Designing a magnet for magnetic refrigeration

Risø-PhD-Report

Rasmus Bjørk
Report nr: Risø-PhD-57(EN)
Publication date: March 2010

Risø DTU
National Laboratory for Sustainable Energy

Author: Rasmus Bjørk
Title: Designing a magnet for magnetic refrigeration
Division: Fuel Cells and Solid State Chemistry Division

This thesis is submitted in partial fulfilment of the requirements for the Ph.D. degree at the Technical University of Denmark.

Abstract:
This thesis investigates the design and optimization of a permanent magnet assembly for use in a magnetic refrigeration device. The heart of magnetic refrigeration is the adiabatic temperature change in the magnetocaloric material which is caused by the magnetic field. In order to design an ideal magnet assembly the magnetocaloric materials and the refrigeration process itself and their properties and performance as a function of magnetic field are investigated. For the magnetocaloric materials it is the magnetization, specific heat capacity and adiabatic temperature that are investigated as functions of the magnetic field. Following this the process utilized by a magnetic refrigerator to provide cooling is investigated using a publicly available one dimensional numerical model. This process is called active magnetic regeneration (AMR). The aim is to determine the performance of the AMR as a function of the magnetic field in order to learn the properties of the optimal magnet assembly. The performance of the AMR as a function of the synchronization and width of the magnetic field with respect to the AMR cycle, the ramp rate and maximum value of the magnetic field are investigated. Other published magnet designs used in magnetic refrigeration devices are also evaluated, using a figure of merit based on the properties of the investigated magnetocaloric materials, to learn the properties of the best magnet designs to date. Following this investigation the Halbach cylinder, which is a hollow permanent magnet cylinder with a rotating remanent flux density, is investigated in detail as it forms the basis of many magnet designs used in magnetic refrigeration. Here the optimal dimensions of a Halbach cylinder, as well as analytical calculations of the magnetic field for a Halbach cylinder of infinite length, are presented.

Once it has been determined which properties are desirable for a magnet used in magnetic refrigeration the design of a new magnet is described. This is a high performance cylindrical magnet for use in a new magnetic refrigeration device being built at Risø DTU. This magnet design must have alternating regions of high and low magnetic field. As a basis for the magnet design the concentric Halbach cylinder design is chosen. This design is then optimized by employing several developed optimization schemes that lower the flux density in a specific region and lower the amount of magnet material used in a given magnet assembly. These schemes are applied to a numerical model of the magnet design. Afterwards the magnet design is dimensioned and segmented to allow construction. This design has been constructed and the flux density measured. Finally, the magnetic forces internally in the magnet design and on the magnetocaloric material inside the magnet assembly have been analyzed.

Risø-PhD-57(EN)
Publication date: March 2010

ISBN 978-87-550-3806-6

Group's own reg. no.:
1960006-00

Pages: 350
Figure: 120
Tables: 8
References: 97

Information Service Department
Risø National Laboratory for Sustainable Energy
Technical University of Denmark
P.O.Box 49
DK-4000 Roskilde

Designing a magnet for magnetic refrigeration

Rasmus Bjørk

Fuel Cells and Solid State Chemistry Division
Risø DTU
Technical University of Denmark

March 2010

Published by:
Risø DTU

Fuel Cells and Solid State Chemistry Division
Risø DTU
Technical University of Denmark - DTU
Building 779, P.O. Box 49
DK-4000 Roskilde
Denmark
Tel +45 4677 5800
Fax +45 4677 5858
web: http://www.risoe.dtu.dk

Publication Reference Data:
Bjørk, R.
Designing a magnet for magnetic refrigeration.
Ph.D. Thesis
Fuel Cells and Solid State Chemistry Division
Risø DTU
Technical University of Denmark - DTU
March 2010
Report number. Risø-PhD-57(EN)
ISBN 978-87-550-3806-6
Keywords: magnetic refrigeration, magnet, magnet design, NdFeB, Active Magnetic Regenerator (AMR), numerical simulation, magnetocaloric materials.

Preface

This thesis was prepared at the Fuel Cells and Solid State Chemistry Division, Risø National Laboratory for Sustainable Energy, Technical University of Denmark - DTU and submitted in partial fulfillment of the requirements for obtaining the PhD degree at the Technical University of Denmark. The work lasted from April 2007 to March 2010 and was financed by Risø National Laboratory for Sustainable Energy through the support of the Programme Commission on Energy and Environment (EnMi) (Contract No. 2104-06-0032) which is part of the Danish Council for Strategic Research.

The PhD project was supervised by Dr. N. Pryds, Dr. C. R. H. Bahl and Dr. A. Smith, all from the Fuel Cells and Solid State Chemistry Division, Risø DTU.

I would like to thank my supervisors Dr. N. Pryds, Dr. C. R. H. Bahl and Dr. A. Smith, who have provided me with constant support, encouragement and many useful discussions throughout my time as a PhD student. I would also like to thank the remainder of the magnetic refrigeration group at Risø DTU and especially K. K. Nielsen for their helpfulness and useful discussions. The technicians, J. Geyti and F. Saxild, who built part of the lab equipment used for the research described in this thesis also have my deepest gratitude. The two companies Sintex A/S, Denmark, and Bakker Magnetics bv, The Netherlands, who built the magnet structures described in this thesis are also thanked for being very cooperative and for allowing me to observe the magnet construction process.

Finally, I would like to thank my wife for being who she is and always supporting me throughout this work.

Risø DTU
National Laboratory for Sustainable Energy

Rasmus Bjørk
March 31, 2010

List of publications

Papers in peer-reviewed journals

Bjørk, R., Bahl, C. R. H., Smith, A. and Pryds, N.: *Optimization and improvement of Halbach cylinder design*, Journal of Applied Physics, **104**, 13910, 2008. Referred to as Paper I.

Nielsen, K. K., Bahl, C. R. H., Smith, A., Bjørk, R., Pryds, N. and Hattel, J.: *Detailed numerical modeling of a linear parallel-plate Active Magnetic Regenerator*, International Journal of Refrigeration, **32**, 1478-1486, 2009. Referred to as Paper IV.

Bjørk, R., Smith, A. and Bahl, C. R. H.: *Analysis of the magnetic field, force, and torque for two-dimensional Halbach cylinders*, Journal of Magnetism and Magnetic Materials, **322**, 133-141, 2010. Referred to as Paper VI.

Bjørk, R., Bahl, C. R. H., Smith A. and Pryds, N.: *Review and comparison of magnet designs for magnetic refrigeration*, International Journal of Refrigeration, **33**, 437-448, 2010. Referred to as Paper VII.

Smith, A., Nielsen, K. K., Christensen, D. V., Bahl, C. R. H., Bjørk, R. and Hattel, J.: *The demagnetizing field of a non-uniform rectangular prism*, Journal of Applied Physics, **107**, 103910, 2010. Referred to as Paper VIII.

Bjørk, R., Bahl, C. R. H., Smith, A., Christensen, D. V. and Pryds, N.: *An optimized magnet for magnetic refrigeration*, Journal of Magnetism and Magnetic Materials, **322**, 3324-3328, 2010. Referred to as Paper XII.

Bjørk, R., Bahl, C. R. H., Smith, A. and Pryds, N.: *Comparison of adjustable permanent magnetic field sources*, Journal of Magnetism and Magnetic Materials, **322**, 3664-3671, 2010. Referred to as Paper IX.

Bjørk, R., Bahl, C. R. H. and Katter, M.: *Magnetocaloric properties of* $LaFe_{13-x-y}Co_xSi_y$ *and commercial grade Gd*, Journal of Magnetism and Magnetic Materials, **322**, 3882-3888, 2010. Referred to as Paper X.

Bjørk, R. and Engelbrecht, K.: *The influence of the magnetic field on the performance of an active magnetic regenerator (AMR)*, International Journal of Refrigeration, doi:10.1016/j.ijrefrig.2010.07.004, 2010. Referred to as Paper XI.

Christensen, D. V., Bjørk. R., Nielsen, K. K., Bahl, C. R. H., Smith. A. and Clausen, S.: *Spatially resolved measurement of the magnetocaloric effect and the local magnetic field using thermography*, Journal of Applied Physics, **108**, 063913, 2010. Referred to as Paper XIV.

Submitted papers

Bjørk, R., Bahl, C. R. H., Smith, A., Pryds, N.: *Improving magnet designs with high and low field regions*, submitted to IEEE Transactions on Magnetics, 2010. Referred to as Paper XV.

Pryds, N., Clemens, F., Menon, M., Nielsen, P. H., Brodersen, K., Bjørk, R., Bahl, C. R. H., Engelbrecht, K., Nielsen, K. K. and Smith, A.: *Monolithic perovskite for magnetic regenerator*, submitted to Journal of the American Ceramic Society, 2010. Referred to as Paper XVI.

Conference proceedings

Nielsen, K. K., Bjørk, R., Jensen, J. B., Bahl, C. R. H., Pryds, N., Smith, A., Nordentoft, A. and Hattel, J.: *Magnetic cooling at Risø DTU*, Proceedings of the 8$^{\text{th}}$ IIF/IIR Gustav Lorentzen Conference on Natural Working Fluids, Copenhagen, Denmark, 2008. Referred to as Paper II.

Bjørk, R., Bahl, C. R. H., Smith, A. and Pryds, N.: *On the optimal magnet design for magnetic refrigeration*, Proceedings of the 3$^{\text{rd}}$ International Conference on Magnetic Refrigeration at Room Temperature, Des Moines, Iowa, USA, 473-480, 2009. Referred to as Paper III.
Note that this paper has also appeared in the Spanish journal Frio-Calor-Aire Acondicionado (2010) under the title *La Refrigeración Magnética: Diseño Óptimo Del Imán*.

Bjørk, R., Bahl, C. R. H., Smith, A., Pryds, N., Nielsen, K. K. and Hattel, J.: *Numerical modeling in magnetic refrigeration*, Proceedings of SIMS 50 - Modelling and Simulation of Energy Technology, Fredericia, Denmark, 323-330, 2010. Referred to as Paper V.

Bahl, C. R. H., Engelbrecht, K., Bjørk, R., Eriksen, D., Smith, A. and Pryds, N.: *Design concepts for a continuously rotating active magnetic regenerator*, Proceedings of the 4$^{\text{rd}}$ International Conference on Magnetic Refrigeration at Room Temperature, Baotou, China, 2010. Referred to as Paper XIII.

Scientific communication

Bjørk, R.: *Magnetic cooling for use in refrigerators*, poster at the yearly meeting of the Danish Physical Society, 2007.

Abstract

This thesis investigates the design and optimization of a permanent magnet assembly for use in a magnetic refrigeration device. The heart of magnetic refrigeration is the adiabatic temperature change in the magnetocaloric material which is caused by the magnetic field. In order to design an ideal magnet assembly the magnetocaloric materials and the refrigeration process itself and their properties and performance as a function of magnetic field are investigated. For the magnetocaloric materials it is the magnetization, specific heat capacity and adiabatic temperature change that are investigated as functions of the magnetic field. Following this the process utilized by a magnetic refrigerator to provide cooling is investigated using a publicly available one dimensional numerical model. This process is called active magnetic regeneration (AMR). The aim is to determine the performance of the AMR as a function of the magnetic field in order to learn the properties of the optimal magnet assembly. The performance of the AMR as a function of the synchronization and width of the magnetic field with respect to the AMR cycle, the ramp rate and maximum value of the magnetic field are investigated. Other published magnet designs used in magnetic refrigeration devices build by different research groups are also evaluated, using a figure of merit based on the properties of the investigated magnetocaloric materials, to learn the properties of the best magnet designs to date. Following this investigation the Halbach cylinder, which is a hollow permanent magnet cylinder with a rotating remanent flux density, is investigated in detail as it forms the basis of many magnet designs used in magnetic refrigeration. Here, the optimal dimensions of a Halbach cylinder, as well as analytical calculations of the magnetic field for a Halbach cylinder of infinite length, are presented.

Once it has been determined which properties are desirable for a magnet used in magnetic refrigeration the design of a new magnet is described. This is a high performance cylindrical magnet for use in a new magnetic refrigeration device being built at Risø DTU. This magnet design must have alternating regions of high and low magnetic field. As a basis for the magnet design the concentric Halbach cylinder design is chosen. This design is then optimized by employing several developed optimization schemes that lower the flux density in a specific region and lower the amount of magnet material used in a given magnet assembly. These schemes are applied to a numerical model of the magnet design. Afterwards the magnet design is dimensioned and segmented to allow construction. This design has been constructed and the flux density measured. Finally, the magnetic forces internally in the magnet design and on the magnetocaloric material inside the magnet assembly have been analyzed.

Resumé (Danish)

I denne afhandling undersøges det, hvordan man designer og optimerer en permanent magnetkonstruktion til brug i en magnetisk kølemaskine. Hjertet i en sådan maskine er den adiabatiske temperaturændring, som skabes af magnetfeltet. For at kunne designe en optimal magnetkonstruktion må egenskaberne af magnetokaloriske materialer undersøges. Disse egenskaber er magnetiseringen, varmekapaciteten og den adiabatiske temperaturændring, der her undersøges som funktion af magnetfelt og temperatur. Efterfølgende undersøges selve den proces, som en magnetisk kølemaskine anvender for at skabe køling. Denne proces eller cykel kaldes aktiv magnetisk regeneration (AMR). Ydelsen af denne proces undersøges som funktion af magnetfeltet ved hjælp af en offentlig tilgængeligt endimensional numerisk model. Målet med denne undersøgelse er at finde de egenskaber, der kendetegner den optimale magnetkonstruktion. Konkret undersøges ydelsen af AMR-cyklen som funktion af synkroniseringen og vidden af magnetfeltet med hensyn til AMR-cyklen, samt ydelsen som funktion af ramperaten og den maksimale værdi af magnetfeltet. Dernæst undersøges publicerede magnetdesigns, der anvendes i magnetisk køling, ved hjælp af en "figure of merit", som er baseret på de undersøgte egenskaber af de magnetokaloriske materialer. Dette gøres for at undersøge hvilke magnetdesigns, der er de bedste, og hvorfor de er det. Efterfølgende undersøges magnetdesignet kaldet en Halbach cylinder. Dette er en magnetkonstruktion formet som en hul cylinder, hvor retningen af den remanente magnetisering roterer. Dette design undersøges, fordi det indgår i mange magnetdesigns til brug i magnetisk køling. De optimale dimensioner samt en analytisk udregning af magnetfeltet fra Halbach cylinderen præsenteres her.

De fundne optimale egenskaber for et magnetdesign til brug i magnetisk køling anvendes til at designe en cylindrisk magnet med høj ydelse til et nyt magnetisk kølesystem, som konstrueres på Risø DTU. Dette magnetdesign skal have alternerende regioner af højt og lavt magnetfelt. Som basis for magnetdesignet anvendes den koncentriske Halbach cylinder. Dette design optimeres efterfølgende ved hjælp af to udviklede optimeringsrutiner, som henholdsvis sænker den magnetiske fluxtæthed i et specifikt område og sænker mængden af magnetisk materiale i et givent magnetdesign. Disse optimeringsrutiner anvendes på en numerisk model af magnetdesignet. Efterfølgende dimensioneres og segmenteres designet, således at det kan konstrueres. Dette design er efterfølgende konstrueret, og fluxtætheden målt. Endelig undersøges magnetkræfterne i magnetdesignet og på det magnetokaloriske materiale, som anvendes i maskinen.

Contents

Chapter 1

Introduction

Refrigeration, both common household and industry sized applications, is today based on a vapor compression cycle. This technology was introduced more than 120 years ago and has been vastly improved since then so that the technology today is cheap and reliable. However, vapor compression refrigeration has also reached a technological level where further improvements to the technology are unlikely. Since it was first introduced refrigeration has become such a widespread technology that in 2002 it accounted for 25% of the residential electricity consumption and 15% of the commercial electricity consumption in the USA (Russek and Zimm, 2006). A serious problem with the vapor compression refrigeration technology is that the refrigerant, typically a hydrofluorocarbon (HFC) gas, is a very potent greenhouse gas and its use is being regulated by the Kyoto Protocol. However, there is ongoing research to use gasses with a lower global warming potential. Previously used refrigerants, such as chlorofluorocarbons (CFC) and hydrochlorofluorocarbons (HCFC), had a damaging effect on the ozone layer. In this century where concern for global warming and rising energy consumption are problems that worry society a great deal, a refrigeration technology that is more energy efficient than vapor based compression and also contains no greenhouse gasses of any kind is in high order.

Magnetic refrigeration is an emerging technology that aims to meet exactly these two criteria. Magnetic refrigeration is based on the magnetocaloric effect (MCE), which has been known since 1881 (Warburg, 1881). The MCE is observed as a temperature change of a magnetic material when this is subjected to a changing magnetic field. A material displaying this effect is called a magnetocaloric material (MCM). This temperature change of the material can be used in a refrigeration device, which is then known as a magnetic refrigeration device. Such a device consists of a number of subsystems that each are necessary to produce cooling. Beside the magnetocaloric material a heat transfer fluid, heat exchangers and a magnet is needed. The purpose of this thesis is to scientifically investigate the design and optimization of a magnet for use in a magnetic refrigeration device. As part of this process the design of a magnet for a magnetic refrigeration device being built at Risø DTU is described.

1.1 Outline of the thesis

This thesis is outlined as follows: In Chapter 2 a general introduction to magnetic refrigeration is presented. The properties of magnetocaloric materials are described and modeled using the Weiss mean field model and measurements of the magnetization, specific heat capacity and adiabatic temperature of the benchmark magnetocaloric material, Gd, are presented. The process utilized by a magnetic refrigerator to provide cooling, the so called active magnetic regeneration (AMR) process, is also presented in this chapter. In Chapter 3 the performance of the AMR as a function of magnetic field is investigated using a publicly available one dimensional numerical model. The performance of the AMR as a function of the synchronization and width

of the magnetic field with respect to the AMR cycle, the ramp rate of the magnetic field, and the maximum value of the magnetic field are determined using a generic magnetic field profile. In Chapter 4 the requirements for a magnet used in magnetic refrigeration are presented along with other published magnet designs used in magnetic refrigeration. These designs are investigated and evaluated using a figure of merit defined in this chapter. In Chapter 5 a description on how to numerically model magnet assemblies as well as a detailed investigation of the Halbach cylinder, which is a hollow permanent magnet cylinder with a rotating remanent flux density, is presented. This magnet design is interesting because it forms the basis of many magnet designs used in magnetic refrigeration. In Chapter 6 the design of a high performance cylindrical magnet for use in a new magnetic refrigeration device being built at Risø DTU is presented. The design is optimized by employing several developed optimization schemes and is subsequently dimensioned and segmented. In Chapter 7 a constructed version of the designed magnet is investigated and measurements of the flux density is reported and compared with a numerical model. The magnetic forces internally in the magnet design and on the magnetocaloric material to be used in conjunction with the magnet design are also analyzed. Finally, in Chapter 8 the work described in this thesis is summarized and concluded.

In Appendix A additional analytical calculations of the magnetic field from a Halbach cylinder of infinite length are presented. In Appendix B photographs of the assembly of the magnet for the new magnetic refrigeration device built at Risø DTU are shown together with photos of a plate of magnetocaloric material. Papers I, II, III, IV, V, VI, VII, VIII, IX, X, XI, XII, XIII, XIV, XV and XVI contains research papers submitted or published during the work on this thesis. The papers are listed in chronological order.

Parts of the results described in Paper X appear in Chapter 2. The research described in Paper XI appear in Chapter 3. Papers III and VII make up parts of Chapter 4. Likewise Papers I and VI form most of Chapter 5. The research from Papers XII and XV are at the core of Chapter 6 while the latter also forms parts of Chapter 7. The remaining papers describe research that have been performed partially by the author of this thesis and are related to magnetic refrigeration but are not directly referred in this thesis. These have been included for completeness.

Chapter 2

The physics of magnetic refrigeration

This chapter provides a general introduction to magnetocaloric materials and magnetic refrigeration. A sufficient knowledge of these subjects are necessary to understand how to design a high performing magnet for a magnetic refrigeration device. The principles of the magnetocaloric effect and magnetic refrigeration are explained and the properties of a magnetocaloric material are investigated as a function of magnetic field in order to learn how to design an ideal magnet for use in magnetic refrigeration.

This chapter is partially based on the results described in Paper X.

2.1 Thermodynamics of magnetocaloric materials

The magnetocaloric effect (MCE) is expressed as a temperature change of a magnetocaloric material (MCM) if the MCM is subjected to an external magnetic field. The physics behind this phenomenon can be understood by considering the entropy for the material. The total specific entropy, s, of a magnetocaloric material can be divided into three sources (Tishin and Spichkin, 2003)

- The magnetic specific entropy, s_{mag}.
- The lattice specific entropy, s_{lat}.
- The electronic specific entropy, s_{ele}.

The magnetic specific entropy results from the magnetic spins in the material, the lattice specific entropy results from vibrations in the lattice, while the electronic specific entropy results from free electrons in the material. The total entropy is given as the sum of these sources; $s = s_{\mathrm{mag}} + s_{\mathrm{lat}} + s_{\mathrm{ele}}$. The two latter parts of the entropy do not depend on the magnetic field while s_{mag} does[1]. During an adiabatic process in which the material is subjected to a positive change in magnetic field, s_{mag} decreases because the magnetic field will align the spins. The remaining two terms, s_{lat} and s_{ele}, must increase correspondingly, which increases the temperature by what is termed the adiabatic temperature change, ΔT_{ad}. Had the temperature been kept constant the specific entropy would instead have been reduced by an amount, Δs_{M}, called the isothermal entropy change. The MCE is illustrated in Fig. 2.1.

The MCE is generally largest near the phase transition of the MCM. It is important to consider the order of the phase transition, i.e. the order of the lowest differential of the free

[1] In at least one case the electronic component do depend on the magnetic field (Burriel et al., 2005), but this is generally not the case.

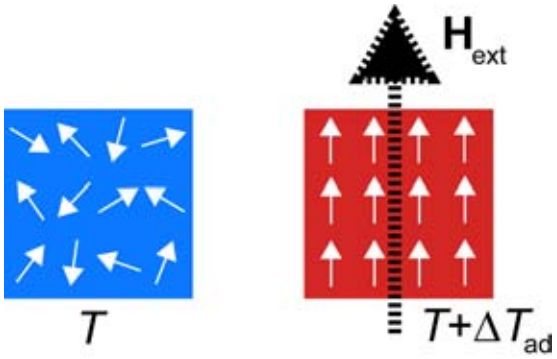

Fig. 2.1: An illustration of the magnetocaloric effect. The left figure shows a magnetic sample at temperature T which is not magnetized and thus the spins are randomly oriented. The right figure shows a sample placed in an external magnetic field, $\mathbf{H}_{\rm ext}$, that has aligned the spins. This has raised the temperature of the sample by $\Delta T_{\rm ad}$.

energy which shows a discontinuity at the transition. A first order material will have a discontinuity in quantities like the magnetization, entropy and volume. These changes give rise to a latent heat in the material. A second order material has a discontinuity in quantities like the heat capacity, compressibility or the gradient of the magnetization. In this thesis only second order materials are considered. The MCE in second order materials are reversible, i.e. the opposite effect of the MCE described above will take place when the external magnetic field is removed, and the material will return to its original temperature. All materials considered in this thesis are assumed to be reversible. The adiabatic temperature change, $\Delta T_{\rm ad}$, is a function of temperature and magnetic field. A substantial number of magnetocaloric material are known (see e.g. Gschneidner Jr et al. (2005)). These can have a different dependence on temperature and magnetic field. The adiabatic temperature change can be used to generate a temperature span and a refrigeration capacity either directly or, as is almost always the case, by using a regenerative process.

To understand the basic properties of magnetocaloric materials a closer look at the thermodynamics behind the MCE is necessary.

The change in specific entropy of a magnetic material can be written as

$$ds(H,P,T) = \left(\frac{\partial s}{\partial H}\right)_{P,T} dH + \left(\frac{\partial s}{\partial P}\right)_{T,H} dP + \left(\frac{\partial s}{\partial T}\right)_{P,H} dT \ , \tag{2.1}$$

where the differentiation is with respect to the three thermodynamic variables, temperature, T, pressure, P, and magnetic field, H. For the materials considered in this thesis the variations in pressure are negligible and thus the term $\left(\frac{\partial s}{\partial P}\right)_{T,H} dP$ is disregarded[2].

[2]Some magnetocaloric material do show a significant variation of the magnetocaloric effect with pressure, but these are not considered here as the pressure change typically must be of the order of gigapascal (de Oliveira, 2008).

The remaining two terms in Eq. (2.1) can both be expressed using the laws of thermodynamics. The first term can be expressed as a Maxwell relation

$$\left(\frac{\partial s}{\partial H}\right)_T = \mu_0 \left(\frac{\partial m}{\partial T}\right)_H \ , \tag{2.2}$$

where μ_0 is the permeability of free space and m is the specific magnetization.

The second term can be replaced by the definition of heat capacity,

$$c_\mathrm{p} = \left(\frac{\partial q}{\partial T}\right)_{P,H} \ , \tag{2.3}$$

where ∂q is the specific dissipated heat during a temperature change of ∂T at constant pressure and magnetic field, combined with the second law of thermodynamics,

$$Tds = dq \ , \tag{2.4}$$

so that we have

$$\left(\frac{\partial s}{\partial T}\right)_H = \frac{c_\mathrm{p}}{T} \ . \tag{2.5}$$

Substituting Eq. (2.2) and (2.5) into Eq. (2.1) yields

$$ds(H,T) = \mu_0 \left(\frac{\partial m}{\partial T}\right)_H dH + \frac{c_\mathrm{p}}{T} dT \ . \tag{2.6}$$

The change in specific entropy due to the magnetocaloric effect can now be determined by integrating Eq. (2.6) at changing magnetic field at isothermal conditions ($dT = 0$).

Integrating for this isothermal process we get

$$\Delta s_\mathrm{M} = \mu_0 \int_{H_\mathrm{i}}^{H_\mathrm{f}} \left(\frac{\partial m}{\partial T}\right)_H dH \ , \tag{2.7}$$

where H_i is the initial magnetic field and H_f is the final magnetic field. Thus if the magnetization is known and the material is second order the change in entropy can be found. For first order materials a latent heat will be present and great care must be taken when integrating Δs_M.

An expression for the adiabatic temperature change can be found by considering an adiabatic process ($ds = 0$). By integrating Eq. (2.6) we get

$$\Delta T_\mathrm{ad} = -\mu_0 \int_{H_\mathrm{i}}^{H_\mathrm{f}} \frac{T}{c_\mathrm{p}} \left(\frac{\partial m}{\partial T}\right)_H dH \ . \tag{2.8}$$

Note that this equation is not as trivial as it seems as the temperature itself is an implicit function of H as the temperature will change due to the adiabatic temperature change as the magnetic field is altered. This must be included when performing the integration. The adiabatic temperature change can of course also be determined directly from observation. For most magnetic materials the magnetization decrease with temperature and thus $(\partial m/\partial T)_H$ will be negative. Thus it is seen that $\Delta s_\mathrm{M} < 0$ and $\Delta T_\mathrm{ad} > 0$ for positive field changes.

As the specific heat capacity is usually a weak function of magnetic field there are two ways to obtain a large Δs_M and ΔT_ad:

- A large magnetic field change.
- A large change in magnetization with respect to temperature.

A small heat capacity will also increase ΔT_{ad}. The change in magnetization and the heat capacity are intrinsic to the material while the change in magnetic field can be externally controlled.

2.1.1 The Curie temperature

The Curie temperature, T_{C}, is defined as the lowest temperature at which the magnetization of a material in the absence of an external field is zero. Above the Curie temperature the thermal vibrations, i.e. the temperature, is powerful enough to randomize the spins, while below the Curie temperature a spontaneous magnetization appears. This magnetization increases with decreasing temperature, due to smaller thermal fluctuations. Experimentally the Curie temperature can be approximated by the temperature at which the change in magnetization, $(\partial m/\partial T)_H$, is maximum, which is also where Δs_{M} will be maximized. However, it is seen from Eq. (2.8) that, as c_{p} is a function of temperature and magnetic field, that ΔT_{ad} might have a maximum at a different temperature than Δs_{M}. However, for most materials the peak value of the heat capacity changes at most by a few degrees, so the peak in ΔT_{ad} will be close to the peak in Δs_{M}.

2.2 Properties of magnetocaloric materials

It is important to consider the properties of actual magnetocaloric materials as it is necessary to optimize the magnet and adapt the refrigeration device to the properties of the magnetocaloric material being used.

For a household magnetic refrigerator, which is the focus of this thesis, the Curie temperature should at least be between 278 K and room temperature, as these constitute the operating range of the refrigerator. Also the change in magnetization of the material must be substantial to provide a large ΔT_{ad}. The benchmark magnetocaloric material used in magnetic refrigeration today is gadolinium (Gd), which has a T_{C} around room temperature and a ΔT_{ad} of ~ 4 K at T_{C} in a field of 1 T (Dan'kov et al., 1998). It is necessary to examine the properties of this benchmark material in greater detail in order to determine how to design an optimal magnet for magnetic refrigeration.

2.2.1 The Weiss mean field theory

It is possible to model the properties of a magnetocaloric material using the Weiss mean field theory (MFT). It is interesting to examine this theory as it can be used to model the properties of Gd. The model is applicable to second order magnetic materials and assumes that the interactions between the individual spins can be described by the interaction of a spin with an effective molecular field. Using this model the specific magnetization can be obtained as described in e.g. Morrish (1965) by

$$m = N_{\mathrm{s}} g J \mu_{\mathrm{B}} B_J(\chi) \ , \tag{2.9}$$

where N_s is the number of magnetic spins per unit mass, g is the Landé factor, J is the total angular momentum in units of $\hbar$ and μ_B is the Bohr magneton. The last factor is the Brillouin function, $B_J(\chi)$, which is defined as

$$\begin{aligned} B_J(\chi) &= \frac{2J+1}{2J}\coth\left(\frac{2J+1}{2J}\chi\right) - \frac{1}{2J}\coth\left(\frac{1}{2J}\chi\right) \\ \chi &= \frac{gJ\mu_B\mu_0 H}{k_B T} + \frac{3T_C J}{T(J+1)}B_J(\chi)\ , \end{aligned} \tag{2.10}$$

where k_B is the Boltzmann constant. As the Brillouin function is a function of itself it must be solved through iteration.

The magnetic part of the total specific entropy can be calculated as

$$s_{mag} = N \ln \frac{\sinh\left(\frac{2J+1}{2J}\chi\right)}{\sinh\left(\frac{1}{2J}\chi\right)} - \chi B_J(\chi) \quad , \tag{2.11}$$

where N is the number of atoms per unit mass of the material.

The Weiss mean field model also estimates the magnetic contribution to the specific heat capacity as

$$c_{mag} = -\mu_0 H\frac{\partial m}{\partial T} - \frac{1}{2}N_{int}\frac{\partial m^2}{\partial T}\ , \tag{2.12}$$

where N_{int} is the mean field constant which is defined as

$$N_{int} = \frac{3k_B T_C}{N_s g^2 \mu_B^2 J(J+1)}. \tag{2.13}$$

The remaining two terms of the specific entropy and the specific heat capacity, i.e. the lattice and electron parts, can be obtained from other models.

The lattice contribution to the specific heat can be obtained from the Debye model as (Ashcroft and Mermin, 1976)

$$c_{lat} = 9Nk_B\left(\frac{T}{\theta_D}\right)^3 \int_0^{\theta_D/T} \frac{x^4 e^x}{(e^x-1)^2}\,\mathrm{d}x\ , \tag{2.14}$$

where N is the number of atoms per unit mass and θ_D is the Debye temperature. The lattice contribution to the specific entropy is estimated from the Debye model as

$$s_{lat} = k_B N \left[-3\ln\left(1-e^{\frac{\theta_D}{T}}\right) + 12\left(\frac{T}{\theta_D}\right)^3 \int_0^{\theta_D/T} \frac{x^3}{e^x-1}\,\mathrm{d}x\right] . \tag{2.15}$$

The free electron contribution to the specific heat capacity can be estimated using the Sommerfeld model (Ashcroft and Mermin, 1976)

$$c_{ele} = \gamma_e T, \tag{2.16}$$

where γ_e is the Sommerfeld constant which is material dependent. The specific entropy in the Sommerfeld model is given by the same expression, $s = \gamma_e T$.

The total specific heat capacity is the sum of the three contributions; $c_{\rm p} = c_{\rm mag} + c_{\rm lat} + c_{\rm ele}$. Likewise, the total entropy is $s = s_{\rm mag} + s_{\rm lat} + s_{\rm ele}$. With the specific magnetization known from Eq. (2.9) the adiabatic temperature change can be calculated using Eq. (2.8). However, when the total entropy is known the adiabatic temperature change can also be determined as

$$s(T, H_{\rm i}) \quad = \quad s(T + \Delta T_{\rm ad}, H_{\rm f}) \ , \tag{2.17}$$

since the temperature change is an adiabatic process.

Before applying this model to obtain the properties of an MCM it is important to consider what magnetic field an MCM actually experiences when it is subjected to an external magnetic field, because the magnetic field used in the model and that experienced by an actual sample must of course be identical.

2.2.2 Demagnetization

When subjecting a magnetic sample to an external magnetic field the internal field of the sample will depend on the geometry of the sample. This is because the magnetization of the sample creates a magnetic field, which is known as the demagnetization field. If the sample has an ellipsoidal shape the internal field will be homogeneous and can be calculated if the magnetization of the sample is known (Osborn, 1945). If the sample has a non-ellipsoidal shape the internal field will not be homogeneous across the sample except in a few limiting cases such as the infinite cylinder or sheet. However, an average internal magnetic field can be found in this case. Assuming that the magnetic anisotropy is negligible the internal field, applied field and the magnetization are all parallel, so only the magnitudes need be considered. This average internal magnetic field, $H_{\rm int}$, can be found by subtracting the demagnetization field $H_{\rm d} = N_{\rm d} M$, where $N_{\rm d}$ is the average demagnetization factor and M is the magnetization, from the applied or external field, $H_{\rm ext}$,

$$H_{\rm int} = H_{\rm ext} - N_{\rm d} M \ . \tag{2.18}$$

If the sample has a rectangular (orthorhombic) shape with dimensions a, b and c, with the external field directed along the c-direction, the average demagnetization factor is given as (Aharoni, 1998)

$$\begin{aligned}
\pi N_{\rm d} \quad = \quad & \frac{b^2 - c^2}{2bc} \ln \quad \frac{\sqrt{a^2 + b^2 + c^2} - a}{\sqrt{a^2 + b^2 + c^2} + a} \quad + \frac{a^2 - c^2}{2ac} \ln \quad \frac{\sqrt{a^2 + b^2 + c^2} - b}{\sqrt{a^2 + b^2 + c^2} + b} \\
& + \frac{b}{2c} \ln \quad \frac{\sqrt{a^2 + b^2} + a}{\sqrt{a^2 + b^2} - a} \quad + \frac{a}{2c} \ln \quad \frac{\sqrt{a^2 + b^2} + b}{\sqrt{a^2 + b^2} - b} \quad + \frac{c}{2a} \ln \quad \frac{\sqrt{b^2 + c^2} - b}{\sqrt{b^2 + c^2} + b} \\
& + \frac{c}{2b} \ln \quad \frac{\sqrt{a^2 + c^2} - a}{\sqrt{a^2 + c^2} + a} \quad + 2 \arctan \left(\frac{ab}{c \sqrt{a^2 + b^2 + c^2}} \right) + \frac{a^3 + b^3 - 2c^3}{3abc} \\
& + \frac{a^2 + b^2 - 2c^2}{3abc} \quad \sqrt{a^2 + b^2 + c^2} + \frac{c}{ab} \left(\quad \sqrt{a^2 + c^2} + \quad \sqrt{b^2 + c^2} \right) \\
& - \frac{(a^2 + b^2)^{3/2} + (b^2 + c^2)^{3/2} + (c^2 + a^2)^{3/2}}{3abc} \ .
\end{aligned} \tag{2.19}$$

Using this equation the average internal field of a rectangular sample can be found.

T_C	N_s	g	J	N	θ_D	γ_e
293.6 K	$3.83 * 10^{24}$ kg^{-1}	2	3.5	$3.83 * 10^{24}$ kg^{-1}	169 K	$6.93 * 10^{-2}$ J kg^{-1} K^{-2}

Table 2.1: The material constants for Gd. All the values are from Lide (2004); Tishin and Spichkin (2003), except the Curie temperature. This has been chosen to be the identical to experimentally observed values (Dan'kov et al., 1998).

It is extremely important to always report magnetocaloric properties as a function of internal field, as comparison with both identical and other materials is otherwise not meaningful[3].

2.2.3 Gadolinium

The properties of an MCM can best be understood by examining the properties of a typical MCM. Here we will consider the benchmark magnetocaloric material for magnetic refrigeration, gadolinium (Gd), as this material is used in almost all magnetic refrigeration devices. It thus makes sense to design the magnet for this magnetocaloric material. Gd is a ferromagnetic material and can thus be modeled by the MFT model. The material dependent constants used for the MFT model of Gd are given in Table 2.1.

The four parameters m, ΔT_{ad}, c_p, and Δs_M have been calculated using MFT for Gd and the results are shown in Fig. 2.2. The magnetic field was varied from 0 to 2 T in steps of 4 mT and the temperature was varied from 200 K to 350 K in steps of 0.3 K. The values for Δs_M has been constructed based on Eq. (2.7) and ΔT_{ad} has been calculated from Eq. (2.17).

The figures show that the magnetization increases with decreasing temperature. Both Δs_M and ΔT_{ad} are seen to have a characteristic shape as a function of temperature and magnetic field. Also, the adiabatic temperature change is seen to be no more than ~ 6 K in a field of 2 T and it is seen to decline rapidly away from the Curie temperature. Finally, the specific heat capacity is seen not to be a strong function of field. At the Curie temperature a discontinuity in the specific heat capacity at zero field is seen, as is expected for a second order material.

These data sets are often used as inputs in models of magnetic refrigeration processes because a direct comparison between different models is possible, if the same data sets are used as input for the models (Zheng et al., 2007; Petersen et al., 2008b; Nielsen et al., 2009).

2.2.3.1 Commercial grade gadolinium

It is also important to establish the properties of actual magnetocaloric materials that are used in magnetic refrigerators. As mentioned previously the benchmark magnetocaloric material is Gd, and therefore it is the properties of this material that are of the most interest. Comparing the measured properties of Gd with the MFT model is of course also of interest. In this subsection the measured properties of Gd are described. The properties of two other magnetocaloric materials, $LaFe_{13-x-y}Co_xSi_y$ and $(La_{0.67}Ca_{0.26}Sr_{0.07})Mn_{1.05}O_3$, have also been measured. Both materials have a lower adiabatic temperature change than Gd. The magnetocaloric properties of these materials are described in Paper X and XVI respectively. These materials are not described in this thesis because they have a lower ΔT_{ad} than Gd.

[3]This can be a problem for first order MCMs because of hysteresis behavior.

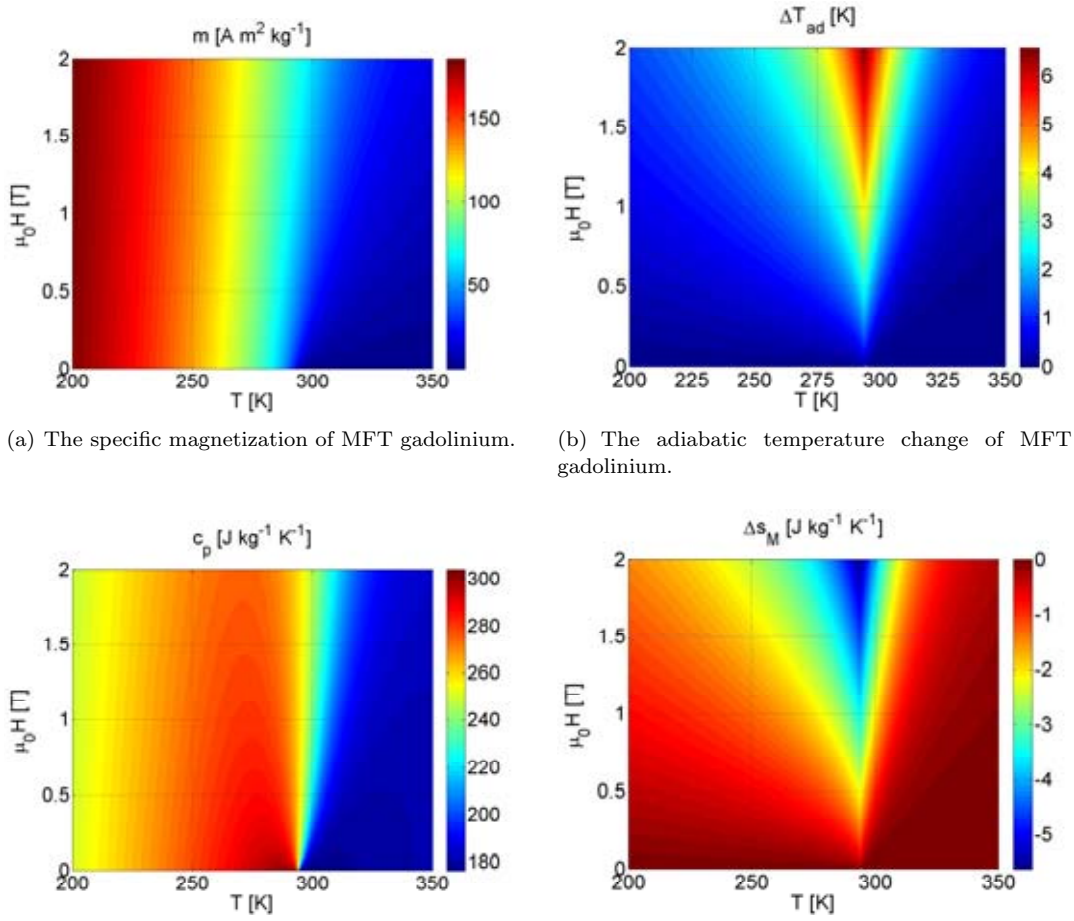

(a) The specific magnetization of MFT gadolinium.

(b) The adiabatic temperature change of MFT gadolinium.

(c) The specific heat capacity of MFT gadolinium.

(d) The change in specific entropy of MFT gadolinium.

Fig. 2.2: The calculated properties of MFT gadolinium.

The gadolinium that has been measured are what will be referred to as "Commercial grade gadolinium". This gadolinium is much cheaper than pure gadolinium, but the purity is also lower. The commercial grade gadolinium contains 99.5% rare earth metal, of which 99.94% is gadolinium. This type of Gd has been used in actual magnetic refrigeration devices (Bahl et al., 2008; Engelbrecht et al., 2009).

The properties of both pure and impure gadolinium have previously been reported (Dan'kov et al., 1998), and the main conclusion of this analysis is that the impure gadolinium have a lower adiabatic temperature change. Also, depending on the impurities of the sample, a small shift of a couple of degrees of the Curie temperature is also seen.

The properties of commercial grade Gd have been measured using different lab equipment at Risø DTU. The magnetization was measured using a LakeShore 7407 Vibrating Sample Magnetometer (VSM). Isothermal magnetization measurements as a function of applied field

were made at a ramp rate of 2.5 mT/s up to a maximum field of $\mu_0 H_{\rm ext} = 1.6$ T and data was measured for every 5 mT. In a sample interval of ± 10 K around the Curie temperature the measurements were taken at 1 K separation, while further from $T_{\rm C}$ the temperature sample rate was smaller. Data was measured from 100 K to 320 K. A surface plot of the measured values of the magnetization, corrected for demagnetization using Eq. (2.19), is shown in Fig. 2.3. The individual measured values of the magnetization are too densely spaced to be shown on the figure.

The change in specific entropy was calculated by using the measured magnetization data in Eq. (2.7) and employing a numerical integration scheme. This is also shown in Fig. 2.3.

Calorimetric data in applied fields up to 1.4 T were obtained using a Differential Scanning Calorimeter (DSC) (Jeppesen et al., 2008) with the magnetic field provided by an adjustable permanent magnet assembly designed by the author of this thesis[4]. The specific heat capacity was measured at external field values of $\mu_0 H_{\rm ext} = 0,\ 0.25,\ 0.50,\ 0.75,\ 1.00$ and 1.40 T in a temperature interval from 223 to 323 K with a ramp of 1 K/min and from 323 to 223 K with a ramp of -1 K/min. As no hysteresis was observed the calculated values of $c_{\rm p}$ from the two data sets were averaged. Data was taken every 12.5 ms. The DSC was calibrated using both copper and titanium reference samples. The measured values of $c_{\rm p}$, corrected for demagnetization using Eq. (2.19) and binned in 0.25 K intervals, are shown as circles in Fig. 2.3, along with a data set constructed from linear interpolation between these values.

Finally, the adiabatic temperature change was measured using an instrument designed at Risø DTU as part of this thesis. A pneumatic piston moves a sample holder in and out of a magnetic field generated by the same adjustable permanent magnet assembly as used for the DSC. A sliding track ensures that the direction of the sample holder with respect to the magnetic field is fixed. The entire setup is placed in a freezer, which is used to control the temperature. The magnet is also cooled in the setup. This changes the magnetic field produced by the magnet slightly, but at 1 T the change is less than 3%. The ramp rate of the temperature was controlled by a 75 W light bulb and heat leakage to the surroundings. In general a complete sweep in temperature took around 9 hours, during which time data was recorded. Due to this substantial time span, parasitic temperature gradients were kept as small as possible. The pneumatic piston was moved in and out of field every 5 seconds, with an actual movement time of no more than 100 ms. Because of the high sweep rate and the thermal isolation conditions can be assumed to be close to adiabatic. The temperature of the sample was recorded every 100 ms.

The sample is prepared by placing a type E thermocouple between two equally sized plates of the given sample which are then glued together. This is done to ensure good thermal contact between the thermocouple and the sample. The sample is packed in isolating foam and placed in a sample holder together with a Hall probe. Data was measured at external field values of $\mu_0 H_{\rm ext} = 0.25,\ 0.50,\ 0.75,\ 1.00$ and 1.40 T in a temperature interval from 253 to 313 K. The measured values of $\Delta T_{\rm ad}$, corrected for demagnetization and binned in 0.25 K intervals, are shown as circles in Fig. 2.3, along with a data set constructed from linear interpolation between these values.

For the measured values of both $c_{\rm p}$ and $\Delta T_{\rm ad}$ the "bending" of the curves with temperature that can be seen in Fig. 2.3 is a direct consequence of correcting for the demagnetization effect. Thus here one can directly see how important it is to correct for demagnetization.

[4]The details of the design of this magnet are described in Paper IX, but as the magnet is not used directly in magnetic refrigeration it is not described in this thesis.

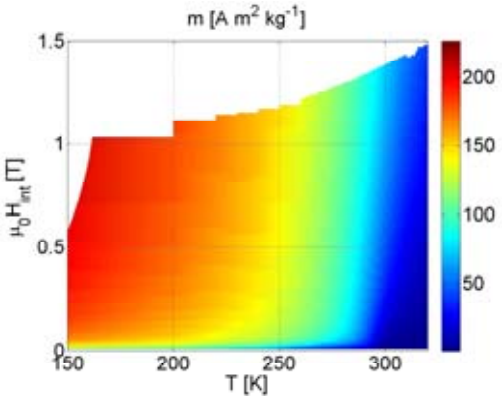

(a) The measured specific magnetization of commercial grade gadolinium, corrected for demagnetization.

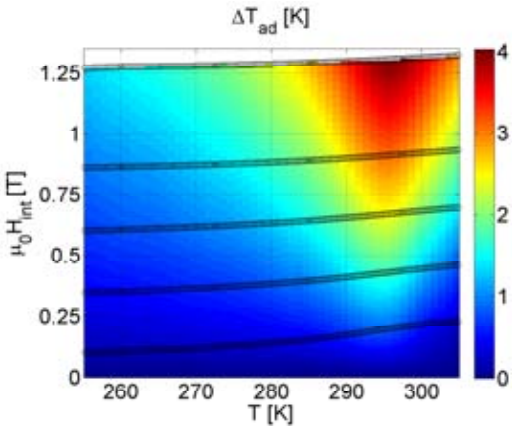

(b) The measured adiabatic temperature change of commercial grade gadolinium, corrected for demagnetization, is shown as circles. The remaining data is constructed from linear interpolation.

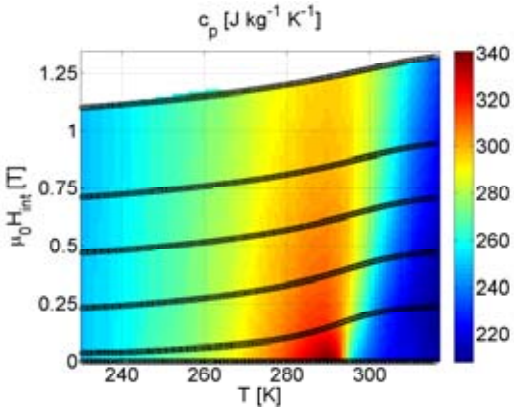

(c) The measured specific heat capacity of commercial grade gadolinium, corrected for demagnetization, is shown as circles. The remaining data is constructed from linear interpolation.

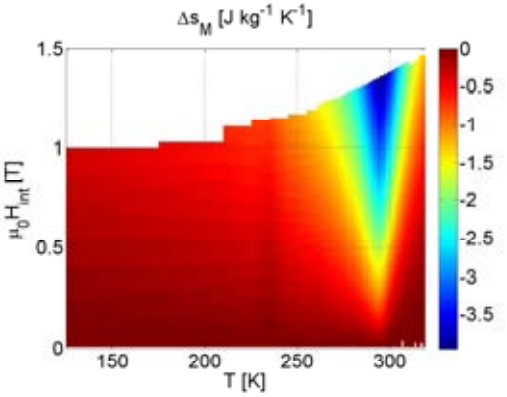

(d) The change in specific entropy of commercial grade gadolinium constructed using the measured magnetization data and Eq. (2.7).

Fig. 2.3: The measured properties of commercial grade gadolinium.

It is seen from Fig. 2.3 that as for the MFT model the magnetization increases with decreasing temperature. The characteristic shape of Δs_{M} and ΔT_{ad} are also seen. The adiabatic temperature change is 3.3 K at the peak temperature in an internal field of 1 T. The specific heat capacity is seen to be fairly constant as a function of magnetic field, and the sharp discontinuity seen in the MFT model at the Curie temperature at zero field has been broadened. This may be caused by impurities in the Gd.

The peak temperature for Δs_{M}, ΔT_{ad} and c_{p} differs. In a field change of 1 T the peak temperatures are 294.8 K, 295.1 K and 289.2 K for the three properties respectively. In zero field the peak temperature of c_{p} does not change.

2.2.4 MFT and commercial grade gadolinium

As previously mentioned it is of interest to compare the MFT and commercial grade gadolinium data to establish how well the model reproduces actual measured material data. A comparison between the measured values and the MFT values are shown in Fig. 2.4. The MFT model has a value of $T_{\mathrm{C}} = 293.6$ K, as this corresponds fairly well with the observed peak temperatures of the measured gadolinium.

The magnetization of the measured Gd is seen to be similar to the MFT model, except at very low fields. Here the discrepancy is an effect of the ordering of the magnetization into domains. The measured sample has a domain structure in which magnetic domains cancel each other at zero field so that the sample appears nonmagnetic. It takes a small field to shift the borders between the domains and thus the sample responds slower to a small magnetic field than the MFT model does since it does not include domains. It is also seen from the figure that the measured values of the specific heat capacity are higher at high temperatures than the MFT values. At temperatures below T_{C} the change in specific entropy is larger for the commercial grade gadolinium than for the MFT gadolinium. Finally, the adiabatic temperature change is seen to be smaller at and below T_{C} and higher above T_{C} than what is expected from MFT. Some of these effects can be caused by the fact that the measured sample of Gd contains impurities.

Even though the MFT does not exactly reproduce the observed material data the model can still be useful as input in a magnetic refrigeration model. If the results produced by a magnetic refrigeration model are of general interest to the scientific community the MFT model can be used, since it is a reproducible model that allows for other researchers to more clearly interpret and reproduce the results of the refrigeration model. In this thesis both the measured Gd data as well as the MFT model will be used to model magnetic refrigeration processes.

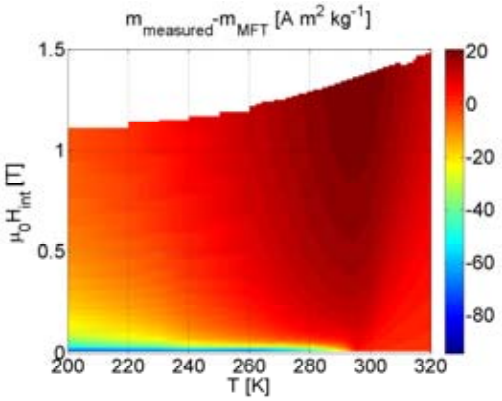

(a) The difference between the measured magnetization and the MFT magnetization.

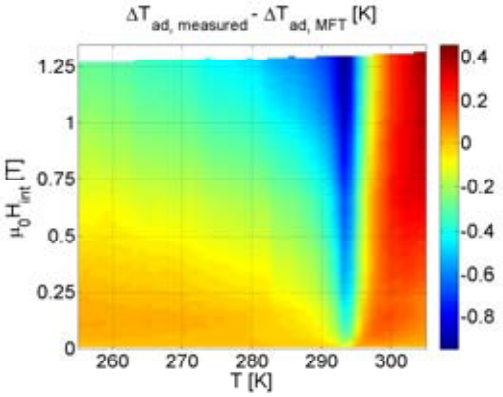

(b) The difference between the measured ΔT_{ad} and the MFT ΔT_{ad}.

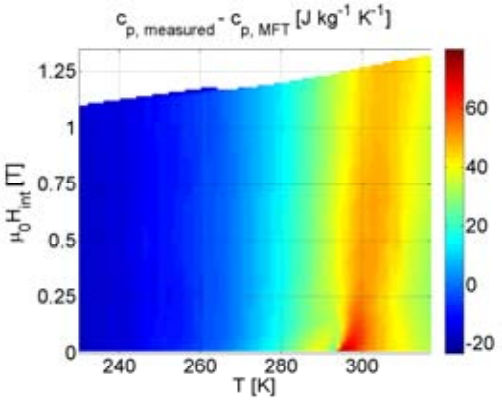

(c) The difference between the measured specific heat capacity and the MFT specific heat capacity.

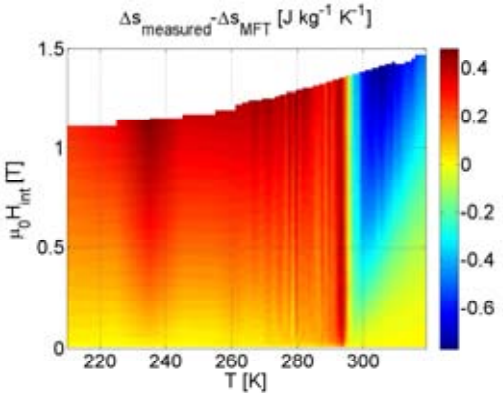

(d) The difference in the change in specific entropy between the measured and MFT gadolinium.

Fig. 2.4: A difference between the properties of MFT and the measured properties of commercial grade gadolinium.

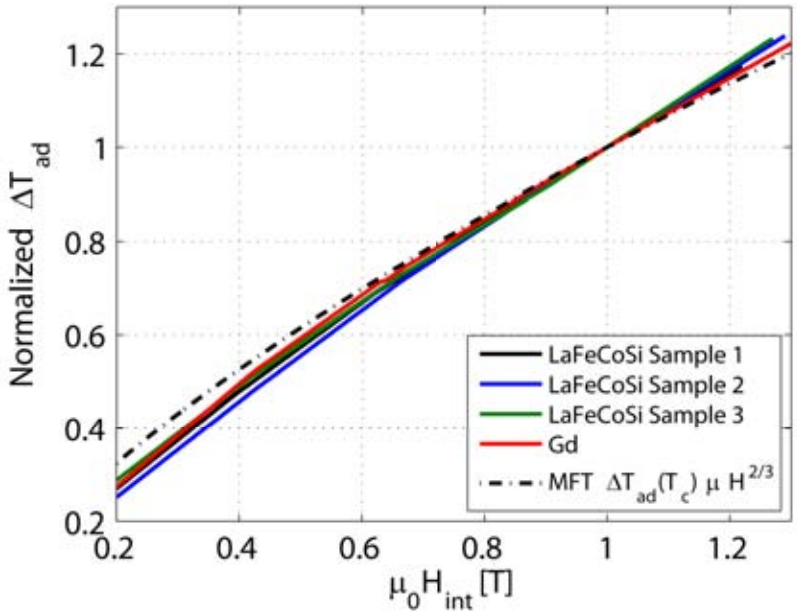

Fig. 2.5: The scaling of the adiabatic temperature change of Gd and three different LaFeCoSi samples as a function of magnetic field at the peak temperature.

2.2.5 Scaling of ΔT_{ad}

An interesting observation concerning the properties of an MCM is that at the Curie temperature ΔT_{ad} does not scale linearly with the magnetic field. In MFT ΔT_{ad} at T_{C} scales with the power of 2/3 of the magnetic field (Oesterreicher and Parker, 1984). Here, we have compared this scaling with the measured commercial grade Gd and also with another second order magnetic material $\mathrm{LaFe}_{13-x-y}\mathrm{Co}_x\mathrm{Si}_y$, termed LaFeCoSi, which is described in detail in Paper X. For this material the adiabatic temperature change of three different samples with (x=0.86, y=1.08), (x=0.94, y=1.01) and (x=0.97, y=1.07) respectively was measured in the same way as for Gd. These are termed Sample 1, 2 and 3 respectively. These have peak temperatures close to 276, 286 and 288 K respectively.

The interpolated normalized adiabatic temperature change at the peak temperature, which is close to the Curie temperature, is shown in Fig. 2.5 for all the above mentioned materials. As can be seen ΔT_{ad} of the materials scales with a power very close to 2/3 for the magnetic field interval considered here. This was also found by Pecharsky and Gschneidner Jr (2006) for the case of Gd, where a scaling with an exponent of 0.7 was found. This scaling is interesting as it means that it is very important to ensure that the magnetocaloric materials experience a very low magnetic field before they are subjected to a high magnetic field in order to obtain the largest temperature change. For a given difference in magnetic field between a high and low field region the scaling of ΔT_{ad} means that this will always be largest if the field in the low field region is zero. Away from T_{C} neither the MFT nor the measured ΔT_{ad} scales as a power law of the magnetic field.

2.3 Active magnetic regeneration

The temperature change in a magnetic field change of 0-1.5 T of the benchmark magnetocaloric material, Gd, is too small to be applied directly for refrigeration purposes. Therefore a magnetic refrigeration device must utilize a regenerative process to produce a large enough temperature span to be useful for refrigeration purposes. The most utilized process for this is called active magnetic regeneration (AMR) (Barclay, 1982).

In the AMR process a heat transfer fluid and a magnetocaloric material, acting as a regenerator, are used to build up a temperature span that can be much larger than the adiabatic temperature change produced by the magnetocaloric material. The regenerator consists of a porous matrix of a solid magnetocaloric material through which a non-magnetic fluid can flow. This fluid exchange heat with the solid material and through a movement of the fluid, by a piston or a pump, the heat is moved to heat exchangers in a cooled space or in contact with the environment. Most AMR devices either have a packed bed regenerator where the MCM is typically packed spheres (Okamura et al., 2005; Tura and Rowe, 2009) or a parallel plate regenerator (Zimm et al., 2007; Bahl et al., 2008). For a review of different magnetic refrigeration devices please see e.g. Gschneidner Jr and Pecharsky (2008).

An AMR cycle proceeds in four steps. First the regenerator is magnetized. This raises the temperature of the solid due to the magnetocaloric effect. The temperature rise is a function of magnetic field but also of temperature, and thus of position in the regenerator. Heat is then transferred from the MCM to the heat transfer fluid in a time span, τ_1, while the fluid is stationary. The heat transfer fluid is then displaced towards the hot heat exchanger where the heat is released to the surroundings through a time span, τ_2. Next, the magnetic field in the regenerator is removed. This is also called the demagnetization of the regenerator[5]. This lowers the temperature of the MCM by the adiabatic temperature change, and heat is transferred from the heat transfer fluid to the MCM through a time span, τ_3, while the fluid is stationary. Then the heat transfer fluid is displaced towards the cold heat exchanger, where heat can be absorbed from a heat load through a time span, τ_4. A total cycle lasts a time span τ, equal to $\tau_1 + \tau_2 + \tau_3 + \tau_4$. The process then starts over again. Using this regenerative process a temperature span between the hot and cold end that is greater than the adiabatic temperature change can be achieved.

Presented as a scheme the AMR process cycle proceeds as below. This process is also illustrated in Fig. 2.6.

1. Magnetization of the regenerator. The temperature of the MCM is raised by $\Delta T_{\mathrm{ad}}(T)$ and heat is transferred from the MCM to the heat transfer fluid (Fig. 2.6a.)

2. The heat transfer fluid is displaced towards the hot heat exchanger and heat is transferred to the hot heat exchanger (Fig. 2.6b.)

3. Demagnetization of the regenerator. The temperature of the MCM is lowered by $\Delta T_{\mathrm{ad}}(T)$ and heat is transferred from the heat transfer fluid to the MCM (Fig. 2.6c.)

4. The heat transfer fluid is displaced towards the cold heat exchanger and heat is absorbed from the cold heat exchanger (Fig. 2.6d.)

[5]Here the term "demagnetized" means "removed from the magnetic field". This term is *not* in any way related to the demagnetization effect described previously.

Notice that the temperature T depends on the position of the MCM in the regenerator. The temperature profile inside the regenerator is also not necessarily linear. This will be considered further in Chapter 7.

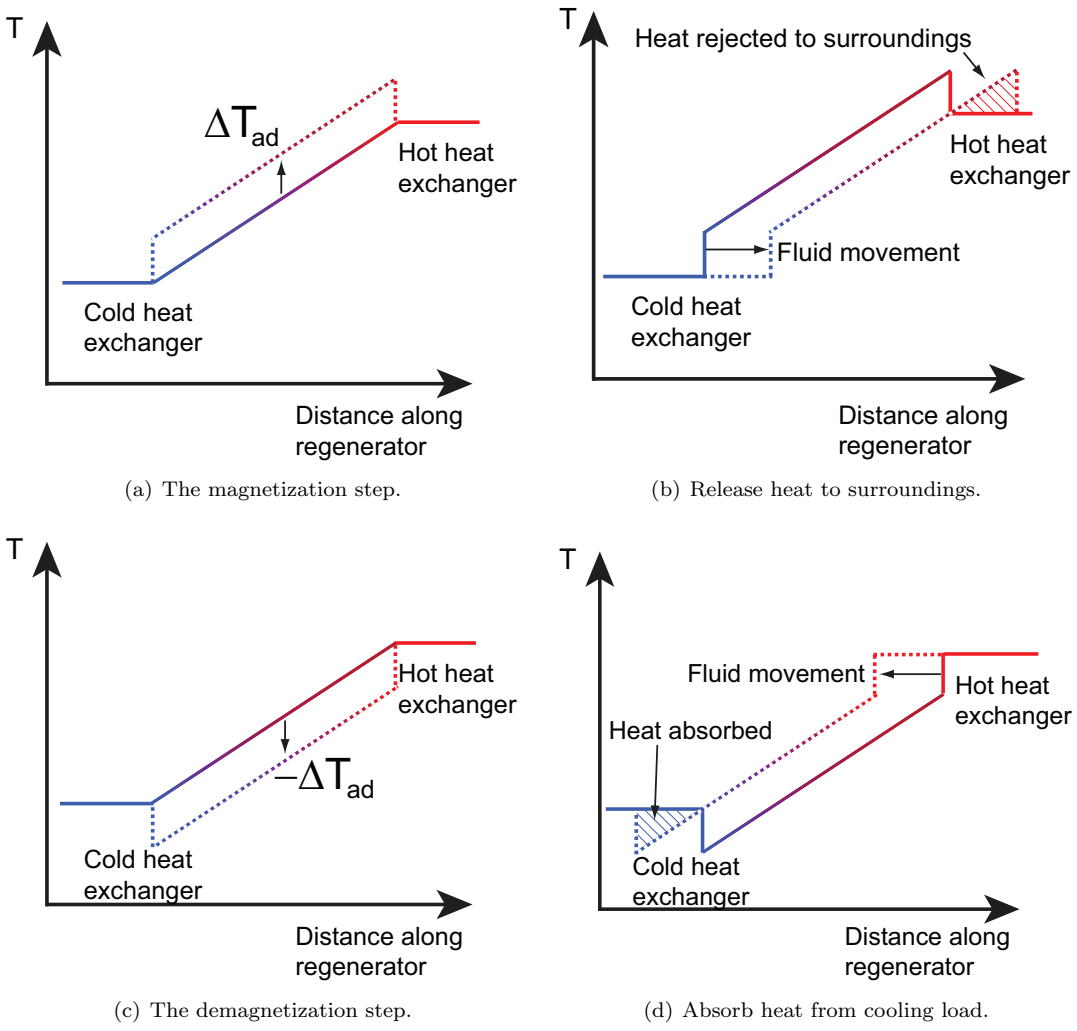

(a) The magnetization step.

(b) Release heat to surroundings.

(c) The demagnetization step.

(d) Absorb heat from cooling load.

Fig. 2.6: An illustration of an AMR cycle. The dashed temperature profiles indicate the change in the given step. Between step (b) and (c) the linear temperature profile is recovered. The same is the case between step (d) and (a).

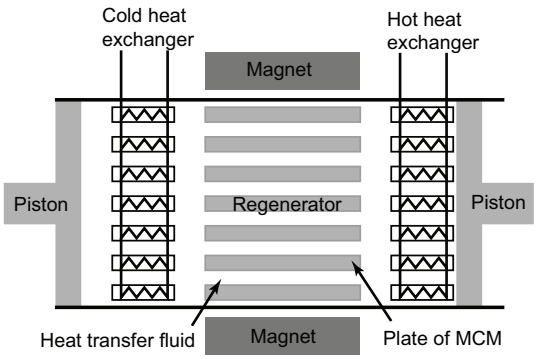

Fig. 2.7: A schematic drawing of the Risø DTU parallel plate regenerator in the magnetization step showing the parallel plates, fluid channels, heat exchangers and pistons.

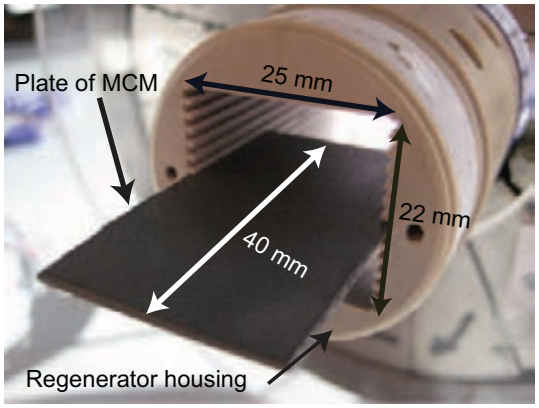

Fig. 2.8: A close-up photo of the experimental AMR regenerator housing with a plate of Gd sticking out of the regenerator. The regenerator bed can contain 13 parallel plates.

An example of an AMR is the parallel plate regenerator built at Risø DTU (Bahl et al., 2008). The regenerator consists of a square opening which is 22 mm high and 25 mm wide. The regenerator core contains 13 precision machined grooves to hold plates of MCM with dimensions 40 mm along the flow direction, 0.9 mm thick and 25 mm wide. The plates are separated by a 0.8 mm spacing which is then the thickness of the fluid channel, although this can be changed by using a different regenerator housing. Two pistons, one in each end, can be moved by a motor and thus the movement of the heat transfer fluid can be controlled. The whole regenerator can be moved in and out of a magnetic field by a second motor. A schematic drawing of the regenerator is shown in Fig. 2.7 while a photograph of the regenerator is shown in Fig. 2.8.

Different AMR devices exist, but these can be divided into two types; a reciprocating device and a rotating device. In a reciprocating device the magnetocaloric material and the magnet is moved linearly away from each other in the demagnetization step, and the movement is reversed in the magnetization step. In a rotating device either the magnetocaloric material or the magnet rotates in order to magnetize and demagnetize the magnetocaloric material. However the AMR process in itself is identical in the two types of devices.

2.3.1 The performance of an AMR

The performance of an AMR device depends on the process parameters specific to each AMR system. These are the shape and packing of the magnetocaloric material, the temperature of the surroundings and the properties of the MCM used, as well as the properties of the heat transfer fluid, flow system etc. The only parameter that is common to all AMR systems is the magnetic field. The magnet might be shaped differently in different AMR systems, but the magnetic field generated by the magnet has the same effect on all AMR systems, namely that it generates the magnetocaloric effect that is the heart of the AMR. Thus the magnetic field sets a fundamental limit on the temperature span and cooling power that an AMR system can produce.

The performance of an AMR is summed up in the cooling curve of the AMR. This curve

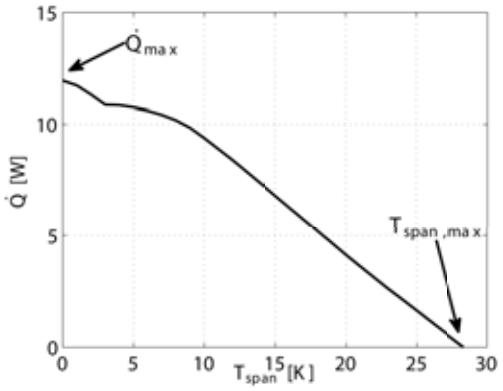

Fig. 2.9: An example of a cooling curve showing $\dot{Q}$ as a function of T_{span}. The maximum temperature span, $T_{\text{span,max}}$, and the maximum refrigeration capacity, $\dot{Q}_{\text{max}}$, have been indicated. The precise shape of the curve is explained in Chapter 3.

shows the cooling capacity, $\dot{Q}$, as a function of temperature span, T_{span}, of the device, for a given set of process parameters. The temperature span is the difference between the temperature of the hot and the cold end, T_{hot} and T_{cold}, respectively. An example of a cooling curve is shown in Fig. 2.9. Examination of the figure shows that the cooling power produced by the AMR is highly dependent on the temperature span. The most often-cited information that can be learned from a cooling curve are the maximum or no load temperature span, $T_{\text{span,max}}$, and the maximum refrigeration capacity, $\dot{Q}_{\text{max}}$. At $T_{\text{span,max}}$ $\dot{Q} = 0$ W, while at $\dot{Q}_{\text{max}}$ $T_{\text{span}} = 0$ K, where in the latter case all the cooling power generated by the device is used to move heat from the cold to the hot end. These two parameters are often used to characterize the efficiency of an AMR. Just as the performance of an MCM was studied as a function of magnetic field so must the performance of an AMR be studied as a function of magnetic field, in order to learn how to design the ideal magnet for magnetic refrigeration.

Chapter 3

The influence of the magnetic field on the AMR process

Before studying the design of a magnet for magnetic refrigeration it is important to study how the magnetic field affects the active magnetic regeneration (AMR) process. If the magnetic field has a different influence on different AMR devices or different AMR process parameters the magnetic field will need to be tailored to the specific AMR. Here, this is investigated along with the performance of the AMR as a function of magnetic field. This is done to learn how to design the ideal magnet for use in magnetic refrigeration.

Previously, detailed and extensive investigation of the AMR process using numerical modeling have been published (Hu and Xiao, 1995; Engelbrecht et al., 2005a,b; Allab et al., 2005; Siddikov et al., 2005; Shir et al., 2005b; Petersen et al., 2008b; Nielsen et al., 2009, 2010), but so far little effort has been put into investigating how the properties and variation of the magnetic field influence the theoretical performance of the AMR cycle and how this knowledge can improve magnet designs for magnetic refrigeration. This will be studied here, also using a numerical model.

This chapter is partially based on the results described in Paper XI.

3.1 Modeling the AMR process

Two types of regenerators are considered here: a packed sphere bed and a parallel plate regenerator. A one dimensional numerical model capable of modeling both packed sphere bed and parallel plate regenerators are used to model the AMR process (Engelbrecht et al., 2006). This model is publicly available. In case of the packed sphere bed regenerator the model has previously been compared with experimental data (Engelbrecht, 2008). For the parallel plate regenerator case the model has been compared with a more detailed two dimensional model (Petersen et al., 2008a), where the latter has been compared with experimental data (Bahl et al., 2008). In the numerical model the temperature span is an input parameter and the refrigeration capacity is calculated for the specified process parameters.

The one dimensional model assumes that the fluid and solid temperature profiles are functions only of the flow direction. The cooling capacity of the AMR is determined by solving the coupled one-dimensional partial differential equations in space and time describing the temperature in the regenerator and in the fluid. Different regenerator parameters such as the position dependent Nusselt number, which determines the heat transfer between the regenerator and the fluid, and the friction factor are determined using established correlations. The model assumes that the edges of both the fluid and the solid are adiabatic except during the blow periods where the fluid enters the regenerator with the prescribed temperature of either the hot or the cold reservoir. The model starts from an initial temperature distribution and takes time steps

until a cyclical steady state has been achieved. This state is reached when the dimensionless value of the absolute change in energy of the regenerator from cycle to cycle is less than a specified tolerance. The governing equations for the model are given in Engelbrecht et al. (2006); Petersen et al. (2008a).

For the parallel plate regenerator model the comparison with the two dimensional model lead to the definition of a "1D correctness" parameter, Γ, which is defined as

$$\Gamma = \frac{\pi^2 k_{\text{fluid}}}{h_{\text{fluid}}^2 \rho_{\text{fluid}} c_{\text{p,fluid}}} \tau_1 \gg 1 \tag{3.1}$$

where the subscript fluid denotes a property of the heat transfer fluid, and where k is the thermal conductivity, ρ is the mass density, c_{p} is the specific heat capacity and h_{fluid} is the height of the fluid channel (Petersen et al., 2008a). A value much greater than one for Γ corresponds to an operating condition in which the one dimensional model produces comparable results to the two dimensional model.

3.1.1 The magnetic field profile

To investigate the relation between AMR performance and the magnetic field four parameters of the magnetic field are varied. These are:

- The synchronization of the magnetic field with the AMR cycle, i.e. when in the AMR cycle the magnetocaloric material is subjected to the magnetic field.
- The ramp rate of the magnetic field, i.e. how quickly does the magnetic field change from its minimum to its maximum value and vice versa.
- The width of the magnetic field profile compared to the fluid flow profile.
- The maximum value of the magnetic field.

A spatial variation of the magnetic field across the AMR is not considered here. In reality, there will be a spatial variation of the magnetic field across e.g. a plate of MCM because the demagnetization field inside such a plate will not be homogeneous, as was also discussed in Chapter 2. However, here we are interested in the theoretical performance of the AMR and thus this effect can be disregarded.

To separately study the effects of each of the properties of the magnetic field a generic magnetic field that varies as a function of time during the AMR cycle is used. This time varying profile is called the magnetic field profile. This profile is shown in Fig. 3.1 along with the fluid flow profile of the AMR. The generic magnetic field profile can be characterized by four parameters. The first parameter is the synchronization, denoted by x_0, which indicates the time in fractions of τ where the magnetic field profile begins to increase, relative to the AMR fluid flow cycle. The second parameter is the maximum value of the magnetic field, $\mu_0 H_{\max}$, which is in general varied between 0.5 and 1.5 T, as this is the range obtainable with permanent magnets. The final two parameters are the top width, w_{top}, and the total width, w_{total}, of the temporal magnetic field profile, which are both defined in terms of τ. These also define the ramp rate.

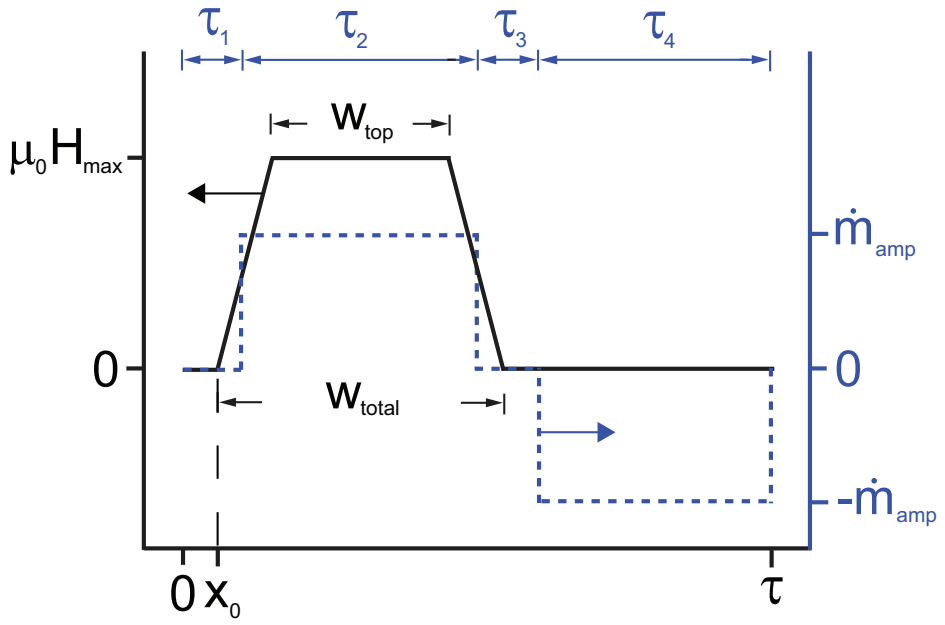

Fig. 3.1: The generic magnetic field profile (full line) and the fluid flow cycle (dotted line) of the AMR cycle. The parameters of the magnetic field profile are indicated, as well as the AMR cycle time parameters τ_{1-4}, which corresponds to different parts of the flow cycle.

3.2 AMR process parameters

The performance of the AMR as a function of magnetic field are studied for a number of process parameters. These must be chosen realistically if the results of the numerical model are to be relevant for magnetic refrigeration test devices. In all models and for all process parameters, a symmetric, or balanced, AMR flow cycle is used. The values of the fluid flow cycle parameters are always $\tau_1 = \tau_3 = 0.1$ and $\tau_2 = \tau_4 = 0.4$ in fractions of the total cycle time, τ. A standard magnetic field profile will be used in some of the numerical experiments. Based on the chosen fluid flow cycle parameters, the standard magnetic field profile is chosen to have $w_{\text{top}} = 0.45$, $w_{\text{total}} = 0.55$ and $x_0 = 0$. For this profile the magnetic field begins to increase at $t = 0$ and reaches its maximum value at $t = \tau_1/2 = 0.05$. It begins to decrease at $t = \tau_2 = 0.5$ and is zero at $t = 0.55$.

The length of the modeled regenerator is 50 mm. The heat transfer fluid is water with the following constant properties: specific heat capacity, $c_{\text{p}} = 4183$ J kg^{-1} K^{-1}, thermal conductivity, $k = 0.595$ W m^{-1} K^{-1}, density, $\rho = 997$ kg m^{-3} and dynamic viscosity, $\mu = 8.91 * 10^{-4}$ kg m^{-1} s^{-1} (Petersen et al., 2008a). The MCM is taken to be gadolinium, modeled using the mean field model as described in Chapter 2 and with $k = 10.5$ W m^{-1} K^{-1} and $\rho = 7900$ kg m^{-3}. Although the mean field model does not exactly reproduce experimental data it is often used as the benchmark model for AMR models because it produces thermodynamically consistent data with smooth derivatives and different numerical models can be more easily compared if the same data set has been used as input. The temperature of the hot end of the AMR is kept fixed at $T_{\text{hot}} = 298$ K.

For the parallel plate regenerator three process parameters must be specified. These are the height of the fluid channel, h_{fluid}, the height of the plate, h_{plate}, and the mass flow rate, $\dot{m}_{\text{amp}}$. Here, 54 different sets of parameters are considered. These are listed in Table 3.1, and have been chosen so that they span realistic values of the different parameters and yet produce similar results to the two dimensional model mentioned previously. The mass flow rate has been chosen so that it is $7.27 * 10^{-3}$ kg s^{-1} for a 1 mm plate for $\tau = 6$ s which is similar to the value chosen by Petersen et al. (2008a). With the chosen values for the height of the plate and fluid channel the porosity is 50%, 66% and 75% respectively.

For the cycle time of $\tau = 0.5$ s the result of the one dimensional model might deviate from a more detailed two dimensional model, as per the Γ parameter defined in Eq. (3.1). If $\Gamma < 3$ the set of process parameters are not considered further. For the $\tau = 0.5$ s parallel plate case these are the parameter sets where $h_{\text{fluid}} > 0.00010$ m. Thus a total of 18 sets of parameters

Table 3.1: Parallel plates regenerator parameters. The parameters are varied individually so the table should not be read as rows but rather as what values the different parameters can assume. In total there are 54 sets of parameters, but 18 sets for $\tau = 0.5$ s are disregarded as the results would differ from a two dimensional AMR model.

h_{fluid} [m]	h_{plate} [m]	$\dot{m}_{\text{amp}}$ [kg s^{-1}]	τ [s]
0.00010	$1 * h_{\text{fluid}}$	$0.5 * 7.27 * 6/\tau * h_{\text{plate}}$	0.5
0.00025	$2 * h_{\text{fluid}}$	$1 * 7.27 * 6/\tau * h_{\text{plate}}$	6
0.00050	$3 * h_{\text{fluid}}$	$2 * 7.27 * 6/\tau * h_{\text{plate}}$	

Table 3.2: Packed sphere bed regenerator parameters. Similarly to the parallel plate parameter table, Table 3.1, the rows in this table are not to be understood as parameter sets, except for the $\dot{m}_{\mathrm{amp}}$ column. Here, e.g., for the case of $h = 0.0002$ m the value of $\dot{m}_{\mathrm{amp}} = 0.0001 * [0.5 \;\; 1 \;\; 2] * 7.27$ kg s^{-1} and not any other values. Similarly for $h = 0.00075$ m the value is $\dot{m}_{\mathrm{amp}} = 0.0005 * [0.5 \;\; 1 \;\; 2] * 7.27$ kg s^{-1} and not any other values and so on. This ensures that $\dot{m}_{\mathrm{amp}}$ is equal for the parallel plate and packed sphere bed cases with the same regenerator volume. There are a total of 54 parameter sets.

h [m]	d_{p} [m]	$\dot{m}_{\mathrm{amp}}$ [kg s^{-1}]	τ [s]
0.00020	0.00010	$0.0001 * [0.5 \;\; 1 \;\; 2] * 7.27 * 6/\tau$	0.5
0.00075	0.00025	$0.0005 * [0.5 \;\; 1 \;\; 2] * 7.27 * 6/\tau$	6
0.00150	0.00050	$0.0010 * [0.5 \;\; 1 \;\; 2] * 7.27 * 6/\tau$	

are disregarded for the case of $\tau = 0.5$ s. For the case of $\tau = 6$ s, the lowest value of Γ occurs for $h_{\mathrm{fluid}} = 0.00050$ m, where $\Gamma = 3.38$, thus all sets of parameters are within the defined requirement for Γ.

A spherical particle packed sphere bed regenerator is also considered. Here, the process parameters are the height of the regenerator, h, the particle size, d_{p}, the mass flow rate, $\dot{m}_{\mathrm{amp}}$, and the porosity. For a randomly packed sphere regenerator used in magnetic refrigeration the latter is generally near 0.36 (Okamura et al., 2005; Jacobs, 2009; Tura and Rowe, 2009) and therefore this parameter is fixed. The height of the regenerator is chosen to be identical to three of the values from the parallel plate case, resulting in an equal regenerator volume for these cases. The particle size, d_{p}, is varied within reasonable values (Okamura et al., 2005; Engelbrecht et al., 2007; Tura and Rowe, 2009). The value of $\dot{m}_{\mathrm{amp}}$ is calculated to give the same value as the parallel plate cases with the same regenerator geometry. Finally, τ assumes the values of 0.5 and 6 s. The parameter sets are listed in Table 3.2.

3.3 The cooling curve

As mentioned in Chapter 2 the performance of an AMR, for a given set of process parameters, is summed up in the cooling curve which shows the cooling capacity, $\dot{Q}$, as a function of temperature span, T_{span}, of the device. The cooling curve is often assumed to be linear which would allow for inter- or extrapolation to find $T_{\mathrm{span,max}}$. This is useful because the model used here calculates $\dot{Q}$ for a chosen T_{span}. Here, we have investigated the linearity of the cooling curve by calculating the R^2 parameter of a linear least-squares fit to the cooling curve for the standard magnetic field profile, i.e. $w_{\mathrm{top}} = 0.45$, $w_{\mathrm{total}} = 0.55$ and $x_0 = 0$, for all parameters sets, and $T_{\mathrm{cold}} = 298$ K to 260 K in steps of 1 K and at $\mu_0 H_{\mathrm{max}} = 0.5$ T to 1.5 T in steps of 0.1 T for both the parallel plates and packed sphere bed regenerator. The parameter R^2 is a goodness-of-fit statistic that measures how well the fit approximates the data points, with an R^2 value of 1.0 indicating a perfect fit. The parameter is defined as

$$R^2 \equiv 1 - \frac{{}_i(y_i - f_i)^2}{{}_i(y_i - \bar{y})^2}, \tag{3.2}$$

where y_i are the values of the data set, f_i are the interpolated values and $\bar{y}$ is the mean of the data.

The shape of a typical cooling curve displays a flattening around the Curie temperature. Here, the temperature of the hot end, $T_{\text{hot}} = 298$ K, is larger than the Curie temperature of the MCM, $T_{\text{c}} = 293.6$ K, and thus this flattening will be present, as can also be seen in the cooling curve shown in Fig. 2.9.

The R^2 parameter is shown in Fig. 3.2 as a function of $T_{\text{span,max}}$ for two different linear functions. For this figure $T_{\text{span,max}}$ has been determined fairly accurately because the temperature has been varied in steps of 1 K. The functions are linear fits of the cooling curve from 298 K, i.e. at $\dot{Q}_{\text{max}}$, to $T_{\text{span,max}}$ and a linear fit from 285 K to $T_{\text{span,max}}$. The first fit is denoted $L(\dot{Q}(298), \dot{Q}(T_{\text{span,max}}))$ and the latter $L(\dot{Q}(285), \dot{Q}(T_{\text{span,max}}))$ in Fig. 3.2. As can clearly be seen from the figure the cooling curve is not linear from $\dot{Q}_{\text{max}}$ to $T_{\text{span,max}}$. However, if only the part after the flattening, i.e. $L(\dot{Q}(285), \dot{Q}(T_{\text{span,max}}))$, is fitted the R^2 parameter is in general higher than 0.998, and thus this part of the cooling curve is extremely close to being linear for both parallel plate and packed sphere bed regenerators.

Having shown that the part of the cooling curve away from T_{c} can be fitted by a linear function, we wish to examine if the $T_{\text{span,max}}$ parameter can be estimated by only calculating the refrigeration capacity at a few selected temperature spans. In Fig. 3.3 four different linear functions have been used to calculate $T_{\text{span,max}}$. The first is a linear function between the two points $\dot{Q}(T_{\text{cold}} = 298)$ and $\dot{Q}(T_{\text{cold}} = 285)$, denoted $L(\dot{Q}(298), \dot{Q}(285))$. Using the same notation the three remaining functions are $L(\dot{Q}(285), \dot{Q}(260))$, $L(\dot{Q}(285), \dot{Q}(270))$ and

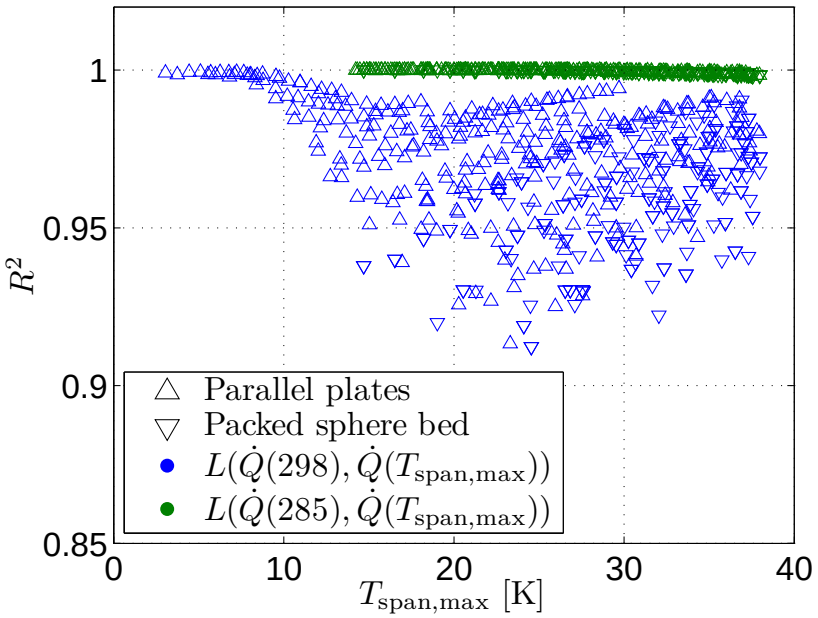

Fig. 3.2: The goodness of fit parameter R^2 as a function of $T_{\text{span,max}}$ for parallel plates and packed sphere bed regenerators for a linear fit to the full cooling curve and the cooling curve from 285 K to $T_{\text{span,max}}$.

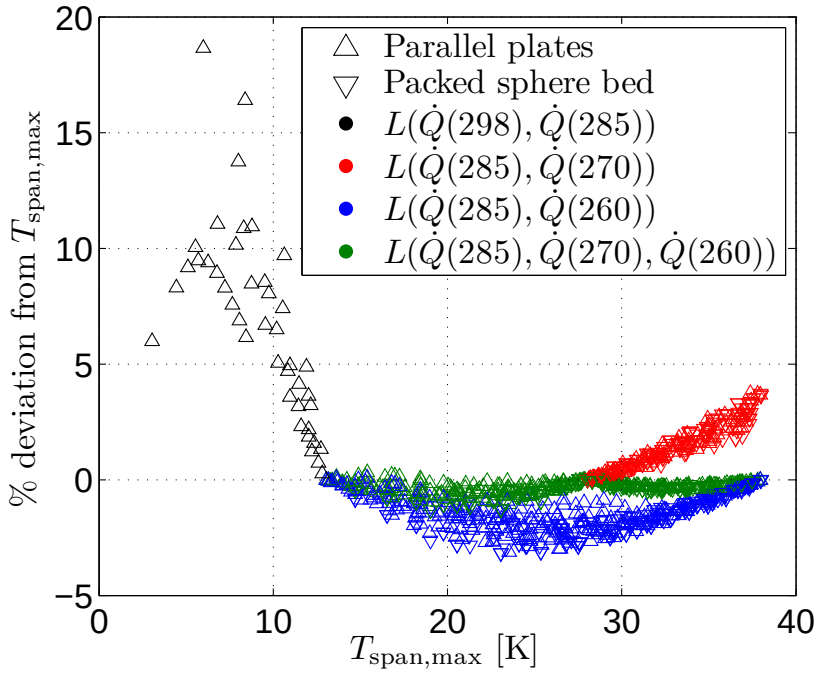

Fig. 3.3: The deviation of the estimated $T_{\text{span,max}}$, based on different linear functions, from the true $T_{\text{span,max}}$. From $T_{\text{cold}} = 285$ K to 270 K the two linear functions $L(\dot{Q}(285), \dot{Q}(270))$ and $L(\dot{Q}(285), \dot{Q}(270), \dot{Q}(260))$ are identical, and thus only $L(\dot{Q}(285), \dot{Q}(270), \dot{Q}(260))$ is shown.

$L(\dot{Q}(285), \dot{Q}(270), \dot{Q}(260))$, where the latter is a two-section linear function, which consists of a linear function from $\dot{Q}(285)$ to $\dot{Q}(270)$ and second from $\dot{Q}(270)$ to $\dot{Q}(260)$. The $T_{\text{span,max}}$ parameter has been interpolated based on these linear functions and the deviation from the true $T_{\text{span,max}}$, found by linear interpolation of the data set where T_{cold} was varied in steps of 1 K, is shown in Fig. 3.3. If the value of $T_{\text{span,max}}$ is higher than 38 K, i.e. outside the temperature interval considered here, it is disregarded. This is the case for the remainder of this chapter.

From Fig. 3.3 it can be seen that all the linear functions provides an accurate estimate of $T_{\text{span,max}}$. However, the two-section linear function $L(\dot{Q}(285), \dot{Q}(270), \dot{Q}(260))$ provides the most precise estimate of $T_{\text{span,max}}$, i.e. one that is accurate to within 1.5% of the true value in the $T_{\text{span,max}}$ interval between 285 K and 260 K. In the interval between 298 K and 285 K the estimate of $T_{\text{span,max}}$ is not very accurate, but as there are few models that have this small a temperature span the linear interpolation will still be used. In the remainder of this chapter the refrigeration capacity will be calculated at $T_{\text{cold}} = 298$, 285, 270 and 260 K, and $T_{\text{span,max}}$ will be estimated based on these values using linear interpolation, unless otherwise stated.

3.4 Synchronization of the magnetic field

It is important to investigate the performance of the AMR cycle as a function of when in the AMR cycle the regenerator is subjected to the magnetic field. This is termed "synchronization" as it describes how synchronized the magnetic field profile is with the AMR fluid flow profile and it is characterized by the synchronization parameter, x_0, as shown previously in Fig. 3.1. At $t = 0$ the synchronization is zero, i.e. $x_0 = 0$. A negative value of x_0 means that the magnetic field profile has been moved so that it begins earlier in the cycle compared to this case.

The effect of the synchronization on $\dot{Q}_{\max}$ and $T_{\text{span,max}}$ has been investigated for all parameter sets for both the parallel plate and packed sphere bed cases. A value of $\mu_0 H_{\max} = 0.5$, 1 and 1.5 T and a magnetic field profile with $w_{\text{top}} = 0.45$ and $w_{\text{total}} = 0.55$ were used in the synchronization study. The synchronization parameter, x_0, was varied from -0.1 to 0.1 in steps of 0.01. Some of the different magnetic field profiles tried are shown in Fig. 3.4.

The results are shown in Figs. 3.5 and 3.6 which show $\dot{Q}_{\max}$ and $T_{\text{span,max}}$ as a function of the synchronization parameter, x_0, for all process parameters and magnetic fields. As can be seen from the figures both $\dot{Q}_{\max}$ and $T_{\text{span,max}}$ show a broad plateau around $x_0 = 0$. The behavior of $\dot{Q}_{\max}$ and $T_{\text{span,max}}$ appears to be much the same across the different sets of AMR process parameters and different magnetic fields that were investigated. The parallel plates show a slightly larger drop in $T_{\text{span,max}}$ than the packed sphere bed regenerator does. For all parameter sets a drop in performance between 20 and 40% is seen if the magnetic field is ramped too early. A smaller performance drop is seen if the field is ramped too late. Shifting the magnetic field to earlier in the cycle can also provide a minimal increase in performance.

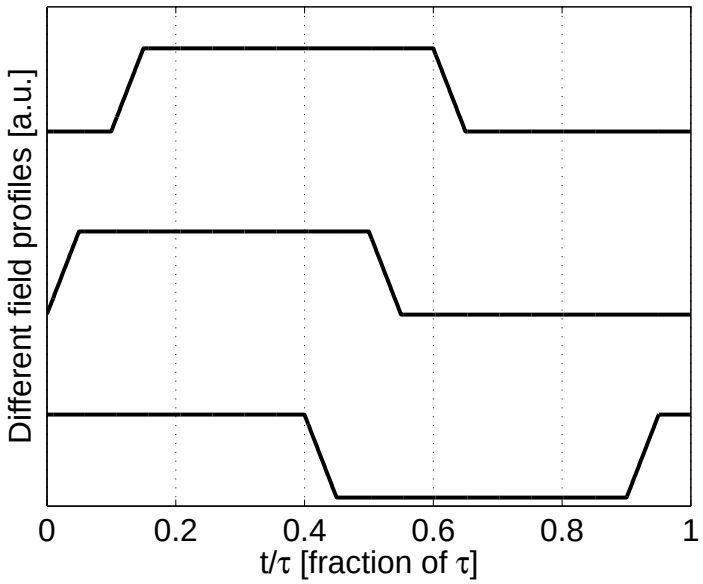

Fig. 3.4: Three of the different magnetic field profiles used in the synchronization experiment. The profiles shown have x_0 = -0.1, 0 and 0.1 respectively.

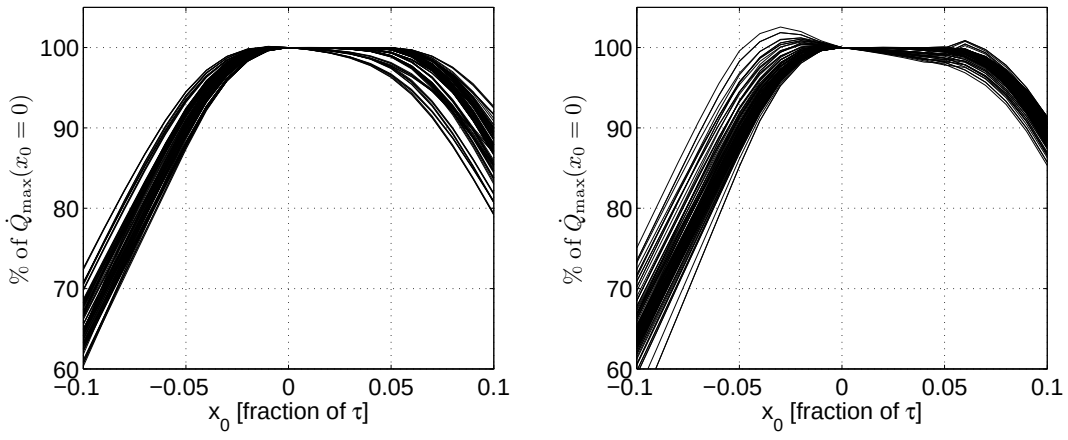

(a) Parallel plates.

(b) Packed sphere bed.

Fig. 3.5: The maximum cooling capacity, $\dot{Q}_{\max}$, as a function of the synchronization parameter, x_0, for all parameter sets.

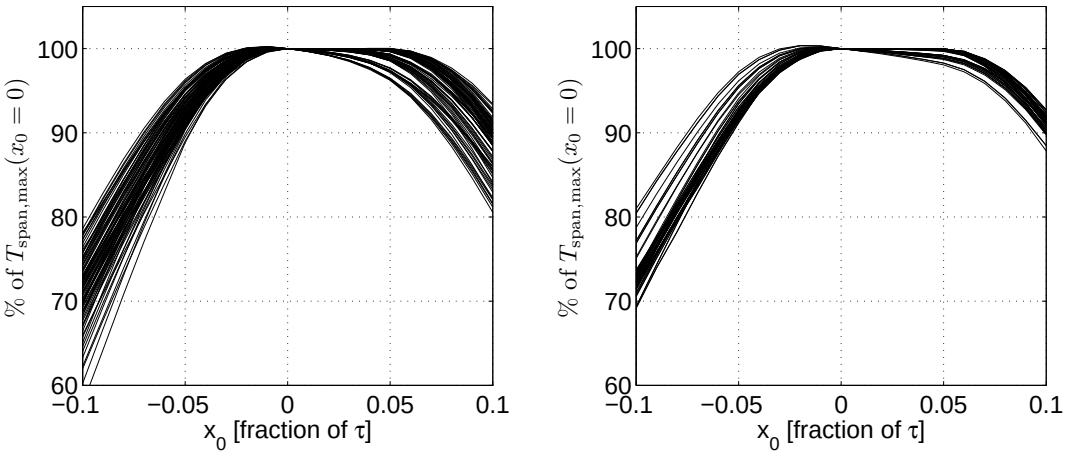

(a) Parallel plates.

(b) Packed sphere bed.

Fig. 3.6: The no load temperature span, $T_{\text{span,max}}$, as a function of the synchronization parameter, x_0, for all parameter sets.

3.5 Ramp rate of the magnetic field

It is also important to investigate the influence of the ramp rate, i.e. the speed of the increase from $\mu_0 H = 0$ T to $\mu_0 H_{\max}$, on the performance of the AMR cycle. The ramp rate can be controlled by varying the w_{top} and w_{total} parameters as the ramp rate is given by Rate $= (w_{\text{total}} - w_{\text{top}})/2$ in fractions of τ.

In the simulations w_{top} is kept constant at 0.45 and $\mu_0 H_{\max} = 1$ T. The total width, w_{total}, was varied from 0.46 to 0.65 in steps of 0.01, which means that the ramp rate was varied from 0.005 to 0.1 in fractions of τ. The synchronization parameter, x_0, was chosen such that the magnetic field profile always begins to ramp down at $t = \tau_1 + \tau_2$. In practice this means that the synchronization parameter was given as $x_0 = (0.55 - w_{\text{total}})/2$. It is ensured that the ramp of the magnetic field is always sufficiently numerically resolved in time. The different magnetic field profiles tried are shown in Fig. 3.7.

The behavior of the AMR system, which was only examined at the maximum refrigeration capacity, is shown in Fig. 3.8 which shows $\dot{Q}_{\max}$ as a function of w_{total} and the ramp rate for all process parameters. The maximum temperature span was not found due to the extensive computation time caused by the high numerical resolution required to resolve the field profiles with fast ramp rates. It is seen that the decrease in performance is only a few percent if a slow ramp rate is used. For a fast ramp rate no gain in performance is seen, but in a few cases a drop in performance is observed. This drop in performance can occur because the magnetic field profile with a slow ramp rate is wider, which can improve performance for some sets of process parameters. This will be considered in more detail shortly.

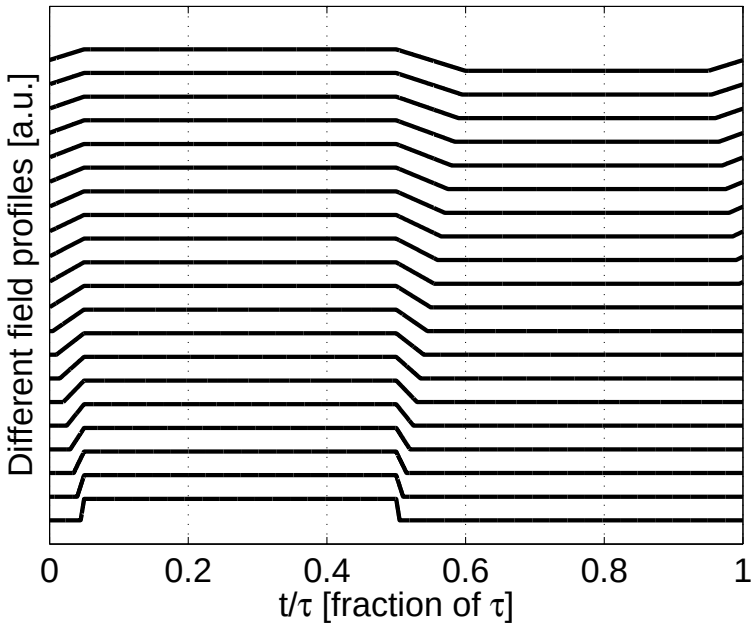

Fig. 3.7: The different magnetic field profiles used in the ramping experiment. The profiles shown at the bottom of the graph have the highest ramp rates.

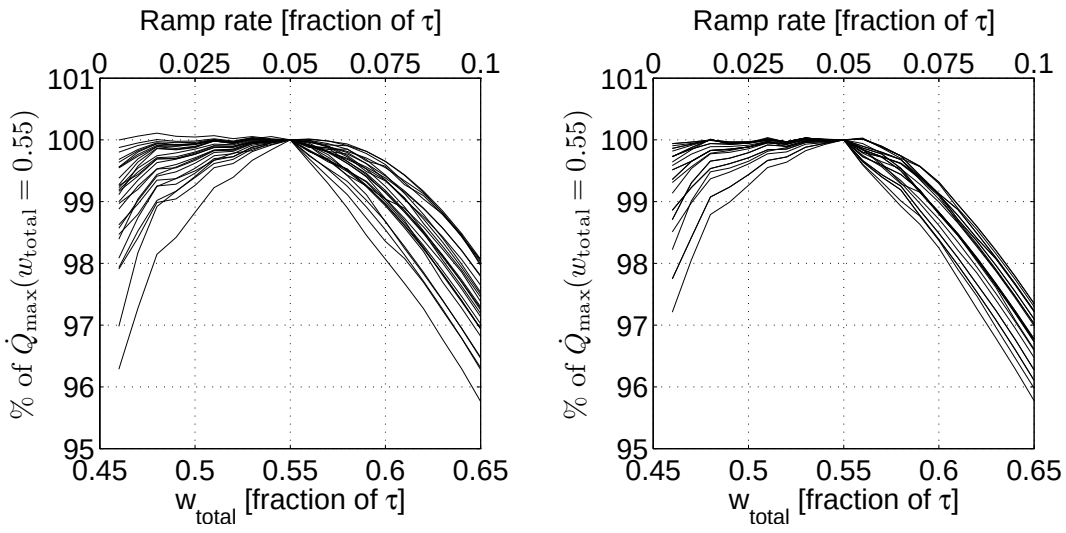

(a) Parallel plates.

(b) Packed sphere bed.

Fig. 3.8: The maximum cooling capacity, $\dot{Q}_{\max}$, as a function of w_{total} and the ramp rate for the parallel plate and packed sphere bed cases. The top x-axis shows the corresponding ramp rate. The lack of smoothness of the curves is due to the very small change of the refrigeration capacity with ramp rate, which is difficult to resolve numerically.

3.6 Maximum value of the magnetic field

Having determined the effect of synchronization and ramping of the magnetic field on the performance of the AMR, we now turn to the study of the effect of the maximum value of the magnetic field, $\mu_0 H_{\max}$.

To study this, the standard magnetic field profile, i.e. $w_{\text{top}} = 0.45$, $w_{\text{total}} = 0.55$ and $x_0 = 0$ is used. The value of $\mu_0 H_{\max}$ was varied from 0.5 to 1.5 T in steps of 0.1 T. The temperature of the cold end of the regenerator was varied from 230 to 260 K in steps of 5 K and from 260 to 298 K in steps of 1 K in order to find $T_{\text{span,max}}$ and $\dot{Q}_{\max}$. The larger temperature interval of the cold end temperature was considered in order to improve the estimate of $T_{\text{span,max}}$ produced by the high values of the magnetic field.

In Figs. 3.9 and 3.10 the maximum cooling capacity and temperature span are plotted as functions of $\mu_0 H_{\max}$ for all process parameters. As can be seen from the figures $\dot{Q}_{\max}$ scales almost identically for the different process parameters. In all cases $\dot{Q}_{\max}$ has a stronger dependency on $\mu_0 H_{\max}$ than $T_{\text{span,max}}$. Thus increasing the magnetic field increases $\dot{Q}_{\max}$ more than $T_{\text{span,max}}$, e.g. increasing $\mu_0 H_{\max}$ from 1 T to 1.5 T increases $\dot{Q}_{\max}$ by $\sim 40\%$ but only $T_{\text{span,max}}$ by $\sim 25\%$. The slope of increase for both $T_{\text{span,max}}$ and $\dot{Q}_{\max}$ with respect to $\mu_0 H_{\max}$ is below 1 for every parameter set modeled. For $T_{\text{span,max}}$ the scaling of ΔT_{ad} at the Curie temperature, i.e. $\Delta T_{\text{ad}}(T_{\text{c}}) \quad (\mu_0 H)^{2/3}$, is also shown. As can be seen $T_{\text{span,max}}$ scales with an exponent that is slightly less than 2/3.

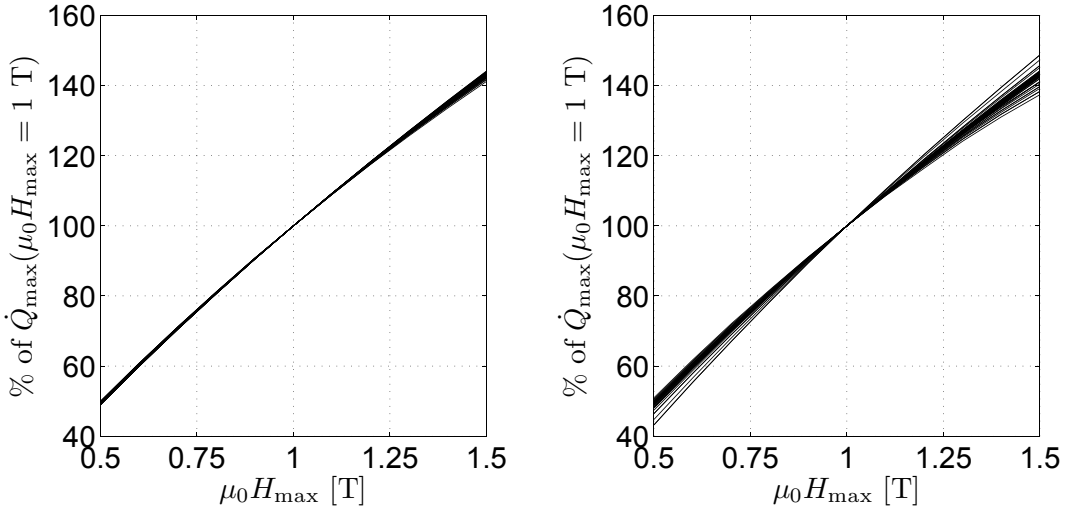

(a) Parallel plates.

(b) Packed sphere bed.

Fig. 3.9: The maximum cooling capacity, $\dot{Q}_{\max}$, as a function of $\mu_0 H_{\max}$ for all parameter sets.

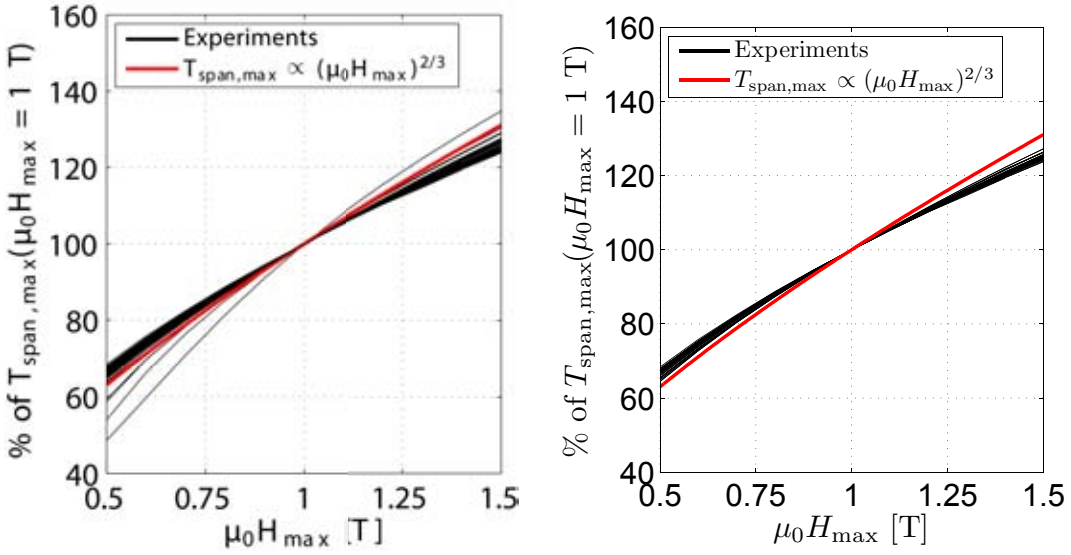

(a) Parallel plates.

(b) Packed sphere bed.

Fig. 3.10: The no load temperature span, $T_{\text{span,max}}$, as a function of $\mu_0 H_{\max}$ for all parameter sets. Also shown is $T_{\text{span,max}} \quad (\mu_0 H_{\max})^{2/3}$.

3.7 Width of the magnetic field

It is important to examine the behavior of the AMR cycle with respect to the width of the magnetic field profile, i.e. the fraction of the AMR cycle in which the regenerator is subjected to the high magnetic field or correspondingly how long time the regenerator is in the low field region. Here, we consider a profile where the ramp time is kept constant at 5% of the total cycle time, i.e. $(w_{\text{total}} - w_{\text{top}})/2 = 0.05$. The w_{top} parameter is varied from 0.35 to 0.55 in steps of 0.01, with the w_{total} parameter given by the ramp time, i.e. $w_{\text{total}} = w_{\text{top}} + 0.1$.

We consider two cases: one case where the magnetic field profile is centered on the flow profile, and one case where the magnetic field profile begins to ramp down at the same time as the flow profile changes from $\dot{m}_{\text{amp}}$ to 0, i.e. at $t = \tau_1 + \tau_2$. The first type of profile will be referred to as the centered profile, whereas the latter will be referred to as the synced profile. The fluid flow profile is kept fixed at the values introduced earlier, i.e. $\tau_1 = \tau_3 = 0.1$ and $\tau_2 = \tau_3 = 0.4$, respectively, in fractions of the total cycle time, τ. Thus as w_{top} is changed the width of the magnetic field profile will change from being "shorter" to "longer" than the fluid flow profile. This can be the case in e.g. a rotating AMR where the high field region can be smaller than the low field region or vice versa. Some of the different field profiles are shown in Fig. 3.11.

The modeling results are shown in Figs. 3.12 and 3.13, which show $\dot{Q}_{\text{max}}$ and $T_{\text{span,max}}$ as a function of w_{total}. As can be seen from the figures, a more or less identical behavior is seen for all parameter sets. The optimum w_{total} is approximately 0.55, and both $\dot{Q}_{\text{max}}$ and $T_{\text{span,max}}$ decrease as the value of w_{total} moves further from 0.55. In general a large width is worse than a short width for the values considered here. The drop in performance for both $\dot{Q}_{\text{max}}$ and $T_{\text{span,max}}$ for $w_{\text{total}} > 0.55$ is greater for the synced profiles than for the centered profiles.

The difference between the centered and synced profiles for all parameter sets are shown in Fig. 3.14 and 3.15. For both $\dot{Q}_{\text{max}}$ and $T_{\text{span,max}}$ it is seen that if the magnetic field profile has a small value of w_{total} it is better to sync the profile with the fluid flow profile, whereas for large values of w_{total} the centered profile has the best performance.

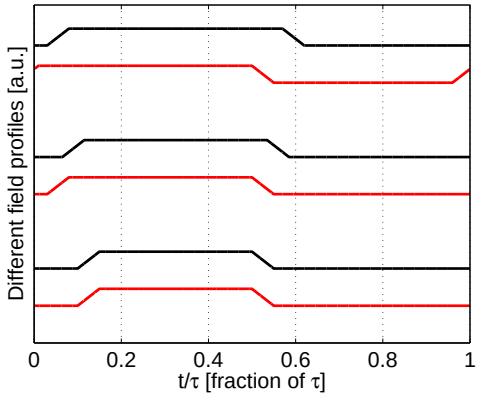

Fig. 3.11: Three of the different magnetic field profiles for the width experiment. The black curves are centered on the fluid flow profile (not shown), while the red curves are synced, i.e. the time at which the magnetic field is ramped down is fixed at $t = \tau_1 + \tau_2 = 0.5$.

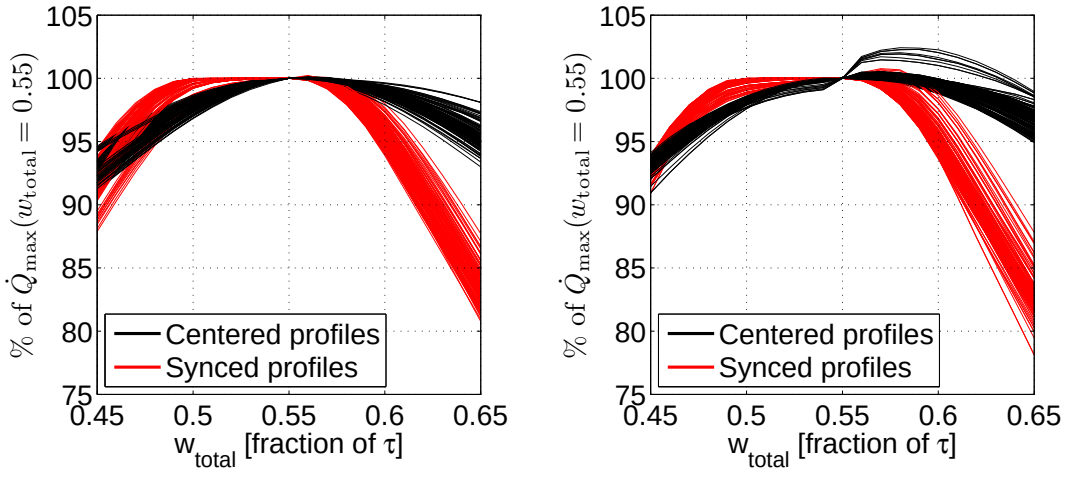

(a) Parallel plates.

(b) Packed sphere bed.

Fig. 3.12: The maximum cooling capacity, $\dot{Q}_{\max}$, as a function of w_{total} for the parallel plate and packed sphere bed cases. Both centered profiles and synced profiles are shown.

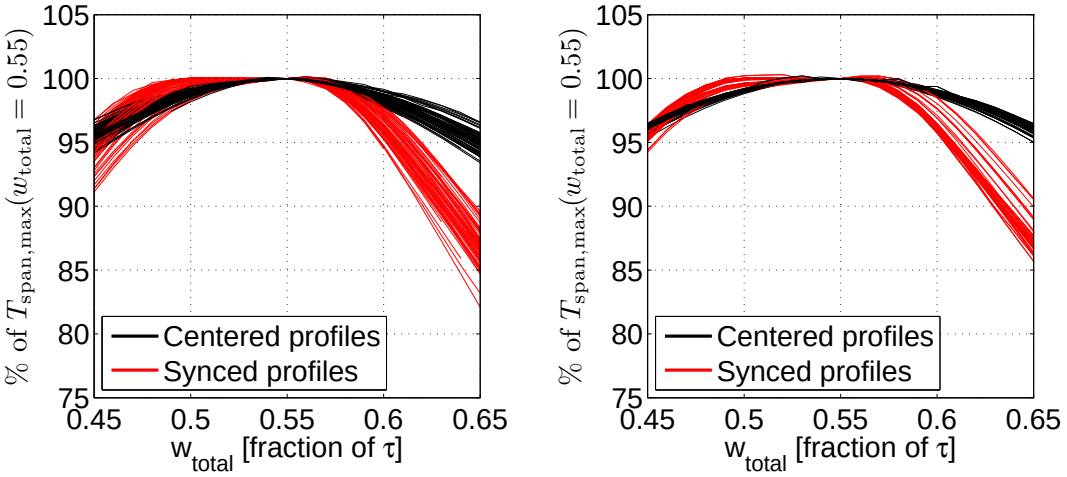

(a) Parallel plates.

(b) Packed sphere bed.

Fig. 3.13: The no load temperature span, $T_{\text{span,max}}$, as a function of w_{total} for the parallel plate and packed sphere bed cases. Both centered profiles and synced profiles are shown.

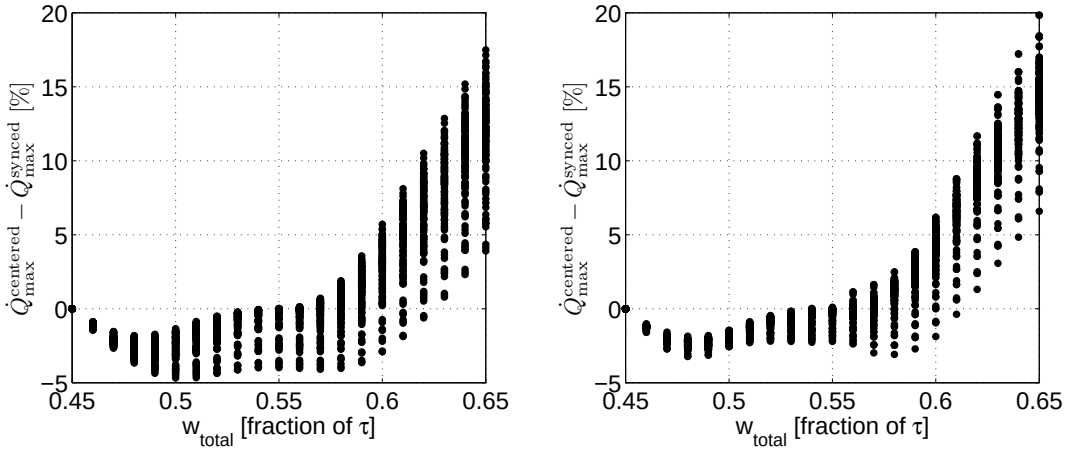

(a) Parallel plates.

(b) Packed sphere bed.

Fig. 3.14: The difference in $Q_{\max}$ in percent between the synced and centered profiles as a function of w_{total} for the parallel plate and packed sphere bed cases.

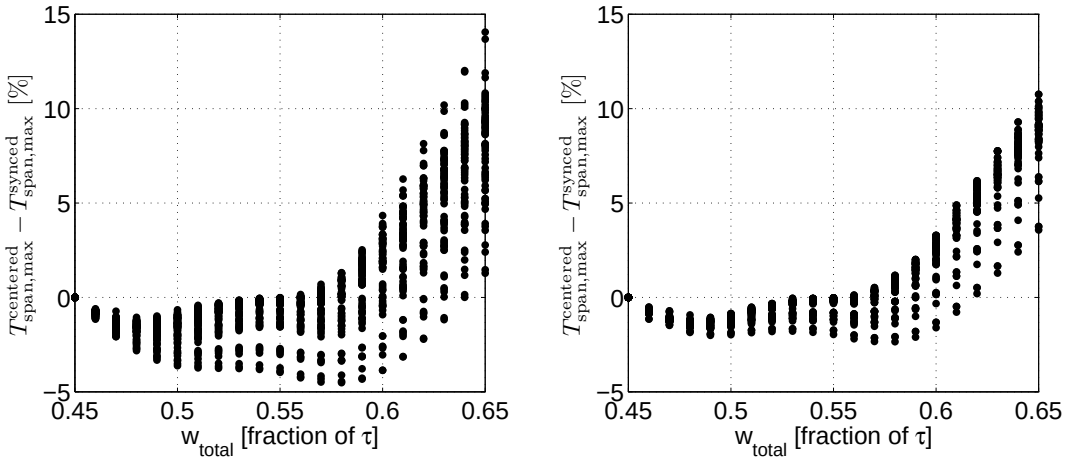

(a) Parallel plates.

(b) Packed sphere bed.

Fig. 3.15: The difference in $T_{\text{span,max}}$ in percent between the synced and centered profiles as a function of w_{total} for the parallel plate and packed sphere bed cases.

3.8 Summary

The influence of four different variables of the magnetic field on the performance of the AMR have been tested and the results are summed up in Table 3.3 where the impact on performance is given for variable of the magnetic field profile that was varied.

In general for each type of variable varied the relative change in performance was seen to be the same for all the different process parameters tested. For the fluid flow profile used here a magnetic field width of 0.55 was found to be optimum although a drop in performance of only 5% was seen if the value was decreased by ± 0.1 in fractions of τ. Also the drop in performance if the magnetic field was ramped slowly was less than 5%. This means that the change from zero to maximum field does not need to be fast. However, it was seen that it was very important to synchronize the fluid flow and magnetic field profiles, but this does not affect the design of the magnetic field profile. Finally, it was shown that $\dot{Q}_{\max}$ has a stronger dependency on $\mu_0 H_{\max}$ than $T_{\text{span,max}}$ and that these scale almost identically for the different process parameters. Also $T_{\text{span,max}}$ was seen to scale almost as a power law with an exponent that is slightly less than 2/3 as a function of the maximum value of the magnetic field.

Based on these findings we conclude that the performance of the AMR for different regenerator geometries and process parameters are the same as a function of magnetic field, which in turn means that the design of the magnet can be done independently of these.

Table 3.3: The performance of the different tested profiles for a magnetic field profile characterized by the value in the "Change" column relative to the performance of a profile with the value given by "Reference value" column. For the Width case (c) means the centered profiles and (s) means the synced profiles.

Case	Reference value	Change	Performance: parallel plate regenerator		Performance: packed bed regenerator	
			$Q_{\max}$	$T_{\text{span,max}}$	$Q_{\max}$	$T_{\text{span,max}}$
Sync.	$x_0 = 0$	x_0 = -0.1	60-75%	60-80%	60-75%	70-80%
		x_0 = 0.1	80-95%	80-95%	85-90%	90-95%
Ramp	Rate = 0.05	Rate = 0.005	96-100%	-	97-100%	-
		Rate = 0.1	96-98%	-	96-98%	-
Max. field	$\mu_0 H_{\max} = 1$ T	$\mu_0 H_{\max} = 0.5$ T	50%	60-70%	40-50%	60-70%
		$\mu_0 H_{\max} = 1.5$ T	140%	130%	130-150%	120-130%
Width (c)	$w_{\text{total}} = 0.55$	$w_{\text{total}} = 0.45$	90-95%	95-100%	90-95%	95-100%
		$w_{\text{total}} = 0.65$	90-100%	90-100%	95-100%	95-100%
Width (s)	$w_{\text{total}} = 0.55$	$w_{\text{total}} = 0.45$	85-95%	90-95%	90-95%	95-100%
		$w_{\text{total}} = 0.65$	80-90%	85-90%	80-90%	85-90%

Chapter 4

Magnet design for magnetic refrigeration

The magnet is a key component of a magnetic refrigeration system. However, so far the design of the magnet seems not to have been prioritized in most magnetic refrigeration devices and little research has been conducted to define the requirements, characterize and optimize the magnet design used in a magnetic refrigerator. This is even though the magnet is often the single most expensive part of a magnetic refrigerator, and it also contributes a significant part of the weight and bulk of the device.

In this chapter the requirements for a magnet used in a magnetic refrigeration device will be discussed based on the findings in the previous two chapters. The different ways that can be used to generate a magnetic field will be discussed in this context, and a novel way to characterize a magnet design will be introduced. To further understand how to design an optimal magnet existing published magnet designs will be compared in order to learn how to design more efficient magnetic structures. This analysis will also serve as a baseline for comparison with future magnet designs.

This chapter is partially based on the results described in Papers III and VII.

4.1 Magnet requirements

There are certain requirements that a magnet used in a magnetic refrigeration device must ideally meet. Preferably a magnet design must generate a high magnetic field over as large a volume as possible while using a minimum amount of magnet material. This is because a high field results in a large magnetocaloric effect, a large volume means that more magnetocaloric material can be subjected to the high field, thus increasing the cooling capacity of the refrigerator, and finally a minimum amount of magnet material must be used as this is both expensive and increases the weight and bulk of the device.

Unfortunately these requirements are contradictory as a large amount of magnet material is needed to generate a high field over a large volume. How to find a compromise between these factors are discussed in the coming sections.

Another requirement that influences the magnet design is that since the magnet is expensive it is important that the magnetic refrigerator itself is designed to continuously utilize the magnetic field generated by the magnet. This is as much a regenerator design issue as it is a magnet design one, but nevertheless some magnet designs allow for a higher utilization time than others. This is discussed in detail later in this chapter.

4.2 Generating a magnetic field

A magnetic field can be generated either by using a permanent magnet or by using an electromagnet. The latter can be subdivided into two categories, the superconducting and non-superconducting electromagnet. All of these three types have been utilized in magnetic refrigeration devices. The first magnetic refrigeration device built used a superconducting electromagnet (Brown, 1976), and other systems also using a superconducting electromagnet have since been built (Zimm et al., 1998; Blumenfeld et al., 2002; Richard et al., 2004; Rowe et al., 2005). Devices using a non-superconducting electromagnet have also been constructed (Bahl et al., 2008; Coelho et al., 2009) but the greater majority of devices built in recent years have used permanent magnets to generate the magnetic field (Lu et al., 2005; Shir et al., 2005a; Vasile and Muller, 2006; Zimm et al., 2006; Buchelnikov et al., 2007; Chen et al., 2007; Okamura et al., 2007; Tura and Rowe, 2007; Vuarnoz et al., 2007; Zimm et al., 2007; Coelho et al., 2009; Dupuis et al., 2009; Engelbrecht et al., 2009; Sari et al., 2009; Zheng et al., 2009).

Permanent magnets are preferred in magnetic refrigeration devices because they do not require power to generate a magnetic field and they can be geometrically small, allowing for a compact refrigerator design. Concerning the power requirement the permanent magnet must be compared to the electromagnet where a large amount of power is needed to generate e.g. a 1 T magnetic flux density in a reasonable volume. This can be seen from the relation between the current, I, and the generated flux density, B, for a solenoidal electromagnet in a single magnetic circuit consisting of a core of soft magnetic material with relative permeability[1], μ_{r}, and where the core has roughly the same cross sectional area throughout its length and the air gap is small compared with the cross sectional dimensions of the core,

$$NI = B\left(\frac{L_{\mathrm{core}}}{\mu_{\mathrm{r}}\mu_0} + \frac{L_{\mathrm{gap}}}{\mu_0}\right) , \tag{4.1}$$

where N is the number of turns in the winding, L_{core} is the length of the soft magnetic material, μ_0 is the permeability of free space and L_{gap} is the length of the air gap. In order to generate a 1.0 T magnetic flux density over e.g. a 30 mm air gap, which is typical for a magnetic refrigeration device, an iron cored solenoid with $\mu_{\mathrm{r}} = 4000$ would need to have 24000 ampere windings. The length of the soft magnetic material is irrelevant as the expression is dominated by the second term. Such an electromagnet with 24000 ampere windings would need a massive power supply and an equally massive cooler to prevent the solenoid from overheating. Based on this simple calculation it is seen why an electromagnet is not preferred in most magnetic refrigeration devices.

The superconducting electromagnet is a better option than the traditional electromagnet as it requires little power to operate once the electromagnet has become superconducting as no power is lost due to ohmic resistance. Although a superconducting electromagnet can create magnetic flux densities of the order of 10 T, continuous cooling is needed. This can be an expensive process and the apparatus surrounding the superconducting electromagnet can be substantial. However, for large scale applications, e.g. large refrigerators for warehouses etc., a superconducting electromagnet might be a relevant solution. For common household refrigeration the superconducting electromagnet is at present not an option.

Based on the above arguments it is seen why permanent magnets are used to generate the magnetic field in most magnetic refrigeration devices. For these reasons this thesis will focus

[1]The relative permeability is defined in the next section.

on the characterization and design of permanent magnet assemblies for magnetic refrigerators. The properties of permanent magnets are considered in the next section.

4.2.1 Properties of magnetic materials

A magnetic material is a material that has a magnetization, **M**, which is the magnetic moment per unit volume, that is different from zero. This magnetization can either be a response of the material when it is subjected to an external magnetic field or it can be a permanent property of the material. The fundamental quantity in magnetism is the vector **B**-field, here termed "the magnetic flux density" and denoted by the letter **B**. This is the quantity that appears in Maxwells equations for electromagnetism. However, inside magnetic materials one can define a new vector field that is the modification of **B** due to the magnetization of the material itself, be that a magnetization that is a result of the external **B** field or a permanent magnetization. This new vector field is termed "the magnetic field" and is denoted by the letter **H**. The magnetic flux density and the magnetic field inside a magnetic material are related by the magnetization through the relation

$$\mathbf{B} = \mu_0(\mathbf{H} + \mathbf{M}) \ . \tag{4.2}$$

This equation is the definition of **H**. In vacuum the quantities **B** and **H** are directly proportional as there is no magnetization. The constant of proportionality, called the permeability of free space, μ_0, is equal to $4\pi 10^{-7}$ N A^{-2}. The magnetic flux density is measured in tesla [T], while the magnetic field is measured in ampere per meter [A m^{-1}]. When the magnitudes of the different fields need be considered these are denoted B, H and M, respectively.

The relation given in Eq. (4.2) between the magnetic flux density and magnetic field is typically visualized as a $B(H)$ curve, i.e. the magnetic flux density of a given material as a function of magnetic field. For some magnetic materials the relation between B and H will not be a function, but will instead depend on the history of the material. If this is the case the material is said to show hysteresis. If the material retains its magnetization once the external magnetic field has been removed it is termed a "hard" magnetic material, while if little or no magnetization remains it is termed a "soft" magnetic material. A hard magnetic material is a permanent magnet. The difference between the two types of magnetic materials can be read directly from the $B(H)$ curve. The intersection of the $B(H)$ curve with the B-axis, i.e. $H = 0$, is called the remanence of the material, B_{rem}, and it is the magnetic flux density that the material produces even though it is not subjected to an external magnetic field. The point at which the curve intersects the H-axis, i.e. $B = 0$, is called the coercivity, H_{c} and at this point there will be no flux density inside the magnet. However, an even greater magnetic field might be required to reverse the direction of the magnetization. This is the point on an $M(H)$ curve where $M = 0$ and it is called the intrinsic coercivity, $H_{\mathrm{c,i}}$, and it is this property that is of interest for a permanent magnet. The properties of the magnet, also called the working point of the magnet, will lie somewhere along the $B(H)$ curve. The place in the second quadrant of the $B(H)$ curve where the product between B and $-H$ is greatest is called the maximum energy density and is the ideal working point for the magnet as here the energy density is greatest. The properties of a hard magnetic material are illustrated in Fig. 4.1.

The permeability, denoted $\mathbb{\mu}$ or μ, is the relation between **B** and **H**, i.e. $\mathbf{B} = \mathbb{\mu}\mathbf{H}$, where $\mathbb{\mu}$ is a tensor and a function of **H**, so that the magnetization of the material is contained within $\mathbb{\mu}$. The permeability is often given as the relative permeability, which is a dimensionless quantity

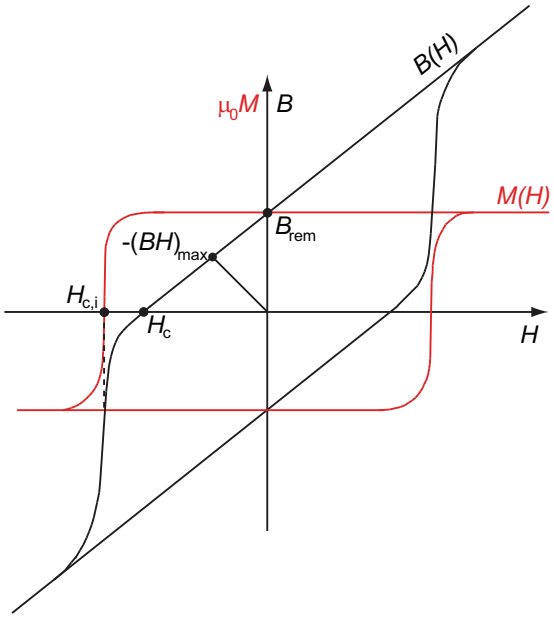

Fig. 4.1: An illustration of the properties of a hard magnetic materials. Both the $B(H)$ and $M(H)$ curve is shown. The remanence, the normal and intrinsic coercivities and the maximum working point, $-(BH)_{\max}$, are indicated on the figure.

defined as $\mu_r = \mu/\mu_0$. This relation between $\mathbf{B}$ and $\mathbf{H}$ is equivalent to defining a relation between the magnetization and the magnetic field as $\mathbf{M} = \chi_{\mathrm{m}}\mathbf{H}$ where χ_{m} is a tensor termed the susceptibility, and so $\mu = \mu_0(1 + \chi_{\mathrm{m}})$. Written as a tensor equation we have $M_i = \chi_{ij}H_j$ where i and j refer to the direction of the applied field and magnetization, respectively. The susceptibility, and likewise the permeability, is thus a tensor of rank 2 with dimension 3×3 that describes the component of magnetization and magnetic flux density, respectively, in the i-th direction from the external field applied in the j-th direction. Both the susceptibility and the permeability are almost always considered to be isotropic, in which case they are denoted μ_{r} and χ_{m} respectively. This is also the case for the remainder of this thesis.

The definition of the permeability and susceptibility are problematic for materials that display hysteresis. Here the magnetization and thus the susceptibility will be a function of both $\mathbf{H}$ and the history of the material and thus care must be taken when considering these materials.

If a material has a permanent magnetization, $\mathbf{M}_0$, and a susceptibility, χ_{m}, the net magnetization is given by

$$\mathbf{M} = \chi_{\mathrm{m}}\mathbf{H} + \mathbf{M}_0 \ . \tag{4.3}$$

Using this relation in Eq. (4.2) along with the definition of the permeability and the definition of the remanence as $\mathbf{B}_{\mathrm{rem}} = \mu_0\mathbf{M}_0$, one obtains the constitutive relation for magnetism,

$$\mathbf{B} = \mu_0\mu_{\mathrm{r}}\mathbf{H} + \mathbf{B}_{\mathrm{rem}} \ . \tag{4.4}$$

The boundary conditions for $\mathbf{B}$ for any surface is that the perpendicular component of $\mathbf{B}$

must be continuous across boundaries, while for **H** it is the parallel components that must be continuous.

An important thing to note is that a magnetostatic problem is scale invariant, i.e. if all dimensions are scaled by the same factor the magnetic field in a given point will be the same if this point is scaled as well. This means that quantities such as the average value and the homogeneity of the magnetic field in a scaled volume of space will be the same, as long as the magnet design is scaled appropriately.

4.2.2 Permanent magnets

As already stated a permanent magnet is simply a hard magnetic material, i.e. a material which has a remanence that is different from zero. However, certain magnetic properties are favorable in producing a large remanence. If the material has an anisotropy in its crystal structure this can favor alignment of the spins, resulting in a so called "easy axis" along which it is energetically favorable for the spontaneous magnetization to align. This increases the remanence if the material is magnetized along this axis. The strength of the anisotropy is characterized by the anisotropy field, which is the magnetic field that is necessary to completely align the magnetization away from the easy axis. The component of the magnetic field perpendicular to the easy axis is given by $K\sin^2(\phi)$, where K is the anisotropy constant and ϕ is the angle between the easy axis and the direction of magnetization.

If an anisotropic material is subjected to an external field that is larger than the intrinsic coercivity the magnetization will "tip" and go from pointing in one direction to pointing in the opposite direction, along the external magnetic field, as also seen in Fig. 4.1. The large value of the gradient in the $B(H)$ curve near the intrinsic coercivity is due to the anisotropy of the material.

For hard magnetic materials the definition of μ_r as B/H can be problematic. This is because for small values of H the material has a large value of B, due to its remanence, which means that μ_r is large. Also for $H = 0$ the value of μ_r is not defined. The solution is to define the relative permeability as $\mu_r = \frac{\partial B}{\partial H}$, also called the differential permeability, for hard magnetic materials.

The most powerful permanent magnet available today is made from an alloy of neodymium, iron and boron and is called the NdFeB magnet. All permanent magnet assemblies used in magnetic refrigerators use this type of magnet. This permanent magnet, which has the chemical composition $Nd_2Fe_{14}B$, has a tetragonal crystalline structure that has a very high anisotropy field of 8 T (Zimmermann, 1993). Other properties of NdFeB magnets are a high remanence of 1.2-1.4 T, an intrinsic coercivity that, depending on manufacturing process as well as the remanence of the magnet, can be as high as 3.2 T and a relative permeability of $\mu_r = 1.05$ (MMPA Standard, 2000). The second and a part of the third quadrant of the $B(H)$ and $M(H)$ curves for two different NdFeB permanent magnets, both made by Vacuumschmelze[2], are shown in Figs. 4.2 and 4.3. In general the properties of magnetic materials are functions of temperature, so the figures show the $B(H)$ and $M(H)$ curves for different temperatures. It is seen that the coercivity is a strong function of temperature. This means that care must be taken not to heat the magnets, as this can cause the direction of magnetization to "flip" and point in the opposite direction.

[2]Vacuumschmelze GMBH & Co. KG, Hanau, Germany

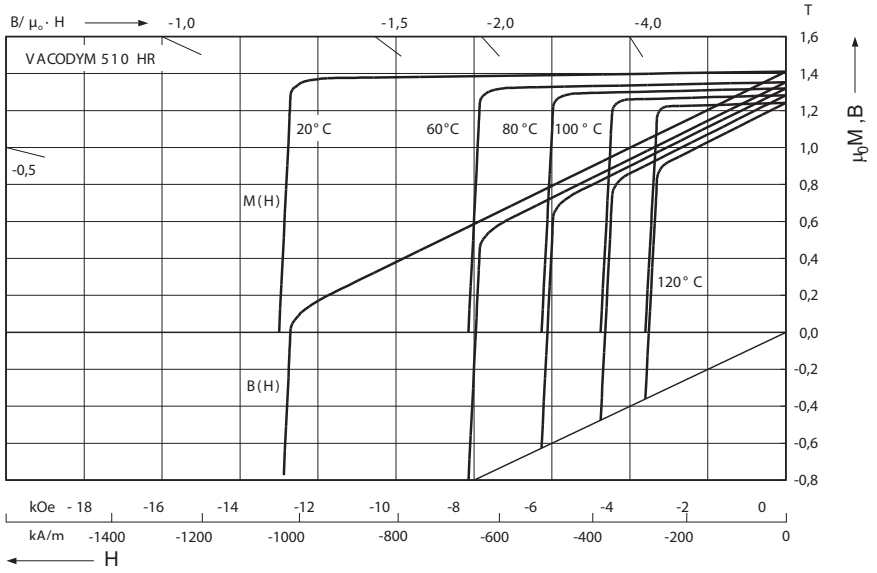

Fig. 4.2: The $B(H)$ and $M(H)$ curves for Vacodym® 510 HR, a high remanence, low coercivity permanent magnet (Vacuumschmelze GMBH & Co, KG, 2007).

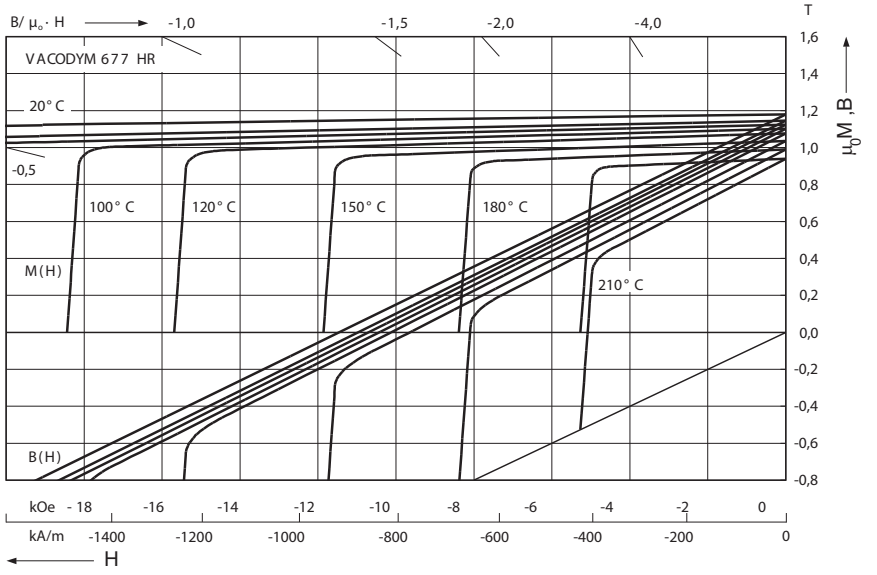

Fig. 4.3: The $B(H)$ and $M(H)$ curves for Vacodym® 677 HR, a permanent magnet with a lower remanence than Vacodym® 510 HR, but with a much higher coercivity (Vacuumschmelze GMBH & Co, KG, 2007).

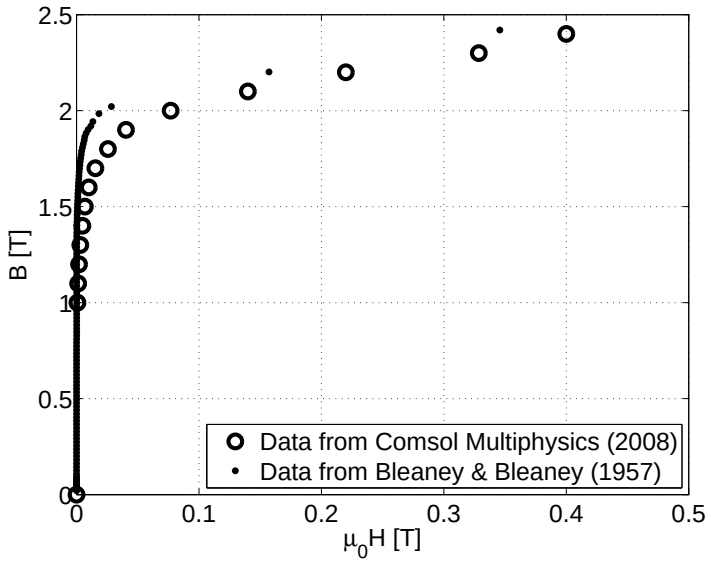

Fig. 4.4: The magnetic flux density as a function of the magnetic field for iron.

4.2.2.1 Soft magnetic materials

A soft magnetic material with a high permeability can be used in a magnetic assembly to guide the magnetic flux through the magnet assembly as well as shield part of the assembly and/or the surroundings from the generated flux density. Therefore a high permeability soft magnetic material is a constituent of almost all magnet assemblies used in magnetic refrigerators.

A high permeability soft magnetic material can also be used for other purposes in a magnet design. These will be described in Chapter 6.

A cheap and easy-to-work-with high permeability soft magnetic material is obviously preferable. The most commonly used high permeability soft magnetic material is iron. The $B(H)$ curve for iron obtained from Bleaney and Bleaney (1957) and Comsol Multiphysics (2008) is shown in Fig. 4.4. As can be seen from the figure iron responds extremely strongly to even a very small magnetic field. The relative permeability of iron is over 8000 at the peak value. Therefore iron is used as the soft magnetic material in almost all magnet assemblies used in magnetic refrigeration.

4.3 Characterizing a magnet design

To design an efficient magnet for use in magnetic refrigeration the advantages of different published magnet designs must be studied and compared to learn the properties of the best design. This is best done using a figure of merit that characterizes the performance of the magnet design. A previous suggestion for a comparison parameter was made by Nikly and Muller (2007) who defined the parameter

$$\xi = \frac{M_{\text{magnet}}}{M_{\text{magnet}} + M_{\text{MCM}}} \tag{4.5}$$

where M_{magnet} is the mass of the magnet and M_{MCM} is the mass of magnetocaloric material used in the device. This is not a useful parameter for two reasons: it contains no information about the magnetic flux density produced by the magnet design and using the same magnetic structure with two different magnetocaloric materials with different densities will yield different characterization results.

A general figure of merit, M^*, used to characterize a magnet design is defined by Jensen and Abele (1996) as

$$M^* = \frac{\int_{V_{\text{field}}} \mathbf{B}^{\ 2} dV}{\int_{V_{\text{mag}}} \mathbf{B}_{\text{rem}}^{\ 2} dV} \tag{4.6}$$

where V_{field} is the volume of the region where the magnetic field is created and V_{mag} is the volume of the magnets. It can be shown that the maximum value of M^* is 0.25, and a structure is considered reasonable efficient if it has $M^* \geq 0.1$.

The strength of the magnetic field that is generated can also be quantified by the dimensionless number (Coey and Ni Mhiochain, 2003)

$$K = \frac{\mathbf{B}}{\mathbf{B}_{\text{rem}}} \ . \tag{4.7}$$

For a two dimensional structure with completely uniform remanence and magnetic flux density the two numbers K and M^* are related by the expression

$$M^* = K^2 \frac{A_{\text{field}}}{A_{\text{mag}}} \ . \tag{4.8}$$

The figure of merit, M^*, often shown as a function of K, is useable for characterizing magnet designs in general, but for magnet designs used in magnetic refrigeration the parameter does not consider the flux density in the low field region of the magnet system where the MCM is placed when it is demagnetized. Also, the scaling of the MCE itself with magnetic field, which is not linear as was shown in Chapter 2, is not taken into account.

Finally, a general performance metric for magnetic refrigerators has been suggested (Rowe, 2009a). The cost and effectiveness of the magnet design is included in this metric as a linear function of the volume of the magnet, along with the generated flux density which is also included linearly. However, the metric does not make it possible to evaluate the efficiency of the magnet design alone.

Here we will characterize a magnet design by a new parameter, termed the Λ_{cool} parameter. This parameter is a figure of merit that depends on a number of different parameters related to the magnet assembly being evaluated.

The Λ_{cool} parameter is defined as

$$\Lambda_{\text{cool}} \equiv \left(\ (\mu_0 H)_{\text{high}}^{2/3} \ - \ (\mu_0 H)_{\text{low}}^{2/3} \ \right) \frac{V_{\text{field}}}{V_{\text{mag}}} P_{\text{field}} \ , \tag{4.9}$$

where V_{mag} is the volume of the magnet(s), V_{field} is the volume where the high field is generated, P_{field} is the fraction of time where magnetocaloric material is placed in the high field region, $(\mu_0 H)_{\text{high}}^{2/3}$ is the volume average of the field in the high field region to the power of 2/3 and $(\mu_0 H)_{\text{low}}^{2/3}$ is the volume average of the field to the power of 2/3 in the region where the

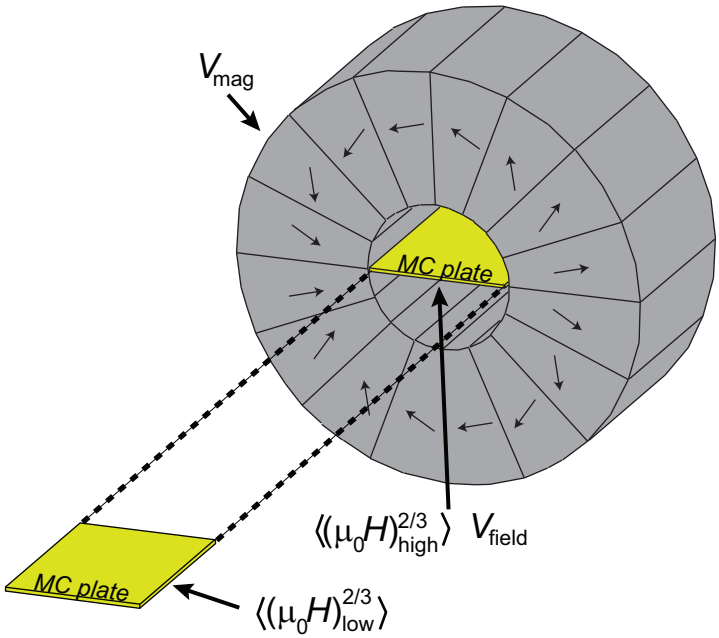

Fig. 4.5: An illustration of some of the different variables in the Λ_{cool} parameter for the case of a cylindrical magnet assembly called a Halbach cylinder, which is a hollow cylinder with a high magnetic field in the cylinder bore. Here the Halbach cylinder is segmented in 16 individual magnet pieces. The direction of magnetization of each segment is shown. A plate of magnetocaloric (MC) material is shown in both the high and low field regions.

magnetocaloric material is placed when it is being demagnetized. Some of these variables are illustrated for the case of a specific magnet design in Fig. 4.5.

The Λ_{cool} parameter depends on the magnetic field to the power of 2/3. The reason for this is that Λ_{cool} is defined to be proportional to the temperature change of a magnetocaloric material, and not the magnetic field, as the former is what is used to generate the temperature span and cooling power of the refrigeration device. As shown in Chapter 2 the temperature change scales with the magnetic field to the power of 2/3 at the Curie temperature in MFT. For actual materials the scaling might deviate from 2/3 but as long as the exponent is below 1 the conclusions based on the Λ_{cool} parameter remain substantially unchanged. Also, note that it was shown in Chapter 3 that the maximum temperature span of an AMR scales with an exponent only slightly below 2/3 with the maximum magnetic field. Finally, as it is the magnetic field generated in an empty volume that is considered $\mathbf{B} = \mu_0\mathbf{H}$, and thus it is equivalent to speak of the magnetic flux density or the magnetic field.

It is not only the field in the high field region that is of importance to the magnetocaloric effect. The field in the volume where the magnetocaloric material is placed when it is demagnetized is equally important. In order to maximize the magnetocaloric effect the field in this region must be as low as possible. In a reciprocating device this can of course be accomplished by simply moving the magnetocaloric material far away from the magnet, but this will increase the physical size and cycle time of the device. In a rotating device the high and low field re-

gions will generally be adjacent and care must be taken to minimize the "leak" of the magnetic field into the low field region. Also because of the 2/3 scaling of ΔT_{ad} with magnetic field even a small magnetic field in the low field region can reduce the adiabatic temperature change significantly.

To take into account the amount of magnetocaloric material that can experience a temperature change, the Λ_{cool} parameter is proportional to the volume of the high field region. Note that Λ_{cool} is proportional to the whole volume of the high field region and not only the volume occupied by the magnetocaloric material. Thus Λ_{cool} does not depend on the porosity of the magnetocaloric material, nor on the amount of e.g. plastic housing used to confine the magnetocaloric material. Also, Λ_{cool} is inversely proportional to the volume of magnet material used, as the more magnet material used the more expensive the design will be.

Finally, the Λ_{cool} parameter is proportional to the fraction of time in which magnetocaloric material is placed in the high field volume. The reason for this is that if, e.g., an AMR cycle lasts six seconds and magnetocaloric material is only placed inside the high field volume for three seconds, the (expensive) magnet is not utilized during the remaining half of the cycle and it is thus essentially being wasted during this time. The fraction of time the magnetic field generated by the magnet is being used to generate a magnetocaloric effect must be maximized.

One should note that the Λ_{cool} parameter will favor a design with a small magnetic field and a large volume of the high field region. This is because usually the magnetic field generated by a magnet scales with a power less than 2/3 with the volume of the magnet. In an actual device, heat transfer rates and thermal losses will set a lower limit on the field needed to produce a given temperature span and cooling capacity. Therefore, for practical applications, one would choose to maximize Λ_{cool} under the condition of a certain minimum field in the high field region.

The remanence of the magnets is not explicitly considered in the Λ_{cool} parameter. The reason for this is twofold. First this information is almost always not available for published magnet designs. Secondly the remanence of the NdFeB magnets used in all magnetic refrigeration magnet assemblies only varies between 1.2-1.4 T and so the exact value is not critical for comparison of different designs. Therefore, geometry accounts for almost all of the differences between different designs. Any soft magnetic material used in the magnet assembly is ignored, as the price of this material is in general much lower than that of the permanent magnets.

4.3.0.2 Example of a Λ_{cool} calculation

To give an example of how the Λ_{cool} parameter is calculated for a given magnet design, consider the design shown in Fig. 4.5. If the magnet has an inner radius of 20 mm, an outer radius of 50 mm and a length of 30 mm the total volume is $V_{\mathrm{mag}} = 0.198$ L. The high field region is the cylinder bore and this has a volume of $V_{\mathrm{field}} = 0.038$ L. The magnetic field in the bore must be measured, but here we assume a value of $(\mu_0 H)^{2/3}_{\mathrm{high}} = 0.6$ T. The magnetocaloric material is moved so far away from the cylinder that the field is essentially zero, so $(\mu_0 H)^{2/3}_{\mathrm{low}} = 0$ T. Finally, assume that the magnetocaloric material spends 5 seconds in the high field volume, is then moved for 1 second whereupon it spends another 5 seconds in the zero field volume and is then moved back again for 1 second. Thus $P_{\mathrm{field}} = \frac{5}{5+1+5+1} = 0.42$ if the magnet is not considered as being in use during the movement times. All in all $\Lambda_{\mathrm{cool}} = 0.048$ T$^{2/3}$. Whether this is a high value for Λ_{cool} can be seen by comparing with other magnet designs.

4.4 Published magnet designs

It is worth studying other published magnet designs to learn which designs are performing well and mostly of course *why* their performance is good. The Λ_{cool} parameter is ideally suited for this purpose. These magnet designs also provide a basis against which to compare new designs.

It should of course be remembered that all existing magnetic refrigerators are scientific test devices and this should be kept in mind when characterizing the associated magnet designs. However, it is also in the test design phase that large improvements to a design should be suggested. Therefore it is extremely relevant to compare and evaluate existing magnet designs, as this can potentially lead to improvements for both current and future magnet designs.

There exists a substantial number of published magnet designs for magnetic refrigerators but unfortunately many publications lack the necessary specifications to either reconstruct or directly calculate the Λ_{cool} parameter. Among these are the designs by Richard et al. (2004); Shir et al. (2005a); Zimm et al. (2006); Buchelnikov et al. (2007); Chen et al. (2007); Vuarnoz et al. (2007); Coelho et al. (2009); Dupuis et al. (2009); Sari et al. (2009). The designs presented in this section are the published designs that represents the main magnets configurations and where sufficient information has been obtained to calculate Λ_{cool}.

For all the designs given here an "ideal" device is considered when estimating the P_{field} parameter. In such a ideal device the time for moving either the magnet or the magnetocaloric regenerator is minimized. This has been chosen in order that the Λ_{cool} parameter will not depend on, e.g., the power of the motor in the device. An example is the rotating magnet design by Okamura et al. (2007), which is considered in detail later. Using the actual rotation speed of the magnet gives $P_{\text{field}} = 0.66$. However, using a more powerful motor would probably allow $P_{\text{field}} = 0.9$. In the calculation of Λ_{cool} for the given design the latter value has been used. The AMR cycle is assumed to be symmetric, i.e. the magnetization and demagnetization steps are assumed to take the same amount of time.

The designs reviewed here have been classified into three groups, depending on the complexity of the design. After all designs have been presented they are compared in Table 4.1.

4.4.1 Simple magnetic circuits

The designs presented in this subsection all have a simple geometric structure and consist of rectangular blocks of magnets.

4.4.1.1 Design by Zheng et al. (2009)

The general refrigerator design by Zheng et al. (2009) is a reciprocating design where the magnet is moving and two packed sphere beds of magnetocaloric material are kept stationary. When one of the beds is in the magnetic field the other bed is out of the field. The field in the design is provided by a single simple magnet and the field lines are guided by a soft magnetic material through a small air gap, as shown in Fig. 4.6. Based on Zheng (2009) the volume of the magnet is 0.5 L and the volume of the high field region is 0.09 L. The mean magnetic flux density is 0.93 T. The flux density as a function of distance out of the air gap is shown in Fig. 4.7. Based on the cycle time, movement speed of the beds and the distance between these, the actual P_{field} parameter is calculated to be 0.60. However, using a faster and more powerful motor to move the magnet, as well as considering that the magnet has to be moved across a finite distance between the beds where no magnetocaloric material is present, it is estimated that the P_{field} parameter could be as high as 0.90.

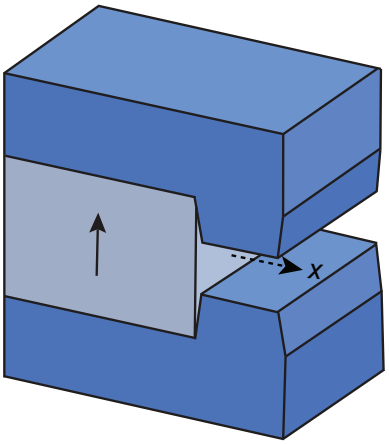

Fig. 4.6: The design by Zheng et al. (2009). From Zheng (2009). The full arrow indicates the direction of magnetization of the magnet. The blue structure consists of soft magnetic material. The magnetocaloric material is placed in the gap in the structure where the dotted arrow is shown.

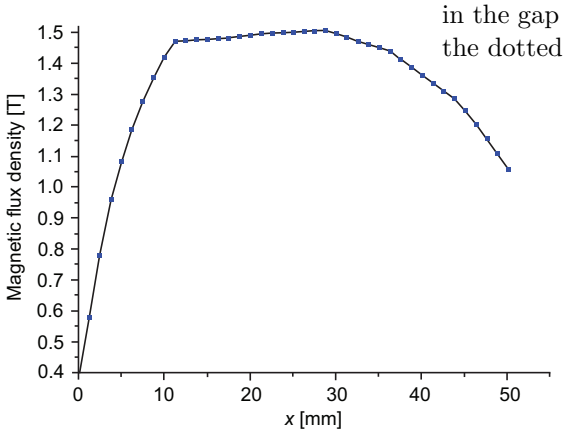

Fig. 4.7: A numerical simulation of the magnetic flux density along the line marked by x on Fig. 4.6. The numerical model assumes an infinite length. This is the reason for the large difference between the plotted flux density and the reported 0.93 T mean flux density given above. From Zheng et al. (2009).

4.4.1.2 Design by Vasile and Muller (2006)

The magnet design by Vasile and Muller (2006) is a "C" shaped magnet assembly of rectangular magnet blocks with soft magnetic material inside and outside of the "C" as seen in Fig. 4.8. In this design the magnets are rotating around a circle with inserts filled with magnetocaloric material. Only two dimensional specifications are given for the design. The cross sectional area of the magnets is estimated to be 9.2 L/m and the high field gap cross sectional area to be 0.75 L/m. The magnetic flux density is given as 1.9 T in the high field region, but this is based on a simulation of infinite length so a real world assembly would have a significantly lower value. As the magnets are rotating continuously and the inserts for the magnetocaloric material fill most of the circle along which the magnet is rotating P_{field} is estimated to be 0.90.

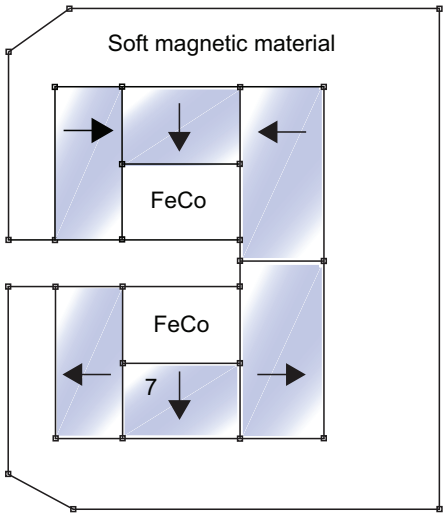

Fig. 4.8: After Vasile and Muller (2006). The arrows indicate the direction of magnetization of the magnets.

4.4.1.3 Design by Bohigas et al. (2000)

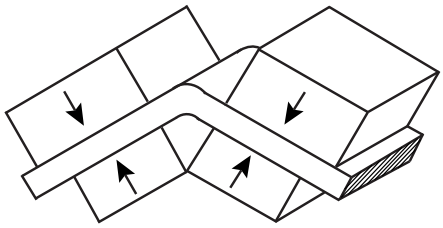

Fig. 4.9: The design by Bohigas et al. (2000).

The design by Bohigas et al. (2000) is a rotating design in which the magnets are stationary and the magnetocaloric material is rotated in and out of the high field region. A total of eight rectangular magnets are used, four of them placed on the inside of the rotating wheel and four placed outside the wheel. The design can be seen in Fig. 4.9. The dimension of one of the inner blocks is given as $40\times40\times20$ mm^3 and one of the outside blocks has dimensions $50\times50\times25$ mm^3. The size of the air gap is given to be 7 mm and there are a total of four air gaps. From these figures we estimate the dimensions of one air gap to be $40\times7\times20$ mm^3. Thus the volume of the magnets is 0.38 L and the volume of the high field region is 0.02 L. The flux density is given as 0.9 T. This design has magnetocaloric material continuously entering the high field region and thus the P_{field} parameter is 1.

4.4.1.4 Design by Tagliafico et al. (2009)

The magnet design by Tagliafico et al. (2009) is a rectangular structure which uses soft magnetic material to guide the field lines round through the magnetic circuit. The magnet has a slot $50 \times 9.5 \times 100$ mm^3 in the center, through which the magnetocaloric material is moved, as seen in Fig. 4.10. The volume of the high field region is thus 0.07 L. The flux density in the center of the slot is 1.55 T. A reported 5 kg of magnet is used, which corresponds to $V_{\text{mag}} = 0.68$ L. As two regenerative beds are run in parallel, and as the beds can be moved fairly quickly in and out of the high field region, the ideal P_{field} parameter is estimated to be 0.95. The actual value for the P_{field} parameter, which can be estimated based on the total cycle time, is very close to this figure.

Fig. 4.10: The magnet design by Tagliafico et al. (2009). The magnetocaloric material passes through the gap in the structure.

4.4.1.5 Design by Tušek et al. (2009)

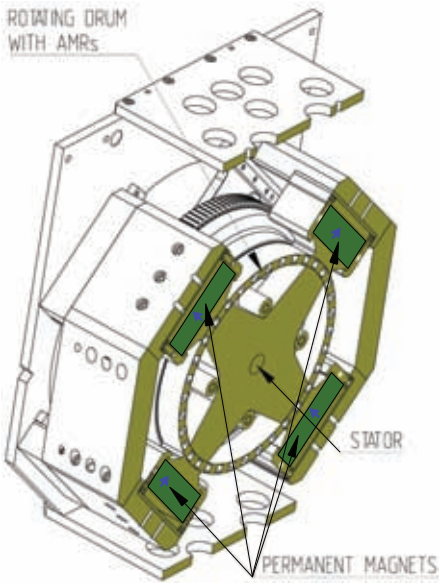

Fig. 4.11: The design by Tušek et al. (2009). The green structures consist of soft magnetic material while the dark green structures are magnets. The small blue arrows indicated the direction of magnetization. From Tušek et al. (2009).

The refrigeration system presented by Tušek et al. (2009) uses a rotating AMR and a stationary magnet system. The magnet system consists of an inner and outer magnetic circuit with the magnetocaloric material placed in between the two structures. There are four high field regions and four low field regions along the circumference between the inner and the outer structure. A drawing of the design can be seen in Fig. 4.11. The volume of the high field regions is four times $48 \times 10 \times 55$ mm^3, or 0.11 L. The amount of magnet material used is four times $90 \times 30 \times 90$ mm^3, or 0.65 L. The average mean flux density in the high field region is 0.97 T while it is 0.1 T in the low field region. The remanence of the magnets is 1.27 T. As magnetocaloric material is continuously rotated into the high field regions the magnets are constantly being used and thus $P_{\text{field}} = 1$.

4.4.2 Halbach type magnet assemblies

The magnetic structures presented in this subsection are all based on the Halbach cylinder design. The Halbach cylinder is a cylindrical magnetic structure with a bore along the cylinder symmetry axis and a direction of the remanence that at any point is given by $B_{\mathrm{rem},r} = B_{\mathrm{rem}}\cos(\phi)$ and $B_{\mathrm{rem},\phi} = B_{\mathrm{rem}}\sin(\phi)$ where B_{rem} is the magnitude of the remanent flux density and subscript r denotes the radial component of the remanence and subscript ϕ the tangential component (Mallinson, 1973; Halbach, 1980). The Halbach cylinder can be characterized by three parameters; the internal and external radii, R_{i} and R_{o} respectively, and the length, L. The Halbach cylinder is often divided into segments, each with their own direction of magnetization, in order to ease construction of the cylinder. Such a segmented cylinder was shown in Fig. 4.5. The properties of a general Halbach cylinder are considered in Chapter 5.

4.4.2.1 Design by Lee et al. (2002)

The magnet design by Lee et al. (2002) is suited to a reciprocating device with a stationary magnet and a moving bed of magnetocaloric material, but no actual device has been built. The magnet system is shaped like the letter "C", with a high homogeneous field in the center. The design resembles an 8 segmented Halbach cylinder where one of the horizontal segments has been removed. The flux density in the center is enhanced by blocks of soft magnetic material, placed in the center of the "C". An illustration of the design can be seen in Fig. 4.12. The cross sectional dimensions of the array are given as 114×128 mm^2, i.e. 14.6 L/m. The cross sectional area of the high field is estimated to be 25×12.7 mm^2, i.e. 0.32 L/m. The magnetic flux density is given to be 1.9 T in the high field region but this is based on a simulation of infinite length. Depending on the length of an actual device this figure will be significantly lower. No actual device has been built so P_{field} is simply taken to be 0.90.

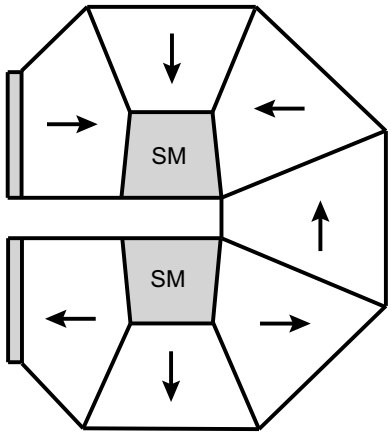

Fig. 4.12: The design by Lee et al. (2002). The blocks labeled "SM" consists of soft magnetic material.

4.4.2.2 Design by Engelbrecht et al. (2009)

The magnetic refrigeration test machine designed at Risø DTU is a reciprocating device in which plates of magnetocaloric material are moved in and out of a stationary magnet (Engelbrecht et al., 2009). The magnet is a Halbach cylinder consisting of 16 blocks of permanent magnets. The cylinder has an inner radius of 21 mm, an outer radius of 60 mm and a length of 50 mm. An illustration of the Halbach cylinder is shown in Fig. 4.13. The average magnetic flux density in the cylinder bore is 1.03 T. The volume of the magnet is 0.50 L and the volume of the high field region, i.e. the cylinder bore, is 0.07 L. The remanence of the magnets used in the Halbach cylinder is 1.4 T. The P_{field} parameter for this system design is 0.5. This is because half the cycle time the regenerator is out of the high field region leaving this empty. The actual P_{field} parameter is slightly less than 0.5 due to the finite velocity of the moving regenerator.

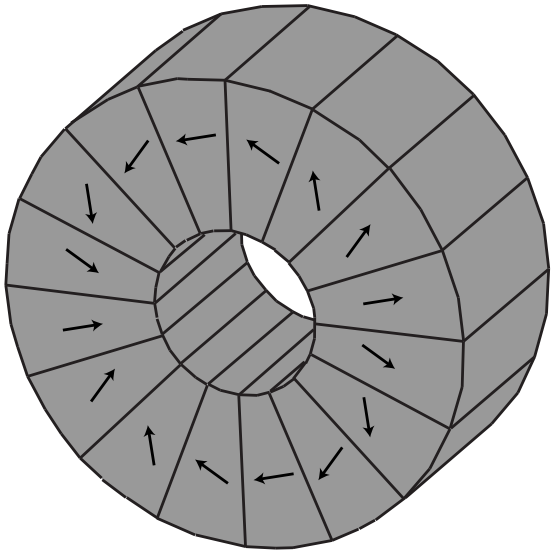

Fig. 4.13: The design by Engelbrecht et al. (2009). The Halbach cylinder has an inner radius of 21 mm, an outer radius of 60 mm and a length of 50 mm.

4.4.2.3 Design by Lu et al. (2005)

The magnetic refrigeration device designed by Lu et al. (2005) is a reciprocating device with two separate packed sphere beds of magnetocaloric material moving in and out of two stationary magnet assemblies to provide force compensation. Both magnets are 16 segmented Halbach cylinders with an inner radius of 15 mm and an outer radius of 70 mm. The flux density produced is given as 1.4 T, and the length of the cylinder is 200 mm. Given these numbers the volume of the magnet is 2.94 L and the volume of the high field region is 0.14 L, for either of the magnets. For the same reason as the design by Engelbrecht et al. (2009) the P_{field} parameter for this device is 0.5.

4.4.2.4 Design by Kim and Jeong (2009)

The magnet design by Kim and Jeong (2009) is a 16 segmented Halbach cylinder. A single bed of magnetocaloric material is reciprocated through the cylinder bore. The radius of the cylinder bore is 8 mm, the outer radius of the cylinder is 38 mm and the length is 47 mm. This means that the volume of the high field region is 0.01 L while the volume of the magnet is 0.20 L. The flux density is 1.58 T at the center of the bore and 1 T at the edge, with a mean value of 1.4 T. As only a single magnetocaloric bed is used the high field region is only used half the time and thus P_{field} is 0.5.

4.4.2.5 Design by Tura and Rowe (2007)

The magnetic refrigerator presented by Tura and Rowe (2007) is a rotating system in which the magnetocaloric material is kept stationary and a magnet is rotated to alter the field. The magnet design used in the device consists of two separate magnets each of which is a concentric Halbach cylinder. The reason that two separate magnets are used is that the system can be run such that the magnetic forces are balanced. In the concentric Halbach cylinder design the field in the inner cylinder bore can be controlled by rotating the inner or outer magnet. An illustration of the design can be seen in Fig. 4.14. Tura and Rowe (2007) report that when the inner magnet is rotated the mean magnetic flux produced can be changed continuously from 0.1 T to 1.4 T. The magnetic field generated by the individual Halbach magnets are shown in Fig. 4.15. The total volume of the magnetic material is 1.03 L, while the total volume of the high field region is 0.05 L (Rowe, 2009b). These values are for one of the concentric Halbach cylinders. The remanence of the blocks in the inner cylinder is 1.15 T while for the outer magnet it is 1.25 T. The P_{field} parameter for this system design is 0.5 as half of a cycle the inner magnet will be turned such that it cancels the magnetic field generated by the outer magnet. In this configuration there is no high field region, and the magnets are not being used to generate cooling.

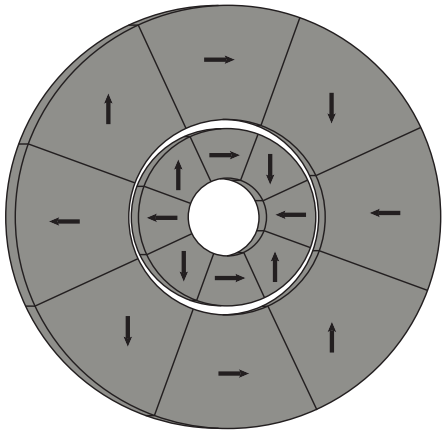

Fig. 4.14: A sketch of the concentric Halbach magnet design by Tura and Rowe (2007), viewed from the front. The inner and outer radius of the inner cylinder is 12.5 mm and 27 mm respectively while the corresponding figures for the outer cylinder is 30 mm and 60 mm respectively. The length of the actual concentric cylinder is 100 mm. The configuration shown here is the high field configuration.

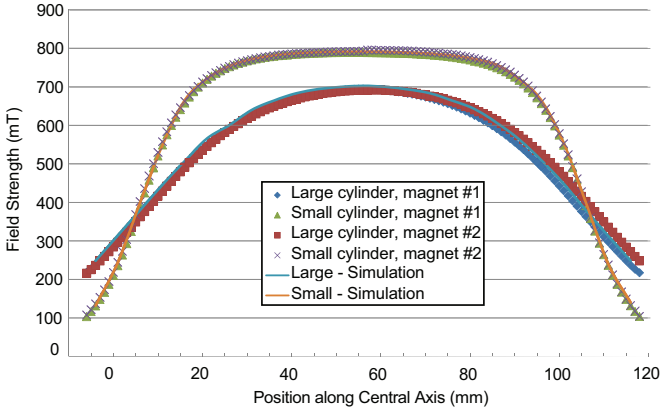

Fig. 4.15: The magnetic field generated by each of the two Halbach cylinders in the concentric Halbach cylinder design. From Rowe (2009b).

4.4.3 Complex magnetic structures

The designs presented in this subsection have a complex structure and consists of irregular shaped magnet blocks.

4.4.3.1 Design by Zimm et al. (2007)

The magnetic refrigeration machine presented by Zimm et al. (2007) utilizes a rotating principle in which the magnetocaloric material is stationary and the magnet is rotating. The magnet design is quite complex, utilizing both magnets and soft magnetic materials, but essentially consists of two double Y-shaped magnetic structures separated by an air gap. The design is shown in Fig. 4.16. The high field region spans an angle of 60 degrees on two opposite sides of the design, as also shown in Fig. 4.17. Based on Chell (2009) the total volume of the magnet assembly is 4.70 L, the volume of the high field region is 0.15 L and the mean flux density is 1.5 T. The P_{field} parameter for this design is essentially given by the speed at which the magnet rotates from one bed of magnetocaloric material to the next. These are separated by an angle of 30 degrees. If the magnet is rotated fast the P_{field} parameter could be as high as 0.90.

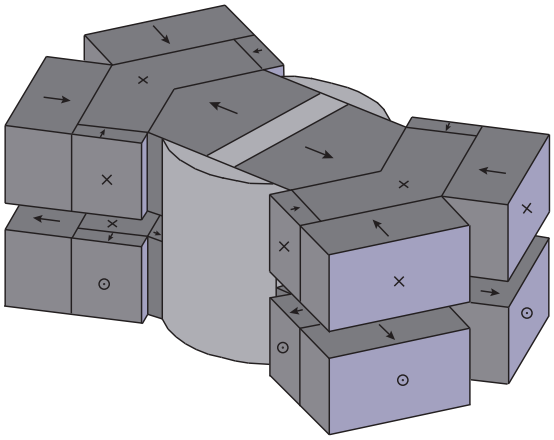

Fig. 4.16: The complex magnet design by Zimm et al. (2007). The magnetocaloric material passes through the gap between the upper and lower double "Y" structures. The dark grey blocks are individual magnets while the light grey structure is made of soft magnetic material. The direction of magnetization of the individual blocks are indicated as given in Chell and Zimm (2006).

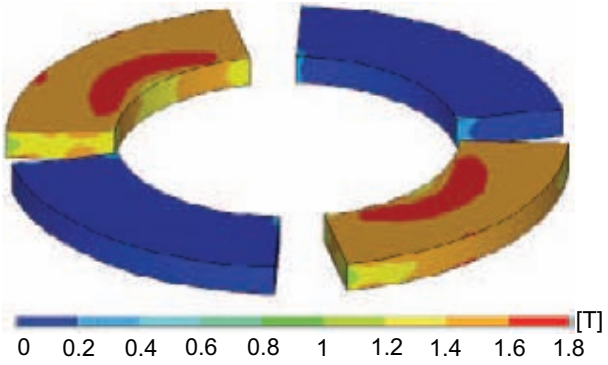

Fig. 4.17: The magnetic field generated by the magnet design. Adapted from Zimm et al. (2007).

4.4.3.2 Design by Okamura et al. (2007)

The design by Okamura et al. (2007) is a rotating device in which the magnet is rotated past ducts packed with magnetocaloric material. The magnet design consists of a complex arrangement of permanent magnets and soft magnetic materials which is assembled in the shape of an inner rotor consisting both of magnets and soft magnetic material with an outer yoke consisting of only soft magnetic material. The magnetocaloric material is placed in four ducts in the air gap between the inner and outer structure. The inner rotor is designed such that magnets with identical poles are facing each other and separated by a soft magnetic material. This increases the field and "pushes" the field lines from the inner rotor to the outer yoke. A photo of the design can be seen in Fig. 4.18, while a sketch of the design is shown in Fig. 4.19. The mean flux density is 1.0 T and the magnet design contains 3.38 L of magnet and 0.80 L of high field region (Okamura, 2009). As with the design by Zimm et al. (2007) the P_{field} parameter for this design is essentially given by the speed at which the magnet rotates from one duct to the next. The actual P_{field} parameter can be estimated using the total cycle time and the time to rotate between two ducts, separated by an angle of 40 degrees, and is found to be 0.66. However a faster rotation might be possible and thus we estimate that the P_{field} parameter can be as high as 0.90.

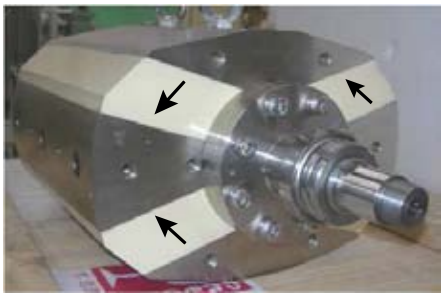

Fig. 4.18: The inner magnetic structure in the design by Okamura et al. (2007). From Okamura (2009). The outer magnetic structure consists of a cylinder of soft magnetic material. The arrows indicate the direction of magnetization of the magnets, which are white in color.

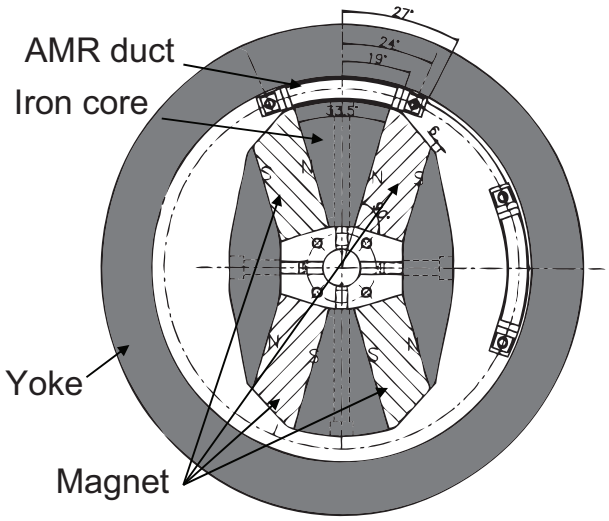

Fig. 4.19: A sketch of the magnetic design by Okamura et al. (2007). Only two of the fours ducts are shown.

Table 4.1: The specifications of different magnet designs used in magnetic refrigeration devices. In all cases it is assumed that $H^{2/3} = H^{2/3}$, which is only true if the field is completely homogeneous.
* designates a quantity estimated by the author of this thesis.
H indicates that the reported value of the field is the highest possible attainable field in the center of the design, and as such is not a representative average of the magnetic field for the whole of the high field region.
2D indicates that the field is based on a two dimensional simulation, i.e. with infinite length. These notoriously overestimate the field except for very long assemblies and so Λ_{cool} will be overestimated for these designs. Some of the two dimensional designs also have their volumes given per meter.

Name	V_{mag} [L]	V_{field} [L]	H_{high} [T]	H_{low} [T]	P_{field}	Magnet type	$\frac{\Lambda_{\text{cool}}}{P_{\text{field}}}$ [$T^{2/3}$]	Λ_{cool} [$T^{2/3}$]
Bohigas et al. (2000)	0.38	0.02	0.9^{H}	0*	1	Rectangular magnets on round surface	0.05	0.05
Engelbrecht et al. (2009)	0.50	0.07	1.03	0	0.5	Halbach cylinder	0.14	0.07
Kim and Jeong (2009)	0.20	0.01	1.4 0	0	0.5	Halbach cylinder	0.06	0.03
Lee et al. (2002)	14.6/m	0.32/m	$1.90^{H,2D}$	0*	0.9*	"C" shaped Halbach cylinder	0.03	0.03
Lu et al. (2005)	2.94	0.14	1.40^{H}	0	0.5	Halbach cylinder	0.06	0.03
Okamura et al. (2007)	3.38	0.80	1.00	0	0.9*	Inner magnet rotor, soft magnetic yoke	0.24	0.21
Tagliafico et al. (2009)	0.68	0.07	1.55^{H}	0	0.95	Rectangular magnetic circuit with slot	0.14	0.13
Tura and Rowe (2007)	1.03	0.05	1.40	0.1	0.5	Concentric Halbach cylinders	0.05	0.03
Tušek et al. (2009)	0.11	0.65	0.97	0.1	1.0	Stationary magnet, rotating MC material	0.13	0.13
Vasile and Muller (2006)	9.2/m	0.75/m	$1.90^{H,2D}$	0*	0.9*	"C" shaped circuit	0.12	0.11
Zheng et al. (2009)	0.50	0.09	0.93	0*	0.9*	Single magnet magnetic circuit	0.17	0.15
Zimm et al. (2007)	4.70	0.15	1.50	0.1*	0.9*	"Y" shaped magnetic structure	0.04	0.03

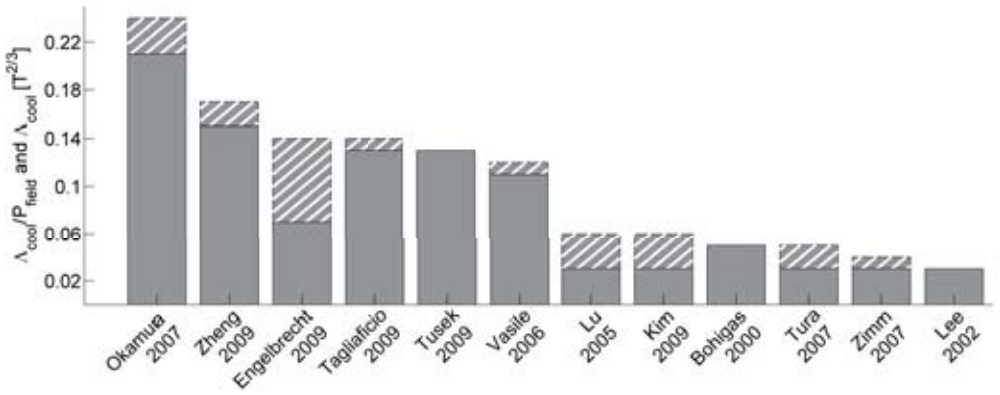

Fig. 4.20: The parameters $\Lambda_{\text{cool}}/P_{\text{field}}$ (hatched) and Λ_{cool} (full). The $\Lambda_{\text{cool}}/P_{\text{field}}$ parameter only takes the magnet design into account and not the fraction of time the magnet is used. As $P_{\text{field}} \leq 1$ the Λ_{cool} parameter is always less than or equal $\Lambda_{\text{cool}}/P_{\text{field}}$. Completely filled bars have $P_{\text{field}} = 1$. Note that the best design is five times as good as the design with the lowest value of $\Lambda_{\text{cool}}/P_{\text{field}}$.

4.5 Comparing the designs

In Table 4.1 the different magnet designs are presented. In the table the Λ_{cool} parameter has been calculated for each design, thus allowing for a direct comparison of the designs.

In Fig. 4.20 the parameter $\Lambda_{\text{cool}}/P_{\text{field}}$, which only takes the magnet assembly into account and not the design of the refrigeration device, as well as the actual Λ_{cool} parameter are shown. From the figure it is seen that the magnet design by Okamura et al. (2007) outperforms the remaining magnet designs. Compared to e.g. Lu et al. (2005) the design by Okamura et al. (2007) uses almost the same amount of magnets but creates a high field region that is more than three times larger. An interesting thing to note is that although the design by Zimm et al. (2007) creates a very high field the design has a rather low Λ_{cool} value because the adiabatic temperature change only scales with the magnetic field to the power of 2/3 at the Curie temperature and this, as mentioned previously, does not favor high fields. However, Λ_{cool} should be optimized under the condition of a certain minimum field in the high field region, e.g. the field required to obtain a given temperature span of the device. It is also seen that many of the reciprocating designs only utilize the magnet in half of the time, i.e. that the P_{field} parameter is 0.5, which is very inefficient. It is also seen that the different Halbach cylinders do not perform equally well. This is because the efficiency of a Halbach cylinder is strongly dependent on the relative dimensions of the cylinder, as will be discussed in Chapter 5.

Note that the actual magnetic refrigeration machines, when ranked by their temperature span and cooling capacity, do not necessarily follow the trend of Fig. 4.20 (Engelbrecht et al., 2007; Gschneidner Jr and Pecharsky, 2008; Rowe, 2009a). This can be caused by e.g. different types of magnetocaloric materials, different regenerator designs and different operating or process parameters.

An interesting thing to note concerning all the designs presented above is that in the original publications none of the designs are presented with a clear description of how the design was

initially envisioned and how it was optimized. All magnet designs presented so far for use in magnetic refrigeration are simply presented "as is", with no thoughts or a clear scientific method of design accompanying the design. The designs presented here have obviously been designed using a scientific process, but this is not described.

There is a natural limit to the effectiveness of a magnet design. The optimal design is limited by the energy density in the magnets themselves. Also a design can be limited by the intrinsic coercivity of the magnet if the magnetic field inside the magnet has a reverse direction compared to the magnetization. A standard grade NdFeB magnet with a remanence of 1.2 T has an intrinsic coercivity of $\mu_0 H_{\mathrm{c,i}} = 3.2$ T, so the reversal of the magnet will only be a problem above this flux density. One should note that for NdFeB magnets with a higher energy density, e.g. 1.4 T, the intrinsic coercivity can be significantly lower, e.g. around $\mu_0 H_{\mathrm{c,i}} = 1.4$ T.

4.5.1 Design of an optimal magnet assembly

Based on the knowledge gained from the magnet assemblies reviewed here certain key features that the magnet assembly must accomplish or provide can be stated. It must produce a region that has a high field preferably with as high uniformity as possible. Also the magnet must be designed such that the amount of leakage of field and stray field is as low as possible. This includes both leakage to the surroundings and leakage to low field regions in the magnet assembly. The recommendations to maximize Λ_{cool} for a given field can be summed up as

- Use the minimum amount of magnets
- Make the volume for the regenerator as large as possible
- Utilize the magnet at all times
- Ensure that the field in the low field region is low
- Minimize leakage to surrounding by e.g. using soft magnetic material as field guides
- Use the lowest possible field necessary to obtain the chosen operating parameters

Some of these criteria relate directly to the magnet design while others relate to the machine design. The recommendations might seem fairly straight forward, and it would obviously be more interesting if more general advise on e.g. how to "Use the minimum amount of magnets" could be presented. However, this will in general depend on the actual magnet design. In Chapter 6 a more general way to limit the amount of magnet used for a given design is presented, but this method does not necessarily turn a bad design into a good one. The reviewed designs will serve as a baseline for comparing designs proposed later in this thesis.

Chapter 5

The Halbach cylinder

As shown in Chapter 4 numerous magnet designs are used in magnetic refrigeration devices. However, a certain design is quite frequently used and also serves as a basis for more complicated designs. This design, which was briefly introduced in Chapter 4, is the Halbach cylinder. This chapter focuses on the design and characteristics of the Halbach cylinder, aiming to provide a deeper understanding of magnet designs in general and magnet designs similar to the Halbach cylinder specifically. Such an understanding would hopefully allow the use of more efficient magnets in magnetic refrigeration.

This chapter is partially based on the results described in Papers I and VI.

5.1 Introduction

The Halbach cylinder (Mallinson, 1973; Halbach, 1980) (also known as a hole cylinder permanent magnet array (HCPMA)) is a hollow permanent magnet cylinder with a remanent flux density at any point that varies continuously as

$$\begin{aligned} B_{\mathrm{rem},r} &= B_{\mathrm{rem}} \cos(p\phi) \\ B_{\mathrm{rem},\phi} &= B_{\mathrm{rem}} \sin(p\phi) \, , \end{aligned} \tag{5.1}$$

where B_{rem} is the magnitude of the remanent flux density and p is an integer. Subscript r denotes the radial component of the remanence and subscript ϕ the tangential component. A positive value of p produces a field that is directed into the cylinder bore, called an internal field, and a negative value produces a field that is directed outwards from the cylinder, called an external field. When the Halbach cylinder was first introduced in Chapter 4 only a remanence with $p = 1$ was considered. In this chapter the more general type of remanence is considered. In Fig. 5.1 four Halbach cylinders with different values of p are shown. The angle ϕ is also shown.

The Halbach cylinder is an interesting magnet design because it is able to generate a homogeneous flux density that is larger than the remanence of the permanent magnets used in the design, as will be shown later in this chapter. Also, the design is well defined geometrically and its dimensions can easily be adapted to the wanted experiment.

In this chapter the Halbach cylinder will be investigated in detail. This is done because the Halbach cylinder is already used in a number of magnetic refrigeration devices, as was seen in Chapter 4, and these devices would benefit from an additional knowledge of Halbach cylinders. Also, the Halbach cylinder is used in a range of other scientific areas, such as nuclear magnetic resonance (NMR) apparatus (Appelt et al., 2006) and accelerator magnets (Lim et al., 2005), and as such the results presented in this chapter will be of general interest to the scientific community.

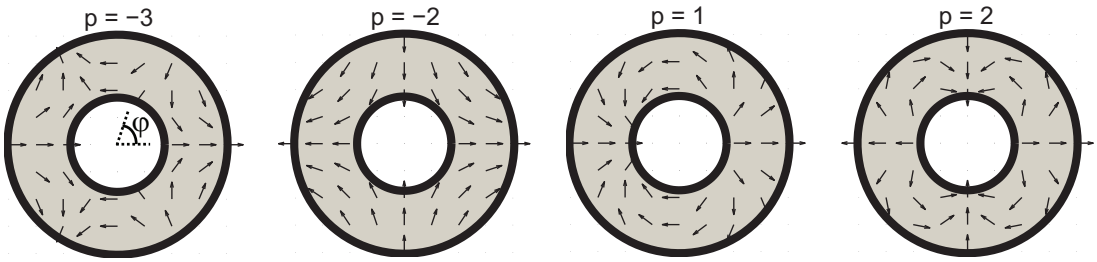

Fig. 5.1: The remanence of a $p = -3$, $p = -2$, $p = 1$ and $p = 2$ Halbach cylinder. The angle ϕ from Eq. (5.1) is also shown.

The properties of the Halbach cylinder will be studied through an analytical derivation of the magnetic field of the Halbach cylinder as well as numerical simulations of the same. Before the Halbach cylinder is discussed the numerical modeling of magnetic materials and the simulation software used in this thesis are considered.

5.2 Modeling magnetism

The numerical modeling of magnetism performed in this thesis is done using the commercially available finite element multiphysics program *Comsol Multiphysics*[1]. The Comsol Multiphysics code has previously been validated through a number of NAFEMS (National Agency for Finite Element Methods and Standards) benchmark studies (Comsol Multiphysics, 2005). Comsol was chosen as the simulation software for its finite element capabilities as well as its ability to solve both two and three dimensional problems and for the ease with which the model geometry can be constructed.

The systems modeled in this thesis are static problems in magnetism, i.e. magnetostatics. In these systems the magnetic flux density, $\mathbf{B}$, and the magnetic field, $\mathbf{H}$, are not functions of time but only of position. For a given system considered here there are no currents and the remanent flux density, $\mathbf{B}_{\mathrm{rem}}$, is known as a function of position and can be used as an initial condition to solve the system.

As previously found in Chapter 4 the relation between the magnetic flux density and the magnetic field is given as

$$\mathbf{B} = \mu_0 \mu_{\mathrm{r}} \mathbf{H} + \mathbf{B}_{\mathrm{rem}} \ , \tag{5.2}$$

where μ_0 is the permeability of free space and μ_r is the relative permeability, which is considered isotropic.

From one of the Maxwell equations in matter, $\times \mathbf{H} = \mathbf{J}_f + \frac{\partial \mathbf{D}}{\partial t}$, where $\mathbf{J}_f$ is the free volume current density and $\mathbf{D}$ is the electric displacement it is seen that if there are no currents or electric fields in the system the magnetic field will have a curl of zero,

$$\times \mathbf{H} = 0 \ . \tag{5.3}$$

[1]Comsol Multiphysics AB, Stockholm, Sweden.

This implies that the magnetic field can be described completely from a scalar potential, called the magnetic scalar potential, V_{m}, which is defined as

$$- \quad V_{\mathrm{m}} \equiv \mathbf{H} \ . \tag{5.4}$$

Using this definition in Eq. (5.2) and applying the divergence operator while at the same time remembering the Maxwell equation, $\quad \cdot \mathbf{B} = 0$, one gets the magnetic scalar potential equation, which is a Poisson equation,

$$- \quad \cdot (\mu_0 \mu_r \quad V_{\mathrm{m}} - \mathbf{B}_{\mathrm{rem}}) = 0 \ . \tag{5.5}$$

This is the equation that is solved in the numerical simulations. The relative permeability is in all cases assumed to be isotropic, but it can of course be either constant or a function of magnetic field, in which case the solution is automatically iterated until convergence is reached.

The equation Eq. (5.5) is solved on a finite element mesh, as this can provide high resolution near geometric connections, e.g. corners. The solver used to solve Eq. (5.5) on the simulation mesh is *Pardiso* which is a parallel sparse direct linear solver (Schenk et al., 2001; Schenk and Gärtner, 2002).

Boundary conditions are chosen such that the boundaries of the computational volume, which is many times larger than the simulated magnetic structure, are magnetically insulating, i.e. $\hat{\mathbf{n}} \cdot \mathbf{B} = 0$, where $\hat{\mathbf{n}}$ is the surface normal, while for all other (internal) boundaries the magnetic boundary conditions apply, i.e. the perpendicular component of $\mathbf{B}$ and the parallel components of $\mathbf{H}$ are continuous across boundaries. With the chosen exterior boundary condition it is important that the computational volume is large enough that the insulating boundaries do not affect the calculations. In general both the size of the computational volume and the mesh has been chosen fine enough that the simulation results does not depend on these.

5.2.1 Modeling magnetic materials

The permanent magnets are modeled as NdFeB magnets with a relative isotropic permeability of $\mu_r = 1.05$ which is taken to be constant unless otherwise stated. The direction of the remanence is fixed, which is only valid if the anisotropy field is very large and if the component of $\mathbf{H}$ that is parallel and opposite to $\mathbf{B}_{\mathrm{rem}}$ is less than the intrinsic coercivity as mentioned in Chapter 4. For an NdFeB magnet the intrinsic coercivity can be as high as 3.2 T and the anisotropy field has a value of 8 T (Zimmermann, 1993), thus this modeling approach is justified.

A soft magnetic material is modeled by the relation $\mathbf{B} = \mu(\ \mathbf{H}\ )\mathbf{H}$, where μ is the isotropic permeability. The soft magnetic material used in the simulations throughout this thesis is iron, as it is both cheap and have an extraordinarily high permeability, as also shown in Chapter 4. The data used are the Comsol Multiphysics data plotted in Fig. 4.4. For values outside the data range a linear extrapolation scheme has been used.

5.3 The ideal Halbach cylinder

Having described how to model a magnetostatic problem we now consider the Halbach cylinder. We begin by considering the ideal Halbach cylinder. The term "ideal" refers to a two dimensional, i.e. infinitely long, Halbach cylinder with a remanence as given by Eq. (5.1). In the remainder of this thesis all models referred to as two dimensional are assumed to be infinitely long. Such a Halbach cylinder is geometrically characterized by two parameters: the internal radius, R_{i}, and the external radius, R_{o}.

For modeling purposes, as well as to characterize and evaluate the effectiveness of the Halbach cylinder design, we wish to determine the magnetic flux density produced by an ideal Halbach cylinder. There already exist several publications where the magnetic field and flux density for some parts of a Halbach cylinder are calculated (Zhu et al., 1993; Atallah et al., 1997; Peng et al., 2003; Xia et al., 2004), but a complete spatial calculation has previously not been presented.

5.3.1 Defining the magnetostatic problem

The magnetic flux density produced by an ideal Halbach cylinder can be found analytically by defining the problem in terms of the magnetic vector potential, $\mathbf{A}$.[2]

The relation between the magnetic flux density and the magnetic vector potential is

$$\mathbf{B} = \quad \times \mathbf{A} \ . \tag{5.6}$$

Using this relation in Eq. (5.2) and applying the curl operator on both sides on the equation gives

$$\times (\quad \times \mathbf{A}) = \quad \times \mathbf{B}_{\mathrm{rem}} \ , \tag{5.7}$$

if there are no currents present as then $\quad \times \mathbf{H} = 0$. Remembering that $\quad \times (\quad \times \mathbf{A}) = (\quad \cdot \mathbf{A}) - \quad ^2\mathbf{A}$ and choosing the Lorenz gauge, i.e. $\quad \cdot \mathbf{A} = 0$, for the magnetic vector potential we get

$$- \quad ^2\mathbf{A} = \quad \times \mathbf{B}_{\mathrm{rem}} \ . \tag{5.8}$$

For the ideal, i.e. two dimensional, case considered here the vector potential only has a z-component, A_z, and the above equation, using Eq. (5.1), is reduced to

$$- \quad ^2A_z(r,\phi) = \frac{B_{\mathrm{rem}}}{r} \ (p+1) \sin(p\phi) \ . \tag{5.9}$$

This differential equation constitutes the magnetic vector potential problem for the Halbach cylinder and must be solved. In the air region of the problem the right hand side reduces to zero as $B_{\mathrm{rem}} = 0$ here.

Once A_z has been determined Eq. (5.6) can be used to find the magnetic flux density. Afterwards the magnetic field can be found through Eq. (5.2).

[2] One might equally well have defined the problem in terms of the magnetic scalar potential, V_{m}, if no currents are present, as was done for the modeling approach. The solution, i.e. the magnetic field and flux density, are of course independent of whether V_{m} or $\mathbf{A}$ are used.

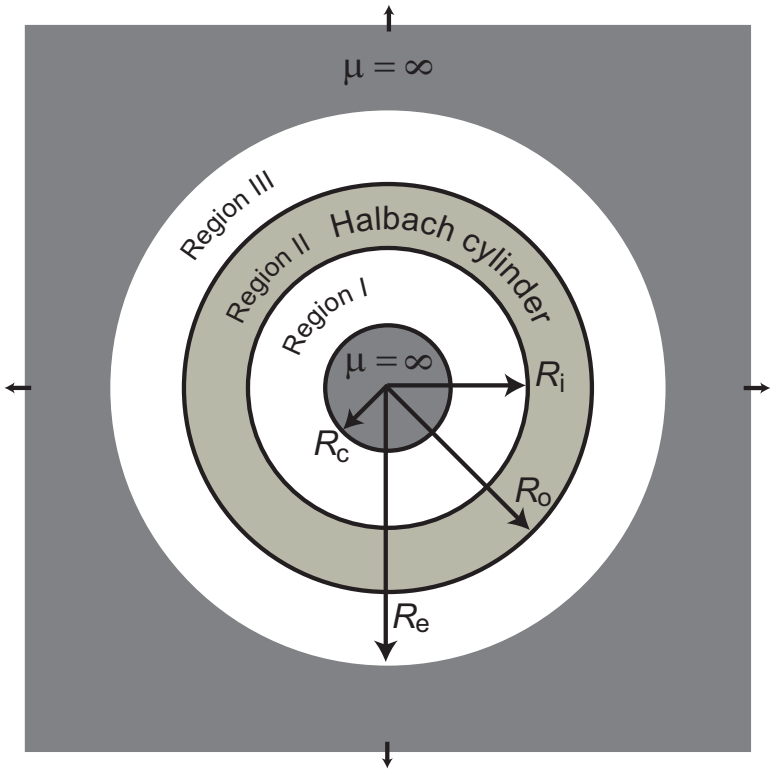

Fig. 5.2: A Halbach cylinder with internal radius R_i and external radius R_o enclosing an infinitely permeable cylinder with radius R_c while itself being enclosed by another infinitely permeable cylinder with internal radius R_e and infinite external radius. The regions marked I and III are air gaps.

5.3.2 Geometry of the problem

Having found the equation governing the magnetostatic problem of the Halbach cylinder we now take a closer look at the geometry of the problem. Following the approach of Xia et al. (2004) we will start by solving the problem of a Halbach cylinder enclosing a cylinder of an infinitely permeable soft magnetic material, while at the same time itself being enclosed by another such cylinder. This is the situation depicted in Fig. 5.2. The Halbach cylinder has an internal radius of R_i and an external radius of R_o and the inner infinitely permeable cylinder has a radius of R_c while the outer enclosing cylinder has an internal radius of R_e and an infinite external radius. The problem of a Halbach cylinder in air will be solved subsequently, by letting R_c 0 and R_e . The use of the soft magnetic cylinders results in a well-defined set of boundary equations as will be shown later. Of course, one can also solve directly for the Halbach cylinder in air using the boundary conditions specific for this case.

When solving the magnetostatic problem three different expressions for the magnetic vector potential, field and flux density will be obtained, one for each of the three different regions shown in Fig. 5.2. The geometry of the problem results in six boundary conditions. The requirement is, as stated previously, that the perpendicular component of $\mathbf{B}$ and the parallel

components of **H** are continuous across boundaries. Here this results in the following boundary conditions,

$$\begin{aligned} H_\phi^I &= 0 && r = R_\mathrm{c} \\ B_r^I &= B_r^{II} && r = R_\mathrm{i} \\ H_\phi^I &= H_\phi^{II} && r = R_\mathrm{i} \\ B_r^{III} &= B_r^{II} && r = R_\mathrm{o} \\ H_\phi^{III} &= H_\phi^{II} && r = R_\mathrm{o} \\ H_\phi^{III} &= 0 && r = R_\mathrm{e}\ . \end{aligned} \tag{5.10}$$

The two equations for $H_\phi = 0$ come from the fact that the soft magnetic material has an infinite permeability.

5.3.3 Solution for the vector potential

The solution to the vector potential equation, Eq. (5.9), is the sum of the solution to the homogeneous equation and a particular solution. The solution is

$$A_z(r,\phi) = \sum_{n=1} (\mathcal{A}_n r^n + \mathcal{B}_n r^{-n})\sin(n\phi) + B_\mathrm{rem}\frac{r}{p-1}\sin(p\phi)\ , \tag{5.11}$$

where $\mathcal{A}_n$ and $\mathcal{B}_n$ are constants that differ for each different region and are different for each n. Using the boundary conditions for the geometry defined above one can show that these are only nonzero for $n = p$. This is shown in Appendix A.

The solution for the defined geometry then becomes

$$A_z(r,\phi) = (\mathcal{A} r^p + \mathcal{B} r^{-p})\sin(p\phi) + B_\mathrm{rem}\frac{r}{p-1}\sin(p\phi)\ , \tag{5.12}$$

where $\mathcal{A}$ and $\mathcal{B}$ are constants that differ for each different region and that are determined by the boundary conditions.

The solution is not valid for $p = 1$. For this special case the solution to Eq. (5.9) is instead

$$A_z(r,\phi) = (\mathcal{A} r + \mathcal{B} r^{-1})\sin(\phi) - B_\mathrm{rem} r \ln(r)\sin(\phi)\ , \tag{5.13}$$

where $\mathcal{A}$ and $\mathcal{B}$ are defined like in Eq. (5.12).

Note that for $p = 0$ we have that $B_{\mathrm{rem},r} = B_\mathrm{rem}$ and $B_{\mathrm{rem},\phi} = 0$ in Eq. (5.1). This means that $A_z = 0$ and consequently **B** is zero everywhere. The magnetic field, **H**, however, will be nonzero inside the magnet material itself, i.e. in region II, but will be zero everywhere else.

We now derive the constants in Eq. (5.12) and (5.13) directly from the boundary conditions.

5.3.4 Deriving the vector potential constants

The constants of the vector potential equation can be derived from the boundary conditions specified in Eq. (5.10). First we note that the magnetic flux density and the magnetic field can be calculated from the magnetic vector potential as

$$\begin{aligned} B_r = \frac{1}{r}\frac{\partial A_z}{\partial \phi} \quad &, \quad B_\phi = -\frac{\partial A_z}{\partial r} \\ H_r = \frac{1}{\mu_0\mu_r}(B_r - B_{\mathrm{rem},r}) \quad &, \quad H_\phi = \frac{1}{\mu_0\mu_r}(B_\phi - B_{\mathrm{rem},\phi}) \end{aligned} \tag{5.14}$$

Using the vector potential in either Eq. (5.12) or (5.13) we get

$$
\begin{aligned}
B_r &= \begin{cases} p\mathcal{A}r^{p-1} + p\mathcal{B}r^{-p-1} + B_{\rm rem}\frac{p}{p-1}\ \cos(p\phi) & p=1 \\ \left[\mathcal{A} + \mathcal{B}r^{-2} - B_{\rm rem}\ln(r)\right]\cos(\phi) & p=1 \end{cases} \\
B_\phi &= \begin{cases} -p\mathcal{A}r^{p-1} + p\mathcal{B}r^{-p-1} - B_{\rm rem}\frac{1}{p-1}\ \sin(p\phi) & p=1 \\ \left[-\mathcal{A} + \mathcal{B}r^{-2} + B_{\rm rem}(\ln(r)+1)\right]\sin(\phi) & p=1 \end{cases} \\
H_r &= \begin{cases} \frac{p}{\mu_0\mu_r}(\mathcal{A}r^{p-1} + \mathcal{B}r^{-p-1}) + \frac{B_{\rm rem}}{\mu_r\mu_0}\left(\frac{p}{p-1} - 1\right)\ \cos(p\phi) & p=1 \\ \frac{1}{\mu_0\mu_r}\left[\mathcal{A} + \mathcal{B}r^{-2} - B_{\rm rem}(\ln(r)+1)\right]\cos(\phi) & p=1 \end{cases} \\
H_\phi &= \begin{cases} \frac{p}{\mu_0\mu_r}(-\mathcal{A}r^{p-1} + \mathcal{B}r^{-p-1}) - \frac{B_{\rm rem}}{\mu_r\mu_0}\left(\frac{1}{p-1} - 1\right)\ \sin(p\phi) & p=1 \\ \frac{1}{\mu_0\mu_r}\left[-\mathcal{A} + \mathcal{B}r^{-2} + B_{\rm rem}\ln(r)\right]\sin(\phi) & p=1 \end{cases}
\end{aligned}
\tag{5.15}
$$

Using the radial component of the magnetic flux density and the tangential component of the magnetic field in the set of boundary equations we get a set of six equations containing the six unknown constants, two for each region. The constants $\mathcal{A}$ and $\mathcal{B}$ will be termed $\mathcal{A}^I$ and $\mathcal{B}^I$ in region I, $\mathcal{A}^{II}$ and $\mathcal{B}^{II}$ in region II, and $\mathcal{A}^{III}$ and $\mathcal{B}^{III}$ in region III, respectively.

Introducing the following new constants

$$
a = \frac{R_{\rm e}^{2p} - R_{\rm o}^{2p}}{R_{\rm e}^{2p} + R_{\rm o}^{2p}} \qquad\qquad b = -\frac{R_{\rm i}^{2p} - R_{\rm c}^{2p}}{R_{\rm i}^{2p} + R_{\rm c}^{2p}}\ , \tag{5.16}
$$

the constants are determined to be

$$
\begin{aligned}
\mathcal{A}^{II} &= \begin{cases} -\mathcal{B}^{II}\frac{\mu_r a-1}{\mu_r a+1}R_{\rm o}^{-2p} - \frac{B_{\rm rem}}{p-1}R_{\rm o}^{1-p} & p=1 \\ -\mathcal{B}^{II}\frac{\mu_r a-1}{\mu_r a+1}R_{\rm o}^{-2} + B_{\rm rem}\ \ln(R_{\rm o}) & p=1 \end{cases} \\
\mathcal{B}^{II} &= \begin{cases} -\left(\frac{\mu_r a-1}{\mu_r a+1}R_{\rm o}^{-2p} - \frac{\mu_r b-1}{\mu_r b+1}R_{\rm i}^{-2p}\right)^{-1}(R_{\rm o}^{1-p} - R_{\rm i}^{1-p})\frac{B_{\rm rem}}{p-1} & p=1 \\ -\left(\frac{a\mu_r-1}{a\mu_r+1}R_{\rm o}^{-2} - \frac{\mu_r b-1}{\mu_r b+1}R_{\rm i}^{-2}\right)^{-1}B_{\rm rem}\ \ln\left(\frac{R_{\rm i}}{R_{\rm o}}\right) & p=1 \end{cases}
\end{aligned}
\tag{5.17}
$$

and

$$
\begin{aligned}
\mathcal{A}^I &= \frac{\mathcal{B}^{II}}{R_{\rm i}^{2p} + R_{\rm c}^{2p}}\left(1 - \frac{\mu_r b - 1}{\mu_r b + 1}\right) \\
\mathcal{B}^I &= \mathcal{A}^I R_{\rm c}^{2p} \\
\mathcal{A}^{III} &= \frac{\mathcal{B}^{II}}{R_{\rm o}^{2p} + R_{\rm e}^{2p}}\left(1 - \frac{\mu_r a - 1}{\mu_r a + 1}\right) \\
\mathcal{B}^{III} &= \mathcal{A}^{III} R_{\rm e}^{2p}\ .
\end{aligned}
\tag{5.18}
$$

The constants $\mathcal{A}^I$, $\mathcal{B}^I$, $\mathcal{A}^{III}$ and $\mathcal{B}^{III}$ are identical for all integer values of p.

Using these constants in Eqs. (5.12), (5.13) and (5.15) allows one to calculate the magnetic vector potential, the magnetic flux density and the magnetic field respectively.

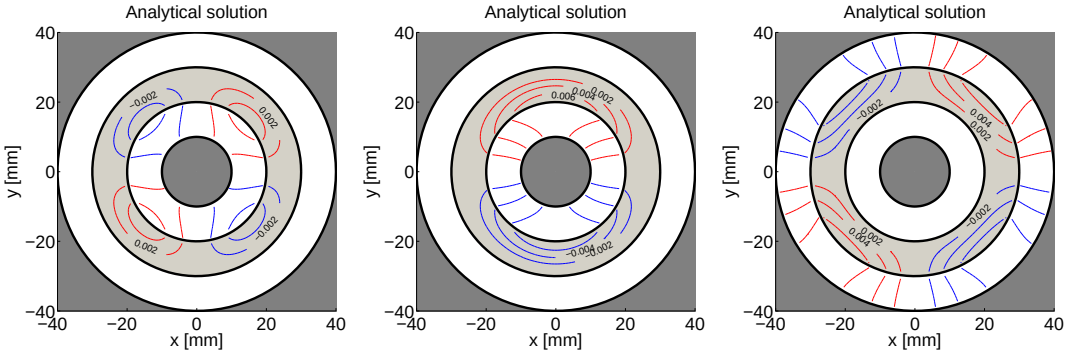

(a) $p = 2$ (b) $p = 1$ (c) $p = -2$

Fig. 5.3: The analytical solution as given by Eqs. (5.12), (5.17) and (5.18). Shown are contours of $A_z = \pm[0.002, 0.004, 0.006]$V s m^{-1} for an enclosed Halbach cylinder with dimensions as given in the text and a value of p as given above. The shaded areas in the figures correspond to the similar shaded areas in Fig. 5.2.

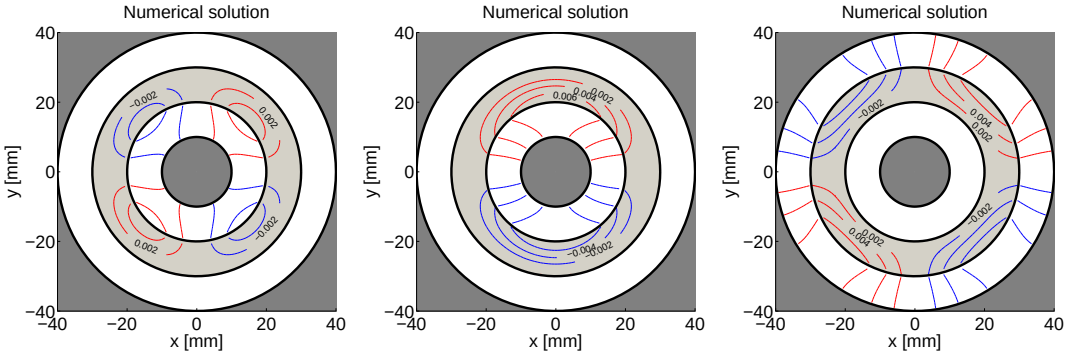

(a) $p = 2$ (b) $p = 1$ (c) $p = -2$

Fig. 5.4: The numerical solution of the identical systems as in Fig. 5.3.

5.3.4.1 Validity of the solution

To show the validity of the analytical solution Eqs. (5.17) and (5.18) we compare this with a numerical simulation. We consider a Halbach cylinder with dimensions $R_\mathrm{c} = 10$ mm, $R_\mathrm{i} = 20$ mm, $R_\mathrm{o} = 30$ mm, $R_\mathrm{e} = 40$ mm, and $B_\mathrm{rem} = 1.4$ T, $\mu_r = 3$.

In Figs. 5.3 and 5.4 the vector potential, A_z, is shown for an enclosed Halbach cylinder with $p = 2$, $p = 1$ and $p = -2$ respectively, as well as the results of a numerical simulation of the identical system. The analytical and numerical solutions are seen to be identical.

5.3.5 Halbach cylinder in air

We can find the solution for a Halbach cylinder in air if we look at the solution for R_c 0 and R_e .

Considering the previous expression for the constants a and b in Eq. (5.16) we see that

$$a \quad \begin{cases} 1 & p \geq 1 \\ -1 & p < 0 \end{cases} \qquad b \quad \begin{cases} -1 & p \geq 1 \\ 1 & p < 0 \end{cases} \tag{5.19}$$

in the limit defined above.

This means that the constants $\mathcal{A}^{II}$ and $\mathcal{B}^{II}$ now become

$$\begin{aligned}
\mathcal{A}^{II} &= \begin{cases}
-\mathcal{B}^{II}\frac{\mu_r-1}{\mu_r+1}R_\mathrm{o}^{-2p} - \frac{B_\mathrm{rem}}{p-1}R_\mathrm{o}^{1-p} & p > 1 \\
-\mathcal{B}^{II}\frac{\mu_r-1}{\mu_r+1}R_\mathrm{o}^{-2} + B_\mathrm{rem}\ln(R_\mathrm{o}) & p = 1 \\
-\mathcal{B}^{II}\frac{\mu_r+1}{\mu_r-1}R_\mathrm{o}^{-2p} - \frac{B_\mathrm{rem}}{p-1}R_\mathrm{o}^{1-p} & p < 0 \\
-\left(\frac{\mu_r-1}{\mu_r+1}R_\mathrm{o}^{-2p} - \frac{\mu_r+1}{\mu_r-1}R_\mathrm{i}^{-2p}\right)^{-1}(R_\mathrm{o}^{1-p} - R_\mathrm{i}^{1-p})\frac{B_\mathrm{rem}}{p-1} & p > 1
\end{cases} \\
\mathcal{B}^{II} &= \begin{cases}
-\left(\frac{\mu_r-1}{\mu_r+1}R_\mathrm{o}^{-2} - \frac{\mu_r+1}{\mu_r-1}R_\mathrm{i}^{-2}\right)^{-1}B_\mathrm{rem}\ln\left(\frac{R_\mathrm{i}}{R_\mathrm{o}}\right) & p = 1 \\
-\left(\frac{\mu_r+1}{\mu_r-1}R_\mathrm{o}^{-2p} - \frac{\mu_r-1}{\mu_r+1}R_\mathrm{i}^{-2p}\right)^{-1}(R_\mathrm{o}^{1-p} - R_\mathrm{i}^{1-p})\frac{B_\mathrm{rem}}{p-1} & p < 0
\end{cases}
\end{aligned} \tag{5.20}$$

and the remaining constants become

$$\begin{aligned}
\mathcal{A}^{I} &= \mathcal{B}^{II}R_\mathrm{i}^{-2p}\left(1 - \tfrac{\mu_r+1}{\mu_r-1}\right) \quad p \geq 1 \\
\mathcal{B}^{I} &= \mathcal{B}^{II}\left(1 - \tfrac{\mu_r-1}{\mu_r+1}\right) \quad p < 0 \\
\mathcal{A}^{III} &= \mathcal{B}^{II}R_\mathrm{o}^{-2p}\left(1 - \tfrac{\mu_r+1}{\mu_r-1}\right) \quad p < 0 \\
\mathcal{B}^{III} &= \mathcal{B}^{II}\left(1 - \tfrac{\mu_r-1}{\mu_r+1}\right) \quad p \geq 1
\end{aligned} \tag{5.21}$$

The remaining constants, i.e. $\mathcal{B}^{I}, \mathcal{A}^{III}$ for $p \geq 1$ and $\mathcal{A}^{I}, \mathcal{B}^{III}$ for $p < 0$, are zero.

This is the solution for a Halbach cylinder in air. Note that the solution is only valid for $\mu_r = 1$. In the special case of $\mu_r = 1$ the constants can be reduced even further.

Combining the above constants in the case of $p = 1$ with Eq. (5.15) we see that the magnetic flux density in the cylinder bore is a constant, and that its magnitude is given by

$$\mathbf{B}^{I} = \left(\frac{\mu_r - 1}{\mu_r + 1}R_\mathrm{o}^{-2} - \frac{\mu_r + 1}{\mu_r - 1}R_\mathrm{i}^{-2}\right)^{-1}\left(\frac{\mu_r + 1}{\mu_r - 1} - 1\right)R_\mathrm{i}^{-2}B_\mathrm{rem}\ln\left(\frac{R_\mathrm{i}}{R_\mathrm{o}}\right), \tag{5.22}$$

for $\mu_r = 1$.

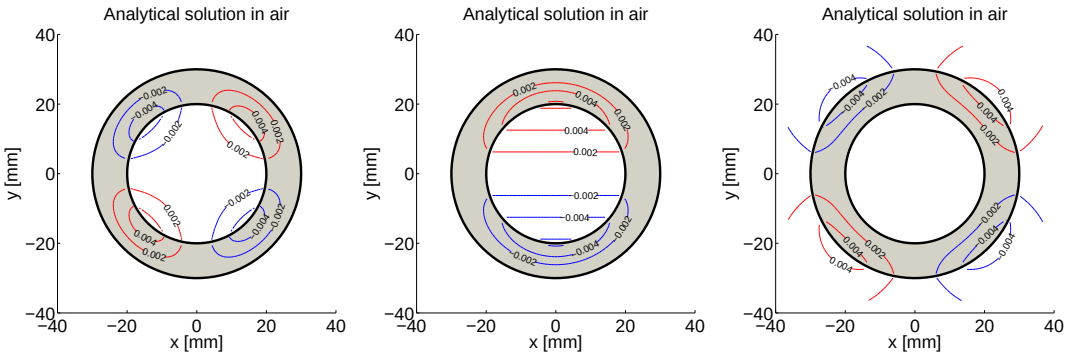

(a) $p = 2$ (b) $p = 1$ (c) $p = -2$

Fig. 5.5: The analytical solution as given by Eqs. (5.12), (5.20) and (5.21). Shown are contours of $A_z = \pm[0.002, 0.004, 0.006]$V s m^{-1} for a Halbach cylinder in air with dimensions as given in the text and a value of p as given above. The shaded areas in the figures correspond to the similar shaded areas in Fig. 5.2.

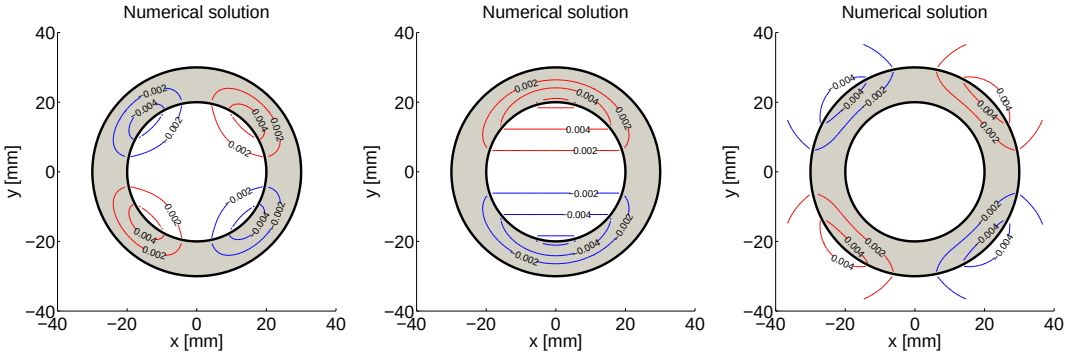

(a) $p = 2$ (b) $p = 1$ (c) $p = -2$

Fig. 5.6: The numerical solution of the identical systems as in Fig. 5.5.

5.3.5.1 Validity of the solution for Halbach cylinder in air

As previously the validity of the analytical solutions, Eqs. (5.20) and (5.21), is found by comparison with a numerical simulation. Again we consider a system with dimensions similar to those previously used.

In Figs. 5.5 and 5.6 the vector potential, A_z, is shown for a Halbach cylinder in air with $p = 2$, $p = 1$ and $p = -2$ respectively, as well as the results of a numerical simulation of the identical system. The analytical and numerical solutions are seen to be identical.

5.3.6 Halbach cylinder in air and $\mu_r = 1$

We now look at the special case of a Halbach cylinder in air with $\mu_r = 1$. This is a relevant case since, as previously mentioned, NdFeB magnets have a relative permeability very close to one.

Using the approximation of $\mu_r \quad 1$ for a Halbach cylinder in air reduces the constant $\mathcal{B}^{II}$ to

$$\mathcal{B}^{II} = 0 \ . \tag{5.23}$$

The remaining constants depend on whether the Halbach cylinder produces an internal or external field, and whether $p = 1$. The constant $\mathcal{A}^{II}$ is

$$\mathcal{A}^{II} = \begin{cases} -\frac{B_{\text{rem}}}{p-1} R_{\text{o}}^{1-p} & p > 1 \\ B_{\text{rem}} \ln(R_{\text{o}}) & p = 1 \\ -\frac{B_{\text{rem}}}{p-1} R_{\text{i}}^{1-p} & p < 0 \end{cases} \tag{5.24}$$

while the remaining constants are

$$\begin{aligned} \mathcal{A}^{I} &= \begin{cases} \frac{B_{\text{rem}}}{p-1} \left(R_{\text{i}}^{1-p} - R_{\text{o}}^{1-p} \right) & p > 1 \\ B_{\text{rem}} \ln\left(\frac{R_{\text{o}}}{R_{\text{i}}} \right) & p = 1 \end{cases} \\ \mathcal{A}^{III} &= \frac{B_{\text{rem}}}{p-1} \left(R_{\text{o}}^{p-1} - R_{\text{i}}^{p-1} \right) \qquad p < 0 \end{aligned} \tag{5.25}$$

The remaining constants, i.e. $\mathcal{B}^{I}$, $\mathcal{A}^{III}$ and $\mathcal{B}^{III}$ for $p \geq 1$ and $\mathcal{A}^{I}$, $\mathcal{B}^{I}$ and $\mathcal{B}^{III}$ for $p < 0$ are zero.

Using Eq. (5.15) the two components of the magnetic flux density in both the cylinder bore, region I, in the magnet, region II, and outside the magnet, region III, can be found.

$$\begin{aligned} B_r^{II} &= \begin{cases} \frac{B_{\text{rem}} p}{p-1} \left(1 - \left(\frac{r}{R_{\text{o}}} \right)^{p-1} \right) \cos(p\phi) & p > 1 \\ B_{\text{rem}} \ln\left(\frac{R_{\text{o}}}{r} \right) \cos(\phi) & p = 1 \\ \frac{B_{\text{rem}} p}{p-1} \left(1 - \left(\frac{R_{\text{i}}}{r} \right)^{-p+1} \right) \cos(p\phi) & p < 0 \end{cases} \\ B_\phi^{II} &= \begin{cases} -\frac{B_{\text{rem}}}{p-1} \left(1 - p \left(\frac{r}{R_{\text{o}}} \right)^{p-1} \right) \sin(p\phi) & p > 1 \\ -B_{\text{rem}} \left(\ln\left(\frac{R_{\text{o}}}{r} \right) - 1 \right) \sin(\phi) & p = 1 \\ -\frac{B_{\text{rem}}}{p-1} \left(1 - p \left(\frac{R_{\text{i}}}{r} \right)^{-p+1} \right) \sin(p\phi) & p < 0 \end{cases} \end{aligned} \tag{5.26}$$

and

$$
\begin{aligned}
B_r^I &= \begin{cases} \frac{B_{\rm rem}p}{p-1}\left(1-\left(\frac{R_{\rm i}}{R_{\rm o}}\right)^{p-1}\right)\left(\frac{r}{R_{\rm i}}\right)^{p-1}\cos(p\phi) & p>1 \\ B_{\rm rem}\ln\left(\frac{R_{\rm o}}{R_{\rm i}}\right)\cos(\phi) & p=1 \end{cases} \\
B_\phi^I &= \begin{cases} -\frac{B_{\rm rem}p}{p-1}\left(1-\left(\frac{R_{\rm i}}{R_{\rm o}}\right)^{p-1}\right)\left(\frac{r}{R_{\rm i}}\right)^{p-1}\sin(p\phi) & p>1 \\ -B_{\rm rem}\ln\left(\frac{R_{\rm o}}{R_{\rm i}}\right)\sin(\phi) & p=1 \end{cases} \\
B_r^{III} &= \frac{B_{\rm rem}p}{p-1}\quad 1-\left(\frac{R_{\rm i}}{R_{\rm o}}\right)^{-p+1}\quad\left(\frac{R_{\rm o}}{r}\right)^{-p+1}\cos(p\phi) \qquad p<0 \\
B_\phi^{III} &= -\frac{B_{\rm rem}p}{p-1}\quad 1-\left(\frac{R_{\rm i}}{R_{\rm o}}\right)^{-p+1}\quad\left(\frac{R_{\rm o}}{r}\right)^{-p+1}\sin(p\phi) \qquad p<0
\end{aligned} \tag{5.27}
$$

Again the remaining constants, B_r^I and B_ϕ^I for $p<0$ and B_r^{III} and B_ϕ^{III} for $p\geq 1$, are zero.

Note that the equations for B_r^{III} and B_ϕ^{III} for $p<0$ are identical to the expressions for B_r^I and B_ϕ^I for $p>1$ except for a minus sign in both equations.

As for the case of $\mu_r=1$ the magnetic flux density in the cylinder bore is a constant for the case of $p=1$. The magnitude of the magnetic flux density in the bore is given by

$$
\mathbf{B}^I = B_{\rm rem}\ln\left(\frac{R_{\rm o}}{R_{\rm i}}\right), \tag{5.28}
$$

which we recognize as the well-known Halbach formula (Halbach, 1980)[3].

[3] All of the above geometries were also solved by Xia et al. (2004), although here only the magnetic flux density was given. The expressions have been compared with those derived in this paper. Unfortunately the solution given by Xia et al. (2004) for the Halbach cylinder in air with $\mu_r=1$ i.e. Eq. (63),(64) and (80),(81) in Xia et al. (2004) as well as the expression for an enclosed Halbach cylinder with internal field, Eq. (20),(22),(24),(26) and (32) are wrong. For the case of the enclosed Halbach cylinder with an internal field the errors in the expressions by Xia et al. (2004) is in Eq. (20) and $\mathcal{A}^{III}$ and $\mathcal{B}^{III}$ in Eq. (32), while for the case of the Halbach in air with $\mu_r=1$ the error in Eq. (80),(81) is a reversal of sign for both equations while in Eq. (63),(64) it is only the latter equation which has the wrong sign.

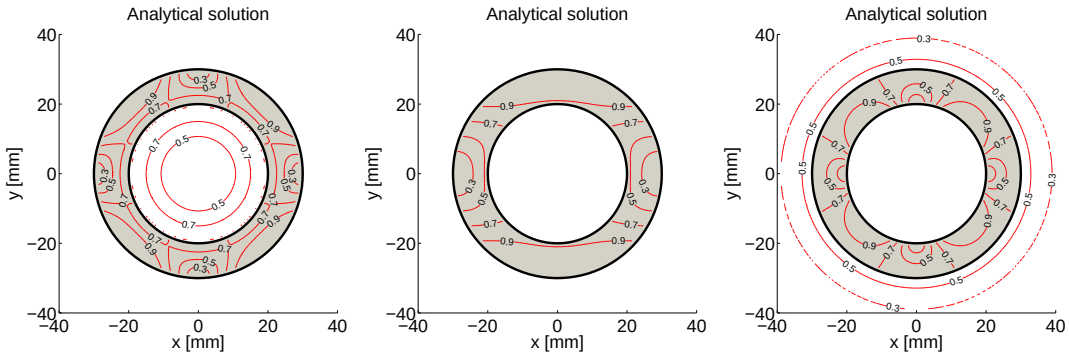

(a) $p = 2$ (b) $p = 1$ (c) $p = -2$

Fig. 5.7: The analytical solution as given by Eqs. 5.26) and (5.27). Shown are contours of $\mathbf{B}$ $= [0.3, 0.5, 0.7, 0.9]$ T for a Halbach cylinder in air with $\mu_r = 1$ and with dimensions as given in the text and a value of p as given above. The shaded areas in the figures correspond to the similar shaded areas in Fig. 5.2.

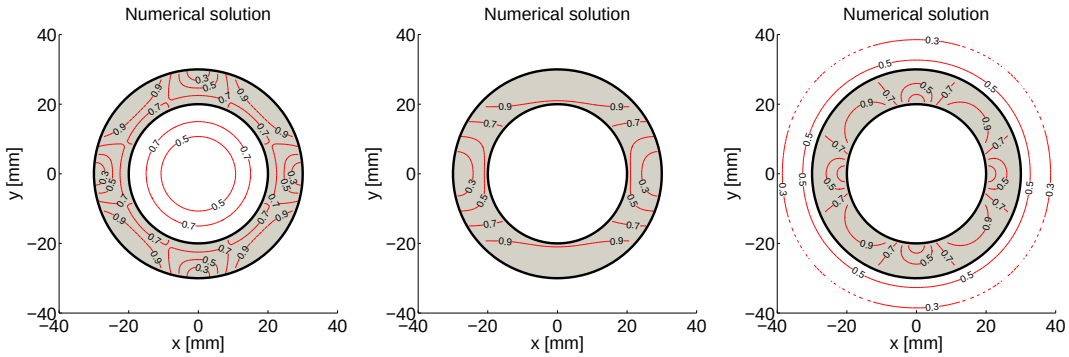

(a) $p = 2$ (b) $p = 1$ (c) $p = -2$

Fig. 5.8: The numerical solution of the identical systems as in Fig. 5.7.

5.3.6.1 Validity of the solution for Halbach cylinder in air and $\mu_r = 1$

As previously the validity of the analytical solutions, Eqs. (5.26) and (5.27), is found by comparison with a numerical simulation. Again we consider a system with dimensions similar to those previously used.

In Figs. 5.7 and 5.8 the norm of the magnetic flux density, $\mathbf{B}$, is shown for a Halbach cylinder in air with $p = 2$, $p = 1$ and $p = -2$ respectively, as well as the results of a numerical simulation of the identical system. The analytical and numerical solutions are seen to be identical.

5.4 The physical Halbach cylinder

Having described the magnetic field produced by an ideal Halbach cylinder we now focus on a Halbach cylinder used in actual applications, i.e. a cylinder with a finite length, L. In published magnetic refrigerators mostly a Halbach cylinder with $p = 1$ is used, and so only this is considered in this section. We wish to examine how to build the optimal Halbach cylinder, i.e. how to dimension and optimize the Halbach cylinder, as well as investigate if the Halbach cylinder design can be improved by using additional blocks of magnet.

5.4.1 Segmenting the Halbach cylinder

We begin by considering the effect of segmenting the Halbach cylinder into pieces. The continuous variation of the direction of magnetization as described in Eq. (5.1) is often not attainable in real-world assemblies, and therefore the Halbach cylinder is often made up of segments, each of which has a direction of magnetization equal to the direction of magnetization of a continuous Halbach cylinder at the center of the segment.

An infinitely long Halbach cylinder consisting of n segments will have its flux density in the cylinder bore reduced to (Halbach, 1980)

$$B(n) = B(\quad)\frac{\sin(2\pi/n)}{2\pi/n}, \tag{5.29}$$

where $B(\quad)$ is the flux density given by Eq. (5.28), i.e. with a continuous magnetization.

The consequence of this segmentation of the Halbach cylinder has been analyzed through a two dimensional simulation by computing the mean value of the magnetic flux density, B , inside the Halbach cylinder bore for a Halbach cylinder consisting of 4, 6, 8, 12, 16, 24 or 32 segments. The calculations were performed both for an infinitely long Halbach cylinder consisting of "perfect" magnets, i.e. with a relative permeability, μ_r, of 1, and magnets where actual material properties were taken into account by increasing μ_r to 1.05. The magnet material was assumed to have a remanent flux density of 1.4 T, equal to standard grade N48 NdFeB magnets (MMPA Standard, 2000). This value for the remanence is used through the remainder of this chapter. The Halbach cylinder examined here has $R_\mathrm{o} = 60$ mm while R_i is varied from 10 mm to 40 mm in steps of 2 mm. The deviation from a non-segmented cylinder, i.e. Eq. (5.29), is found for all the considered cases. The mean of the deviation for all cases is shown in Fig. 5.9. Taking the mean is justified as the largest deviation from the mean is 0.75%. It is seen that Eq. (5.29) describes the numerical data with $\mu_r = 1$ extremely well. It is also seen that choosing a small number of segments severely limits the flux density.

A reasonable compromise between complexity and flux density is a 16 segmented Halbach cylinder, which is thus chosen as the Halbach cylinder that is considered in the remainder of this chapter. Also $\mu_r = 1.05$ is used in the remainder of this chapter.

5.4.2 A finite length Halbach cylinder

A Halbach cylinder with a finite length, L, will have its flux density in the cylinder bore reduced compared to that of an infinitely long cylinder because flux will leak out of the ends of the cylinder. Here this effect is studied using numerical simulations instead of an analytical approach as used for the case of a cylinder of infinite length. The reason for this is that finding

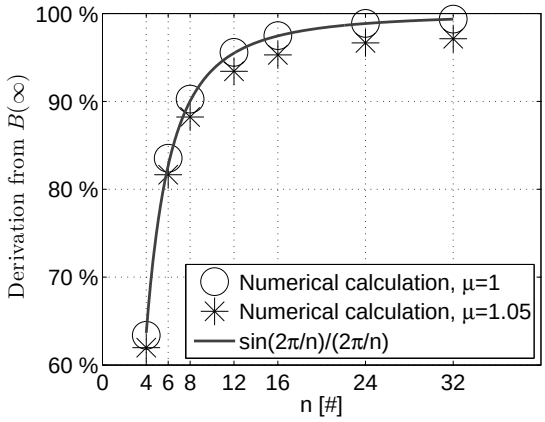

Fig. 5.9: Dividing an infinitely long Halbach cylinder into n segments makes the flux density differ from that of a perfect Halbach cylinder. The deviation is given by Eq. (5.29) for "perfect" magnets, $\mu_r = 1$, while magnets with $\mu_r = 1.05$ deviate more from the ideal Halbach cylinder.

an analytical expression for the magnetic field of a finite length Halbach cylinder is cumbersome. However, this can be done but the analytical expression is extremely complicated, making it impractical for direct application (Ni Mhiochain et al., 1999). The effect of a finite length Halbach cylinder has only been studied previously for two specific Halbach cylinders of a fixed length (Ni Mhiochain et al., 1999; Xu et al., 2004), and not the general case, which is considered here.

The physical properties of a finite length Halbach cylinder have been studied through a parameter study where the physical parameters of the Halbach cylinder were varied as given in Table 5.1. In each of the configurations the mean magnetic flux density inside the cylinder bore has been computed. The results are shown as a contour plot of the mean flux density as a function of L and R_o in Fig. 5.10 for $R_\mathrm{i} = 20$ mm. It is seen that the configuration producing the highest mean flux density is the configuration with the largest R_o and L. This is in agreement with Eq. (5.28) and the fact that for a long Halbach cylinder the loss of flux through the ends of the cylinder will be relatively smaller than for a short cylinder.

It is not sufficient to characterize a design only by the value of the mean flux density, as increasing the length of the Halbach cylinder increases the volume of the bore, which allows for more MCM to be placed inside the Halbach cylinder bore. On the other hand increasing

Table 5.1: The variation of the Halbach parameters, length, L, external radius, R_o, and internal radius, R_i.

	From [mm]	To [mm]	Stepsize [mm]
L	41	130	1
R_o	22	200	2
R_i	10	30	10

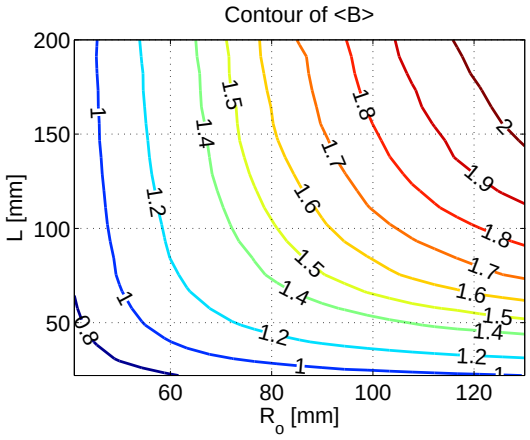

Fig. 5.10: Contours of the mean flux density for the Halbach cylinders with $R_\mathrm{i} = 20$ mm. Each contour is labeled by its mean flux density.

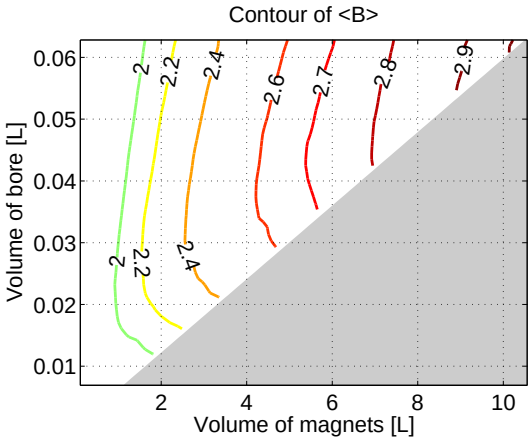

Fig. 5.11: Contours of the mean flux density as a function of the volume of magnets used and the volume of the cylinder bore for $R_\mathrm{i} = 10$ mm. No data exist for the greyed area.

the external radius does of course not affect the volume of the bore. Consequently, a better way of characterizing each Halbach cylinder configuration is by the volume of its magnets and the volume of the bore, and then calculate contour plots with lines of equal mean flux density. These are shown in Figs. 5.11-5.13 for the three different values of R_i considered here. On Figs. 5.11-5.13 the volume of the bore scales directly with the length of the Halbach cylinder because the internal radius is kept constant in each figure.

Looking at, e.g., Fig. 5.12 it can be seen that for a mean flux density of 1.6 T a Halbach cylinder can be constructed with a ∼50% increase in magnet material but a ∼250% larger volume of the bore compared to the design using the least amount of magnet material. It is possible to attain this substantial increase in the volume of the bore because the latter configuration is a very long Halbach cylinder with a small external radius, while the configuration with the smallest volume of the magnets is a shorter Halbach cylinder with a large external radius.

In Fig. 5.14 the total volume of magnet material is shown as a function of the mean flux density in the bore for $R_\mathrm{i} = 20$ mm for all varied parameters. Two data series where R_o has been fixed and L has been varied are highlighted on the plot (one could also have chosen to vary R_o and kept L fixed. The curves display the same behavior). Here one can see that as R_o is increased the mean flux density is increased as well. At some point each data series becomes the rightwards edge of the data plot, and then the increase in the volume of the magnets with mean flux density becomes too steep and the data points move upwards, leaving the rightwards edge of the data plot.

The reason for this behavior is that the data series start with a short Halbach cylinder. This configuration looses a lot of flux through the ends of the cylinder and as the length is increased the average flux density increases quite rapidly. When a certain length of the Halbach cylinder is reached there is not as much to be gained by increasing the length of the cylinder further and so the average flux density only increases slowly as the volume of the magnets is increased.

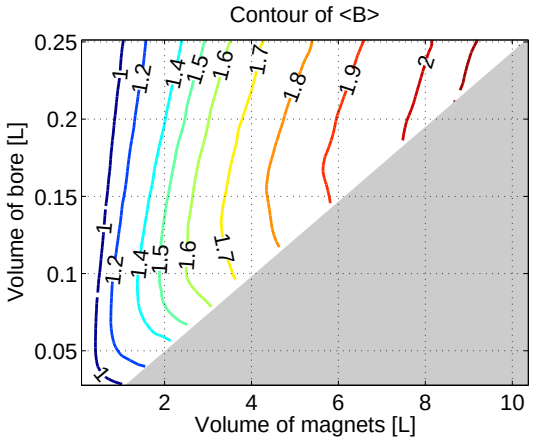

Fig. 5.12: Contours of the mean flux density as a function of the volume of magnets used and the volume of the cylinder bore for $R_\mathrm{i} = 20$ mm. No data exist for the greyed area. The conclusion of Fig. 5.11 applies here as well.

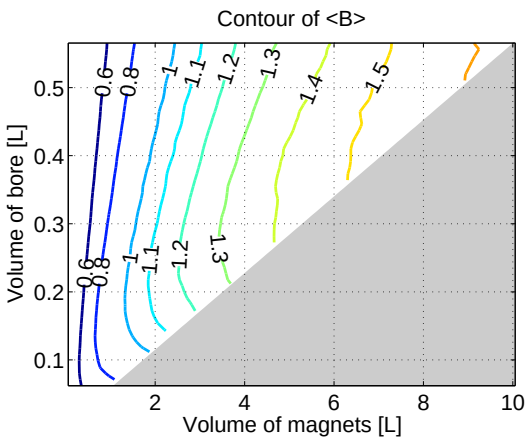

Fig. 5.13: Contours of the mean flux density as a function of the volume of magnets used and the volume of the cylinder bore for $R_\mathrm{i} = 30$ mm. No data exist for the greyed area. The conclusion of Fig. 5.11 applies here as well.

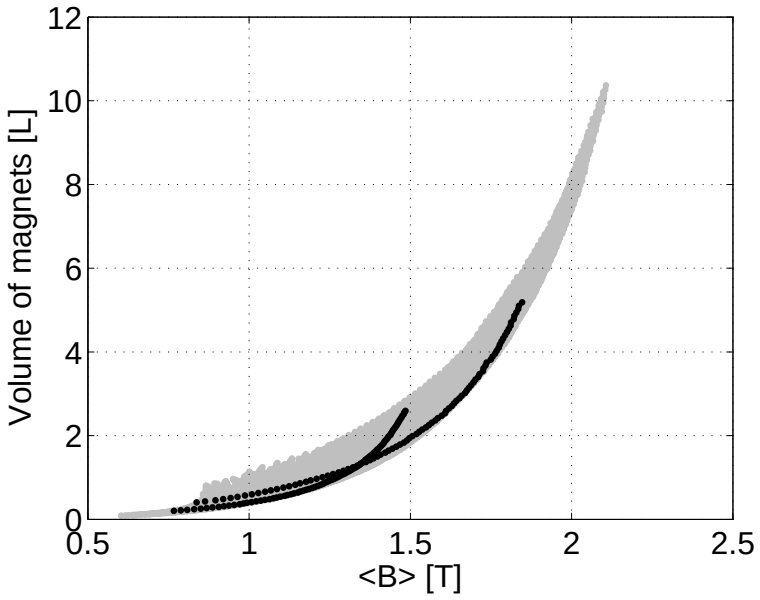

Fig. 5.14: The total volume of the magnet material as a function of the mean flux density for $R_\mathrm{i} = 20$ mm for all varied parameters. The data have been produced in series where R_o has been fixed and L has been varied. Two of these data series have been highlighted in black and starting from the left both series can be seen to first approach the rightwards edge of the data plot and then leave it again. A similar behavior is seen for $R_\mathrm{i} = 10$ mm and 30 mm.

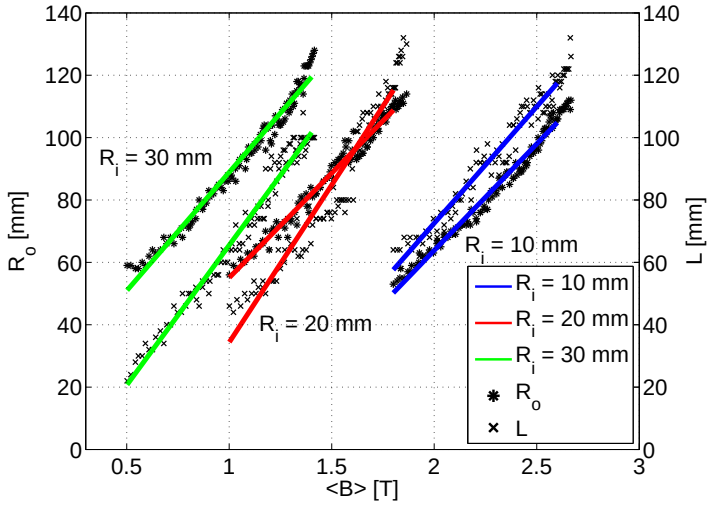

Fig. 5.15: The optimal R_o and L as functions of the mean flux density in the cylinder bore for Halbach cylinders with $R_i = 10$, 20 and 30 mm. Building a Halbach cylinder with dimensions different from the dimensions given here means that more magnet material is used than need be, if one is only interested in obtaining the maximum flux density possible and does not care about the size of the cylinder bore.

As this is the case for all data series where the length of the Halbach cylinder is gradually increased it is possible to characterize the rightwards edge of the data plotted in Fig. 5.14 as the optimal configurations, i.e. the configurations with the smallest volume of the magnet at a given mean flux density.

In Fig. 5.15 the values of R_o and L are plotted as functions of the mean flux density for these optimal configurations. Thus one can directly use this figure to find the external radius and length for the Halbach cylinder with the minimum volume of magnets at a given mean flux density. Straight lines have been fitted to the data.

The conclusion of this parameter variation is twofold. First, it can be concluded from Figs. 5.11-5.13 that it is possible, at a constant mean flux density, to increase the volume of the bore significantly by increasing the volume of the magnets slightly for a Halbach cylinder with a fixed R_i. Secondly, the length and external radius of the minimum magnet material Halbach cylinder at a given mean flux density was found and can be read off directly from Fig. 5.15. Thus if one wishes to build a Halbach cylinder with a given mean flux density where the volume of the bore is not essential and the limiting factor is the price of magnet material, one should always choose the optimal configuration from this figure. However such a design would not be ideal for use in magnetic refrigeration, as here the volume of the bore is of great importance.

Although the above results are useful in choosing the optimal Halbach cylinder design, methods for improving the design of a Halbach cylinder also exists. The problem with especially the short Halbach cylinders is that they loose a relatively large amount of flux through the ends of the cylinder. In the next section it is investigated whether it is possible to limit the amount of flux escaping through the ends of the cylinder by appending blocks of permanent magnets to the end faces of the Halbach cylinder and thus in this way improve the design.

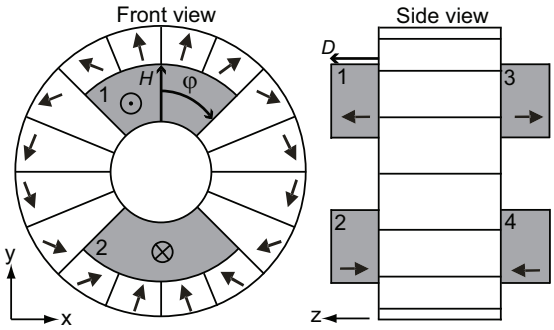

Fig. 5.16: This figure shows the height, H, angular span, ϕ, and depth, D, of the additional blocks, colored in grey. The blocks are always symmetrically placed and blocks diagonally opposite each other have the same direction of magnetization. The black arrows show the direction of magnetization.

5.5 Improving the Halbach cylinder design

The loss of flux through the ends of the Halbach cylinder bore can be remedied by "covering" the ends of the Halbach cylinder with magnetic blocks in the shape of an equipotential surface(Potenziani et al., 1987). However, this also blocks access to the cylinder bore. Instead we wish to investigate if some of the escaping flux may be confined by placing additional magnets, of a given size and direction of magnetization, at the end faces of the cylinder, in such a way that they do not block access to the cylinder bore but still increase the flux density in the cylinder bore and ensure a low flux density outside of the Halbach cylinder. We also investigate whether it is better to use the additional magnets or if one might as well use the additional magnet material for building a larger Halbach cylinder.

To maximize the amount of magnet material capable of being used in the additional blocks we use a design of the additional blocks that follows the curvature of the cylinder bore, i.e. a circular design as can be seen in Fig. 5.16. In total four additional blocks are used, placed symmetrically around the Halbach cylinder symmetry axis. In this design an additional block is characterized by three parameters, namely the angular extent of the block, ϕ, the block's depth, D, and its height, H. The direction of magnetization of the individual additional block is perpendicular to the Halbach cylinder end face and the blocks diagonally opposite have the same direction of magnetization.

The height, angular span and depth of the additional blocks are varied to find the optimal configuration for several different Halbach cylinders. Calculating the flux density for each of the original Halbach cylinders with additional magnets is a too time consuming task, and thus the calculations were only done on a few carefully chosen Halbach cylinder designs. These are given in Table 5.2.

The results of the simulations are shown in Fig. 5.17 which shows the mean flux density in the bore as a function of the total volume of the magnet material used. The figure shows both the Halbach cylinders without any additional blocks, i.e. those shown in Fig. 5.14, and the Halbach cylinders with additional blocks. One can see from the figure that placing additional blocks on a relatively short Halbach cylinder will improve the mean flux density in the cylinder bore significantly, while for a longer cylinder this is not the case.

Table 5.2: The additional magnets were placed on the four different Halbach cylinders given in column 5. The parameters of the additional blocks were varied as given in this table for each Halbach cylinder.

	From	To	Step size	Halbach dimensions [mm]
ϕ [°]	10	80	10	$L = 100$
H [mm]	100	30	10	$R_o = 100$
D [mm]	50	5	5	$R_i = 20$
ϕ [°]	10	80	10	$L = 92$
H [mm]	130	25	15	$R_o = 130$
D [mm]	46	4.6	4.6	$R_i = 20$
ϕ [°]	10	80	10	$L = 200$
H [mm]	60	25	5	$R_o = 60$
D [mm]	100	10	10	$R_i = 20$
ϕ [°]	10	80	10	$L = 50$
H [mm]	130	25	15	$R_o = 130$
D [mm]	25	2.5	2.25	$R_i = 20$

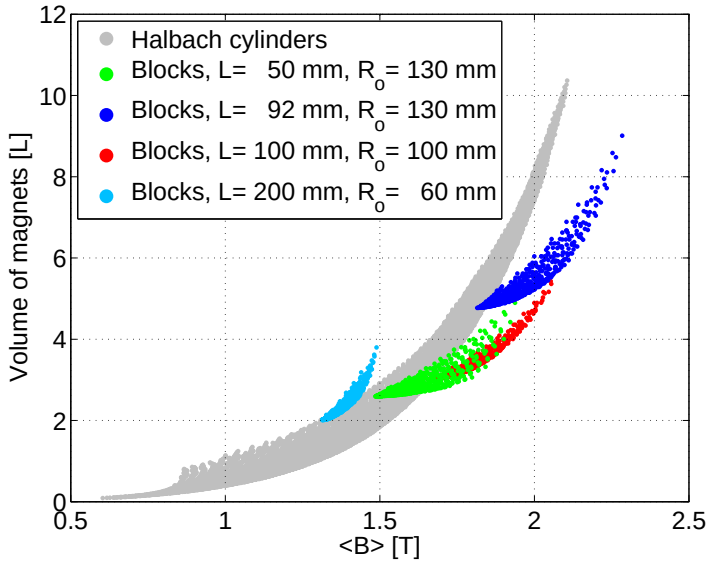

Fig. 5.17: Placing additional blocks on a specific Halbach cylinder improves the mean flux density in the cylinder bore but the improvement depends on L and R_o of the Halbach cylinder. The legend shows which Halbach cylinder the additional blocks was placed on. Without the additional blocks the figure is identical to Fig. 5.14.

5.6 Halbach cylinders in magnetic refrigeration

To evaluate the Halbach cylinder magnet design with respect to magnetic refrigeration the Λ_{cool} parameter can be used. The parameter was introduced in Chapter 4 but is repeated here for convenience.

The Λ_{cool} parameter is defined as

$$\Lambda_{\text{cool}} \equiv \left(\ (\mu_0 H)^{2/3}_{\text{high}} \ - \ (\mu_0 H)^{2/3}_{\text{low}} \ \right) \frac{V_{\text{field}}}{V_{\text{mag}}} P_{\text{field}} \ , \tag{5.30}$$

where each factor is described in Chapter 4.

In the case of the Halbach cylinder, V_{field} is the volume of the cylinder bore, $(\mu_0 H)^{2/3}_{\text{high}}$ is the volume average of the field in the cylinder bore to the power of 2/3 and $(\mu_0 H)^{2/3}_{\text{out}}$ is the volume average of the field to the power of 2/3 in the region shown in Fig. 5.18, i.e. the volume just outside the cylinder bore where the magnetocaloric material is placed when it is demagnetized. It has the same size and shape as the cylinder bore. This placement of the demagnetization volume is the worst case scenario, as the magnetocaloric material could be placed further from the magnet where the stray field from the cylinder bore is lower. Finally, P_{field} is 0.5, as the magnetocaloric material has to be moved out of the Halbach cylinder half of the time of a full AMR cycle. This could of course be improved by using two separate regenerators with the same Halbach cylinder, such that one regenerator is moved into the Halbach cylinder when the other is moved out. However, this solution requires a complicated flow system, and is not considered here.

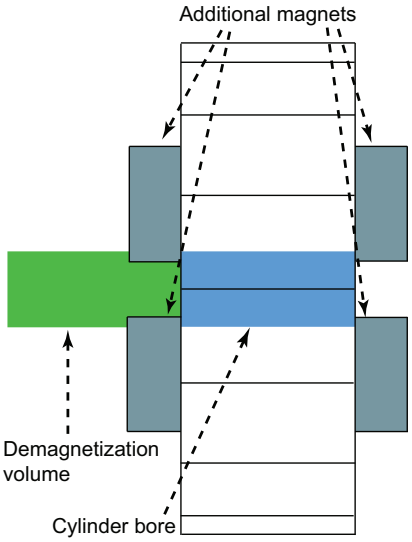

Fig. 5.18: A side view of the Halbach cylinder with additional blocks. The volume inside which $(\mu_0 H)^{2/3}_{\text{low}}$ is calculated is labeled "Demagnetization volume". The volume is identical in shape to the cylinder bore and is located directly outside the end of the cylinder bore. Also shown are the additional blocks of magnets. The edges of the 16 segments that make up the Halbach cylinder can also be seen on the figure.

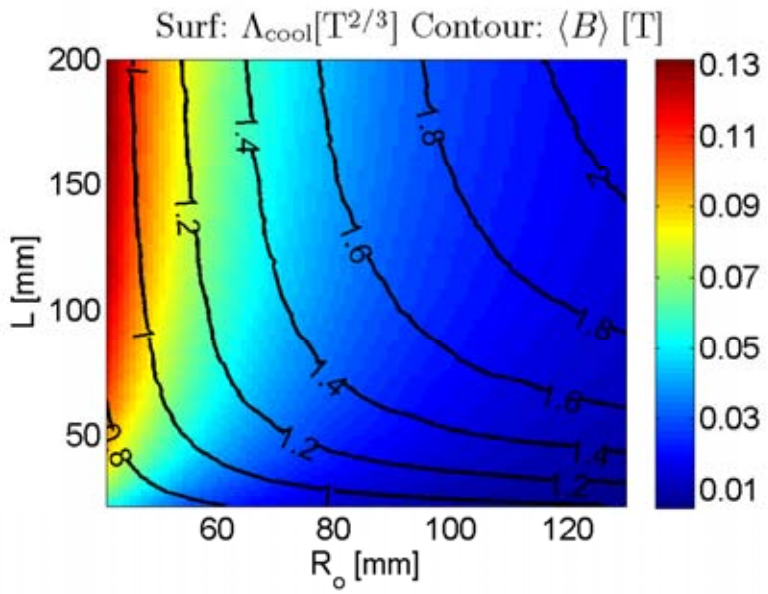

Fig. 5.19: A surface plot showing the magnetic cooling parameter, Λ_{cool}, for the Halbach cylinders without additional blocks and with $R_{\text{i}} = 20$ mm. Also B is shown as contours.

The Λ_{cool} parameter is shown for the Halbach cylinders without additional blocks and with $R_{\text{i}} = 20$ mm in Fig. 5.19. Here we see that the optimal design is the Halbach cylinder with the largest L and smallest R_{o}. Note that this design is not the overall optimal design, as it lies on the edge of the parameter space, i.e. simulations have not been conducted with a larger L and smaller R_{o}.

There are several reasons that the long, thin Halbach cylinder has the largest value of Λ_{cool}. The primary reason is that the volume of the magnet increases faster than the magnetic field when R_{o} is increased. Secondary reasons are that the relative loss of flux through the ends of the cylinder bore is greatly reduced in the long Halbach cylinder and that due to its long length, the volume where $(\mu_0 H)_{\text{low}}^{2/3}$ is calculated is also long (as previously mentioned the shape of the cylinder bore and this volume are identical), and thus the end furthest from the cylinder bore will only experience a very small stray field, thus lowering $(\mu_0 H)_{\text{low}}^{2/3}$. For practical applications one would choose to maximize Λ_{cool} under a criterion of a minimum flux density in the cylinder bore, i.e. find the Halbach cylinder with the maximum Λ_{cool} that at the same time has a minimum flux density in the cylinder bore.

It is interesting to investigate the effect the additional blocks of magnets have on the Λ_{cool} parameter. In Fig. 5.17 we saw that the additional blocks increase the flux density in the cylinder bore, but this might not mean that Λ_{cool} is increased as well, as additional magnet material is also used.

In Fig. 5.20 Λ_{cool} is shown for the different Halbach cylinders with additional blocks, i.e. the ones given in Table 5.2. Here we can see that some configurations of the additional blocks do increase Λ_{cool} by as much as $\sim$15%. Shown in the figure are also Halbach cylinders with no additional blocks that have the same R_{i} and L as the Halbach cylinders with additional

blocks but where R_o has been expanded by up to 30 mm. These are shown such that it can be estimated if it is better to spend any additional magnet material on the additional blocks or on enlarging the external radius of the Halbach cylinder. As one can see from the figure in three of the cases it is better to spend the additional magnet material on the additional blocks.

The design that is the most improved by the additional blocks is a short Halbach cylinder with a large external radius, i.e. $L = 50$ mm, $R_o = 130$ mm. For the longest Halbach cylinder with the smallest external radius, $L = 200$ mm, $R_o = 60$ mm, the additional blocks do not improve Λ_{cool}. The reason for this is that the short designs are also the ones that have the greatest relative loss of flux through the ends of the cylinder bore, which is exactly what the additional magnets reduce.

The optimal design of the additional blocks, i.e. the angular span, height and depth, vary between the four optimal Halbach cylinders in Fig. 5.20, and the results can be read in Table 5.3. Here it is seen that the optimal design of the additional blocks seems to be an angular span of around 60°, a height in the range $45-60$ mm and a depth in the range $22.5-27.5$ mm, at least for the three systems used in these simulations.

It can thus be concluded that for a short Halbach cylinder with a large external radius it is possible to optimize the Λ_{cool} parameter by using additional magnets placed at the ends of the cylinder. However, as can be seen by comparing Fig. 5.19 and 5.20 the improvement gained

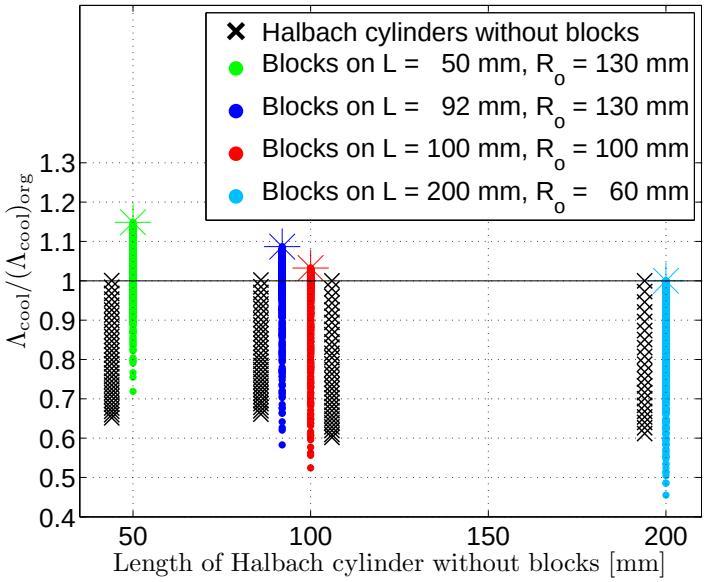

Fig. 5.20: The relative improvement of the magnetic cooling parameter compared to the original Halbach cylinder without any additional blocks, for the designs listed in Table 5.2. For each Halbach cylinder the best configuration of the additional blocks have been marked by a star. The black crosses in the figure are Halbach cylinder with the same R_i and L as the Halbach cylinder with blocks, but with a bigger R_o and no blocks. The black crosses are displaced by ± 6 mm on the x-axis to make the comparison with the Halbach cylinders with additional blocks possible.

Table 5.3: The optimal configuration of the additional blocks, i.e. the configurations that maximize the magnetic cooling parameter. $(\Lambda_{\text{cool}})_{\text{org}}$ refers to the "original" Halbach cylinder without any additional blocks.

Halbach dimensions [mm]	ϕ [°]	H [mm]	D [mm]	$\frac{\Lambda_{\text{cool}}}{(\Lambda_{\text{cool}})_{\text{org}}}$
$R_{\text{o}} = 130$ $L = 50$	80	47.5	22.5	1.15
$R_{\text{o}} = 130$ $L = 92$	60	61.2	27.6	1.09
$R_{\text{o}} = 100$ $L = 100$	60	50.0	25.0	1.03
$R_{\text{o}} = 60$ $L = 200$	60	30.0	10.0	1.00

by using the additional blocks is small compared to building a long Halbach cylinder with a small R_{o} in the first place. For example the design improved the most by the additional blocks, $L = 130$ mm and $R_{\text{o}} = 50$ mm, has the magnetic cooling parameter improved 1.15 times. This is not as impressive when one considers that the magnetic cooling parameter for this Halbach cylinder has a value of 0.011 $\text{T}^{2/3}$ (the lower right corner in Fig. 5.19), and even multiplied by 1.15 this is still much lower than the longer Halbach cylinders. However, in specific cases with a limited geometry due to the application the additional blocks can still be used to improve the flux density.

5.6.1 Homogeneity of the field

In most Halbach cylinder applications it is not only the flux density that is important but also the homogeneity of the field in the cylinder bore. In order to characterize the homogeneity of the flux density in the cylinder bore the quantity,

$$\eta \equiv \frac{\langle(\mu_0 H)^2\rangle - \langle\mu_0 H\rangle^2}{\langle(\mu_0 H)^2\rangle}, \tag{5.31}$$

where the angled brackets denote volume average, is defined. In Fig. 5.21 this parameter is shown for the Halbach cylinders with additional blocks. Also shown in the figure are Halbach cylinders with the same R_{i} and L as the Halbach with additional blocks but with a larger R_{o} and no blocks. It can clearly be seen that the no-block designs with larger R_{o} have a homogeneity parameter comparable to the "original" Halbach cylinder without blocks, while a number of the designs with additional blocks clearly improve the homogeneity of the field in the cylinder bore, i.e. lower η/η_{org}.

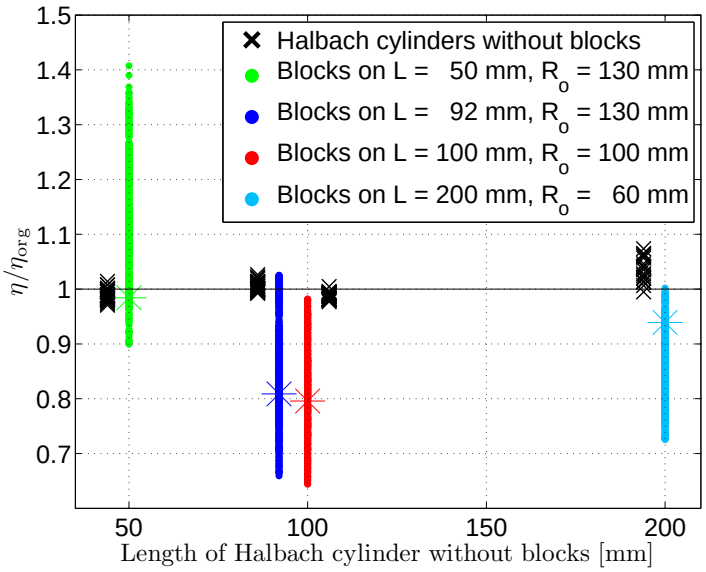

Fig. 5.21: The parameter η/η_{org} describing the homogeneity of the field in the Halbach cylinder bore. The data points marked with a star represent the best data points from Fig. 5.20. The black crosses are Halbach cylinders with the same R_{i} and L as the Halbach with additional blocks but with a larger R_{o} and no blocks. The black crosses are displaced by ± 6 mm on the x-axis to make the comparison with the Halbach cylinders with additional blocks possible.

5.7 Summary

In this chapter the Halbach cylinder have been analyzed in detail. The analytical solution for the magnetic field for a cylinder of infinite length has been found. Also, the three dimensional Halbach cylinder has been analyzed and the optimal dimensions, i.e. the dimensions of a Halbach cylinder with a minimum volume of magnet material for a given mean flux density, have been found. With regards to magnetic refrigeration the Λ_{cool} parameter was considered for a Halbach cylinder and was found to favor long cylinders. Finally, it was considered whether the Halbach cylinder could be improved by using additional blocks of magnet, which was found to be the case for short designs although for magnetic refrigeration purposes a long cylinder is always preferable.

Chapter 6

Design of a new magnet

The knowledge gained about magnet design in the previous chapters will in this chapter be used to design a magnet for use in a new magnetic refrigeration device currently being built at Risø DTU. The design of this device and the design process of the magnet is described in this chapter.

This chapter is partially based on the results described in Papers XII and XV.

6.1 The new refrigeration device

One aim of the magnetic refrigeration group at Risø DTU has been to design and build a magnetic refrigeration device powerful enough to produce a temperature span of $T_{\text{span}} = 40$ K while at the same time producing a cooling capacity of $\dot{Q} = 100$ W.

The design of this new magnetic refrigeration device, hereafter termed the "New Machine", is such that plates of magnetocaloric material rotate in an air gap in between a stationary inner and outer magnetic structure. The position of the fluid inlets and outlets for the heat transfer fluid are fixed relative to the position of the high and low magnetic field regions. This means that the heat transfer fluid is injected in between the plates at certain fixed positions, as the plates are rotating around in the air gap. The temperature gradient will be along the plates, from one end of the machine to the other. A drawing of the design is shown in Fig. 6.1.

This design is advantageous because as plates are continuously rotating around in the air gap the magnetic field is utilized at all times. Also, there is no rotating valve as the position of the fluid inlets and outlets are fixed. However, there is a need for a rotating seal between the regenerator itself, which is rotating, and the fluid inlets and outlets. The overall design of the New Machine is described in Bahl et al. (2009).

It is part of the aim of this thesis to design a magnet for the New Machine. This magnet will be referred to as the "New Magnet".

6.1.1 Requirements for the magnet

The magnet for the New Machine must provide a magnetic field that changes magnitude from ideally zero to a high value a certain number of times round in the air gap between the inner and outer magnetic structure.

Several different possibilities were considered for the number of poles of the magnetic field, i.e. the number of times that the field has a maximum (or minimum) round in the air gap. The number of AMR cycles that a plate of magnetocaloric material will experience during a complete rotation in the machine is equal to the number of poles of the magnetic field. Twice as many inlets and outlets are needed for the heat transfer fluid as there are poles. In order for the AMR cycle to have a duration of the order of seconds, as is needed to produce a high

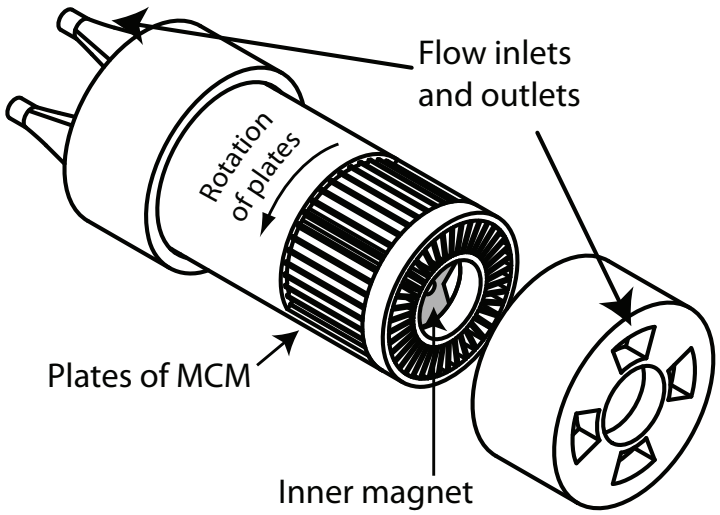

Fig. 6.1: A drawing of the design idea for the magnetic refrigeration device. The plates of MCM rotate, while the magnet and the fluid inlets and outlets are stationary. The outer magnetic structure is not shown in this drawing. The temperature gradient is along the plates. Adapted from Bahl et al. (2009).

performance (Nielsen et al., 2010), the rotation frequency of the plates would have to be quite fast for a magnet design with a low pole number. This is unfavorable as high rotation frequency increases friction and heating in the rotating seal. The opposite situation, i.e. a magnet design with a large number of poles, is unfavorable as it is hard to obtain a high flux density gradient between the high and low field regions over a short angular span. It is also difficult to make room for sufficient inlets and outlets for the heat transfer fluid. Based on these arguments a four pole magnet design, i.e. a design with four high field regions and four low field regions round the air gap, was chosen.

For ease of construction and handling of the New Machine the overall magnetic structure is chosen to be cylindrical in shape. This means that the air gap will have the shape of a hollow cylinder. Both the inner and outer magnetic structures need in principle only be round on the side facing the air gap and could be any shape along the other edges. This is e.g. the case for the magnet design by Tušek et al. (2009), described in Chapter 4, which utilizes a similar refrigerator design as described above. Here we will only consider structures with cylindrical symmetry to reduce the complexity of the design. Thus, the shape of the outer magnetic structure will be round on the outside. A 10 mm shaft needs to be passed through the center of the inner magnetic structure so the structure will be fitted to the shape of the shaft. A schematic drawing of the magnet design and the rotating plates of MCM is shown in Fig. 6.2.

As previously mentioned the temperature gradient is generated along the plates, i.e. along the length of the machine. As also described in Bahl et al. (2009) the plates of magnetocaloric material can be graded, i.e. have different Curie temperatures, along the length of the machine to ensure that they have a large adiabatic temperature change at the temperature that they are operating at. This is a well known way to increase the performance of an AMR (Rowe and Tura, 2006). It would also be possible to grade the magnets along the length of the machine, i.e.

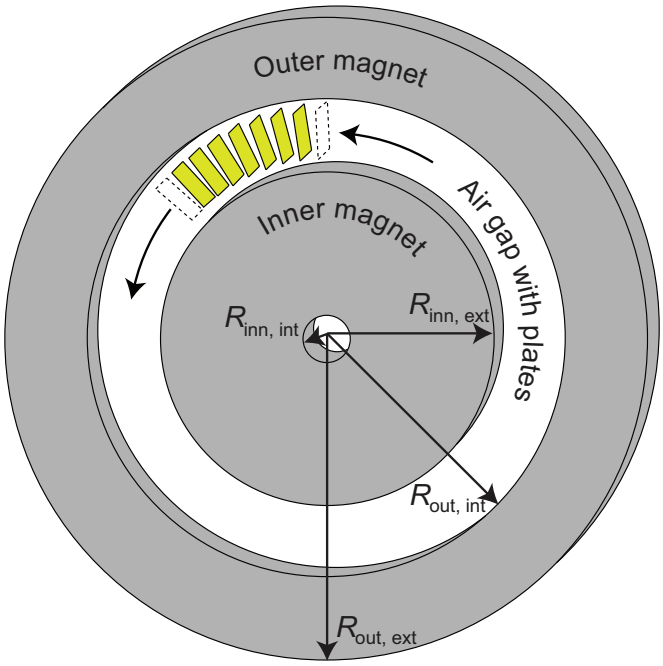

Fig. 6.2: A schematic drawing of the magnet design. The plates of MCM in the air gap are along the entire circumference, but for illustrative purposes only a few are shown. These are green in color. The dimensions of the two magnets, the internal radius of the inner magnet, $R_{\mathrm{inn,int}}$, the external radius of the inner magnet, $R_{\mathrm{inn,ext}}$, and likewise for the outer magnet, $R_{\mathrm{out,int}}$ and $R_{\mathrm{out,ext}}$ respectively, are shown.

to have more powerful magnets (higher remanence) in one end of the device and less powerful magnets (lower remanence) in the other end, if there was a need to generate a higher adiabatic temperature change in one end of the device than in the other. This could decrease the overall cost of the magnet structure as cheaper magnets could be used where appropriate. However, here we will only consider the same type of magnets along the whole length of the regenerator.

6.1.2 Dimensioning the New Machine

As mentioned previously the New Machine must produce $T_{\mathrm{span}} = 40$ K and $\dot{Q} = 100$ W. Based on experiments with the prototype magnetic refrigeration device described in Bahl et al. (2008) as well as detailed numerical modeling of the AMR process using the model described in Nielsen et al. (2009) it was decided that the air gap volume must be 4 liters in order that enough magnetocaloric material be present to provide the desired cooling capacity (Nielsen, 2009). This volume is the complete volume for the regenerator and includes the total volume of magnetocaloric plates, fluid channels and support structure for the plates.

The height of the air gap must in general be chosen small, as it is easier to generate a high flux density in a small air gap. However, there must of course be sufficient room for the plates, as well as for the flow inlets and outlets. A compromise between these two factors resulted in an air gap size of 30 mm, as this was the smallest value that the engineers designing the

regenerator and flow inlets could accept. The actual height of the plates of MCM will be only 20 mm, as there must be room for rotational clearance as well as for a support structure on both the inner and outer side of the air gap.

To decide the outer gap radius, $R_{\text{out,int}}$, the number of plates that would need to be placed inside the air gap was considered. As the volume of the air gap, V_{gap}, and the height of air gap, h_{gap}, has been fixed the value of $R_{\text{out,int}}$ also decides the length of the device, L, as

$$V_{\text{gap}} = \pi(R_{\text{out,int}}^2 - (R_{\text{out,int}} - h_{\text{gap}})^2)L \, , \tag{6.1}$$

where $V_{\text{gap}} = 4$ L and $h_{\text{gap}} = 30$ mm.

The number of plates of MCM inside the air gap can be calculated if we assume that the plates have a width, w_{plate}, of 0.5 mm and the width of the fluid channel in between the plates in the middle of the air gap, w_{channel}, is also 0.5 mm. This is a reasonable size for both the plate and fluid channel (Nielsen, 2009). The plates are put radially in the air gap, thus the height of the fluid channel will vary from the bottom to the top of the air gap. The number of plates in the air gap is given by

$$N_{\text{plates}} = \frac{2\pi(R_{\text{out,int}} - \frac{h_{\text{gap}}}{2})}{w_{\text{plate}} + w_{\text{channel}}} \, . \tag{6.2}$$

The number of plates is shown as a function of the outer gap radius in Fig. 6.3. Here it can be seen that there is room for a substantial number of plates in the air gap. Numerical simulation results of the AMR model indicate that it is preferable if the regenerator has a length of more than 200 mm (Nielsen, 2009). Also long plates are needed if these are to be graded. It was also shown in Chapter 5 that a long Halbach cylinder results in a better Λ_{cool} value. However, as the length of the device is increased $R_{\text{out,int}}$ is reduced, which leaves less volume for the inner magnetic structure, which in turn makes it harder to generate a high flux density. Based on these results as well as on the difficult task of stacking a large number of plates it was decided that $R_{\text{out,int}}$ must be 100 mm and thus $R_{\text{inn,ext}} = 70$ mm and $L = 250$ mm. Thus there will be about 530 plates in the machine.

6.2 Designing the magnet

Having decided on the dimensions of the New Machine the design of the magnet can be discussed. The ideal magnet could be designed by defining an optimization criterion and based on this alone calculate the optimal shape, placement and direction of magnetization of the permanent magnets, as well as the shape and placement of any blocks of soft magnetic material. This can be done using the approach described in Jensen and Abele (1996). Unfortunately, this is not possible due to the complexity of the problem. One could employ a numerical approach where small volumes predefined in shape and placement could either be magnet (with varying direction of magnetization) or a soft magnetic material and then find the optimal configuration by maximizing the optimization criteria. However, such an approach would be extremely computationally intensive due to the many degrees of freedom of the problem. Also, changing the properties of a small volume from magnet to soft magnetic material would not be a smooth transition and thus it would present problems for the numerical optimization routine. However, if the ideal placement of soft magnetic material was known it would be possible to optimize the direction of magnetization of the blocks of magnet, as this can be varied continuously.

An alternative design strategy for the magnet must be used. As the internal radius of the inner magnet, $R_{\text{inn,int}}$ and the external radius of the outer magnet, $R_{\text{out,ext}}$, have not been fixed it is important to consider a magnet design that can be easily parameterized, such that the optimal values for $R_{\text{inn,int}}$ and $R_{\text{out,ext}}$ can be found.

Several magnet designs have been considered but it was chosen to focus on a design with as few parameters as possible and then try to develop ways to optimize this design. Also, it was chosen to design a two dimensional magnet, i.e. of infinite length. Based on these choices a concentric Halbach cylinder design was chosen as a starting point for the magnet design for the New Machine.

6.2.1 The concentric Halbach cylinder design

The concentric Halbach cylinder design is a cylindrical magnet with an air gap in between an inner and outer cylindrical magnet structure. Each cylinder is a Halbach cylinder, i.e. the cylinder is magnetized such that the remanent flux density at any point varies continuously as,

$$\begin{aligned} B_{\text{rem},r} &= B_{\text{rem}} \cos(p\phi) \\ B_{\text{rem},\phi} &= B_{\text{rem}} \sin(p\phi), \end{aligned} \tag{6.3}$$

as also described in Chapter 5. As we are interested in designing a magnet with four high and four low field regions, we choose a $p = 2$ outer Halbach cylinder and a $p = -2$ inner Halbach cylinder. The magnetization of such a concentric Halbach cylinder is shown in Fig. 6.4.

Using a numerical two dimensional model the magnetic field for this setup has been calculated using magnets with a remanence of 1.4 T and a relative permeability of 1.05. The magnetic flux density for a quadrant of the magnet design is shown in Fig. 6.5 for $R_{\text{inn,int}} =$ 10 mm and $R_{\text{out,ext}} = 135$ mm which has been chosen as an example. Here we define the high and low field regions to be of the same size and to span an angle of 45 degrees each. The high

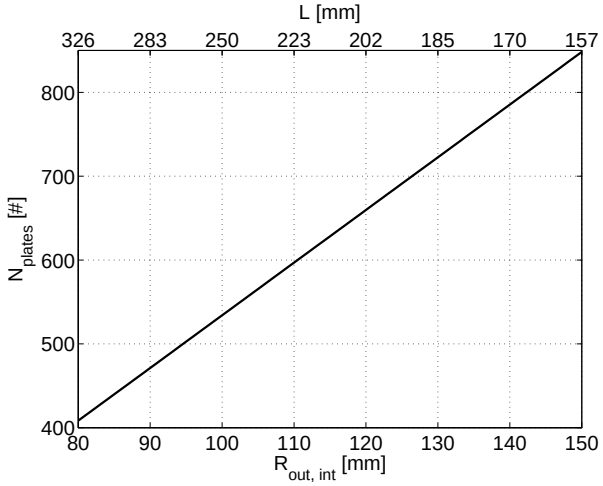

Fig. 6.3: The number of 0.5 mm plates of MCM with 0.5 mm fluid channels as a function of the outer gap radius (and length of the device) for a 30 mm gap.

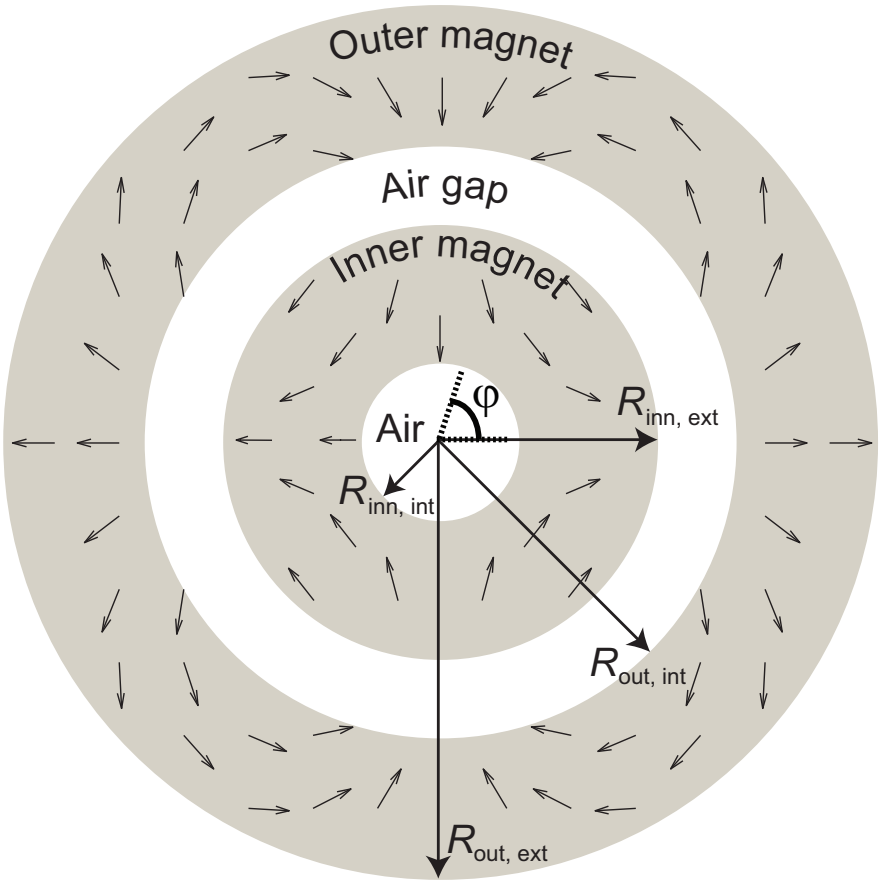

Fig. 6.4: The concentric Halbach cylinder design. The outer magnet has $p = 2$ and the inner magnet has $p = -2$. The direction of magnetization is shown as arrows. The different radii have been indicated. The angle, ϕ, is also shown.

field region extends from -22.5 to 22.5 degrees and so on. The magnet design produces a high flux density in the high field region but unfortunately also a rather high flux density in the low field region. The reason a numerical model is used even though the solution for the magnetic field can be calculated analytically as shown in Chapter 5 will become apparent shortly.

6.3 Optimizing and improving the magnet design

The concentric Halbach cylinder design presented above does not have the desired flux distribution with a large flux density gradient and equally large high and low field regions. For the example dimensions chosen earlier the volume of magnet is 41 L/m and $B_{\text{high}} = 1.03$ T and $B_{\text{low}} = 0.50$ T. The design can be improved by either increasing the flux density in the high field region, lowering the flux density in the low field region or lowering the amount of magnet material used. The first suggestion can be accomplished by adding more magnet material or by using shims of soft magnetic material to concentrate the flux density. However, as the adia-

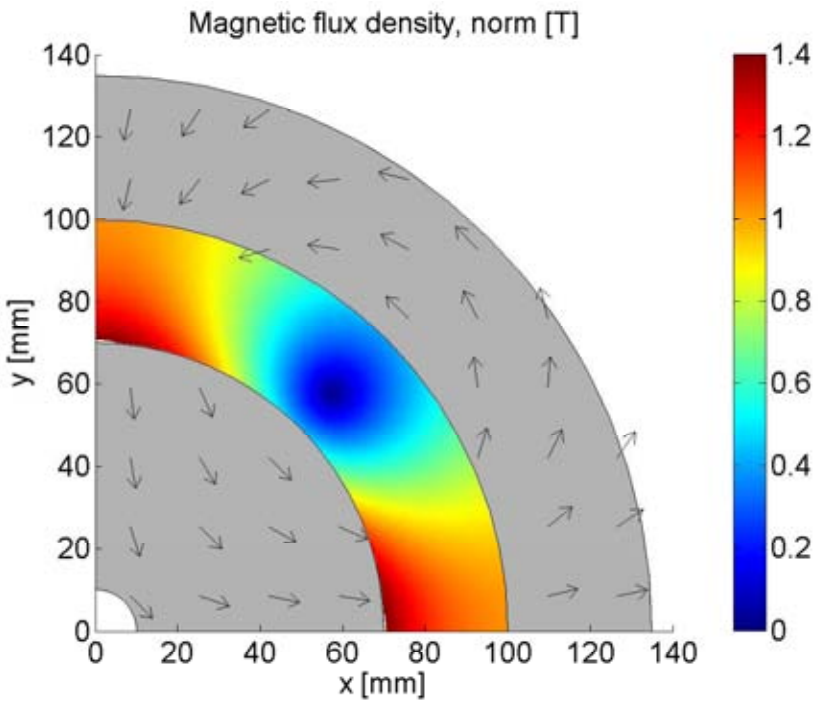

Fig. 6.5: A quadrant of the magnet design shown in Fig. 6.4 consisting of two concentric Halbach cylinders with $p = 2$ for the outer magnet and $p = -2$ for the inner magnet. The magnetization is shown as black arrows on the magnets, which are grey. The norm of the flux density in the air gap between the cylinders is shown as a color map. The ramining quadrants can be obtained by mirror symmetry.

batic temperature change scales with the magnetic field to the power of 2/3 more "temperature change" is gained by lowering the flux density in the low field region than by increasing the flux density correspondingly in the high field region. Therefore, we will focus on improving the concentric magnet design by focusing on the two latter improvements to performance; lowering the flux density in the low field region and lowering the amount of magnet material used.

6.3.1 Lowering the low flux density

The flux density in a given area can be minimized by exploiting the properties of field lines of the magnetic flux density. The following scheme will be referred to as the "optimization scheme". A field line is a curve whose tangent at every point is parallel to the vector field at that point. These lines can be constructed for any vector field. The magnitude of the magnetic flux density, $\mathbf{B}$, is proportional to the density of field lines. For a two dimensional problem, as we consider here, with a static magnetic field, lines of constant magnetic vector potential, A_z, are identical to field lines of $\mathbf{B}$ if the Lorenz gauge, i.e. $\cdot\mathbf{A} = 0$, is chosen (Haznadar and Stih, 2000). We begin by calculating a field line of the magnetic flux density, i.e. an equipotential line of constant A_z, that encloses the area in which the flux density is to be minimized. All

field lines enclosed by the calculated field line are confined to the enclosed area as field lines do not cross. These enclosed field lines are "creating" the flux density inside the calculated area. This procedure only works for a two dimensional case, as in three dimensions a field line will not enclose a volume.

If we remove all magnet material enclosed within the chosen field line, no field lines should be present inside the area and the flux density should be zero. However, this is not the case since by removing some magnet material the magnetostatic problem is no longer the same and a new solution, with new field lines of $\mathbf{B}$, must be calculated. Thus a new field line that confines the area in which we wish to minimize the flux density can be found and the procedure can be iteratively repeated.

It should be made clear that the magnet material inside the calculated field line, i.e. the material that is removed, does contribute a non-zero flux density to areas outside the enclosing field line. This can be seen by considering each little piece of a magnet as a dipole, which will generate a flux density at any point in space. Thus by removing the enclosed magnet material the flux density will also be lowered in the high field region. However, this is compensated by the lowering of $\mathbf{B}$ in the low field region, making it possible to increase the *difference* between the high and low field regions.

Field lines that do not pass through the high field region do not contribute to the flux density there. The optimization scheme can also be used to remove the magnet material enclosed by these field lines.

The optimization scheme must be run until a stopping criterion has been reached. This can be that the flux density in the low field region has dropped below a certain value or that the volume of magnet material has been reduced by a certain fraction. In some cases successive applications of the optimization scheme might result in removal of all magnet material. If, e.g., one tried to remove the flux density on one side of an ordinary bar magnet by applying the optimization scheme, one would simply remove slices of the bar magnet, until the magnet would be removed completely. This results in zero flux density, but does not leave any region with flux at all.

As an additional improvement, the removed magnet material can be replaced by a high permeability soft magnetic material, to shield the low flux density region from field lines from the new magnet configuration. This will lower the flux density in the low field region further. If the magnet material is replaced by air this is henceforth referred to as optimization scheme (Air), while if magnet material is replaced by soft magnetic material the reference term is optimization scheme (Iron). The difference between these two cases is illustrated in the next section.

Due to the high permeability of the soft magnetic material one would not necessarily have to replace all the enclosed magnet material with a soft magnetic material. Removing the magnet material and using only a small layer of soft magnetic material along the edge of the remaining magnet to shield the low field region will in general result in the same magnetic field as replacing all the magnet material with soft magnetic material. This will be an attractive option if the weight of the final assembly is an issue. However, the only difference between these two solutions is the amount of soft magnetic material used. Therefore, this option will not be considered further here.

In practice the optimization scheme is implemented numerically and applied to a numerical simulation of a magnet design.

The optimization scheme is presented as a flow diagram in Fig. 6.6.

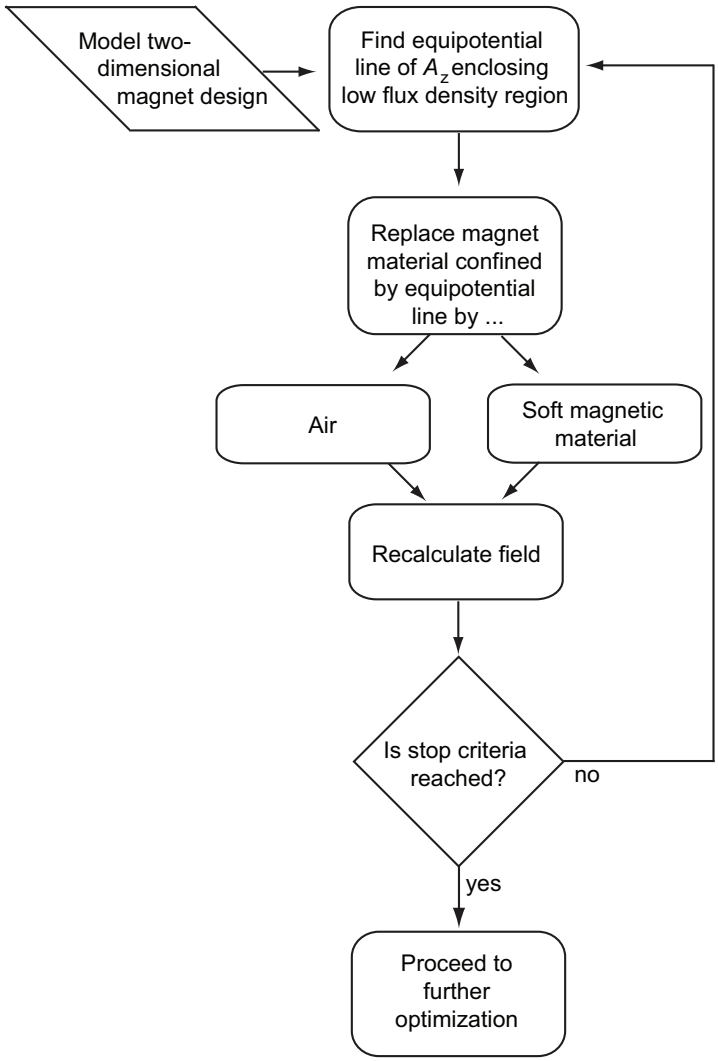

Fig. 6.6: The flow diagram for the optimization scheme.

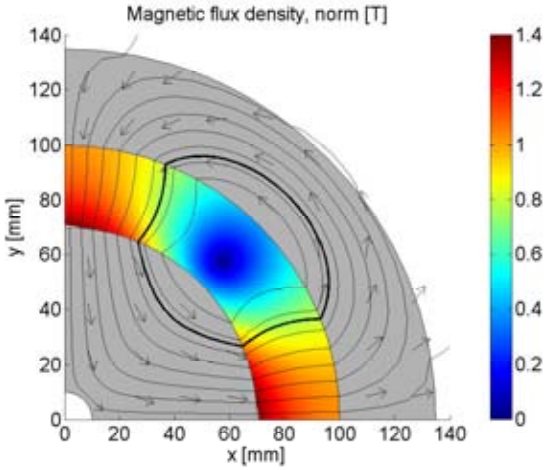

Fig. 6.7: A quadrant of the concentric Halbach cylinder design, as also shown in Fig. 6.5. The equipotential line of A_z that passes through the point ($r = 85$ mm, $\phi = 22.5°$) is shown as a thick black line, whereas other contours of A_z are shown as thin black lines.

6.3.1.1 The optimization scheme applied

The optimization scheme is applied to the concentric Halbach cylinder design. To show the effect of applying the optimization scheme we consider a concentric Halbach cylinder design with $R_{\text{inn,int}} = 10$ mm and $R_{\text{out,ext}} = 135$ mm. The remaining dimensions are as described previously. To find an encircling equipotential line of A_z we choose a given starting point that the equipotential line will pass through. The shape of the equipotential line of A_z will depend strongly on this starting point. First we consider the equipotential line of A_z to be the line that goes through the point ($r = 85$ mm, $\phi = 22.5°$), i.e. in the middle of the air gap, half way between the centers of the high and low field regions. This equipotential line is shown in Fig. 6.7 and it is seen that it encircles the low field region.

The magnet design where the optimization scheme (Air) has been applied is shown in Fig. 6.8, while the same scheme where the magnet material is replaced by iron is shown in Fig. 6.9. Iron was chosen as the soft magnetic material because it has a very high permeability as well as being easily workable and reasonably priced. It is seen that applying the optimization scheme several times removes more and more magnet material which in turn reduces the flux density in the low field region, but also the flux density in the high field region.

We now consider another equipotential line of A_z. This line goes through the point ($r = 100$ mm, $\phi = 22.5°$), i.e. the point on the internal radius of the outer magnet, half way between the centers of the high and low field regions. This line also encircles the low field region. In Figs. 6.10 and 6.11 the optimization scheme applied to the concentric Halbach cylinder design using this line is shown. As can be seen from the figure the optimization routine alters the design quite differently than was the case for when the point ($r = 85$ mm, $\phi = 22.5°$) was used as a starting point. The first iterations are almost identical but the following iterations produce completely different shapes. The reason for the different behavior can be seen in Fig. 6.12 which shows equipotential lines of A_z for the two different starting points after the

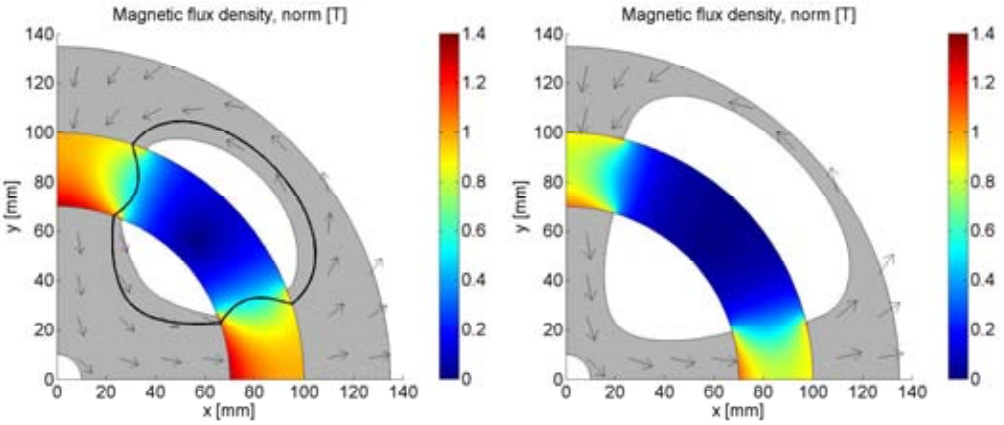

(a) Iteration 1. (b) Iteration 4.

Fig. 6.8: The optimization scheme (Air) applied to a quadrant of the magnet design. The first iteration step and the fourth step are shown. In the first step the magnet material enclosed by the thick black line in Fig. 6.7 has been removed. Fig. (a) also shows the equipotential line for the next iteration of the scheme, i.e. the equipotential line of A_z that passes through $(r = 85 \text{ mm}, \phi = 22.5°)$.

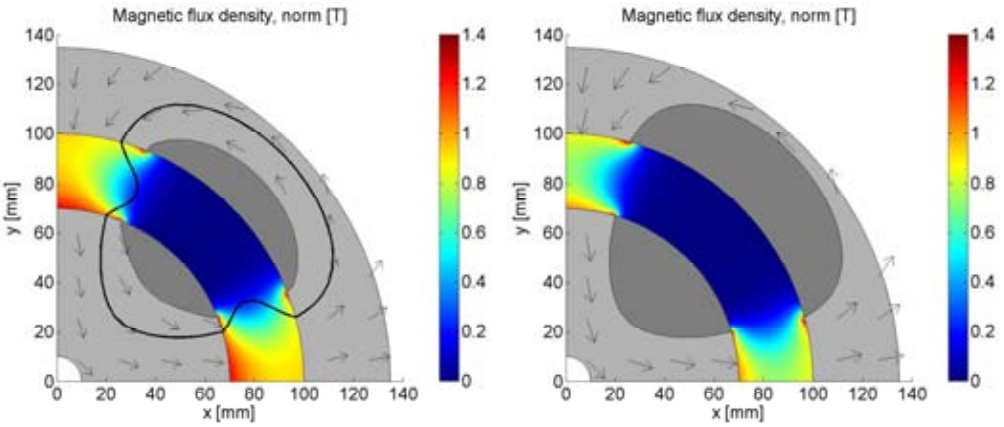

(a) Iteration 1. (b) Iteration 2.

Fig. 6.9: The optimization scheme (Iron) applied to a quadrant of the magnet design. Areas of iron are indicated by dark grey. The first iteration step and the second step are shown. The first iteration is identical to the first iteration in Fig. 6.8, expect that iron has been substituted instead of air. Fig. (a) also shows the equipotential line for the next iteration of the scheme.

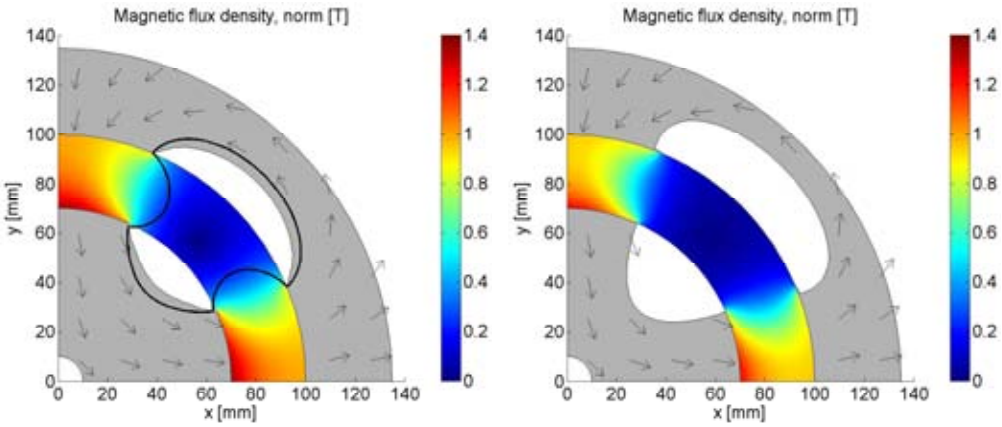

(a) Iteration 1. (b) Iteration 7.

Fig. 6.10: The optimization scheme (Air) applied to a quadrant of the magnet design. The first iteration step and the seventh step are shown. Fig. (a) also shows the equipotential line for the next iteration of the scheme.

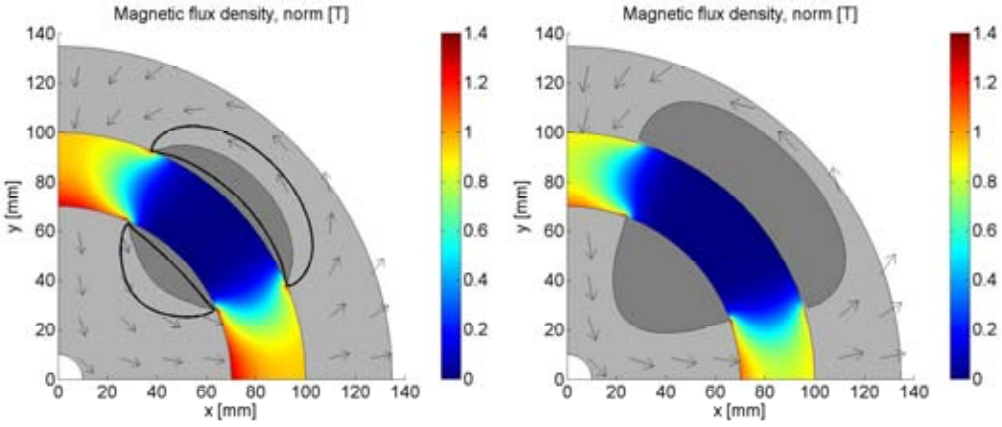

(a) Iteration 1. (b) Iteration 4.

Fig. 6.11: The optimization scheme (Iron) applied to a quadrant of the magnet design. The first iteration step and the fourth step are shown. The first iteration is identical to the first iteration in Fig. 6.10, expect that iron has been substituted instead of air. Fig. (a) are also shows the equipotential line for the next iteration of the scheme.

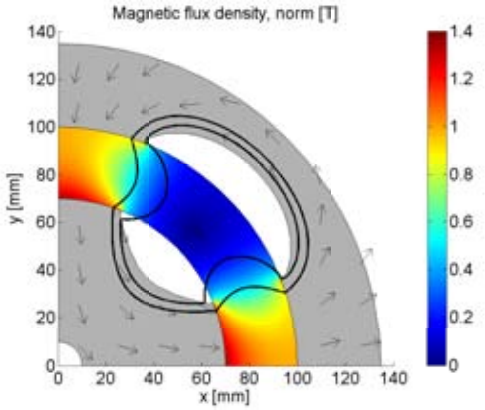

Fig. 6.12: The equipotential contours of A_z after the optimization scheme (Air) ($r = 100$ mm) has been applied a single time. The inner contour intersects the point ($r = 100$ mm, $\phi = 22.5°$) while for the outer contour the intersected point is ($r = 85$ mm, $\phi = 22.5°$).

optimization scheme (Air) with starting point $r = 100$ mm, hereafter termed optimization scheme (Air) ($r = 100$ mm), has been applied a single time.

The effect of applying the different versions of the optimization schemes is shown in Fig. 6.13 where the difference in flux density as a function of the volume of the magnet is plotted. Even though we are interested in optimizing the flux difference to the power of 2/3, we first consider just the flux difference to show the general improvement in performance gained by applying the scheme. As can be seen applying the optimization scheme increases the flux difference substantially. At the same time the amount of magnet material is reduced. Subsequent applications of especially the optimization scheme (Air) with starting point ($r = 85$ mm, $\phi = 22.5°$) reduces the magnet volume significantly.

The effect of applying the optimization scheme is also shown in Fig. 6.14, which shows the magnetic flux density in the middle of the air gap as a function of the angle, ϕ. It is seen from the figure that some flux is lost in the high field region as the optimization scheme is applied, but the flux density in the low field region is also almost completely removed. Substituting with a soft magnetic material lowers the flux density in the low field region more than substituting with air. The ramp rate of the magnetic field, i.e. the gradient between the high and low field regions, is not very steep but as shown in Chapter 3 this does not have a significant effect on the performance of the AMR.

Based on Figs. 6.13 and 6.14 and remembering that the optimization scheme is meant to increase the difference in flux density between the high and low field regions and not reduce the amount of magnet material, we choose the first iteration of the optimization scheme (Iron) with starting point ($r = 100$ mm, $\phi = 22.5°$) as the model that will be further improved. It has been verified for other values of $R_{\text{inn,int}}$ and $R_{\text{out,ext}}$ than used above that the first iteration of the optimization scheme (Iron) produces the highest difference in flux density. For the model with dimensions as used above the volume of magnet has been reduced by 13% and the flux density difference has been improved by 39% compared to the original design.

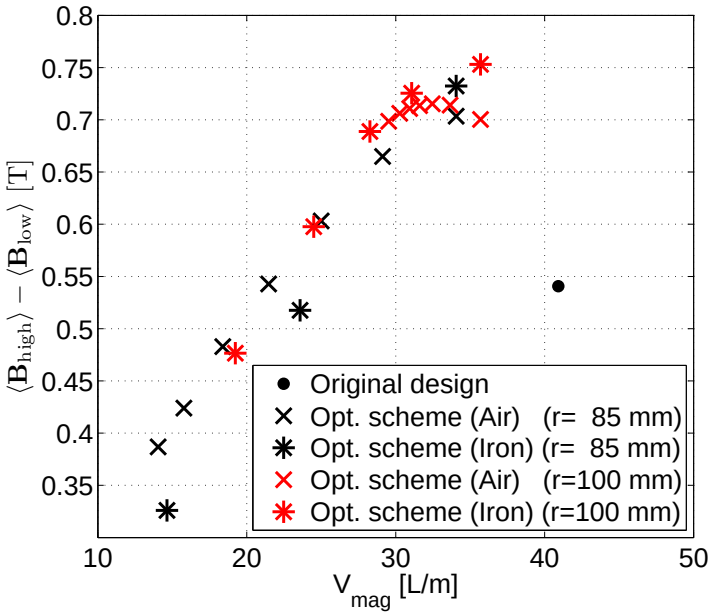

Fig. 6.13: The difference in flux density as a function of the volume of the magnet for the different versions and iteration steps of the optimization scheme. For all schemes decreasing values of V_{mag} indicates further iteration steps.

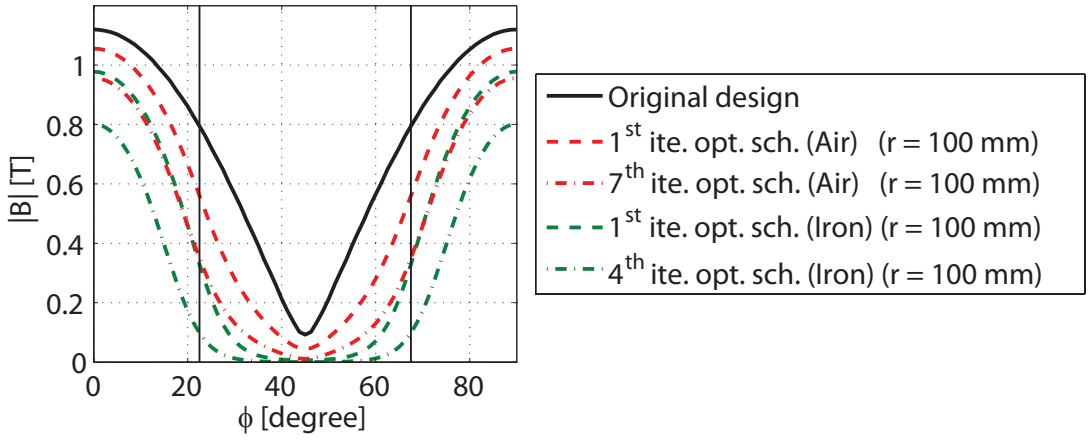

Fig. 6.14: The norm of the flux density as a function of angle in the middle of the air gap for the models shown in Figs. 6.10 and 6.11. The vertical lines separate the high and low field regions.

6.3.2 Lowering amount of magnet material

A magnet design can also be improved by examining the design for places where magnet material can be substituted for a high permeability soft magnetic material in order to lower the amount of magnet material used. A procedure for this improvement will be termed the "improvement scheme".

For an ideal hard magnet the anisotropy field is infinite, and so components of $\mathbf{H}$ and $\mathbf{B}$ that are perpendicular to the direction of the remanence, $\hat{\mathbf{B}}_{\mathrm{rem}}$, have no effect on the magnet. Here $\hat{\mathbf{B}}_{\mathrm{rem}} = \mathbf{B}_{\mathrm{rem}}/\ \mathbf{B}_{\mathrm{rem}}\ $, i.e. the unit vector in the direction of $\mathbf{B}_{\mathrm{rem}}$. Thus the working point and the demagnetization curve for the magnet need only be considered for the components of $\mathbf{H}$ and $\mathbf{B}$ that are parallel to the direction of $\hat{\mathbf{B}}_{\mathrm{rem}}$.

In areas where the component of $\mathbf{B}$ along $\hat{\mathbf{B}}_{\mathrm{rem}}$ is greater than $\ \mathbf{B}_{\mathrm{rem}}\ $ the magnet has a working point in the first quadrant of the demagnetization curve. This means that $\mathbf{H}$ and $\mathbf{B}$ are parallel, in the same way as in a soft magnetic material. Thus if the magnet material is replaced by a high permeability soft magnetic material this will produce a similar value of $\ \mathbf{B}\ $ as the magnet produces, thus allowing an interchange between the two. The requirement that the component of $\mathbf{B}$ along $\hat{\mathbf{B}}_{\mathrm{rem}}$ is greater than $\ \mathbf{B}_{\mathrm{rem}}\ $ is equivalent to requiring that the component of $\mathbf{H}$ along $\hat{\mathbf{B}}_{\mathrm{rem}}$ is greater than zero.

The direction of $\mathbf{B}$, and consequently $\mathbf{H}$, inside the soft magnetic material that replaces the magnet will depend on both components of $\mathbf{H}$, but will in general be such that the field lines of $\mathbf{B}$ are similar in shape to those before the substitution of magnet material with soft magnetic material.

Thus it can be advantageous to replace magnet material with a high permeability soft magnetic material in areas where

$$\mathbf{H} \cdot \hat{\mathbf{B}}_{\mathrm{rem}} > 0\ . \tag{6.4}$$

The requirement above can be further improved by considering that any magnet material that has a small negative value of $\ \mathbf{H}\cdot\hat{\mathbf{B}}_{\mathrm{rem}}\ $ has a poor working point far from the maximum energy density, $(\ \mathbf{B}\cdot\hat{\mathbf{B}}_{\mathrm{rem}}\ \ \mathbf{H}\cdot\hat{\mathbf{B}}_{\mathrm{rem}}\ )_{\mathrm{max}}$, of the magnet. Thus to remove some magnet material with a poor working point and thus lower the amount of magnet material, more material can be replaced. Of course, this will also affect the flux density generated in the air gap, so care must be taken not to remove too much magnetic material. This is done by altering the criterion in Eq. (6.4) such that

$$\mu_0 \mathbf{H} \cdot \hat{\mathbf{B}}_{\mathrm{rem}} > -\gamma\ , \tag{6.5}$$

where γ is a positive number in units of tesla. The value for γ can be changed depending on the demagnetization curve for the magnet material being used. The improvement gained by using different values of γ will be discussed subsequently. The $B(H)$ curve for a magnet along with the value of γ is indicated in Fig. 6.15.

As with the optimization scheme, the magnetic flux density will change when magnet material is replaced by soft magnetic material, and thus the scheme can be applied to the model again. This must be done until the model converges, which is the case if there are no additional areas where Eq. (6.5) applies.

The improvement scheme is presented as a flow diagram in Fig. 6.16.

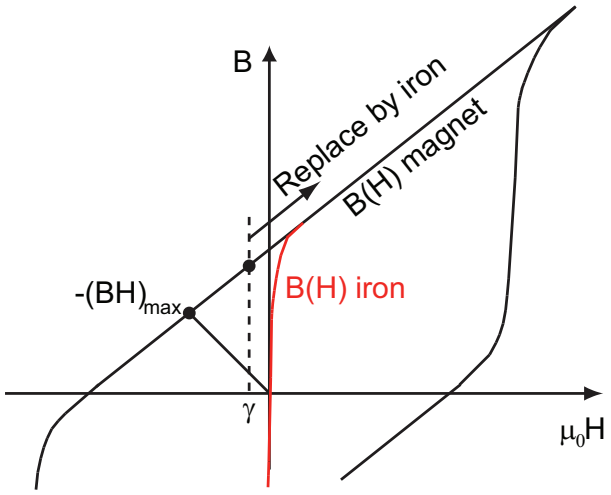

Fig. 6.15: Part of the $B(H)$ curve for a magnet and the soft magnetic material iron. Also shown is the value of γ. The arrow indicates from where the working point of the magnet is so sufficiently poor that it can be replaced by iron.

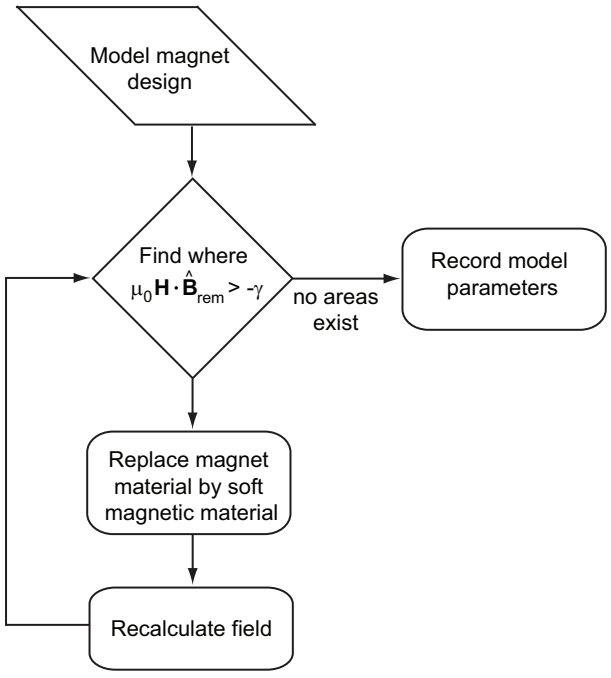

Fig. 6.16: The flow diagram for the improvement scheme.

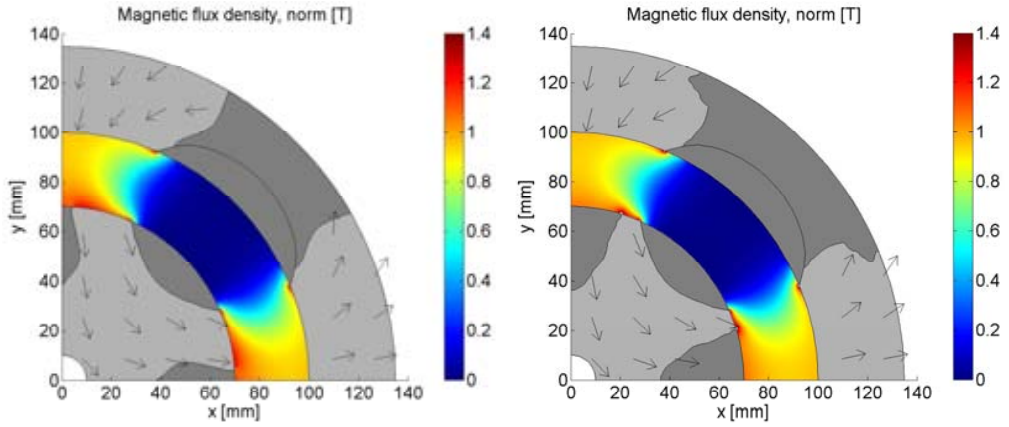

(a) Iteration 1.

(b) Iteration 9.

Fig. 6.17: The improvement scheme with $\gamma = 0.125$ T applied to the first iteration of the optimization scheme (Iron), i.e. Fig. 6.11a. The first iteration step and the ninth step, where the model has converged, are shown.

6.3.2.1 The improvement scheme applied

The result of applying the improvement scheme with a value of $\gamma = 0.125$ T to the model produced by a single application of the optimization scheme (Iron) ($r = 100$ mm) is shown in Fig. 6.17 for the example dimensions considered earlier and where the soft magnetic material used is iron. The improvement scheme is run until the change in magnet volume from one iteration to the next is less than 5%. This criterion has been chosen for numerical stability and the results do not depend on the exact number, as long as this is chosen sufficiently small. This is due to the fact that if the change in magnet volume from one iteration to the next is very small there are only very small areas left where it would be appropriate to replace magnet material with iron. As can be seen from the figure the flux density in the air gap hardly changes as the scheme is applied while the volume of magnet is significantly reduced.

The effect of applying the improvement scheme is shown in Fig. 6.18 where the difference in flux density as a function of the volume of the magnet is plotted. As can be seen successive applications of the improvement scheme reduces the volume of magnet material while the difference in flux density is kept almost constant. It can be seen that the model converges, i.e. successive application of the improvement scheme reduces V_{mag} by smaller and smaller amounts. For the converged improvement model the volume of the magnet is reduced by 33% while the difference in flux density remains the same compared to the model before the improvement scheme was applied. In total the volume of magnet is reduced by 41% compared to the original model.

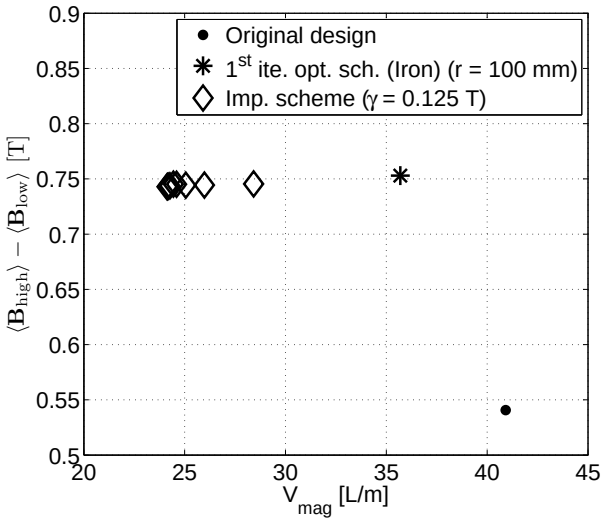

Fig. 6.18: The difference in flux density as a function of the volume of the magnet for the improvement scheme. This has been applied to the model produced by applying the optimization scheme (Iron) ($r = 100$ mm) a single time. Decreasing values of V_{mag} indicates further iteration steps.

6.3.2.2 Varying γ

Choosing a different value of γ will result in a larger or smaller part of the magnet being replaced. In Fig. 6.19 the difference in flux density is shown as a function of the volume of the magnet for the improvement scheme with different values of γ. The improvement scheme has been applied to the first iteration of the optimization scheme (Iron) ($r = 100$ mm) applied to a model with dimensions as used until now. As can be seen from the figure for high values of γ the flux difference drops as too much of the magnet is removed. The large change between $\gamma = 0.1$ T and $\gamma = 0.125$ T is because for the former value no magnet material is replaced in the inner magnet while this is the case for the latter value. In general the optimal value of γ will depend on the specific geometry of the design considered. This is illustrated in Fig. 6.20 which shows a single iteration of the improvement scheme with two different values of γ applied to the first iteration of the optimization scheme (Iron) ($r = 100$ mm). As can be seen a large value of γ means that significantly more of the magnet material is replaced. For the low value of γ no magnet material is replaced in the inner magnet.

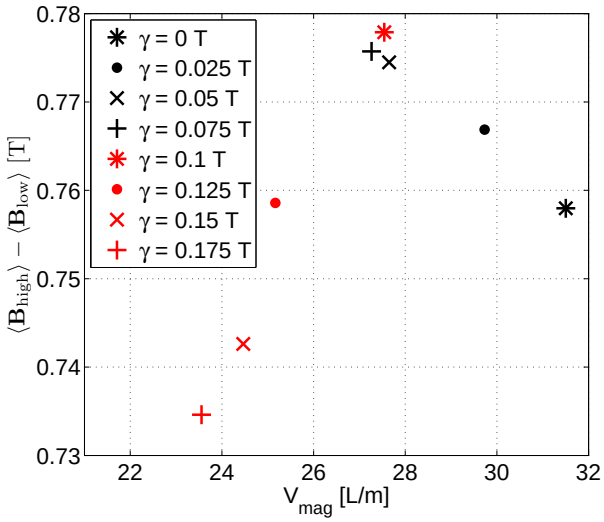

Fig. 6.19: The difference in flux density between the high and low field regions as a function of the volume of the magnet for different values of γ. All models have converged.

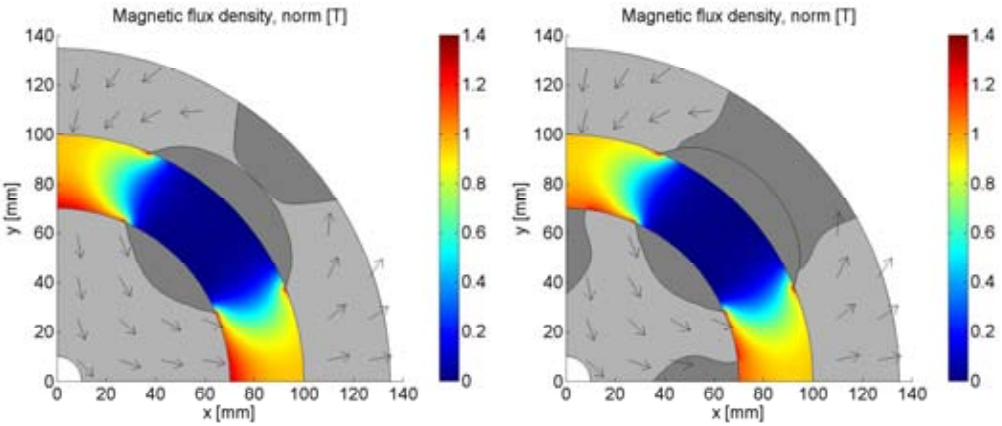

(a) $\gamma = 0$ T (b) $\gamma = 0.15$ T

Fig. 6.20: A single iteration of the improvement scheme with two different values of γ applied to the first iteration of the optimization scheme (Iron) ($r = 100$ mm).

6.3.3 Dimensioning of the design

Having developed two methods for improving the magnet design the two remaining dimensions of the concentric Halbach cylinder, i.e. $R_{\text{out,ext}}$ and $R_{\text{inn,int}}$, can be chosen based on a parameter variation of the concentric Halbach cylinder design with the optimization and improvement schemes applied. Here $R_{\text{out,ext}}$ was varied from 115 mm to 155 mm in steps of 5 mm while $R_{\text{inn,int}}$ was varied from 10 mm to 50 mm in seven equidistant steps.

The optimization scheme (Iron) ($r = 100$ mm) was applied a single time and then the improvement scheme was applied until convergence was reached. For the improvement scheme a value of $\gamma = 0.125$ T was used as this ensured that magnet material was also replaced in the inner magnet. Ensuring a numerically stable improvement routine proved difficult for all parameter sets. All cases have been manually inspected to ensure that convergence has been reached. If this was not the case the parameter set has been excluded, but this was only the case for a few sets of dimensions. Also, the value chosen for γ might not be the optimal value for all parameter cases, as in the previous subsection γ was only investigated for a single example. However, it would too computationally intensive to perform the parameter variation for all values of γ. The difference in flux density between the high and low field regions to the power of 2/3 as a function of the volume of the magnet is shown in Fig. 6.21.

To limit the cost of the magnet, a size of 25 L/m was chosen. Based on this value and Fig. 6.21 the optimal design was chosen. This design has $R_{\text{out,ext}} = 135$ mm and $R_{\text{inn,int}} = 10$ mm.

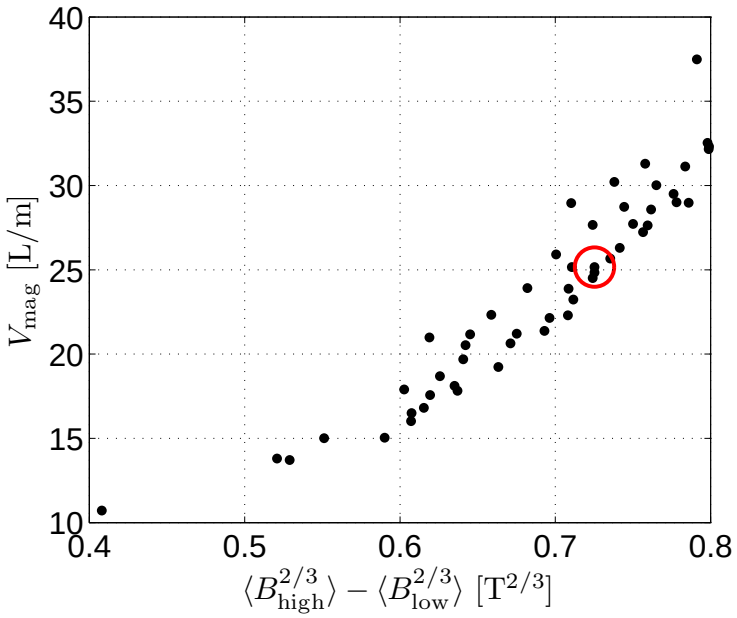

Fig. 6.21: The volume of the magnet as a function of the difference in flux between the high and low field regions to the power of 2/3 for a range of different external radii of the outer magnet, $R_{\text{out,ext}}$, and internal radii of the inner magnet, $R_{\text{inn,int}}$. The model with the chosen set of dimensions has been encircled. A lookup table is needed to find the parameters for each data point.

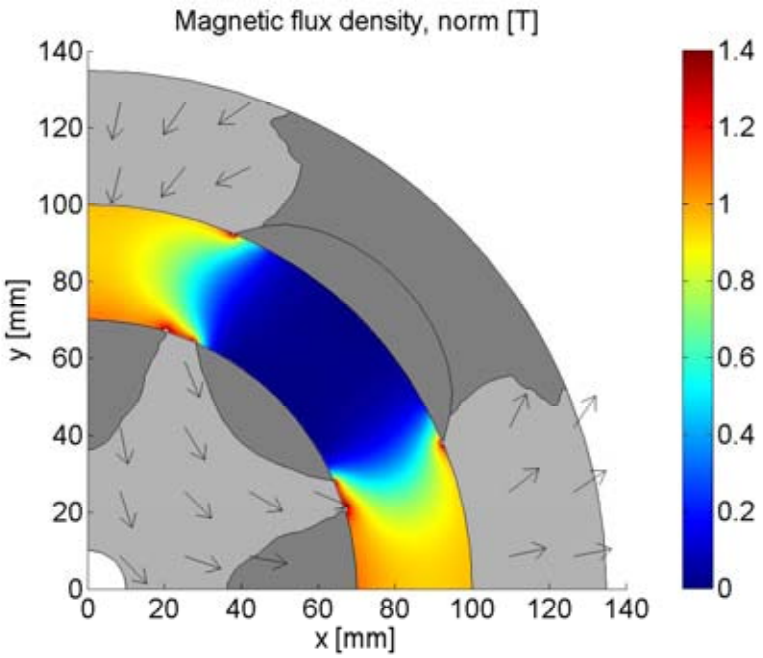

Fig. 6.22: The final design after the optimization and improvement schemes have been applied. First a single iteration of the optimization scheme (Iron) was applied and then nine iterations of the improvement scheme with $\gamma = 0.125$ T were applied.

The magnet design after the application of the optimization and improvement schemes for the chosen dimensions are shown in Fig. 6.22.

The volume of magnet material of the concentric Halbach cylinder design with the chosen dimensions before either of the schemes had been applied was 41 L/m and $B_{\text{high}} = 1.03$ T and $B_{\text{low}} = 0.50$ T. The flux density to the power of 2/3 was $B_{\text{high}}^{2/3} = 1.02$ T$^{2/3}$ and $B_{\text{low}}^{2/3} = 0.61$ T$^{2/3}$. After applying both schemes the volume of the magnet material was 25.4 L/m and $B_{\text{high}} = 0.85$ T and $B_{\text{low}} = 0.09$ T , while the flux density to the power of 2/3 was $B_{\text{high}}{}^{2/3} = 0.89$ T$^{2/3}$ and $B_{\text{low}}^{2/3} = 0.17$ T$^{2/3}$, respectively. Thus there has been a significant reduction of magnet material and at the same time a significant increase in the difference in flux density between the high and low field region.

6.3.4 Segmentation of the final design

To allow construction of the magnet, the design shown in Fig. 6.22 must be segmented into regular pieces. The number of segments is an important parameter as the more segments used the more expensive the manufacturing process becomes. Generally, it is the number of segments with different geometric shapes that determines the cost together with the overall magnet volume (Bendixen, 2009). If different segments have the same geometrical shape but different directions of magnetization these introduce little additional cost.

The segmentation of the optimized design is done manually. The size of the iron regions are decreased a bit compared to Fig. 6.22 in order to generate a higher flux density in the high field region and make the magnetic field profile wider, as this was shown in Chapter 3 to be favorable. In order to find the optimal direction of magnetization of the individual magnet segments an optimization procedure has been applied. The optimization routine used is a modified version of the Matlab[1] function `FMINSEARCH` (Matlab, 2008), called `FMINSEARCHBND`, which finds the minimum of an unconstrained multivariable function with boundaries using a derivative-free method (D'Errico, 2006). A Comsol model with a predefined geometry is used as input, with the direction of magnetization as variables. The optimization criterion is that the difference between $B_{\text{high}}^{2/3}$ and $B_{\text{low}}^{2/3}$ must be maximized. Several different initial directions of magnetization were tried and all converged to the same result. The segmentation of the magnet design and the resulting directions of magnetization are shown in Fig. 6.23.

The segmented design has 29.1 L/m of magnet material and $B_{\text{high}} = 0.97$ T and $B_{\text{low}} = 0.10$ T , while the flux density to the power of 2/3 is $B_{\text{high}}^{2/3} = 0.96$ T$^{2/3}$ and $B_{\text{low}}^{2/3} = 0.18$ T$^{2/3}$, respectively. Thus the flux density in the high field region has been increased compared to the design before segmentation. The amount of magnet volume has been slightly increased because the size of the iron regions has been decreased.

The effectiveness of the magnet design can be judged from the working point of the magnets, i.e. the norm of the magnetic field times the norm of the flux density both in the direction of the remanence, $\mathbf{B} \cdot \hat{\mathbf{B}}_{\text{rem}} \quad \mathbf{H} \cdot \hat{\mathbf{B}}_{\text{rem}}$. In Fig. 6.24 the working point is shown as calculated from a model of the magnet design. For magnets with a remanence of 1.44 T, as will be used for the construction of the design, the maximum energy density, i.e. the optimal working point, $(\mathbf{B} \cdot \hat{\mathbf{B}}_{\text{rem}} \quad \mathbf{H} \cdot \hat{\mathbf{B}}_{\text{rem}})_{\max}$, is 400 kJ m^{-3} (Vacuumschmelze GMBH & Co, KG, 2007). As can be seen from the figure most parts of the magnets are close to the maximum energy density thus illustrating the efficiency of the design.

[1] The MathWorks, Inc., Natick, Massachusetts, USA.

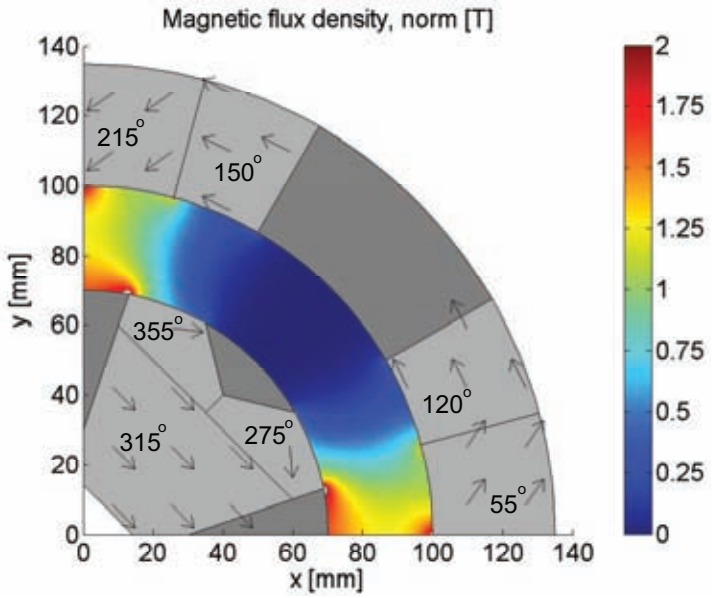

Fig. 6.23: The segmentation of the final design. The direction of magnetization has been found by maximizing $B_{\text{high}}^{2/3} - B_{\text{low}}^{2/3}$ and is indicated on each segment. Note that the flux density scale on this figure is larger than on the previous figures in this chapter.

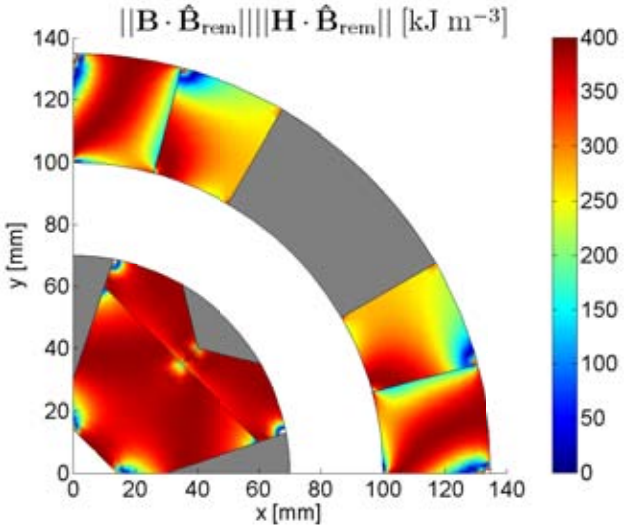

Fig. 6.24: The working point, $\mathbf{B}\cdot\hat{\mathbf{B}}_{\text{rem}}$ $\mathbf{H}\cdot\hat{\mathbf{B}}_{\text{rem}}$, of the magnets. The maximum working point for a 1.44 T remanence magnet, as is used here, is 400 kJ m^{-3}.

Chapter 7

Characterizing the New Magnet

In Chapter 6 the final design for the New Magnet was chosen and now the design must be realized. The inner and outer magnet was constructed and assembled at Bakker Magnetics[1] following the final design presented in the previous chapter.

The magnets used in the construction are of type N50M, which have a typical remanence of 1.44 T, a minimum intrinsic coercivity of 1114 kA m^{-1}, a typical maximum energy product of 398 kJ m^{-3} and a maximum operating temperature of 363 K (Bakker Magnetics, 2008). These magnets have the highest remanence available on the market today.

The assembly of the magnets can be a dangerous process, as there are substantial forces between the individual magnets. In Appendix B some photos taken during the assembly process are shown. The final realized magnet design is shown in Figs. 7.1 and 7.2. The magnets and iron pieces have been coated red and the outer magnet has been encased in a stainless steel ring. The magnet has a length of 250 mm.

This chapter is partially based on the results described in Paper XII.

7.1 Magnetic flux density profile

All spatial components of the flux density in the air gap of the magnet have been measured using a Hall probe (AlphaLab Inc, Model: DCM) as a function of angle, ϕ, radius, r, and length, z, of the device. The measuring apparatus was designed as part of this thesis but the actual flux density measurements were carried out by D. V. Christensen. A three dimensional simulation of the magnet design has also been performed.

The norm of the radial and angular components of the flux density is shown in Fig. 7.3 as a function of z for 16 different angles equidistantly spaced by 22.5 degrees. The z component of the magnetic flux density is very small and has not been included. These angles correspond to the center of the high and low field regions, 0 and 45 degrees respectively, and the angles half way between these, 22.5 and 67.5 degrees respectively, and so on. As can be seen from the figure there is a four-fold symmetry in the angular direction, as expected. In the four high field regions the flux density is around 1.24 T while it is very close to 0 T in the four low field regions. The high field region at 180 degrees was not measured as detailed along the z-direction as the remaining high field regions because the axial supports of the inner magnet prevented proper access to this region. There is a "bump" in the flux density at 157.5 and 247.5 degrees, respectively, which is unexpected. The New Magnet is assembled from five 50 mm long identical magnet rings in order to make it 250 mm long. The bump occurs right at the boundary between two such rings, though this does not explain the cause of the bump. Also shown in Fig. 7.3 is the result of a three dimensional numerical simulation of the magnet design. An excellent agreement between the simulated and measured flux density is seen. It is

[1] Bakker Magnetics bv, Eindhoven, The Netherlands

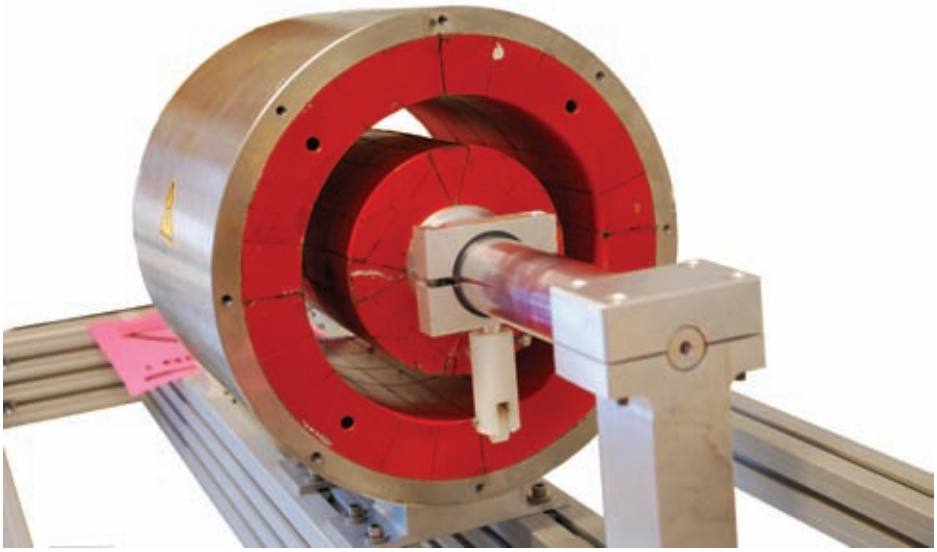

Fig. 7.1: A photo of the actual constructed magnet (in red) including stand and an outer stainless steel casing. The individual segments can be discerned. A small placeholder for a rod to fixate a Hall probe can also be seen.

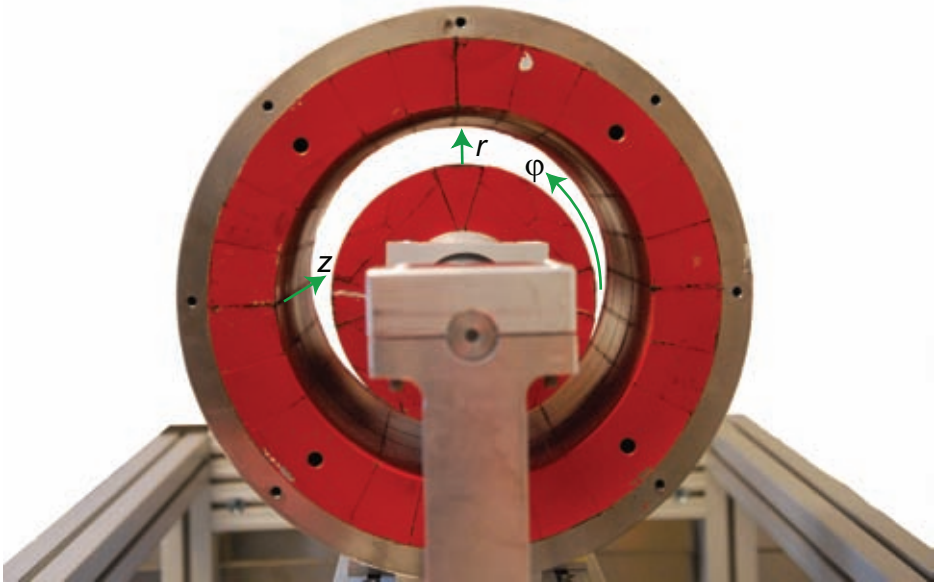

Fig. 7.2: A front photo of the actual constructed magnet (in red) including the axial support structure for the inner magnet. The coordinate system that will be used in this chapter is also shown. In the middle of the magnet $z = 0$.

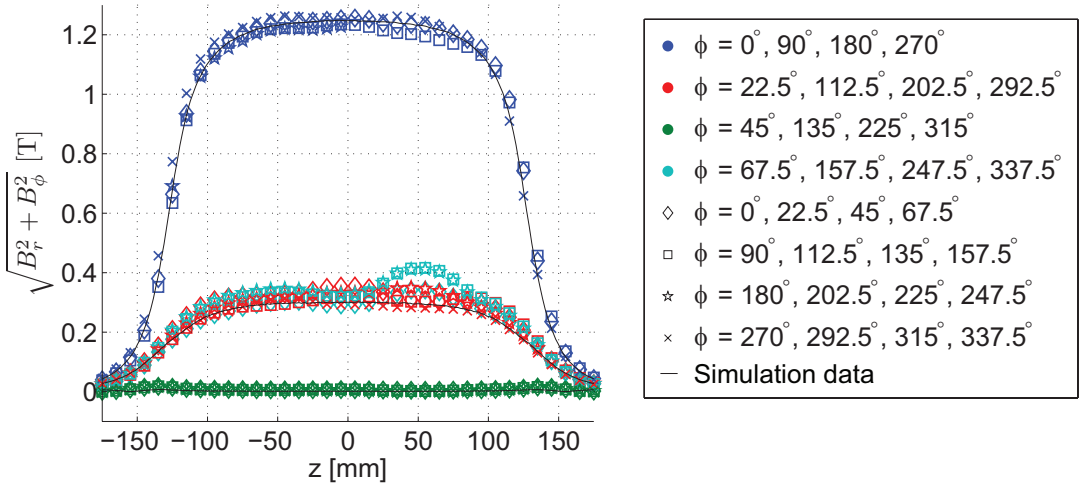

Fig. 7.3: The flux density as a function of z at different angles in the middle of the air gap in the New Magnet.

also seen that the flux density in the high field region is high along almost the entire length of the device, and only decrease very near the ends of the device.

Having shown that the measured flux density is periodic with a period of 90 degrees a more detailed measurement of the flux density for 0-90 degrees was performed. Both the r, ϕ and z components of the magnetic flux density were measured. The norm of the flux density as a function of angle for this quadrant of the New Magnet is shown in Fig. 7.4. As can be seen the flux density decreases from the high field region to the low field region exactly as predicted by the simulation. One exception is that the field at one end of the New Magnet, at $z = 125$ mm, appears to be slightly higher than at the other end.

All components of the flux density were also measured as a function of the height in the air gap at selected places in the New Magnet. The norm of the flux density as a function of r for these locations are shown in Fig. 7.5. The flux density is lowest in the center of the air gap and increases towards both the inner and outer magnet. A good agreement between the measurements and simulation is seen.

7.1.1 Performance of the magnet

Having measured the flux density the performance of the magnet with regard to magnetic refrigeration can be evaluated using the Λ_{cool} parameter introduced in Chapter 4.

As previously mentioned other published magnet designs for magnetic refrigeration devices have Λ_{cool} parameters between 0.03 and 0.21 $\text{T}^{2/3}$. The magnet designed here has $V_{\text{mag}} = 7.3$ L, $V_{\text{field}} = 2.0$ L, $B_{\text{high}}^{2/3} = 0.91$ T and $B_{\text{low}}^{2/3} = 0.15$ T. Assuming $P_{\text{field}} = 1$, as is the aim of the device, the design achieves $\Lambda_{\text{cool}} = 0.21$ $\text{T}^{2/3}$, thus equal to the best performing magnet published to date, which is the design by Okamura et al. (2007). The numbers differ from the numbers reported in Chapter 6 because there a model with infinite length was considered.

For the New Magnet the choice of the size of the high and low field regions is arbitrary and

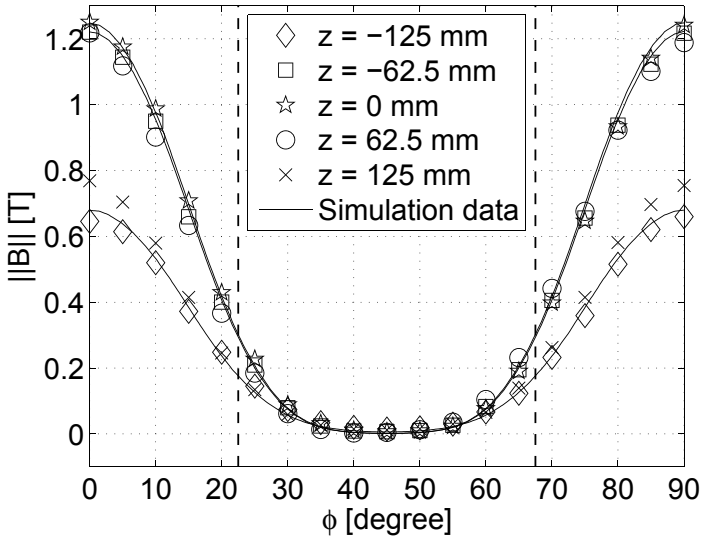

Fig. 7.4: The norm of the flux density as a function of angle in the middle of the air gap of the New Magnet compared with numerical simulations. The dotted lines separate the high and low field regions.

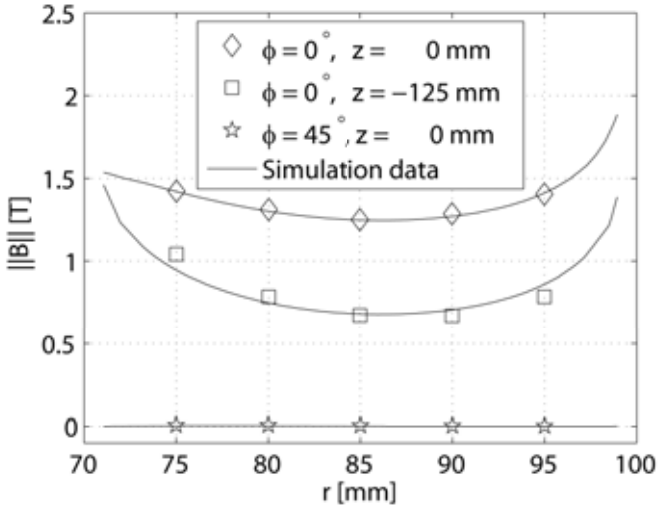

Fig. 7.5: The norm of the flux density as a function of radius at selected locations in the air gap of the New Magnet compared with numerical simulations. The locations are the center of the high field region in the middle and at the end of the magnet and the center of the low field region in the middle of the magnet, respectively.

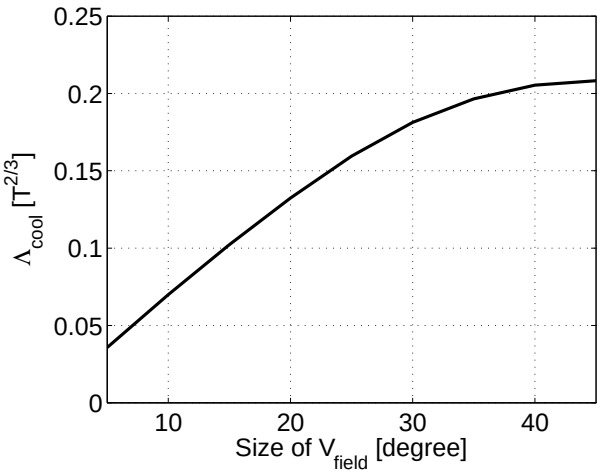

Fig. 7.6: The Λ_{cool} parameter as a function of the size of V_{field} for the New Magnet.

so they could have been chosen to span less than 45 degrees. This would lead to a higher value for $B_{\text{high}}^{2/3}$ and a lower value of $B_{\text{low}}^{2/3}$ but also to a lower value of V_{field}. The P_{field} parameter would remain constant. In Fig. 7.6 Λ_{cool} is shown as a function of the size of V_{field}. As can be seen Λ_{cool} attains the highest value for this design when the high and low field regions combined span the entire air gap circumference.

Having determined the flux density and performance of the New Magnet it is now time to investigate another important property of the design namely the magnetic forces in the design.

7.2 Forces in the New Magnet design

There are substantial forces present in the New Magnet design. Besides the forces between the individual magnets in the inner and outer magnets there is a force between these two magnets. Also there is a significant force on the plates of MCM that will be rotating inside the air gap. The forces between the individual magnets in the inner and outer magnets will not be considered here, as Bakker Magnetics has ensured that the magnets has been constructed in such a way that the inner and outer magnets are structurally safe. The remaining forces will be estimated using numerical simulations. Here the force on a magnetic material is calculated using the Maxwell stress tensor, $\mathbb{T}$, formulation. The force on a body is given by

$$\mathbf{F} = \frac{1}{\mu_0} \int_S \mathbb{T} \cdot \hat{\mathbf{n}} ds \, . \tag{7.1}$$

where $\hat{\mathbf{n}}$ is the outwards normal of the integration surface S that is defined by a closed loop in free space that surrounds the object on which the force is calculated. The tensor $\mathbb{T}$ is Maxwell's stress tensor and its components are given by

$$T_{ij} = B_i B_j - \frac{1}{2} \delta_{ij} B^2 \, , \tag{7.2}$$

where δ_{ij} is the Kronecker delta, which has a value of one if the indices are the same and zero otherwise.

The torque on a body can be calculated as

$$\tau = \frac{1}{\mu_0} \int_S \mathbf{r} \times \mathbb{T} \cdot \hat{\mathbf{n}} ds \,, \tag{7.3}$$

Both the computed force and torque will be independent of the chosen closed loop.

7.3 Forces between the two magnets

It is necessary to consider the force between the inner and outer magnets so that these can be fixed in a structure capable of withstanding this force. There will be both a radial and a tangential component of the force between the two magnets. The radial force is by far the most critical, as this force attracts the magnets. The tangential force acts as a torque and will want to turn either of the magnets until the force is minimized. The force and torque are illustrated in Fig. 7.7.

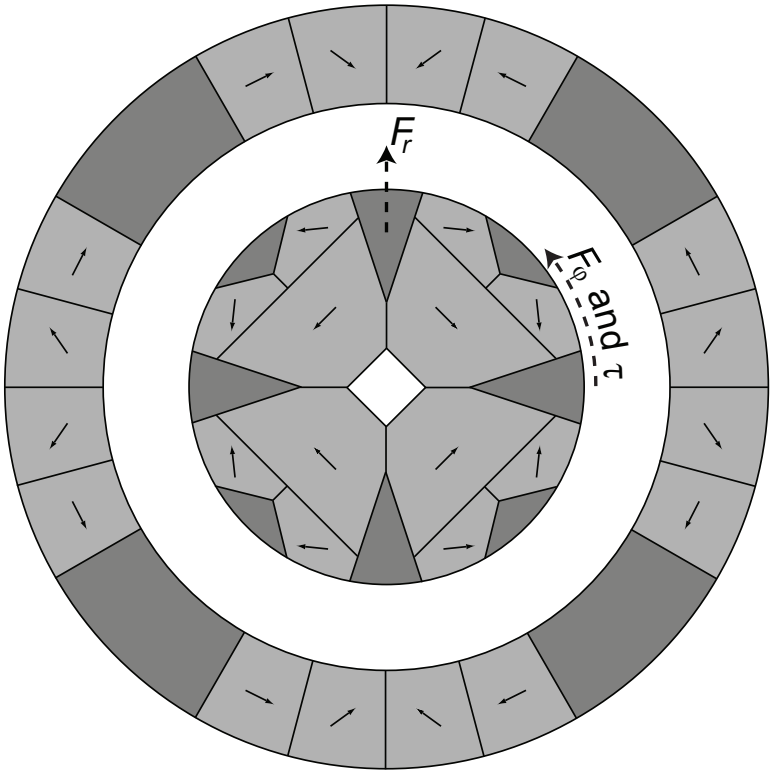

Fig. 7.7: An illustration of the radial force, F_r, tangential force, F_ϕ, and torque, τ, respectively, between the inner and outer magnets, as well as the starting configuration from which these forces are calculated.

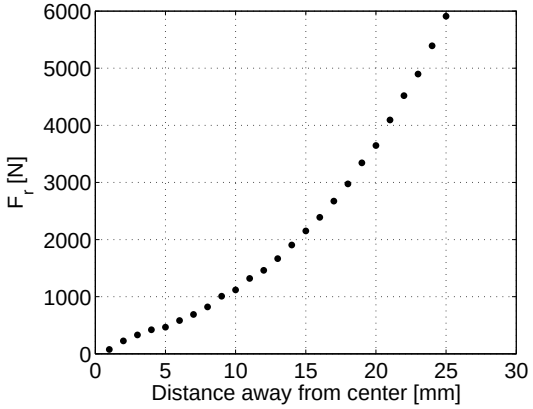

Fig. 7.8: The force between the inner and outer magnet as a function of distance if the inner magnet is moved closer to the outer magnet.

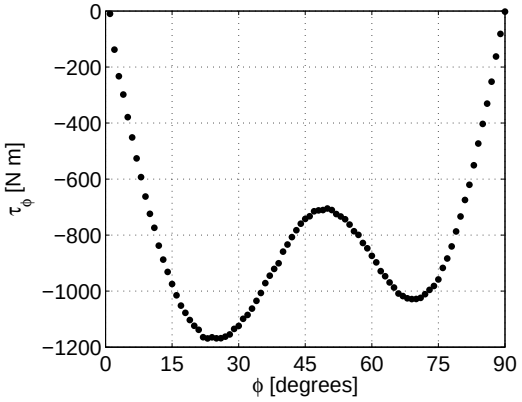

Fig. 7.9: The torque between the inner and outer magnet as a function of the angle the inner magnet has been rotated.

7.3.1 The radial force

The inner and outer magnets will attract each other as a high field region is created by opposite magnetic poles on the inner and outer magnets. However, as there is an even number of equidistantly spaced high field regions the radial force will be balanced in an unstable equilibrium.

Using a numerical two dimensional model, where the results are afterwards multiplied by the length of the New Magnet, the force has been calculated between the inner and outer magnets. The two dimensional model will overestimate the force because the loss of flux through the ends of the device is ignored, but this is not a concern here as the calculated force is primarily used to design a sufficiently strong support structure for the New Magnet. In Fig. 7.8 the radial force is shown for the case where the inner magnet is moved closer to the outer magnet, i.e. moved away from the center, or symmetric, position. The inner magnet is moved in a direction along a high field region i.e. along the F_r arrow shown in Fig. 7.7. As can be seen from the figure the force increases dramatically if the magnets are brought out of equilibrium. This is a serious concern and the structure supporting the inner magnet must be constructed such that this cannot happen.

7.3.2 The tangential force

The tangential force between the two magnets results in a torque around the central axis that will turn either of the magnets if these are not properly aligned or fixed. The torque is shown in Fig. 7.9 for different rotations of the inner magnet. As can be seen from the figure there is no torque in the starting position but as the inner magnet is turned the torque increases significantly. The torque is in a restoring direction, i.e. towards the original position, which is fortunate as this means that the magnet design is stable towards rotation. It is also seen that if the inner magnet is turned a full 90 degrees it reaches an equilibrium position. However, as can be seen this position is an unstable equilibrium, as a north pole of the inner magnet is pointing towards a north pole of the outer magnet and so on. The asymmetry in Fig. 7.9 is due to the

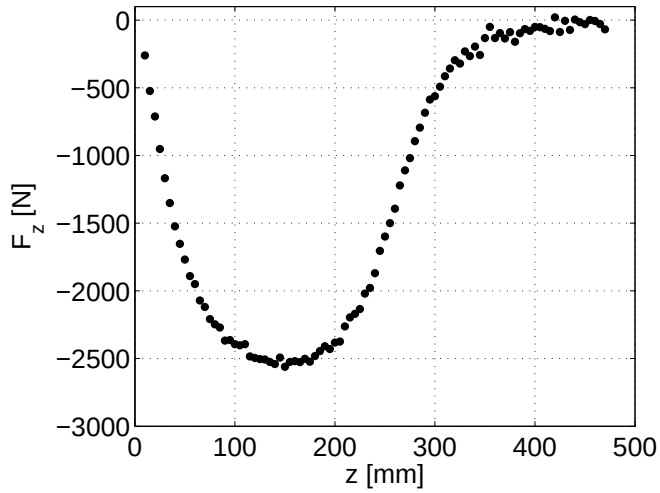

Fig. 7.10: The force as a function of distance if the inner magnet is pulled out from within the outer magnet. The small scatter of the data points is due to the numerical resolution. The force is directed towards the center of the magnet.

fact that the torque is reduced when the iron areas of the inner and outer magnets line up.

7.3.3 Removing the inner magnet

It is not possible to mount the flow heads for the flow inlets and outlets or the regenerator housing, i.e. the structure containing the plates of MCM, if the inner magnet is axially supported in both ends of the New Magnet. The axial support can be seen in Figs. 7.1 and 7.2. Either of the axial supports must be removed in turn to allow the flow heads to be mounted. To overcome this problem it was considered to pull the inner magnet completely out from within the outer magnet while the flow heads and the regenerator housing were mounted. In order to evaluate if this was a feasible solution the force needed to pull the inner magnet away from the outer magnet was calculated. This was done using a three dimensional model of the New Magnet.

The force on the inner magnet as a function of distance pulled is shown in Fig. 7.10. The total work required to remove the inner magnet, which is found by integrating the force along the distance moved, is 580 J. Because of the significant force involved this idea was abandoned and it was instead chosen to enforce the central axis and the two axial supports such that the inner magnet can be suspended in a single support while the flow head and regenerator is mounted.

7.4 Forces on the regenerator

It is important to calculate the force on the magnetocaloric plates in the regenerator, both when the machine is running and when the regenerator is mounted, i.e. inserted into the magnet. The force will be calculated using both a two and a three dimensional numerical model. In general the three dimensional model is used when the force on a single plate is calculated while the two dimensional model is used to calculate the force on the entire regenerator at once. The reason this approach is used is that it is not possible to model the whole of the regenerator in a three dimensional simulation, as the resolution becomes to large to handle numerically. The regenerator is modeled as consisting of 500 plates of Gd, where a plate has dimensions $0.5 \times 20 \times 250$ mm^3. The plates are located in the middle of the air gap, which leaves a gap of 5 mm on either side of the plates for regenerator housing and rotational clearance. The plates are positioned radially, so the fluid channels between the plates will be small near the inner magnet and large near the outer magnet. As there are 500 plates and the circumference in the center of the air gap is $2\pi * 85$ mm, the width of the fluid channel is 0.568 mm in the middle of the air gap. At the top of the plates the fluid channel is 0.694 mm while at the bottom it is 0.442 mm. In Appendix B a picture of a magnetocaloric plate as will be used in the actual machine is shown.

The Gd is modeled using the measured values of the magnetization and the adiabatic temperature change described in Chapter 2.

7.4.1 Mounting the regenerator

When the regenerator is removed from (or mounted into) the air gap the plates will experience a gradient in the magnetic field and will tend to move towards the middle of the New Magnet. The force required to remove a single plate of Gd has been calculated as a function of z for different angle positions in the regenerator. The plate has a starting temperature of 293 K when in the magnet, but as the plate is removed the temperature is lowered as the magnetic field decreases, because of the adiabatic temperature change. Note that this changes the magnetization, making the plate more magnetic. As mentioned the force is calculated for a single plate and thus demagnetization effects from nearby plates are ignored. This is a justified approach as it was shown by Bahl and Nielsen (2009) that the difference in adiabatic temperature change between a single and a stack of magnetocaloric plates is small if the stack is aligned such that the plates have a small demagnetization factor, as is the case here. An illustration of the force that is calculated is shown in Fig. 7.11.

The force, F_z, on a single plate located at an angle ϕ and at a distance z from the center of the magnet is shown in Fig. 7.12 as a surface plot. It can clearly be seen that the force on the plate is largest if the plate is moved out from the center of the high field region ($\phi = 0°$), as the field gradient out of the magnet is the largest here. Summing up the individual 500 plates the total force on the regenerator as a function of distance can be found. The total force on the entire regenerator is shown in Fig. 7.13 as a function of z. It is seen that a substantial force is needed to completely remove the regenerator. Integrating this force gives the total work required to remove the regenerator, which is 155 J.

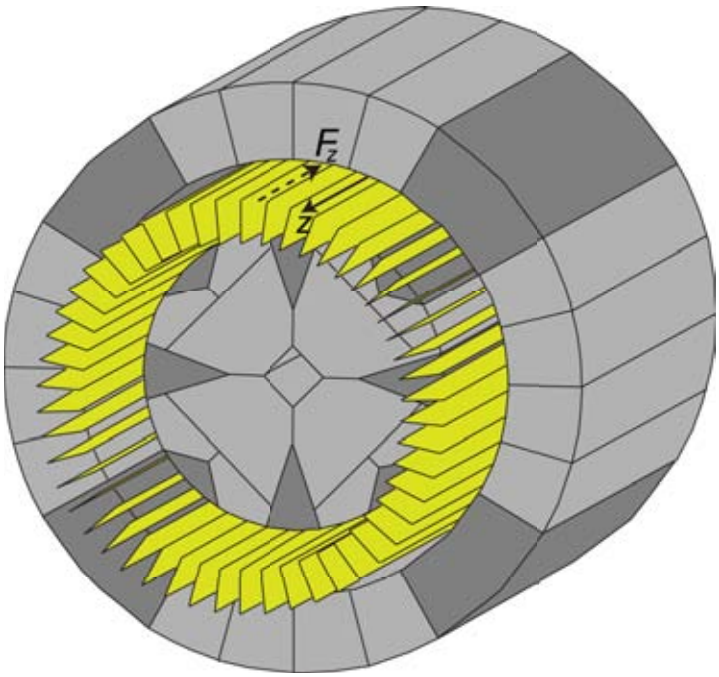

Fig. 7.11: An illustration of the force, F_z, required to remove the regenerator from the air gap. The actual regenerator has 500 plates but here only 50 are shown. The regenerator (in green) is shown pulled 50 mm out of the magnet. In the model the force is calculated on a single plate.

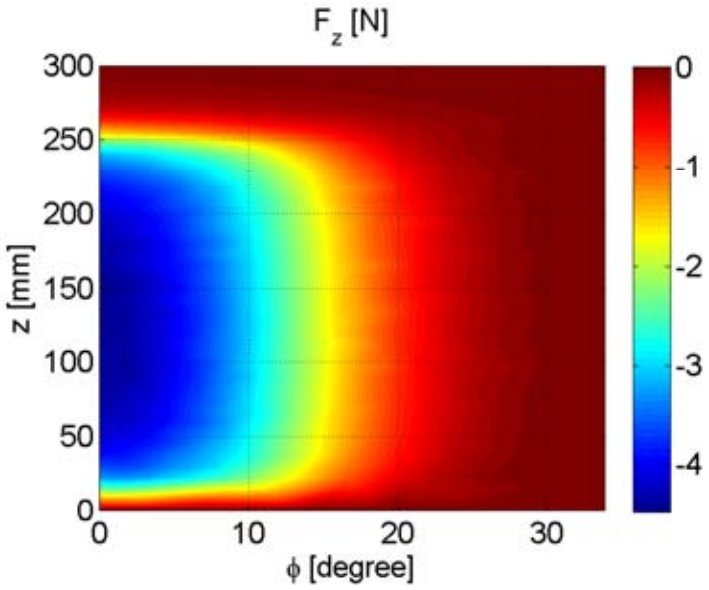

Fig. 7.12: The force, F_z, on a single plate of Gd with a starting temperature of 293 K located at an angle, ϕ, and at a distance, z, from the center of the regenerator.

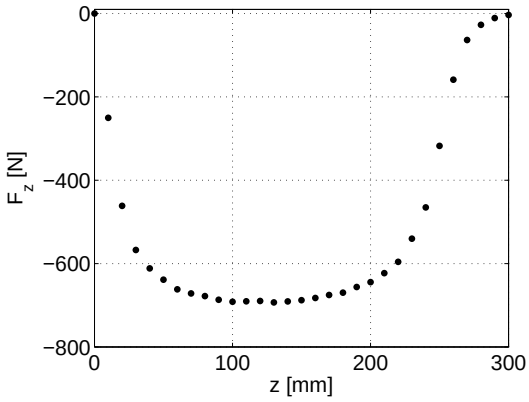

Fig. 7.13: The force on the whole 500 plate regenerator as a function of distance the regenerator is moved out of the air gap. The force is directed into the magnet.

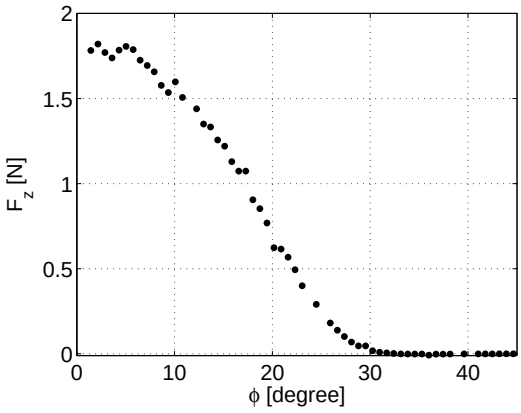

Fig. 7.14: The force on a single plate of Gd with a linear temperature profile from 273 K to 303 K located at an angle ϕ if it is centered in the magnet. Some scatter due to the numerical resolution can be seen.

7.4.2 Fixing the regenerator

There will be a force on the regenerator in the z-direction during operation of the magnetic refrigeration device when the regenerator shown in Fig. 7.11 is centered in the magnet because one end of the regenerator will be cold whereas the other will be hot. This means that one end of the regenerator will be more magnetic than the other and this results in a magnetic force along the z-direction directed from the cold end of the regenerator and towards the middle of the magnet.

This force has been calculated assuming a linear temperature profile inside the Gd regenerator and a cold, T_{cold}, and hot, T_{hot}, temperature of 273 K and 303 K respectively. As with the force for mounting the regenerator the force considered here has been found by calculating the force on a single plate, thus ignoring demagnetization effects from nearby plates. The force for a single plate located at an angle ϕ is shown in Fig. 7.14. The total force for the entire regenerator is summed to be 360 N. The flow caps at the end of the regenerator need to be able to withstand this force in order to keep the regenerator fixed in the middle of the magnet.

7.4.3 Rotating the regenerator

The most important force in the refrigeration system is the force experienced by an MCM plate as it is rotating around in the air gap. This force is the cause of the work that will be required to turn the regenerator. If heat were not removed from the plates by the flow of the heat transfer fluid there would be no net force on the regenerator, as an equal number of equally magnetic plates would be entering and exiting the high field region. However, as heat is removed at the center of the high field region the plates exiting the high field region will be slightly colder than the plates entering, thus they will be more magnetic, which results in a net force. Had the plates been heated by the heat transfer fluid in the high field region there would be a net force directed into the high field region in the direction of rotation and the device would work as an

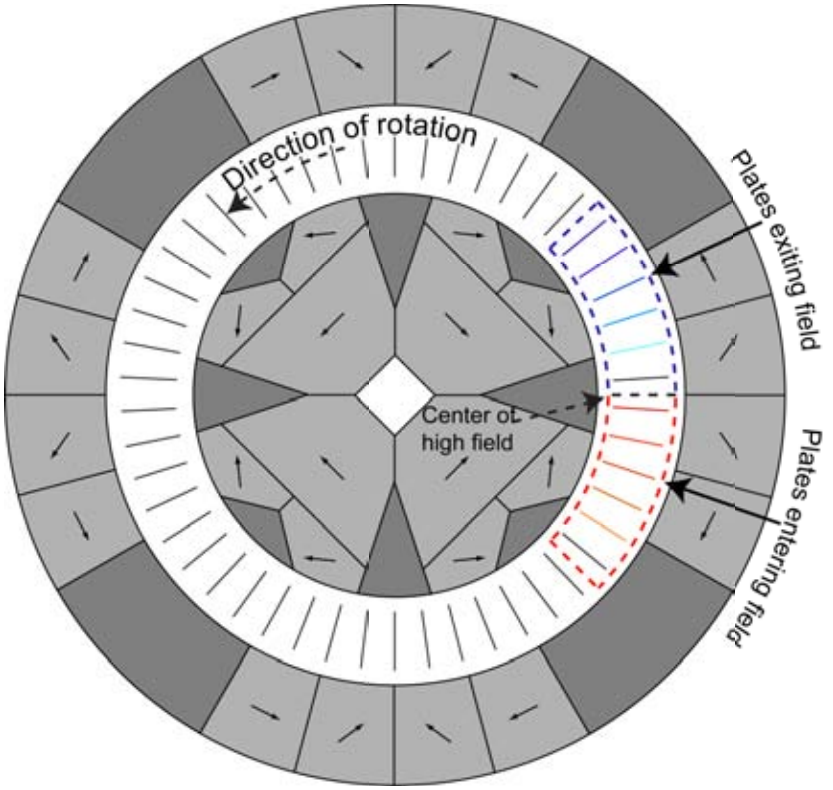

Fig. 7.15: An illustration of the force required to turn the regenerator. The actual regenerator has 500 plates but here only 50 are shown. The plates in the illustrated region are colored according to their temperature. The heat is removed from the plate at the center of the high field region.

engine. The force is illustrated in Fig. 7.15.

In order to estimate the force needed to turn the regenerator the system is modeled as a two dimensional model consisting of 500 plates of Gd. It is not possible to model this many plates in a three dimensional model. Any eddy current heating of the plates is ignored as the system is modeled as a magnetostatic system. The force in the direction of rotation is calculated on each plate but the full system is modeled so each plate is affected by the magnetization of nearby plates. The force is calculated from a two dimensional simulation, which is then multiplied by the length of the plate. This will overestimate the force, as the drop in magnetic flux density near the ends of the magnet is disregarded.

The error of using a two dimensional simulation can be estimated by comparing the calculated force from the two dimensional model with the three dimensional model used to calculate the force to fix the regenerator since here F_ϕ was also calculated. The force resulting from the two and three dimensional simulations is shown in Fig. 7.16, which shows the force as a function of angle for a plate with a linear temperature profile from 273 K to 303 K that is centered, i.e. situated from $z = -125$ mm to 125 mm, in the magnet. As can be seen there is a difference in the calculated force, as the two dimensional model overestimates this. However, the order

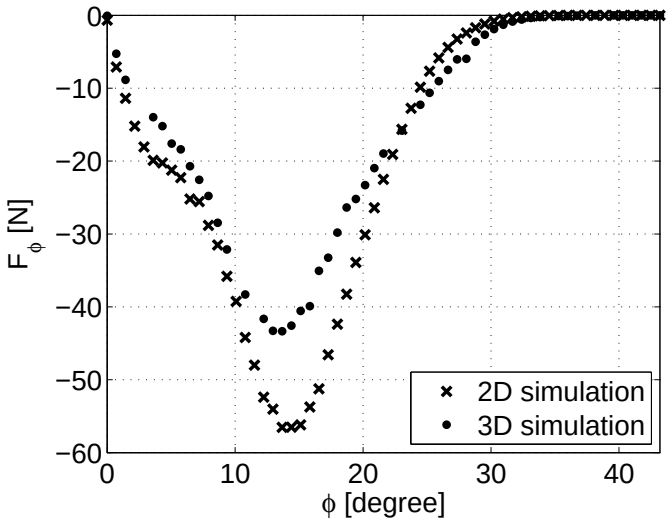

Fig. 7.16: The force on a plate with a linear temperature profile from 273 K to 303 K as a function of angle in a two and three dimensional simulation, respectively.

of magnitude of the two dimensional result is correct. The calculation of the force will be used to dimension an appropriate motor for turning the regenerator in the New Machine, and so an overestimation of the force will not present a problem, as this will just lead to a slightly over dimensioned motor. Thus, the results from the two dimensional model are acceptable.

Having determined that the two dimensional model is sufficient, the force in the direction of rotation has been calculated on a single plate in a 500 plate regenerator. First the case where no heat is removed in the center of the high field region is considered. The initial temperature of the plate has been varied from 260 K to 320 K in steps of 1 K and the angular position of the plate from 0 to 45 degrees in steps of 0.72 degrees, which is the spacing between the plates, i.e. 360/500 degrees. For the remaining angles the solution is mirror symmetric. All 500 plates in the regenerator are present, and their temperature and magnetization are corrected for the adiabatic temperature change depending on the experienced magnetic field.

The force per unit length as a function of angle and initial temperature, i.e. the temperature that a plate would have if it were in a magnetic field of $\mu_0 H = 0$ T, is shown in Fig. 7.17. The force is largest when the plate is cold, as it is more magnetic, and when the plate is located where the largest magnetic field gradient is present, which is between the high and low field regions.

Because of the difference in temperature along a plate different parts of the plate will experience a different force. This can clearly be seen from Fig. 7.17 by considering the force as a function of temperature for a fixed angle. For an angle around 15 degrees, which is between the high and low field regions, the force along a single plate can differ from -100 N m^{-1} to -300 N m^{-1} if the temperature along the plate goes from 260 K to 300 K. Thus it is extremely important to construct the regenerator housing such that it can withstand this force, which will try to twist the plate. Also, and more importantly, the plates must be structurally stable in order not to crack or break due to this force.

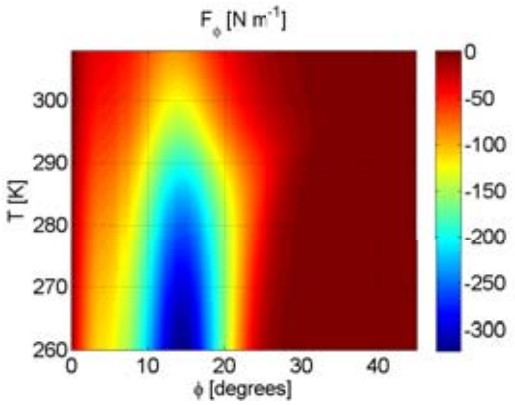

Fig. 7.17: The force per unit length in the direction of rotation on a plate of Gd with an initial temperature, T, located at an angle, ϕ. The force for the remaining angles can be obtained by mirror symmetry and by reversal of the sign of F_ϕ depending on whether the plate is entering of exiting the high field region.

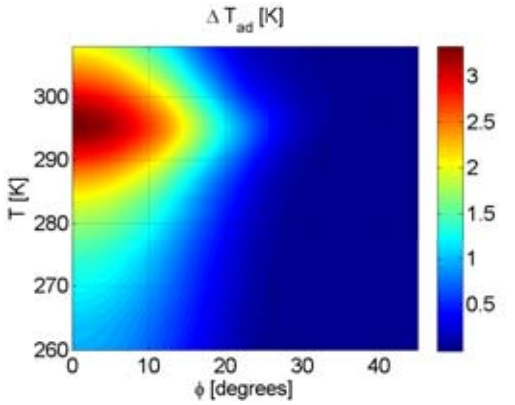

Fig. 7.18: The adiabatic temperature change in a plate at starting temperature, T, located at an angle, ϕ. The temperature change for the remaining angles can be obtained by mirror symmetry.

Along with the force the magnetic field is also calculated. This can be used to find the adiabatic temperature change of a plate, which is shown in Fig. 7.18 as a function of angle and initial temperature. The adiabatic temperature change of Gd is found based on the interpolated data set described in Chapter 2. As expected the adiabatic temperature change is greatest in the center of the high field region and near the Curie temperature.

The total force and work needed to turn the entire regenerator must also be estimated. These will depend on the temperature span of the regenerator. The work needed to turn the regenerator is the difference in work gained by moving a plate into the high field region and the work needed to remove the same plate once it has had its temperature lowered by the flow of the heat transfer fluid.

In order to calculate the force and work on a plate entering and exiting the high field region we assume that when a plate reaches the exact center of the high field region all generated heat is completely removed from the plate, which is thus brought back to its original linear temperature profile. As the plate is then moved out of the high field region the temperature drops along the plate, though not in a uniform way since the adiabatic temperature change depends on temperature. In Fig. 7.19 the temperature along the plate with a linear temperature profile from 273 K to 303 K before it has entered the high field region, at the center of the high field region before the heat is removed and after it has completely exited the high field region is shown. The heat has been removed as described above. As can be seen there is nonlinear drop in temperature along the plate.

The removal of heat gives rise to a difference in force between the plates entering and exiting the high field region. This difference is shown in Fig. 7.20 which shows the force as a function of absolute angle for a 250 mm plate with a linear temperature profile from 273 K to 303 K. The absolute angle is shown, since plates entering the high field region have negative ϕ and

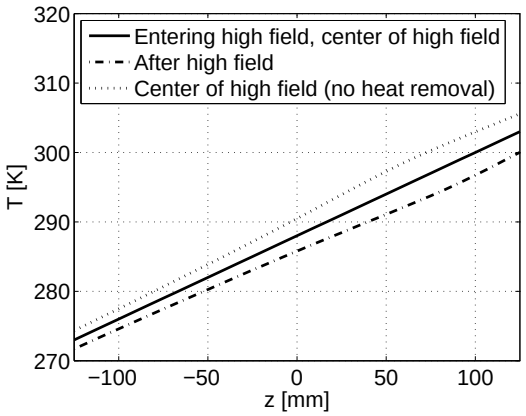

Fig. 7.19: The temperature along a plate before and after it has been through the high field region. At the center of the high field region the generated heat is removed and the plate brought back to its original linear temperature profile.

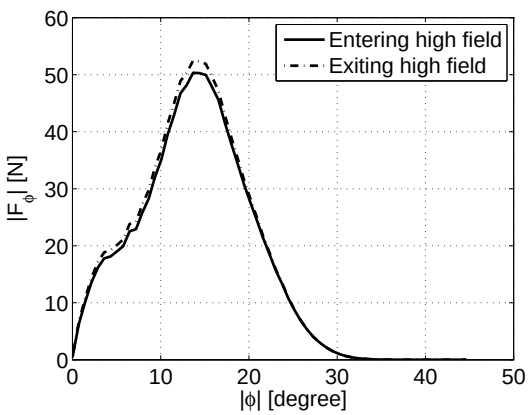

Fig. 7.20: The force on a plate with a linear temperature profile from 273 K to 303 K as it enters and exits the high field region. At the center of the high field region, $\phi = 0$, the generated heat is removed and the plate brought back to its original linear temperature profile. The exiting force is negative.

plates exiting have positive ϕ for the high field region centered around $\phi = 0°$. The rotation of the regenerator is counterclockwise, i.e. along positive ϕ. As can be seen from the figure the force is slightly larger on the plate exiting the high field region than entering the high field. As previously stated this is because the plate gets colder as it is moved out of the field. The force entering the high field region is positive, i.e. along the direction of rotation, and the force exiting is negative.

The total force on the eighth of the regenerator entering and the eighth exiting a high field region is shown in Fig. 7.21 as a function of T_{cold}, where a linear temperature profile between $T_{\text{hot}} = 303$ K and T_{cold} has been assumed. These eights of the regenerator correspond to the areas shown in Fig. 7.15. The total force increases as T_{cold} decreases, since to the plates become more magnetic. The difference between the force entering and exiting the regenerator is shown in Fig. 7.22. This is the force necessary to turn a quarter of the regenerator. For the whole regenerator the the maximum rotational force is 240 N, which is the case for $T_{\text{cold}} = 291$ K.

The total work performed on a single plate entering and exiting the high field region can be found by integrating the force shown in Fig. 7.21 along the distance moved. This work is shown in Fig. 7.23, and is equal to the magnetic work performed on the plate. When the plate is moved into the high field region the force is along the direction of motion and the work is positive, while the opposite is true when the plate is removed from the high field region.

There will also be a force on the plates in the radial direction because of the difference in magnetic field across the gap, as was shown in Fig. 7.5. However, as the plates are fixed in the regenerator and it is cylindrically symmetric there will be an equal but opposite force on each of the parts of the regenerator in the high field regions. These forces cancel each other and thus this component of the force can be ignored.

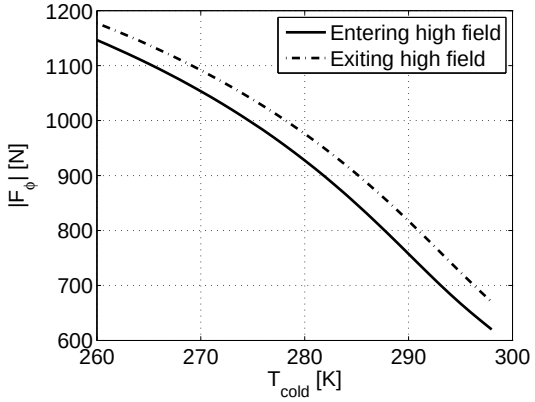

Fig. 7.21: The total force on the eighth of the regenerator that is entering and exiting the high field region as a function of the temperature of the cold end of the regenerator.

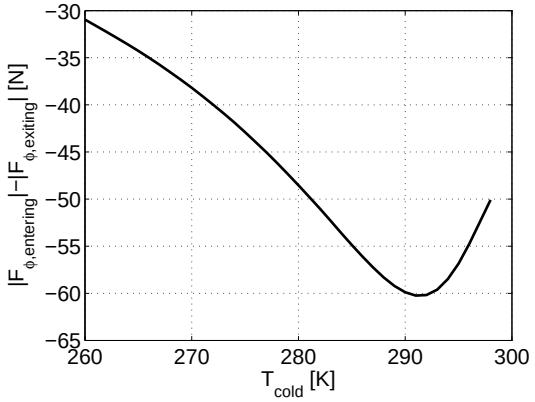

Fig. 7.22: The difference in force between the eighth of the regenerator entering and exiting the high field region as a function of the temperature of the cold end of the regenerator.

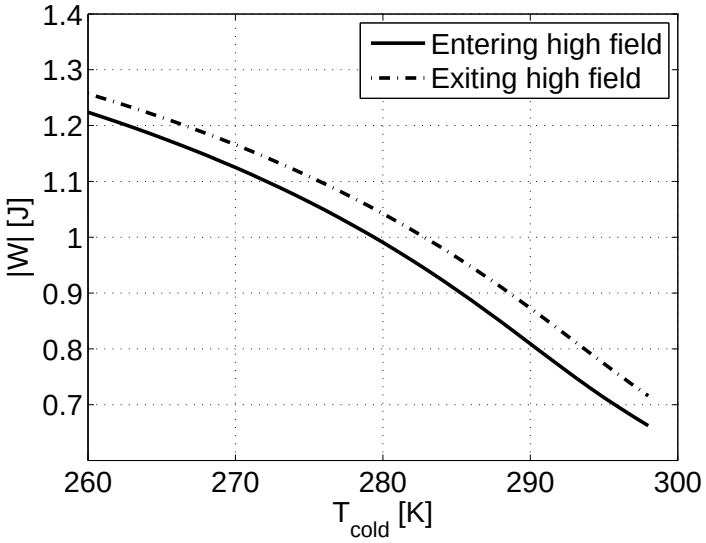

Fig. 7.23: The absolute total work on a single plate entering and exiting the high field region as a function of T_{cold}. The work entering the high field region is negative, i.e. energy is gained, while the work is positive when the plate is removed, i.e. energy is needed.

7.4.4 Plates in compartments

It is also a possibility to arrange the plates in compartments. Here we consider a case where the regenerator is divided into 25 equidistantly spaced compartments with 11 plates in each compartment. In between the compartments is empty space. The plates inside the compartments are spaced as in the 500 plate regenerator case considered previously, which means that the empty space in the regenerator also corresponds to the space of 11 plates in the 500 plate regenerator. For this compartmented regenerator the force as parts of it enters and exists the high field region differs from the equidistantly spaced regenerator, as there are no longer the same number of plates entering and exiting the high field region at the same time.

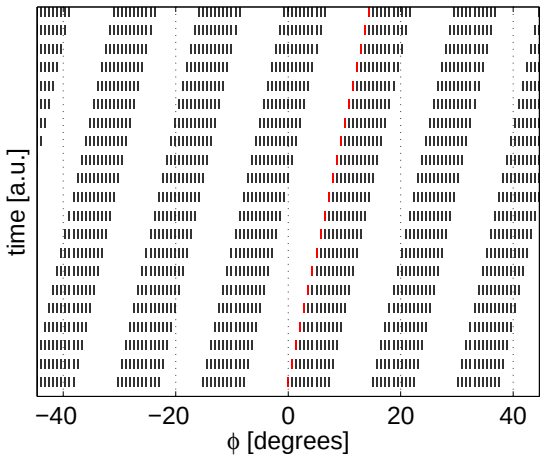

Fig. 7.24: The movement of the plates as a function of time. The angle ϕ, used in Fig. 7.25 is indicated by the red plate.

In Fig. 7.24 the plates in compartments are shown as they enter and exit a high field region centered at $\phi = 0°$. In 7.25 the total force for a quarter of the regenerator in compartments is shown as a function of angle and T_{cold}. The force for the remaining angles can be obtained by simply symmetry. As can be seen the force is of the order of the equidistant case, i.e. Fig. 7.22, but here the force also becomes positive, i.e. there will be a net force dragging the regenerator into the high field region.

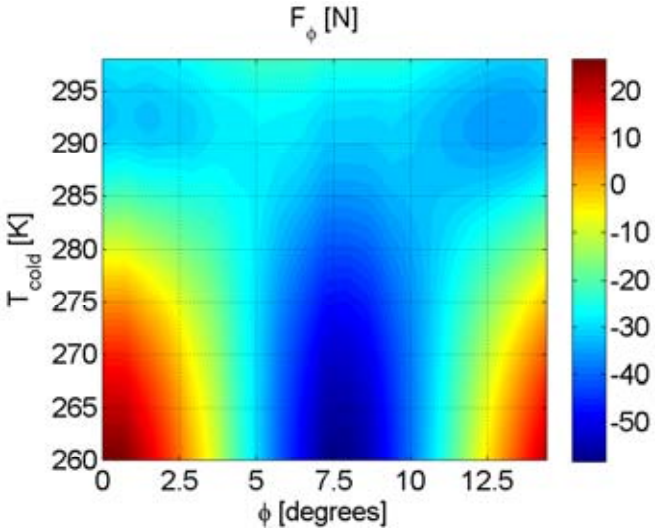

Fig. 7.25: The total force on a quarter of the regenerator in compartments as a function of the angle ϕ, indicated in Fig. 7.24, and T_{cold}.

7.5 Summary

In this chapter measurements of the magnetic flux density were compared to a three dimensional model of the magnet and an excellent agreement was seen. Next, the radial and tangential forces between the inner and outer magnets were considered. The radial force was found to be significant if the magnets are brought out of equilibrium, while the tangential force was found to be in the restoring direction.

The force on the regenerator was also considered. Here the temperature profile along the MCM plates will cause a force to be present on the regenerator. The force to fix the regenerator so that it does not move in the z-direction during operation was found to be 360 N for a linear temperature profile from 273 K to 303 K along the plates. Assuming that the heat is removed from the plates in the center of the high field region the force to rotate the regenerator was found as a function of the temperature of the cold end of the regenerator. The maximum rotational force was 240 N at $T_{\text{cold}} = 291$ K.

The tangential force on a single plate was also considered and it was shown that this force can differ between -100 N m^{-1} to -300 N m^{-1} along a plate with a linear temperature profile from 260 K to 300 K. Thus the plates must be structurally stable.

Finally, the force on the regenerator if the plates are separated into compartments was calculated and found to be both positive and negative along the direction of rotation. This was different from the non-compartmented case where the force is always against the direction of rotation.

Chapter 8

Conclusion

The aim of this thesis was to investigate how to design a magnet for use in magnetic refrigeration. In order to gain an understanding of the requirements for such a magnet the properties of both magnetocaloric materials and the magnetic refrigeration process itself were investigated as a function of magnetic field and temperature.

First, the properties of the benchmark magnetocaloric material Gd were investigated. Here it was determined that the adiabatic temperature change at the Curie temperature scales with the magnetic field to the power of 2/3. This was also shown to be true for other magnetocaloric materials. This is extremely important as it shows that a magnet assembly must be designed such that the magnetocaloric material experiences a very low field in order to gain the largest adiabatic temperature change possible. Next, the active magnetic regeneration (AMR) cycle, which generates the cooling capacity and temperature span in a magnetic refrigeration device, was investigated for a number of process parameters using a publicly available one dimensional numerical model. Here, it was determined that in general the relative change in AMR performance as a function of magnetic field was generally the same for a range of different process parameters. The performance of the AMR was shown to be a weak function of the width and ramp rate of the magnetic field. However, it was seen that it was very important to synchronize the fluid flow and magnetic field profiles. Finally, it was shown that the maximum refrigeration capacity has a stronger dependency on the maximum value of the magnetic field than the maximum temperature span and that these almost scales identically for the different process parameters. The temperature span scales with the magnetic field with a power slightly less than the 2/3 exponent found for the scaling of the magnetocaloric materials at the Curie temperature. Based on these findings it was concluded that the performance of the AMR for different regenerator geometries and process parameters is the same as a function of magnetic field which in turn means that the design of the magnet can be done independently of these.

Having determined these facts other published magnet designs used in magnetic refrigeration were reviewed and evaluated using the introduced Λ_{cool} figure of merit to learn the properties of the best magnet designs to date. A permanent magnet design was shown to be preferable to an electromagnet for common household refrigeration. It was shown that there is a great span in the efficiency of the different magnet designs, e.g. two designs used almost the same amount of magnets but one created a high field region that is over three times larger than the other. Some key points for designing an efficient magnet was also found. Next, the Halbach cylinder was investigated and an analytical expression of the magnetic field for a Halbach cylinder of infinite length was found and the optimal dimensions, i.e. the dimensions that give a minimum volume of magnets for a given mean flux density, of a three dimensional Halbach cylinder were found.

Based on the knowledge gained from the magnetocaloric materials, the performance of the AMR, the reviewed magnet designs and the Halbach cylinder a high performance cylindrical magnet for use in a new magnetic refrigeration device being built at Risø DTU was designed.

This magnet design was based on the concentric Halbach cylinder design to which two optimization schemes were applied. These schemes were developed in order to lower the flux density in the low field region and lower the amount of magnet material used and can be applied to any magnet design. The schemes reduced the volume of magnet material from 41 L/m to 25.4 L/m while at the same time increasing the difference in flux density between the high and low field regions in the concentric Halbach cylinder magnet from 0.53 T to 0.76 T. Following this optimization the design was segmented and the direction of magnetization of the different segments optimized. This resulted in an increase in flux density in the high field regions, raising the flux density difference to 0.87 T. The working point of the magnets in the design was investigated and shown to be close to the theoretical maximum value.

The magnet design was constructed and the flux density measured and found to be in excellent agreement with a numerical model. The forces between the inner and outer magnet were investigated and found be to substantial if the magnets were brought out of equilibrium. Finally, the forces on the magnetocaloric regenerator were found through numerical simulation.

The work and methods presented in this thesis can be used directly by other researchers working on designing a magnet for magnetic refrigeration. The work relating to the performance of an AMR as a function of the magnetic field can also be used to optimize existing magnetic refrigeration devices. The optimal dimensions found for the Halbach cylinder are directly useable for researchers building these. And finally the schemes presented that lower the flux density in the low field region and lower the amount of magnet material used in a magnet design can be applied to any permanent magnet assembly and will thus be of use in designing permanent magnet assemblies for a great number of applications.

Appendix A

A single analytical solution

As found in Chapter 5 the solution to the vector potential equation for $p = 1$ is

$$A_z(r,\phi) = \sum_{n=1} (\mathcal{A}_n r^n + \mathcal{B}_n r^{-n})\sin(n\phi) + B_{\text{rem}}\frac{r}{p-1}\sin(p\phi)\ . \tag{A.1}$$

By writing out the term for $n = p$ this can also be written as

$$\begin{aligned} A_z(r,\phi) &= \sum_{n=p} (\mathcal{A}_n r^n + \mathcal{B}_n r^{-n})\sin(n\phi) \\ &\quad +(\mathcal{A}_p r^p + \mathcal{B}_n r^{-p})\sin(p\phi) + B_{\text{rem}}\frac{r}{p-1}\sin(p\phi)\ . \end{aligned} \tag{A.2}$$

The radial component of the magnetic field is

$$\begin{aligned} B_r &= \frac{1}{r}\frac{\partial A_z}{\partial \phi} \\ &= \sum_{n=p} n(\mathcal{A}_n r^{n-1} + \mathcal{B}_n r^{-n-1})\cos(n\phi) \\ &\quad +p(\mathcal{A}_p r^{p-1} + \mathcal{B}_n r^{-p-1})\cos(p\phi) + B_{\text{rem}}\frac{p}{p-1}\cos(p\phi)\ . \end{aligned} \tag{A.3}$$

The boundary conditions of the magnetic field and flux density for the geometry defined in Chapter 5 are

$$\begin{aligned} H_\phi^I &= 0 && r = R_{\text{c}} \\ B_r^I &= B_r^{II} && r = R_{\text{i}} \\ H_\phi^I &= H_\phi^{II} && r = R_{\text{i}} \\ B_r^{III} &= B_r^{II} && r = R_{\text{o}} \\ H_\phi^{III} &= H_\phi^{II} && r = R_{\text{o}} \\ H_\phi^{III} &= 0 && r = R_{\text{e}}\ . \end{aligned} \tag{A.4}$$

From the boundary condition $B_r^{III} = B_r^{II}$ we have

$$\begin{aligned} &\sum_{n=p} n(\mathcal{A}_n^{III} R_{\text{o}}^{n-1} + \mathcal{B}_n^{III} R_{\text{o}}^{-n-1})\cos(n\phi) \\ &\quad +p(\mathcal{A}_p^{III} R_{\text{o}}^{p-1} + \mathcal{B}_p^{III} R_{\text{o}}^{-p-1})\cos(p\phi) = \sum_{n=p} n(\mathcal{A}_n^{II} R_{\text{o}}^{n-1} + \mathcal{B}_n^{II} R_{\text{o}}^{-n-1})\cos(n\phi) \\ &\qquad +p(\mathcal{A}_p^{II} R_{\text{o}}^{p-1} + \mathcal{B}_p^{II} R_{\text{o}}^{-p-1})\cos(p\phi) \\ &\qquad +B_{\text{rem}}\frac{p}{p-1}\cos(p\phi)\ , \end{aligned} \tag{A.5}$$

where the last term is due to the remanence inside the magnet.

We must thus have that

$$\sum_{n=\,p} n(\mathcal{A}_n^{III} R_{\rm o}^{n-1} + \mathcal{B}_n^{III} R_{\rm o}^{-n-1})\cos(n\phi) = \sum_{n=\,p} n(\mathcal{A}_n^{II} R_{\rm o}^{n-1} + \mathcal{B}_n^{II} R_{\rm o}^{-n-1})\cos(n\phi)\ . \quad \text{(A.6)}$$

The exact same argument as above must be true for the boundary condition between region I and II, $B_r^I = B_r^{II}$, i.e. at $R_{\rm i}$, and so we get the following equations

$$\begin{aligned} \mathcal{A}_n^{III} R_{\rm o}^{n-1} + \mathcal{B}_n^{III} R_{\rm o}^{-n-1} &= \mathcal{A}_n^{II} R_{\rm o}^{n-1} + \mathcal{B}_n^{II} R_{\rm o}^{-n-1} \\ \mathcal{A}_n^{I} R_{\rm i}^{n-1} + \mathcal{B}_n^{II} R_{\rm i}^{-n-1} &= \mathcal{A}_n^{II} R_{\rm i}^{n-1} + \mathcal{B}_n^{II} R_{\rm i}^{-n-1}\ , \end{aligned} \quad \text{(A.7)}$$

or

$$\begin{aligned} \mathcal{A}_n^{III} &= \mathcal{A}_n^{II} + (\mathcal{B}_n^{II} - \mathcal{B}_n^{III}) R_{\rm o}^{-2n} \\ \mathcal{A}_n^{I} &= \mathcal{A}_n^{II} + (\mathcal{B}_n^{II} - \mathcal{B}_n^{I}) R_{\rm i}^{-2n}\ . \end{aligned} \quad \text{(A.8)}$$

We must also look at the angular component of the magnetic field, H_ϕ, which is

$$H_\phi = \frac{1}{\mu_0\mu_r}(B_\phi - B_{{\rm rem},\phi}) \quad \text{(A.9)}$$

$$\begin{aligned} &= \frac{1}{\mu_0\mu_r} \sum_{n=\,p} n(-\mathcal{A}_n r^{n-1} + \mathcal{B}_n r^{-n-1})\sin(n\phi) + p(-\mathcal{A}_p r^{p-1} + \mathcal{B}_n r^{-p-1})\sin(p\phi) \\ &\quad -\frac{M}{\mu_r}\frac{1}{p-1}\sin(p\phi) - \frac{M}{\mu_r}\sin(p\phi)\ . \end{aligned} \quad \text{(A.10)}$$

For the boundary condition at $H_\phi^I = H_\phi^{II}$ we get

$$\begin{aligned} &\sum_{n=\,p} n(-\mathcal{A}_n^I R_{\rm i}^{n-1} + \mathcal{B}_n^I R_{\rm i}^{-n-1})\sin(n\phi) \\ &\quad -p(\mathcal{A}_p^I R_{\rm i}^{p-1} + \mathcal{B}_p^I R_{\rm i}^{-p-1})\sin(p\phi) = \frac{1}{\mu_r} \sum_{n=\,p} n(-\mathcal{A}_n^{II} R_{\rm i}^{n-1} + \mathcal{B}_n^{II} R_{\rm i}^{-n-1})\sin(n\phi) \\ &\qquad + \frac{p}{\mu_r}(-\mathcal{A}_p^{II} R_{\rm i}^{p-1} + \mathcal{B}_p^{II} R_{\rm i}^{-p-1})\sin(p\phi) \\ &\qquad - \frac{B_{\rm rem}}{\mu_r}\frac{1}{p-1}\sin(p\phi)\ , \end{aligned} \quad \text{(A.11)}$$

while for $H_\phi^{II} = H_\phi^{III}$ we get

$$\begin{aligned} &\sum_{n=\,p} n(-\mathcal{A}_n^{III} R_{\rm o}^{n-1} + \mathcal{B}_n^{III} R_{\rm o}^{-n-1})\sin(n\phi) \\ &\quad -p(\mathcal{A}_p^{III} R_{\rm o}^{p-1} + \mathcal{B}_p^{III} R_{\rm o}^{-p-1})\sin(p\phi) = \frac{1}{\mu_r} \sum_{n=\,p} n(-\mathcal{A}_n^{II} R_{\rm o}^{n-1} + \mathcal{B}_n^{II} R_{\rm o}^{-n-1})\sin(n\phi) \\ &\qquad + \frac{p}{\mu_r}(-\mathcal{A}_p^{II} R_{\rm o}^{p-1} + \mathcal{B}_p^{II} R_{\rm o}^{-p-1})\sin(p\phi) \\ &\qquad - \frac{B_{\rm rem}}{\mu_r}\frac{1}{p-1}\sin(p\phi)\ . \end{aligned} \quad \text{(A.12)}$$

Just as with the boundary condition for B_r these can be reduced to

$$\begin{aligned} \mathcal{A}_n^{III} &= \mathcal{A}_n^{II}\mu_r^{-1} + (\mathcal{B}_n^{II}\mu_r^{-1} - \mathcal{B}_n^{III})R_{\rm o}^{-2n} \\ \mathcal{A}_n^{I} &= \mathcal{A}_n^{II}\mu_r^{-1} + (\mathcal{B}_n^{II}\mu_r^{-1} - \mathcal{B}_n^{I})R_{\rm i}^{-2n} \ . \end{aligned} \tag{A.13}$$

So we now have the two sets of equations, Eq. (A.8) and (A.13). Putting these equations equal to one another we get

$$\begin{aligned} \mathcal{A}_n^{II} + (\mathcal{B}_n^{II} - \mathcal{B}_n^{III})R_{\rm o}^{-2n} &= \mathcal{A}_n^{II}\mu_r^{-1} + (\mathcal{B}_n^{II}\mu_r^{-1} - \mathcal{B}_n^{III})R_{\rm o}^{-2n} \\ \mathcal{A}_n^{II} + (\mathcal{B}_n^{II} - \mathcal{B}_n^{I})R_{\rm i}^{-2n} &= \mathcal{A}_n^{II}\mu_r^{-1} + (\mathcal{B}_n^{II}\mu_r^{-1} - \mathcal{B}_n^{I})R_{\rm i}^{-2n} \ , \end{aligned} \tag{A.14}$$

or

$$\begin{aligned} \mathcal{A}_n^{II} + \mathcal{B}_n^{II}R_{\rm o}^{-2n} &= \mu_r^{-1}(\mathcal{A}_n^{II} + \mathcal{B}_n^{II}R_{\rm o}^{-2n}) \\ \mathcal{A}_n^{II} + \mathcal{B}_n^{II}R_{\rm i}^{-2n} &= \mu_r^{-1}(\mathcal{A}_n^{II} + \mathcal{B}_n^{II}R_{\rm i}^{-2n}) \ . \end{aligned} \tag{A.15}$$

These equations can only be true for $\mu_r = 1$ if

$$\begin{aligned} \mathcal{A}_n^{II} &= -\mathcal{B}_n^{II}R_{\rm o}^{-2n} \\ \mathcal{A}_n^{II} &= -\mathcal{B}_n^{II}R_{\rm i}^{-2n} \ . \end{aligned} \tag{A.16}$$

But this is only true if $\mathcal{A}_n^{II} = \mathcal{B}_n^{II} = 0$.

So the above equations can be deduced to

$$\begin{aligned} \mathcal{A}_n^{III} &= -\mathcal{B}_n^{III}R_{\rm o}^{-2n} \\ \mathcal{A}_n^{I} &= -\mathcal{B}_n^{I}R_{\rm i}^{-2n} \ . \end{aligned} \tag{A.17}$$

Finally from the $H_\phi^I = H_\phi^{III} = 0$ boundary conditions we get

$$\begin{aligned} \sum_{n=\ p} (-\mathcal{A}_n^{I}R_{\rm c}^{n-1} + \mathcal{B}_n^{I}R_{\rm c}^{-n-1}) &= 0 \\ \sum_{n=\ p} (-\mathcal{A}_n^{III}R_{\rm e}^{n-1} + \mathcal{B}_n^{III}R_{\rm e}^{-n-1}) &= 0 \ . \end{aligned} \tag{A.18}$$

From these two equations we get

$$\begin{aligned} \mathcal{B}_n^{III} &= \mathcal{A}_n^{III}R_{\rm e}^{2n} \\ \mathcal{B}_n^{I} &= \mathcal{A}_n^{I}R_{\rm c}^{2n} \ . \end{aligned} \tag{A.19}$$

Combining this with Eq. (A.17) leads to

$$\begin{aligned} \mathcal{A}_n^{III} &= -\mathcal{A}_n^{III}R_{\rm e}^{2n}R_{\rm o}^{-2n} \\ \mathcal{A}_n^{I} &= -\mathcal{A}_n^{I}R_{\rm c}^{2n}R_{\rm i}^{-2n} \ , \end{aligned} \tag{A.20}$$

which means that $\mathcal{A}_n^{III}$ and $\mathcal{A}_n^{I}$ are also zero. Thus we have shown that all $\mathcal{A}_n$ and $\mathcal{B}_n$ are zero for $n = \ p$. The argument is identical for the case of $p = 1$.

Appendix B

Assembling the magnet and a plate of magnetocaloric material

The New Magnet was assembled by Bakker Magnetics bv, Eindhoven, The Netherlands. K. Engelbrecht from the magnetic refrigeration group at Risø DTU visited Bakker Magnetics during the assembly of the magnet and took the photographs shown below. These are presented solely to illustrate how the New Magnet was assembled.

Also shown is a plate of a ceramic magnetocaloric material, as will be used in the regenerator.

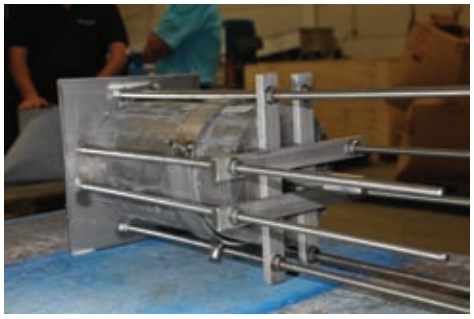

Fig. B.1: The inner magnet, assembled from five identical 50 mm long magnets. These are glued together while being fixed in the apparatus shown here.

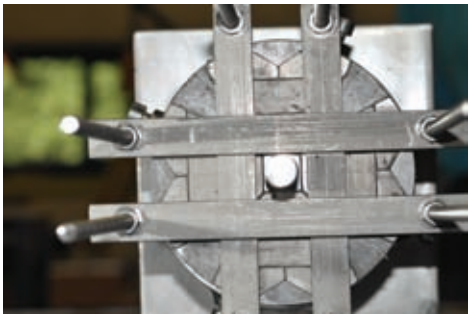

Fig. B.2: A front view of the fixed inner magnet.

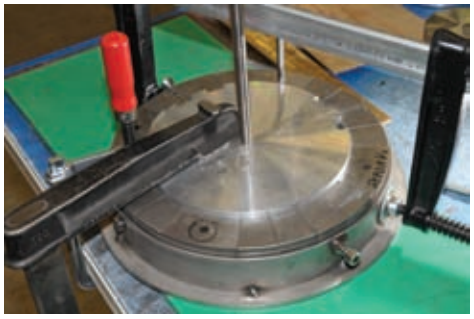

Fig. B.3: The outer magnet is also assembled from five 50 mm long identical pieces. Here the magnets are being fixed while one of the five identical pieces is assembled.

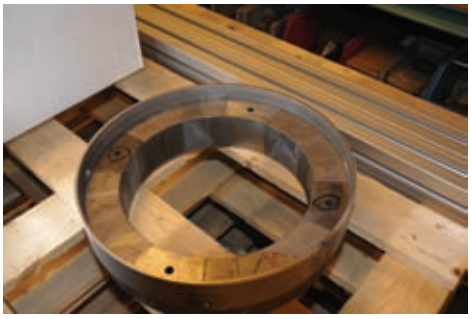

Fig. B.4: One of the five identical 50 mm pieces of the outer magnet inside an outer stainless steel casing.

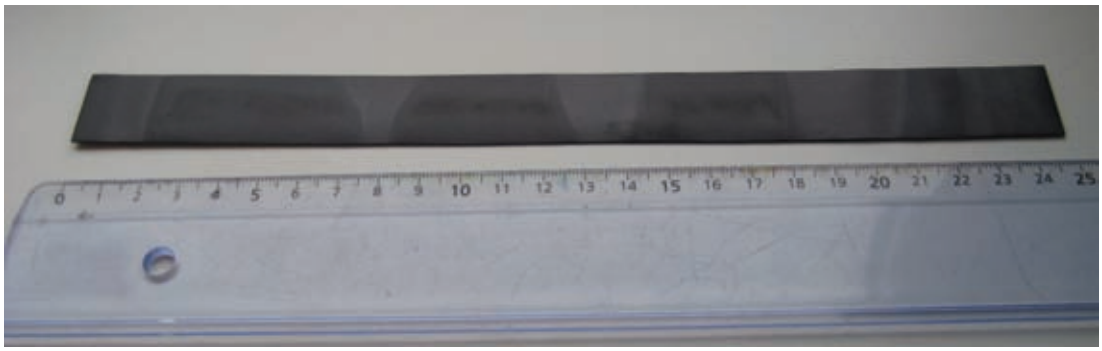

Fig. B.5: A plate of magnetocaloric material similar to those that will be used for the regenerator. The plates are made of a ceramic magnetocaloric material and not Gd. The dimensions of the plate are $250 \times 20 \times 0.5$ mm^3.

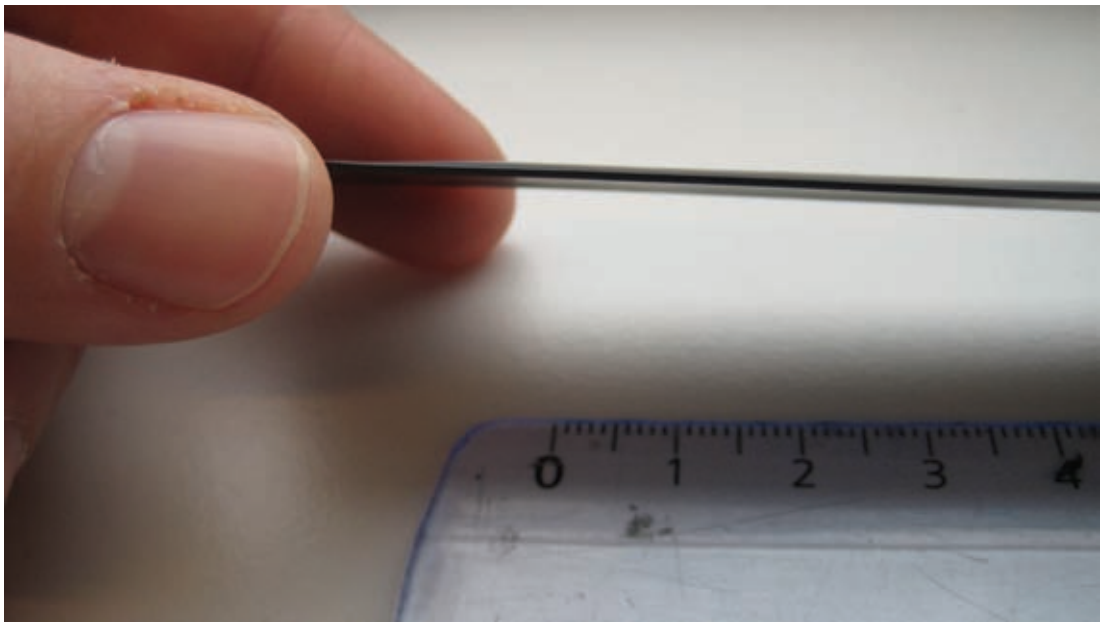

Fig. B.6: The same plate as shown in Fig. B.5.

Paper I

Paper published in Journal of Applied Physics, 2008

Bjørk, R., Bahl, C. R. H., Smith, A. and Pryds, N.

Optimization and improvement of Halbach cylinder design

Journal of Applied Physics, 104, 13910, 2008

Optimization and improvement of Halbach cylinder design

R. Bjørk,[a] C. R. H. Bahl, A. Smith, and N. Pryds
Department of Fuel Cells and Solid State Chemistry, National Laboratory for Sustainable Energy, Technical University of Denmark, Frederiksborgvej 399, DK-4000 Roskilde, Denmark

(Received 6 December 2007; accepted 7 May 2008; published online 9 July 2008)

In this paper we describe the results of a parameter survey of a 16 segmented Halbach cylinder in three dimensions in which the parameters internal radius, r_{in}, external radius, r_{ex}, and length, L, have been varied. Optimal values of r_{ex} and L were found for a Halbach cylinder with the least possible volume of magnets with a given mean flux density in the cylinder bore. The volume of the cylinder bore could also be significantly increased by only slightly increasing the volume of the magnets, for a fixed mean flux density. Placing additional blocks of magnets on the end faces of the Halbach cylinder also improved the mean flux density in the cylinder bore, especially so for short Halbach cylinders with large r_{ex}. Moreover, magnetic cooling as an application for Halbach cylinders was considered. A magnetic cooling quality parameter, Λ_{cool}, was introduced and results showed that this parameter was optimal for long Halbach cylinders with small r_{ex}. Using the previously mentioned additional blocks of magnets can improve the parameter by as much as 15% as well as improve the homogeneity of the field in the cylinder bore. © *2008 American Institute of Physics*.
[DOI: 10.1063/1.2952537]

I. INTRODUCTION

Configurations of permanent magnets that produce a strong homogeneous field in a confined region of space and a very weak field elsewhere are useful in many applications such as particle accelerators,[1] nuclear magnetic resonance (NMR) apparatus,[2] or magnetic cooling applications.[3]

The design known as a Halbach cylinder is especially good at producing this type of magnetic field. A Halbach cylinder is a long cylinder made of a magnetic material with a bore along the cylinder symmetry axis. The Halbach cylinder can be characterized by three parameters: the internal and external radii, r_{in} and r_{ex}, respectively, and the length, L. The magnetic material around the bore is magnetized such that the direction of magnetization at any point is at an angle

$$\eta = 2\theta \tag{1}$$

from the vertical axis.[4,5] This arrangement means that a uniform field will be created across the bore in the vertical direction without creating, in the ideal case, any stray field outside the cylinder. Figure 1 shows a drawing of a Halbach cylinder.

It is well known that the flux density inside the bore of an infinitely long Halbach cylinder is[5]

$$B = B_r \ln\left(\frac{r_{ex}}{r_{in}}\right), \tag{2}$$

where B_r is the remanent flux density of the magnetic material.

Halbach cylinders have previously been investigated in detail in two dimensions, but there exist only a few investigations of Halbach cylinders in three dimensions, where the effect of the finite length of the Halbach cylinder has been studied. In one example[6] the reduction in flux density due to a finite length Halbach cylinder was investigated, but the field was only calculated for a single fixed length. An analytical formula for the magnetic flux of a Halbach cylinder of any given length was derived, however this formula is extremely complicated, making it impractical for direct application. In another publication[7] the effects of a finite length Halbach cylinder were also explored, as well as the effect of dividing the Halbach cylinder into a number of segments, each with its own direction of magnetization. However, both investigations were only performed for one specific Halbach cylinder of a fixed length.

In this paper the three dimensional Halbach cylinder will be investigated in greater detail, and the flux density will be computed for a multitude of different configurations and not only a single specific case.

First, the effect of dividing the Halbach cylinder into segments each with their own direction of magnetization will

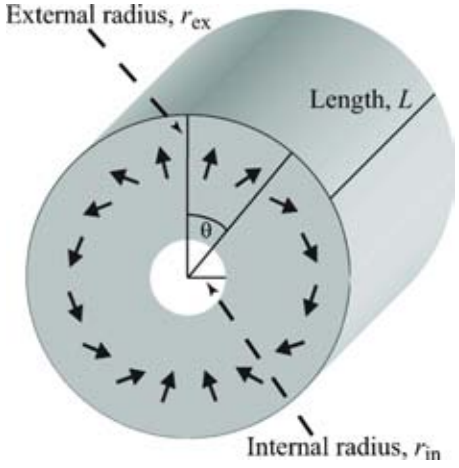

FIG. 1. (Color online) A sketch of a Halbach cylinder showing the internal radius, r_{in}, external radius, r_{ex}, and length, L. Also shown as arrows is the direction of the remanent magnetization of the magnetic material.

[a]Electronic mail: rasmus.bjoerk@risoe.dk.

be investigated. To measure only the effect of segmentation the calculations are performed in two dimensions, so that any effects from a finite length Halbach cylinder are avoided. We then assume that the effect of segmentation in two dimensions is similar in three dimensions.

Thereafter the Halbach cylinder will be investigated in three dimensions, with focus on how to build a Halbach cylinder with a certain mean flux density using a minimum of magnetic material, i.e., find the configuration of r_{in}, r_{ex}, and L that generates the strongest flux density for the minimum amount of magnetic material.

Finally, it will be investigated if the magnetic flux density can be improved by placing additional blocks of permanent magnets on the end faces of the Halbach cylinder.

The results of this investigation of Halbach cylinder design are useful in many different fields, e.g., magnetic cooling[3] or tabletop NMR.[8] These applications typically require a flux density of around 1–3 T, and this is also the range of flux density that we will concern ourselves with in this paper.

All numerical work in this paper was done using the commercially available finite element multiphysics program, *Comsol Multiphysics*.[9] The Comsol Multiphysics code has previously been validated through a number of NAFEMS (National Agency for Finite Element Methods and Standards) benchmark studies.[10]

The equation solved in the following simulations is the magnetic vector potential equation,

$$\nabla \times (\mu_0^{-1}\mu_r^{-1}(\nabla \times \mathbf{A} - \mathbf{B}_r)) = 0, \tag{3}$$

where $\mathbf{A}$ is the magnetic vector potential, $\mathbf{B}_r$ is the remanent flux density, μ_0 is the permeability of free space, and μ_r is the relative permeability assumed to be isotropic.

The solver used to solve this equation on the simulation mesh is *Pardiso*, which is a parallel sparse direct linear solver.[11,12]

Boundary conditions are chosen such that the boundaries of the computational volume, which is many times larger than the Halbach cylinder, are magnetically insulating, while all other (internal) boundaries are continuous.

II. SEGMENTED HALBACH CYLINDER

An infinitely long Halbach cylinder is equivalent to a two dimensional situation, so it fulfills Eq. (2) if the direction of magnetization varies continuously through the magnetic material as prescribed by Eq. (1). This continuous variation of the direction of magnetization is often not attainable in real-world assemblies, and therefore the Halbach cylinder is often made up of segments, each of which has a direction of magnetization equal to the direction of magnetization of a continuous Halbach cylinder at the center of the segment.

A Halbach cylinder consisting of n such segments will have its flux density reduced to[5]

$$B(n) = B(\infty)\frac{\sin(2\pi/n)}{2\pi/n}, \tag{4}$$

where $B(\infty)$ is the flux density given by Eq. (2), i.e., with a continuous magnetization.

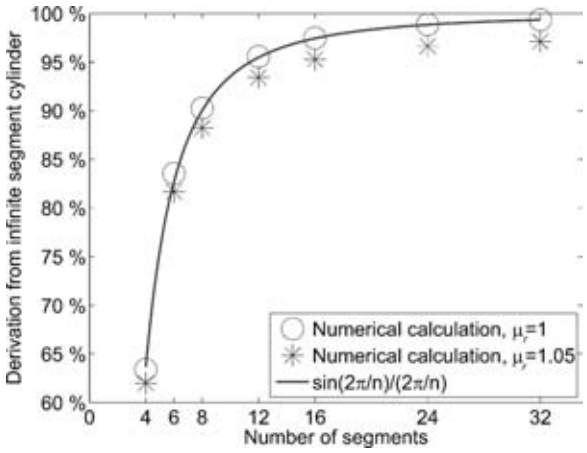

FIG. 2. Dividing a Halbach cylinder into n segments makes the flux density differ from that of a perfect Halbach cylinder. The deviation is given by Eq. (4) for "perfect magnets," $\mu_r=1$, while magnets with $\mu_r=1.05$ deviate more from the ideal Halbach cylinder.

We have analyzed the consequence of this segmentation of the Halbach cylinder by computing the mean value of the magnetic flux density inside the Halbach cylinder bore for a Halbach cylinder consisting of 4, 6, 8, 12, 16, 24, and 32 segments. The calculations were performed both for a Halbach cylinder consisting of "perfect" magnets, i.e., with a relative permeability, μ_r, of 1, and magnets where actual material properties were taken into account by increasing μ_r to 1.05. The magnetic material was assumed to have a remanent flux density of 1.4 T, equal to standard grade N48 neodymium-iron-boron (NdFeB) magnets.[13] This value for the remanent flux density will be used in the remainder of this paper.

The results of the computations together with Eq. (4) are shown in Fig. 2. Here it is seen that Eq. (4) describes the numerical data with $\mu_r=1$ extremely well. It is also seen that choosing a small number of segments severely limits the flux density.

Based on the results shown in Fig. 2 we choose, in the calculations and computations presented in the following sections, to use a 16 segmented Halbach cylinder with $\mu_r=1.05$. This configuration obtains 95% of the flux density of a perfect Halbach cylinder and is realizable in real-world assemblies.

Having determined the configuration to be used in the following simulations we now proceed to investigate if there exist optimal dimensions for a Halbach cylinder design. For this three dimensional simulation must be used in order to study how the loss of flux density through the ends of the cylinder bore varies with r_{ex} and L.

III. HALBACH CYLINDER 3D STUDY

A parameter study of Halbach cylinder configurations has been performed by varying the parameters L, r_{ex}, and r_{in} as given in Table I. In each of the $90\times90\times3$ configurations the mean flux density of the magnetic field inside the cylinder bore has been computed. The results are shown as a contour plot of the mean flux density as a function of L and r_{ex} in Fig. 3 for $r_{in}=20$ mm.

TABLE I. The variation of the Halbach parameters. In total there are 90 $\times 90 \times 3$ different configurations.

	From (mm)	To (mm)	Step size (mm)
L	41	130	1
r_{ex}	22	200	2
r_{in}	10	30	10

Figure 3 shows that the configuration producing the strongest mean flux density is the configuration with the largest r_{ex} and L. This is in agreement with Eq. (2) and the fact that for a long Halbach cylinder the loss of flux through the ends of the cylinder will be relatively smaller than for a short cylinder.

It is not sufficient to characterize a design only by the value of the mean flux density. It should be considered that increasing the length of the Halbach cylinder increases the volume of the bore, thus allowing a larger sample to be placed inside the Halbach cylinder bore. On the other hand, increasing the external radius does not affect the volume of the bore. Consequently, a better way of characterizing each Halbach cylinder configuration is by the volume of its magnets and the volume of the bore, and then calculating contour plots with lines of equal mean flux density. These are shown in Figs. 4–6 for the three different values of r_{in}. In Figs. 4–6 the volume of the bore scales directly with the length of the Halbach cylinder because the internal radius is kept constant in each figure.

Looking at, e.g., Fig. 5 it can be seen that for a mean flux density of 1.6 T a Halbach cylinder can be constructed with an ~50% increase in magnetic material but an ~250% larger volume of the bore compared to the design using the least amount of magnetic material.

It is possible to attain this substantial increase in the volume of the bore because the latter configuration is a very long Halbach cylinder with a small external radius, while the configuration with the smallest volume of the magnets is a short Halbach cylinder with a large external radius. In these two configurations the shape of the bore is different, but the mean flux density.

In Fig. 7 the total volume of the magnetic material is shown as a function of the mean flux density in the bore for $r_{in}=20$ mm. In this plot there are 90×90 data points. Two data series where r_{ex} has been fixed and L has been varied are highlighted on the plot. (One could also have chosen to vary r_{ex} and kept L fixed. The curves look the same.) Here one can see that as L is increased, the mean flux density is increased as well. At some point each data series becomes the rightwards edge of the "feather," and then the increase in the volume of the magnets with mean flux density becomes too steep and the data points move upwards, leaving the edge of the feather.

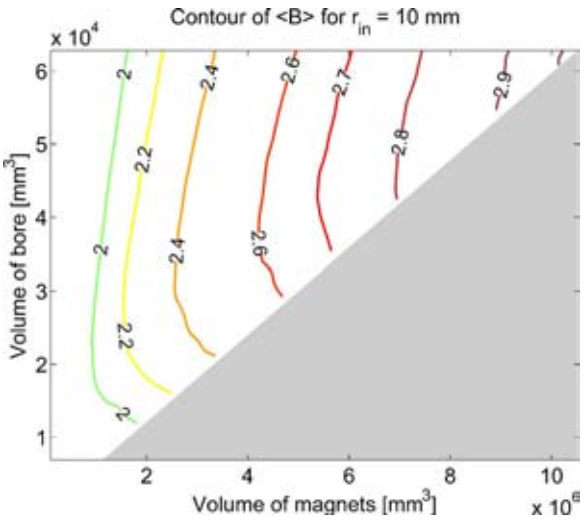

FIG. 4. (Color online) Contours of the mean flux density as a function of the volume of magnets used and the volume of the cylinder bore for $r_{in}=10$ mm. It is seen that the volume of the bore can be significantly increased by slightly increasing the volume of the magnets. Note that the range is not the same on the two axes. A look-up table is necessary such that each data point (these are not shown) is uniquely tied to a specific Halbach cylinder, i.e., a given r_{in}, r_{ex}, and L.

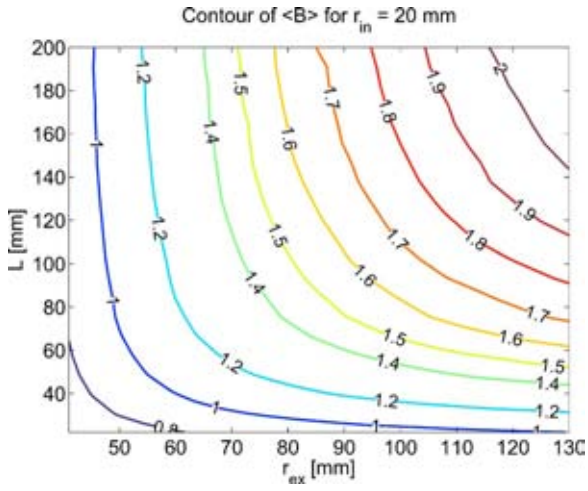

FIG. 3. (Color online) Contours of the mean flux density for the Halbach cylinders with $r_{in}=20$ mm. Each contour is labeled by its mean flux density. As is expected the maximum flux density is obtained by maximizing both r_{ex} and L.

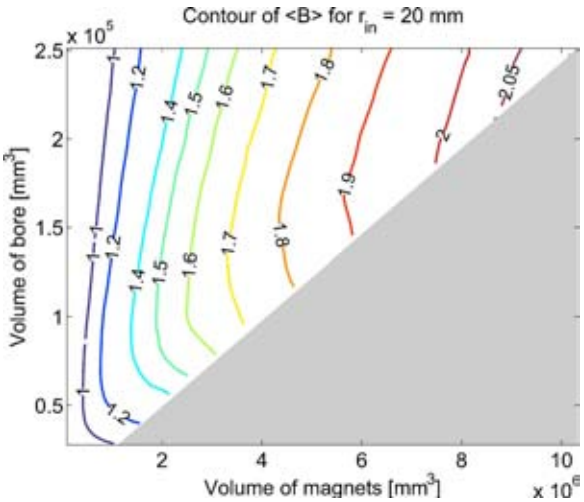

FIG. 5. (Color online) Contours of the mean flux density as a function of the volume of magnets used and the volume of the cylinder bore for $r_{in}=20$ mm. The conclusion of Fig. 4 applies here as well.

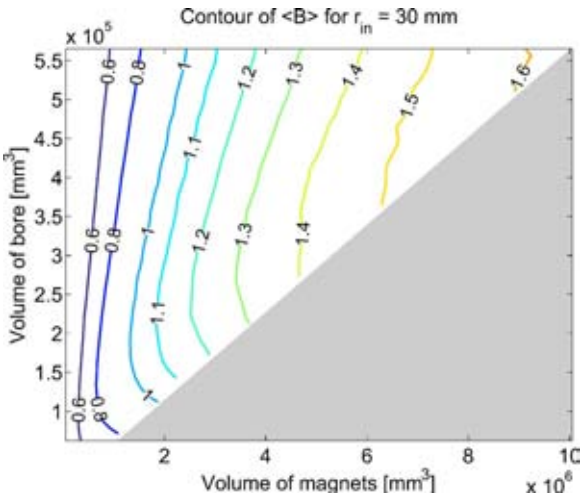

FIG. 6. (Color online) Contours of the mean flux density as a function of the volume of magnets used and the volume of the cylinder bore for $r_{in}=30$ mm. The conclusion of Fig. 4 applies here as well.

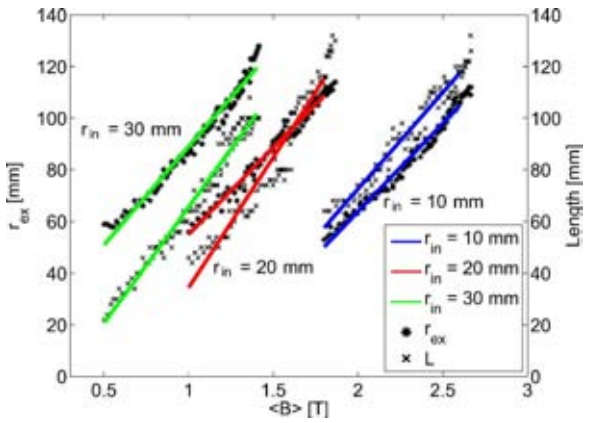

FIG. 8. (Color online) The optimal r_{ex} and L as functions of the mean flux density in the cylinder bore for Halbach cylinders with $r_{in}=10$, 20, and 30 mm. Building a Halbach cylinder with dimensions different from the dimensions given here means that more magnetic material is used than need be, if one is only interested in obtaining the maximum flux density possible and does not care about the size of the cylinder bore.

The reason for this behavior is that the data series start with a short Halbach cylinder. This configuration loses a lot of flux through the ends of the cylinder and so as the length is increased the average flux density increases quite rapidly. When a certain length of the Halbach cylinder is reached there is not as much to be gained by increasing the length of the cylinder further and so the average flux density only increases slowly as the volume of the magnets is increased.

As this is the case for all data series where the length of the Halbach cylinder is gradually increased, it is possible to characterize the rightwards edge of the feather as the optimal configuration, i.e., the configuration with the smallest volume of the magnets at a given mean flux density.

In Fig. 8 the values of r_{ex} and L are plotted as functions of the mean flux density for the optimal points. Thus one can directly use this figure to find the external radius and length for the Halbach cylinder with the minimum volume of magnets at a given mean flux density. Straight lines have been fitted to the data.

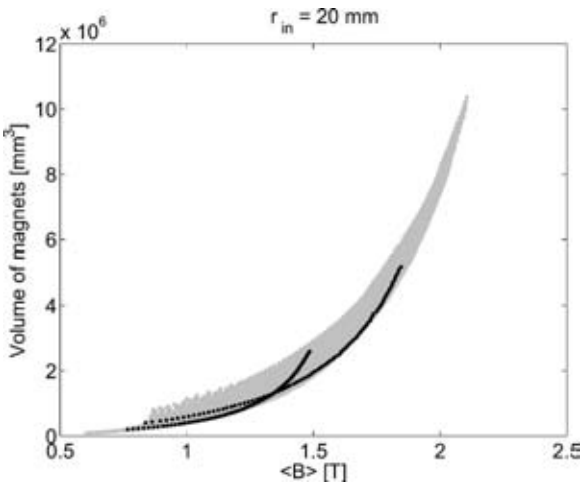

FIG. 7. The total volume of the magnetic material as a function of the mean flux density for $r_{in}=20$ mm. The data points somewhat resemble a feather, and so this plot will be referred to as the "feather plot." The data have been produced in series where r_{ex} has been fixed and L has been varied. Two of these data series have been highlighted in black and, starting from the left, both series can be seen to first approach the rightwards edge of the feather and then leave it again. Similar plots exist for $r_{in}=10$ and 30 mm.

The conclusion of this parameter investigation is twofold. First, it can be concluded from Figs. 4–6 that it is possible, at a constant mean flux density, to increase the volume of the bore significantly by only increasing the volume of the magnets slightly for a Halbach cylinder with a fixed r_{in}. Second, the length and external radius of the minimum magnetic material Halbach cylinder at a given mean flux density was found and can be read off directly from Fig. 8. Thus if one wishes to build a Halbach cylinder with a given mean flux density and the limiting factor is the price of magnetic material, one should always choose the optimal configuration from this figure.

A few remarks on the precision of the simulations are in order. With the chosen boundary conditions, i.e., a magnetically insulating computational volume, it is important that the computational volume is large enough that the insulating boundaries do not effect the calculations. Also, as the solution method used is a finite element method, the mesh applied to the geometry must be as detailed as needed for the desired precision. The resolution of the mesh used for the simulations presented in this paper is chosen such that the results have a high degree of precision. To give an example, the mean flux density of the cylinder bore was calculated at different precisions for a random Halbach cylinder. The Halbach cylinder chosen had $r_{in}=20$ mm, $r_{ex}=102$ mm, and $L=70$ mm, and a mean flux density of 1.54 T. This result, calculated using the precision used throughout this paper, deviated by only 1.13% from a simulation using 173% more mesh elements all in all, and 1845% more mesh elements in the cylinder bore. The influence of the size of the computational volume on the mean flux density in the bore has also been tested for a number of different values of r_{in}, r_{ex}, and L and found to be less than 1%. Thus we conclude that at least the relative precision of the numerical experiments is satisfactory.

Although the above results are useful in choosing the

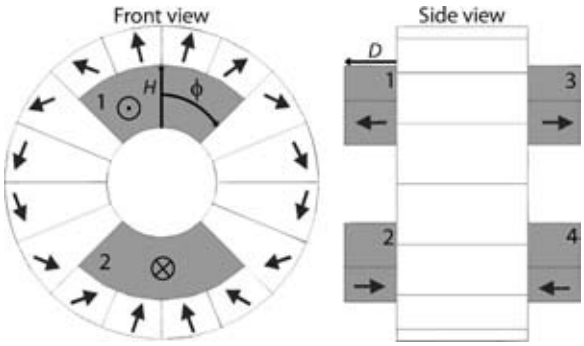

FIG. 9. This figure shows the height, H, angular span, ϕ, and depth, D, of the additional round blocks, colored in gray. The blocks are always symmetrically placed. The black arrows show the direction of magnetization. The additional blocks diagonally opposite each other have the same direction of magnetization.

optimal Halbach cylinder design, alternative methods for improving the design of a Halbach cylinder exist. The problem with especially the short Halbach cylinders is that they lose a relatively large amount of flux through the ends of the cylinder. This is the reason that their flux density is not well described by Eq. (2). In the next section it is investigated if it is possible to limit the amount of escaping flux through the ends of the cylinder by appending blocks of permanent magnets to the end faces of the Halbach cylinder and thus in this way improve the design.

IV. IMPROVING THE HALBACH CYLINDER DESIGN

The main loss of flux from the bore of the Halbach cylinder is through the ends of the cylinder bore. It has previously been shown[14] that by "covering" the ends of the Halbach cylinder with magnetic blocks in the shape of an equipotential surface, all of the flux can be confined inside the Halbach cylinder. However, this also blocks access to the cylinder bore. Instead we propose that some of the escaping flux may be confined by placing additional magnets, of a given size and direction of magnetization, at the end faces of the cylinder, in such a way that they do not block access to the cylinder bore but still increase the flux density in the cylinder bore and ensure a low flux density outside of the Halbach cylinder.

In this section we investigate what specific design and placement are optimal for these additional magnets. We also discuss whether it is better to use the additional magnets or if one might as well use the additional magnetic material for building a larger Halbach cylinder.

To maximize the amount of magnetic material capable of being used in the additional blocks we use a design of the additional blocks that follows the curvature of the cylinder bore, i.e., a circular design as can be seen in Fig. 9. In total four additional blocks are used, placed symmetrically around the Halbach cylinder symmetry axis. In this design an additional block is characterized by three parameters, namely the angular extent of a block, ϕ, the block's depth, D, and the height, H. The direction of magnetization of the individual additional block is perpendicular to the Halbach cylinder end face. Furthermore, the blocks diagonally opposite have the same direction of magnetization.

TABLE II. The additional magnets were placed on the four different Halbach cylinders given in column 5. The parameters of the additional blocks were varied as given in this table, resulting in $10\times8\times8$ different configurations of the additional blocks for each Halbach cylinder.

	From	To	Step size	Halbach dimensions (mm)
ϕ (°)	10	80	10	$L=100$
H (mm)	100	30	10	$r_{ex}=100$
D (mm)	50	5	5	$r_{in}=20$
ϕ (°)	10	80	10	$L=92$
H (mm)	130	25	15	$r_{ex}=130$
D (mm)	46	4.6	4.6	$r_{in}=20$
ϕ (°)	10	80	10	$L=200$
H (mm)	60	25	5	$r_{ex}=60$
D (mm)	100	10	10	$r_{in}=20$
ϕ (°)	10	80	10	$L=50$
H (mm)	130	25	15	$r_{ex}=130$
D (mm)	25	2.5	2.25	$r_{in}=20$

The height, H, angular span, ϕ, and depth, D, of the additional blocks are varied to find the optimal configuration for several different Halbach cylinders. Calculating the flux density for each of the original $90\times90\times3$ Halbach cylinders with additional magnets is a too time consuming task, and thus the calculations were only done on a few carefully chosen Halbach cylinder designs. These are given in Table II.

The results of the simulations are shown in Fig. 10. Here the mean flux density in the bore as a function of the total volume of the magnetic material used in the simulated design is shown. The figure shows both the Halbach cylinders without any additional blocks, and the simulations of the Halbach cylinders with additional blocks.

One can see from the figure that placing additional blocks on a relatively short Halbach cylinder will improve the mean flux density in the cylinder bore significantly.

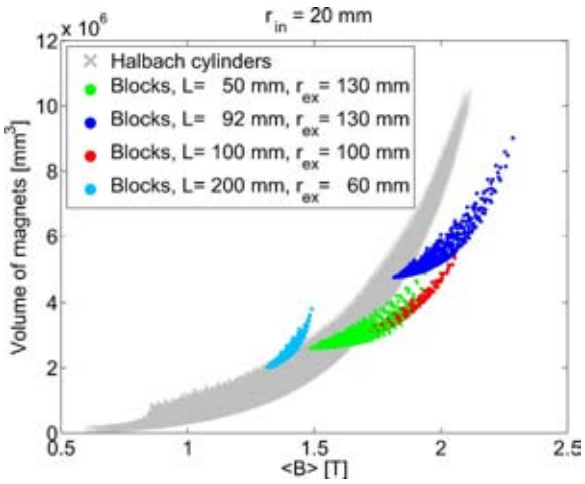

FIG. 10. (Color online) Placing additional blocks on a specific Halbach cylinder improves the mean flux density in the cylinder bore but the improvement depends on L and r_{ex} of the Halbach cylinder. The legend shows which Halbach cylinder the additional block was placed on. Without the additional blocks the figure is identical to Fig. 7.

V. HALBACH CYLINDERS FOR USE IN MAGNETIC COOLING

We have shown that using additional blocks of magnets on the sides of the Halbach cylinder can increase the mean flux density in the cylinder bore. However, in some cases the additional magnetic material might as well be used to enlarge the Halbach cylinder's external radius and in this way also increase the flux density. We will consider this more closely in the context of one particular application for Halbach cylinders, namely magnetic cooling. For this type of application the Halbach cylinder must be designed such that it has a high flux density in a large volume and with a minimum of magnetic material.

The magnetic cooling process relies on a magnetocaloric material. The temperature of such a material is increased upon the application of a magnetic field and decreased again upon the removal of the magnetic field. A large number of different materials have been suggested as the active component of a magnetic refrigeration machine.[15]

From experimental studies it is known that the adiabatic temperature change of gadolinium, the "benchmark" magnetocaloric material at room temperature, has a magnetocaloric effect that scales with the flux density of the magnetic field[16] to the power of 0.7. This is in good accordance with the power of $\frac{2}{3}$ predicted by mean field theory.[17]

However, it is not only the flux density inside the cylinder bore that is of importance to the magnetocaloric effect. The volume outside the cylinder bore where the magnetocaloric material is placed when it is moved to the "out of field" position is also important. In order to maximize the magnetocaloric effect the flux density in this region must be as low as possible. It can, of course, be argued that one could simply move the magnetocaloric material further away than right outside the end of the cylinder bore, but this would increase the physical size of the magnetic refrigeration machine. Finally, it is important that the cylinder bore has as large a volume as possible and that the volume of the magnets be as small as possible.

Taking all this into account we propose to characterize a configuration of magnets for use in magnetic cooling applications by the parameter

$$\Lambda_{\mathrm{cool}} \equiv (\langle B^{0.7}\rangle - \langle B_{\mathrm{out}}^{0.7}\rangle)\frac{V_{\mathrm{field}}}{V_{\mathrm{mag}}}P_{\mathrm{field}}, \tag{5}$$

where V_{mag} is the volume of the magnets, V_{field} is the volume with a high flux density, i.e., the volume of the cylinder bore, P_{field} is the fraction of the total volume of the cylinder bore and the volume outside the cylinder bore that is filled with magnetocaloric material, $\langle B_{\mathrm{out}}^{0.7}\rangle$ is the volume average of the flux density in the high flux volume, i.e., the cylinder bore, to the power of 0.7, and $\langle B_{\mathrm{out}}^{0.7}\rangle$ is the volume average of the flux density to the power of 0.7 in the region shown in Fig. 11, i.e., the volume just outside the cylinder bore where the magnetocaloric material is placed when it is moved out of the magnetic field. It has the same size and shape as the cylinder bore.

The magnetic cooling parameter is shown for the Halbach cylinders without additional blocks and with r_{in} =20 mm in Fig. 12 for P_{field}=0.5, i.e., we assume that the total volume is only half filled with magnetocaloric material at any given moment. Here we see that the optimal design is the Halbach cylinder with the largest L and smallest r_{ex}. Note that this design is not the overall optimal design, as it lies on the edge of the parameter space, i.e., simulations have not been conducted with a larger L and smaller r_{ex}.

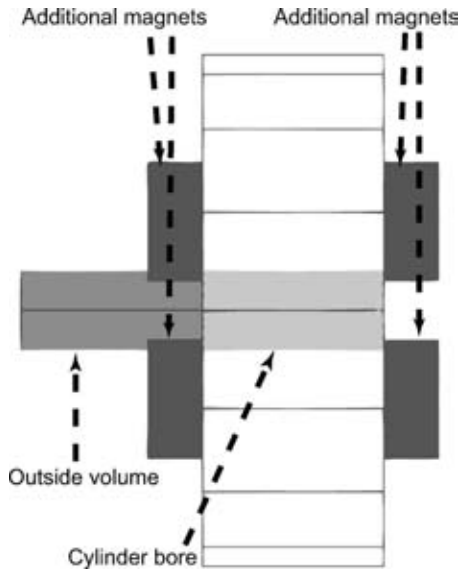

FIG. 11. A side view of the Halbach cylinder with additional blocks. The volume inside which $\langle B_{\mathrm{out}}^{0.7}\rangle$ is calculated is shown. The volume is identical in shape to the cylinder bore, also shown, and is located directly outside the end of the cylinder bore. Also shown are the additional blocks of magnets. The edges of the 16 segments that make up the Halbach cylinder can also be seen in the figure.

There are several reasons that the long, thin Halbach cylinder has the largest Λ_{cool}. The primary cause is due to the fact that the loss of flux through the ends of the cylinder bore is greatly reduced in the long Halbach cylinder. Another effect is, due to its long length, the volume inside which $\langle B_{\mathrm{out}}^{0.7}\rangle$ is calculated is also long (as previously mentioned the shape

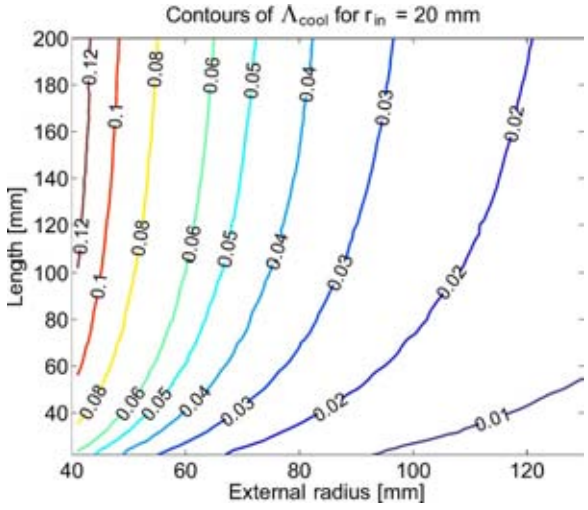

FIG. 12. (Color online) A contour plot showing the magnetic cooling parameter, Λ_{cool}, defined in Eq. (5) for the Halbach cylinders without additional blocks and with r_{in}=20 mm. The optimum design is the longest and thinnest Halbach cylinder.

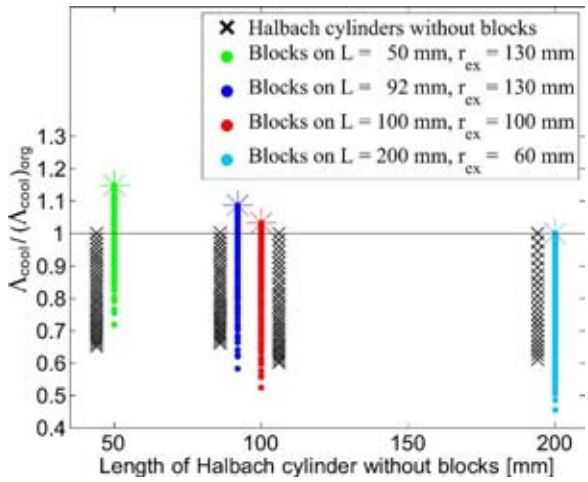

FIG. 13. (Color online) The relative improvement of the magnetic cooling parameter compared to the original Halbach cylinder without any additional blocks, for the designs listed in Table II. The design most improved is the short Halbach cylinder with a large external radius, i.e., $L=50$ mm, $r_{ex}=130$ mm. For each Halbach cylinder the best configuration of the additional blocks have been marked by a star. The black crosses in the figure are Halbach cylinders with the same r_{in} and L as the Halbach cylinder with blocks, but with a bigger r_{ex} and no blocks. The black crosses are displaced by ± 6 mm on the x-axis, to make the comparison with the Halbach cylinders with additional blocks possible.

of the cylinder bore and this volume are identical), and thus the end furthest from the cylinder bore will only experience a very small field, thus lowering $\langle B_{out}^{0.7}\rangle$. For practical applications one would choose to optimize Λ_{cool} under a criterion of a minimum flux density in the cylinder bore, i.e., find the Halbach cylinder with the maximum Λ_{cool} that at the same time has a minimum flux density of, e.g., 1 T in the cylinder bore.

We are also interested in knowing what effect the additional blocks of magnets have on the magnetic cooling parameter. In Fig. 10 we saw that the additional blocks increase the flux density in the cylinder bore, but this might not mean that Λ_{cool} is increased as well, as additional magnetic material is also used.

In Fig. 13 Λ_{cool} is shown for the different Halbach cylinders with additional blocks, i.e., the ones given in Table II. Here we can see that some configurations of the additional blocks do increase Λ_{cool} by as much as $\sim 15\%$. Shown in the figure are also Halbach cylinders with no additional blocks that have the same r_{in} and L as the Halbach cylinders with additional blocks but where r_{ex} has been expanded by up to 30 mm. These are shown such that it can be estimated if it is better to spend any additional magnetic material on the additional blocks or on enlarging the external radius of the Halbach cylinder. As one can see from the figure, in three of the cases it is better to spend the additional magnetic material on the additional blocks.

The design that is the most improved by the additional blocks is a short Halbach cylinder with a large external radius, i.e., $L=50$ mm, $r_{ex}=130$ mm. For the longest Halbach cylinder with the smallest external radius, $L=200$ mm, $r_{ex}=60$ mm, the additional blocks do not improve Λ_{cool}. The reason for this is that the short designs are also the ones that have the greatest loss of flux through the ends of the cylinder bore, which is exactly what the additional magnets reduce.

TABLE III. The optimal configuration of the additional blocks, i.e., the configurations that maximize the magnetic cooling parameter. $(\Lambda_{cool})_{org}$ refers to the "original" Halbach cylinder without any additional blocks.

Halbach dimensions (mm)	ϕ (°)	H (mm)	D (mm)	$\Lambda_{cool}/(\Lambda_{cool})_{org}$
$r_{ex}=130$, $L=50$	80	47.5	22.5	1.15
$r_{ex}=130$, $L=92$	60	61.2	27.6	1.09
$r_{ex}=100$, $L=100$	60	50	25	1.03
$r_{ex}=60$, $L=200$	60	30	10	1.00

The optimal design of the additional blocks, i.e., the angular span, height, and depth, varies between the four Halbach cylinders presented in Fig. 13, and the results can be read in Table III. Here it is seen that the optimal design of the additional blocks seems to be an angle span of around 60°, a height in the range 45–60 mm, and a depth in the range 22.5–27.5 mm, at least for the three systems used in these simulations. The parameters were varied as given in Table II.

It can thus be concluded that for a short Halbach cylinder with a large external radius it is possible to optimize the magnetic cooling parameter by using additional magnets placed at the ends of the cylinder. However, as can be seen by comparing Figs. 12 and 13, the improvement gained by using the additional blocks is small compared to building a long Halbach cylinder with a small r_{ex} in the first place. For example, the design improved the most by the additional blocks, $r_{ex}=130$ mm and $L=50$ mm, has the magnetic cooling parameter improved 1.15 times. This is not as impressive when one considers that the magnetic cooling parameter for this Halbach cylinder has a value of 0.011 (the lower right corner in Fig. 12), and even multiplied by 1.15 this is still much lower than the longer Halbach cylinders. However, in specific cases with a limited geometry due to the application the additional blocks can still be used to improve the flux density.

A. Homogeneity of the field

In most Halbach cylinder applications it is not only the flux density that is important but also the homogeneity of the field in the cylinder bore.

To characterize the homogeneity of the flux density in the cylinder bore the quantity

$$\eta \equiv \frac{\langle B^2\rangle - \langle B\rangle^2}{\langle B^2\rangle}, \tag{6}$$

where the angled brackets denoting volume average, is defined. In Fig. 14 this parameter is shown for the Halbach cylinders with additional blocks. Also shown in the figure are Halbach cylinders with the same r_{in} and L as the Halbach cylinder with additional blocks but with a larger r_{ex} and no blocks. It can clearly be seen that the no-block designs with larger r_{ex} have a homogeneity parameter comparable to the "original" Halbach cylinder without blocks, while a number of the designs with additional blocks clearly improve the homogeneity of the field in the cylinder bore, i.e., lower η/η_{org}.

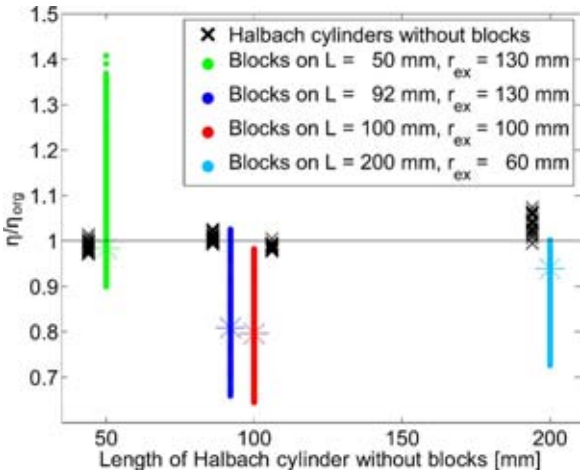

FIG. 14. (Color online) The parameter η/η_{org} describing the homogeneity of the field in the Halbach cylinder bore. The data point marked with a star represents the best data point from Fig. 13. The black crosses are Halbach cylinders with the same r_{in} and L as the Halbach cylinder with additional blocks but with a larger r_{ex} and no blocks. The black crosses are displaced by ± 6 mm on the x-axis to make the comparison with the Halbach cylinders with additional blocks possible.

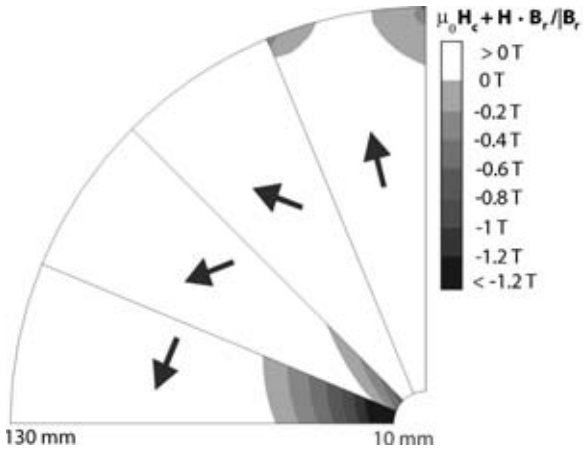

FIG. 15. A quarter of a 2D Halbach cylinder with $r_{in}=10$ mm and $r_{ex}=130$ mm. Shown as a color map is the expression $\mu_0\mathbf{H_c}+\mathbf{H}\cdot\mathbf{B_r}/|\mathbf{B_r}|$. When this expression is negative the magnetic field intensity is stronger than the intrinsic coercivity of the magnet (taken to be $\mu_0 H_c=1.2$ T) and the magnet will be reversed. The directions of the magnetization of the blocks are shown as black arrows.

B. Direction of magnetization

As previously mentioned, the additional blocks all have a direction of magnetization perpendicular to the end face of the Halbach cylinder. This might not be the optimal configuration, so various directions of magnetization have been tested to find the greatest enhancement of the flux density. The direction of magnetization was given by $(0, B_r\cos(\theta), B_r\sin(\theta))$ where θ was varied in steps of 1°. The Halbach cylinder symmetry axis is oriented along the z-axis.

The result indicates that the mean flux density in the bore could only be improved by less than 1% by changing the direction of magnetization from the 90 ° orientation used in the preceding simulations.

VI. DISCUSSION

It is important to discuss the possible influence of the coercivity of the individual magnets in the Halbach cylinder assembly. A serious problem in this context is that the assumed linearity of the magnets is only valid when the magnetic field is above the value of the intrinsic (polarization) coercivity, H_c. For typical 1.4 T NdFeB magnets $\mu_0 H_c$ is around 1.2 T at room temperature. Once the reverse component of the magnetic field reaches this value the linearity of the magnets breaks down and a small increase in the magnetic field will reverse the direction of magnetization of the magnet. We have not modeled this nonlinearity but have assumed that the linear relation is always valid. This is of course problematic when the magnetic field strength is too high. The reason the nonlinearity is not modeled is that due to hysteresis a complete history of the magnet material would be needed, including the physical building of the Halbach array, and this is not possible to model.

The part of the Halbach cylinder where this is a problem is around the inner equator.[18] In Fig. 15 the projection of the magnetic field intensity along the direction of the remanent magnetism is shown for the largest Halbach considered in this paper. Anisotropy is typically larger than coercivity for NdFeB magnets so any reverse field component is important.[18] It can be seen that the magnetic field is strong enough to reverse the direction of magnetization of typical industry 1.4 T magnets at several locations.

The problem is present for a Halbach cylinder with a flux density in the bore larger than 1.2 T. To overcome this problem one can replace the magnets in the affected volume of the Halbach cylinder with magnets with a higher intrinsic coercivity. Such magnets are readily available at slightly lower remanences, e.g., a typical industry NdFeB magnet with a remanence of 1.2 T has $\mu_0 H_c=3.2$ T, which is sufficiently strong to keep the relative permeability constant and thus the material linear. Otherwise the best solution is to remove the magnets from this part of the Halbach cylinder and replace them with a nonmagnetic material.

An additional remark on the conducted numerical simulations is that because the Halbach cylinder consists of magnets with a relative permeability close to one, the magnetostatic problem of calculating the flux density is linear in the remanence. This means that the mean flux density both inside and outside the Halbach cylinder depends linearly on the remanence of the magnets. In this paper we have used magnets with a remanence of 1.4 T. If one would, e.g., replace all these magnets in the Halbach cylinder with magnets with a remanence of 1.2 T, the mean flux density both inside and outside the Halbach cylinder would decrease by a factor of $1.2/1.4=0.86$. This has been verified numerically.

There are still factors that have not been taken into account. We have, for example, discussed the use of additional blocks while taking their shape for granted. It is necessary to test if the circular design used for the additional blocks is the proper design to use. One could just as well have used, e.g., a square design of the additional blocks. It is also important to investigate the effect of the additional blocks on a much larger sample of Halbach designs, including designs with varying internal radii.

VII. CONCLUSION

In this paper we found the optimal values of r_{ex} and L for a Halbach cylinder with a given mean flux density and r_{in}. These configurations have the smallest volume of the magnet possible for a given mean flux density in the cylinder bore. Also, we found that placing blocks of additional permanent magnets on the sides of the Halbach cylinder can improve the flux density in the cylinder bore significantly. Finally, we introduced a magnetic cooling efficiency parameter, Λ_{cool}, and showed that the additional blocks can improve this by as much as 15% compared to ordinary Halbach cylinders. However, one must always take care that the polarization coercivity, H_c, is always higher than the flux density in the Halbach cylinder gap.

ACKNOWLEDGMENTS

The authors would like to acknowledge the support of the Programme Commission on Energy and Environment (EnMi) (Contract No. 2104-06-0032), which is part of the Danish Council for Strategic Research.

[1]M. Sullivan, G. Bowden, S. Ecklund, D. Jensen, M. Nordby, A. Ringwall, and Z. Wolf, Proceedings of the 1997 Particle Accelerator Conference **3**, 3330 (1998).
[2]S. Appelt, H. Kühn, F. W. Häsing, and B. Blümich, Nat. Phys. **2**, 105 (2006).
[3]J. M. D. Coey, J. Magn. Magn. Mater. **248**, 441 (2002).
[4]J. C. Mallinson, IEEE Trans. Magn. **9**, 678 (1973).
[5]K. Halbach, Nucl. Instrum. Methods **169**, 1 (1980).
[6]T. R. Ni Mhiochain, D. Weaire, S. M. McMurry, and J. M. D. Coey, J. Appl. Phys. **86**, 6412 (1999).
[7]X. N. Xu, D. W. Lu, G. Q. Yuan, Y. S. Han, and X. Jin, J. Appl. Phys. **95**, 6302 (2004).
[8]G. Moresi, and R. Magin, Concepts Magn. Reson., Part B **19B**(1), 35 (2003).
[9]COMSOL AB, Tegnérgatan 23, SE-111 40 Stockholm, Sweden.
[10]Comsol, Comsol Multiphysics Model Library, 3rd ed. COMSOL AB, Chalmers Teknikpark 412 88 G (2005).
[11]O. Schenk, K. Gärtner, W. Fichtner, and A. Stricker, FGCS, Future Gener. Comput. Syst. **18**, 69 (2001).
[12]O. Schenk and K. Gärtner, Parallel Comput. **28**, 187 (2002).
[13]Standard Specifications for Permanent Magnet Materials, Magnetic Materials Producers Association, 8 South Michigan Avenue, Suite 1000, Chicago, IL 60603.
[14]E. Potenziani, J. P. Clarke, and H. A. Leupold, J. Appl. Phys. **61**, 3466 (1987).
[15]K. A. Gschneidner, Jr., V. K. Pecharsky, and A. O. Tsokol, Rep. Prog. Phys. **68**, 1479 (2005).
[16]V. K. Pecharsky and K. A. Gschneidner, Jr., Int. J. Refrig. **29**, 1239 (2006).
[17]H. Oesterreicher and F. T. Parker, J. Appl. Phys. **55**, 4334 (1984).
[18]F. Bloch, O. Cugat, G. Meunier, and J. C. Toussaint, IEEE Trans. Magn. **34**, 2465 (1998).

Paper II

Paper presented at the 8th IIF/IIR Gustav Lorentzen Conference on Natural Working Fluids, 2008

Nielsen, K. K., Bjørk, R., Jensen, J. B., Bahl, C. R. H., Pryds, N., Smith, A., Nordentoft, A. and Hattel, J.

Magnetic cooling at Risø DTU

Proceedings of the 8th IIF/IIR Gustav Lorentzen Conference on Natural Working Fluids, Copenhagen, Denmark, 2008

Magnetic cooling at Risø DTU

K.K. Nielsen[a,b], R. Bjørk[b], J.B. Jensen[b], C.R.H Bahl[b], N. Pryds[b], A. Smith[b], A. Nordentoft[b], J. Hattel[a]

[a] Technical University of Denmark, Department for Mechanical Engineering, Produktionstorvet, building 425 room 024, 2800 Kgs. Lyngby, Denmark, kaspar.kirstein.nielsen@risoe.dk

[b] Department for Fuel Cells and Solid State Chemistry, Risø National Laboratory for Sustainable Energy, Technical University of Denmark - DTU, building 232, Frederiksborgvej 399, 4000 Roskilde

ABSTRACT

Magnetic refrigeration at room temperature is of great interest due to a long-term goal of making refrigeration more energy-efficient, less noisy and free of any environmentally hostile materials.
A refrigerator utilizing an active magnetic regenerator (AMR) is based on the magnetocaloric effect, which manifests itself as a temperature change in magnetic materials when subjected to a varying magnetic field.
In this work we present the current state of magnetic refrigeration research at Risø DTU with emphasis on the numerical modeling of an existing AMR test machine. A 2D numerical heat-transfer and fluid-flow model that represents the experimental setup is presented. Experimental data of both no-heat load and heat load situations are compared to the model. Moreover, results from the numerical modeling of the permanent magnet design used in the system are presented.

1. INTRODUCTION

The magnetocaloric effect (MCE) was discovered by E. Warburg in 1881. Warburg found that iron got heated up when placed in a magnetic field and when the magnetic field was removed the iron sample cooled down (Warburg 1881). The basic principle of the MCE is that the ordering of the magnetic moments is increased when an external magnetic field is applied to a magnetic material. This means that the spin-entropy decreases. The process is virtually adiabatic if the field is applied rapidly. This means that the total entropy of the system must remain constant and thus the lattice and electron entropies must increase, which is equivalent to an increase in temperature. The process is reversible (for some materials) and thus the opposite will take place when the field is removed again (i.e. the ordering of the magnetic moments decrease and the temperature thus decreases). The MCE is strongest at the phase-transition between the ferromagnetic and the paramagnetic phases. This phase transition takes place at the Curie temperature T_C, which can vary significantly depending on the material. In the past materials have been used mainly for cryogenic applications, but some 30 years ago research into the MCE at room temperature was commenced (Brown 1976) .
The MCE yields, for the benchmark magnetocaloric material (MCM) gadolinium (Gd), an adiabatic temperature change of about 3.6 K at room temperature for a 1 tesla (T) magnetic flux density. This rather low temperature change is obviously too small for direct usage in a cooling device. However, if the material is used in an AMR it is possible to achieve, due to regeneration, a higher temperature difference (Brown 1976). In his experiments Brown reached a temperature span of 46 K using Gd with the hot end at 319 K using a 7 T magnetic flux density from a super conducting magnet. The MCE of Gd is proportional to the magnetic flux density to the power of 0.7 (Pecharsky and Gschneidner 2006). Today's state-of-the-art permanent magnets yield a magnetic flux density of about 1.5 T (Tura and Rowe 2007). Therefore it is crucial to develop a high-performing and efficient AMR.
This work is primarily concerned with developing a model describing an existing AMR test machine based on parallel plates, and using a permanent magnet based on the Halbach design yielding around 1.1 T (Halbach 1980) . In Section 2 the experimental test machine is described. In Section 3 the corresponding numerical model is presented. In Section 4 results from the test machine and the model are compared both including no-load and load-situations. In Section 5 the results are discussed and the work is concluded with some future aspects briefly discussed.

2. EXPERIMENTAL SETUP

Figure 1 shows photos of the test machine, which consists of a regenerator core in the middle of a plastic tube with outer diameter 40 mm and inner diameter 34 mm. The regenerator core is built up of 13 plates of 99.9 % pure Gd (obtained from China Rare Metal Materials Co). The plates with dimensions 40x0.9x25 mm have a total mass of 92 g. At both ends of the Gd plates (in the flow direction) 20 mm long plastic flow guides are placed to ensure a fully developed laminar flow across the plates. The plates and flow guides are fixed by precision machined grooves and are stacked with a spacing of 0.8 mm, which is then the height of the fluid channel.

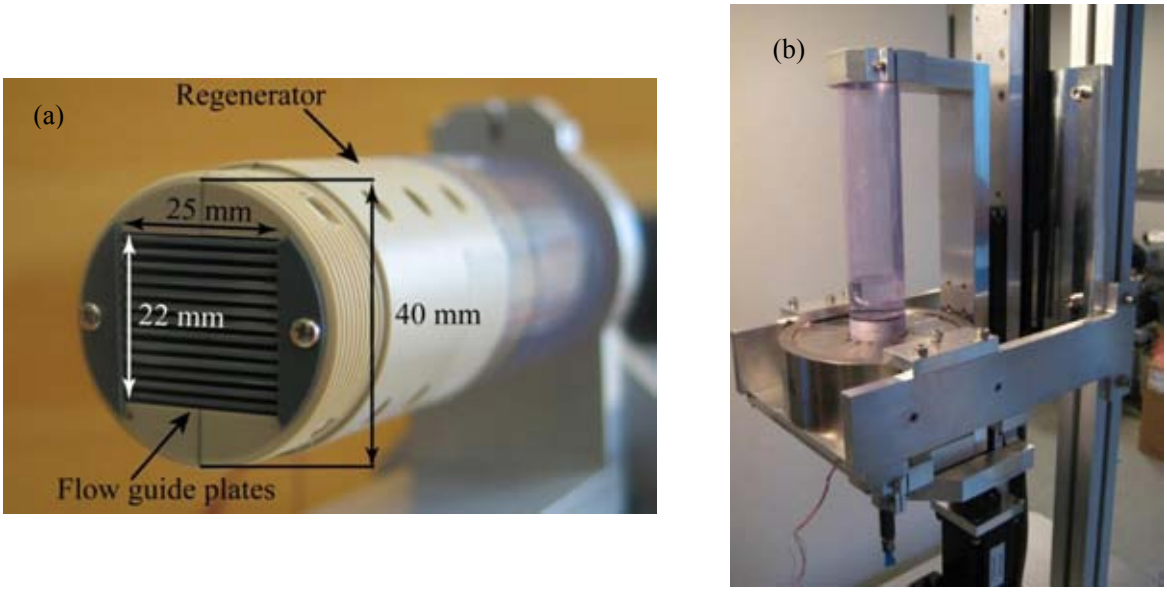

Figure 1: Figure (a) shows a close-up of the experimental AMR test machine where the 13 parallel channels can be seen as well as the plastic tube. Figure (b) is a picture of the machine in its operational environment. The permanent Halbach magnet can be seen with the plastic tube including the regenerator core penetrating it.

The heat transfer fluid is moved by a piston. The regenerator block and its parent plastic tube are suspended vertically in a mounting as shown in Figure 1b and can be moved in and out of the field of the permanent Halbach magnet using stepper motors. This magnet has a maximum magnetic flux density of 1.1 T.
One of the most important results of the experiment – as well as in the model – is to be able to measure the temperature gradient across the regenerator core. This is done via five type E thermo-couples placed equidistantly in the center flow channel as sketched in Figure 2a.

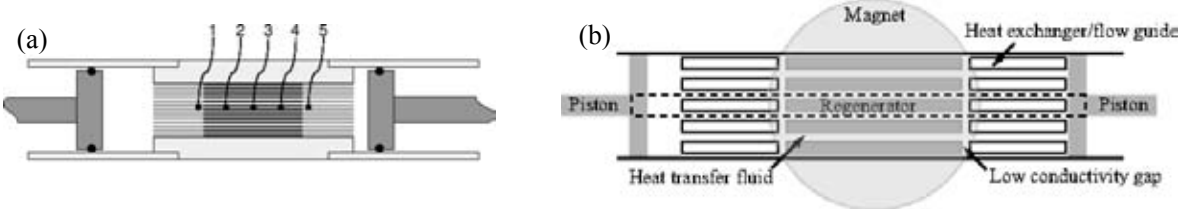

Figure 2: Drawing (a) is a schematic of the regenerator pictured in Figure 1a. The locations of the five thermo-couples are indicated with their appropriate numbers. Thermo-couples 1and 5 are placed at the cold and hot ends respectively. Figure (b) shows how the numerical model represents the full geometry of the AMR. The model breaks the geometry down into a single replicating cell consisting of one half of a complete flow channel (indicated with a dashed line in the figure and magnified in Figure 3).

The system evolves transiently through a number of AMR cycles until cyclic steady-state has been reached. Each cycle consists of four different steps, which have four different characteristic times τ_1, τ_2, τ_3 and τ_4. The cycle is symmetric meaning that $\tau_1 = \tau_3$ and $\tau_2 = \tau_4$. In the first step the magnetic field is applied thus increasing the temperature of the MCM and at this stage the fluid is stationary. In the second step, the pistons move the fluid for τ_2 seconds towards the hot end of the regenerator to reject heat. At the third step the magnetic field is switched off and thus the temperature in the MCM decreases and again at this stage the fluid is stationary. Finally, the piston pushes the fluid towards the cold end for τ_4 seconds. The total cycle-time is $\tau_{total} = 2(\tau_1 + \tau_2)$. In this way the MCM is used as the active material in a regenerator and a

temperature gradient is built up. The magnitude of this gradient depends mainly on the geometry, material and operational properties, i.e. the piston stroke length, τ_1 and τ_2, the height of the fluid channel, the MCM, and how strong the magnetic field is. It is therefore quite a challenge to predict the behavior of a certain system for different process parameters.

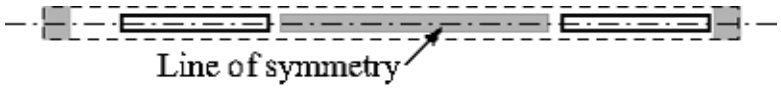

Figure 3: A close-up of the line of symmetry from the replicating cell marked with a dashed line in Figure 2b.

The geometrical simplicity of such an experimental setup makes it ideal for studies of parallel plate regenerators, facilitating direct comparison to the numerical model. Validating the model against the experiment is crucial since a high-quality model can predict the performance of configurations otherwise not thought of and span a much larger parameter-space than possible with the experiment.

3. NUMERICAL MODELING

3.1 Thermal model of the regenerator

The numerical model is "2.5-dimensional" as illustrated geometrically in Figure 4 and Figure 5. For technical reasons the heat transfer fluid is chosen to be stationary and the solid domains are moved relative to this. Thus, the piston movement is modeled as a coordinate transformation of the solid domains with a suitable convective term in the thermal equation for the fluid. The spatial discretization is the classical 2nd order finite difference scheme with a equidistant grid where $\Delta x = 1\,\mathrm{mm}$ and $\Delta y = 0.05\,\mathrm{mm}$, and the temporal integration is done using an Alternate Direction Implicit (ADI) solver with a timestep chosen to be 0.001 second. Since the system includes moving boundaries it is extremely important to make sure that there is energy conservation. Therefore the finite difference (FD) formulation is preferred and validation-tests show that the energy-conservation is virtually the precision of the computer. The computational time on a 2.0 GHz Intel Core 2 Duo CPU is roughly 0.7 CPU-seconds pr physical second in the model.

Due to symmetry considerations only half a replicating cell is modeled (as indicated in Figure 3). This is a good assumption at least for the central channels and plates (which have virtually no loss through the top and bottom of the regenerator).

Figure 4a and Figure 5 show a schematic of the boundary conditions of the model in the (x,y)-plane and (x,z)-plane respectively. The various thermal resistances are labeled with their respective names.

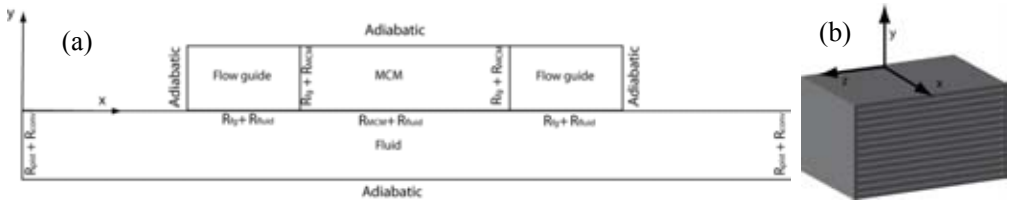

Figure 4 : Figure (a) shows a schematic of the modeled domain in the (x,y)-plane, i.e. half a replicating cell with the boundaries being either adiabatic (symmetry boundaries) or coupled via thermal resistances to the ambient. The x-direction is the direction of the flow and the y-direction is orthogonal to the plates (labeled MCM). The left end is defined as the cold end and the right end as the hot end. Figure (b) shows a 3D sketch of the regenerator block with the coordinate system visualized.

The governing equations for the thermal system are

$$\frac{\partial T_{fl}}{\partial t} = \frac{k_{fl}}{\rho_{fl} c_{p,fl}} \nabla^2 T_{fl} - (\boldsymbol{u} \cdot \nabla) T_{fl} \tag{1}$$

$$\frac{\partial T_s}{\partial t} = \frac{k_s}{\rho_s c_{p,s}} \nabla^2 T_s \tag{2}$$

where the temperatures of the fluid and solid domains are denoted by T_{fl} and T_s respectively. For simplicity all the solid domains are labeled with an s, although they have different physical properties. The thermal properties, i.e. the thermal conductivities k_{fl} and k_s, the mass densities ρ_{fl} and ρ_s and the heat capacities $c_{p,fl}$ and $c_{p,s}$ are all assumed constant except the heat capacity of Gd, which varies as function of both temperature and magnetic field (see Figure 6). The material properties used are given in Table 1.

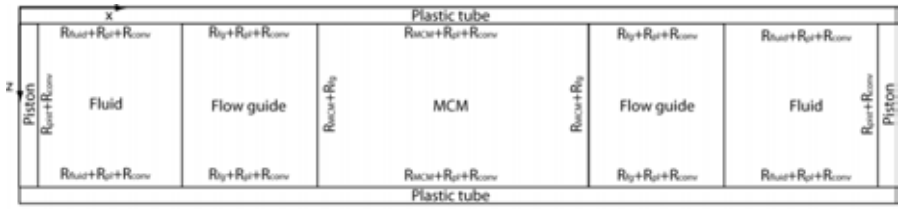

Figure 5 : The model in the (x, z)-plane. The z-direction is only resolved by one grid cell meaning that the model is effectively 2.5-dimensional with the x- and y-dimensions being the two regular dimensions and the finite extension of the z-direction as the half dimension (and most importantly including losses via boundary conditions).

The velocity field in the fluid is denoted by $\boldsymbol{u} = (u, v)$ and is prescribed by the analytical expression for a parallel-plate laminar flow with piston velocity u_p, see e.g. (T. F. Petersen 2007):

$$u = \frac{H_{fl}^2}{2\mu}\frac{\partial p}{\partial x}\left(1 - \frac{y^2}{H_{fl}^2}\right) + u_p \tag{3}$$

$$v = 0 \tag{4}$$

$$\frac{\partial p}{\partial x} = \frac{96}{Re}\,\rho_{fl}\,\frac{1}{4H_{fl}}\,\frac{u_p^2}{2} \tag{5}$$

The Reynolds' number $Re = u_p 4H_{fl}\rho_{fl}/\mu$, ρ_{fl} is the mass density of the fluid, H_{fl} is half the height of the fluid channel, μ is the viscosity of the fluid and y is the vertical coordinate, i.e. orthogonal to the flow direction.

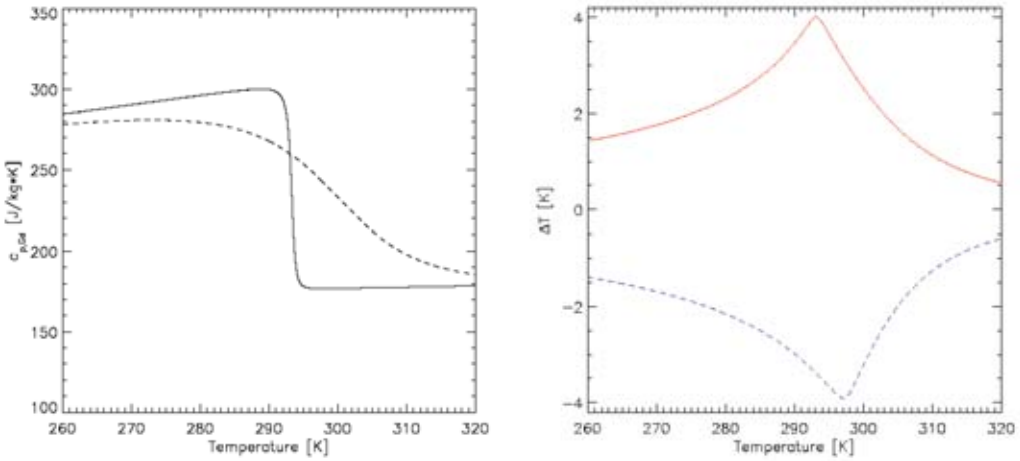

.

Figure 6 : Left: c_p for Gd as function of temperature in zero field (solid line) and in a 1 T field (dashed line). The change around 293 K is rather significant and is actually the definition of the Curie temperature. Right: The adiabatic temperature change of Gd around room-temperature in a 1 T field. The red/solid line is the temperature increase when the field is applied and the blue/dashed line is the corresponding curve for when the field is removed. The data are calculated from the mean field model of Gd compiled in e.g. (Petersen, et al. 2008).

The internal boundaries between the fluid domain and the solid domains are implemented through thermal resistances in Fourier's law of thermal conduction:

$$q_{bd} = -\frac{T_1 - T_2}{R_1 + R_2}. \tag{6}$$

Here the flux across the boundary between two domains (e.g. fluid and MCM) is denoted by q_{bd}, the temperature of the boundary cells in the two adjacent domains are T_1 and T_2 and their corresponding thermal resistances are R_1 and R_2 respectively. The thermal resistance is simply given by the distance from the grid cell's centre to the boundary face divided by the thermal conductivity of the material multiplied by the area of the face boundary.

Table 1 : Material properties used in the model obtained from (Petersen, et al. 2008) and (Holman 1987).

Material	k [W/m · K]	ρ [kg/m^3]	c_p [J/kg · K]	μ [kg/m · s]
Water/ethanol mixture	0.52	981	4330	$8.91 \cdot 10^{-4}$
Plastic	0.2	1200	840	n/a
Gd	10.5	7900	170-300	n/a

The outer boundaries are either adiabatic, if they are symmetry boundaries, or they simulate heat loss in the z-direction, which is not directly resolved (hence this is what we call a 2.5-dimensional model). These losses are calculated via thermal resistances and they contain the thicknesses and thermal conductivities of the particular domain (fluid or solid) and the insulating material surrounding the entire system. On the outer part of the insulating material there is assumed to be natural convection modeled via the parameter h_{conv}, which has a value in the range $5 - 20$ W/Km^2 and corresponds to free convection of air on a plate (Holman 1987).

3.2 The permanent magnet

The magnetic field that generates the MCE can be produced by an electromagnet or a permanent magnet assembly. For this machine we have chosen the latter as this requires no external power source to produce a strong magnetic field. The requirement of the permanent magnet assembly is that it must produce a strong homogenous magnetic field in a confined region of space and a very weak field elsewhere. The design known as a Halbach cylinder (Mallinson 1973), (Halbach 1980) fulfills these requirements and has therefore been chosen for the test machine. An ideal Halbach cylinder consists of a permanent magnetic material with a bore along the cylinder symmetry axis. The magnetic material is magnetized such that the direction of magnetization varies as shown in Figure 7. This produces a strong homogeneous field in the cylinder bore. In the case of an infinitely long cylinder the flux density in the bore is given by $B = B_r \ln\left(\frac{r_{ex}}{r_{in}}\right)$. An ideal Halbach cylinder is not physically realizable, as it is both necessary to make the Halbach cylinder of a finite length and to divide the continuously magnetized cylinder into parts consisting of permanent magnets each with their own directions of magnetization. Based on the design of the regenerator the Halbach cylinder for the test machine consists of 16 blocks of permanent magnets and with dimensions $r_{in} = 2.1$ cm, $r_{ex} = 6$ cm, and $L = 5$ cm.

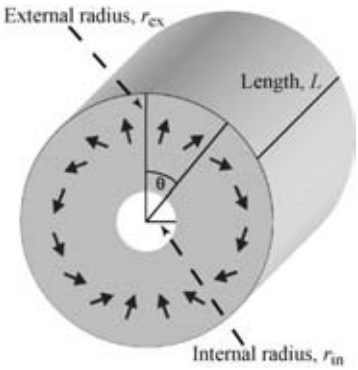

Figure 7: A drawing of a Halbach cylinder showing the internal radius, r_{in}, external radius, r_{ex}, and length, L. Also shown are arrows in the direction of the remanent magnetization of the magnetic material. This varies as 2θ. The figure is from (Bjørk, et al. 2008)

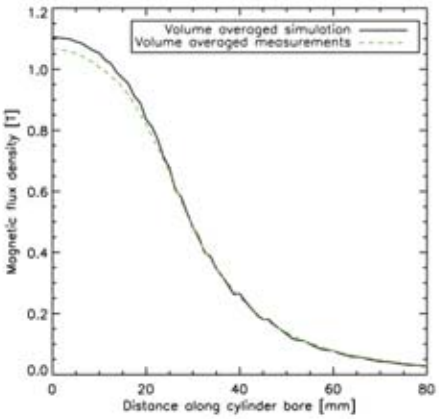

Figure 8: Flux density for the simulated and the physical Halbach cylinder for the test machine. There is good agreement between data.

To investigate the magnetic field produced by this Halbach cylinder we have performed numerical simulations using the commercially available finite element multiphysics program, *Comsol Multiphysics* (Comsol 2005), see also (Bjørk, et al. 2008) for details.

As well as modeling the magnet assembly we have also performed measurements of the flux density of the physical magnet assembly, seen in Figure 1. In Figure 8 the average flux density of the magnetic field as a function of distance from the center of the Halbach cylinder for both simulation and measurement is shown. As can be seen from the figure the numerical simulation and the experimental measurements agree, and show that a high flux density is produced in the center of the cylinder bore.

4. RESULTS

The experimental and modeling results are divided in two parts. First a sensitivity analysis of how far the regenerator is taken out of the Halbach's magnetic field is addressed under no-load conditions. Secondly a load-situation is investigated.

4.1 Sensitivity to the magnetic field

Since the magnetic field of the Hallbach magnet strays outside of the central bore in the cylinder (see Figure 8), the distance which the regenerator block is moved away from the centre of the Halbach must have some influence on the performance of the regenerator. The experiments were adjusted to move the regenerator out of the magnetic field with a distance varying from 30 mm to 150 mm (see Figure 9). The operating conditions were the same for each experiment, which was allowed to reach steady-state in each case (see Table 2). The model was set with the same parameters and the varying magnetic field was implemented via a volumetric source term in the heat equation for the MCM:

$$\frac{dQ_{MCM}}{dt} = -\rho_{Gd} T_{Gd} \frac{\partial \sigma}{\partial T} \frac{dB}{dt}. \tag{7}$$

This is obtained from the mean field theory of Gd, see e.g. (Petersen, et al. 2008). The change with respect to temperature of the magnetization is denoted by $\partial\sigma/\partial T$ and the magnetic flux density is denoted by B. The magnetic field only varies in the x-direction in the regenerator. The crucial term in this formulation is the time variation of the magnetic field. This is implemented simply using the finite extent of the regenerator block and the velocity of which the regenerator is moved in and out of field.

As seen in Figure 9 there is one series of experimental data and two model series. The data sets show the no-load steady-state temperature span between thermo-couples one and five as function of how far the regenerator is taken out of the magnetic field. It is seen from the experimental data that at distances above 70 mm the temperature span does not increase anymore; hence, the full yield of the magnet is utilized.

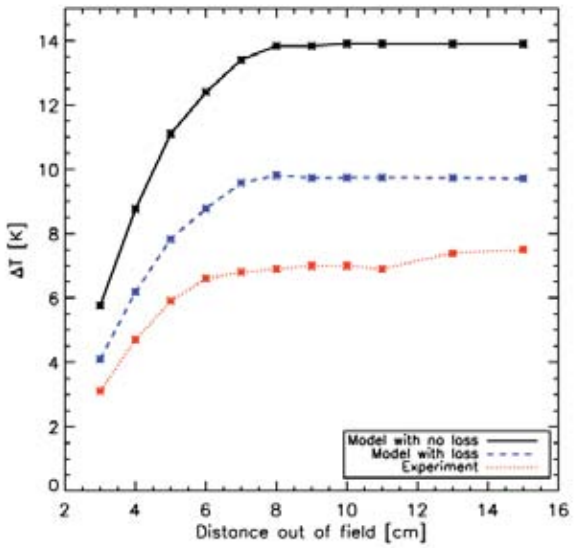

Figure 9: The figure shows how the steady-state and no-load temperature span behaves when the regenerator is not taken completely out of the magnetic field (the red/dotted line). Each asterisk in the graph represents a data point. Also included are the results of two slightly different numerical simulations; one without losses (the black/solid line) and one with ideal losses (blue/dashed line). The tendencies are clearly the same on all three graphs. The absolute values of the temperature spans differ somewhat, however, including losses is seen to improve the correspondence between experiment and model significantly.

The model simulations were done for two cases: One with no loss to the surroundings, i.e. perfect thermal insulation, and one with realistic losses via the boundary conditions described in Section 3.1. The tendencies of all three data sets are virtually the same, which clearly shows that the numerical model catches many of the aspects of the magnetic regeneration. It is not surprising that the ideal adiabatic model overestimates the temperature span somewhat as significant losses to the ambient are expected in the test device. When the losses are included, however, the model comes much closer at the experimental values still showing the exact same tendency.

Table 2 : The operational properties of the two experiment series.

Experiment	Effective piston stroke length (% of plate length)	τ_1(s)	τ_2(s)
Magnetic field variation	40 %	3.0	2.9
Heat load experiment	53 %	1.5	2.9

4.2 Load experiment

The piston at the cold end has been equipped with a copper plate connected to a power supply which makes it possible to apply a heat load through ohmic dissipation to the water. An experiment was run with the

parameters given in Table 2 and heat loads from 0 to 1.6 W. The model was set with the same parameters and a spatially constant magnetic flux density of 1 T. Figure 10 shows both an example of the transient evolution of a specific heat load experiment (left-hand) and the results of the heat-load series (right-hand).

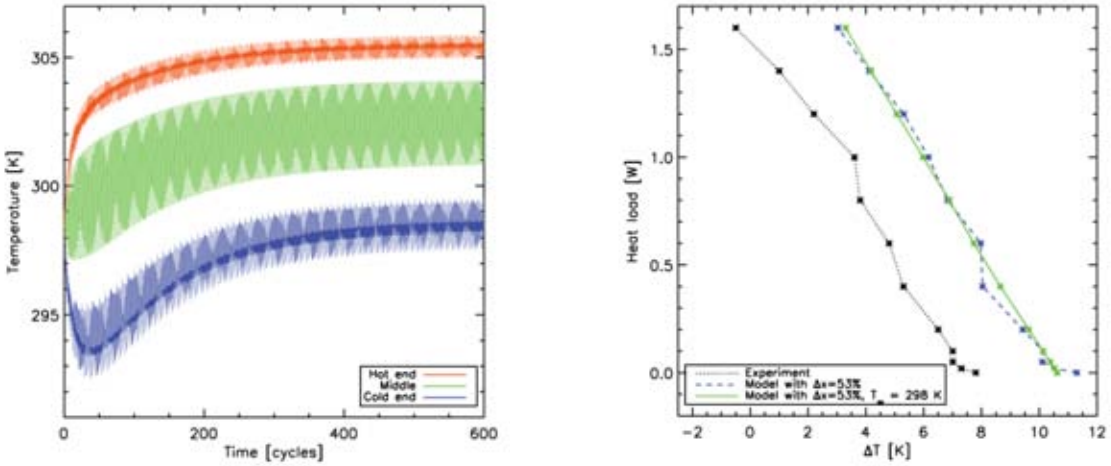

Figure 10: Left: The transient evolution of the cold, middle and hot parts of the regenerator (simulated). The particular example is for a piston stroke (Δx) of 53% with a load of 0.8 W. Right: A load-experiment and the corresponding model results. The model assumed $h_{conv} = 20\,W/m^2K$. *Note that there are two model-series in the right graph. The green/solid line data set was performed with a constant ambient temperature whereas the blue/dashed line data set corresponds directly to the circumstances during the experimental data acquisition (black line/dotted).*

The experimental series was performed over a period of two days since it takes around an hour to reach steady-state for each configuration. Therefore the ambient temperature T_∞ varied slightly (from 296-299 K). This is possible to adjust in the model as well, and therefore the two data sets are directly comparable. The model and the experimental data are very similar in behavior, though the model over-estimates the temperature span. Generally the temperature span decreases linearly with the increasing cooling capacity as one would expect. There are, however, minor fluctuations in the linearity. If the experimental data are considered isolated, the small variations may be regarded as experimental noise. However, when compared to the model data, virtually the same variations are seen. To investigate this, a model-series was performed with the ambient temperature set to the constant value 298 K. This is seen as the green/solid line in the right graph of Figure 10. Thus, the variations away from the linearly decreasing cooling capacity are interpreted as a result of the fluctuations in the ambient temperature. The slopes of each of the three graphs were found by linear regression. The values are all -0.2 $\pm$0.01 W/K.

5. DISCUSSION, CONCLUSIONS AND OUTLOOK

5.1 Discussion

The numerical model has been successfully validated against real experiments in different situations including no-load and load-experiments, varying the magnetic field and some of the operational parameters, namely piston stroke length, τ_1 and τ_2. The discrepancies between the model and the experiment seen in Figure 9 and Figure 10 are, however, something that should be considered and the model should be improved to minimize these. We have used an ideal model for the behavior of Gd in terms of c_p and ΔT_{ad}. We have independently measured the actual adiabatic temperature change of the Gd used in the test machine and it has turned out that due to impurities the actual adiabatic temperature change is roughly 20 % lower than in the ideal mean field model used in the numerical model. We have chosen not to include this in the present work since we have not yet performed enough measurements of the utilized Gd in order to cover the range in magnetic fields and temperature span needed.

A result of this work is that the model is directly capable of catching the effect of the ambient temperature on the system. This may have been interpreted as an experimental feature (e.g. noise) if the model had not caught it and if not the constant-ambient temperature modeling had resulted in the completely straight line seen in the right part of Figure 10.

5.2 Conclusions and outlook

The experimental AMR at Risø DTU has been demonstrated to be quite versatile in terms of operational parameters and various aspects of the cooling capacity. The corresponding numerical model is to a large extent successful in predicting the behavior of the system. Many interesting aspects still need to be investigated though. They include obtaining more reliable and realistic data of the Gd we actually use in our test machine, testing other potential MCM materials and changing the thickness of the plates and the fluid channels as well as the operating parameters. Having a powerful numerical model that predicts the behavior seen experimentally is crucial for the further development of a new AMR with significantly improved performance. The fact that there is a very strong correspondence between the experimental and modeling results in both series presented in Section 4 strongly indicates that the model indeed captures the general behavior of the parallel-plate AMR system.

ACKNOWLEDGEMENTS

The authors thank Mr. Jørgen Geyti for his technical assistance. Furthermore the authors would like to acknowledge the support of the Programme Commission on Energy and Environment (EnMi) (Contract no. 2104-06-0032) which is part of the Danish Council for Strategic Research.

REFERENCES

Bjørk, R., C.R.H. Bahl, A. Smith, and N. Pryds. "Optimization and improvement of Halbach cylinder design." *Journal of Applied Physics, in press*, 2008.

Brown, G. V. "Magnetic heat pumping near room temperature." *Journal of Applied Physics* (AIP) 47 (1976): 3673-3680.

Comsol. *Comsol Multiphysics Model Library, third ed.* COMSOL AB, Chalmers Teknikpark 412 88 G., 2005.

Halbach, K. "Design of permanent multipole magnets with oriented rare earth cobalt material." *Nuclear instruments and methods* 169 (1980).

Holman, J.P. *Heat Transfer.* 6. McGraw-Hill, 1987.

Mallinson, J. C. "One-sided Fluxes - A Magnetic Curiosity?" *IEEE Transactions on magnetics* 9 (4) (1973): 678-682.

Pecharsky, V. K., and K.A. Gschneidner. "Advanced magnetocaloric materials: What does the future hold?" *International Journal of Refrigeration* 29 (2006): 1239-1249.

Petersen, T. F., N. Pryds, A. Smith, J. Hattel, H. Schmidt, and H.J.H Knudsen. "Two-dimensional mathematical model of a reciprocating room-temperature Active Magnetic Regenerator." *International Journal of Refrigeration* 31 (2008): 432-443.

Petersen, Thomas Frank. "Numerical modelling and analysis of a room temperature magnetic refrigeration system." PhD Thesis, Risø National Laboratory and Technical University of Denmark, 2007.

Tura, A., and A. Rowe. "Design and Testing of a Permanent Magnet Magnetic Refrigerator." *2nd International Conference on Magnetic Refrigeration at Room Temperature.* 2007. 363-370.

Warburg, E. "Magnetische untersuchungen." *Ann.Phys (Leipzig)* 13 (1881): 141-164.

Paper III

Paper presented at the 3rd International Conference on Magnetic Refrigeration at Room Temperature, 2010

Bjørk, R., Bahl, C. R. H., Smith, A. and Pryds, N.

On the optimal magnet design for magnetic refrigeration

Proceedings of the 3rd International Conference on Magnetic Refrigeration at Room Temperature, Des Moines, Iowa, USA, 473-480, 2009

ON THE OPTIMAL MAGNET DESIGN FOR MAGNETIC REFRIGERATION

R. Bjørk[*], C. R. H. Bahl, A. Smith and N. Pryds
Fuel Cells and Solid State Chemistry Division, Risø National Laboratory for Sustainable Energy, Technical University of Denmark, Frederiksborgvej 399, 4000 Roskilde

[*]Corresponding author: e-mail address: rasmus.bjoerk@risoe.dk

ABSTRACT

One of the key issues in magnetic refrigeration is generating the magnetic field that the magnetocaloric material must be subjected to. The magnet constitutes a major part of the expense of a complete magnetic refrigeration system and a large effort should therefore be invested in improving the magnet design. In this paper we analyze the different efficiency and usability of permanent magnets and electromagnets/superconducting magnets. We then present an overview of different published magnet designs used in magnetic refrigeration applications. These designs are analyzed based on the generated magnetic flux density and the amount of magnetic material used. This is done by characterizing each design by a magnet design efficiency parameter, Λ_{cool}. The analyses of the different published permanent magnet designs allows us to present recommendations for improving existing magnet designs as well as discussing the features of the best magnet design for magnetic refrigeration.

1. INTRODUCTION

The magnet is an essential yet often overlooked part of a magnetic refrigerator. Although a number of review articles on magnetic refrigeration devices have been published these have only concerned themselves with the temperature span and cooling power of the devices and not the magnet design in detail (Gschneidner and Pecharsky, 2008). Little effort has yet been made to compare existing magnet designs.

It is important to investigate the design of the magnet in detail because the magnet can be the single most expensive part of a magnetic refrigerator. If we consider the commercial viability of magnetic refrigeration it is extremely important that the magnetic structure used generates a high magnetic flux density over as large a volume as possible while using the minimum amount of magnets possible. It is also important that the magnetic refrigerator itself is designed to utilize the magnetic flux density generated by the magnet at all times. By comparing different magnet assemblies and showing which designs perform best, we hope to learn some fundamental key features that must be present in an efficient magnet design.

1.1. The different types of magnets

There are essentially three different types of magnets that can be used in a magnetic refrigeration device. These are the electromagnet, the superconducting magnet and the permanent magnet. We will consider the usability of each in turn.

The electromagnet generates a magnetic flux density by passing a current through a solenoid. The relation between the current, I, and the generated flux density, B, for an electromagnet in a single magnetic circuit consisting of a soft magnetic material with relative permeability, μ_r, and where the core has roughly the same cross sectional area throughout its length and the air gap is small compared with the cross sectional dimensions of the core, is

$$NI = B\left(\frac{L_{core}}{\mu_r \mu_0} + \frac{L_{gap}}{\mu_0}\right), \tag{1}$$

where N in the number of turns in the winding, L_{core} is the length of the soft magnetic material, μ_0 is the permeability of free space and L_{gap} is the length of the air gap. To generate a 1.0 T magnetic flux density over a 30 mm air gap an iron cored solenoid with $\mu_r = 4000$ would need to have 24000 ampere windings. The length of the soft magnetic material is irrelevant as the expression is dominated by the second term. An electromagnet having 24000 ampere windings would need a massive power supply and an equally massive cooler to prevent the solenoid from melting. Based on this simple calculation we can rule out electromagnets as applicable to commercially viable magnetic refrigerators.

The superconducting magnet is a better option than the traditional electromagnet as it requires little power to operate once the electromagnet has become superconducting as no power is lost to ohmic resistance. Although a superconducting magnet can create magnetic flux densities of the order of 10 T it has to be continuously cooled. This can be an expensive process and the apparatus surrounding the superconducting magnet can be substantial. However for large scale applications, e.g. large refrigerators for warehouses etc., a superconducting magnet might be a relevant solution. For common household refrigeration the superconducting magnet is at present not a relevant option.

Having considered the electromagnet and superconducting magnet and ruled out both of these for common household magnetic refrigeration we will now consider the permanent magnet. As these provide a constant magnetic flux density they are ideal for use in applications which aim at a low power consumption, such as magnetic refrigeration. The magnetic flux density generated across an air gap by a permanent magnet depends on the remanence of the magnet, which is typically of the order 1.2-1.4 T for NdFeB magnets, and the magnetic circuit in which the magnet is placed. In this paper we review and characterize different permanent magnet assemblies previously published in the magnetic refrigeration literature.

2. CHARACTERIZING A MAGNET DESIGN

To easily compare different magnet designs it is important to be able to characterize a magnet design by a single parameter. A previous suggestion for such a parameter was given by Nikly and Muller (2007) who proposed characterizing a magnet design by

$$\xi = \frac{M_{magnet}}{M_{magnet} + M_{MCM}}, \tag{2}$$

where M_{magnet} is the mass of the magnet and M_{MCM} is the mass of the magnetocaloric material.

The parameter ξ can take values in the range of zero to one, where zero corresponds to no magnet at all and one corresponds to no magnetocaloric material present. The problem with using ξ for magnet characterization is that it contains no information about the magnetic flux density produced by the magnet design. Two designs might have the same value of ξ but produce very different flux densities. Also because the ξ parameter contains the masses and not the volume of the magnet and magnetocaloric material, the same magnetic refrigerator will have a different ξ value if two magnetocaloric materials with different densities or regenerators with different porosities are used.

We propose instead to characterize a magnet design for use in magnetic refrigeration by the Λ_{cool} parameter introduced in Bjørk *et al.* (2008). This parameter is designed to favor magnet designs that generate a high magnetic flux density in a large volume using a minimum of magnetic material. It also favors system designs where the amount of time where the magnetic flux density is "wasted" by not magnetizing a magnetocaloric material is minimized.

2.1. The Λ_{cool} parameter

If the Λ_{cool} parameter is to be used to express the efficiency of a given permanent magnet assembly it must be dependent on the temperature change that the magnetic flux density can induce in the magnetocaloric material placed in the assembly gap. The temperature change scales with the magnetic flux density but not necessary linearly. It is important to note that the Λ_{cool} parameter will be proportional to the temperature change of the magnetocaloric material and not the magnetic flux density because the temperature change of the magnetocaloric material is what is used to generate the temperature span and cooling power of the refrigeration device.

A large number of different materials have been suggested as the active component of a magnetic refrigeration machine (Gschneidner *et al.*, 2005). However the material most often used, i.e. the ``benchmark" magnetocaloric material at room temperature, Gadolinium, has a magnetocaloric effect that scales with the flux density of the magnetic field to the power of 0.7 at the Curie temperature (Pecharsky and Gschneidner, 2006). This is in good accordance with the power of 2/3 predicted by mean field theory for a general second order magnetocaloric phase transition material (Oesterreicher and Parker, 1984). Taking this into consideration the Λ_{cool} parameter is chosen to be proportional to the magnetic flux density to the power of 2/3.

It is not only the flux density inside the air gap that is of importance to the magnetocaloric effect. The volume in which the magnetocaloric material is placed when it is demagnetized is equally important. In

order to maximize the magnetocaloric effect the flux density in this volume must be as low as possible. In a reciprocating device this can of course be accomplished by simply moving the magnetocaloric material far away from the magnet, but this will increase the physical size and cycle time of the magnetic refrigeration machine. In a rotating device the high and low flux density regions will generally be adjacent and care must be taken to minimize the "leak" of flux into the low flux density region.

To take into account the amount of magnetocaloric material that can experience a temperature change, the Λ_{cool} parameter is proportional to the volume of the high flux density region. Note that Λ_{cool} is proportional to the whole volume of the gap and not only the volume occupied by the magnetocaloric material. Thus Λ_{cool} does not depend on the porosity of the magnetocaloric material, nor on the amount of e.g. plastic housing used to confine the magnetocaloric material. Also Λ_{cool} is inversely proportional to the volume of magnetic material used, as the more magnetic material used the more expensive the design will be.

Finally, the Λ_{cool} parameter is proportional to the fraction of an active magnetic regenerator (AMR) cycle of which magnetocaloric material is placed in the high flux density volume. The reason for this is that if e.g. magnetocaloric material is only placed inside the high flux density region half the time of a full AMR cycle the (expensive) magnet is not utilized during the remaining half of the cycle and it is thus essentially being wasted during this time. The fraction of time the magnetic flux generated by the magnet is being used to generate a magnetocaloric effect must be maximized.

Taking all this into account we will characterize a magnet design for use in magnetic cooling applications by the parameter

$$\Lambda_{cool} \equiv \left(\left\langle B^{2/3} \right\rangle - \left\langle B_{out}^{2/3} \right\rangle \right) \frac{V_{field}}{V_{mag}} P_{field} , \tag{3}$$

where V_{mag} is the volume of the magnets, V_{field} is the volume with a high flux density, P_{field} is the fraction of an AMR cycle that magnetocaloric material is placed in the high flux density volume, $\left\langle B^{2/3} \right\rangle$ is the volume average of the flux density in the high flux volume to the power of 2/3 and $\left\langle B_{out}^{2/3} \right\rangle$ is the volume average of the flux density to the power of 2/3 in the volume where the magnetocaloric material is placed when it is being demagnetized.

One should note that the Λ_{cool} parameter will favor a design with a small magnetic flux density and large volume of the high flux density region. This is because the magnetic flux generated by a magnet scales with a power less than 0.7 with the volume of the magnet. Therefore for practical applications one would choose to optimize Λ_{cool} under the condition of a certain minimum flux density in the high flux density region. We do not explicitly consider the remanence of the permanent magnets used in the assembly. This is not critical for the comparison of different designs as the remanence of the NdFeB magnets used in all magnetic refrigeration magnet assemblies varies only between 1.2-1.4 T. Therefore, geometry accounts for the most of the differences between different designs. Any soft magnetic material used in the magnet assembly is ignored, as the price of this material is much lower than that of the permanent magnets.

3. PUBLISHED MAGNET DESIGNS

Having defined the Λ_{cool} parameter we can now compare different published magnet designs. There exist several published designs of magnetic refrigerators; unfortunately many publications lack the necessary specifications to either reconstruct or directly calculate the Λ_{cool} parameter. The designs presented below are among the few that contain sufficient information to calculate Λ_{cool}. A short description of each design is given prior to the calculation.

We are aware that many of the magnetic refrigerators presented here are test devices and should be evaluated as such. However it is also in the test design phase that large improvements to the design should be suggested. Therefore we hope that the evaluation of the designs can lead to improvement for both current and future magnetic refrigerators.

3.1. Simple magnetic circuits

Design by Zheng *et al.* (2009)

The general refrigerator design by Zheng *et al.* (2009) is a reciprocating design where the magnet is kept stationary and two packed beds of magnetocaloric material are moved in and out of the magnetic field. When one of the beds is in the magnetic field the other bed is out of the field. The flux density in the design is provided by a single simple magnet and the flux lines are guided by a soft magnetic material through a small air gap. Based on Zheng (2009) the volume of the magnet is 0.5 L and the volume of the high flux density region is 0.09 L. The mean magnetic flux density is 0.93 T.

The P_{field} parameter can easily be estimated for this design as the cycle time, movement speed of the magnet and the distance between the ducts are given. The latter distance is 80 mm and as the permanent magnet moves with a speed of 0.02 m/s it will take the magnet 4 seconds to move between the ducts. The magnet has to go back and forth in one cycle, thus moving the magnet takes a total of 8 seconds. The magnetization parts of the cycle are given as two times 2 seconds, and from this we conclude that P_{field} is 0.33.

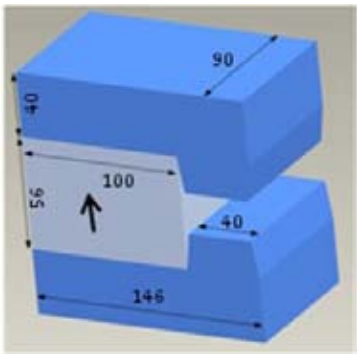

Fig 1: The magnet design by Zheng *al* (2007). From Zheng (2009). The blue material is soft magnetic material. All dimensions are in mm. The arrow indicates the direction of magnetization.

Design by Lee *et al.* (2002)

The design by Lee *et al.* (2002) is a reciprocating design with a stationary magnet and a moving bed of magnetocaloric material. The magnet is shaped like the letter C, with a high homogenous flux density in the center. The flux density in the center is enhanced by blocks of soft magnetic material. These are placed in the center of the "C". The height of the air gap is 12.7 mm and the cross sectional dimensions is given as 114x128 mm^2 i.e. 14.6 L/m. The cross sectional area of a magnetocaloric bed is given as 15.2x10 mm^2, and from this we estimate the total cross sectional area of the high flux region to be 25x12.7mm^2, i.e. 0.32 L/m. The magnetic flux density is given to be 1.9 T in the high flux region but this is based on a two dimensional simulation. Depending on the length of an actual device this figure will be significantly lower. As the paper is mostly about magnet design and less about an actual magnetic refrigeration device it is impossible to estimate the P_{field} parameter. For an optimistic estimate we take P_{field} to be 0.95.

Design by Vasile and Muller (2006)

The magnet design by Vasile and Muller (2006) is almost identical to the design by Lee *et al.* (2002). A "C" shaped magnet assembly with soft magnetic material inside, but this time also outside the array of magnets. In this design the magnets are rotating around a circle with inserts filled with magnetocaloric material. Based on a drawing included in the paper we estimate the cross sectional area of the magnets to be 9.2 L/m and the high field gap cross sectional area to be 0.75 L/m. The magnetic flux density is given as 1.9 T in the high field region, but this is based on a two dimensional simulation so a real world assembly would have a lower value. As the magnets are rotating continuously and the inserts for the magnetocaloric material fill most of the circle along which the magnet is rotating we estimate the P_{field} parameter to be 0.90.

Design by Bohigas *et al.* (2000)

The design by Bohigas *et al.* (2000) is a rotating design in which the magnets are stationary and the magnetocaloric material is rotated in and out of the high flux density region. A total of eight rectangular magnets are used, four of them placed in the inside of the rotating wheel and four placed outside the wheel. The dimension of one of the inner blocks is given as 40x40x20 mm and one of the outside blocks has dimensions 50x50x25 mm. The size of the air gap is given to be 7 mm and there are a total of four air gaps. From these figures we estimate the dimensions of one air gap to be 40x7x20 mm. Thus the volume of the magnets is 0.38 L and the volume of the high flux density region is 0.02 L. The flux density is given as 0.9 T. This design has magnetocaloric material continuously entering the high flux density region and thus the P_{field} parameter is 1.

3.2. Halbach type magnet assemblies

Design by Tura and Rowe (2007)

The magnetic refrigerator presented by Tura and Rowe (2007) is a rotating system in which the magnetic material is kept stationary and a magnet is rotated to alter the magnetic flux density. The magnet design used in the device consists of two separate magnets each of which consists of two concentric Halbach cylinders. The reason that two separate magnets are used is that the system can be run such that the magnetic forces are balanced.

In the concentric Halbach cylinder design the flux density in the inner cylinder bore can be controlled by rotating the inner or outer magnet. Tura and Rowe (2007) report that when the inner magnet is rotated the mean magnetic flux produced can be changed continuously from 0.1 T to 1.4 T. From Rowe (2009) we know the total volume of the magnetic material to be 1.03 L, while the total volume of the high flux density region is 0.05 L. These values are for one of the concentric Halbach cylinders. The P_{field} parameter for this system design is 0.5 as half the cycle time the inner magnet will be turned such that it approximately cancels the magnetic flux generated by the outer magnet. In this configuration there is no high flux density region, and the magnets are essentially not being used.

Design by Engelbrecht *et al.* (2009)

The magnetic refrigeration test machine designed at Risø DTU Engelbrecht *et al.* (2009) is a reciprocating device in which plates of magnetocaloric material are moved in and out of a stationary magnet. The magnet is a Halbach cylinder consisting of 16 blocks of permanent magnets. The cylinder has an inner radius of 21 mm, an outer radius of 60 mm and a length of 50 mm. The average magnetic flux density in the cylinder bore is 1.03 T. The volume of the magnet is 0.50 L and the volume of the high field region, i.e. the cylinder bore, is 0.07 L. The P_{field} parameter for this system design is 0.5. This is because for half the cycle time the stack of plates is out of the high field region leaving this to be empty.

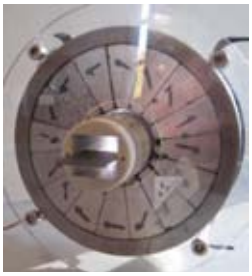

Fig 2: The Halbach design by Engelbrecht *et al* (2007). The regenerator with a magnetocaloric plate can also be seen.

Design by Lu *et al.* (2005)

The magnetic refrigeration device designed by Lu *et al.* (2005) is a reciprocating device with two separate packed beds of magnetocaloric material moving in and out of two stationary magnet assemblies thus allowing force compensation. Both magnets are 16 segmented Halbach cylinders with an inner radius of 15 mm and an outer radius which is claimed to be 700 mm. We take this as a typo and assume the outer radius is of 70 mm. The flux density produced is given as 1.4 T, and the length of the cylinder is 200 mm. Given these number the volume of the magnet is 2.94 L and the volume of the high flux density region is 0.14 L, for either of the magnets. For the same reasons as the design by Engelbrecht *et al.* (2009) the P_{field} parameter for this system design is 0.5.

3.3. Complex magnetic structures

Design by Zimm *et al.* (2007)

The magnetic refrigeration machine presented by Zimm *et al.* (2007) utilizes a rotating principle, in which the magnetocaloric material is stationary and the magnet is rotating. The magnet design is quite complicated, utilizing both magnets and soft magnetic materials, but essentially consists of two Y-shaped magnetic structures separated by an air gap. The high flux density region spans an angle of 60 degrees on two opposite sides of the design. Based on Chell (2009) the total volume of the magnet assembly is 4.70 L, the volume of the high flux density region is 0.145 L and the mean flux density is 1.5 T. The P_{field} parameter for this design is essentially given by the speed at which the magnet rotates from one high flux region to the next. In this design these are separated by an angle of 30 degrees. We do not know the rotation speed therefore we take the P_{field} parameter to be 0.90.

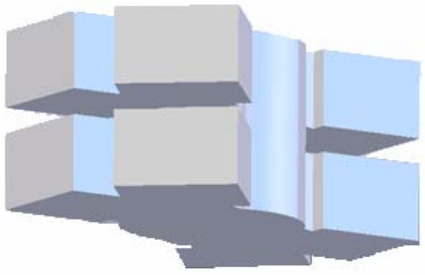

Fig 3: The magnet design by Zimm *et al* (2007). From Chell (2009). The high flux density is generated in the gap between the two "Y"-shaped structures. The direction of magnetization for the individual magnets is too complex to illustrate on this figure.

Name	V_{mag} [L]	V_{field} [L]	$\langle B \rangle$ [T]	$\langle B_{out} \rangle$ [T]	$\langle B^{2/3} \rangle$ [T$^{2/3}$]	$\langle B_{out}^{2/3} \rangle$ [T$^{2/3}$]	P_{field}	Magnet type	Λ_{cool} without P_{field}	Λ_{cool}
Zheng *et al.* (2009)	0.5	0.09	0.93	0*	0.95[a]	0*	0.33	Single magnet magnetic circuit	0.17	0.06
Lee *et al.* (2002)	14.6/m	0.32/m	1.9[H, 2D]	0*	1.53[a, H]	0*	0.95*	"C" shaped circuit	0.03	0.03
Vasile and Muller (2006)	9.2/m	0.75/m	1.9[H, 2D]	0*	1.53[a, H]	0*	0.90*	"C" shaped circuit	0.12	0.11
Bohigas *et al.* (2000)	0.38	0.02	0.9[H]	0*	0.93[a, H]	0*	1	Rectangular magnet on round surface	0.049	0.049
Tura and Rowe (2007)	1.03	0.05	1.4	0.1	1.25[a]	0.2[a]	0.5	Concentric Halbach cylinders	0.05	0.03
Engelbrecht *et al.* (2009)	0.5	0.07	1.03	0.01	1.02	0.06	0.5	Halbach cylinder	0.13	0.07
Lu *et al.* (2005)	2.94	0.14	1.4[H]	0	1.25[a, H]	0	0.5	Halbach cylinder	0.06	0.03
Zimm *et al.* (2007)	4.70	0.15	1.5	0.1	1.31[a]	0.2[a]	0.90*	"Y" shaped magnetic structure	0.04	0.03
Okamura *et al.* (2007)	3.38	0.80	1.0	0	1.0[a]	0	0.66	Inner magnet rotor, soft magnetic yoke	0.24	0.16

Table 1: This table lists the specifications for a number of different magnet designs. Each design has been described in some detail in this paper. For further information on each model we refer to the original papers.

*designates an estimated quantity.

[a] means that in the columns $\langle B^{2/3} \rangle$ and $\langle B_{out}^{2/3} \rangle$ the mean value of the magnetic flux density has simply been taken to the power of 0.7. The value of $\langle B \rangle^{2/3}$ and $\langle B^{2/3} \rangle$ will only be equal if the flux density is completely homogenous.

[H] indicates that the value given for the magnetic field might be the highest possible attainable flux density in the center of the high field region, and as such not a representative average of the magnetic flux density for the whole of the high field region.

[2D] indicates that the flux density is based on a two dimensional simulation. These notoriously overestimate the flux density except for very long assemblies and so Λ_{cool} will be overestimated for these designs. Some of the two dimensional designs also have their volumes given pr meter.

Design by Okamura *et al.* (2007)

The design used by Okamura *et al.* (2007) is a rotating device in which the magnet is rotated past ducts packed with magnetocaloric material. The magnet design consists of a complex arrangement of permanent magnets and soft magnetic materials which is assembled as an inner rotor consisting both of magnets and soft magnetic material with an outer yoke consisting of only soft magnetic material. The magnetocaloric material is placed in four ducts in the air gap, each spanning 34 degrees. The inner rotor is designed such that magnets with identical poles are put facing each other and separated by a soft magnetic material. This increases the flux density and "pushes" the flux lines from the inner rotor to the outer stator. Based on Okamura (2009) the mean flux density is 1.0 T and the magnet design to contain 3.38 L of magnet and 0.80 L of high flux density region.

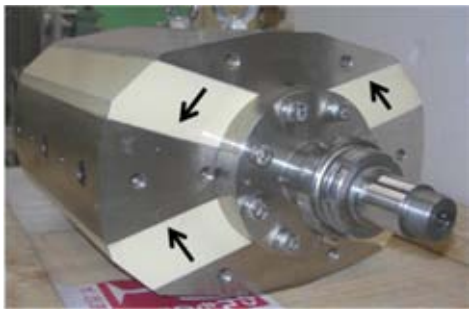

Fig 4: The magnet design by Okamura (2009). The arrows show the direction of magnetization of the magnets (white). The outer yoke is not shown.

As with the design by Zimm *et al.* (2007) the P_{field} parameter for this design is essentially given by the speed at which the magnet rotates from one duct to the next. In this design these are separated by an angle of 40 degrees. The total cycle time is given as 1.2 seconds and the time to rotate between two ducts is given as 0.5 seconds. Based on these numbers we estimate the P_{field} parameter to be 0.66.

4. COMPARING THE DESIGNS

In Table 1 we compare the different magnet designs mentioned above. In the table the Λ_{cool} parameter has also been calculated for each design, thus allowing a direct comparison between the designs. From Table 1 we can see that the magnet design by Okamura *et al.* (2007) significantly outperforms the remaining magnet designs. Compared to e.g. Lu *et al.* (2005) the design by Okamura *et al.* (2007) uses almost the same amount of magnets but creates a high flux density region that is over three times larger. An interesting thing to note is that although the design by Zimm *et al.* (2007) creates a very high magnetic flux density the design has a rather low Λ_{cool} value because the magnetocaloric temperature change scales with the magnetic flux density to the power of 0.7 and this, as mentioned previously, does not favor high magnetic flux densities. However Λ_{cool} should be optimized under the condition of a certain minimum flux density in the high flux density region, where this magnetic flux density is what is required to obtain a sufficient temperature span of the device. Looking at the designs reviewed in this paper we also see that many of the reciprocating designs only utilize the magnet in half of the AMR cycle, i.e. that their P_{field} parameter is 0.5. This means that the expensive magnet is only utilized half the time, which is very inefficient.

Having evaluated existing magnet designs we now analyze the advantages of these designs and focus on how to design the optimal magnet for a magnetic refrigerator. As the magnet is the most expensive part of the magnetic refrigerator it is very important to consider how to design an optimal magnet configuration. By optimal we mean a magnet design that produces a high amount of magnetic flux over a large volume but with a minimum amount of magnetic material. There is a theoretical limit of the flux density that may be generated by a given magnet design. The energy density in the magnets themselves is what limits the maximum possible flux density per mass of magnet. The coercivity of the magnet is a limiting factor for e.g. very large Halbach cylinders, because the magnetic field has a reverse direction compared to the magnetization around the inner equator of the Halbach cylinder (Bloch *et al.,* 1998, Bjørk *et al.,* 2008). A standard grade NdFeB magnet with a remanence of 1.2 T has a coercivity of $\mu_0 H_C = 3.2$ T, so the reversal of the magnet will only be a problem above this flux density. One should note that for NdFeB magnets with a higher energy density, e.g. 1.4 T, the coercivity can be significantly lower, e.g. around $\mu_0 H_C = 1.4$ T.

4.1. Design of a optimal magnet assembly

Based on the knowledge gained from the magnet assemblies reviewed above we have learned that there are certain key features that the magnet assembly must accomplish or provide. It must produce a region that has a high flux density preferably with as high uniformity as possible. Also the magnet must be designed such that the amount of leakage of flux or stray field is as low as possible. This includes both leakage to the surroundings and leakage to e.g. low flux density regions in the magnet assembly. The recommendations can be summed up as

1) Maximize Λ_{cool} for a given flux density
   a) Use minimum amount of magnets
   b) Make the gap as large as possible
   c) Utilize the magnet at all times
   d) Make sure the flux density in the low field region is low
2) Minimize leakage to surrounding by e.g. using soft magnetic material as flux guides

Concerning the first point there are several parameters that can be tuned to optimize Λ_{cool}. Besides the obvious optimization done by reducing the amount of magnet used and maximizing the high flux density volume it is also important to maximize the amount of time the magnetic flux density is used to generate a magnetocaloric effect, i.e. maximize the P_{field} parameter. Looking at the designs reviewed in this paper we see that many of the reciprocating designs only utilize the magnet in half of the AMR cycle. If magnetic refrigeration is to become a viable alternative to conventional refrigeration technology this figure must be increased to as close to one as possible.

ACKNOWLEDGEMENTS

The authors would like to acknowledge the support of the Programme Commission on Energy and Environment (EnMi) (Contract No. 2104-06-0032) which is part of the Danish Council for Strategic Research. The authors also wish to thank T. Okamura, A. Rowe, C. Zimm, J. Chell and Z.G. Zheng for useful discussions and for providing some of the figures in this article.

REFERENCES

1. Bjørk, R., Bahl, C. R. H., Smith, A. and Pryds, N. 2008. *Journal of Applied Physics*, 104:13910.
2. Bloch, F., Cugat, O., Meunier, G. and Toussaint, J. C. 1998. *IEEE Transactions on magnetic*, 34:2465-2468.
3. Bohigas, X., Molins, E., Roig, A., Tejada, J. and Zhang, X.X. 2000. *IEEE Transactions on Magnetics*, 36:538-544.
4. Chell, J. 2009. Astronautics Technology Center. Private communication.
5. Gschneidner, K. A. Jr., Pecharsky, V. K. and Tsokol, A. O. 2005. *Rep. Prog. Phys*, 68:1479-1539.
6. Gschneidner, K. A. Jr., and Pecharsky, V.K. 2008. *International Journal of Refrigeration*, 31: 945-961.
7. Engelbrecht, K., Jensen, J. B., Bahl, C. R. H. and Pryds, N. 2009. *Proc. 3rd International Conference on Magnetic Refrigeration at Room Temperature*, IIF/IIR.
8. Lee, S.J., Kenkel, J.M., Pecharsky, V.K. and Jiles, D.C. 2002. *Journal of Applied Physics*, 91:8894-8896.
9. Lu, D. W., Xu, X. N., Wu, H. B. and Jin, X. 2005. *Proc. 1st International Conference on Magnetic Refrigeration at Room Temperature*, IIF/IIR:1-6
10. Nikly, G., and Muller, C. 2007. *Proc. 2nd International Conference on Magnetic Refrigeration at Room Temperature, Portoroz, Solvenia*, IIF/IIR:59-70.
11. Oesterreicher, H. and Parker, F.T. 1984. *Journal of Applied Physics*, 55:4334-4338.
12. Okamura, T., Rachi, R., Hirano, N., and Nagaya, S. 2007. *Proc. 2nd International Conference on Magnetic Refrigeration at Room Temperature, Portoroz, Solvenia*, IIF/IIR:377-382.
13. Okamura, T. 2009. Private communication.
14. Pecharsky, V. K. and Gschneidner, K. A. Jr. 2006. *International Journal of Refrigeration*, 29:1239-1249.
15. Rowe, A. 2009. Private communication.
16. Tura, A., and Rowe, A. 2007. *Proc. 2nd International Conference on Magnetic Refrigeration at Room Temperature, Portoroz, Solvenia*, IIF/IIR:363-370.
17. Vasile, C. and Muller, C. 2006. *International Journal of Refrigeration*, 29:1318-1326.
18. Zheng, Z.G., Yu, H.Y., Zhong, X.C., Zeng, D.C. and Liu, Z.W. 2009. *International journal of refrigeration*, 32:78–86.
19. Zheng, Z.G. 2009. Private communication.
20. Zimm, C., Auringer, J., Boeder, A., Chell, J., Russek, S. and Sternberg, A. 2007. *Proc. 2nd International Conference on Magnetic Refrigeration at Room Temperature, Portoroz, Solvenia*, IIF/IIR:341-347.

III.1 Paper published in Frio-Calor-Aire Acondicionado, 2010

Bjørk, R., Bahl, C. R. H., Smith A. and Pryds, N.

La Refrigeración Magnética: Diseño Óptimo Del Imán

Frio-Calor-Aire Acondicionado, 2010

This is a Spanish translation of Paper III

LA REFRIGERACIÓN MAGNÉTICA: DISEÑO ÓPTIMO DEL IMÁN

El equipo de investigación constituido por Rasmus BJØRK, C.R.H. BAHL, A. SMITH y N. PRYDS, de Fuel Cells and Solid State Chemistry Division, Risø National Laboratory for Sustainable Energy, Technical University of Denmark (Roskilde, Dinamarca) han analizado la eficiencia y la capacidad de uso de imanes permanentes e imanes electromagnéticos/superconductores para equipos con refrigeración magnética. Dicho análisis ha sido recogido en un documento titulado **"ON THE OPTIMAL MAGNET DESIGN FOR MAGNETIC REFRIGERATION"** [(*)], que ha sido presentado por sus autores como ponencia durante la celebración del evento "**3rd International Conference on Magnetic Refrigeration at Room Temperature**[(**)]**,** en Des Moines(Iowa,2009), bajo el patrocinio del **International Institute of Refrigeration (IIR)** y organizado por la **Universidad de Iowa (Estados Unidos)** conjuntamente con **Ames Laboratory United States Department of Energy ,** centro donde se descubrió una nueva familia de aleaciones magnéticas refrigerantes, en estrecha colaboración con **Astronautics Corporation of America** en Milwaukee.

SINOPSIS

Uno de los temas clave en la refrigeración magnética es la generación de un campo magnético al que tiene que estar sometido el material magnetocalórico. El imán constituye la parte principal del coste de un sistema completo de refrigeración magnética, y por lo tanto debería invertirse un gran esfuerzo en mejorar el diseño del imán. En el presente documento analizamos las diferentes eficiencias y capacidad de uso de imanes permanentes y de imanes electromagnéticos/superconductores. Exponemos una visión general de los diferentes diseños publicados sobre imanes en las aplicaciones de la refrigeración magnética. Estos diseños se analizan en base a la densidad de flujo magnético generado y a la cantidad de material magnético utilizado. Esto se hace mediante la caracterización de cada diseño mediante un parámetro Λ_{cool} de eficiencia del diseño del imán. Los análisis de los diferentes diseños publicados sobre imanes permanentes nos permiten exponer las recomendaciones para mejorar los diseños de los imanes existentes, así como discutir acerca de las características del mejor diseño del imán para la refrigeración magnética.

1. INTRODUCCIÓN

El imán es una parte esencial del frigorífico magnético, que a veces se pasa por alto. Aunque se han publicado numerosos artículos revisando los equipos para refrigeración magnética, dichos artículos sólo se han referido al intervalo de temperatura y a la potencia de los mismos, y no han tratado en detalle el diseño del imán (Gschneidner y Pecharsky, 2008). Se ha realizado ahora un pequeño esfuerzo para comparar los diseños existentes de imanes.

Es importante investigar en detalle el diseño del imán, porque éste puede constituir la única parte más costosa de un frigorífico magnético. Si consideramos la viabilidad de la refrigeración magnética, es extremadamente importante que la estructura magnética utilizada genere una elevada densidad de flujo magnético sobre un volumen tan grande como sea posible, empleando la mínima cantidad posible de imanes. También es importante que el propio frigorífico magnético esté diseñado para utilizar en todo momento la densidad de flujo magnético generada por el imán. Al comparar los diferentes conjuntos de imanes y mostrando cuáles son los diseños de mejor rendimiento, esperamos aprender algunas características clave fundamentales que han de tenerse presentes en el diseño de un imán eficiente.

1.1. Los diferentes tipos de imanes

Esencialmente existen tres tipos diferentes de imanes que se pueden usar en un equipo de refrigeración magnética. Éstos son el imán electromagnético, el superconductor y el permanente. Tendremos en cuenta la posibilidad de uso de cada uno de ellos en su momento.

El imán electromagnético genera una densidad de flujo magnético al pasar la corriente a través de un solenoide. La relación entre la corriente, I, y la densidad generada de flujo, B, para un imán electromagnético en un circuito magnético sencillo consistente en un material magnético suave con permeabilidad relativa, μ_r, y en el que el núcleo tiene aproximadamente la misma superficie en sección transversal en toda su longitud, y el espacio de aire es pequeño comparado con las dimensiones en sección transversal del núcleo, viene dada por la expresión:

$$NI = B\left(\frac{L_{core}}{\mu_r \mu_o} + \frac{L_{gap}}{\mu_o}\right) \qquad 1$$

en la que N es el número de vueltas del devanado, L_{core} es la longitud del material magnético dulce, μ_o es la permeabilidad del espacio libre y L_{gap} es la longitud del espacio de aire. Para generar una densidad de flujo magnético de 1,0 T en todo el espacio de aire de 30 mm se necesitaría un solenoide con núcleo de hierro con μ_r = 4.000 para tener devanados de 24.000 amperios. La longitud del material magnético dulce es irrelevante, ya que en la expresión dada domina el segundo término. Un imán electromagnético con devanados de 24.000 amperios necesitaría un aporte masivo de potencia eléctrica e igualmente un enfriamiento masivo para prevenir que el solenoide se funda. En base a este simple cálculo podemos descartar los imanes electromagnéticos como aplicables en frigoríficos magnéticos comercialmente viables.

El imán superconductor es una opción mejor que el imán electromagnético tradicional ya que precisa de poca potencia eléctrica para funcionar, una vez que el electroimán se ha convertido en superconductor, ya que no se pierde potencia eléctrica en la resistencia óhmica. Aunque el imán superconductor puede crear densidades de flujo magnético del orden de 10 T, hay que enfriarlo continuamente. Esto puede representar un proceso costoso y puede ser importante el aparato que rodee el imán superconductor. Sin embargo, en aplicaciones a gran escala, es decir grandes frigoríficos para almacenes, etc., un imán superconductor podría ser una solución relevante. En este momento el imán superconductor no es una opción relevante para la refrigeración doméstica común.

Vistos el imán electromagnético y el superconductor, y descartados ambos para la refrigeración magnética a nivel doméstico común, consideraremos ahora el imán permanente. Ya que estos imanes proporcionan una densidad constante de flujo magnético, son ideales para utilizarlos en aplicaciones con bajo consumo de energía eléctrica, como es el caso de la refrigeración magnética. La densidad de flujo magnético generada a través de un espacio de aire por un imán permanente depende de la remanencia del imán, que es típicamente del orden de 1,2 – 1, 4 T para imanes de NdFeB, y del circuito magnético en el que se coloca el imán. En este documento revisamos y caracterizamos los diferentes conjuntos de imanes permanentes dados a conocer anteriormente a través de las publicaciones sobre refrigeración magnética.

2. CARACTERIZACIÓN DEL DISEÑO DE UN IMÁN

Para comparar fácilmente los diferentes diseños de imanes, es importante ser capaces de caracterizar un diseño de imán mediante un parámetro único. Para dicho parámetro se hizo una sugerencia por parte de Nikly y Muller (2207), quienes propusieron la caracterización del diseño de un imán mediante la expresión:

$$\xi = \frac{M_{magnet}}{M_{magnet} + M_{MCM}} \qquad 2$$

en la que M_{magnet} es la masa del imán y M_{MCM} es la masa del material magnetocalórico.

El parámetro ξ pueden tomar valores comprendidos entre cero y uno, correspondiendo el valor cero a sin imán y el valor uno a la no presencia de material magnetocalórico. El problema al usar ξ para la caracterización del imán es que no contiene información alguna acerca de la densidad de flujo magnético producida por el diseño del imán. Dos diseños podrían tener el mismo valor de ξ, pero producirían densidades muy diferentes de flujo. Debido a que también el parámetro ξ contiene las masas y no el volumen del imán y del material magnetocalórico, el mismo frigorífico magnético tendrá un valor diferente de ξ si se usan materiales magnetocalóricos con densidades diferentes o componentes regeneradores con diferentes porosidades.

Proponemos en su lugar caracterizar el diseño del imán para uso en refrigeración magnética mediante el parámetro Λ_{cool}, introducido por Bjørk *et al*. (2008). Este parámetro está concebido para favorecer los diseños de imanes que generan una alta densidad de flujo magnético en un gran volumen usando un mínimo de material magnético. También favorece a los diseños del sistema donde se minimiza la cantidad de tiempo durante la que "se desperdicia" densidad de flujo magnético por no magnetización de un material magnetocalórico.

2.1. El parámetro Λ_{cool}

Si el parámetro Λ_{cool} se va a utilizar para expresar la eficiencia de un conjunto dado de imán permanente, tiene que depender del cambio de temperatura que la densidad de flujo magnético puede inducir en el material magnetocalórico colocado en el espacio del conjunto. El cambio de temperatura se va escalando con la densidad de flujo magnético, pero no necesariamente de forma lineal. Es importante hacer la observación de que el parámetro Λ_{cool} será proporcional al cambio de temperatura del material magnetocalórico y no a la densidad de flujo magnético, porque el cambio de temperatura del material magnetocalórico se usa para generar el salto de temperatura y la potencia frigorífica del equipo de refrigeración.

Como componentes activos de una máquina de refrigeración magnética se han sugerido una gran variedad de diferentes materiales (Gschneidner *et al.,* 2005). Sin embargo, el material utilizado con más frecuencia, es decir el material magnetocalórico según "antecedentes" a temperatura ambiente, el Gadolinio, tiene un efecto magnetocalórico que se va escalando con la densidad de flujo del campo magnético hasta una potencia de 0,7 a temperatura Curie (Pecharsky y Gschneidner, 2006). Esto está en consonancia con la potencia de 2/3 predicha por la teoría del campo medio para un material magnetocalórico general con transición de fase de segundo orden (Oesterreicher y Parker, 1984). Teniendo esto en cuenta, el parámetro Λ_{cool} se elige para que sea proporcional a la densidad de flujo magnético a la potencia de 2/3.

No sólo la densidad de flujo dentro del espacio de aire tiene su importancia para el efecto magnetocalórico. Es igualmente importante el volumen en el que se coloca el material magnetocalórico cuando se desmagnetiza. La densidad de flujo en este volumen tiene que ser tan baja como sea posible con el fin de maximizar el efecto magnetocalórico. Con el fin de maximizar el efecto magnetocalórico, la densidad de flujo en este volumen tiene que ser tan baja como sea posible. En un componente de tipo alternativo esto puede lograrse, por supuesto, moviendo sencillamente el material magnetocalórico lejos del imán, pero esto aumentará el tamaño físico y el tiempo del ciclo de la máquina de refrigeración magnética. En un componente rotativo, las regiones de alta y baja densidad de flujo generalmente serán adyacentes, y ha de tenerse cuidado en minimizar la "fuga" de flujo hacia la región de baja densidad.

Para tener en cuenta la cantidad de material magnetocalórico que puede experimentar un cambio de temperatura, el parámetro Λ_{cool} es proporcional al volumen total del hueco y no sólo al volumen ocupado por el material magneto calórico. Así pues, Λ_{cool} no depende de la porosidad del material magnetocalórico, ni de la cantidad, por ejemplo, de carcasa de plástico utilizada para confinar el material magnetocalórico. También Λ_{cool} es inversamente proporcional al volumen de material magnético usado, ya que a más material magnético utilizado tanto más costoso será el diseño.

Finalmente, el parámetro Λ_{cool} es proporcional a la fracción de un ciclo de regenerador magnético activo (RMA) (*AMR, en el original, acrónimo en inglés de:* ***a****ctive* ***m****agnetic* ***r****egenerator)* del cual el material magnetocalórico se coloca en el volumen de alta densidad de flujo. La razón de esto, es que si, por ejemplo, el material magnetocalórico se coloca sólo dentro de la mitad del tiempo de un ciclo completo de RMA en la región de alta densidad de flujo, el (costoso) imán no se utiliza durante la mitad del ciclo remanente, y así se está desperdiciando durante este tiempo. La fracción de tiempo en el que se genera el flujo magnético por el imán está siendo utilizada para generar un efecto magnetocalórico que tiene que maximizarse.

Teniendo en cuenta todo esto, caracterizaremos un diseño del imán para uso en aplicaciones de refrigeración magnética mediante el parámetro:

$$\Lambda_{cool} \equiv \left\langle B^{2/3} \right\rangle - \left\langle B_{out}^{2/3} \right\rangle \frac{V_{field}}{V_{mag}} P_{field} \qquad 3$$

Siendo V_{mag} el volumen de los imanes, V_{field} es volumen con alta densidad de flujo, P_{field} la fracción del ciclo RMA en el que se coloca el material magnetocalórico en el volumen de alta densidad de flujo. $\left\langle B^{2/3} \right\rangle$ es la media del volumen de la densidad de flujo en el volumen de alto flujo para la potencia de 2/3, y $\left\langle B_{out}^{2/3} \right\rangle$ es la media de volumen de la densidad de flujo para la potencia de 2/3 en el volumen donde se coloca el material magnetocalórico, cuando está siendo desmagnetizado.

Hay que tener en cuenta que el parámetro Λ_{cool} favorecerá un diseño con una pequeña densidad de flujo magnético y un volumen grande para la región de alta densidad de flujo. Esto es debido a que el flujo magnético generado por un imán escala a una potencia inferior a 0,7 con el volumen del imán. Por lo tanto, para las aplicaciones prácticas uno elegiría por optimizar Λ_{cool}, bajo la condición de una determinada densidad mínima de flujo en la región de alta densidad de flujo. No consideramos de forma explícita la remanencia de los imanes permanentes utilizados en el ensamblaje. Esto no es crítico para la comparación de diferentes diseños, ya que la remanencia de los imanes de NdFeB usados en todos los ensamblajes de imanes para refrigeración magnética varía sólo entre 1,2 y 1,4 T. Por consiguiente, la geometría cuenta para la mayoría de las diferencias entre diseños diferentes. Cualquier material magnético dulce utilizado en el ensamblaje del imán se ignora, ya que el precio de este materiales es mucho menor que el de los imanes permanentes.

3. DISEÑOS PUBLICADOS DE IMANES

Habiendo definido el parámetro Λ_{cool}, podemos comparar ahora los diferentes diseños publicados de imanes. Existen varios diseños publicados de frigoríficos magnéticos; desafortunadamente muchas publicaciones carecen de la especificaciones necesarias para reconstruir o bien calcular directamente el parámetro Λ_{cool}. Los diseños presentados a continuación están entre los pocos que contienen información suficiente para calcular Λ_{cool}. Se ofrece una breve descripción de cada diseño antes de proceder al cálculo.

Somos conscientes de que muchos de los frigoríficos magnéticos presentados aquí son equipos para ensayo y deben evaluarse como tales. Sin embargo, también se considera en la fase de diseño para el ensayo que debieran sugerirse grandes mejoras al diseño. Por lo tanto, esperamos que la evaluación de los diseños pueda llevar a mejorar tanto los frigoríficos magnéticos actuales como los futuros.

3.1. Circuitos magnéticos simples

Diseño de Zheng *et al.* (2009)

El diseño general del frigorífico de Zheng *et al.*, (2009) es un diseño tipo alternativo en el que el imán se mantiene estacionario y los dos lechos empaquetados de material magnetocalórico se desplazan hacia dentro y hacia fuera del campo magnético. Cuando uno de los lechos está en el campo magnético el otro se encuentra fuera del mismo. La densidad de flujo en el diseño viene proporcionada por un solo imán simple, y las líneas de flujo están guiadas por el material magnético dulce a través de un pequeño espacio de aire. Basándose en Zheng (2009), el volumen del imán es de 0,5 L, y el volumen de la región de alta densidad de flujo es 0,09 L. La densidad media de flujo magnético es de 0,93 T.

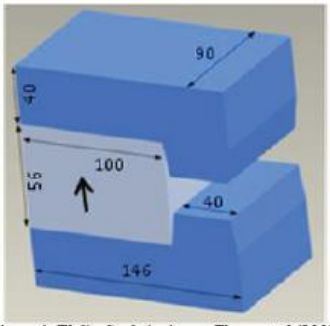

Figura 1: El diseño de imán por Zheng et al (2007). De Zheng (2009). El material en color azul es el material magnético dulce. Dimensiones en mm. La flecha indica la dirección de la magnetización

El parámetro P_{field} puede estimarse fácilmente para este diseño ya que se dan el tiempo del ciclo, la velocidad de desplazamiento del imán y la distancia entre conductos. Esta última distancia es de 80 mm, y como el imán permanente se mueve a una velocidad de 0,02 m/s, el imán tardará 4 segundos para desplazarse entre los conductos. El imán tiene que retroceder y progresivamente en un ciclo, así que el desplazamiento del imán lleva en total 8 segundos. Las partes de magnetización del ciclo se dan como dos veces en 2 segundos, y a partir de esto llegamos a la conclusión de que P_{field} es de 0,33.

Diseño de Lee *et al.* (2002)

El diseño de Lee *et al.*, (2002) es un diseño tipo alternativo con imán estacionario y un lecho móvil de material magnetocalórico. El imán tiene forma de la letra "C", con una elevada densidad de flujo homogéneo en el centro. La densidad de flujo en el centro está intensificada por bloques de material magnético dulce. Dichos bloques están colocados en el centro de la "C". La altura del espacio de aire es de 12,7 mm y las dimensiones de la sección transversal de 114 x 128 mm^2, es decir 14,6 L/m. El área de la sección transversal de un lecho magnetocalórico es de 15,2 x 10 mm^2, y a partir de aquí estimamos que el área total de la sección transversal de la región de flujo alto es de 25 x 12,7 mm^2, es decir 0,32 L/m. La densidad de flujo magnético viene a ser de 1,9 T en la región de flujo alto, pero está basado en una simulación bidimensional. Dependiendo de la longitud del equipo actual, esta cifra será significativamente más baja. Ya que en la documentación se trata más sobre el diseño del imán y menos sobre el equipo actual para refrigeración magnética, es imposible estimar el parámetro P_{field}. Haciendo una estimación optimista, tomaremos para P_{field} el valor de 0,95.

Diseño de Vasile y Muller (2006)

El diseño del imán por Vasile y Muller (2006) es casi idéntico al de Lee *et al.*, (2002). Un ensamblaje del imán en forma de "C" con material magnético dulce en el interior, pero esta vez también fuera de la disposición de los imanes. En este diseño los imanes rotan alrededor de un círculo con inserciones rellenas de material magnetocalórico. En base a un dibujo incluido en el documento, estimamos que el área de la sección transversal de los imanes es de 9,2 L/m, y el área de la sección transversal del hueco en el campo de alta es de 0,75 L/m. La densidad de flujo magnético se da como 1,9 T en la región del campo de alta, pero esto está basado en una simulación bidimensional, así que un ensamblaje real en la práctica tendría un valor mas bajo. Ya que los imanes están en rotación continua y las inserciones para el material magnético llenan la mayor parte del círculo a lo largo del cual está rotando el imán, estimamos que el parámetro P_{field} es de 0.90.

Diseño de Bohigas et al. (2000)

El diseño de Bohigas *et al.*, (2000) es un diseño tipo rotativo en el que los imanes son estacionarios y el material magnetocalórico se rota dentro y fuera de la región de alta densidad de flujo. Se usan un total de ocho imanes rectangulares, cuatro de los cuales situados en el interior de la rueda giratoria y cuatro colocados fuera de la rueda. La dimensión de uno de los bloques interiores viene a ser de 40 x 40 x 20 mm, y uno de los bloques exteriores tiene unas dimensiones de 50 x 50 x 25mm. El tamaño del espacio de aire viene a ser de 7 mm, y aquí existen un total de cuatro espacios de aire. A partir de estos datos estimamos las dimensiones de un hueco de aire que son 40 x 7 x 20. Así pues el volumen de los imanes es de 0,38 L y el volumen de la región de alta densidad de flujo es de 0,02 L. La densidad de flujo está dada como 0,9 T. Este diseño tiene un

material magnetocalórico entrando continuamente dentro de la región de alta densidad de flujo, por lo que el parámetro P_{field} es 1.

3.2 Conjuntos de imanes tipo Halbach

Diseño de Tura y Rowe (2007)

El frigorífico magnético presentado por Tura y Rowe (2007) es un sistema tipo rotativo en el que el material magnético se mantiene estacionario y el imán se rota para alterar la densidad de flujo magnético. El diseño del imán utilizado en el equipo consta de dos imanes separados, cada uno de los cuales consisten en dos cilindros concéntricos de Halbach. La razón por la que se usan dos imanes separados es que el sistema puede funcionar de modo que se equilibren las fuerzas magnéticas.

En el diseño de cilindro concéntrico de Halbach, la densidad de flujo en el interior del agujero del cilindro se puede controlar por rotación del imán interior o exterior. Tura y Rowe (2007) informaron que cuando el imán interior se gira, el flujo medio producido puede cambiarse de forma continuada desde 0,1 T hasta 1,4 T. Por parte de Rowe (2009) conocemos el volumen total del material magnético que es 1,03 L, mientras que el volumen total de la región de alta densidad de flujo es de 0,05 L. Estos valores son para uno de los cilindros concéntricos de Halbach. El parámetro P_{field} para este sistema es de 0,5, ya que la mitad del tiempo del ciclo, el imán interior se girará de modo que cancela aproximadamente el flujo magnético generado por el imán exterior. En esta configuración no existe una región de alta densidad de flujo, y esencialmente los imanes no se están usando.

Diseño de Engelbrecht *et al.* (2009).

La máquina de refrigeración magnética de ensayo diseñada por Risø DTU Engelbrecht *et al.*, (2009) es una máquina alternativa en la que las placas de material magnetocalórico se mueven dentro y fuera de un imán estacionario. El imán es un cilindro de Halbach consistente en 16 bloques de imanes permanentes. El cilindro tiene un radio interior de 21 mm, un radio exterior de 60 m y una longitud de 50 mm. La densidad media de flujo magnético en el agujero del cilindro es de 1,03 T. El volumen del imán de 0,50 L y el volumen de la región de alta, es decir el agujero del cilindro, es de 0,07 L. El parámetro P_{field} para este diseño del sistema es de 0,5. Esto es porque para la mitad del tiempo del ciclo, la pila de placas está fuera de la región de alta, abandonando ésta hasta estar vacía.

Figura 2: El diseño de de Halbach por Engelbrecht et al (2007). Puede verse también el regenerador con una placa magnetocalórica

Diseño de Lu *et al.* (2005)

El aparato de refrigeración magnética diseñado por Lu *et al.*, (2005) es un equipo tipo alternativo con dos lechos empaquetados separados de material magnético moviéndose dentro y fuera de dos conjuntos estacionarios de imanes, permitiendo así la compensación de fuerzas. Ambos imanes son 16 cilindros segmentados de Halbach, con un radio interior de 15 mm y un radio exterior que se confirma que es 700 mm. Tomamos este como tipo y suponemos que el radio exterior es de 70 mm. La densidad de flujo producida viene a ser como de 1,4 T, y la longitud del cilindro es de 200. Dadas estas cifras, el volumen del imán es de 2,94 L, y el volumen de la región de alta densidad de flujo es de 0,14 L para cualquiera de los imanes. Por las mismas razones expuestas para el diseño de Engelbrecht *et al.*, (2009), el P_{field} es de 0,5 para este diseño del sistema.

3.3. Estructuras magnéticas complejas

Diseño por Zimm *et al.* (2007).

La máquina de refrigeración magnética presentado por Zimm *et al.*, (2007), utiliza un principio de rotación, en el que el material magnetocalórico es estacionario y el imán es rotativo. El diseño del imán es bastante complicado, utilizando ambos imanes y materiales magnéticos dulces, pero esencialmente consiste en estructuras en forma de "Y" separados por en espacio de aire. La región de alta densidad de flujo se abre en un ángulo de 60 grados en los dos lados opuestos del diseño. Basándose en Cell (2009), el volumen total del conjunto magnético es de 4,70 L, el volumen de la región de alta densidad de flujo es de 0,145 L y la densidad media de flujo es de 1,5 T. El parámetro P_{field} para este diseño viene esencialmente dado por la velocidad a la que el imán rota desde una región de alto flujo hasta la

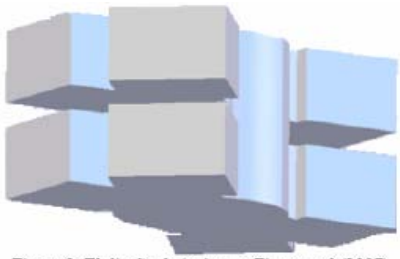

Figura 3: El diseño de imán por Zimm et al (2007). De Chell (2009). La alta densidad de flujo se genera en el hueco entre las dos estructuras en forma de "Y". La dirección de la magnetización para los imanes individuales es demasiado compleja para mostrarla en la figura.

siguiente. En este diseño dichas regiones están separadas por un ángulo de 30 grados. No conocemos la velocidad de rotación, por lo que tomamos como valor de P_{field} 0,90.

3.4. Diseño de Okamura *et al.* (2007)

El diseño utilizado por Okamura *et al.*, (2997) es un aparato rotativo en el que el imán se gira pasados unos conductos empaquetados con material magnetocalórico. El diseño de imán consiste de una disposición compleja de imanes permanentes y materiales magnéticos dulces, que se montan como un rotor interno consistentes ambos en imanes y el material magnético dulce con un yugo externo, compuesto sólo de material magnético dulce. El material magnetocalórico se coloca en cuatro conductos en el espacio de aire, cada uno desplazado 34 grados. El rotor interno está diseñado de manera que los imanes con polos idénticos se colocan enfrentados uno con otro y separados por material magnético dulce. Esto aumenta la densidad de flujo e "impulsa" las líneas de flujo desde el rotor interno al estator exterior. Según Okamura (2009), la densidad media de flujo es 1,0 T y el diseño magnético es para contener 2,38 L de imán y 0,80 L de la región de alta densidad de flujo. Como con el diseño de Zimm *et al.*, (2007), el parámetro P_{field} para este diseño viene esencialmente determinado por la velocidad a la que el imán gira desde un conducto al siguiente. En este diseño, éstos están separados por un ángulo de 40 grados. El tiempo total del ciclo viene a ser de 1,2 segundos y el tiempo para rotar entre dos conductos es de 0,5 segundos. En base a estas cifras, estimamos que el parámetro P_{field} es de 0,66.

Figura 4: El diseño de imán por Okamura (2009). Las flechas muestran la dirección de la magnetización de los imanes (en blanco). No se muestra el yugo exterior.

4. COMPARACIÓN ENTRE DISEÑOS

En la Tabla 1 (al final) comparamos los diseños de los diferentes imanes antes mencionados. En la tabla, el parámetro Λ_{cool} se ha calculado también para cada diseño, permitiendo así una comparación directa entre diseños. A partir de la Tabla 1, podemos ver que el diseño del imán de Okamura *et al.*, (2007) supera significativamente los restantes diseños de imanes. Por ejemplo, al compararlo con Lu *et al.*, (2005), el diseño de Okamura et al., (2007) usa casi la misma cantidad de imanes, pero crea una región de alta densidad de flujo que es más de tres veces mayor. Una cosa interesante a observar, es que si bien el diseño de Zimm *et al.*, (2007) crea una densidad muy alta de flujo magnético, el diseño tiene un valor de Λ_{cool} más bien bajo porque el cambio de temperatura magnetocalórica escala con la densidad de flujo magnético hasta una potencia de 0,7, y esto, como se mencionó previamente, no favorece altas densidades de flujo magnético. Sin embargo, Λ_{cool} debería optimizarse bajo la condición de una determinada densidad mínima de flujo en la región de alta densidad de flujo. Mirando los diseños repasados en el presente documento, vemos también que muchos de los diseños de tipo alternativo utilizan solamente el imán en la mitad del ciclo de RMA, es decir que su parámetro P_{field} es de 0,5. Esto significa que el imán caro sólo se utiliza la mitad del tiempo, lo que es muy ineficiente.

Habiendo evaluado los diseños existentes de imanes, analizamos ahora las ventajas de estos diseños, y nos centramos en cómo diseñar el imán óptimo para un frigorífico magnético. Ya que el imán es la parte más costosa del frigorífico magnético, es muy importante considerar cómo diseñar una configuración óptima de imán. Por óptimo entendemos un diseño de imán que produce una elevada cantidad de flujo magnético por todo un gran volumen, pero con una mínima cantidad de material magnético. Existe un límite teórico de densidad de flujo que puede generarse mediante un determinado diseño de imán. La densidad de energía en los propios imanes es que limita la densidad máxima posible de flujo por masa de imán. La coercitividad del imán es un factor limitativo, por ejemplo para cilindros muy grandes de Halbach, porque el campo magnético tiene una dirección opuesta comparada con la magnetización alrededor del ecuador interno del cilindro de Halbach (Bloch *et al.*, 1998, Bjørk *et al.*, 2008). Un imán de grado estándar de NdFeB con una remanencia de 1,2 T tiene una coercitividad de $\mu_0 H_C$ = 3,2 T, de modo que la reversión del imán será sólo un problema por encima de esta densidad de flujo. Habría que observar que para los imanes de NdFeB con una densidad de energía superior, por ejemplo 1,4 T, la coercitividad puede ser significativamente más baja, por ejemplo casi $\mu_0 H_C$ = 1,4 T.

4.1 Diseño de un conjunto óptimo del imán.

En base al conocimiento adquirido a partir de los montajes de imanes repasados anteriormente, hemos aprendido que hay determinadas características clave que la disposición del imán tiene que cumplir o proporcionar. Tiene que producir una región que tenga una alta densidad de flujo, preferiblemente con una uniformidad tan alta como sea posible. También el imán tiene que estar diseñado de manera que la cantidad de fuga de flujo o de campo de dispersión sea lo más bajo posible. Esto incluye

tanto la fuga hacia los alrededores como la fuga, por ejemplo, a las regiones de baja densidad de flujo en el conjunto del imán. Estas recomendaciones pueden resumirse como sigue:

1) Maximizar Λcool para una densidad dada de flujo
    a) Utilizar la mínima cantidad de imanes
    b) Hacer el espacio tan grande como seas posible
    c) Utilizar el imán todo el tiempo
    d) Cerciorarse que es baja la densidad de flujo en la región del campo de baja
2) Minimizar la figa al entorno, por ejemplo utilizando material magnético dulce como guía de flujos

En lo concerniente al primer punto, existen varios parámetros que pueden ajustarse para optimizar Λcool. Aparte de la optimización obvia hecha mediante reducción de cantidad de imán utilizada y maximizando el volumen de alta densidad de flujo, también es importante maximizar la cantidad de tiempo que la densidad de flujo magnético se utiliza para generar un efecto magnetocalórico, es decir maximizar el parámetro Pfield. Observando los diseños repasados en este documento, vemos que muchos de los diseños de tipo alternativo sólo utilizan el imán en la mitad del ciclo de RMA. Si la refrigeración magnética llega a convertirse en una alternativa viable para la tecnología de refrigeración convencional, esta cifra tiene que aumentarse lo más posible.

Nombre	V_{mag} [L]	V_{field} [L]	$\langle B \rangle$ [T]	$\langle B_{out} \rangle$ [T]	$\langle B^{2/3} \rangle$ [T$^{2/3}$]	$\langle B_{out}^{2/3} \rangle$ [T$^{2/3}$]	P_{field}	Tipo de imán	Λ_{eval} sin P_{field}	Λ_{eval}
Zheng *et al.* (2009)	0.5	0.09	0.93	0*	0.95*	0*	0.33	Circuito magnético con un imán solo	0.17	0.06
Lee *et al.* (2002)	14.6/m	0.32/m	1.9[H,2D]	0*	1.53*,[H]	0*	0.95*	Circuito en "C"	0.03	0.03
Vasile and Muller (2006)	9.2/m	0.75/m	1.9[H,2D]	0*	1.53*,[H]	0*	0.90*	Circuito en "C"	0.12	0.11
Bohigas *et al.* (2000)	0.38	0.02	0.9[H]	0*	0.93*,[H]	0*	1	Imán rectangular en superficie redonda	0.049	0.049
Tura and Rowe (2007)	1.03	0.05	1.4	0.1	1.25[a]	0.2[a]	0.5	Cilindros concéntricos de Halbach	0.05	0.03
Engelbrecht *et al.* (2009)	0.5	0.07	1.03	0.01	1.02	0.06	0.5	Cilindro de Halbach	0.13	0.07
Lu *et al.* (2005)	2.94	0.14	1.4[H]	0	1.25*,[H]	0	0.5	Cilindro de Halbach	0.06	0.03
Zimm *et al.* (2007)	4.70	0.15	1.5	0.1	1.31*	0.2[a]	0.90*	Estructura magnética en "Y"	0.04	0.03
Okamura *et al.* (2007)	3.38	0.80	1.0	0	1.0[a]	0	0.66	Rotor magnético interno, yugo magnético dulce	0.24	0.16

Tabla 1: Listado de especificaciones para un determinado número de diseños diferentes de imanes. Cada diseño se ha descrito con detalle en este documento. Para más información sobre cada modelo nos referimos a los documentos originales.

* Designa una cantidad estimada

[a] Significa que en las columnas $\langle B^a \rangle$ y $\langle B_{out}^a \rangle$, el valor medio de la densidad de flujo magnético se ha tomado a la potencia de 0,7. El valor de $\langle B \rangle^a$ y $\langle B^a \rangle$ será sólo igual si la densidad de flujo es completamente homogénea.

[H] indica que le valor dado para el campo magnético podría se la máxima densidad alcanzable posible de flujo para la región alta del campo, y como tal no una media representativa de la densidad de flujo magnético para toda la región alta del campo.

[2D] indica que la densidad de flujo se basa en una simulación bidimensional. Notoriamente ésta sobrestima la densidad de flujo, excepto para conjuntos muy largos, y así Λ_{eval} estará sobrestimado para estos diseños. Algunos de los diseños bidimensioanles tienen sus volúmenes expresador por metro.

REFERENCIAS

(*) Fuente: *3rd IIR Conference on Magnetic Refrigeration at Room Temperature – Proceedings [#1021]*

(**) The International Institute of Refrigeration – Institute International du Froid – IIR bajo la organización de la **Universidad de Iowa** ha celebrado las reuniones de las Comisiones **A1- Criotecnología, B2- Equipos de Refrigeración, E2- Bomba de Calor** en el marco de la **3ª Conferencia Internacional sobre Refrigeración Magnética a Temperatura Ambiente,** cuya presidencia estuvo ostentada conjuntamente por **Karl A. Gschneidner y Vitalij K. Pecharsky.** La Primera Reunión se instituyó en Montreux, 2005 (Suiza), concebida y planificada por **Peter Egolf y Andrej Kitanovskii**, ambos de la Universidad de Ciencia Aplicada de Suiza Occidental, y la Segunda tuvo lugar en Portoroz, 2007 (Eslovenia).

1. Bjørk, R., Bahl, C. R. H., Smith, A. and Pryds, N. 2008. *Journal of Applied Physics*, 104:13910.
2. Bloch, F., Cugat, O., Meunier, G. and Toussaint, J. C. 1998. *IEEE Transactions on magnetic*, 34:2465-2468.
3. Bohigas, X., Molins, E., Roig, A., Tejada, J. and Zhang, X.X. 2000. *IEEE Transactions on Magnetics*, 36:538-544.
4. Chell, J. 2009. Astronautics Technology Center. Private communication.
5. Gschneidner, K. A. Jr., Pecharsky, V. K. and Tsokol, A. O. 2005. *Rep. Prog. Phys*, 68:1479-1539.
6. Gschneidner, K. A. Jr., and Pecharsky, V.K. 2008. *International Journal of Refrigeration*, 31: 945-961.
7. Engelbrecht, K., Jensen, J. B., Bahl, C. R. H. and Pryds, N. 2009. *Proc. 3rd International Conference on Magnetic Refrigeration at Room Temperature*, IIF/IIR.
8. Lee, S.J., Kenkel, J.M., Pecharsky, V.K. and Jiles, D.C. 2002. *Journal of Applied Physics*, 91:8894-8896.
9. Lu, D. W., Xu, X. N., Wu, H. B. and Jin, X. 2005. *Proc. 1st International Conference on Magnetic Refrigeration at Room Temperature*, IIF/IIR:1-6
10. Nikly, G., and Muller, C. 2007. *Proc. 2nd International Conference on Magnetic Refrigeration at Room Temperature, Portoroz, Solvenia*, IIF/IIR:59-70.
11. Oesterreicher, H. and Parker, F.T. 1984. *Journal of Applied Physics*, 55:4334-4338.
12. Okamura, T., Rachi, R., Hirano, N., and Nagaya, S. 2007. *Proc. 2nd International Conference on Magnetic Refrigeration at Room Temperature, Portoroz, Solvenia*, IIF/IIR:377-382.
13. Okamura, T. 2009. Private communication.
14. Pecharsky, V. K. and Gschneidner, K. A. Jr. 2006. *International Journal of Refrigeration*, 29:1239-1249.
15. Rowe, A. 2009. Private communication.
16. Tura, A., and Rowe, A. 2007. *Proc. 2nd International Conference on Magnetic Refrigeration at Room Temperature, Portoroz, Solvenia*, IIF/IIR:363-370.
17. Vasile, C. and Muller, C. 2006. *International Journal of Refrigeration*, 29:1318-1326.
18. Zheng, Z.G., Yu, H.Y., Zhong, X.C., Zeng, D.C. and Liu, Z.W. 2009. *International journal of refrigeration*, 32:78–86.
19. Zheng, Z.G. 2009. Private communication.
20. Zimm, C., Auringer, J., Boeder, A., Chell, J., Russek, S. and Sternberg, A. 2007. *Proc. 2nd International Conference on Magnetic Refrigeration at Room Temperature, Portoroz, Solvenia*, IIF/IIR:341-347.

El Laboratorio Nacional de Risø para Energía Sostenible en la Universidad Técnica de Dinamarca lleva a cabo investigaciones centradas en el desarrollo de las tecnologías energéticas y sistemas que tengan un mínimo impacto en el clima. Risø tiene 700 empleados. La División de Pilas de Combustible y de Química de Estado Sólido realiza las investigaciones y el desarrollo en cerámicas funcionales para las tecnologías energéticas. Los temas principales de investigación en la División son las pilas de combustible de óxido sólido, electrolisis a alta temperatura, membranas cerámicas para separación de gases, purificación electroquímica de gases de combustión y refrigeración magnética.

AGRADECIMIENTOS

- Los autores del presente documento desean manifestar su agradecimiento al apoyo financiero de la Comisión del Programa sobre Energía y Medio Ambiente (EnMi) (Contrato No. 2104.06-0032), que forma parte del Consejo Danés para Investigación Estratégica. Los autores desean agradecer también a T. Okamura, A. Rowe, C. Zimm, J. Chell y Z.G. Zheng todas las discusiones útiles y por proporcionar algunas de las figuras expuestas en este documento.
- La Dirección Técnica de FRIO CALOR AIRE ACONDICIONADO S.L. desea mostrar su agradecimiento a los autores del mencionado estudio, así como a **Mme.Susan Phalippou**, Directora de Conferencias & Promoción del **International Institute of Refrigeration – IIR-IIF (www.iifiir.org) (iif-iir@iifiir.org)**, por la amable atención dispensada al autorizar la publicación de la citada ponencia en nuestra Revista.

Paper IV

Paper published in International Journal of Refrigeration, 2009

Nielsen, K. K., Bahl, C. R. H., Smith, A., Bjørk, R., Pryds, N. and Hattel, J.

Detailed numerical modeling of a linear parallel-plate Active Magnetic Regenerator

International Journal of Refrigeration, 32, 1478-1486, 2009

available at www.sciencedirect.com

ScienceDirect

journal homepage: www.elsevier.com/locate/ijrefrig

Detailed numerical modeling of a linear parallel-plate Active Magnetic Regenerator

K.K. Nielsen[a,b,*], C.R.H. Bahl[b], A. Smith[b], R. Bjørk[b], N. Pryds[b], J. Hattel[a]

[a]Department of Mechanical Engineering, Technical University of Denmark, Building 425, Niels Koppels Allé, DK-2800 Kgs. Lyngby, Denmark
[b]Fuel Cells and Solid State Chemistry Division, Risø National Laboratory for Sustainable Energy, Technical University of Denmark, Frederiksborgvej 399, DK-4000, Denmark

ARTICLE INFO

Article history:
Received 10 December 2008
Received in revised form
2 March 2009
Accepted 16 March 2009
Published online 24 March 2009

Keywords:
Magnetic refrigerator
Modelling
Simulation
Magnetic field
Heat
Loss

ABSTRACT

A numerical model simulating Active Magnetic Regeneration (AMR) is presented and compared to a selection of experiments. The model is an extension and re-implementation of a previous two-dimensional model. The new model is extended to 2.5D, meaning that parasitic thermal losses are included in the spatially not-resolved direction.
The implementation of the magnetocaloric effect (MCE) is made possible through a source term in the heat equation for the magnetocaloric material (MCM). This adds the possibility to model a continuously varying magnetic field.
The adiabatic temperature change of the used gadolinium has been measured and is used as an alternative MCE than mean field modeling. The results show that using the 2.5D formulation brings the model significantly closer to the experiment. Good agreement between the experimental results and the modeling was obtained when using the 2.5D formulation in combination with the measured adiabatic temperature change.

Modélisation numérique d'un régénérateur magnétique linéaire à plaques parallèles

Mots clés : Réfrigérateur magnétique ; Modélisation ; Simulation ; Champ magnétique ; Chaleur ; Perte

1. Introduction

Magnetic refrigeration at room temperature is a topic that spans several research areas. These include the optimal design of permanent magnet assemblies, focused research into relevant magnetocaloric materials and system/regenerator designs (e.g. Bjørk et al., 2008; Pecharsky and Gschneidner, 2006; Rowe and Barclay, 2003; Rowe and Tura, 2008).

The theoretical advantages of magnetic refrigeration compared to conventional gas vaporization based refrigeration

Abbreviations: AMR, Active Magnetic Regeneration; MCE, Magnetocaloric effect; MCM, Magnetocaloric material; MFT, Mean field theory; HHEX, Hot heat exchanger; CHEX, Cold heat exchanger; PDE, Partial Differential Equation; FEM, Finite Element Method; ADI, Alternate Direction Implicit; TDMA, Tri-diagonal Matrix Algorithm; Gd, Gadolinium.

* *Corresponding author*. Tel.: +45 4677 4758.
E-mail address: kaspar.kirstein.nielsen@risoe.dk (K.K. Nielsen).

0140-7007/$ – see front matter © 2009 Elsevier Ltd and IIR. All rights reserved.
doi:10.1016/j.ijrefrig.2009.03.003

Nomenclature

Variables

ΔT_{ad}	Adiabatic temperature change [K]
T	Temperature [K]
T_∞	Ambient temperature [K]
c_p	Specific heat capacity [J/kg K]
ρ	Mass density [kg/m^3]
k	Thermal conductivity [W/m K]
h	Convective heat transfer coefficient [W/m^2 K]
t	Time [s]
Δt	Timestep [s]
τ_1	Timing of magnetization part of the AMR cycle [s]
τ_2	Timing of hot blow part of the AMR cycle [s]
τ_3	Timing of demagnetization part of the AMR cycle [s]
τ_4	Timing of cold blow part of the AMR cycle [s]
τ_{rel}	Equal to $\tau_1/\tau_2 = \tau_3/\tau_4$ [–]
τ_{tot}	Equal to $2(\tau_1 + \tau_2)$ [s]
μ_0	Vacuum permeability equal to $4\pi 10^{-7}$ (N/A^2)
$\mu_0 H$	Magnetic field [T]
B	Magnetic flux density [T]
m	Magnetization [Am^2/kg]
$\mathbf{u}$	Velocity vector [m/s]
u	x-direction velocity component [m/s]
v	y-direction velocity component [m/s]
$\breve{u}$	Inlet fluid velocity [m/s]
μ	Dynamic viscosity [kg/m s]
Re	Reynolds number [–]
H	Height [m]
L	Regenerator length [m]
p	Absolute pressure [N/m^2]
Δp	Pressure drop [N/m^2]
Δx	Finite difference length in the x-direction [m]
Δy	Finitee difference length in the y-direction [m]
Δz	Finite difference length in the z-direction [m]
R	Thermal resistance [K/W]
Q	Thermal source term [W]

Sub- and super-scripts

f	Fluid
s	Solid
r	Regenerator
m	Material (solid or fluid)
l	Summation dummy index
pl	Plate
conv	Convection
i	x-direction index
j	y-direction index
0	Value at time t
*	Value at time $t + 1/2\Delta t$
**	Value at time $t + \Delta t$

are: significantly higher energy efficiency, low-noise operation and non-toxic magnetocaloric materials and heat transfer fluids.

So far numerous experiments have been done that are based on the Active Magnetic Regenerator (AMR) cycle (e.g. Rowe et al., 2004; Gao et al., 2006; Okamura et al., 2006; Bahl et al., 2008). These experiments show in general that it is certainly possible to utilize the magnetocaloric effect (MCE), which manifests itself as an adiabatic temperature change (ΔT_{ad}), inherent in the magnetocaloric material (MCM), to lift the temperature span of the AMR device to several times that of ΔT_{ad} of the used material. The experiments differ mainly in the basic design of the regenerator; some use porous packed beds and some parallel plates (of MCM). The optimal geometrical configuration of the regenerator is not obvious and since building experiments that span a sufficient number of configurations is both time-consuming and demands a great amount of resources, the need for fast and in particular accurate modeling is great.

The AMR models previously published have been one-dimensional (e.g. Dikeos et al., 2006; Li et al., 2006; Engelbrecht et al., 2005; Shir et al., 2005; Allab et al., 2005) with the exception of one, published in Petersen et al. (2008), which is a two-dimensional model of a parallel-plate design. In the one-dimensional models the regenerator is discretized with a sufficient number of grid cells in the x-direction (parallel to the flow) and thus a lumped analysis needs to be employed in order to describe the heat transfer between the active MCM and the heat transfer fluid. This description is the main simplification compared to a two-dimensional model that also resolves the thickness of both the fluid channels and MCM-plates. The model is developed for a parallel-plate based design; it would be much more tedious to develop a consistent 2D model of a porous bed-based design.

This work presents a 2.5-dimensional model that is a further development and re-implementation of the model presented in Petersen et al. (2008). This new model was developed in order to decrease computation time, make it much more versatile in terms of geometrical and operational configurations and to include parasitic thermal losses in a physically realistic way in order to resemble the current experimental AMR device situated at Risø DTU in Denmark (see Bahl et al., 2008).

The outline of this paper is the following: In Section 2 the model is presented. In Section 3 the conditions of the experimental setup are implemented into the model. The model is validated in various geometrical and operational configurations. Finally in Section 4 the conclusions are drawn and future work is presented and proposed.

2. The numerical model

The model is designed to resemble a reciprocating linear parallel-plate based AMR design. The basic model is thoroughly discussed in Petersen et al. (2008). The following subsection is a short summary of that model and in Subsections 2.2–2.4 new additions are presented.

2.1. *Summary of the original model*

Fig. 1 shows the geometry and boundary conditions in detail. The plates are stacked with an equal spacing that defines the

fluid channel thickness. The plates can be made of any MCM and the heat transfer fluid can be any liquid of interest. The x-direction is defined to be parallel to the flow. The y-direction is perpendicular to the plane of the MCM-plates. The z-direction, which is not resolved in the basic model denotes the width of the fluid channel and MCM-plate. Placed at either end in the x-direction are a cold and a hot heat exchanger, respectively. The model includes half a plate and half a fluid channel in the y-direction in a so-called replicating cell thus exploiting the symmetry of both the fluid channel and plate.

When the fluid displacement is modeled the fluid-domain is kept stationary and the solid domains (i.e. heat exchangers (HEXs) and the MCM-plate) are subject to a movement correspondingly and an appropriate fluid-flow profile is applied to the fluid-domain. The heat exchangers at either end ensure a smooth way of measuring the temperature span for a no heat-load modeling situation. In the case of a heat-load modeling situation the cold heat exchanger (CHEX) is kept at a fixed temperature via its upper boundary. The hot heat exchanger (HHEX) is at all times kept at the ambient temperature T_∞ via its upper boundary condition.

The AMR cycle simulated includes four steps. The total cycle time is denoted by τ_{tot} and the timings of the four substeps are denoted by τ_1, τ_2, τ_3 and τ_4 respectively. The cycle is symmetric meaning that $\tau_1 = \tau_3$ and $\tau_2 = \tau_4$. The first step is the magnetization of the MCM. The second step is the so-called ''hot blow'', i.e. where the fluid is moved from the cold towards the hot end. In the third step the MCM is demagnitized. The fourth step is called the ''cold blow'' and during this step the fluid is moved from the hot end towards the cold end. The timing fraction of the magnetization periods to the blow periods is defined as $\tau_{re} \equiv \tau_1/\tau_2 = \tau_3/\tau_4$.

The MCE is modeled via mean field theory (MFT) (see Petersen et al., 2008) and the resulting ΔT_{ad} is directly applied as a discrete temperature increase/decrease in the control volume under consideration. The specific heat capacity $c_p(H, T)$ is also calculated (as a function of both temperature and field) from MFT and is updated in every timestep. The MCE is highly sensitive to impurities and variations in the MCM, which are not modeled by MFT. It is therefore imperative that experimental data are used when available.

The equation system solved consists of four partial differential equations (PDEs) coupled via inner boundaries. For the solid domains (subscript s) the equations are all unsteady diffusion equations (for convenience subscript s has been adopted for all three solid domains, though the material properties ρ, k and c_p are not the same):

$$\rho_s c_{p,s} \frac{\partial T_s}{\partial t} = k_s \nabla^2 T_s. \tag{1}$$

Here, the mass density is ρ, the temperature is T, time is t and the thermal conductivity is k. The PDE describing the transient thermal behaviour of the fluid-domain, subscript f, includes an extra term, namely the convective heat transfer:

$$\rho_f c_{p,f} \left(\frac{\partial T_f}{\partial t} + (u \cdot \nabla) T_f \right) = k_f \nabla^2 T_f. \tag{2}$$

The fluid velocity is denoted by $\boldsymbol{u} = (u, v)$. Thus, all the thermal properties except c_p for the MCM are assumed constant.

2.1.1. *Velocity profile*

The applied velocity field is a steady, incompressible, fully developed and laminar flow de-coupled from the thermal system. The boundary conditions are non-slip on the boundary between the fluid-domain and the solid domains and slip on the symmetry boundary.

The assumption of incompressible flow is certainly valid since water (or a water + ethanol mixture) is used as the heat transfer fluid. Since the thermal properties (ρ, c_p and k) of water do not change significantly under the present working conditions, these are safely assumed to be constant and thus de-coupled from the thermal system.

The Reynolds number of the system is given by

$$Re = \frac{2 H_f \tilde{u} \rho_f}{\mu}, \tag{3}$$

where $\tilde{u}$ is the inlet velocity, H_f the fluid channel thickness and μ the dynamic viscosity of the fluid. The mass density and viscosity are constant ($\rho_f = 997\ \mathrm{kg/m^3}$ and $\mu = 8.91 \times 10^{-4}\ \mathrm{kg/m\,s}$) and the most extreme (i.e. in this case maximum) values of $\tilde{u}$ and H_f are 0.01 m/s and 0.8×10^{-3} m, respectively. This yields a maximum value of the Reynolds number to be ≈ 24. This value is well within the range of laminar flows justifying our assumption.

Balancing the convective and viscous terms in the incompressible Navier–Stokes equations the entrance length, L, of a laminar pipe-flow can be found to be $L = 0.06 H_f Re$ (e.g. Lautrup, 2005). For the extreme case where $\tilde{u}$ and H_f attain their maximum values the entrance length is about 0.001 m and thus compared to the length of the flow channel ($L_f = 0.16$ m) the assumption of fully developed flow is valid.

The only non-zero velocity component is the x-direction velocity u. The steady incompressible Navier–Stokes equations for laminar flows can thus be reduced to

$$\mu \frac{\partial^2 u}{\partial y^2} = \frac{\partial p}{\partial x}, \tag{4}$$

where the pressure gradient in the flow-direction is given by $\partial p/\partial x = \Delta p / L_f$. We assume the pressure drop to be constant,

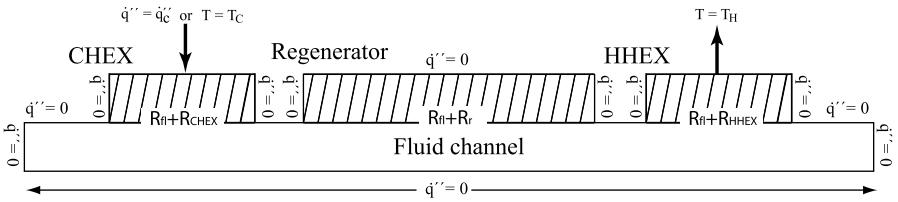

Fig. 1 – Two-dimensional slice of the original model. Half a fluid channel, MCM-plate and HEXs are seen. The thermal boundary conditions are indicated.

given by $\Delta p = 12L_f\mu\tilde{u}/H_f^2$ (Fox and McDonald, 1994). Integration of Eq. (4) and utilization of the boundary conditions $u(y = 1/2H_f) = \tilde{u}$ and $\partial U/\partial y|_{y=0} = 0$, where $y = 0$ is defined as the middle of the flow channel and $y = 1/2H_f$ is the upper boundary between the fluid channel and solid domain, gives the well-known velocity profile

$$u(y) = \tilde{u}\left(\frac{6y^2}{H_f^2} - 1/2\right). \quad (5)$$

2.2. The numerical scheme

In the original model Eqs. (1) and (2) were solved using the commercial software package Comsol (Comsol, 2005). The numerical discretization was based on the Finite Element Method (FEM) and the temporal integration was done fully implicit. The current model has been re-written using finite differences of second order and the Alternate Direction Implicit (ADI) temporal integration method. The code is written by the authors and is currently available in generic Fortran.

The reason for choosing finite differences is that total energy conservation across boundaries is guaranteed at all times due to the nature of that formalism as opposed to the FEM where the conservation of energy has to rely on interpolation methods between node points. The reason why strict energy conservation is crucial in this work is the nature of the moving boundaries. It is very important that the thermal energy exchange between the subdomains is fully conserved at all times. This can be achieved by the FEM (see Petersen et al., 2008). But the cost is a large computational time. The original Comsol model uses around 50 h to complete a simulation of 600 AMR cycles whereas this new code uses around 30 min, in both cases on an Intel Core 2 Duo 2.0 GHz Windows-based PC.

The reason for using the ADI method (see e.g. Patankar, 1980) is that the benefit from the implicit solution of each timestep is achieved and the speed of the explicit integration method is almost reached. The ADI scheme for two-dimensional problems is split into two sub-timesteps. In the first sub-timestep one direction is determined implicitly and the other is used explicitly. In the second sub-timestep the situation is reversed. The term ''explicitly used'' means that the variable solved for (e.g. temperature T) is known at the beginning of the timestep. Likewise, the term ''implicitly determined'' means that the variable is solved for at the new point in time.

If the index-pair (i,j) defines the position in the x- and y-direction and $T^0_{i,j}, T^*_{i,j}$ and $T^{**}_{i,j}$ are chosen to denote the temperatures at times t, $t + 1/2\Delta t$ and $t + \Delta t$, respectively, for the grid cell centered at (i, j) the unsteady discretized equation for the thermal conduction becomes:

$$\rho c_p \Delta x\Delta y\Delta z\frac{T^*_{i,j} - T^0_{i,j}}{1/2\Delta t} = \frac{k\Delta y\Delta z}{\Delta x}\left[\left(T^*_{i+1,j} - T^*_{i,j}\right) - \left(T^*_{i,j} - T^*_{i-1,j}\right)\right] + \frac{k\Delta x\Delta z}{\Delta y}\left[\left(T^0_{i,j+1} - T^0_{i,j}\right) - \left(T^0_{i,j} - T^0_{i,j-1}\right)\right], \quad (6)$$

$$\rho c_p \Delta x\Delta y\Delta z\frac{T^{**}_{i,j} - T^*_{i,j}}{1/2\Delta t} = \frac{k\Delta y\Delta z}{\Delta x}\left[\left(T^*_{i+1,j} - T^*_{i,j}\right) - \left(T^*_{i,j} - T^*_{i-1,j}\right)\right] + \frac{k\Delta x\Delta z}{\Delta y}\left[\left(T^{**}_{i,j+1} - T^{**}_{i,j}\right) - \left(T^{**}_{i,j} - T^{**}_{i,j-1}\right)\right], \quad (7)$$

when applying Fourier's law of heat conduction and using the formalism of the ADI method. The numerical grid cell size is denoted $\Delta x \times \Delta y \times \Delta z$. The x-direction has – arbitrarily – been chosen to be the implicit direction in the first sub-timestep (where super-scripts 0 and * mean explicit and implicit, respectively) and explicit in the second (where super-scripts * and ** mean explicit and implicit, respectively). The inclusion of Δz in Eqs. (6) and (7) is done in order to emphasize the importance of using the correct control volume when including the loss terms defined below in Eq. (12).

Eqs. (6) and (7) can be re-written in the form

$$a_{i,j}T^*_{i,j} = b_{i,j}T^*_{i+1,j} + c_{i,j}T^*_{i-1,j} + d\left(T^0_{i,j}; T^0_{i,j+1}; T^0_{i,j-1}\right), \quad (8)$$

$$a_{i,j}T^{**}_{i,j} = b_{i,j}T^{**}_{i,j+1} + c_{i,j}T^{**}_{i,j-1} + d\left(T^*_{i,j}; T^*_{i+1,j}; T^*_{i-1,j}\right), \quad (9)$$

where $a_{i,j}$, $b_{i,j}$ and $c_{i,j}$ are assumed constant throughout the timestep and d includes the explicit and other additive terms. This function may be spatially dependent. Solving Eqs. (8) and (9) is equivalent to inverting a tri-diagonal matrix. Such an inversion is linearly time-consuming in the number of mesh points and can be done using the well-known Tri-Diagonal Matrix Algorithm (TDMA) given in, e.g., Patankar (1980).

The coupling between the four domains is done using Fourier's law of heat conduction formulated through the use of thermal resistances (see the schematic in Fig. 2).

The heat capacity of the MCM is typically a strong function of both temperature and magnetic field. It is calculated from MFT and in this implementation a large dataset of c_p values has been tabulated with a sufficient range in both temperature and field. The value of c_p needed for every sub-timestep is then spline-interpolated in this dataset using a natural cubic spline (Press et al., 1992).

The forced convection term, due to the fluid movement, is implemented following the ''up-wind scheme'' (see Patankar, 1980). This ensures that the thermal energy of the up-wind cell influences the convection term rather than using the centered difference.

The boundary conditions are given in Figs. 1 and 4. The initial condition was for all experiments set to be a uniform temperature of 298 K throughout the domains.

In Petersen et al. (2008) the original numerical model is thoroughly validated. The new implementation has been exposed to the same tests and is equally numerically valid and in some cases (especially when heat conservation is crucial) the new implementation is more accurate.

2.3. The magnetocaloric effect as a source term

Previously the change in magnetic field was modeled as an abrupt or discrete change as described in Petersen et al. (2008). This approach is obviously not physically correct, but may be sufficient to a certain extent. In order to improve this aspect of the modeling, the change in magnetic field could be implemented to happen through a number of timesteps. One approach would be a simple ramping of the field through an appropriate function, e.g. linear, sinosoidal or hyperbolic tangent. An even more realistic solution is to model the physical movement of the regenerator in and out of the magnetic field from a specific magnet configuration. If the

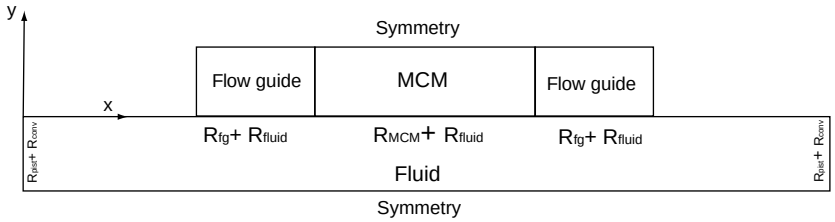

Fig. 2 – The xy-plane of the replicating cell (half a fluid channel and half a plate of MCM and flow guides). The two boundaries marked "symmetry" are symmetric, or adiabatic, due to the nature of the representation using half a replicating cell. The internal boundaries are marked with their respective thermal resistances.

field profile is known then the magnetic flux density as a function of time (and space) is trivial to derive.

Whichever method is used for modeling the magnetic field change in a continuous way, the MCE has to be formulated as a source term in the thermal equation for the MCM. Assuming adiabatic magnetization through each timestep, the heat energy released from the change in magnetic field from time t to $t+\Delta t$ is calculated on basis of the known, or explicit, temperature (i.e. $T_{i,j}(t)$). The differential adiabatic temperature change can be written as

$$\left.\frac{d\Delta T_{ad}}{dt}\right|_t = -\mu_0 \frac{T(t)}{c_p(t)} \left.\frac{\partial m}{\partial T}\right|_t \left.\frac{dH}{dt}\right|_t. \tag{10}$$

Here indices i, j have been omitted for simplicity and μ_0 is the vacuum permeability, m is the specific magnetization and H is the magnetic field. Multiplying by $\Delta x\Delta y\Delta z\rho c_p$ on both sides of Eq. (10) the MCE source term Q_{MCE} becomes

$$Q_{MCE} = -\mu_0 \rho T(t) \left.\frac{\partial m}{\partial T}\right|_t \left.\frac{dH}{dt}\right|_t \Delta x\Delta y\Delta z. \tag{11}$$

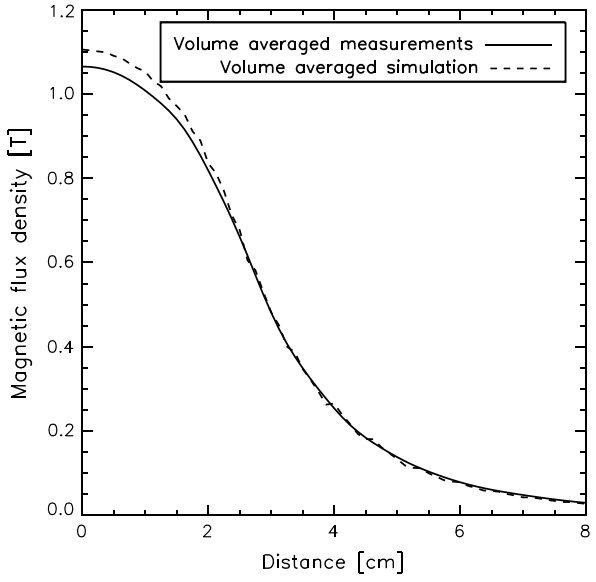

Fig. 3 – The profile of the magnetic flux density of the permanent Halbach magnet used in the experiments. Shown are both the measured data values and the corresponding model results.

Eq. (11) can be inserted directly on the right hand side of Eqs. (6) and (7) as a source term.

The temporal rate of change of the magnetic field dH/dt is derived from the field profile of the used magnet system. In Fig. 3 the flux density of the permanent Halbach magnet system used in the AMR experiments is given as a function of distance from the centre of the bore of the Halbach cylinder. The figure shows both the measured flux density and modeling data using the model from Bjørk et al. (2008).

2.4. The 2.5D heat loss formulation

The experimental setup (Bahl et al., 2008) does not include heat exchangers but does of course leak heat to the surroundings. These are two major differences between the model and the experiment. It is expected that the performance in general will be over-estimated by the model since it is somewhat ideal without losses and that the trends in performance (both in load and no-load situations) will be reproduced fairly well by the model. This is due to the fact that the model actually resolves the important parts of the experimental geometry well and the geometrical parameters are expected to be crucial for the trends of a parallel-plate AMR device.

However, to improve the model, heat losses have been implemented as an alternative to the original HEXs modeled as copper plates. The heat loss is implemented through a lumped analysis and under the assumption that the replicating cell under consideration looses most of its heat in the not-resolved z-direction. The loss can then be implemented as an additional term in Eqs. (6) and (7) using the formalism of thermal resistance:

$$Q_{loss} = \frac{T_\infty - T_{i,j}}{\sum_l R_l}, \tag{12}$$

where the total thermal resistance from the centre of the cell (in terms of the z-direction) to the ambient is denoted by $\sum_l R_l$. There are three terms in this sum. First the thermal resistance through the material within the regenerator R_m (fluid or solid). Second, the housing of the regenerator block R_{pl} (made of a plastic material) and finally loss via natural convection to the ambient R_{conv}

$$\sum_l R_l = R_m + R_{pl} + R_{conv} = \frac{1/2\Delta z}{k_m \Delta x\Delta y} + \frac{1/2\Delta z}{k_{pl}\Delta x\Delta y} + \frac{1}{h_{conv}\Delta x\Delta y}. \tag{13}$$

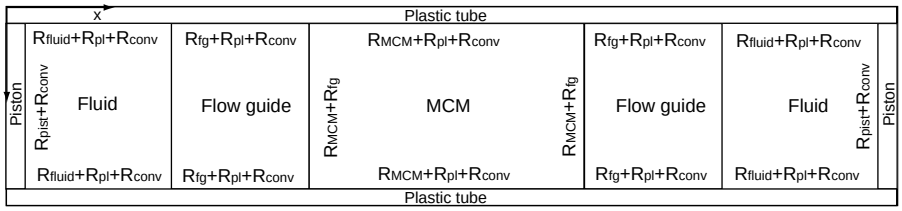

Fig. 4 – The *xz*-plane of the system. The *z*-direction is not resolved, however, the 2.5D model takes the distance from the centre of the control volumes to the ambient into account when calculating the thermal losses, as indicated in the figure.

This 2.5D thermal loss formulation is schematically visualized in Fig. 4. The loss to the ambient through natural convection is characterized by the parameter h_{conv}. Textbook values suggest that h_{conv} lies in the range 5–20 W/K m^2 (Holman, 1987). The thermal properties of the plastic housing are given in Table 1.

3. Results and discussion

In this section the numerical model is compared to various experiments performed with the experimental AMR device located at Risø DTU (Bahl et al., 2008). The model is able to operate in different configurations (2D ideal with no thermal losses, 2.5D with thermal losses, discrete or continuous magnetic field, etc.). Therefore various situations have been picked out for investigation. First, in Section 3.1 variation of the fluid displacement is investigated and compared to the experimental and original model data. Second, in Section 3.2 variation in the timing of the AMR cycle is explored. Third, in Section 3.3 the variation in the application of the magnetic field is compared between the ideal model, the 2.5D loss model and the experiment.

Table 2 gives the specifications of each experiment/model. All experiments were carried out with 0.9 mm thick plates of pure Gd (obtained from China Rare Earth Materials Co.) with a spacing of 0.8 mm. The experiments were all equipped with 13 plates. For further details on the experimental setup see Bahl et al. (2008).

3.1. *Fluid displacement experiments*

The fluid displacement, δx, is one of the key process parameters for an AMR. In Bahl et al. (2008) the dependency of the AMR performance on this parameter is studied using the experimental device and a slightly changed version of the numerical model of Petersen et al. (2008). However, the model did not include losses in the *z*-direction and the plastic flow guides were lumped to represent the entire loss of the plastic tube and regenerator housing. The geometric and operational parameters in the 2.5D loss model were set to resemble the configuration of the original experiment and to use MFT for modeling the MCE. The results are seen in Fig. 5.

The directly measured adiabatic temperature change of the Gd plates when using the Halbach magnet assembly is taken from Bahl and Nielsen (2008). A new experiment series was performed varying the fluid displacement. The model was adjusted to use MFT for calculating the MCE and also to use the directly measured ΔT_{ad} values. The heat capacity was in both cases determined from MFT. The results are seen in Fig. 6.

The fluid displacement experiments show a clearly asymmetric bell-shaped curve (Figs. 5 and 6). This shape is reproduced fairly well by the model. The peak in the curve is situated at a fluid movement around 40%. There is a significant improvement when the experimentally determined values for the adiabatic temperature change are used instead of the mean field model.

3.2. *Timing experiments*

The timing of the AMR cycle is important for the performance of the system. There are two critical questions that need answering. First of all how long the entire cycle (τ_{tot}) should be. Secondly, the amount of time used for magnetizing/demagnetizing and afterwards reaching thermal equilibrium (τ_1 and τ_3) compared to the time spent moving the fluid during the blow periods (τ_2 and τ_4). In Bahl et al. (2008) experimental and model results are given for AMR setups where τ_{rel} and τ_{tot} are

Table 1 – Values of the various thermal properties of the materials used

Material/property	k [W/m K]	ρ [kg/m^3]	c_p [J/kg K]
Copper	401	8933	385
Water	0.595	997	4183
Gadolinium	10.5	7900	170–300 (temperature and field dependent)
Plastic	0.2	800	1250

Table 2 – An overview of the experiments conducted in this work. The process parameters (fluid movement, timing and magnet assembly) are presented. The parameters apply both for the experiment and the corresponding modeling

Model	δx %	τ_{tot} [s]	τ_{rel}	Magnet
Stroke, (Bahl et al., 2008)	5–95	12	1	Electro
Stroke, new experiments	5–95	8.2	0.51	Halbach
Timing, (Bahl et al., 2008)	50	12–18	0.25–4.5	Electro
Timing, new experiments	50	9	0.25–3.0	Halbach
Varying magnetic flux density	40	11.8	1.03	Halbach

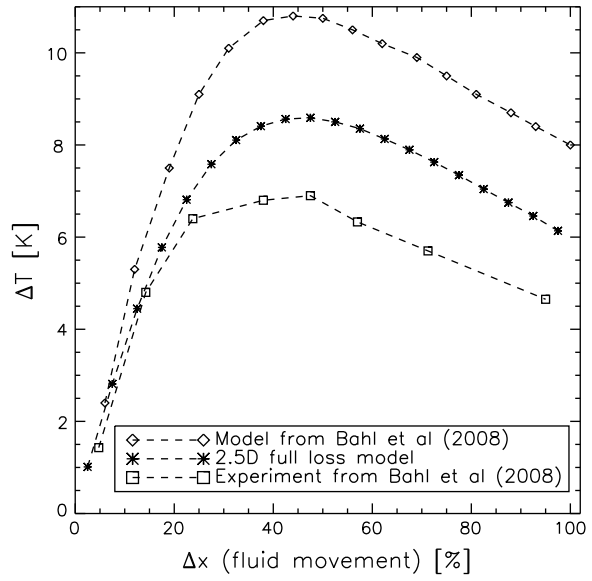

Fig. 5 – Fluid movement experiment from Bahl et al. (2008) with modeling results from both the original paper and this work. The model from this work used MFT to calculate the MCE, since it is not possible to translate the measured ΔT_{ad} values to a different magnetic field profile (the original experiment used an electromagnet).

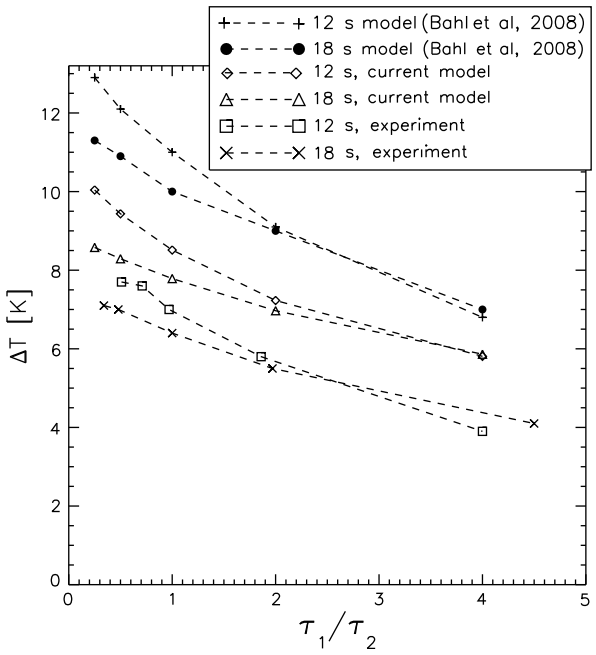

Fig. 7 – Timing experiment and corresponding modeling from Bahl et al. (2008) with the MFT-based 2.5D loss model from this work overplotted.

varied. The 2.5D loss model was setup to the same geometrical and process parametric configuration. The results are given in Fig. 7.

A new experiment series, again using the Halbach magnet was performed varying τ_{rel} and the input parameters to the 2.5D loss model were set accordingly. Both the MFT and the directly measured ΔT_{ad} were used for modeling the MCE. The results are given in Fig. 8.

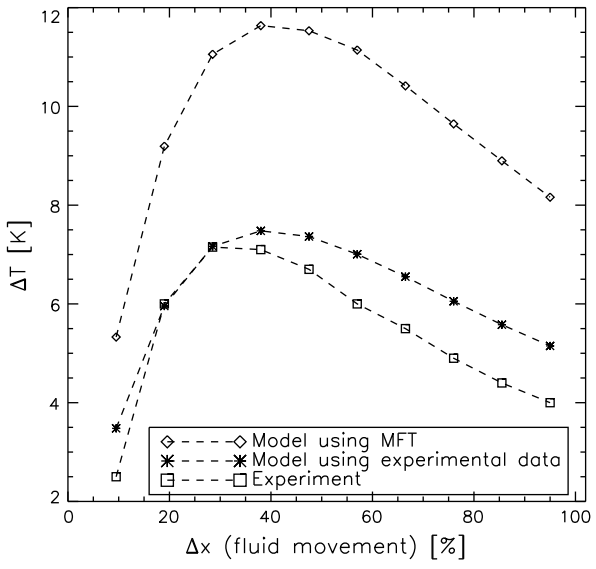

Fig. 6 – A new fluid movement experiment performed using the permanent Halbach magnet and modeled both using MFT and the measured adiabatic temperature changes.

The timing experiments, presented in Figs. 7 and 8, show that the no-load temperature span decreases as a function of the fraction τ_{rel}. This behaviour is also well reproduced by all the models. In Fig. 7 a cross-over is seen between the curves for $\tau_{tot} = 12$ and 18 s at large τ_{rel}. This is also a feature that the models reproduce.

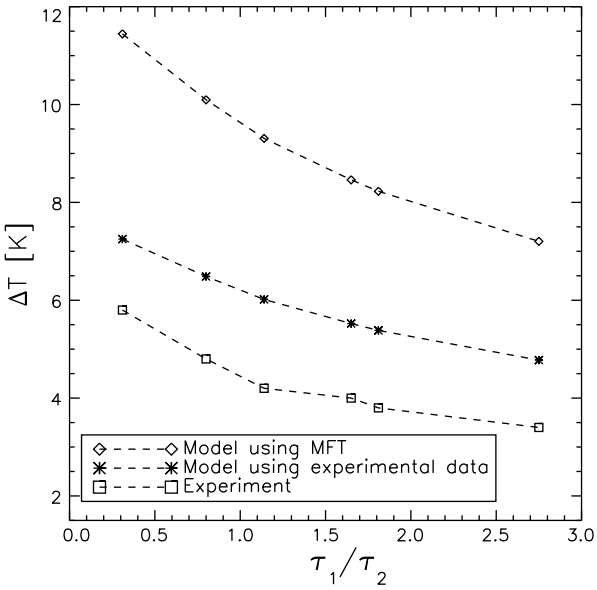

Fig. 8 – New timing experiment performed using the permanent Halbach magnet. The corresponding modeling has been performed for two cases, one using MFT and one using the measured ΔT_{ad} values. Both were done using the 2.5D loss formulation.

However, all the models using MFT for calculating ΔT_{ad} over-estimate the temperature span significantly. Using the measured ΔT_{ad} values the model is seen to reproduce the absolute temperature spans to a higher degree. This is the same conclusion as for the fluid displacement experiments.

3.3. *Varying the magnetic flux density*

The magnetic flux density of the Halbach cylinder as a function of distance from the centre of the bore is given in Fig. 3. An experiment has been conducted where the regenerator was moved from the centre of the Halbach magnet out to various distances in an otherwise identical experiment. It is seen from the results in Fig. 9 that at a certain distance (approximately 7 cm) the magnetic flux density is low enough that moving the regenerator further out does not increase the temperature span.

The modeling of the varying magnetic flux density was done in two ways, both using the MCE described as a source term (see Subsection 2.3). One model-series was performed with the ideal (no heat loss) setup and the other with the 2.5D loss formulation. The results are shown in Fig. 9.

The experimental and modeling investigations of the sensitivity towards the change in field result in two interesting conclusions. First, the need for moving the regenerator far out of the field is limited to roughly 7 cm for the present system configuration. This fact is important. The timing of the experiment is to a certain degree dependent on how much time is spent moving the regenerator in and out of field. As seen from the timing experiments the time spent during this process should be as short as possible. Second, in Fig. 9 it is seen that including thermal parasitic losses in the model significantly improves the results of the model compared to the experiment. In both cases the MFT was used to model the MCE. Thus, only the inclusion of thermal parasitic losses can explain the clear improvement of the modeling results. It should be emphasized that the remaining difference between the model and the experiments is probably due to the additional heat losses in the experimental setup which have not been included in the model due to the lack of knowledge for the origin of these losses.

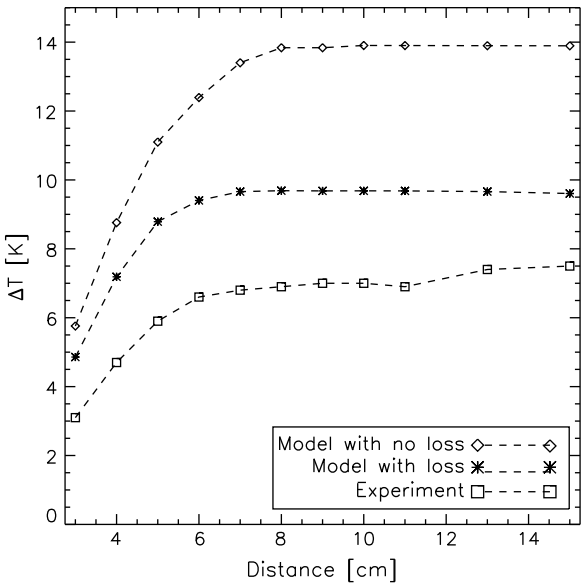

Fig. 9 – Experiment performed by altering the distance from the centre of the magnet bore that the regenerator is moved out to. Two modeling cases are seen. One with the ideal (not including 2.5D losses) and one with the 2.5D loss formulation. The trends are clearly seen to be reproduced, though the absolute values are not quite the same in the models as in the experiment.

3.4. *Overall discussion*

The three different no heat-load situations experimentally investigated and numerically modeled here all point in the same direction. When keeping all parameters except one fixed the tendency in no-load temperature span is well described by the models. However, there is a tendency for the models to over-estimate the absolute values of the temperature span. The reason for this is primarily that the MFT is too idealized and that real experimental data should be used instead. This is supported by the results from the modeling when using the measured values of the adiabatic temperature change.

Furthermore, passive regeneration in the plastic housing may be significant for the performance of the AMR. Generally, the thermal losses to the ambient may be more tightly dependent temporarily (through the cycle). This cannot be investigated in the present model and full three-dimensional modeling is needed to investigate this.

4. Conclusion

A re-definition, re-implementation and feature-upgrade of the numerical 2D AMR model (Petersen et al., 2008) were presented. The computation time has been reduced by a factor of 100. This allows for large parameter space surveys which are under preparation for future publication.

The current state of the 2D AMR model has been investigated and presented. It is concluded that the 2.5D loss model is a significant improvement in terms of reproducing the experimental results. The continuous description of the change in magnetic flux density is recognized as an important improvement of the model in terms of operating the experiment and confidence that the model is well-represented using the discrete change if needed.

Including the measured adiabatic temperature change in the experimental setup with the Halbach magnet has enabled the model to reproduce all aspects of the no heat-load experiments reasonably well.

On the basis of the results presented in this paper it is concluded that the ideal 2D model can be used to explore the performance of a linear reciprocating parallel-plate based AMR design. Once the optimal configuration settings have been found, the 2.5D full loss model can be used to explore the expected experimental performance in more detail. The reason for not only using the loss model is that the ideal AMR work is independent of experimental shortcomings and choices. The results from such an ideal AMR study can thus be used by other experiments and provide a more general understanding of the details and theory of AMR.

Acknowledgements

The authors thank Jørgen Geyti for technical assistance. Furthermore the authors would like to acknowledge the support of the Programme Commission on Energy and Environment (EnMi) (Contract no. 2104-06-0032) which is part of the Danish Council for Strategic Research.

REFERENCES

Allab, F., Kedous-Lebouc, A., Fournier, J., Yonnet, J., 2005. Numerical modeling for active magnetic regenerative refrigeration. IEEE Transactions on Magnetics 41 (10), 3757–3759.

Bahl, C., Nielsen, K., 2008. The effect of demagnetization on the magnetocaloric properties of gadolinium. Journal of Applied Physics 105, 013916.

Bahl, C., Petersen, T., Pryds, N., Smith, A., 2008. A versatile magnetic refrigeration test device. Review of Scientific Instruments 79 (9), 093906.

Bjørk, R., Bahl, C.R.H., Smith, A., Pryds, N., 2008. Optimization and improvement of Halbach cylinder design. Journal of Applied Physics 104 (1), 013910.

Comsol, 2005. In: Comsol Multiphysics Model Library, third ed. COMSOL AB, Chalmers Teknikpark 412 88 G.

Dikeos, J., Rowe, A., Tura, A., 2006. Numerical analysis of an active magnetic regenerator (amr) refrigeration cycle. AIP Conference Proceedings 823 (1), 993–1000.

Engelbrecht, K., Nellis, G., Klein, S., Boeder, A., 2005. Modeling active magnetic regenerative refrigeration systems. In: Egolf, P.W. (Ed.), First International Conference on Magnetic Refrigeration at Room Temperature. Refrigeration Science and Technology Proceedings, vol. 1, pp. 265–274.

Fox, R.W., McDonald, A.T., 1994. Introduction to Fluid Mechanics. John Wiley and Sons, Inc.

Gao, Q., Yu, B., Wang, C., Zhang, B., Yang, D., Zhang, Y., 2006. Experimental investigation on refrigeration performance of a reciprocating active magnetic regenerator of room temperature magnetic refrigeration. International Journal of Refrigeration 29, 1274–1285.

Holman, J., 1987. In: Heat Transfer, first ed. McGraw-Hill.

Lautrup, B., 2005. Physics of continuous matter. Exotic and Everyday Phenomena in the Macroscopic World. Institute of Physics.

Li, P., Gong, M., Yao, G., Wu, J., 2006. A practical model for analysis of active magnetic regenerative refrigerators for room temperature applications. International Journal of Refrigeration 29, 1259–1266.

Okamura, T., Yamada, K., Hirano, N., Nagaya, S., 2006. Performance of a room-temperature rotary magnetic refrigerator. International Journal of Refrigeration 29, 1327–1331.

Patankar, S.V., 1980. Numerical Heat Transfer and Fluid Flow. Taylor & Francis.

Pecharsky, V.K., Gschneidner, K., 2006. Advanced magnetocaloric materials: what does the future hold? International Journal of Refrigeration 29, 1239–1249.

Petersen, T.F., Pryds, N., Smith, A., Hattel, J., Schmidt, H., Knudsen, H., 2008. Two-dimensional mathematical model of a reciprocating room-temperature active magnetic regenerator. International Journal of Refrigeration 31, 432–443.

Press, W.H., Teukolsky, S.A., Vetterling, W.T., Flannery, B.P., 1992. Numerical recipes in FORTRAN. In: The Art of Scientific Computing, second ed. University Press, Cambridge.

Rowe, A., Barclay, J., 2003. Ideal magnetocaloric effect for active magnetic regenerators. Journal of Applied Physics 93 (3), 1672–1676.

Rowe, A., Tura, A., 2008. Active magnetic regenerator performance enhancement using passive magnetic materials. Journal of Magnetism and Magnetic Materials 320 (7), 1357–1363.

Rowe, A., Tura, A., Richard, M.-A., Chahine, R., Barclay, J., 2004. Magnetic refrigeration – an overview of operating experience using the amr test apparatus. Advances in Cryogenic Engineering 49 (B), 1721.

Shir, F., Mavriplis, C., Benneth, L., Torre, E., 2005. Analysis of room temperature magnetic regenerative refrigeration. International Journal of Refrigeration 28, 616–627.

Paper V

Paper presented at SIMS 50 - Modelling and Simulation of Energy Technology, 2010

Bjørk, R., Bahl, C. R. H., Smith, A., Pryds, N., Nielsen, K. K. and Hattel, J.

Numerical modeling in magnetic refrigeration

Proceedings of SIMS 50 - Modelling and Simulation of Energy Technology, Fredericia, Denmark, 323-330, 2010

Proceedings of SIMS 50
Fredericia, Denmark
October 7–8, 2009

NUMERICAL MODELING IN MAGNETIC REFRIGERATION

R. Bjørk[*], C. R. H. Bahl, A. Smith and N. Pryds,
Technical University of Denmark
Fuel Cells and Solid State Chemistry Division
Risø National Laboratory for Sustainable Energy
DK-4000 Roskilde
Denmark

K. K. Nielsen and J. Hattel
Technical University of Denmark
Department of Mechanical Engineering
DK-2800 Lyngby
Denmark

ABSTRACT

A magnetic refrigeration device built at Risø DTU is presented. For this device there are two important physical systems whose design must be carefully considered. The first is the permanent magnet assembly where the optimal economic values for the magnet design are found based on numerical simulations. A physical magnet was constructed and measurements of the flux density are compared with simulation, showing a good agreement. The second is the design of the so-called Active Magnetic Regenerator (AMR) which is the active core of the refrigeration system. A transient heat transfer 2.5-dimensional numerical model to model AMR is presented. The model is shown to reproduce experimental data from the Risø DTU magnetic refrigeration device.
Keywords: **Magnetic refrigeration, Magnetic field, Heat transfer, Finite element, Finite difference**

INTRODUCTION

Magnetic refrigeration is an evolving technology that has the potential of high energy efficiency and the usage of environmentally friendly refrigerants [1]. Magnetic refrigeration is based on the magnetocaloric effect (MCE). The MCE is observed in magnetic materials when subjected to a change in magnetic field. Under adiabatic conditions, most materials exhibit an increase in temperature when the field change is positive and a decrease when the change is negative. An increase in magnetic field tends to order the magnetic moments and thus lowers the magnetic entropy. Since the total entropy is constant under adiabatic conditions the lattice and electron entropies must increase and thus the temperature of the material rises. If the MCE of the material is reversible, the temperature will decrease when the field is removed since the direction of the magnetic moments will be randomized when no external field is present. This increase/decrease in temperature is called the adiabatic temperature change, ΔT_{ad}. Magnetocaloric materials exhibit a maximum in the MCE at the transition temperature between a ferromagnetic and a paramagnetic phase, known as the Curie temperature, T_{c}. Different magnetocaloric materials have different values of T_{c}[2].

One of the keystones of using magnetocaloric materials (MCMs) as refrigerants is their inherent reversibility (for materials of interest), which allows for an efficient refrigeration process. However, the MCE in the best materials currently available show a temperature change of no more than around 4 K in an magnetic field of around 1 T. Thus a simple reverse thermodynamic cycle will not be able to produce significant refrigeration at reachable magnetic

[*]Corresponding author: E-mail:rab @risoe.dtu.dk

fields from permanent magnets. Therefore the active magnetic regeneration (AMR) cycle is applied. This process combines the MCE of the MCM as work input with the MCM, i.e. the refrigerant, at the same time working as a regenerator. A heat transfer fluid is used to exchange heat between the solid and heat exchangers at the hot and cold ends respectively. Four steps are normally used to characterize the AMR process. These are

1. Adiabatic magnetization, which increases the temperature of the refrigerant.
2. The hot blow period, where the heat transfer fluid is blown from the cold to the hot end, allowing heat from the solid to be rejected at the hot end.
3. Adiabatic demagnetization, which lowers the temperature of the refrigerant.
4. The cold blow where the heat transfer fluid is blown from the hot end to the cold end and thus absorbs a cooling load in the cold end.

The regenerator is a porous structure made of the MCM, with the heat transfer fluid filling the void space. The AMR system cannot be described by a conventional refrigeration cycle since each differential element of the regenerator undergoes its own specific thermodynamic cycle. The scientific problem of magnetic refrigeration consists of a combination of regenerator-effectiveness, the non-linear MCE and an application of an external magnetic field.

In this paper the focus is on the numerical modeling of a magnetic refrigeration test machine constructed at Risø DTU [3, 4]. The test machine is a reciprocating device using parallel plates of magnetocaloric material and using a cylindrical permanent magnet assembly to create the magnetic field.

THE RISØ DTU MAGNETIC REFRIGERATION DEVICE

The test machine, which is pictured in Fig. 1, consists of a regenerator core in the middle of a plastic tube with an outer diameter of 40 mm and an inner diameter of 34 mm. The regenerator core contains 13 precision machined grooves to hold plates of magnetocaloric material with dimensions 40 mm along the flow direction, 0.9 mm thick and 25 mm wide. The plates are separated by a 0.8 mm spacing which is then the thickness of the fluid channel. A close up photo of the regenerator can be seen in Fig. 2.

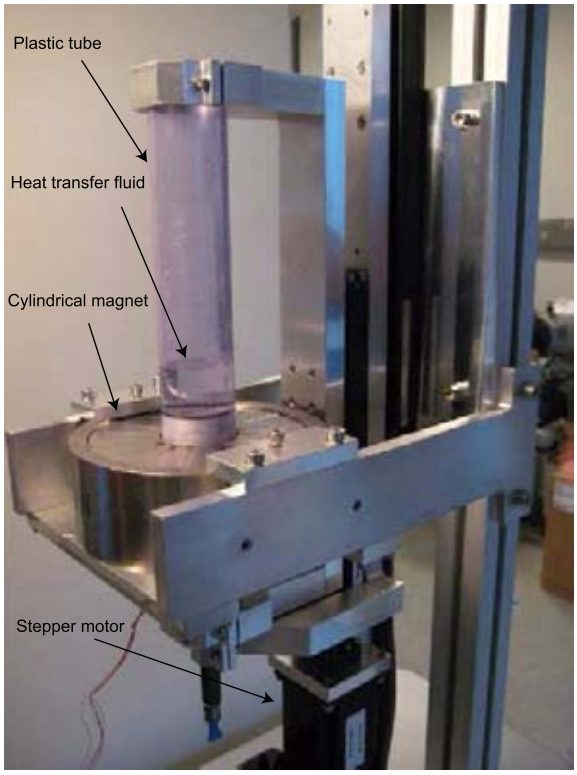

Figure 1: The test machine in its operational environment. The cylindrical permanent magnet assembly can be seen in the center of the picture. Also the plastic tube, filled with water, holding the regenerator core (not visible) can be seen. The regenerator core is inside the magnet. The motor for moving the regenerator core is visible at the bottom of the photo.

The heat transfer fluid is moved using a piston. Five type E thermocouples are placed in the center flow channel of the regenerator so the temperature profile in the AMR can be recorded during an experiment. The permanent magnet assembly that provides the magnetic field can be seen in Fig. 1. This has the shape of a cylinder. The assembly provides a maximum magnetic field of 1.1 T. The regenerator is moved in and out of the magnetic field by a stepper motor.

The total system is compact and is generally easy to handle. The setup allows for easy change of the plates of MCM as well as the heat transfer fluid. Dif-

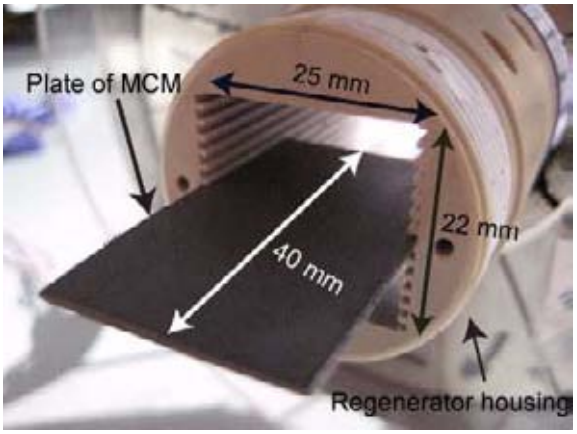

Figure 2: A close-up of the experimental AMR regenerator bed with a plate of MCM material sticking out of the regenerator. The regenerator bed can contain 13 parallel plates.

ferent AMR parameters such as piston stroke length and cycle time are easily adjustable using a custom LabView computer controlled interface.

THE PERMANENT MAGNET ASSEMBLY

In general a magnetic field can be produced by an electromagnet or by a permanent magnet assembly. For the test machine the permanent magnet assembly was chosen as it requires no external power source to produce a magnetic field. The design requirement for the permanent magnet assembly is that it produces a homogenous high flux density magnetic field in a confined region of space and a very weak field elsewhere. The Halbach cylinder design [5, 6] was chosen, because it fulfills the requirements, is compact and relatively simple to assemble.

A Halbach cylinder consists of a permanent magnetic material with a bore along the cylinder symmetry axis in which the magnetic field is concentrated. The magnet is magnetized such that the direction of magnetization varies continuously as, in polar coordinates,

$$\begin{aligned} B_{\mathrm{rem},r} &= B_{\mathrm{rem}} \cos(\ ) \\ B_{\mathrm{rem},} &= B_{\mathrm{rem}} \sin(\ ) , \end{aligned} \qquad (1)$$

where B_{rem} is the magnitude of the remanent flux density. An illustration of the Halbach cylinder can be seen in Fig. 3. The Halbach cylinder can be characterized by three parameters: the internal and external radii, r_{in} and r_{ex}, respectively, and the length, L. For practical applications the Halbach cylinder is built up from segments each with their own direction of magnetization. The Halbach cylinder used for the test machine consists of 16 blocks of permanent magnets. This configuration yields 95% of the flux density of an unsegmented continuous Halbach cylinder [7].

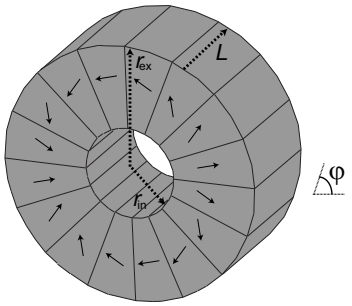

Figure 3: A illustration of a 16 segmented Halbach magnet. Shown as arrows is the direction of magnetization. The internal and external radii, r_{in} and r_{ex}, respectively, and the length, L are also shown.

Dimensioning the magnet

As the magnet is the single most expensive part of a magnetic refrigeration device the magnet must be dimensioned such that it uses the minimum amount of magnetic material while at the same time producing a homogenous high flux density over as large a volume as possible. Based on these requirements a magnet assembly can be characterized by three parameters. The first is the volume in which the magnetic field is created, in this case the volume of the cylinder bore. The second is the volume of magnet used to create the magnetic field, in this case the volume of the Halbach cylinder. The third is the flux density of the created magnetic field.

To find the optimal dimensions of the Halbach cylinder for the test machine we have conducted a series of parameter variation simulations using the commercially available finite element multiphysics program, *Comsol Multiphysics*[8]. The Comsol Multiphysics code has previously been validated through a number of NAFEMS (National Agency for Finite Element Methods and Standards) benchmark studies [9].

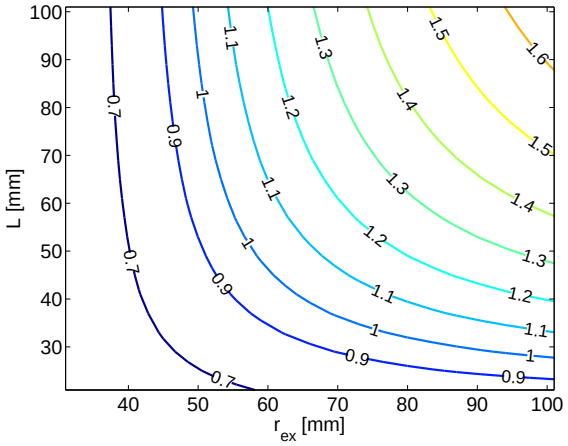

Figure 4: Contours of the mean flux density as a function of external radius and length. Each contour is labeled by its mean flux density. The maximum flux density is obtained by maximizing both r_{ex} and L.

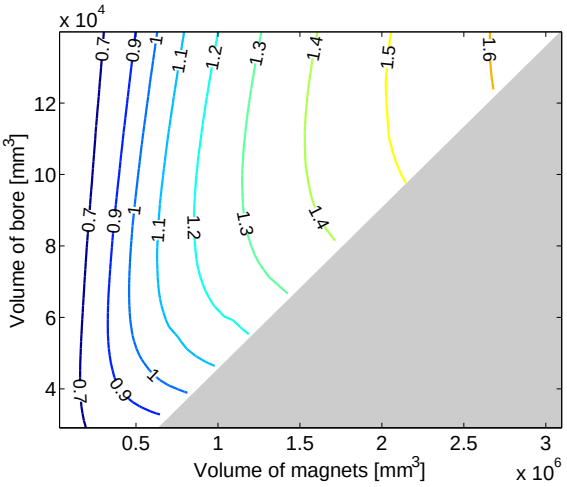

Figure 5: Contours of the mean flux density as a function of the volume of magnets used and the volume of the cylinder bore. It is seen that there is a minimum amount of magnet for each mean flux density contour. Also the volume of the bore can be significantly increased by slightly increasing the volume of the magnets.

The equation solved in the simulations is the magnetic vector potential equation,

$$\nabla \times (\ {}^{-1}_{0}\ \ {}^{-1}_{r}(\nabla \times \mathbf{A} - \mathbf{B}_{\text{rem}})) = 0, \qquad (2)$$

where $\mathbf{A}$ is the magnetic vector potential, $\mathbf{B}_{\text{rem}}$ is the remanent flux density, $_0$ is the permeability of free space and $_r$ is the relative permeability assumed to be isotropic. A finite element mesh is used as this provides high resolution near geometric connections, e.g. corners. The solver used to solve Eq. 2 on the simulation mesh is *Pardiso* which is a parallel sparse direct linear solver [10, 11]. Boundary conditions are chosen such that the boundaries of the computational volume, which is many times larger than the Halbach cylinder, are magnetically insulating, while all other (internal) boundaries are continuous.

The parameters that were varied were the external radius and the length of the Halbach cylinder. The internal radius of the Halbach cylinder was fixed at $r_{\text{in}} = 21$ mm to fit the regenerator bed. The external radius was varied in the range $r_{\text{ex}} = 31 - 101$ mm in steps of 1 mm while the length was varied in the range $L = 21 - 101$ mm in steps of 1 mm. All in all 5751 simulations were performed. For all simulations a remanent magnetization of the individual magnet of 1.4 T was used.

Shown in Fig. 4 are contours of equal mean flux density in the cylinder bore as a function of external radius and length. From this figure it can be seen that increasing the external radius or the length will increase the mean flux density in the cylinder bore. However it cannot be seen which parameters produce the largest flux density over the biggest volume with the minimum amount of magnetic material.

In Fig. 5 contours of equal mean flux density are plotted as a function of the volume of the magnet and the volume of the bore. Using these variables it can be seen that for each flux density there is a minimum value of the volume of the magnet. This is the most economic design as it uses the minimum amount of magnetic material to produce a given mean flux density. However it can also be seen that by increasing the amount of magnetic material slightly the volume of the bore can be significantly increased.

The data points in Fig. 5 (not shown) can be mapped to a specific value of the external radius and length. By finding the minimum value of the volume of the magnet for a range of mean flux densities and recording the external radius and length for this configuration the optimal economic values for r_{ex} and L are found. These are shown in Fig. 6.

From this figure one can get the external radius and length of the Halbach cylinder with the minimum volume of the magnet that produces a given mean

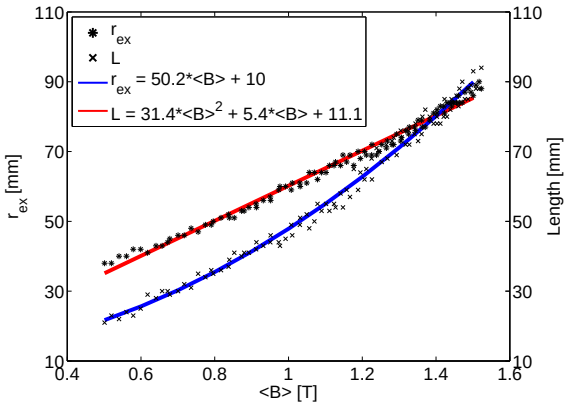

Figure 6: The optimal r_{ex} and L as functions of the mean flux density. Polynomia have been fitted to the data to ease interpolation. Building a Halbach cylinder with an internal radius of 21 mm with dimensions different from the dimensions given here means that more magnetic material is used than need be, if one does not care about the volume of the bore.

flux density. A first order polynomial has been fitted to the external radius data points while a second order polynomial has been fitted to the length data points.

Based on Fig. 6 and a design requirement that the magnet for the test machine should provide a mean flux density of around 1 T, an external radius of the Halbach cylinder of 60 mm and a length of 50 mm was chosen.

The physical magnet

Having found the dimensions of the ideal Halbach cylinder for the test machine a magnet was constructed. The actual Halbach cylinder, part of which can be seen on Fig. 1, has an inner radius of 21 mm, an outer radius of 60 mm and a length of 50 mm. The volume of the magnet is 0.50 L and the volume of the cylinder bore is 0.07 L. We have measured the flux density along the central axis of the Halbach cylinder using a Hall probe and the result is shown in Figure 7. Also shown is the flux density obtained from simulation. As can be seen from the figure the numerical simulation and the experimental measurements agree, and show that a high flux density is produced in the center of the cylinder bore. The small difference between simulation and measurement can be due to uncertainty in the

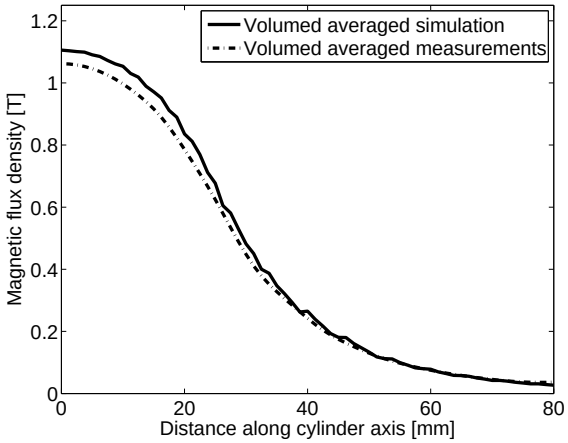

Figure 7: The measured and simulated flux density for the Halbach cylinder for the test machine.

magnet specifications and manufacturing processes as well as measuring uncertainty.

THE AMR MODEL

As the coupling between magnetic field, MCE, fluid-solid heat transfer and the thermal properties of the MCM is highly non-linear, numerical modeling is needed to understand the physics and response of the AMR system to changes in geometry, operating parameters and material composition. Such a model has developed at Risø DTU [12, 14]. The model is 2-dimensional, resolving the flow-direction (parallel to the MCM plates) and the direction perpendicular to the flow and the plane of the plates. Thus the internal gradients are resolved, while the plates are assumed wide enough that boundary effects are negligible. However, the model features an option to model the ambient temperature in the not-resolved dimension through a simple thermal resistive formulation. The governing equations are for the fluid

$$ {}_{\mathrm{f}}c_{\mathrm{p,f}} \left(\frac{T_{\mathrm{f}}}{t} + (\mathbf{u} \cdot \nabla) T_{\mathrm{f}} \right) = k_{\mathrm{f}} \nabla^2 T_{\mathrm{f}}, \qquad (3) $$

and solid

$$ {}_{\mathrm{s}}c_{\mathrm{p,s}} \frac{T_{\mathrm{s}}}{t} = k_{\mathrm{s}} \nabla^2 T_{\mathrm{s}}, \qquad (4) $$

respectively. Subscripts f and s stand for fluid and solid respectively. The thermal properties are mass density, , and thermal conductivity k, both assumed constant, and specific heat capacity, c_{p}, which is a

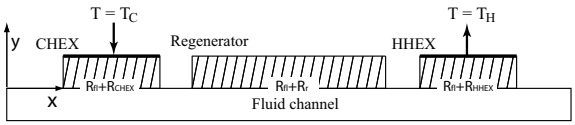

Figure 8: The 2-dimensional geometry of the AMR model. The model exploits symmetry and thus only half a fluid channel and half the solid domains are modeled. All thermal boundary conditions are isolating except those otherwise indicated.

function of temperature and magnetic field. Temperature is denoted T and time is t. Finally, the velocity of the fluid is denoted $\mathbf{u}$. The solid and fluid domains are coupled via inner boundaries. These slide to simulate the fluid movement and the resulting velocity profile is

$$u(y) = \tilde{u}\left(\frac{6y^2}{H_{\mathrm{f}}^2} - 1/2\right). \tag{5}$$

Here the $y-$direction is perpendicular to the flow and the plane of the MCM-plates. The velocity profile only has a component in the $x-$direction (parallel to the flow) since it is assumed to be fully developed, laminar and incompressible. The mean fluid velocity is denoted $\tilde{u}$ and the thickness of the fluid channel is H_{f}.
The geometry of the model is displayed in Fig. 8. The model exploits symmetry and thus only half a fluid channel and half a solid domain are modeled.
The model is solved using a spatial discretization based on finite differences of 2nd order and the alternate direction implicit (ADI) method for the temporal integration. The code is written by the authors and maintained at Risø DTU and available in generic Fortran. A detailed description of the model is available in [12].
The magnetocaloric effect (MCE) can be modeled either using the mean field theory (MFT) [13] or using experimental data when available).

Thermal parasitic losses

The model is able to include thermal parasitic losses to the ambient in the z-direction, i.e. the dimension not resolved spatially. This formulation is straightforwardly written in terms of thermal resistances

$$Q_{\mathrm{loss}} = \frac{T_\infty - T}{\sum_i R_i}. \tag{6}$$

The ambient temperature is denoted T_∞ and the thermal resistances are denoted R_i. This expression is applied for each grid cell, which individually has the temperature T. The thermal resistance sum has three main contributors namely the resistance in the domain under consideration (MCM or fluid), the plastic housing and finally natural convection between the housing and the ambient. Thus, the sum becomes

$$\sum R_i = \frac{1/2\Delta z_{\mathrm{f}}}{k_{\mathrm{f}}\Delta x\Delta y} + \frac{\Delta z_{\mathrm{pl}}}{k_{\mathrm{pl}}\Delta x\Delta y} + \frac{1}{h_{\mathrm{conv}}\Delta x\Delta y}, \tag{7}$$

in the case of the fluid (the subscript is simply substituted for the appropriate domain). In this expression the thickness of the domain, Δz_{f}, has been introduced as well as the area of the individual grid cell perpendicular to the $z-$direction, $\Delta x\Delta y$. The subscript pl stands for plastic. Finally, the natural convection parameter is denoted h_{conv}.
The purpose of including the parasitic losses to the ambient is to model in detail the exterior circumstances to a specific AMR experiment. For ideal modeling, i.e. where the optimal performance is sought for the theoretical AMR device, such losses are without meaning. However, when modeling experimental results they can be of great significance. The expression in Eq. 6 is added as a source term in Eqs. 3 and 4.

Results from the AMR modeling

A wide range of results exist from the current AMR model. These range from theoretical AMR modeling, which aims at understanding the basic principles of active magnetic regeneration both in terms of regenerator efficiency and material composition [15], to modeling of the actual test machine located at Risø DTU [16]. In the latter case e.g. the thermal parasitic losses are taken into account. This way of modeling the AMR problem from different perspectives provides a basis for understanding how to obtain the optimal performance as well as understanding the short-commings of the experiment (e.g. significance of thermal losses, demagnetization effects [17] etc).
Results from a fluid-displacement variation experiment using gadolinium as MCM and water as heat transfer fluid are showed in Fig. 9. The figure shows a clear dependency of the zero heat-load temperature span as function of fluid displacement. Furthermore,

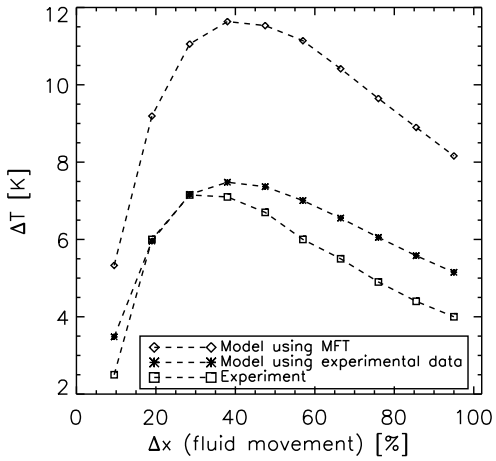

Figure 9: An example of a result from the numerical AMR model compared to the experimental device. The ambient temperature was set to 298 K and gadolinium was used as the MCM and water as the heat transfer fluid. In this figure the no heat-load temperature span is plotted as function of fluid displacement during the AMR process. The two different modeling situations are different in the sense that one uses the mean field theory (MFT) to calculate the MCE and the other uses experimental data from [17]. Reproduced from [12].

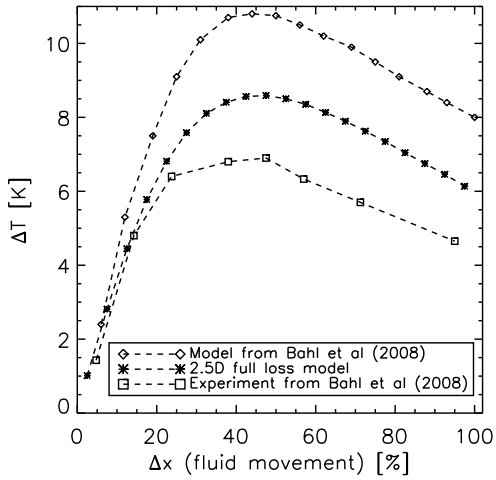

Figure 10: An example of the impact of including the thermal parasitic losses (denoted 2.5D full loss model). The losses are seen to have a significant impact on the experimental results. Reproduced from [12].

it is evident from the figure that the input MCE should be carefully used. The clearly overestimating model-curve is from a modeling series where the mean field theory (MFT) was used to calculated the MCE (see [18] for details on the MFT). The model-curve that is almost overlying with the experimental values uses experimentally obtained data. This shows that the model is quite sensitive to the input MCE, which is important since magnetocaloric data in general are not abundant for most MCMs and thus an effort towards characterizing MCMs in detail is needed.

Figure 10 shows the significance of including the thermal parasitic losses. The experiment was run using gadolinium as MCM and water as heat transfer fluid at a total cycle timing of about 9 seconds, and thus the parasitic losses have plenty of time to destroy the regeneration.

CONCLUSION

A magnetic refrigeration test device made at Risø DTU was presented. The Halbach cylinder magnet design for the device was discussed and optimal economic dimensions for the magnet were found. The magnet was constructed and the flux density was measured and compared with simulation and a good agreement was found. Also a numerical AMR model was presented and some results discussed. The modeling shows that the magnetocaloric effect should be carefully implemented, i.e. when modeling experiments real experimental MCE data should be applied when available. Furthermore, it was shown that including the thermal parasitic losses to the ambient greatly improves the resembles of the model and the experiment. Thus, an important point when designing an AMR experiment is to minimize the impact of parasitic losses. This can be done be e.g. increasing the operating frequency.

ACKNOWLEDGEMENTS

We thank Mr. Jørgen Geyti for his technical help. The authors further acknowledge the support of the Programme Commission on Energy and Environment (EnMi) (Contract No. 2104-06-0032), which is part of the Danish Council for Strategic Research.

REFERENCES

[1] Gschneidner Jr K A and Pecharsky V. *Thirty years of near room temperature magnetic cooling: Where we are today and future prospects.* Int. J. Refrig., 2008;31(6):945.

[2] Pecharsky V K and Gschneidner K A Jr. *Advanced magnetocaloric materials: What does the future hold?* Int. J. Refrig. 2006;29:1239-1249.

[3] Bahl C R H, Petersen T F, Pryds N and Smith, A. *A versatile magnetic refrigeration test device* Rev. Sci. Inst. 2008;79(9):093906

[4] Engelbrecht K, Jensen J B, Bahl C R H and Pryds N. 2009. *Experiments on a modular magnetic refrigeration device* Proc. 3rd Int. Conf. on Magn. Refrig. at Room Temp. 2009;IIF/IIR.

[5] Mallinson J C. *One-sided Fluxes - A Magnetic Curiosity?* IEEE Trans. Magn. 1973;9(4):678.

[6] Halbach K. *Design of permanent multipole magnets with oriented rare earth cobalt material* Nucl. Instrum. Methods 1980;169.

[7] Bjørk R, Bahl C R H, Smith A and Pryds N. *Optimization and improvement of Halbach cylinder design* J. Appl. Phys. 2008;104:13910.

[8] COMSOL AB, Tegnrgatan 23, SE-111 40 Stockholm, Sweden.

[9] Comsol, Comsol Multiphysics Model Library, third ed. COMSOL AB, Chalmers Teknikpark 412 88 G (2005).

[10] Schenk O, Gärtner K, Fichtner W and Stricker A., *PARDISO: A High-Performance Serial and Parallel Sparse Linear Solver in Semiconductor Device Simulation* J. of Future Gener. Comput. Syst. 2001;18:69.

[11] Schenk O and Gärtner K. *Two-Level Scheduling in PARDISO: Improved Scalability on Shared Memory Multiprocessing Systems* Parallel Comput. 2002;28

[12] Nielsen K K, Bahl C R H, Smith A, Pryds N, Bjørk R and Hattel J. *Detailed numerical modeling of a linear parallel-plate active magnetic regenerator* Int. J. Refrig. 2009, doi:10.1016/j.ijrefrig.2009.03.003

[13] Morrish *The physical principles of magnetism*. New York: John Wiley and Sons Inc., 1965.

[14] Nielsen K K , Pryds N, Smith A, Bahl C R H and Hattel J. *2-dimensional numerical modeling of active magnetic regeneration* Proc. 3rd Int. Conf. on Magn. Refrig. at Room Temp. 2009;IIF/IIR.

[15] Nielsen K K , Bahl C R H, Smith A., Pryds N. and Hattel J. *On the ideal cooling capacity of gadolinium in active magnetic regenerative refrigeration* 2009;In prep.

[16] Nielsen K K, Engelbrecht K, Bahl C R H, Smith A, Pryds N and Hattel J. *Numerical modeling of multi-material active magnetic regeneration* Proc. 7th World Conf. on Exp. Heat Transf., Fluid Mech. and Thermodyn. 2009.

[17] Bahl, C R H and Nielsen, K K. *The effect of demagnetization on the magnetocaloric properties of gadolinium.* J. Appl. Phys. 2009;105:013916.

[18] Petersen T F, Pryds N, Smith A, Hattel J, Schmidt H and Knudsen H. *Two-dimensional mathematical model of a reciprocating room-temperature active magnetic regenerator.* Int. J. Refrig. 2008;31:432.

[19] Rowe A & Barclay J. *Ideal magnetocaloric effect for active magnetic regenerators* J. Appl. Phys. 2003;93:1672

Paper VI

Paper published in Journal of Magnetism and Magnetic Materials, 2010

Bjørk, R., Smith, A. and Bahl, C. R. H.

Analysis of the magnetic field, force, and torque for two-dimensional Halbach cylinders

Journal of Magnetism and Magnetic Materials, 322, 133-141, 2010

Journal of Magnetism and Magnetic Materials 322 (2010) 133–141

Contents lists available at ScienceDirect

Journal of Magnetism and Magnetic Materials

journal homepage: www.elsevier.com/locate/jmmm

Analysis of the magnetic field, force, and torque for two-dimensional Halbach cylinders

R. Bjørk *, A. Smith, C.R.H. Bahl

Fuel Cells and Solid State Chemistry Division, Risø National Laboratory for Sustainable Energy, Technical University of Denmark - DTU, Frederiksborgvej 399, DK-4000 Roskilde, Denmark

ARTICLE INFO

Article history:
Received 15 April 2009
Received in revised form
19 August 2009
Available online 4 September 2009

PACS:
85.70.Ay
07.55.Db

Keywords:
Halbach cylinder
Magnetic field
Permanent magnet flux source
Magnetic force
Magnetic torque

ABSTRACT

The Halbach cylinder is a construction of permanent magnets used in applications such as nuclear magnetic resonance apparatus, accelerator magnets and magnetic cooling devices. In this paper the analytical expression for the magnetic vector potential, magnetic flux density and magnetic field for a two dimensional Halbach cylinder are derived. The remanent flux density of a Halbach magnet is characterized by the integer p. For a number of applications the force and torque between two concentric Halbach cylinders are important. These quantities are calculated and the force is shown to be zero except for the case where p for the inner magnet is one minus p for the outer magnet. Also the force is shown never to be balancing. The torque is shown to be zero unless the inner magnet p is equal to minus the outer magnet p. Thus there can never be a force and a torque in the same system.

1. Introduction

The Halbach cylinder [1,2] (also known as a hole cylinder permanent magnet array (HCPMA)) is a hollow permanent magnet cylinder with a remanent flux density at any point that varies continuously as, in polar coordinates,

$$B_{\mathrm{rem},r} = B_{\mathrm{rem}}\cos(p\phi), \quad B_{\mathrm{rem},\phi} = B_{\mathrm{rem}}\sin(p\phi), \tag{1}$$

where B_{rem} is the magnitude of the remanent flux density and p is an integer. Subscript r denotes the radial component of the remanence and subscript ϕ the tangential component. A positive value of p produces a field that is directed into the cylinder bore, called an internal field, and a negative value produces a field that is directed outwards from the cylinder, called an external field.

A remanence as given in Eq. (1) can, depending on the value of p, produce a completely shielded multipole field in the cylinder bore or a multipole field on the outside of the cylinder. In Fig. 1 Halbach cylinders with different values of p are shown.

The Halbach cylinder has previously been used in a number of applications [3,4], such as nuclear magnetic resonance (NMR) apparatus [5], accelerator magnets [6] and magnetic cooling devices [7].

In these applications it is very important to accurately calculate the magnetic flux density generated by the Halbach cylinder. There exist several papers where the magnetic field and flux density for some parts of a Halbach cylinder are calculated [8–11], but a complete spatial calculation as well as a detailed derivation of the magnetic vector potential has previously not been published.

In this paper we wish to calculate the magnetic vector potential and subsequently the magnetic flux density at any point in a two dimensional space resulting from a Halbach cylinder.

Once the analytical solution for the magnetic flux density has been obtained we will proceed to calculate the force and torque between two concentric Halbach cylinders.

For $p=1$ and a relative permeability of 1 the more complicated problem of computing the torque between two finite length concentric Halbach cylinders has been considered [12], and it is shown that a torque arises due to end effects. However, neither the field nor the torque is evaluated explicitly. Below we show that for special values of p a nonzero force and torque may arise even in the two dimensional case.

2. Defining the magnetostatic problem

The problem of finding the magnetic vector potential and the magnetic flux density for a Halbach cylinder is defined in terms of

* Corresponding author.
E-mail address: rabj@risoe.dtu.dk (R. Bjørk).

0304-8853/$ - see front matter © 2009 Elsevier B.V. All rights reserved.
doi:10.1016/j.jmmm.2009.08.044

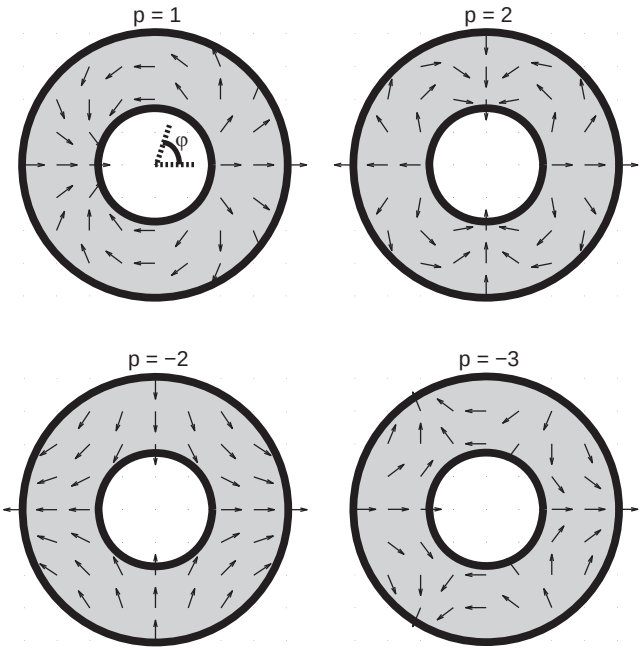

Fig. 1. The remanence of a $p=1, 2, -2$ and -3 Halbach cylinder. The angle ϕ from Eq. (1) is also shown.

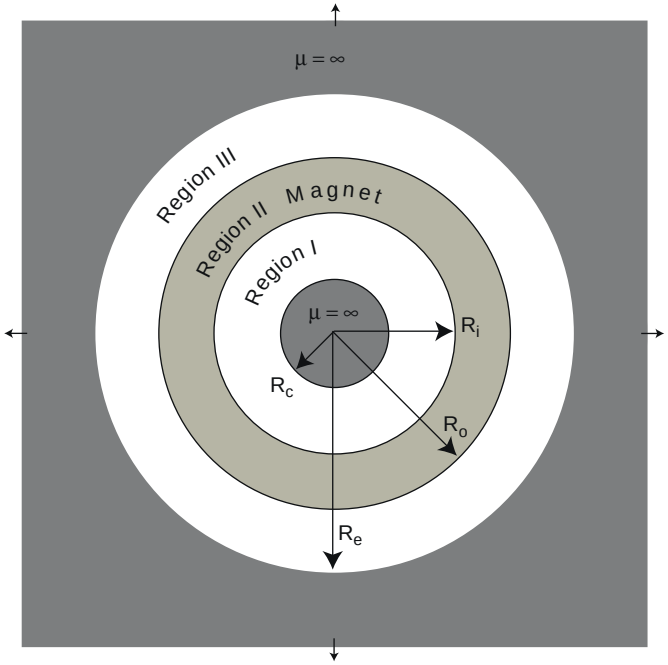

Fig. 2. A Halbach cylinder with inner radius R_i and outer radius R_o enclosing an infinitely permeable cylinder with radius R_c while itself being enclosed by another infinitely permeable cylinder with inner radius R_e and infinite outer radius. The regions marked I and III are air gaps.

the magnetic vector potential equation through the relation between the magnetic flux density, **B**, and the magnetic vector potential, **A**,

$$\mathbf{B} = \nabla \times \mathbf{A}. \tag{2}$$

If there are no currents present it is possible to express the magnetic vector potential as

$$-\nabla^2 \mathbf{A} = \nabla \times \mathbf{B}_{\text{rem}}. \tag{3}$$

For the two dimensional case considered here the vector potential only has a z-component, A_z, and the above equation, using Eq. (1), is reduced to

$$-\nabla^2 A_z(r,\phi) = \frac{B_{\text{rem}}}{r}(p+1)\sin(p\phi). \tag{4}$$

This differential equation constitutes the magnetic vector potential problem and must be solved. In the air region of the problem the right hand side reduces to zero as here $B_{\text{rem}} = 0$.

Once A_z has been determined Eq. (2) can be used to find the magnetic flux density. Afterwards the magnetic field, **H**, can be found through the relation

$$\mathbf{B} = \mu_0 \mu_r \mathbf{H} + \mathbf{B}_{\text{rem}}, \tag{5}$$

where μ_r is the relative permeability assumed to be isotropic and independent of **B** and **H**. This is generally the case for hard permanent magnetic materials.

2.1. Geometry of the problem

Having found the equation governing the magnetostatic problem of the Halbach cylinder we now take a closer look at the geometry of the problem. Following the approach of Xia et al. [11] we will start by solving the problem of a Halbach cylinder enclosing a cylinder of an infinitely permeable soft magnetic material, while at the same time itself being enclosed by another such cylinder. This is the situation depicted in Fig. 2. This configuration is important for e.g. motor applications. The Halbach cylinder has an inner radius of R_i and an outer radius of R_o and the inner infinitely permeable cylinder has a radius of R_c while the outer enclosing cylinder has a inner radius of R_e and an infinite outer radius. Later in this paper we will solve the magnetostatic problem of the Halbach cylinder in air by letting $R_c \to 0$ and $R_e \to \infty$. The use of the soft magnetic cylinders results in a well defined set of boundary equations as will be shown later. Of course one can also solve directly for the Halbach cylinder in air using the boundary conditions specific for this case.

When solving the magnetostatic problem three different expressions for the magnetic vector potential, field and flux density will be obtained, one for each of the three different regions shown in Fig. 2. The geometry of the problem results in six boundary conditions. The requirement is that the radial component of **B** and the parallel component of **H** are continuous across boundaries, i.e.

$$\begin{aligned}
&H_\phi^{\text{I}} = 0 \,|\, r = R_c,\\
&B_r^{\text{I}} = B_r^{\text{II}} \,|\, r = R_i,\\
&H_\phi^{\text{I}} = H_\phi^{\text{II}} \,|\, r = R_i,\\
&B_r^{\text{III}} = B_r^{\text{II}} \,|\, r = R_o,\\
&H\phi\text{III} = H_\phi^{\text{II}} \,|\, r = R_o,\\
&H_\phi^{\text{III}} = 0 \,|\, r = R_e.
\end{aligned} \tag{6}$$

The two equations for $H_\phi = 0$ come from the fact that the soft magnetic material has an infinite permeability.

2.2. Solution for the vector potential

The solution to the vector potential equation, Eq. (4), is the sum of the solution to the homogenous equation and a particular

solution. The solution is

$$A_z(r,\phi)=\sum_{n=1}^{\infty}(\mathcal{A}_n r^n+\mathcal{B}_n r^{-n})\sin(n\phi)+B_{\rm rem}\frac{r}{p-1}\sin(p\phi), \tag{7}$$

where $\mathcal{A}_n$ and $\mathcal{B}_n$ are constants that differ for each different region and that are different for each n. Using the boundary conditions for the geometry defined above one can show that these are only nonzero for $n=p$.

Thus the solution for the defined geometry becomes

$$A_z(r,\phi)=(\mathcal{A}r^p+\mathcal{B}r^{-p})\sin(p\phi)+B_{\rm rem}\frac{r}{p-1}\sin(p\phi), \tag{8}$$

where $\mathcal{A}$ and $\mathcal{B}$ are constants that differ for each different region and that are determined by boundary conditions.

The solution is not valid for $p=1$. For this special case the solution to Eq. (4) is instead

$$A_z(r,\phi)=(\mathcal{A}r+\mathcal{B}r^{-1})\sin(\phi)-B_{\rm rem}r\ln(r)\sin(\phi), \tag{9}$$

where $\mathcal{A}$ and $\mathcal{B}$ are defined like for Eq. (8).

Note that for $p=0$ we have that $B_{{\rm rem},r}=B_{\rm rem}$ and $B_{{\rm rem},\phi}=0$ in Eq. (1). This means that $A_z=0$ and consequently $\mathbf{B}$ is zero everywhere. The magnetic field, $\mathbf{H}$, however, will be nonzero inside the magnetic material itself, i.e. in region II, but will be zero everywhere else.

We now derive the constants in Eqs. (8) and (9) directly from the boundary conditions.

3. Deriving the vector potential constants

The constants of the vector potential equation can be derived from the boundary conditions specified in Eq. (6). We first derive the constants for the case of $p\neq 1$.

First we note that the magnetic flux density and the magnetic field can be calculated from the magnetic vector potential

$$B_r=\frac{1}{r}\frac{\partial A_z}{\partial\phi},\quad B_\phi=-\frac{\partial A_z}{\partial r},$$
$$H_r=\frac{1}{\mu_0\mu_r}(B_r-B_{{\rm rem},r}),\quad H_\phi=\frac{1}{\mu_0\mu_r}(B_\phi-B_{{\rm rem},\phi}). \tag{10}$$

Performing the differentiation gives

$$\begin{aligned}
B_r&=\left[p\mathcal{A}r^{p-1}+p\mathcal{B}r^{-p-1}+B_{\rm rem}\frac{p}{p-1}\right]\cos(p\phi),\\
B_\phi&=\left[-p\mathcal{A}r^{p-1}+p\mathcal{B}r^{-p-1}-B_{\rm rem}\frac{1}{p-1}\right]\sin(p\phi),\\
H_r&=\left[\frac{p}{\mu_0\mu_r}(\mathcal{A}r^{p-1}+\mathcal{B}r^{-p-1})+\frac{B_{\rm rem}}{\mu_r\mu_0}\left(\frac{p}{p-1}-1\right)\right]\cos(p\phi),\\
H_\phi&=\left[\frac{p}{\mu_0\mu_r}(-\mathcal{A}r^{p-1}+\mathcal{B}r^{-p-1})-\frac{B_{\rm rem}}{\mu_r\mu_0}\left(\frac{1}{p-1}-1\right)\right]\sin(p\phi).
\end{aligned} \tag{11}$$

Using the radial component of the magnetic flux density and the tangential component of the magnetic field in the set of boundary equations we get a set of six equations containing the six unknown constants, two for each region. The constants $\mathcal{A}$ and $\mathcal{B}$ will be termed $\mathcal{A}^{\rm I}$ and $\mathcal{B}^{\rm I}$ in region I, $\mathcal{A}^{\rm II}$ and $\mathcal{B}^{\rm II}$ in region II, and $\mathcal{A}^{\rm III}$ and $\mathcal{B}^{\rm III}$ in region III.

Introducing the following new constants:

$$a=\frac{R_{\rm e}^{2p}-R_{\rm o}^{2p}}{R_{\rm e}^{2p}+R_{\rm o}^{2p}},\quad b=-\frac{R_{\rm i}^{2p}-R_{\rm c}^{2p}}{R_{\rm i}^{2p}+R_{\rm c}^{2p}}, \tag{12}$$

the constants are determined to be

$$\mathcal{B}^{\rm II}=-\frac{R_{\rm o}^{1-p}-R_{\rm i}^{1-p}}{\frac{\mu_r a-1}{\mu_r a+1}R_{\rm o}^{-2p}-\frac{\mu_r b-1}{\mu_r b+1}R_{\rm i}^{-2p}}\frac{B_{\rm rem}}{p-1} \tag{13}$$

and

$$\begin{aligned}
\mathcal{A}^{\rm I}&=\frac{\mathcal{B}^{\rm II}}{R_{\rm i}^{2p}+R_{\rm c}^{2p}}\left(1-\frac{\mu_r b-1}{\mu_r b+1}\right),\\
\mathcal{B}^{\rm I}&=\mathcal{A}^{\rm I}R_{\rm c}^{2p},\\
\mathcal{A}^{\rm II}&=-\mathcal{B}^{\rm II}\frac{\mu_r a-1}{\mu_r a+1}R_{\rm o}^{-2p}-\frac{B_{\rm rem}}{p-1}R_{\rm o}^{1-p},\\
\mathcal{A}^{\rm III}&=\frac{\mathcal{B}^{\rm II}}{R_{\rm o}^{2p}+R_{\rm e}^{2p}}\left(1-\frac{\mu_r a-1}{\mu_r a+1}\right),\\
\mathcal{B}^{\rm III}&=\mathcal{A}^{\rm III}R_{\rm e}^{2p}.
\end{aligned} \tag{14}$$

Using these constants in Eqs. (8) and (11) allows one to calculate the magnetic vector potential, the magnetic flux density and the magnetic field, respectively.

The constants are not valid for $p=1$. The solution for this case will be derived in a later section.

3.1. Halbach cylinder in air

We can find the solution for a Halbach cylinder in air if we look at the solution for $R_{\rm e}\to\infty$ and $R_{\rm c}\to 0$. Looking at the previous expression for the constants a and b we see that

$$\begin{aligned}
\text{for } p>1:&\quad a\to 1,\quad b\to -1\\
\text{for } p<0:&\quad a\to -1,\quad b\to 1
\end{aligned} \tag{15}$$

in the limit defined above.

This means that the constant $\mathcal{B}^{\rm II}$ now becomes

$$\mathcal{B}^{\rm II}=\begin{cases}
-\dfrac{R_{\rm o}^{1-p}-R_{\rm i}^{1-p}}{\frac{\mu_r-1}{\mu_r+1}R_{\rm o}^{-2p}-\frac{\mu_r+1}{\mu_r-1}R_{\rm i}^{-2p}}\dfrac{B_{\rm rem}}{p-1} & p>1,\\
-\dfrac{R_{\rm o}^{1-p}-R_{\rm i}^{1-p}}{\frac{\mu_r+1}{\mu_r-1}R_{\rm o}^{-2p}-\frac{\mu_r-1}{\mu_r+1}R_{\rm i}^{-2p}}\dfrac{B_{\rm rem}}{p-1} & p<0
\end{cases} \tag{16}$$

and the remaining constants for $p>1$ become

$$\begin{bmatrix}\mathcal{A}^{\rm I}\\ \mathcal{B}^{\rm I}\\ \mathcal{A}^{\rm II}\\ \mathcal{A}^{\rm III}\\ \mathcal{B}^{\rm III}\end{bmatrix}=\begin{cases}
\mathcal{B}^{\rm II}R_{\rm i}^{-2p}\left(1-\frac{\mu_r+1}{\mu_r-1}\right),\\
0,\\
-\mathcal{B}^{\rm II}\frac{\mu_r-1}{\mu_r+1}R_{\rm o}^{-2p}-\frac{B_{\rm rem}}{p-1}R_{\rm o}^{1-p},\\
0,\\
\mathcal{B}^{\rm II}\left(1-\frac{\mu_r-1}{\mu_r+1}\right)
\end{cases} \tag{17}$$

while for $p<0$ they become

$$\begin{bmatrix}\mathcal{A}^{\rm I}\\ \mathcal{B}^{\rm I}\\ \mathcal{A}^{\rm II}\\ \mathcal{A}^{\rm III}\\ \mathcal{B}^{\rm III}\end{bmatrix}=\begin{cases}
0,\\
\mathcal{B}^{\rm II}\left(1-\frac{\mu_r-1}{\mu_r+1}\right),\\
-\mathcal{B}^{\rm II}\frac{\mu_r+1}{\mu_r-1}R_{\rm o}^{-2p}-\frac{B_{\rm rem}}{p-1}R_{\rm o}^{1-p},\\
\mathcal{B}^{\rm II}R_{\rm o}^{-2p}\left(1-\frac{\mu_r+1}{\mu_r-1}\right),\\
0.
\end{cases} \tag{18}$$

This is the solution for a Halbach cylinder in air. Note that the solution is only valid for $\mu_r \neq 1$. In the special case of $\mu_r = 1$ the constants can be reduced even further.

3.2. Halbach cylinder in air and $\mu_r = 1$

We now look at the special case of a Halbach cylinder in air with $\mu_r = 1$. This is a relevant case as e.g. the highest energy density type of permanent magnet produced today, the so-called neodymium–iron–boron (NdFeB) magnets have a relative permeability very close to one: $\mu_r = 1.05$ [13].

Using the approximation of $\mu_r \to 1$ for a Halbach cylinder in air reduces the constant $\mathcal{B}^{\mathrm{II}}$ to

$$\mathcal{B}^{\mathrm{II}} = 0. \tag{19}$$

The remaining constants depend on whether the Halbach cylinder produces an internal or external field.

For the internal field case, $p > 1$, the constant $\mathcal{A}^{\mathrm{II}}$ will be given by

$$\mathcal{A}^{\mathrm{II}} = -\frac{B_{\mathrm{rem}}}{p-1} R_{\mathrm{o}}^{1-p}. \tag{20}$$

The constant $\mathcal{A}^{\mathrm{I}}$ determining the field in the inner air region is equal to

$$\mathcal{A}^{\mathrm{I}} = \frac{B_{\mathrm{rem}}}{p-1}(R_{\mathrm{i}}^{1-p} - R_{\mathrm{o}}^{1-p}). \tag{21}$$

The remaining constants, $\mathcal{B}^{\mathrm{I}}$, $\mathcal{A}^{\mathrm{III}}$ and $\mathcal{B}^{\mathrm{III}}$ are zero.

Using Eq. (11) the two components of the magnetic flux density in both the cylinder bore, region I, and in the magnet, region II, can be found.

$$\begin{aligned}
B_r^{\mathrm{I}} &= \frac{B_{\mathrm{rem}} p}{p-1}\left(1 - \left(\frac{R_{\mathrm{i}}}{R_{\mathrm{o}}}\right)^{p-1}\right)\left(\frac{r}{R_{\mathrm{i}}}\right)^{p-1}\cos(p\phi),\\
B_\phi^{\mathrm{I}} &= -\frac{B_{\mathrm{rem}} p}{p-1}\left(1 - \left(\frac{R_{\mathrm{i}}}{R_{\mathrm{o}}}\right)^{p-1}\right)\left(\frac{r}{R_{\mathrm{i}}}\right)^{p-1}\sin(p\phi),\\
B_r^{\mathrm{II}} &= \frac{B_{\mathrm{rem}} p}{p-1}\left(1 - \left(\frac{r}{R_{\mathrm{o}}}\right)^{p-1}\right)\cos(p\phi),\\
B_\phi^{\mathrm{II}} &= -\frac{B_{\mathrm{rem}}}{p-1}\left(1 - p\left(\frac{r}{R_{\mathrm{o}}}\right)^{p-1}\right)\sin(p\phi).
\end{aligned} \tag{22}$$

Considering now the external field case, $p < 0$, the constant $\mathcal{A}^{\mathrm{II}}$ is given by

$$\mathcal{A}^{\mathrm{II}} = -\frac{B_{\mathrm{rem}}}{p-1} R_{\mathrm{i}}^{1-p}. \tag{23}$$

The constant $\mathcal{A}^{\mathrm{III}}$ determining the field in the outer air region is given by

$$\mathcal{A}^{\mathrm{III}} = \frac{B_{\mathrm{rem}}}{p-1}(R_{\mathrm{o}}^{p-1} - R_{\mathrm{i}}^{p-1}). \tag{24}$$

The remaining constants, $\mathcal{A}^{\mathrm{I}}$, $\mathcal{B}^{\mathrm{I}}$ and $\mathcal{B}^{\mathrm{III}}$, are zero.

Again using Eq. (11) we find the two components of the magnetic flux density in regions II and III to be

$$\begin{aligned}
B_r^{\mathrm{III}} &= \frac{B_{\mathrm{rem}} p}{p-1}\left(1 - \left(\frac{R_{\mathrm{i}}}{R_{\mathrm{o}}}\right)^{-p+1}\right)\left(\frac{R_{\mathrm{o}}}{r}\right)^{-p+1}\cos(p\phi),\\
B_\phi^{\mathrm{III}} &= -\frac{B_{\mathrm{rem}} p}{p-1}\left(1 - \left(\frac{R_{\mathrm{i}}}{R_{\mathrm{o}}}\right)^{-p+1}\right)\left(\frac{R_{\mathrm{o}}}{r}\right)^{-p+1}\sin(p\phi),\\
B_r^{\mathrm{II}} &= \frac{B_{\mathrm{rem}} p}{p-1}\left(1 - \left(\frac{R_{\mathrm{i}}}{r}\right)^{-p+1}\right)\cos(p\phi),\\
B_\phi^{\mathrm{II}} &= -\frac{B_{\mathrm{rem}}}{p-1}\left(1 - p\left(\frac{R_{\mathrm{i}}}{r}\right)^{-p+1}\right)\sin(p\phi).
\end{aligned} \tag{25}$$

The equations for B_r^{III} and B_ϕ^{III} are identical to the expressions for B_r^{I} and B_ϕ^{I} in Eq. (22) except for a minus sign in both equations.

3.3. The constants for a $p = 1$ Halbach cylinder

Having determined the solution to the vector potential equation and found the constants in the expression for the magnetic flux density and the magnetic vector potential for a Halbach cylinder both in air and enclosed by a soft magnetic cylinder for all cases except $p = 1$ we now turn to this specific case. This case is shown in Fig. 1. We have already shown that the solution to the vector potential problem for this case is given by Eq. (9). The boundary conditions are the same as previous, i.e. they are given by Eq. (6).

In order to find the constants the components of the magnetic field and the magnetic flux density must be calculated for $p = 1$ as the boundary conditions relate to these fields. Using Eq. (10) we obtain

$$\begin{aligned}
B_r &= [\mathcal{A} + \mathcal{B} r^{-2} - B_{\mathrm{rem}}\ln(r)]\cos(\phi),\\
B_\phi &= [-\mathcal{A} + \mathcal{B} r^{-2} + B_{\mathrm{rem}}(\ln(r)+1)]\sin(\phi),\\
H_r &= \frac{1}{\mu_0\mu_r}[\mathcal{A} + \mathcal{B} r^{-2} - B_{\mathrm{rem}}(\ln(r)+1)]\cos(\phi),\\
H_\phi &= \frac{1}{\mu_0\mu_r}[-\mathcal{A} + \mathcal{B} r^{-2} + B_{\mathrm{rem}}\ln(r)]\sin(\phi).
\end{aligned} \tag{26}$$

Using these expressions for the magnetic flux density and the magnetic field we can again write a set of six equations through which we can determine the six constants, two for each region.

Reintroducing the two constants from Eq. (12)

$$a = \frac{R_{\mathrm{e}}^2 - R_{\mathrm{o}}^2}{R_{\mathrm{e}}^2 + R_{\mathrm{o}}^2}, \quad b = -\frac{R_{\mathrm{i}}^2 - R_{\mathrm{c}}^2}{R_{\mathrm{i}}^2 + R_{\mathrm{c}}^2}, \tag{27}$$

the following equations for the constants are obtained:

$$\begin{aligned}
\mathcal{A}^{\mathrm{I}} &= \frac{\mathcal{B}^{\mathrm{II}}}{R_{\mathrm{i}}^2 + R_{\mathrm{c}}^2}\left(1 - \frac{\mu_r b - 1}{\mu_r b + 1}\right),\\
\mathcal{B}^{\mathrm{I}} &= \mathcal{A}^{\mathrm{I}} R_{\mathrm{c}}^2,\\
\mathcal{A}^{\mathrm{II}} &= -\mathcal{B}^{\mathrm{II}}\frac{\mu_r a - 1}{\mu_r a + 1} R_{\mathrm{o}}^{-2} + B_{\mathrm{rem}}\ln(R_{\mathrm{o}}),\\
\mathcal{B}^{\mathrm{II}} &= -\left(\frac{a\mu_r - 1}{a\mu_r + 1} R_{\mathrm{o}}^{-2} - \frac{\mu_r b - 1}{\mu_r b + 1} R_{\mathrm{i}}^{-2}\right)^{-1} B_{\mathrm{rem}}\ln\left(\frac{R_{\mathrm{i}}}{R_{\mathrm{o}}}\right),\\
\mathcal{A}^{\mathrm{III}} &= \frac{\mathcal{B}^{\mathrm{II}}}{R_{\mathrm{e}}^2 + R_{\mathrm{o}}^2}\left(1 - \frac{\mu_r a - 1}{\mu_r a + 1}\right),\\
\mathcal{B}^{\mathrm{III}} &= \mathcal{A}^{\mathrm{III}} R_{\mathrm{e}}^2.
\end{aligned} \tag{28}$$

We see that the constants $\mathcal{A}^{\mathrm{I}}$, $\mathcal{B}^{\mathrm{I}}$, $\mathcal{A}^{\mathrm{III}}$ and $\mathcal{B}^{\mathrm{III}}$ are identical to the constants in Eq. (14).

The magnetic flux density and the magnetic field can now be found through the use of Eq. (26).

3.4. Halbach cylinder in air, $p = 1$

We can find the solution for a $p = 1$ Halbach cylinder in air if we look at the solution for $R_{\mathrm{e}} \to \infty$ and $R_{\mathrm{c}} \to 0$. In this limit the previously introduced constants are reduced to

$$a \to 1, \quad b \to -1. \tag{29}$$

The expressions for the constants can then be reduced to

$$\begin{aligned}
\mathcal{A}^{\mathrm{I}} &= \mathcal{B}^{\mathrm{II}} R_{\mathrm{i}}^{-2}\left(1 - \frac{\mu_r + 1}{\mu_r - 1}\right),\\
\mathcal{B}^{\mathrm{I}} &= 0,
\end{aligned}$$

$$\mathcal{A}^{\mathrm{II}} = -\mathcal{B}^{\mathrm{II}}\frac{\mu_r-1}{\mu_r+1}R_{\mathrm{o}}^{-2}+B_{\mathrm{rem}}\ln(R_{\mathrm{o}}),$$
$$\mathcal{B}^{\mathrm{II}} = -\left(\frac{\mu_r-1}{\mu_r+1}R_{\mathrm{o}}^{-2}-\frac{\mu_r+1}{\mu_r-1}R_{\mathrm{i}}^{-2}\right)^{-1}B_{\mathrm{rem}}\ln\left(\frac{R_{\mathrm{i}}}{R_{\mathrm{o}}}\right),$$
$$\mathcal{A}^{\mathrm{III}} = 0,$$
$$\mathcal{B}^{\mathrm{III}} = \mathcal{B}^{\mathrm{II}}\left(1-\frac{\mu_r-1}{\mu_r+1}\right). \tag{30}$$

Again we see that the constants $\mathcal{A}^{\mathrm{I}}$, $\mathcal{B}^{\mathrm{I}}$, $\mathcal{A}^{\mathrm{III}}$ and $\mathcal{B}^{\mathrm{III}}$ are equal to the constants in Eq. (17). This solution is valid for all μ_r except $\mu_r = 1$.

Combining the above constants with Eq. (26) we see that the magnetic flux density in the cylinder bore is a constant, and that its magnitude is given by

$$\|\mathbf{B}^{\mathrm{I}}\| = \left(\frac{\mu_r-1}{\mu_r+1}R_{\mathrm{o}}^{-2}-\frac{\mu_r+1}{\mu_r-1}R_{\mathrm{i}}^{-2}\right)^{-1}\left(\frac{\mu_r+1}{\mu_r-1}-1\right)R_{\mathrm{i}}^{-2}B_{\mathrm{rem}}\ln\left(\frac{R_{\mathrm{i}}}{R_{\mathrm{o}}}\right), \tag{31}$$

for $\mu_r \neq 1$.

3.5. Halbach cylinder in air, $p = 1$ and $\mu_r = 1$

For the special case of $\mu_r = 1$ for a $p = 1$ Halbach cylinder in air the constants can be reduced further to

$$\mathcal{A}^{\mathrm{I}} = B_{\mathrm{rem}}\ln\left(\frac{R_{\mathrm{o}}}{R_{\mathrm{i}}}\right), \quad \mathcal{A}^{\mathrm{II}} = B_{\mathrm{rem}}\ln(R_{\mathrm{o}}), \quad \mathcal{B}^{\mathrm{I}}, \mathcal{B}^{\mathrm{II}}, \mathcal{A}^{\mathrm{III}}, \mathcal{B}^{\mathrm{III}} = 0. \tag{32}$$

Combining the above constants with Eq. (26) one can find the magnetic flux density in the bore, region I, and in the magnet, region II,

$$B_r^{\mathrm{I}} = B_{\mathrm{rem}}\ln\left(\frac{R_{\mathrm{o}}}{R_{\mathrm{i}}}\right)\cos(\phi),$$
$$B_\phi^{\mathrm{I}} = -B_{\mathrm{rem}}\ln\left(\frac{R_{\mathrm{o}}}{R_{\mathrm{i}}}\right)\sin(\phi),$$
$$B_r^{\mathrm{II}} = B_{\mathrm{rem}}\ln\left(\frac{R_{\mathrm{o}}}{r}\right)\cos(\phi),$$
$$B_\phi^{\mathrm{II}} = -B_{\mathrm{rem}}\left(\ln\left(\frac{R_{\mathrm{o}}}{r}\right)-1\right)\sin(\phi). \tag{33}$$

As for the case of $\mu_r \neq 1$ the magnetic flux density in the cylinder bore is a constant. The magnitude of the magnetic flux density in the bore is given by

$$\|\mathbf{B}^{I}\| = B_{\mathrm{rem}}\ln\left(\frac{R_{\mathrm{o}}}{R_{\mathrm{i}}}\right), \tag{34}$$

which we recognize as the well known Halbach formula [2].

3.6. Validity of the solutions

To show the validity of the analytical solutions we compare these with a numerical calculation of the vector potential and the magnetic flux density.

We have chosen to show a comparison between the expressions derived in this paper and numerical calculations for two selected cases. These are shown in Figs. 3 and 4.

In Fig. 3 the magnitude of the magnetic flux density is shown for an enclosed Halbach cylinder. Also shown in Fig. 3 is a numerical calculation done using the commercially available finite element multiphysics program, *Comsol Multiphysics* [14]. The Comsol Multiphysics code has previously been validated through a number of NAFEMS (National Agency for Finite Element Methods and Standards) benchmark studies [15]. As can be seen the analytical solution closely matches the numerical solution.

In Fig. 4 we show the magnetic vector potential, A_z, as calculated using Eqs. (8) and (18) compared with a numerical Comsol simulation. As can be seen the analytical solution again closely matches the numerical solution.

We have also tested the expressions for the magnetic flux density given by Xia et al. [11] and compared them with those derived in this paper and with numerical calculations. Unfortunately the equations given by Xia et al. [11] contain erroneous expressions for the magnetic flux density of a Halbach cylinder in air with $\mu_r = 1$ as well as for the expression for a Halbach cylinder with internal field enclosed by soft magnetic material.

4. Force between two concentric Halbach cylinders

Having found the expressions for the magnetic vector potential and the magnetic flux density for a Halbach cylinder we now turn to the problem of calculating the force between two concentric Halbach cylinders, e.g. a situation as shown in Fig. 5. In a later section we will calculate the torque for the same configuration. This configuration is interesting for e.g. motor applications and

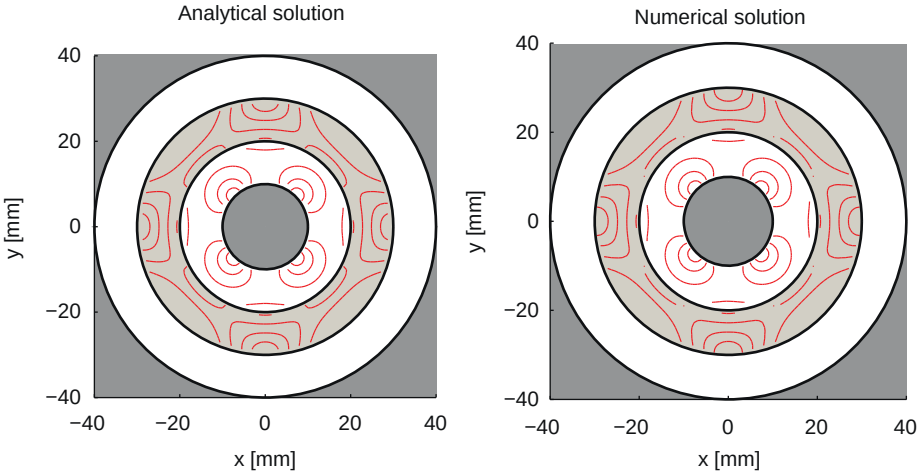

Fig. 3. (Color online) Comparing the analytical solution as given by Eqs. (11) and (14) with a numerical solution computed using Comsol. Shown are contours of $\|\mathbf{B}\| = [0.3, 0.5, 0.7, 0.9]$ T for an internal field $p = 2$ enclosed Halbach cylinder with dimensions $R_{\mathrm{c}} = 10$ mm, $R_{\mathrm{i}} = 20$ mm, $R_{\mathrm{o}} = 30$ mm, $R_{\mathrm{e}} = 40$ mm, and $B_{\mathrm{rem}} = 1.4$ T, $\mu_r = 1.05$. The solutions are seen to be identical. The shaded areas in the figures correspond to the similar shaded areas in Fig. 2.

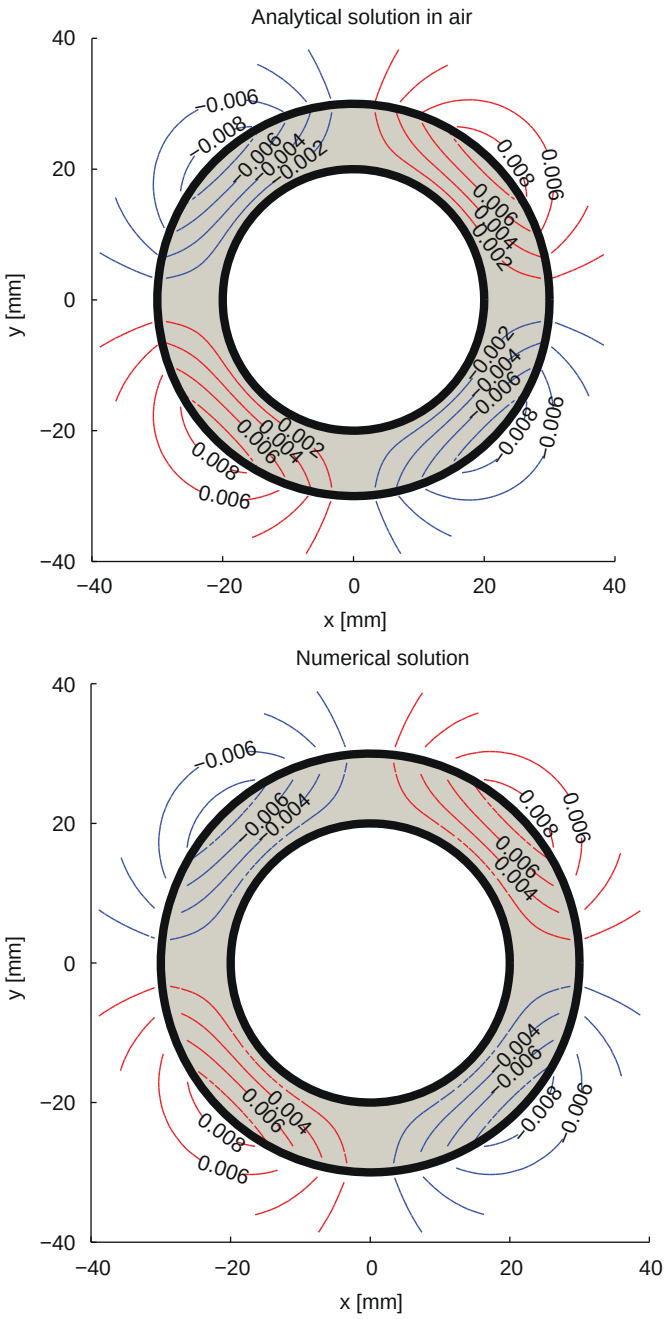

Fig. 4. (Color online) Comparing the analytical solution as given by Eqs. (8) and (18) with a numerical solution computed using Comsol. Shown are contours of $A_z = \pm[0.002, 0.004, 0.006, 0.008]\,\mathrm{V\,s\,m^{-1}}$ for an external field $p = -2$ Halbach cylinder in air with dimensions $R_i = 20\,\mathrm{mm}$, $R_o = 30\,\mathrm{mm}$ and $B_{rem} = 1.4\,\mathrm{T}$, $\mu_r = 1.05$. The red contours are positive values of A_z while the blue are negative values. As with Fig. 3 the solutions are seen to be identical. (For interpretation of the references to color in this figure legend, the reader is referred to the web version of this article.)

drives as well as applications where the magnetic flux density must be turned "on" and "off" without the magnet being displaced in space [7].

The force between the two Halbach cylinders can be calculated by using the Maxwell stress tensor, $\overleftrightarrow{\mathbf{T}}$, formulation. The force per unit length is given by

$$\mathbf{F} = \frac{1}{\mu_0}\oint_S \overleftrightarrow{\mathbf{T}}\, dS. \tag{35}$$

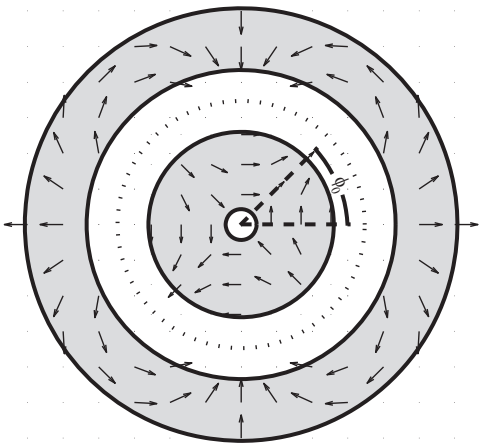

Fig. 5. An example of a concentric Halbach cylinder configuration for which the force and torque is calculated. The outer magnet has $p = 2$ while the inner magnet is a $p = -2$. The inner magnet has also been rotated an angle of $\phi_0 = 45^\circ$. The dotted circle indicates a possible integration path.

The Cartesian components of the force are given by

$$F_x = \frac{1}{\mu_0}\oint_S (T_{xx}n_x + T_{xy}n_y)\,ds, \quad F_y = \frac{1}{\mu_0}\oint_S (T_{yy}n_y + T_{yx}n_x)\,ds, \tag{36}$$

where n_x and n_y are the Cartesian components of the outwards normal to the integration surface and where T_{xx}, T_{yy} and T_{xy} are the components of the Maxwell stress tensor which are given by

$$T_{xx} = B_x^2 - \tfrac{1}{2}(B_x^2 + B_y^2), \quad T_{yy} = B_y^2 - \tfrac{1}{2}(B_x^2 + B_y^2), \quad T_{xy}, T_{yx} = B_xB_y. \tag{37}$$

When using the above formulation to calculate the force a closed integration surface in free space that surrounds the object must be chosen. As this is a two dimensional problem the surface integral is reduced to a line integral along the air gap between the magnets. If a circle of radius r is taken as the integration path, the Cartesian components of the outwards normal are given by

$$n_x = \cos(\phi), \quad n_y = \sin(\phi). \tag{38}$$

Expressing the Cartesian components through the polar components as

$$B_x = B_r\cos(\phi) - B_\phi\sin(\phi), \quad B_y = B_r\sin(\phi) + B_\phi\cos(\phi), \tag{39}$$

the relation for computing the force per unit length becomes

$$F_x = \frac{r}{\mu_0}\int_0^{2\pi}\left(\frac{1}{2}(B_r^2 - B_\phi^2)\cos(\phi) - B_rB_\phi\sin(\phi)\right)d\phi,$$
$$F_y = \frac{r}{\mu_0}\int_0^{2\pi}\left(\frac{1}{2}(B_r^2 - B_\phi^2)\sin(\phi) + B_rB_\phi\cos(\phi)\right)d\phi, \tag{40}$$

where r is some radius in the air gap. The computed force will turn out to be independent of the radius r as expected.

We consider the scenario where the outer magnet is kept fixed and the internal magnet is rotated by an angle ϕ_0, as shown in Fig. 5. Both cylinders are centered on the same axis. Both of the cylinders are considered to be in air and have a relative permeability of one, $\mu_r = 1$, so that their magnetic flux density is given by Eqs. (22) and (25) for $p \neq 1$. For $p = 1$ Eq. (33) applies instead.

As $\mu_r = 1$ the magnetic flux density in the air gap between the magnets will be a sum of two terms, namely a term from the outer magnet and a term from the inner magnet. If the relative permeability were different from one the magnetic flux density of one of the magnets would influence the magnetic flux density of the other, and we would have to solve the vector potential

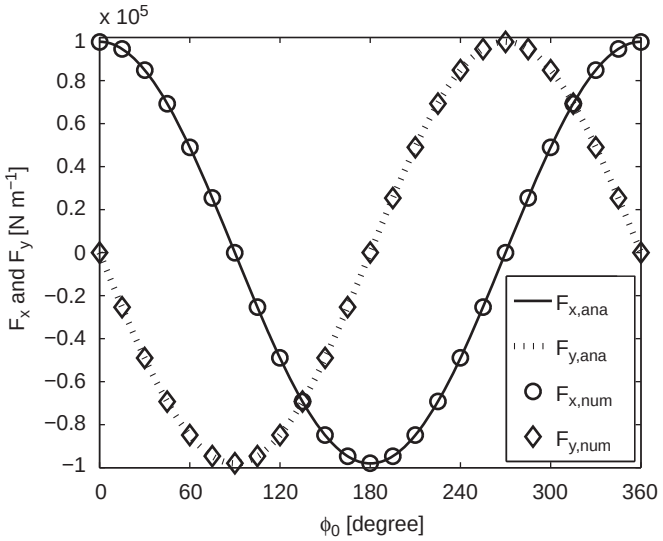

Fig. 6. The two cartesian components of the force per unit length given by Eq. (42) compared with a Comsol calculation for a system where the outer magnet has $p_2 = 2$, $R_{i,2} = 45$ mm, $R_{o,2} = 75$ mm and $B_{rem,2} = 1.4$ T and the inner magnet has $p_1 = -1$, $R_{i,1} = 15$ mm, $R_{o,1} = 35$ mm and $B_{rem,1} = 1.4$ T. The analytical expression is in excellent agreement with the numerical data. The force is per unit length as we consider a two dimensional system.

equation for both magnets at the same time in order to find the magnetic flux density in the air gap.

Assuming the above requirements the flux density in the air gap is thus given by

$$B_r = B^{III}_{r,1} + B^{I}_{r,2}, \quad B_\phi = B^{III}_{\phi,1} + B^{I}_{\phi,2}, \tag{41}$$

where the second subscript refers to either of the two magnets. The inner magnet is termed "1" and the outer magnet termed "2", e.g. $R_{o,1}$ is the inner magnets outer radius. The integer p_1 thus refers to the inner magnet and p_2 to the outer magnet.

There can only be a force between the cylinders if the inner cylinder produces an external field and the outer cylinder produces an internal field. Otherwise the flux density in the gap between the magnets will be produced solely by one of the magnets and the force will be zero.

Performing the integrals in Eq. (40) one only obtains a nonzero solution for $p_1 = 1 - p_2$ and $p_2 > 1$. In this case the solution is

$$F_x = \frac{2\pi}{\mu_0} K \cos(p_1 \phi_0), \quad F_y = \frac{2\pi}{\mu_0} K \sin(p_1 \phi_0), \tag{42}$$

where K is a constant given by

$$K = B_{rem,1} B_{rem,2} (R^{p_1}_{i,2} - R^{p_1}_{o,2})(R^{p_2}_{o,1} - R^{p_2}_{i,1}). \tag{43}$$

Notice that the force is independent of r, as expected.

In Fig. 6 we compare the above equation with a numerical calculation of the force. The results are seen to be in excellent agreement. Notice that the forces never balance the magnets, i.e. when F_x is zero, F_y is nonzero and vice versa.

If $p_2 = 1$ the magnetic flux density produced by the outer magnet is not given by Eq. (22) but is instead given by Eq. (33). However, this equation has the same angular dependence as Eq. (22) and thus the force will also be zero for this case.

5. Torque between two concentric nested Halbach cylinders

Having calculated the force between two concentric Halbach cylinders we now focus on calculating the torque for the same system.

The torque can also be calculated by using the Maxwell stress tensor, $\overleftrightarrow{\mathbf{T}}$, formulation. The torque per unit length is given by

$$\tau = \frac{1}{\mu_0} \oint_S \mathbf{r} \times \overleftrightarrow{\mathbf{T}}\, dS = \frac{1}{\mu_0} \oint_S \mathbf{r} \left((\mathbf{B} \cdot \mathbf{n})\mathbf{B} - \frac{1}{2}\mathbf{B}^2 \mathbf{n} \right) dS, \tag{44}$$

where again the integration surface is a closed loop in free space that surrounds the object. Again choosing a circle of radius r as the integration path, the relation for computing the torque per unit length around the central axis becomes

$$\tau = \frac{1}{\mu_0} \int_0^{2\pi} r^2 B_r B_\phi \, d\phi, \tag{45}$$

where B_r and B_ϕ are the radial and tangential components of the magnetic flux density in the air gap and r is some radius in the air gap. Again the computed torque will be shown to be independent of the radius r when r varies between the inner and outer radii of the air gap.

We consider the same case as with the force calculation, i.e. the outer magnet is kept fixed, both magnets have the same axis, the internal magnet is rotated by an angle ϕ_0 and both of the cylinders are considered to be in air and have a relative permeability of one. Again there can only be a torque between the cylinders if the inner cylinder produces an external field and the outer cylinder produces an internal field.

To find the torque per unit length we must thus integrate

$$\tau = \frac{1}{\mu_0} \int_0^{2\pi} r^2 (B^{III}_{r,1} + B^{I}_{r,2})(B^{III}_{\phi,1} + B^{I}_{\phi,2}) \, d\phi. \tag{46}$$

This integration will be zero except when $p_1 = -p_2$. For this special case the integral gives

$$\tau = \frac{2\pi}{\mu_0} \frac{p_2^2}{1 - p_2^2} K_1 K_2 \sin(p_2 \phi_0), \tag{47}$$

where the constants K_1 and K_2 are given by

$$K_1 = B_{rem,2}(R^{1-p_2}_{i,2} - R^{1-p_2}_{o,2}), \quad K_2 = B_{rem,1}(R^{p_2+1}_{o,1} - R^{p_2+1}_{i,1}). \tag{48}$$

The validity of this expression will be shown in the next section. It is seen that there are p_2 periods per rotation.

For $p_2 = 1$ the expression for the magnetic flux density produced by the outer magnet is not given by Eq. (22) but instead by Eq. (33), and so we must look at this special case separately.

5.1. The special case of $p_2 = 1$

For the special case of a $p_2 = 1$ outer magnet the flux density produced by this magnet in the air gap will be given by Eq. (33). The external field produced by the inner magnet is still given by Eq. (25).

Performing the integration defined in Eq. (46) again gives zero except when $p_2 = 1$ and $p_1 = -1$. The expression for the torque becomes

$$\tau = -\frac{\pi}{\mu_0} K_2 K_3 \sin(\phi_0), \tag{49}$$

Table 1
The parameters for the two cases shown in Figs. 7 and 8.

	Magnet	R_i [mm]	R_o [mm]	p	B_{rem} [T]
Case 1:	Inner	5	15	−2	1.4
	Outer	20	30	2	1.4
Case 2:	Inner	10	35	−1	1.4
	Outer	45	75	1	1.4

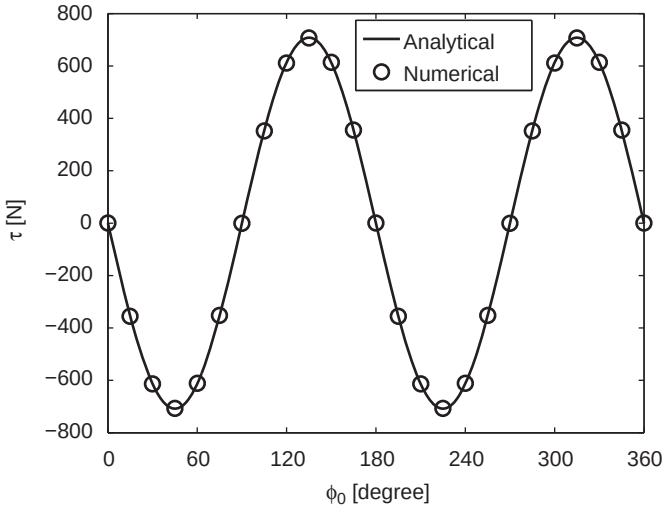

Fig. 7. A numerical calculation of the torque per unit length between two concentric Halbach cylinders compared with the expression given in Eq. (47) for the physical properties given for Case 1 in Table 1. The analytical expression is in excellent agreement with the numerical data. τ is per unit length as we consider a two dimensional system.

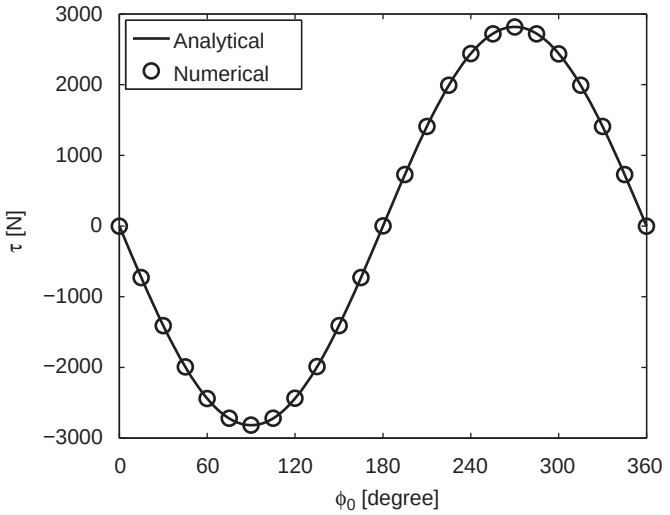

Fig. 8. The torque per unit length given by Eq. (49) compared with a numerical calculation for the physical properties given for Case 2 in Table 1. As with the case for $p_2 \neq 1$, i.e. Fig. 7, the analytical expression is in excellent agreement with the numerical data. τ is per unit length as we consider a two dimensional system.

where the two constants K_2 and K_3 are given by

$$K_2 = B_{\mathrm{rem},1}(R_{\mathrm{o},1}^2 - R_{\mathrm{i},1}^2), \quad K_3 = B_{\mathrm{rem},2}\ln\left(\frac{R_{\mathrm{o},2}}{R_{\mathrm{i},2}}\right). \tag{50}$$

Note that K_2 is identical to the constant K_2 in Eq. (48) for $p_2 = 1$. We also see that Eq. (49) is in fact just $\tau = \mathbf{m} \times \mathbf{B}$ for a dipole in a uniform field times the area of the magnet.

5.2. Validating the expressions for the torque

We have shown that there is only a torque between two Halbach cylinders if $p_1 = -p_2$ for $p_2 > 0$, with the torque being given by Eq. (47) for $p_2 \neq 1$ and Eq. (49) for $p_2 = 1$.

To verify the expressions given in Eqs. (47) and (49) we have computed the torque as a function of the angle of displacement, ϕ_0, for the two cases given in Table 1, and compared this with a numerical calculation performed using Comsol. The results can be seen in Figs. 7 and 8.

As can be seen from the figures the torque as given by Eqs. (47) and (49) are in excellent agreement with the numerical results.

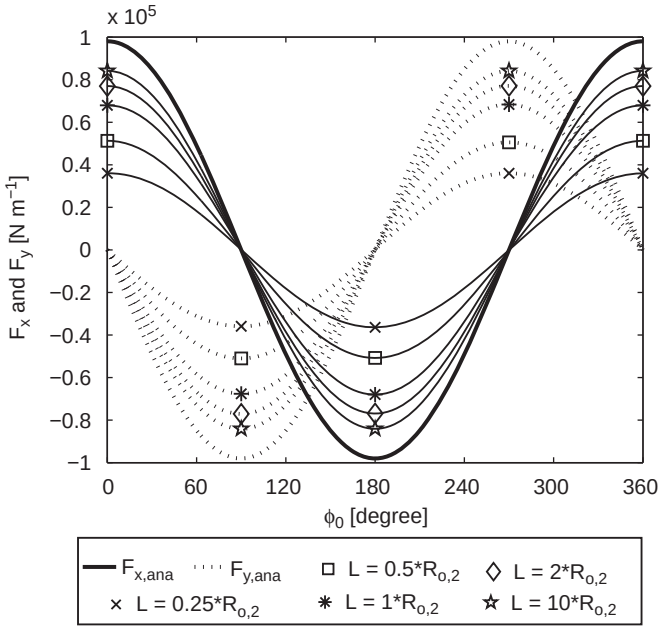

Fig. 9. The two cartesian components of the force per unit length for a three dimensional system with dimensions as those given in Fig. 6. The analytical expressions as well as the results of a three dimensional numerical simulation are shown.

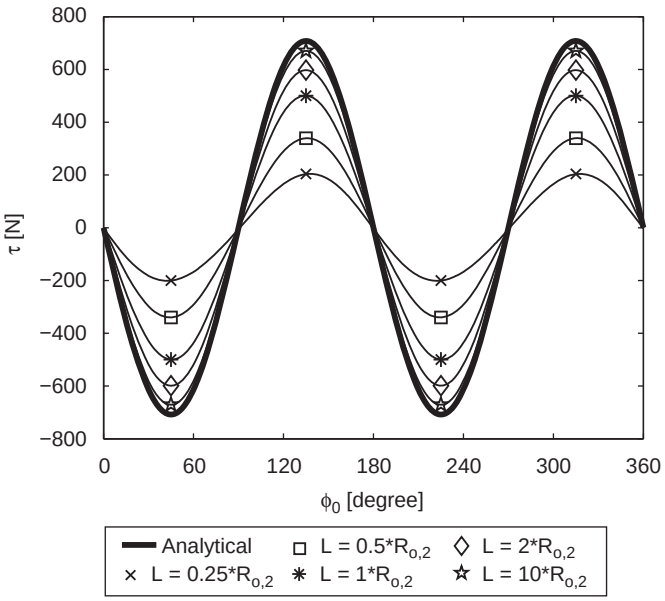

Fig. 10. The torque per unit length for a three dimensional system with dimensions as those given as Case 1 in Table 1. The analytical expressions as well as the results of a three dimensional numerical simulation are shown.

6. Force and torque for finite length cylinders

The force and torque for finite length cylinders will be different than the analytical expressions derived above, because of flux leakage through the ends of the cylinder bore.

To investigate the significance of this effect three dimensional numerical simulations of a finite length system corresponding to the system shown in Fig. 6 has been performed using Comsol. For this system the force has been calculated per unit length for different lengths. The results of these calculations are shown in Fig. 9. From this figure it can be seen that as the length of the system is increased the force becomes better approximated by the analytical expression of Eq. (42). A short system produces a lower force due to the leakage of flux through the ends of the cylinder. However, even for relatively short systems the two-dimensional results give the right order of magnitude and the correct angular dependence of the force.

Similarly, the torque for a three dimensional system has been considered. Here the system given as Case 1 in Table 1 was considered. Numerical simulations calculating the torque were performed, similar to the force calculations, and the results are shown in Fig. 10. The results are seen to be similar to Fig. 9. The torque approaches the analytical expression as the length of the system is increased. As before the two dimensional results are still qualitatively correct.

Above we have considered cases where the two dimensional results predict a force ($p_1 = 1 - p_2$) or a torque ($p_1 = -p_2$). However, for finite length systems a force or a torque can be presented in other cases. One such case is given by Mhiochain et al. [12] who report a maximum torque of $\approx 12\,\mathrm{N\,m}$ for a system where both magnets have $p = 1$, are segmented into eight pieces and where the outer magnet has $R_{i,2} = 52.5\,\mathrm{mm}$, $R_{o,2} = 110\,\mathrm{mm}$, $L_2 = 100\,\mathrm{mm}$ and $B_{rem,2} = 1.17\,\mathrm{T}$ and the inner magnet has $R_{i,1} = 47.5\,\mathrm{mm}$, $R_{o,1} = 26\,\mathrm{mm}$, $L_1 = 100\,\mathrm{mm}$ and $B_{rem,1} = 1.08\,\mathrm{T}$. This torque is produced mainly by the effect of finite length and to a lesser degree by segmentation. The torque produced by this system is $\approx 120\,\mathrm{N}$ per unit length, which is significant compared to the expected analytical value of zero. The torque for finite length systems with $p_1 \neq -p_2$ is, as noted above, a higher order effect. This makes it significantly smaller per unit length than for the corresponding system with $p_1 = -p_2$.

The end effects due to a finite length of the system can be remedied by several different techniques. By covering the ends of the concentric cylinder with magnet blocks in the shape of an equipotential surface, all of the flux can be confined inside the Halbach cylinder [16]. Unfortunately this also blocks access to the cylinder bore. The homogeneity of the flux density can also be improved by shimming, i.e. placing small magnets or soft magnetic material to improve the homogeneity [17–19]. Finally by sloping the cylinder bore or by placing strategic cuts in the magnet the homogeneity can also be improved [20]. However, especially the last two methods can lower the flux density in the bore significantly.

7. Discussion and conclusion

We have derived expressions for the magnetic vector potential, magnetic flux density and magnetic field for a two dimensional Halbach cylinder and compared these with numerical results.

The force between two concentric Halbach cylinders was calculated and it was found that the result depends on the integer p in the expression for the remanence. If p for the inner and outer magnet is termed p_1 and p_2, respectively, it was shown that unless $p_1 = 1 - p_2$ there is no force. The torque was also calculated for a similar system and it was shown that unless $p_1 = -p_2$ there is no torque. We compared the analytical expressions for the force and torque to numerical calculations and found an excellent agreement. Note that either there can be a force or a torque, but not both.

The derived expressions for the magnetic vector potential, flux density and field can be used to do e.g. quick parameter variation studies of Halbach cylinders, as they are much more simple than the corresponding three dimensional expressions.

An interesting use for the derived expressions for the magnetic flux density would be to derive expressions for the force between two concentric Halbach cylinders, where one of the cylinders has been slightly displaced. One could also consider the effect of segmentation of the Halbach cylinder, and of course the effect of a finite length in greater detail. Both effects will in general result in a nonzero force and torque for other choices of p_1 and p_2, but as shown these will in general be smaller than for the $p_1 = 1 - p_2$ and $p_1 = -p_2$ cases.

It is also worth considering computing the force and torque for Halbach cylinders with $\mu_r \neq 1$. Here one would have to solve the complete magnetostatic problem of the two concentric Halbach cylinders to find the magnetic flux density in the gap between the cylinders.

Acknowledgements

The authors would like to acknowledge the support of the Programme Commission on Energy and Environment (EnMi) (Contract no. 2104-06-0032) which is part of the Danish Council for Strategic Research.

References

[1] J.C. Mallinson, IEEE Trans. Magn. 9 (4) (1973) 678.
[2] K. Halbach, Nucl. Instrum. Methods 169 (1980).
[3] Z.Q. Zhu, D. Howe, IEE Proc. Elec. Power. Appl. 148 (4) (2001) 299.
[4] J.M.D. Coey, J. Magn. Magn. Mater. 248 (2002) 441.
[5] S. Appelt, H. Kühn, F.W. Häsing, B. Blümich, Nat. Phys. 2 (2006) 105.
[6] J.K. Lim, P. Frigola, G. Travish, J.B. Rosenzweig, S.G. Anderson, W.J. Brown, J.S. Jacob, C.L. Robbins, A.M. Tremaine, Phys. Rev. ST Accel. Beams 8 (2005) 072401.
[7] A. Tura, A. Rowe, in: Proceedings of the Second International Conference on Magnetic Refrigeration at Room Temperature, Portoroz, Solvenia, IIF/IIR:363, 2007.
[8] Z.Q. Zhu, D. Howe, E. Bolte, B. Ackermann, IEEE Trans. Magn. 29 (12) (1993) 124.
[9] K. Atallah, D. Howe, P.H. Mellor, in: Eighth International Conference on Electric Machine and Drive (Conf. Publ. No. 444), 1997, p. 376.
[10] Q. Peng, S.M. McMurry, J.M.D. Coey, IEEE Trans. Magn. 39 (42) (2003) 1983.
[11] Z.P. Xia, Z.Q. Zhu, D. Howe, IEEE Trans. Magn. 40 (2004) 1864.
[12] T.R. Ni Mhiochain, D. Weaire, S.M. McMurry, J.M.D. Coey, J. Appl. Phys. 86 (1999) 6412.
[13] Standard Specifications for Permanent Magnet Materials, Magnetic Materials Producers Association, Chicago, USA.
[14] COMSOL AB, Tegnérgatan 23, SE-111 40 Stockholm, Sweden.
[15] Comsol, Comsol Multiphysics Model Library, third ed. COMSOL AB, Chalmers Teknikpark 412 88 G, 2005.
[16] E. Potenziani, J.P. Clarke, H.A. Leupold, J. Appl. Phys. 61 (1987) 3466.
[17] M.G. Abele, H. Rusinek, W. Tsui, J. Appl. Phys. 99 (8) (2006) 903.
[18] R. Bjørk, C.R.H. Bahl, A. Smith, N. Pryds, J. Appl. Phys. 104 (2008) 13910.
[19] A. Rowe, A. Tura, J. Magn. Magn. Mater. 320 (2008) 1357.
[20] J.E. Hilton, S.M. McMurry, IEEE Trans. Magn. 43 (5) (2007) 1898.

Paper VII

Paper published in International Journal of Refrigeration, 2010

Bjørk, R., Bahl, C. R. H., Smith A. and Pryds, N.

Review and comparison of magnet designs for magnetic refrigeration

International Journal of Refrigeration, 33, 437-448, 2010

available at www.sciencedirect.com

ScienceDirect

journal homepage: www.elsevier.com/locate/ijrefrig

Review

Review and comparison of magnet designs for magnetic refrigeration

R. Bjørk, C.R.H. Bahl, A. Smith, N. Pryds*

Fuel Cells and Solid State Chemistry Division, Risø National Laboratory for Sustainable Energy, Technical University of Denmark – DTU, Frederiksborgvej 399, DK-4000 Roskilde, Denmark

ARTICLE INFO

Article history:
Received 11 July 2009
Received in revised form
8 December 2009
Accepted 12 December 2009
Available online 28 December 2009

Keywords:
Magnetic refrigerator Review
Design
Technology
Magnetic

ABSTRACT

One of the key issues in magnetic refrigeration is generating the magnetic field that the magnetocaloric material must be subjected to. The magnet constitutes a major part of the expense of a complete magnetic refrigeration system and a large effort should therefore be invested in improving the magnet design. A detailed analysis of the efficiency of different published permanent magnet designs used in magnetic refrigeration applications is presented in this paper. Each design is analyzed based on the generated magnetic flux density, the volume of the region where this flux is generated and the amount of magnet material used. This is done by characterizing each design by a figure of merit magnet design efficiency parameter, Λ_{cool}. The designs are then compared and the best design found. Finally recommendations for designing the ideal magnet design are presented based on the analysis of the reviewed designs.

Tour d'horizon et comparaison des conceptions d'aimants pour le froid magnétique

Mots clés : Réfrigérateur magnétique ; Enquête ; Conception ; Technologie ; Aimant

* *Corresponding author*. Tel.: +4546775800; fax: +4546775858.
E-mail address: rabj@risoe.dtu.dk (R. Bjørk).

0140-7007/$ – see front matter © 2009 Elsevier Ltd and IIR. All rights reserved.
doi:10.1016/j.ijrefrig.2009.12.012

Nomenclature

Variables

ΔT_{ad}	Adiabatic temperature change (K)
T_c	Curie temperature (K)
I	Current (A)
B	Magnetic flux density (T)
N	Number of winding turns (–)
L_{core}	Length of soft magnetic material (m)
L_{gap}	Length of air gap (m)
B_{rem}	Magnetic remanence (T)
V_{mag}	Volume of magnet(s) (m^3)
V_{field}	Volume of high flux density region (m^3)
M^*	Magnet figure of merit from Jensen and Abele (1996) (–)
K	Strength of magnetic field from Coey and Ni Mhiochain (2003) (–)
A_{field}	Area of the high flux density region (m^2)
A_{mag}	Area of the magnet (m^2)
B_{out}	Flux density of low flux density region (T)
P_{field}	Fraction of AMR cycle where magnet is in use (–)
H	Magnetic field ($A\,m^{-1}$)
H_C	Intrinsic Coercivity ($A\,m^{-1}$)

Greek

μ_r	Relative permeability (–)
μ_0	Permeability of free space ($N\,A^{-2}$)
Λ_{cool}	Magnet characterization parameter ($T^{2/3}$)

1. Introduction

Magnetic refrigeration is an evolving cooling technology that has the potential of high energy efficiency using environmentally friendly refrigerants. Magnetic refrigeration utilizes the magnetocaloric effect (MCE), which is the temperature change that most magnetic materials exhibit when subjected to a changing magnetic field. This temperature change is called the adiabatic temperature change, ΔT_{ad}, and is a function of temperature and magnetic field. The temperature change is greatest near the Curie temperature, T_c, which is different for different magnetocaloric materials (Pecharsky and Gschneidner, 2006). Because the MCE in the best magnetocaloric materials currently available exhibit a temperature change of no more than 4 K in a magnetic field of 1 T, a magnetic refrigeration device must utilize a regenerative process to produce a large enough temperature span to be useful for refrigeration purposes. The most utilized process for this is called active magnetic regeneration (AMR).

At present, a great number of magnetic refrigeration test devices have been built and examined in some detail, with focus on the produced temperature span and cooling power of the devices (Barclay, 1988; Yu et al., 2003; Gschneidner and Pecharsky, 2008). So far the magnet, a key component in the magnetic refrigeration system, has been largely overlooked, even though it is often the single most expensive part of a magnetic refrigerator. Also little effort has been made to compare existing magnet designs in order to learn to design more efficient magnetic structures.

In general, a magnet design that generates a high magnetic flux density over as large a volume as possible while using a minimum amount of magnet material is to be preferred. Since the magnet is expensive it is also important that the magnetic refrigerator itself is designed to continuously utilize the magnetic flux density generated by the magnet.

1.1. *Magnetic refrigeration magnets*

As previously stated a substantial number of magnetic refrigeration devices have been built. In all devices, one of three types of magnets has been used to generate the magnetic field. The first magnetic refrigeration device used a superconducting electromagnet (Brown, 1976), and other systems also using a superconducting electromagnet have since been built (Zimm et al., 1998; Blumenfeld et al., 2002; Rowe and Barclay, 2002). Devices using a non-superconducting electromagnet have also been constructed (Bahl et al., 2008; Coelho et al., 2009), but the greater majority of devices built in recent years have used permanent magnets to generate the magnetic field (Bohigas et al., 2000; Lee et al., 2002; Lu et al., 2005; Vasile and Muller, 2006; Okamura et al., 2007; Tura and Rowe, 2007; Zimm et al., 2007; Zheng et al., 2009; Engelbrecht et al., 2009).

The reason permanent magnets are preferred is that they do not require power to generate a magnetic field. This is not the case for an the electromagnet where a large amount of power is needed to generate, e.g. a 1 T magnetic flux density in a reasonable volume. This can be seen from the relation between the current, I, and the generated flux density, B, for an electromagnet in a single magnetic circuit consisting of a soft magnetic material with relative permeability, μ_r, and where the core has roughly the same cross sectional area throughout its length and the air gap is small compared with the cross sectional dimensions of the core,

$$NI = B\left(\frac{L_{core}}{\mu_r \mu_0} + \frac{L_{gap}}{\mu_0}\right), \tag{1}$$

where N is the number of turns in the winding, L_{core} is the length of the soft magnetic material, μ_0 is the permeability of free space and L_{gap} is the length of the air gap. In order to generate a 1.0 T magnetic flux density over e.g. a 30 mm air gap, which is typical for a magnetic refrigeration device, an iron cored solenoid with $\mu_r = 4000$ would need to have 24,000 ampere windings. The length of the soft magnetic material is irrelevant as the expression is dominated by the second term. Such an electromagnet with 24,000 ampere windings would need a massive power supply and an equally massive cooler to prevent the solenoid from overheating. Based on this simple calculation, it can be seen why an electromagnet is not preferred in most magnetic refrigeration devices.

A superconducting electromagnet is a better option than the traditional electromagnet because it requires little power

to operate once the electromagnet has become superconducting as no power is lost to ohmic resistance. Although a superconducting electromagnet can create magnetic flux densities of the order of 10 T, continuous cooling is needed. This can be an expensive process and the apparatus surrounding the superconducting electromagnet can be of substantial size. However for large scale applications, e.g. large refrigerators for warehouses, etc., a superconducting electromagnet might be a relevant solution. For common household refrigeration the superconducting electromagnet is at present not an option.

The only suitable choice left for generating the magnetic field is permanent magnets, which require no power to generate a flux density. The remainder of this paper will be concentrating on permanent magnet magnetic refrigerators, useable in common household refrigeration, as almost all research in magnetic refrigeration is focussed on this area. However the conclusions from this article will be applicable to any device using magnetocaloric materials, e.g. heat pumps, and not only magnetic refrigeration devices.

2. Characterizing a magnet design

When reviewing different magnet designs it is of the utmost importance that the different designs can be compared using a simple figure of merit. A previous suggestion for a comparison parameter was defined using the masses of the magnet and that of the magnetocaloric material used in the device (Nikly and Muller, 2007). This parameter is not useful for two reasons: it contains no information about the magnetic flux density produced by the magnet design and using the same magnetic structure with two different magnetocaloric materials with different densities will yield different characterization results.

A general figure of merit, M^*, used to characterize a magnet design is defined by Jensen and Abele (1996) as:

$$M^* = \frac{\int_{V_{field}} B^2 \, dV}{\int_{V_{mag}} B_{rem}^2 \, dV} \tag{2}$$

where V_{field} is the volume of the region where the magnetic field is created and V_{mag} is the volume of the magnets. It can be shown that the maximum value of M^* is 0.25, and a structure is considered reasonably efficient if it has $M^* \geq 0.1$.

The strength of the magnetic field that is generated can also be quantified by a dimensionless number, K, which is the ratio between the magnetic flux density and the remanence of the magnets (Coey and Ni Mhiochain, 2003). For a two-dimensional structure with completely uniform remanence and magnetic flux density the two numbers K and M^* are related by the expression

$$M^* = K^2 \frac{A_{field}}{A_{mag}} \tag{3}$$

Where A_{field} is the area of the high flux density region and A_{mag} is the area of the magnet. The figure of merit, M^*, often shown as a function of K, is useable for characterizing magnet designs in general, but for magnet design used in magnetic refrigeration the parameter does not take into account the flux density in the low field region of the magnet system where the magnetocaloric material is placed when it is demagnetized. Also, and more importantly, the scaling of the magnetocaloric effect itself with magnetic field is not taken into account. The importance of this will be considered shortly.

Finally, a general performance metric for active magnetic refrigerators has been suggested (Rowe, 2009a). The cost and effectiveness of the magnet design is included in this metric as a linear function of the volume of the magnet. The generated flux density is also included in the metric. However, the metric does not make it possible to evaluate the efficiency of the magnet design alone.

Here the Λ_{cool} parameter proposed by Bjørk et al. (2008) will be used to characterize a magnet design for use in magnetic refrigeration. This parameter is designed to favor magnet designs that generate a high magnetic flux density in a large volume using a minimum of magnetic material. It also favors system designs in which the amount of time where the magnetic flux density is ''wasted'' by not magnetizing a magnetocaloric material is minimized.

2.1. The Λ_{cool} parameter

The Λ_{cool} parameter is a figure of merit that depends on a number of different parameters related to the magnetic assembly being evaluated.

The Λ_{cool} parameter is defined as

$$\Lambda_{cool} \equiv \left(\langle B^{2/3} \rangle - \langle B_{out}^{2/3} \rangle \right) \frac{V_{field}}{V_{mag}} P_{field} \tag{4}$$

where V_{mag} is the volume of the magnet(s), V_{field} is the volume where a high flux density is generated, P_{field} is the fraction of an AMR cycle that magnetocaloric material is placed in the high flux density volume, $\langle B^{2/3} \rangle$ is the volume average of the flux density in the high flux density volume to the power of 2/3 and $\langle B^{2/3}{}_{out} \rangle$ is the volume average of the flux density to the power of 2/3 in the volume where the magnetocaloric material is placed when it is being demagnetized. Some of these variables are illustrated for the case of a Halbach cylinder in Fig. 1.

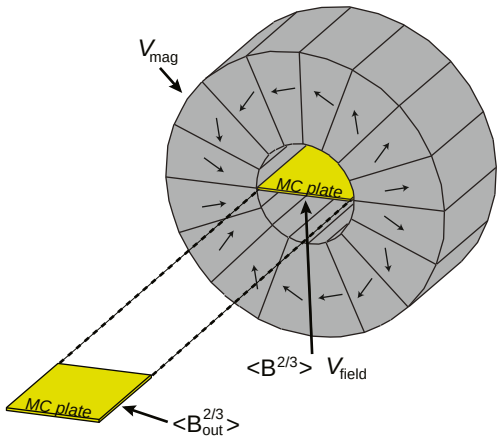

Fig. 1 – An illustration of some of the different variables in the Λ_{cool} parameter for the case of a Halbach cylinder. A plate of magnetocaloric (MC) material is shown in both the in and out of field position.

Note that it is the magnetic flux density generated in an empty volume that is considered, and so $\mathbf{B} = \mu_0\mathbf{H}$, and thus it is equivalent to speak of the magnetic flux density or the magnetic field.

Notice that Λ_{cool} depends on the flux density to the power of 2/3. The reason for this is that Λ_{cool} is defined to be proportional to the temperature change of the magnetocaloric material, and not the magnetic flux density, as the former is what is used to generate the temperature span and cooling power of the refrigeration device. This temperature change does not scale linearly with the magnetic flux density. A large number of different materials have been suggested as the active component of a magnetic refrigeration machine (Gschneidner et al., 2005). The adiabatic temperature change at the Curie temperature of a general second order magnetocaloric phase transition material is predicted by mean field theory to scale with the power of 2/3 of the magnetic field (Oesterreicher and Parker, 1984). This is in good accordance with the material most often used, i.e. the "benchmark" magnetocaloric material at room temperature, gadolinium, which has a magnetocaloric effect that scales with the magnetic field to the power of 0.7 at the Curie temperature (Pecharsky and Gschneidner, 2006), as also shown in Fig. 2. This is why the Λ_{cool} parameter is proportional to the magnetic flux density to the power of 2/3. The scaling of the adiabatic temperature change away from T_c will in general be different from 2/3, but as long as the exponent is below 1 the conclusions of this article remain substantially unchanged. It should be noted that the entropy change of a number of magnetocaloric materials also scales as a power law with an exponent that in general is of the order of 2/3 (Franco et al., 2007; Dong et al., 2008).

It is not only the flux density in the magnetization region that is of importance to the magnetocaloric effect. The volume in which the magnetocaloric material is placed when it is demagnetized is equally important. In order to maximize the magnetocaloric effect, the flux density in this volume must be as low as possible. In a reciprocating device this can of course be accomplished by simply moving the magnetocaloric material far away from the magnet, but this will increase the physical size and cycle time of the magnetic refrigeration machine. In a rotating device the high and low flux density regions will generally be adjacent and care must be taken to minimize the "leak" of flux into the low flux density region.

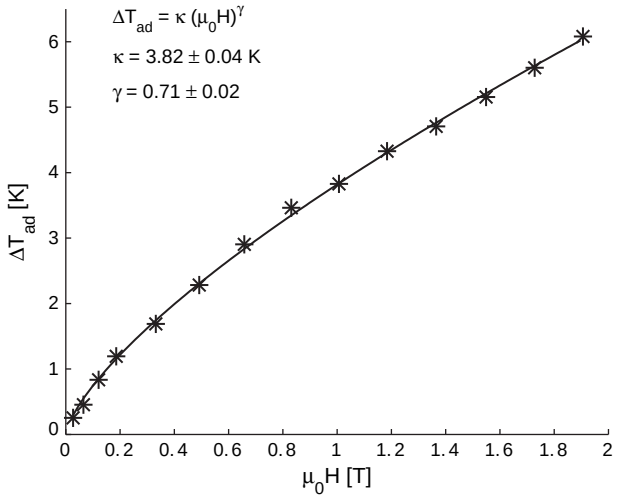

Fig. 2 – The scaling of the adiabatic temperature change of Gadolinium as a function of magnetic field at T_c (293.6 K). Data are from Pecharsky and Gschneidner (2008) and are corrected for demagnetization using Aharoni (1998).

To take into account the amount of magnetocaloric material that can experience a temperature change, the Λ_{cool} parameter is proportional to the volume of the high flux density region. Note that Λ_{cool} is proportional to the whole volume of the high flux density region and not only the volume occupied by the magnetocaloric material. Thus Λ_{cool} does not depend on the porosity of the magnetocaloric material, nor on the amount of e.g. plastic housing used to confine the magnetocaloric material. Also Λ_{cool} is inversely proportional to the volume of magnet material used, as the more magnet material used the more expensive the design will be.

Finally, the Λ_{cool} parameter is proportional to the fraction of the AMR cycle in which magnetocaloric material is placed in the high flux density volume. The reason for this is that if, e.g., magnetocaloric material is only placed inside the high flux density volume half the time of a full AMR cycle, the (expensive) magnet is not utilized during the remaining half of the cycle and it is thus essentially being wasted during this time. The fraction of time the magnetic flux generated by the magnet is being used to generate a magnetocaloric effect must be maximized.

One should note that the Λ_{cool} parameter will favor a design with a small magnetic flux density and large volume of the high flux density region. This is because the magnetic flux generated by a magnet scales with a power less than 2/3 with the volume of the magnet. In an actual device, heat transfer rates and thermal losses will set a lower limit on the flux density needed to produce a given temperature span and cooling capacity. Therefore for practical applications one would choose to optimize Λ_{cool} under the condition of a certain minimum flux density in the high flux density region.

The remanence of the magnets is not explicitly considered in the Λ_{cool} parameter. The reason for this is twofold. First this information is almost always not available for published magnet designs. Secondly the remanence of the NdFeB magnets used in all magnetic refrigeration magnet assemblies varies only between 1.2 and 1.4 T and so the exact value is not critical for comparison of different designs. Therefore, geometry accounts for almost all of the differences between different designs. Any soft magnetic material used in the magnet assembly is ignored, as the price of this material is in general much lower than that of the permanent magnets.

3. Published magnet designs

Having introduced the Λ_{cool} parameter, different published magnet designs can now be compared. There exist a substantial number of published designs of magnetic refrigerators but unfortunately many publications lack the

necessary specifications to either reconstruct or directly calculate the Λ_{cool} parameter (Richard et al., 2004; Shir et al., 2005; Zimm et al., 2006; Buchelnikov et al., 2007; Chen et al., 2007; Vuarnoz et al., 2007; Coelho et al., 2009; Dupuis et al., 2009; Sari et al., 2009). The designs presented below are the ones that represents the main magnets configurations and contain sufficient information to calculate Λ_{cool}. A short description of each design is given prior to the calculation.

It should be noted that many of the magnetic refrigerators presented here are test devices and should be evaluated as such. However, it is also in the test design phase that large improvements to the design should be suggested. Therefore, the evaluation of the designs can potentially lead to improvements for both current and future magnetic refrigerators.

For all designs an ''ideal'' device is considered when estimating the P_{field} parameter. In such a device the time for moving either the magnet or a bed of magnetocaloric material is minimized. This has been done in order that the Λ_{cool} parameter will not depend on, e.g., the power of the motor in the device. An example is the rotating design by Okamura et al. (2007), shown in a later section. Using the actual rotation speed of the magnet gives $P_{field} = 0.66$. However, we estimate that using a more powerful motor would allow $P_{field} = 0.9$. In the calculation of Λ_{cool} for the given design the latter value will be used. The AMR cycle is assumed to be symmetric, i.e. the magnetization and demagnetization steps are assumed to take the same amount of time.

The designs reviewed here have been classified into three groups, depending on the complexity of the design. After all designs have been presented the designs are compared in Table 1.

3.1. *Simple magnetic circuits*

The designs presented in this subsection all have a simple geometric structure and consist of rectangular blocks of magnets.

3.1.1. *Design by Zheng et al. (2009)*

The general refrigerator design by Zheng et al. (2009) is a reciprocating design where the magnet is moving and two packed beds of magnetocaloric material are kept stationary. When one of the beds is in the magnetic field the other bed is out of the field. The flux density in the design is provided by a single rectangular magnet and the flux lines are guided by a soft magnetic material through a small air gap, as shown in Fig. 3. Based on Zheng (2009) the volume of the magnet is 0.5 L and the volume of the high flux density region is 0.09 L. The mean magnetic flux density is 0.93 T. Based on the cycle time, movement speed of the beds and the distance between these the actual P_{field} parameter is calculated to be 0.60. However using a faster and more powerful motor to move the magnet, as well as considering that the magnet has to be moved across a finite distance between the beds where no magnetocaloric material is present, the P_{field} parameter could be as high as 0.90.

3.1.2. *Design by Vasile and Muller (2006)*

The magnet design by Vasile and Muller (2006) is a ''C'' shaped magnet assembly of rectangular magnet blocks with soft magnetic material inside and outside of the ''C'' as seen in Fig. 4. In this design the magnets are rotating around a circle with inserts filled with magnetocaloric material. The cross sectional area of the magnets is estimated to be 9.2 L/m and

Table 1 – The specifications of different magnet designs used in magnetic refrigeration devices.

Name	V_{mag} [L]	V_{field} [L]	$\langle B \rangle$ [T]	$\langle B_{out} \rangle$ [T]	P_{field}	Magnet type	$\frac{\Lambda_{cool}}{P_{field}}$	Λ_{cool}
Bohigas et al. (2000)	0.38	0.02	0.9[b]	0[a]	1	Rectangular magnets on round surface	0.05	0.05
Engelbrecht et al. (2009)	0.5	0.07	1.03	0	0.5	Halbach cylinder	0.14	0.07
Kim and Jeong (2009)	0.20	0.01	1.4	0	0.5	Halbach cylinder	0.06	0.03
Lee et al. (2002)	14.6/m	0.32/m	1.9[b,c]	0[a]	0.90[a]	''C'' shaped Halbach cylinder	0.03	0.03
Lu et al. (2005)	2.94	0.14	1.4[b]	0	0.5	Halbach cylinder	0.06	0.03
Okamura et al. (2007)	3.38	0.80	1.0	0	0.90[a]	Inner magnet rotor, soft magnetic yoke	0.24	0.21
Tagliafico et al. (2009)	0.68	0.07	1.55[b]	0	0.95	Rectangular magnetic circuit with slot	0.14	0.13
Tura and Rowe (2007)	1.03	0.05	1.4	0.1	0.5	Concentric Halbach cylinders	0.05	0.03
Tušek et al. (2009)	0.11	0.65	0.97	0.1	1	Stationary magnet, rotating MC material	0.13	0.13
Vasile and Muller (2006)	9.2/m	0.75/m	1.9[b,c]	0[a]	0.90[a]	''C'' shaped circuit	0.12	0.11
Zheng et al. (2009)	0.5	0.09	0.93	0[a]	0.90[a]	Single magnet magnetic circuit	0.17	0.15
Zimm et al. (2007)	4.70	0.15	1.5	0.1[a]	0.90[a]	''Y'' shaped magnetic structure	0.04	0.03

In all cases is it assumed that $\langle B \rangle^{2/3} = \langle B^{2/3} \rangle$, which is only true if the flux density is completely homogenous.

a A quantity estimated by the authors of this article.

b The value of the flux density is the highest possible attainable flux density in the center of the design, and as such is not a representative average of the magnetic flux density for the whole of the high flux density region.

c The flux density is based on a two dimensional simulation. These notoriously overestimate the flux density except for very long assemblies and so Λ_{cool} will be overestimated for these designs. Some of the two dimensional designs also have their volumes given per meter.

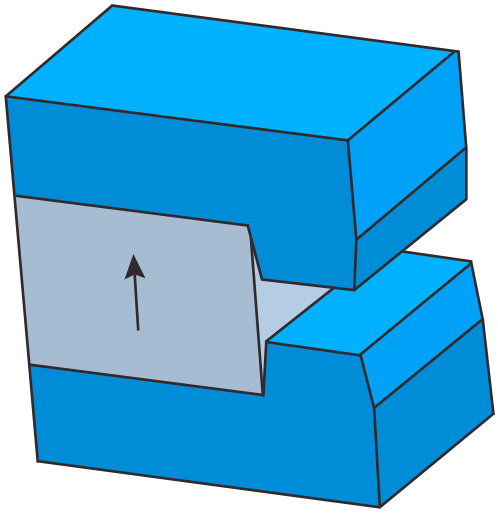

Fig. 3 – The design by Zheng et al. (2009). From Zheng (2009). The arrow indicate the direction of magnetization of the magnet. The dark structure consists of soft magnetic material.

the high field gap cross sectional area to be 0.75 L/m. The magnetic flux density is given as 1.9 T in the high field region, but this is based on a two dimensional simulation so a real world assembly would have a significantly lower value. As the magnets are rotating continuously and the inserts for the magnetocaloric material fill most of the circle along which the magnet is rotating P_{field} is estimated to be 0.90.

3.1.3. *Design by Bohigas et al. (2000)*

The design by Bohigas et al. (2000) is a rotating design in which the magnets are stationary and the magnetocaloric material is

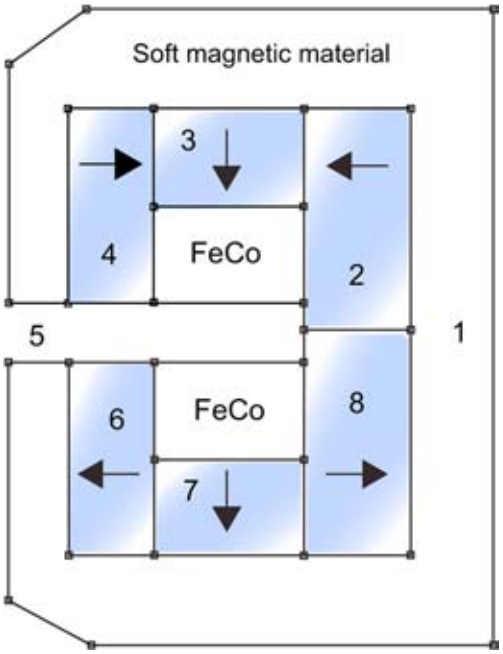

Fig. 4 – After Vasile and Muller (2006). Reprinted with permission. (©2006 Elsevier). The arrows indicate the direction of magnetization of the magnets.

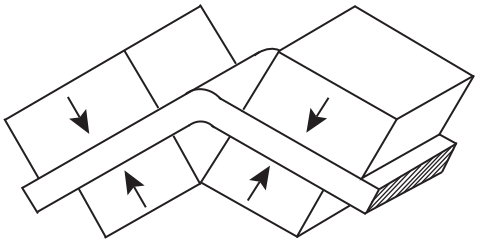

Fig. 5 – The design by Bohigas et al. (2000). Reprinted with permission. (©2000 IEEE).

rotated in and out of the high flux density region. A total of eight rectangular magnets are used, four of them placed on the inside of the rotating wheel and four placed outside the wheel. The design can be seen in Fig. 5. The dimension of one of the inner blocks is given as $40 \times 40 \times 20$ mm^3 and one of the outside blocks has dimensions $50 \times 50 \times 25$ mm^3. The size of the air gap is given to be 7 mm and there are a total of four air gaps. From these figures we estimate the dimensions of one air gap to be $40 \times 7 \times 20$ mm^3. Thus the volume of the magnets is 0.38 L and the volume of the high flux density region is 0.02 L. The flux density is given as 0.9 T. This design has magnetocaloric material continuously entering the high flux density region and thus the P_{field} parameter is 1.

3.1.4. *Design by Tagliafico et al. (2009)*

The magnet design by Tagliafico et al. (2009) consists of ten magnets in a rectangular structure which uses soft magnetic material to guide the flux lines round through the magnetic circuit. The magnet has a slot $50 \times 9.5 \times 100$ mm^3 in the center, through which the magnetocaloric material is moved, as seen in Fig. 6. The volume of the high flux density region is thus 0.07 L. The flux density in the center of the slot is 1.55 T. A reported 5 kg of magnet is used, which corresponds to $V_{mag} = 0.68$ L. As two regenerative beds are run in parallel, and as the beds can be moved fairly quickly in and out of the high flux density region, the ideal P_{field} parameter is estimated to be

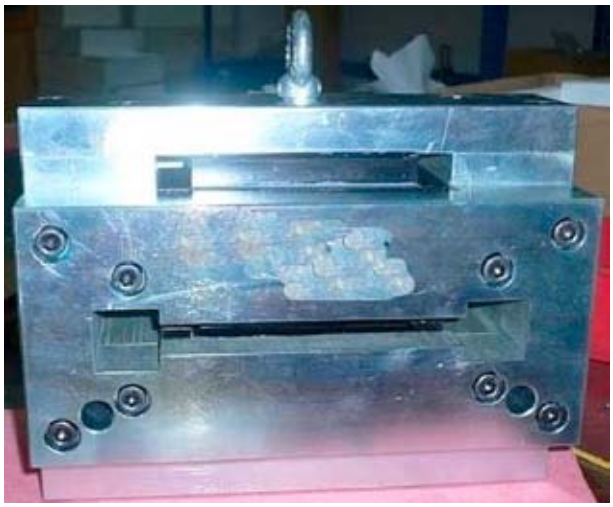

Fig. 6 – The magnet design by Tagliafico et al. (2009) (©2009 IIR/IIF). The magnetocaloric material passes through the gap in the structure.

0.95. The actual value for the P_{field} parameter, which can be estimated based on the total cycle time, is very close to this figure.

3.1.5. *Design by Tušek et al. (2009)*

The refrigeration system presented by Tušek et al. (2009) uses a rotating AMR and a stationary magnet system. The magnet system consists of an inner and outer magnetic circuit with the magnetocaloric material placed in between the two structures. There are four high flux density regions and four low flux density regions along the circumference between the inner and the outer structure. A drawing of the design can be seen in Fig. 7. The volume of the high flux density regions is four times $48 \times 10 \times 55\ mm^3$, or 0.11 L. The amount of magnet material used is four times $90 \times 30 \times 90\ mm^3$, or 0.65 L. The average mean flux density in the high field region is 0.97 T while it is 0.1 T in the low flux density region. The remanence of the magnets is 1.27 T. As magnetocaloric material is continuously rotated into the high field regions the magnets are constantly being used and thus $P_{field} = 1$.

3.2. *Halbach type magnet assemblies*

The magnetic structures presented in this subsection are all based on the Halbach cylinder design (Halbach, 1980; Mallinson, 1973).

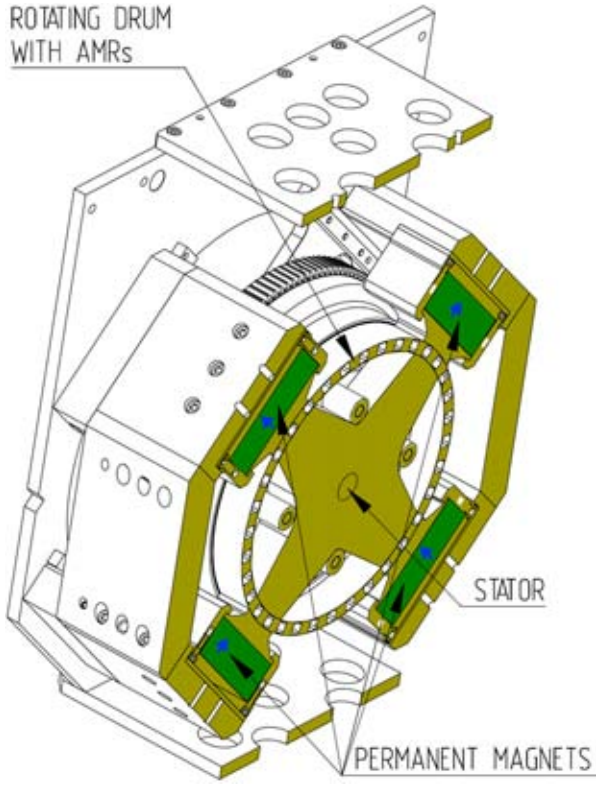

Fig. 7 – The design by Tušek et al. (2009). The magnetocaloric material is placed between the inner and outer magnetic structure. The direction of magnetization is shown as arrows on the magnet blocks. Adapted from Tušek et al. (2009).

3.2.1. *Design by Lee et al. (2002)*

The magnet design by Lee et al. (2002) is suited to a reciprocating design with a stationary magnet and a moving bed of magnetocaloric material, but no actual device has been built. The magnet system is shaped like the letter "C", with a high homogenous flux density in the center. The design resembles an eight-segmented Halbach cylinder where one of the horizontal segmented has been removed. The flux density in the center is enhanced by blocks of soft magnetic material, placed in the center of the "C". An illustration of the design can be seen in Fig. 8. The design is very similar to the design by Vasile and Muller (2006) shown in Fig. 4. However, this design is presented in this section because the shape of the magnets are more complex than in the latter design. The cross sectional dimensions of the array are given as $114 \times 128\ mm^2$, i.e. 14.6 L/m. The cross sectional area of the high flux region is estimated to be $25 \times 12.7\ mm^2$, i.e. 0.32 L/m. The magnetic flux density is given to be 1.9 T in the high flux region but this is based on a two dimensional simulation. Depending on the length of an actual device this figure will be significantly lower. No actual device has been built so the P_{field} is simply taken to be 0.90.

3.2.2. *Design by Engelbrecht et al. (2009)*

The magnetic refrigeration test machine designed at Risø DTU is a reciprocating device in which plates of magnetocaloric material are moved in and out of a stationary magnet (Engelbrecht et al., 2009). The magnet is a Halbach cylinder consisting of 16 blocks of permanent magnets. The cylinder has an inner radius of 21 mm, an outer radius of 60 mm and a length of 50 mm. An illustration of the Halbach cylinder is shown in Fig. 9. The average magnetic flux density in the cylinder bore is 1.03 T. The volume of the magnet is 0.50 L and the volume of the high flux density region, i.e. the cylinder bore, is 0.07 L. The remanence of the magnets used in the Halbach cylinder is 1.4 T. The P_{field} parameter for this system design is 0.5. This is because for half the cycle time the stack of plates is out of the high field region leaving this empty. The actual P_{field} is slightly less than 0.5 due to the finite velocity of the moving regenerator.

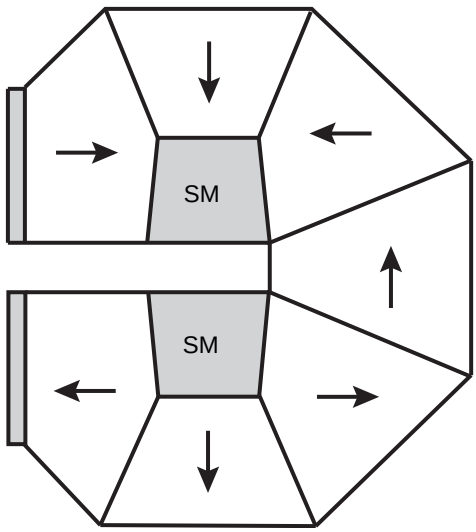

Fig. 8 – The design by Lee et al. (2002). The blocks labeled "SM" consists of soft magnetic material. Reprinted with permission. (©2002 American Institute of Physics).

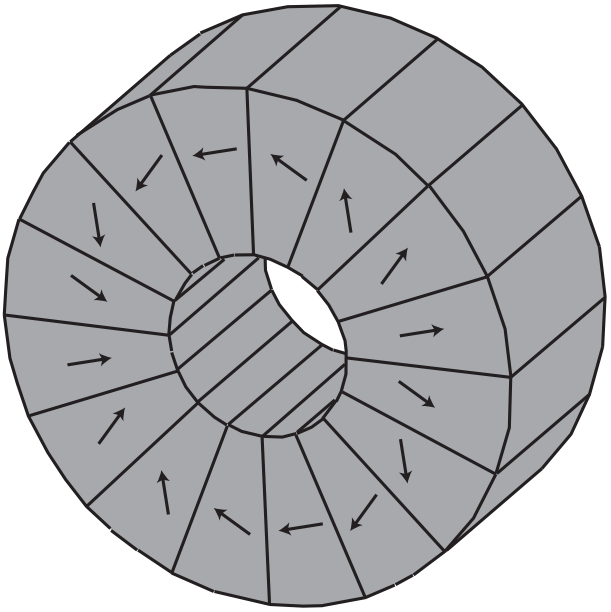

Fig. 9 – The design by Engelbrecht et al. (2009). The Halbach cylinder has an inner radius of 21 mm, an outer radius of 60 mm and a length of 50 mm.

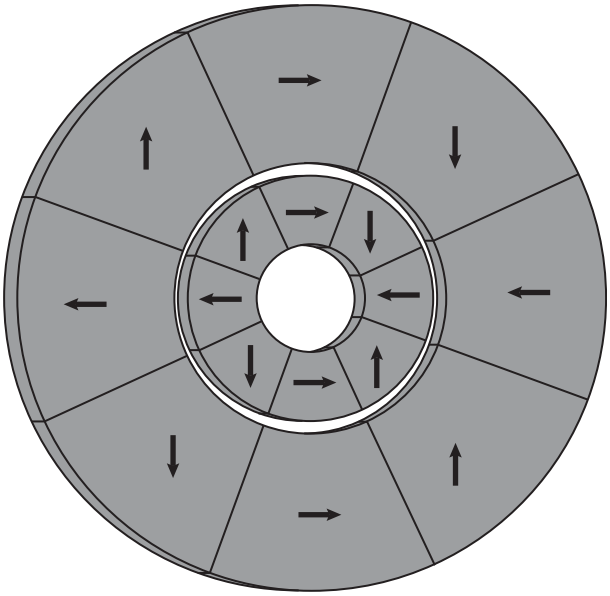

Fig. 10 – A sketch of the concentric Halbach magnet design by Tura and Rowe (2007), viewed from the front. The inner and outer radius of the inner cylinder is 12.5 mm and 27 mm, respectively while the corresponding figures for the outer cylinder is 30 mm and 60 mm, respectively. The rotational length of the actual concentric cylinder is 100 mm. The configuration shown here is the high flux density configuration.

3.2.3. *Design by Lu et al. (2005)*

The magnetic refrigeration device designed by Lu et al. (2005) is a reciprocating device with two separate packed beds of magnetocaloric material moving in and out of two stationary magnet assemblies to provide force compensation. Both magnets are 16 segmented Halbach cylinders with an inner radius of 15 mm and an outer radius of 70 mm. An illustration of the design is not shown as this design is very similar to the one shown in Fig. 9. The flux density produced is given as 1.4 T, and the length of the cylinder is 200 mm. Given these numbers the volume of the magnet is 2.94 L and the volume of the high flux density region is 0.14 L, for either of the magnets. For the same reasons as for the design by Engelbrecht et al. (2009) the P_{field} parameter for this device is 0.5.

3.2.4. *Design by Kim and Jeong (2009)*

The magnet design by Kim and Jeong (2009) is a 16-segmented Halbach cylinder. A single bed of magnetocaloric material is reciprocated through the cylinder bore. The radius of the cylinder bore is 8 mm, the outer radius of the cylinder is 38 mm and the length is 47 mm. An illustration of the design is not shown as this design is very similar to the one shown in Fig. 9. The volume of the high flux density region is 0.01 L while the volume of the magnet is 0.20 L. The flux density is 1.58 T at the center of the bore and 1 T at the edge, with a mean value of 1.4 T. As only a single magnetocaloric bed is used the high flux density region is only used half the time, and thus P_{field} is 0.5.

3.2.5. *Design by Tura and Rowe (2007)*

The magnetic refrigerator presented by Tura and Rowe (2007) is a rotating system in which the magnetocaloric material is kept stationary and a magnet is rotated to alter the flux density. An illustration of the design can be seen in Fig. 10. The magnet design used in the device consists of two separate magnets each of which consists of two concentric Halbach cylinders. The reason that two separate magnets are used is that the system can be run such that the magnetic forces are balanced. In the concentric Halbach cylinder design the flux density in the inner cylinder bore can be controlled by rotating the inner or outer magnet. Tura and Rowe (2007) report that when the inner magnet is rotated the mean magnetic flux produced can be changed continuously from 0.1 T to 1.4 T. The total volume of the magnetic material is 1.03 L, while the total volume of the high flux density region is 0.05 L (Rowe, 2009b). These values are for one of the concentric Halbach cylinders. The remanence of the blocks in the inner cylinder is 1.15 T while for the outer magnet it is 1.25 T. The P_{field} parameter for this system design is 0.5 as half of a cycle the inner magnet will be turned such that it cancels the magnetic flux generated by the outer magnet. In this configuration there is no high flux density region, and the magnets are not being used to generate cooling.

3.3. *Complex magnetic structures*

The designs presented in this subsection have a complex structure and consists of irregularly shaped magnet blocks.

3.3.1. *Design by Zimm et al. (2007)*

The magnetic refrigeration machine presented by Zimm et al. (2007) utilizes a rotating design in which the magnetocaloric

material is stationary and the magnet is rotating. The magnet design is quite complex, utilizing both magnets and soft magnetic materials, but essentially consists of two Y-shaped magnetic structures separated by an air gap. The design is shown in Fig. 11. The high flux density region spans an angle of 60° on two opposite sides of the design. Based on Chell (2009) the total volume of the magnet assembly is 4.70 L, the volume of the high flux density region is 0.15 L and the mean flux density is 1.5 T. The P_{field} parameter for this design is essentially given by the speed at which the magnet rotates from one bed of magnetocaloric material to the next. These are separated by an angle of 30°. If the magnet is rotated fast the P_{field} parameter could be as high as 0.90.

3.3.2. *Design by Okamura et al. (2007)*

The design by Okamura et al. (2007) is a rotating device in which the magnet is rotated past ducts packed with magnetocaloric material. The magnet design consists of a complex arrangement of permanent magnets and soft magnetic materials which is assembled in the shape of an inner rotor consisting both of magnets and soft magnetic material with an outer yoke consisting of only soft magnetic material. The magnetocaloric material is placed in four ducts in the air gap between the inner and outer structure. The inner rotor is designed such that magnets with identical poles are facing each other and separated by a soft magnetic material. This increases the flux density and "pushes" the flux lines from the inner rotor to the outer yoke. A photo of the design can be seen in Fig. 12. The mean flux density is 1.0 T and the magnet design contains 3.38 L of magnet and 0.80 L of high flux density region (Okamura, 2009). As with the design by Zimm et al. (2007) the P_{field} parameter for this design is essentially given by the speed at which the magnet rotates from one duct to the next. The actual P_{field} parameter can be estimated using the total cycle time and the time to rotate between two ducts, separated by an angle of 40°, and is found to be 0.66. However a faster rotation might be possible and thus we estimate that the P_{field} parameter can be as high as 0.90.

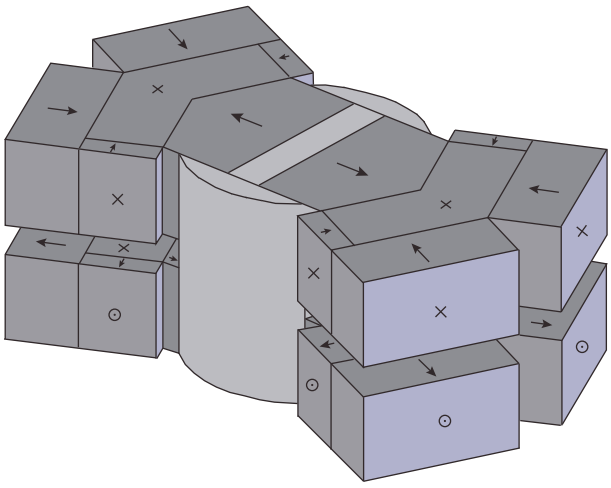

Fig. 11 – The complex magnet design by Zimm et al. (2007) (©2007 IIR/IIF). The magnetocaloric material passes through the gap between the upper and lower "Y" structures. The dark grey blocks are individual magnets, while the light grey structure is made of soft magnetic material. The direction of magnetization of the individual blocks are taken from Chell and Zimm (2006).

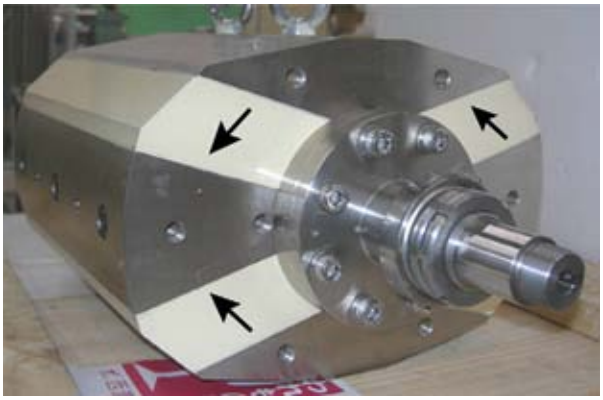

Fig. 12 – The inner magnetic structure in the design by Okamura et al. (2007). From Okamura (2009). The outer magnetic structure consists of a cylinder of soft magnetic material (not shown). The arrows indicate the direction of magnetization of the magnets, which are white in color.

4. Comparing the designs

In Table 1 the different magnet designs are presented. In the table the Λ_{cool} parameter has been calculated for each design, thus allowing a direct comparison of the designs.

In Fig. 13 the parameter Λ_{cool}/P_{field}, which only takes the magnet assembly into account and not the design of the refrigeration device, as well as the actual Λ_{cool} parameter are shown. From the figure, it is seen that the magnet design by Okamura et al. (2007) outperforms the remaining magnet designs. Compared to Lu et al. (2005) the design by Okamura et al. (2007) uses almost the same amount of magnets but creates a high flux density region over three times larger. An interesting thing to note is that although the design by Zimm et al. (2007) creates a very high flux density the design has a rather low Λ_{cool} value because the magnetocaloric temperature change only scales with the magnetic field to the power of 2/3 at the Curie temperature and this, as mentioned previously, does not favor high flux densities. However Λ_{cool} should be optimized under the condition of a certain minimum flux density in the high flux density region, e.g. the flux density required to obtain a given temperature span of the device. It is also seen that many of the reciprocating designs only utilize the magnet in half of the AMR cycle, i.e. that the P_{field} parameter is 0.5. This means that the expensive magnet is only utilized half the time, which is very inefficient. It is also seen that the different Halbach cylinders do not perform equally well. This is because the efficiency of a Halbach cylinder is strongly dependent on the relative dimensions of the cylinder (Bjørk et al., 2008).

Note that the actual magnetic refrigeration machines, when ranked by their temperature span and cooling capacity, does not necessarily follow the trend of Fig. 13 (Engelbrecht

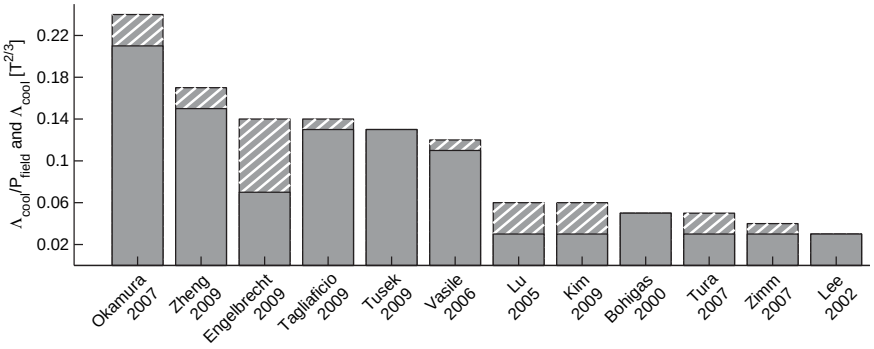

Fig. 13 – The parameters Λ_{cool}/P_{field} (hatched) and Λ_{cool} (full). The Λ_{cool}/P_{field} parameter only takes the magnet design into account and not the fraction of a cycle the magnet is used. As $P_{field} \leq 1$ the Λ_{cool} parameter is always less than or equal Λ_{cool}/P_{field}. Completely filled bars have $P_{field} = 1$. Note that the best design is five times as good as the design with the lowest value of Λ_{cool}/P_{field}.

et al., 2007; Gschneidner and Pecharsky, 2008; Rowe, 2009a). This can be caused by different types of magnetocaloric material, different regenerator designs and different operating parameters.

Having evaluated existing magnet designs we now analyze the advantages of these designs and focus on how to design the optimal magnet for a magnetic refrigerator. The optimal design is limited by the energy density in the magnets themselves. Also for, e.g., very large Halbach cylinders the coercivity of the magnet is a limiting factor because the magnetic field is opposite to the direction of magnetization around the inner equator of the Halbach cylinder (Bloch et al., 1998; Bjørk et al., 2008). A standard grade NdFeB magnet with a remanence of 1.2 T has a intrinsic coercivity of $\mu_0 H_C = 3.2$ T, so the reversal of the magnet will only be a problem above this flux density. One should note that for NdFeB magnets with a higher energy density, e.g. 1.4 T, the intrinsic coercivity can be significantly lower, e.g. around $\mu_0 H_C = 1.4$ T.

4.1. *Design of an optimal magnet assembly*

Based on the knowledge gained from the magnet assemblies reviewed certain key features that the magnet assembly must accomplish or provide can be stated. It must produce a region that has a high flux density preferably with as high uniformity as possible. Also the magnet must be designed such that the amount of leakage of flux or stray field is as low as possible. This includes both leakage to the surroundings and leakage to low flux density regions in the magnet assembly. The recommendations to maximize Λ_{cool} for a given flux density can be summed up as

- Use minimum amount of magnets.
- Make the volume for magnetocaloric material as large as possible.
- Utilize the magnet at all times.
- Ensure that the flux density in the low flux density region is low.
- Minimize leakage to surrounding by e.g. using soft magnetic material as flux guides.
- Use the lowest possible flux density necessary to obtain the chosen temperature span and cooling capacity.

If magnetic refrigeration is to become a viable alternative to conventional refrigeration technology these simple design criteria must be followed.

5. Conclusion

Different ways of generating the magnetic field used in a magnetic refrigeration device have been discussed and it has been shown that permanent magnets are the only viable solution, at present, to common household magnetic refrigeration devices. Twelve published magnet designs were reviewed in detail and were compared using the Λ_{cool} parameter. The best design was found to be five times better than the worst design. Finally guidelines for designing an optimal magnet assembly was presented.

Acknowledgements

The authors would like to acknowledge the support of the Programme Commission on Energy and Environment (EnMi) (Contract No. 2104-06-0032) which is part of the Danish Council for Strategic Research. The authors also wish to thank T. Okamura, A. Rowe, C. Zimm, J. Chell, Z.G. Zheng and J. Tušek for useful discussions and for providing some of the figures and values in this article.

REFERENCES

Aharoni, A., 1998. Demagnetizing factors for rectangular ferromagnetic prisms. Journal of Applied Physics 83, 3432.

Bahl, C., Petersen, T., Pryds, N., Smith, A., Petersen, T., 2008. A versatile magnetic refrigeration test device. Review of Scientific Instruments 79 (9), 093906.

Barclay, J.A., 1988. Magnetic refrigeration: a review of a developing technology. Advances in Cryogenic Engineering 33, 719–731.

Bjørk, R., Bahl, C.R.H., Smith, A., Pryds, N., 2008. Optimization and improvement of Halbach cylinder design. Journal of Applied Physics 104 (1), 13910.

Bloch, F., Cugat, O., Meunier, G., Toussaint, J., 1998. Innovating approaches to the generation of intense magnetic fields: design and optimization of a 4 Tesla permanent magnet flux source. IEEE Transactions on Magnetics 34 (5), 2465–2468.

Blumenfeld, P.E., Prenger, F.C., Sternberg, A., Zimm, C., 2002. Magnetic refrigerators – high temperature superconducting magnetic refrigeration. Advances in Cryogenic Engineering 47 (A), 1019.

Bohigas, X., Molins, E., Roig, A., Tejada, J., Zhang, X., 2000. Room-temperature magnetic refrigerator using permanent magnets. IEEE Transactions on Magnetics 36, 538–544.

Brown, G., 1976. Magnetic heat pumping near room temperature. Journal of Applied Physics 47 (8), 3673–3680.

Buchelnikov, V., Taskaev, S., Bychkov, I., Chernets, I., Denisovskiy, A., 2007. The prototype of effective device for magnetic refrigeration. In: Proceedings of the 2nd International Conference of Magnetic Refrigeration at Room Temperature, Portoroz, Slovenia, pp. 371–376.

Chell, J., 2009. Private communication.

Chell, J., Zimm, C.B., 2006. Permanent magnet assembly. US Patent 7148777.

Chen, Y., Tang, Y., Wang, B., Xue, Q., Tu, M., 2007. A permanent magnet rotary magnetic refrigerator. In: Proceedings of the 2nd International Conference of Magnetic Refrigeration at Room Temperature, Portoroz, Slovenia, pp. 309–313.

Coelho, A., Gama, S., Magnus, A., Carvalho, G., 2009. Prototype of a Gd-based rotating magnetic refrigerator for work around room temperature. In: Proceedings of the 3rd International Conference on Magnetic Refrigeration at Room Temperature, Des Moines, Iowa, USA, pp. 381–386.

Coey, J.M.D., Ni Mhiochain, T.R., 2003. Permanent magnets. High Magnetic Fields. World Scientific, pp. 25–47.

Dong, Q., Zhang, H., Sun, J., Shen, B., Franco, V., 2008. A phenomenological fitting curve for the magnetocaloric effect of materials with a second-order phase transition. Journal of Applied Physics 103 (11), 116101–116103.

Dupuis, C., Vialle, A.J., Legait, U., Kedous-Lebouc, A., Ronchetto, D., 2009. New investigations in magnetic refrigeration device, AMR cycle and refrigerant bed performance evaluation. In: Proceedings of the 3rd International Conference on Magnetic Refrigeration at Room Temperature, Des Moines, Iowa, USA, pp. 437–442.

Engelbrecht, K., Jensen, J.B., Bahl, C.R.H., Pryds, N., 2009. Experiments on a modular magnetic refrigeration device. In: Proceedings of the 3rd International Conference on Magnetic Refrigeration at Room Temperature, Des Moines, Iowa, USA, pp. 431–436.

Engelbrecht, K.L., Nellis, G.F., Klein, S.A., Zimm, C.B., 2007. Recent developments in room temperature active magnetic regenerative refrigeration. HVAC and R Research 13 (4), 525–542.

Franco, V., Conde, A., Pecharsky, V.K., Gschneidner Jr., K.A., 2007. Field dependence of the magnetocaloric effect in Gd and (Er1-xDyx)Al2: does a universal curve exist? EPL (Europhysics Letters) 79 (4), 47009.

Gschneidner Jr., K.A., Pecharsky, V., 2008. Thirty years of near room temperature magnetic cooling: where we are today and future prospects. International Journal of Refrigeration 31 (6), 945–961.

Gschneidner Jr., K.A., Pecharsky, V.K., Tsokol, A.O., 2005. Recent developments in magnetocaloric materials. Reports on Progress in Physics 68, 1479–1539.

Halbach, K., 1980. Design of permanent multipole magnets with oriented rare earth cobalt material. Nuclear Instruments and Methods 169.

Jensen, J.H., Abele, M.G., 1996. Maximally efficient permanent magnet structures. Journal of Applied Physics 79 (2), 1157–1163.

Kim, Y., Jeong, S., 2009. Investigation on the room temperature active magnetic regenerative refrigerator with permanent magnet array. In: Proceedings of the 3rd International Conference on Magnetic Refrigeration at Room Temperature, Des Moines, Iowa, USA, pp. 393–400.

Lee, S.J., Kenkel, J.M., Pecharsky, V.K., Jiles, D.C., 2002. Permanent magnet array for the magnetic refrigerator. Journal of Applied Physics 91 (10), 8894–8896.

Lu, D.W., Xu, X.N., Wu, H.B., Jin, X., 2005. A permanent magnet magneto-refrigerator study on using Gd/Gd–Si–Ge/Gd–Si–Ge–Ga alloys. In: Proceedings of the 1st International Conference on Magnetic Refrigeration at Room Temperature, Montreux, Switzerland, pp. 1–6.

Mallinson, J.C., 1973. One-sided fluxes – a magnetic curiosity? IEEE Transactions on Magnetics 9 (4), 678–682.

Nikly, G., Muller, C., 2007. Technical and economical criteria to design and realize a magneto-caloric heat pump. In: Proceedings of the 2nd International Conference of Magnetic Refrigeration at Room Temperature, Portoroz, Slovenia, pp. 59–70.

Oesterreicher, H., Parker, F., 1984. Magnetic cooling near curie temperatures above 300 K. Journal of Applied Physics 55, 4334–4338.

Okamura, T., 2009. Private communication.

Okamura, T., Rachi, R., Hirano, N., Nagaya, S., 2007. Improvement of 100w class room temperature magnetic refrigerator. In: Proceedings of the 2nd International Conference of Magnetic Refrigeration at Room Temperature, Portoroz, Slovenia, pp. 377–382.

Pecharsky, V.K., Gschneidner Jr., K.A., 2006. Advanced magnetocaloric materials: what does the future hold? International Journal of Refrigeration 29 (8), 1239–1249.

Pecharsky V.K., Gschneidner, Jr., K.A., 2008. Private communication.

Richard, M.A., Rowe, A., Chahine, R., 2004. Magnetic refrigeration: single and multimaterial active magnetic regenerator experiments. Journal of Applied Physics 95 (4), 2146–2150.

Rowe, A., Barclay, J.A., 2002. Design of an active magnetic regenerator test apparatus. Advances in Cryogenic Engineering 47, 325–333.

Rowe, A., 2009a. Performance metrics for active magnetic refrigerators. In: Proceedings of the 3rd International Conference on Magnetic Refrigeration at Room Temperature, Des Moines, Iowa, USA, pp. 195–206.

Rowe, A., 2009b. Private communication.

Sari, O., Balli, M., Trottet, G., Bonhote, P., Egolf, P., Muller, C., Heitzler, J., Bour, S., 2009. Initial results of a test-bed magnetic refrigeration machine with practical running conditions. In: Proceedings of the 3rd International Conference on Magnetic Refrigeration at Room Temperature, Des Moines, Iowa, USA, pp. 371–380.

Shir, F., Bennett, L., Della Torre, E., Mavriplis, C., Shull, R., 2005. Transient response in magnetocaloric regeneration. IEEE Transactions on Magnetics 41 (6), 2129–2133.

Tagliafico, L., Scarpa, F., Tagliafico, G., Valsuani, F., Canepa, F., Cirafici, S., Napoletano, M.C.B., 2009. Design and assembly of a linear reciprocating magnetic refrigerator. In: Proceedings of the 3rd International Conference on Magnetic Refrigeration at Room Temperature, Des Moines, Iowa, USA, pp. 425–430.

Tura, A., Rowe, A., 2007. Design and testing of a permanent magnet magnetic refrigerator. In: Proceedings of the 2nd International Conference of Magnetic Refrigeration at Room Temperature, Portoroz, Slovenia, pp. 363–370.

Tušek, J., Zupan, S., Sarlah, A., Prebil, I.A.P., 2009. Development of a rotary magnetic refrigerator. In: Proceedings of the 3rd International Conference on Magnetic Refrigeration at Room Temperature, Des Moines, Iowa, USA, pp. 409–414.

Vasile, C., Muller, C., 2006. Innovative design of a magnetocaloric system. International Journal of Refrigeration 29 (8), 1318–1326.

Vuarnoz, D., Kitanovski, A., Diebold, M., Gendre, F., Egolf, P., 2007. A magnetic heat pump with porous magneto caloric material. Physica Status Solidi (C) Current Topics in Solid State Physics 4 (12), 4552–4555.

Yu, B., Gao, Q., Zhang, B., Meng, X., Chen, Z., 2003. Review on research of room temperature magnetic refrigeration. International Journal of Refrigeration 26 (6), 622–636.

Zheng, Z., 2009. Private communication.

Zheng, Z., Yu, H., Zhong, X., Zeng, D., Liu, Z., 2009. Design and performance study of the active magnetic refrigerator for room-temperature application. International Journal of Refrigeration 32, 78–86.

Zimm, C., Auringer, J., Boeder, A., Chell, J., Russek, S., Sternberg, A., 2007. Design and initial performance of a magnetic refrigerator with a rotating permanent magnet. In: Proceedings of the 2nd International Conference of Magnetic Refrigeration at Room Temperature, Portoroz, Slovenia, pp. 341–347.

Zimm, C., Boeder, A., Chell, J., Sternberg, A., Fujita, A., Fujieda, S., Fukamichi, K., 2006. Design and performance of a permanent-magnet rotary refrigerator. International Journal of Refrigeration 29 (8), 1302–1306.

Zimm, C., Jastrab, A., Pecharsky, A.S.V., Gschneidner Jr., K., Osborne, M., Anderson, I., 1998. Cryocoolers: regenerative – description and performance of a near-room temperature magnetic refrigerator. Advances in Cryogenic Engineering 43 (B), 1759.

Paper VIII

Paper published in Journal of Applied Physics, 2010

Smith, A., Nielsen, K. K., Christensen, D. V., Bahl, C. R. H., Bjørk, R. and Hattel, J.

The demagnetizing field of a non-uniform rectangular prism

Journal of Applied Physics, 107, 103910, 2010

The demagnetizing field of a nonuniform rectangular prism

A. Smith,[1] K. K. Nielsen,[1,2,a)] D. V. Christensen,[1,3] C. R. H. Bahl,[1] R. Bjørk,[1] and J. Hattel[2]
[1]*Fuel Cells and Solid State Chemistry Division, Risø National Laboratory for Sustainable Energy, Technical University of Denmark, Frederiksborgvej 399, DK-4000 Roskilde, Denmark*
[2]*Department of Mechanical Engineering, Technical University of Denmark, Building 425, Niels Koppels Alle, DK-2800 Kongens Lyngby, Denmark*
[3]*The Niels Bohr Institute, University of Copenhagen, Blegdamsvej 17, DK-2100 Copenhagen, Denmark*

(Received 8 February 2010; accepted 12 March 2010; published online 20 May 2010)

The effect of demagnetization on the magnetic properties of a rectangular ferromagnetic prism under nonuniform conditions is investigated. A numerical model for solving the spatially varying internal magnetic field is developed, validated, and applied to relevant cases. The demagnetizing field is solved by an analytical calculation and the coupling between applied field, the demagnetization tensor field, and spatially varying temperature is solved through iteration. We show that the demagnetizing field is of great importance in many cases and that it is necessary to take into account the nonuniformity of the internal field, especially for nonconstant temperature distributions and composite magnetic materials. © *2010 American Institute of Physics*. [doi:10.1063/1.3385387]

I. INTRODUCTION

The importance of demagnetization for the properties of a magnetic body has long been recognized. The long-range nature of the dipolar force acting between individual magnetic moments will give rise to a demagnetizing field inside the body and can give rise to shape dependence of the thermodynamic properties, e.g., the heat capacity, of the body.[1] Only in uniform ellipsoidal samples (and a few other limiting cases such as an infinite sheet or an infinite cylinder) is the demagnetizing field uniform. Even in these cases, calculations of the demagnetizing field can be quite involved.[2] The results can be expressed in terms of a demagnetization tensor $\mathbb{N}$

$$\mathbf{H} = \mathbf{H}_{\text{appl}} - \mathbb{N} \cdot \mathbf{M}, \tag{1}$$

where $\mathbf{H}$ is the total internal magnetic field, $\mathbf{H}_{\text{appl}}$ is the applied magnetic field, and $\mathbf{M}$ is the constant magnetization. The demagnetization tensor is symmetrical and has a trace equal to one.

If the coordinate axes are chosen to coincide with the principal axes of the ellipsoid, the demagnetization tensor becomes diagonal. Thus, the demagnetizing field is determined by three quantities N_{xx}, N_{yy}, and N_{zz} whose sum is unity. When both the applied field and $\mathbf{M}$ are along a principal axis, Eq. (1) becomes the scalar equation

$$H = H_{\text{appl}} - NM, \tag{2}$$

where N is the relevant demagnetization factor. This equation is often used for other geometries as well. In such cases N should be interpreted as an average demagnetization factor.[3] This approach can be sufficient if one is only interested in the average demagnetizing field over the entire sample. Otherwise, it becomes necessary to consider the spatial variation in the demagnetization explicitly. In particular, this is the case when the relevant physical properties of the material depend nonlinearly on the local field.

In cases where the demagnetizing field is nonuniform, the calculation of it is nontrivial. Since the magnetization of the sample at a given point is dependent on the local field, which in its turn depends on the entire magnetization of the sample, the demagnetizing field has to be calculated self-consistently, e.g., through an iterative approach. Often, the simplifying assumption that the magnetization can be considered as constant and independent of the external field is made. In this case, calculations for a wide range of nonellipsoidal bodies have been carried out.[4–7] In Ref. 4 the case of letting the direction (but not the magnitude) of the magnetization vary is considered and analytical expressions for the demagnetizing field to second order are given for a few special geometries.

To go beyond such simple magnetic equations of state requires numerical methods. For thin disks with cylindrical symmetry Ref. 8 calculated the demagnetizing field for homogeneous applied fields and four different magnetic equations of state: constant susceptibility, constant susceptibility with step discontinuity, hyperbolic tangential field-dependent susceptibility and finally the equation of state for a mean field ferromagnet. In Ref. 9 an axisymmetric model was applied to the problem of demagnetization in an active magnetic regeneration (AMR) device.

In this work we present a full three-dimensional modeling of a rectangular prism based only on the assumption of discretizing the prism into a mesh of grid cells each assumed to have a constant temperature and magnetization. A similar approach was followed in Ref. 10 however, only the demagnetization tensor was calculated and not the demagnetizing field.

The model is introduced in Sec. II. Then, in Sec. III the model is applied to the case of a flat prism with the magnetic field aligned along different axes and with different internal temperature distributions. Two main cases are considered: a

a)Electronic mail: kaki@risoe.dtu.dk.

single-material prism with an internal temperature gradient and a multimaterial prism, i.e., a single prism consisting of several materials, uniformly distributed for simplicity, each having an individual Curie temperature. In Sec. IV the model is compared to the average expression given in Ref. 3. The results, and in particular their relevance to the construction and optimization of an AMR magnetic refrigeration system where multiple materials are expected to be crucial for performance, are discussed in Sec. V.

II. DEMAGNETIZATION MODEL OF A RECTANGULAR PRISM

The internal magnetic field can be written in the general form

$$\mathbf{H} = \mathbf{H}_{\text{appl}} + \mathbf{H}_{\text{dem}}, \tag{3}$$

where the difference between the internal and external field is the demagnetizing field $\mathbf{H}_{\text{dem}}$.

The demagnetizing field can be expressed as an integral over the interior Ω of the body in the following manner

$$\mathbf{H}_{\text{dem}}(\mathbf{r},T) = \frac{1}{4\pi}\int_{\Omega} d\mathbf{r}'\mathbb{D}(\mathbf{r}-\mathbf{r}')\cdot\mathbf{M}[\mathbf{H}(\mathbf{r}',T),\mathbf{r}',T], \tag{4}$$

where $\mathbb{D}$ is a symmetric 3×3 tensor whose components are given in Appendix A. This expression is valid both for points $\mathbf{r}$ inside and outside the body. The magnetization is in general a function of both the internal field, position and temperature. The explicit position dependence is relevant when, e.g., a multimaterial prism is considered. Due to the appearance of the internal field in $\mathbf{M}$, Eq. (4) becomes an implicit equation for the demagnetizing field. Only when the magnetization is independent of the internal field, the equation may be evaluated explicitly. For constant magnetization this may be done either by direct integration[4] or through a Fourier transform approach.[6,7]

At low applied fields the magnetization within a soft ferromagnetic body will form domains in order to minimize the magnetostatic energy. Upon application of a modest magnetic field the domains will be aligned bringing the ferromagnet into a single-domain, saturated state. This saturated state is always assumed in the following.

To assume that the magnetization will not depend on the internal field will be a fair approximation for ferromagnetic bodies at temperatures far below the Curie temperature. However, close to the Curie temperature the magnetization has a strong field dependence. In the following, we will assume that the mean field equation of state captures the essential aspects of this dependence for the purpose of calculating the demagnetizing field. We do not expect our results to differ markedly for more realistic equations of state.

For concreteness we will only consider rectangular prisms. However, the procedure below may readily be adapted to, e.g., multimaterial spheres or cylinders. Considering now a rectangular prism bounded by the inequalities $-a\le x\le a$, $-b\le y\le b$, and $-c\le z\le c$ (see Fig. 1) the demagnetizing field may be expressed as

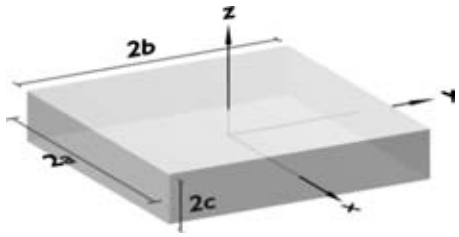

FIG. 1. The coordinate system of the modeled rectangular prism with the coordinate system defined with Origo at the center of the prism. Note that the z-direction is the "thin" direction, i.e., $2c \ll 2a$.

$$\mathbf{H}_{\text{dem}}(\mathbf{r},T) = \frac{1}{4\pi}\int_{-a}^{a} dx'\int_{-b}^{b} dy'\int_{-c}^{c} dz'\mathbb{D}(\mathbf{r}-\mathbf{r}') \cdot\mathbf{M}\{\mathbf{H}[\mathbf{r}',T(\mathbf{r}')],\mathbf{r}',T(\mathbf{r}')\}. \tag{5}$$

Dividing the prism into $n_x\times n_y\times n_z$ rectangular cells (following Refs. 10 and 11) the integral in Eq. (5) may be written as a sum of integrals over each cell

$$\mathbf{H}_{\text{dem}}(\mathbf{r},T) = \frac{1}{4\pi}\sum_{i=1}^{n_x}\sum_{j=1}^{n_y}\sum_{k=1}^{n_z}\int_{-a'}^{a'} dx'\int_{-b'}^{b'} dy'\int_{-c'}^{c'} dz' \mathbb{D}(\mathbf{r}-\mathbf{r}')\cdot\mathbf{M}\{\mathbf{H}[\mathbf{r}',T(\mathbf{r}')],\mathbf{r}',T(\mathbf{r}')\} \tag{6}$$

with $a'=a/n_x$, $b'=b/n_y$, and $c'=c/n_z$. Each cell has the same relative dimensions as the original prism.

Assuming each cell to be sufficiently small to have constant magnetization, $\mathbf{M}_0(\mathbf{r}'_{i,j,k},T_{i,j,k})$, Eq. (6) may be approximated by

$$\mathbf{H}_{\text{dem}}(\mathbf{r},T) \approx -\sum_{i=1}^{n_x}\sum_{j=1}^{n_y}\sum_{k=1}^{n_z} \mathbb{N}(\mathbf{r}-\mathbf{r}'_{i,j,k})\cdot\mathbf{M}_0[\mathbf{H}(\mathbf{r}'_{i,j,k},T_{i,j,k}),\mathbf{r}'_{i,j,k},T_{i,j,k}], \tag{7}$$

where $\mathbb{N}$ denotes the symmetric 3×3 demagnetization tensor field with the components given in Eqs. (A8) and (A12) below. The vector $\mathbf{r}'_{i,j,k}$ denotes the center of the cell with index i,j,k.

The magnetization is generally a function of both the magnitude of the internal field, H, and temperature, T. Therefore, Eq. (3) has to be solved by iteration. For simplicity the magnetization is assumed to be aligned with $\mathbf{H}$, i.e., there is no magnetocrystalline anisotropy.[4]

To obtain the magnitude of the magnetization, M, the mean field equation of state for a ferromagnet is assumed[12]

$$M(T,H) = \mathrm{N_s} g J \mu_{\mathrm{B}} \rho B_J(\chi) \tag{8}$$

with $\mathrm{N_s}$ denoting the number of magnetic spins per unit mass, g the Landé factor, J the total angular momentum in units of $\hbar$, μ_{B} the Bohr magneton, and ρ the mass density. The Brillouin function, B_J, is defined as

$$B_J(\chi) = \frac{2J+1}{2J}\coth\left(\frac{2J+1}{2J}\chi\right) - \frac{1}{2J}\coth\left(\frac{1}{2J}\chi\right), \tag{9}$$

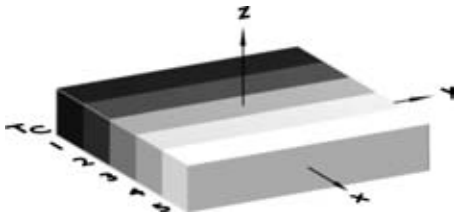

FIG. 2. The concept of grading the prism with different ferromagnets. In this case five materials are illustrated. The Curie temperatures differ from layer to layer as indicated by T_{C1-5}.

$$\chi = \frac{gJ\mu_B\mu_0 H}{k_B T} + \frac{3T_C J}{T(J+1)} B_J(\chi). \tag{10}$$

Here the vacuum permeability, μ_0, the Boltzmann constant, k_B, and the Curie temperature, T_C, were introduced. Equation (10) is iterated to obtain a self-consistent solution. In Appendix B a numerical model solving the coupled problem in Eqs. (3)–(10) is described in detail.

III. APPLICATION OF THE MODEL

Four different cases are investigated in the following. Two cases with a rectangular prism made of a single magnetic material, i.e., having one Curie temperature, and two cases with a so-called graded material, i.e., a composite material which contains regions with different Curie temperatures. In the latter case, the grading is assumed to be along the *x*-direction; for concreteness we consider five equal-sized regions each with its own Curie temperature (illustrated in Fig. 2). This is presented in Sec. III B.

Both materials configurations are considered under two different temperature situations: one with a constant temperature and one with an imposed temperature gradient. The latter case is relevant to investigate for, e.g., magnetic refrigeration, or in other cases where a thermal gradient is present in the system. In general, such a gradient may cause the prism to be in different magnetic phases at the same time. This is the typical operation mode of a magnetic material used in magnetic refrigeration, which will be roughly centered around the Curie temperature for optimal utilization of the magnetocaloric effect.[13]

As a magnetic material, gadolinium (Gd) is used since it can be fairly well described by the mean field equation of state, Eq. (8);[14] additionally it acts as a de facto benchmark material in magnetic refrigeration. The Curie temperature of Gd is taken to be 293 K, and the other input parameters for the mean field equation of state are given in Table I. The dimensions of the prism are taken to be $2a=0.02$ m, $2b=0.02$ m, and $2c=0.001$ m in all cases. The coordinate system is illustrated in Fig. 1.

TABLE I. Parameters for the mean field equation of state, Eq. (8), for Gd. Data taken from Refs. 15 and 16.

Parameter	N_s (kg^{-1})	g (−)	J ($\hbar$)	ρ ($kg\ m^{-3}$)	T_C (K)
Value	3.83×10^{24}	2	7/2	7900	293

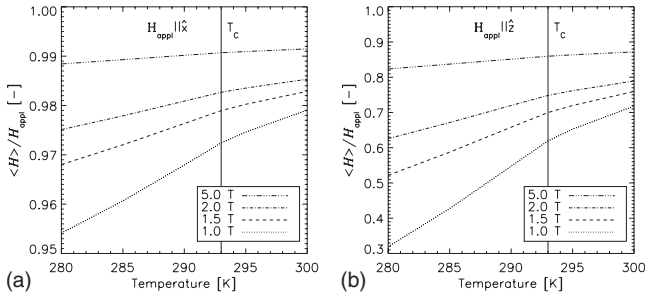

FIG. 3. The normalized mean of the magnetic field as a function of the (spatially constant) temperature for four different applied fields in the case of a rectangular prism consisting of one magnetic material. (a) The applied field is along the *x*-direction. (b) The applied field is along the *z*-direction.

A. Single Curie-point flat prism

1. Constant temperature

We first consider the case of a single material with a constant temperature to validate our approach. This is a well-known situation and will only briefly be discussed. In Fig. 3 the normalized mean of the magnitude of the internal field is plotted as a function of the (spatially constant) prism temperature for four different applied fields. It is evident from the figure that the effect of demagnetization decreases at higher applied fields in the ferromagnetic phase. This follows directly from the fact that the magnetization is saturated in the ferromagnetic phase and thus the demagnetizing field becomes constant. However, a field of more than 5 T is needed in order for this to be the case (this field value is material dependent, of course). Furthermore, when applying the field in the *xy*-plane of the prism, the magnetic field is reduced with a few percent whereas it is reduced with up to 70% in the case of applying the field along the *z*-direction. The decrease is dependent on temperature and material properties.

2. Linear temperature profile

In the following, the rectangular prism is assumed to have an imposed temperature profile ranging linearly from 280 to 300 K along the *x*-direction. This will make the magnetic state of the prism depend on *x*. This is a special case of great importance in, e.g., magnetic refrigeration where a magnetic material acts both as a regenerator material, i.e., upholding a thermal gradient, and as an active magnetic material through the magnetocaloric effect.

Figure 4 shows the two cases where the applied field is along the *x*-direction and *z*-direction, (a) and (b), respectively. Four different fields have been applied, namely 1.0, 1.5, 2.0, and 5.0 T. The same trends as in Fig. 3 are observed. The rather large applied magnetic field of 5 T saturates the magnetization (in the ferromagnetic phase) and the effect of demagnetization is thus small here. However, considering the cases of applied fields of 1.0–2.0 T a rather large gradient in the internal field is observed when the applied field is along the *z*-direction [Fig. 4(b)]. In the case of applying the field along the *x*-direction [Fig. 4(a)], the internal field is generally not affected greatly by the demagnetizing field. However, on the low temperature edge, i.e., where $x/a=-1$, the field drops rapidly. A similar, though not as large, drop is seen on the

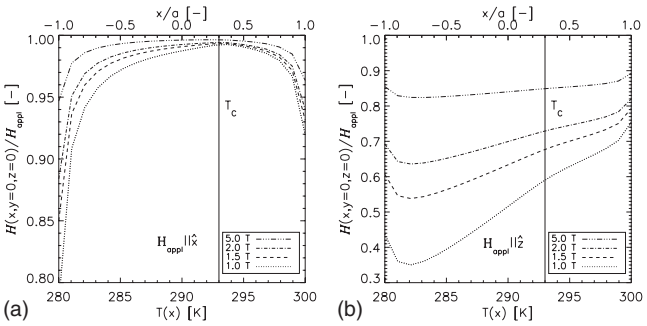

FIG. 4. The magnetic field along the line $y=0$, $z=0$, and $-1 \leq x/a \leq 1$. The prism has an imposed thermal gradient along the x-direction ranging from 280 to 300 K and consists of one magnetic material with a Curie temperature of 293 K. (a) The applied field is along the x-direction. (b) The applied field is along the z-direction.

high temperature edge (at $x/a=1$). These two drops in the internal field are due to the fact that the demagnetization tensor field is largest on the edges perpendicular to the direction of the applied field. The reason that the lower temperature edge has the somewhat greater drop in internal field is because this part of the prism is in the ferromagnetic phase and thus the magnetization is largest here and consequently the demagnetizing field is greater.

B. Flat prism with multiple Curie temperatures

In the following a rectangular prism consisting of five equally distributed magnetic materials resembling Gd but with Curie temperatures 280 K, 285 K, 290 K, 295 K, and 300 K, respectively, is considered. The grading of the prism is along the x-axis. With the temperature of the prism in the interval 280 to 300 K the individual parts of the prism will be in different magnetic phases but still in the vicinity of their respective Curie temperatures.

1. Constant temperature

Considering the case with the prism having a constant temperature the magnitude of the internal field across the prism in the direction of the grading is plotted in Fig. 5 for five different constant temperatures. The applied field is in all cases equal to 1 T. The magnetic field is seen to be discontinuous in the x-direction when applying the field in this direction [Fig. 5(a)], whereas it is continuous in the x-direction when applying the field along the y-direction and z-direction [Figs. 5(b) and 5(c)]. This is to be expected since in the former case the magnetic field lines are crossing material boundaries and the normal component of **H** is discontinuous. In the latter cases the field lines are perpendicular to the materials boundaries and the parallel component of **H** across boundaries is continuous as expected. It should be noted that the largest component of **H** is along the direction of the applied field. Considering the magnetic flux density,

$$\mathbf{B} = \mu_0(\mathbf{H} + \mathbf{M}), \tag{11}$$

the opposite is true, i.e., the normal component is continuous whereas the parallel component is discontinuous. This is seen in Figs. 6(a) and 6(c). Figure 6(b) shows a plot of the magnitude of the magnetic flux density along the x-axis

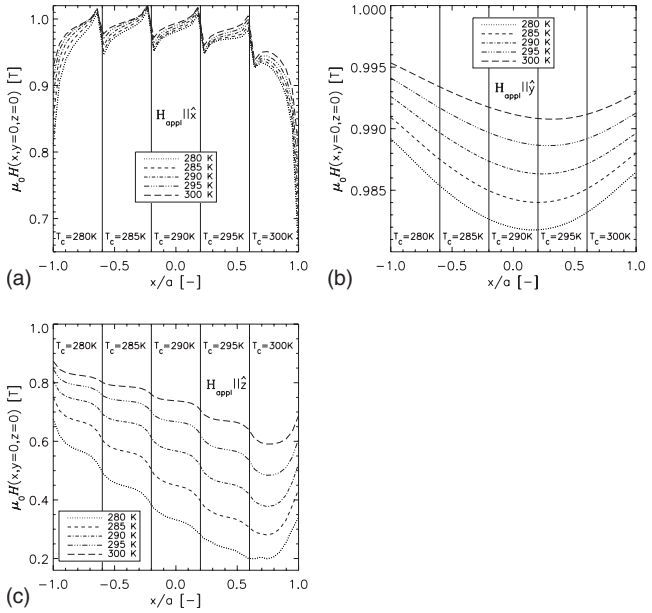

FIG. 5. The magnitude of the magnetic field along the line defined as $-1 \leq x/a \leq 1$, $y=0$, and $z=0$ through the prism for five different constant temperatures. The prism is divided in five regions each being a magnetic material resembling Gd but with different Curie temperatures (280 K, 285 K, 290 K, 295 K, and 300 K, respectively), as illustrated in Fig. 2. (a) The applied field is along the x-direction. (b) The applied field is along the y-direction. (c) The applied field is along the z-direction. In all cases $\mu_0 H_{\text{appl}}=1.0$ T.

when the magnetic field is applied along the y-axis. Since H is virtually constant (to within a few per mille; see Fig. 5), the magnetization is dominating the spatial variation in B. This is seen in the staircaselike plot on Fig. 6(b). At, e.g., a constant temperature of 280 K, the value of B in the part of the prism with a Curie temperature of 280 K is equal to B at a temperature of 285 K in the part of the prism with a Curie

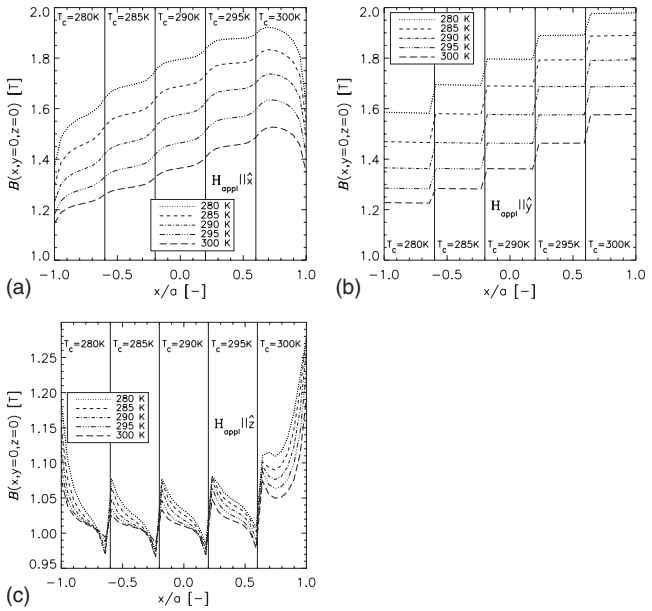

FIG. 6. The magnitude of the magnetic flux density, B, along the same line as in Fig. 5, i.e., $-1 \leq x/a \leq 1$, $y=0$, $z=0$ for five different temperatures. The prism is the same as considered in Fig. 5. (a) The applied field is along the x-direction. (b) The applied field is along the y-direction. (c) The applied field is along the z-direction. In all cases $\mu_0 H_{\text{appl}}=1.0$ T.

point of 285 K, etc. The discontinuities across the internal materials boundaries are expected again due to the boundary conditions.

When applying the magnetic field along the *x*-direction, which causes minimal demagnetization, it is observed that the variation in the temperature of the prism does not change the internal field significantly. However, when applying the field along the *z*-direction, Fig. 5(c), a significant difference is observed between the various temperature cases. The lower the temperature of the prism the more of the individual composites are in their ferromagnetic state. This produces higher magnetization values and thus also a larger demagnetizing field. For increasing Curie temperature (along the *x*-axis) the magnetic field decreases because of the larger magnetization. It should be noted that for a constant temperature of 280 K the average internal field is about 60% of the applied field. The maximum decrease is observed to be around 80% for the cases studied here. The reason for the increase in magnetic field at either ends for all temperature cases is the relatively low demagnetization factor on the boundary. It is noted that the internal field may actually be greater than the applied field locally. This is seen in Fig. 5(a) and can be explained by flux shimming due to the discontinuity in the permeability on the boundary between two different magnetic materials.[9]

Finally, it is noted that applying the field along the *y*-direction [Fig. 5(b)] yields both a continuous and large internal magnetic field. The difference in this situation between the largest and smallest values of the magnitude of the internal field is only a few percent whereas in the case of applying the field along the *x*-direction may give a decrease in as much as 30%, though only in relatively small regions.

2. Linear temperature profile

Figure 7 shows the magnetic field in the *x*-direction of a prism similar to the one considered in Sec. III B 1 but with an imposed linear temperature profile ranging from 280 to 300 K. For the four different applied fields, 1, 1.5, 2.0, and 5.0 T, Figs. 7(a)–7(c) show the case when magnetizing along the *x*-direction, *y*-direction, and *z*-direction, respectively. A magnetic field similar to that obtained in the constant temperature case, Fig. 5, is produced in this case. However, when applying the field along the *x*-direction the drop in magnetic field at either end is similar to the edge defined as $x=-a$ in Fig. 5(a).

Again, as discussed in Sec. III B 1, applying the field along the *y*-direction [Fig. 7(b)] yields both a smooth and large internal field. This may be explained by the simple fact that the normal component of **H** is continuous across materials boundaries and the demagnetization is low when the field is applied in the *y*-direction.

Finally, when applying the field along the *z*-direction the internal field is more smooth than in the constant temperature case [see Figs. 5(c) and 7(c)]. This is due to the fact that each section of the prism having a specific Curie temperature is relatively close to this temperature. Thus, the magnetization across the prism is fairly constant as opposed to the decrease with increasing *x* in Fig. 5(b). This results in a more constant demagnetizing field. It is also observed in Figs. 7(a)–7(c)

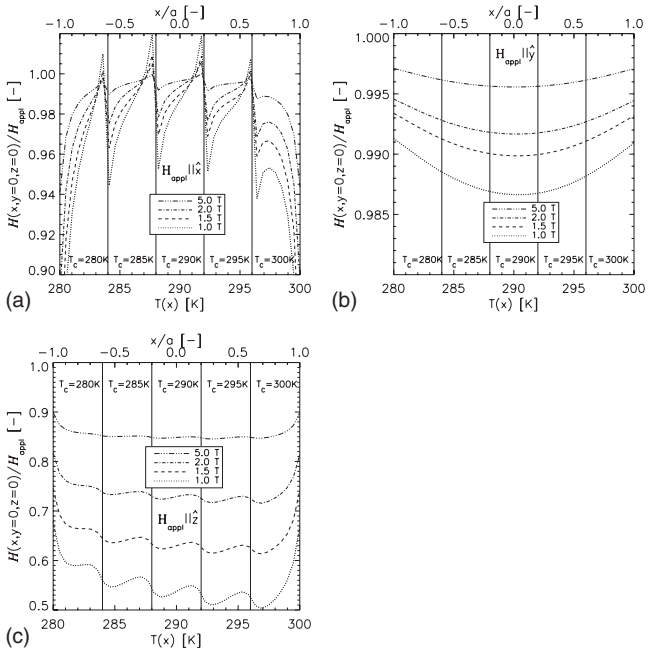

FIG. 7. The magnitude of the internal field along the line $-1 \le x \le 1$, $y=0$, and $z=0$ for four different applied fields. The prism is divided into five materials each having a different Curie temperature as in Fig. 5. The prism has an imposed linear temperature profile along the *x*-direction ranging from 280 K to 300 K. (a) The applied field is along the *x*-direction. (b) The applied field is along the *y*-direction. (c) The applied field is along the *z*-direction.

that lower applied fields induce larger variation along the *x*-direction, which is due to the fact that the magnetization becomes saturated above a certain field and thus the demagnetizing field becomes constant.

IV. COMPARISON TO THE AVERAGE DEMAGNETIZATION FACTOR

In Ref. 3 the average demagnetization factor, *N*, of a prism under the assumption that the magnetization and internal field are homogeneous and constant was calculated by Aharoni. In the following a comparison between the results of the model presented here and this average value is performed. Experimentally, the applied field and the mean magnetization along the direction of the applied field may be obtained. This leads to the definition of a representative average demagnetization factor, $N_{0,i}$

$$\langle H_i \rangle = H_{\mathrm{appl},i} - N_{0,i}\langle M_i \rangle \tag{12}$$

with the subscript *i* denoting the component of the field. It should be noted that with this definition, $N_{0,i}$, is not the average of the demagnetization tensor field given in Eqs. (A8) and (A12). In particular, the sum of $N_{0,x}$, $N_{0,y}$, and $N_{0,z}$ need not be unity. It should rather be interpreted as a simplification of the model results in terms of a single number, which is useful when analyzing experimental data.

Figure 8(a) shows $N_{0,x}$ for the case of a constant temperature, single material rectangular prism with an applied field of 1 T along the *x*-direction. The prism has a symmetric *yz*-cross section and the length is varied in the *x*-direction giving rise to a variation in the aspect ratio. The average demagnetization factor is seen to coincide with the Aharoni

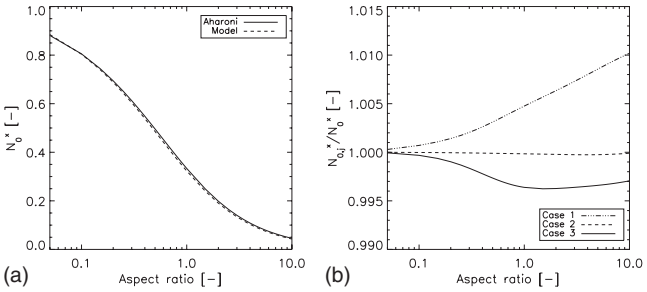

FIG. 8. The representative average demagnetization factor as defined in Eq. (12). (a) Shows this factor as a function of aspect ratio for a rectangular prism with quadratic cross section (in the *yz*-plane) and varying length (along the *x*-direction). The applied field is along the *x*-direction and has a magnitude of 1 T. The temperature is fixed at 293 K, i.e., the Curie temperature. (b) Three specific cases where the temperature and composition of the magnetic material are varied. Case 1 is for a constant temperature of 293 K with five materials, with Curie temperatures 280 K, 285 K, 290 K, 295 K, and 300 K, respectively, spaced evenly along the *x*-direction. Case 2 is for the same composition as in Case 1 but with a linear temperature profile ranging from 280–300 K. Case 3 is for a single material prism with an imposed linear temperature profile also from 280–300 K. In all cases the graphs show the ratio between the respective average demagnetization factor and the single material, constant temperature average demagnetization factor.

expression almost completely. In the limits where the aspect ratio goes to zero and infinity, respectively, the demagnetization factors are equal. However, for aspect ratios from one to five the Aharoni demagnetization factor is a few percent larger than the representative average defined in Eq. (12). This may be explained from the fact that the corners of the prism have a relative large impact on the demagnetization factor in these cases, i.e., the magnetization and thus internal field deviate mostly from being parallel to the applied field for this range of aspect ratios. Since the Aharoni expression assumes the magnetization to be completely parallel to the applied field, a discrepancy is to be expected.

Figure 8(b) shows the average demagnetization factor for the constant temperature and single material case compared to the three cases: (1) a rectangular prism graded with five materials as discussed in Sec. III B 1, (2) same as in (1) but with an imposed linear temperature profile, i.e., as discussed in Sec. III B 2, and finally (3) a single material prism with an imposed linear temperature profile as discussed in Sec. III A 2. It is clearly evident from the figure that the representative average demagnetization factor is not purely geometric. In the cases investigated here the effect of grading the material or imposing a linear temperature profile is of the order of 1% only. This should be taken as a consequence of the selected cases rather than as a general rule. Indeed, Ref. 8 found their effective demagnetization factor to vary with as much as 10%–20% due to nongeometric factors.

V. CONCLUSIONS AND DISCUSSION

A numerical solution to the fully coupled problem of solving for the internal magnetic field in a three-dimensional rectangular prism with spatially varying temperature, applied magnetic field and magnetization has been derived and implemented. The model was applied to several relevant cases where the orientation of a magnetic material and an applied magnetic field is crucial combined with imposed temperature gradients. The magnetic material was assumed to be either homogeneous or a multilayered composite.

From the results presented in this paper it can be concluded that detailed knowledge of the demagnetizing field throughout the sample is important in many cases. This includes the situations when the temperature is not spatially constant or the sample is a composite material consisting of several materials each having a distinct Curie temperature. Imposing a temperature gradient across the sample makes the internal magnetic field become spacially asymmetric and especially when the demagnetization tensor field is rather large the internal field may be approximately linear as shown in Fig. 4(b). In this case the largest value of the internal field in the sample may be 50% greater than the smallest, which certainly invalidates any assumption of constant magnetization throughout the sample.

When applying a magnetic field along the direction of the grading of the material (in this case the *x*-direction) discontinuities on each internal boundary are observed. This is a direct consequence of the boundary conditions that apply generally for **H** and **B**. This leaves two preferred directions to apply the magnetic field in (the *x*-direction and *y*-direction, respectively), in order to minimize the demagnetizing field. However, a large difference is observed in the behavior of the internal magnetic field between these two cases. When the external magnetic field is applied along the *x*-direction, discontinuities exist at every internal material boundary due to the boundary conditions for **H**. In the other case, when the applied magnetic field is along the *y*-direction, no discontinuities are present. Furthermore, the magnitude of the internal magnetic field is generally seen to be larger in this case. It may therefore be concluded that great care should be taken when deciding along which direction the magnetic field should be applied with respect to both the demagnetizing field and a possible grading of the magnetic material.

In the case of applying the magnetic field in the *z*-direction to a constant temperature sample a difference between single and multiple material prisms is observed. In the former case the internal field is fairly constant. In the latter case the internal field becomes almost linear in the *x*-direction for a range of temperatures [see Fig. 5(c)]. However, when imposing a temperature gradient in the *x*-direction the virtually opposite is the case [compare Figs. 4(b) and 7(c)].

An average demagnetization factor was introduced and compared to the analytical expression calculated in Ref. 3 which is based on the assumptions that the magnetization is constant and completely aligned with the applied field. However, when the prism does not have a constant temperature or is made of a composite of different magnetocaloric materials, the demagnetization factor of Eq. (12) changes slightly.

Finally, it is concluded that the internal magnetic field is far from being constant under realistic circumstances and that it may be a poor approximation to assume so. As expected, when imposing a temperature gradient across the rectangular prism and assuming a composite material the internal field can become highly inhomogeneous, depending on the orientation of the applied field. Such inhomogeneities

are important in any case where a good representation of the internal field is sought. It is noted that the results of this paper are valid for single prisms only. In many situations stacks or arrays of prisms will be relevant. A future paper on this using the model presented here is in preparation.

ACKNOWLEDGMENTS

The authors thank the support of the Programme Commission on Energy and Environment (EnMi) (Contract No. 2104-06-0032) which is part of the Danish Council for Strategic Research.

APPENDIX A: CALCULATING THE $\mathbb{D}$ TENSOR FIELD

The vector potential of a single magnetic dipole at $\mathbf{r}'$ is

$$\mathbf{A}_i(\mathbf{r}) = \frac{\mu_0}{4\pi}\frac{\mathbf{m}_i \times (\mathbf{r}-\mathbf{r}')}{|\mathbf{r}-\mathbf{r}'|^3}. \tag{A1}$$

The total vector potential of a magnetic body is obtained by integrating over the interior of the body (with $\mathbf{m}_i = \mathbf{M}dV$):

$$\mathbf{A}(\mathbf{r}) = \frac{\mu_0}{4\pi}\int_\Omega d\mathbf{r}'\frac{\mathbf{M}(\mathbf{r}')\times(\mathbf{r}-\mathbf{r}')}{|\mathbf{r}-\mathbf{r}'|^3}. \tag{A2}$$

Note that this gives the vector potential both inside and outside of the prism.

The resulting **H**-field is

$$\mathbf{H}(\mathbf{r}) = \frac{1}{\mu_0}\mathbf{B}(\mathbf{r}) - \mathbf{M}(\mathbf{r}) = \frac{1}{\mu_0}\nabla \times \mathbf{A} - \mathbf{M}(\mathbf{r})$$
$$= -\frac{1}{4\pi}\int_\Omega d\mathbf{r}'(\mathbf{M}(\mathbf{r}')\cdot\nabla)\frac{\mathbf{r}-\mathbf{r}'}{|\mathbf{r}-\mathbf{r}'|^3}, \tag{A3}$$

which is the required demagnetizing field, $\mathbf{H}_{\mathrm{dem}}$.

The differentiations can be performed straightforwardly, giving rise to the following equation

$$\mathbf{H}_{\mathrm{dem}}(\mathbf{r}) = \frac{1}{4\pi}\int_\Omega d\mathbf{r}'\mathbb{D}(\mathbf{r}-\mathbf{r}')\cdot\mathbf{M}(\mathbf{r}'), \tag{A4}$$

with $\mathbb{D}$ being a symmetrical 3×3 tensor with elements

$$D_{ii}(\mathbf{r}) = -\frac{1}{|\mathbf{r}|^3} + \frac{3x_i^2}{|\mathbf{r}|^5} \tag{A5}$$

$$D_{ij}(\mathbf{r}) = \frac{3x_i x_j}{|\mathbf{r}|^5}, \quad i \neq j \tag{A6}$$

Considering a rectangular prism with constant magnetization, $\mathbf{M}(\mathbf{r}) = \mathbf{M}_0$,[4] the demagnetizing field becomes

$$\mathbf{H}_{\mathrm{dem}}(\mathbf{r}) = \frac{1}{4\pi}\int_{-a}^{a}dx'\int_{-b}^{b}dy'\int_{-c}^{c}dz'\mathbb{D}(\mathbf{r}-\mathbf{r}')\cdot\mathbf{M}_0$$
$$= -\mathbb{N}(\mathbf{r})\cdot\mathbf{M}_0, \tag{A7}$$

where the symmetric 3×3 demagnetization tensor $\mathbb{N}(\mathbf{r})$ has the components

$$N_{ii}(\mathbf{r}) = \frac{1}{4\pi}[\arctan f_i(x,y,z) + \arctan f_i(-x,y,z)$$
$$+ \arctan f_i(x,-y,z) + \arctan f_i(x,y,-z)$$
$$+ \arctan f_i(-x,-y,z) + \arctan f_i(x,-y,-z)$$
$$+ \arctan f_i(-x,y,-z) + \arctan f_i(-x,-y,-z)] \tag{A8}$$

where

$$f_x(x,y,z) = \frac{(b-y)(c-z)}{(a-x)[(a-x)^2+(b-y)^2+(c-z)^2]^{1/2}} \tag{A9}$$

$$f_y(x,y,z) = \frac{(a-x)(c-z)}{(b-y)[(a-x)^2+(b-y)^2+(c-z)^2]^{1/2}} \tag{A10}$$

$$f_z(x,y,z) = \frac{(b-y)(a-x)}{(c-z)[(a-x)^2+(b-y)^2+(c-z)^2]^{1/2}}. \tag{A11}$$

The off-diagonal elements are

$$N_{ij}(\mathbf{r}) = -\frac{1}{4\pi}\ln\left[\frac{F_{ij}(\mathbf{r},a,b,c)F_{ij}(\mathbf{r},-a,-b,c)F_{ij}(\mathbf{r},a,-b,-c)F_{ij}(\mathbf{r},-a,b,-c)}{F_{ij}(\mathbf{r},a,-b,c)F_{ij}(\mathbf{r},-a,b,c)F_{ij}(\mathbf{r},a,b,-c)F_{ij}(\mathbf{r},-a,-b,-c)}\right], \quad i \neq j \tag{A12}$$

where

$$F_{xy}(\mathbf{r},a,b,c) = (c-z) + [(a-x)^2+(b-y)^2+(c-z)^2]^{1/2} \tag{A13}$$

$$F_{yz}(\mathbf{r},a,b,c) = (a-x) + [(a-x)^2+(b-y)^2+(c-z)^2]^{1/2} \tag{A14}$$

$$F_{xz}(\mathbf{r},a,b,c) = (b-y) + [(a-x)^2+(b-y)^2+(c-z)^2]^{1/2}. \tag{A15}$$

APPENDIX B: NUMERICAL IMPLEMENTATION OF THE MODEL

This appendix describes the implementation of a numerical model for solving the demagnetization problem as stated in Eqs. (3) and (7). First a simple scheme for optimized

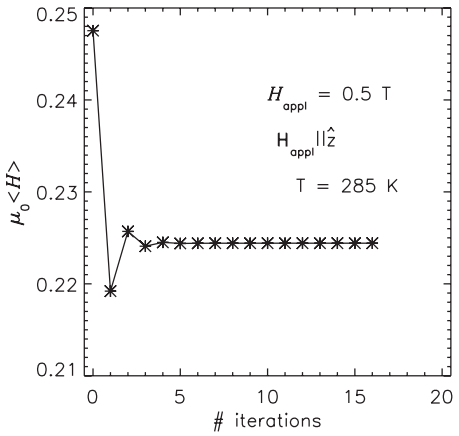

FIG. 9. The mean of the internal magnetic field as a function of number of iterations for the case when applying the magnetic field in the *z*-direction, setting the temperature to be constant at 285 K (below the Curie temperature) and $\mu_0 H_{appl}=0.5$ T.

convergence conditions is presented. Second, the resolution of the model is discussed. Finally, symmetry conditions and parallelization are considered since the problem is of order n^2 with $n=n_x\times n_y\times n_z$.

1. Convergence

The criterium for convergence is defined as the maximum difference between the internal magnetic fields in two following iterations should be less than 10^{-8} T. This is a criterium that is very similar to that of Ref. 8. An under-relaxation technique on the magnetization for obtaining convergence *in situ*ations with small applied fields and/or temperatures below the Curie temperature was applied in Ref. 8. By thorough testing, we found that under-relaxing on the internal field was better for convergence. This may be expressed as

$$\mathbf{H}_{n+1}=\mathbf{H}_n+\lambda_n[\mathbf{H}(M_n)-\mathbf{H}_n], \tag{B1}$$

where n denotes the iteration step, $\mathbf{H}_0=\mathbf{H}_{appl}$, $M_n=M(H_n)$ using Eq. (8) and assuming $\mathbf{M}$ to be parallel to $\mathbf{H}$ in the previous step and $\mathbf{H}(M_n)$ is obtained through Eqs. (3) and (7). The under-relaxation parameter for the nth iteration is denoted λ_n, which attains a value in the interval $0<\lambda_n\leq 1$. Finally, it is noted that Eq. (B1) is used on every mesh point and the convergence is determined from the mesh point where two consecutive iterations yield $\max[\mathrm{abs}(\mathbf{H}_n-\mathbf{H}_{n+1})]$ ensuring the slowest but most precise convergence. Figure 9 shows an example of the under-relaxation technique.

2. Resolution

A variation in resolution is shown in Fig. 10. The resolution of the prism is in all cases, except when comparing to the average demagnetization factor, $(n_x,n_y,n_z)=k(2a,2b,10\times 2c)$ with k being an arbitrary scaling constant. As can be seen from the figure a fairly low resolution is sufficient. This corresponds to $(n_x,n_y,n_z)=(20,20,10)$ for the case discussed in this work.

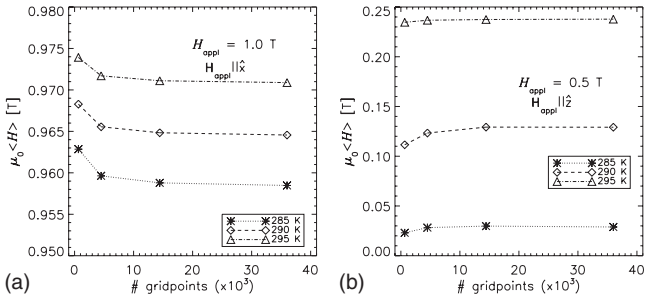

FIG. 10. The mean of the internal magnetic field as a function of the number of grid points for three different constant temperatures and an applied field of 1.0 T applied along the *x*-direction (a) and an applied field of 0.5 T applied along the *z*-direction (b).

3. Symmetry and optimization

The solution to the problem stated in Eqs. (3) and (7) both involves iteration of Eq. (3) and an n^2 problem from Eq. (7). Optimization in the form of exploitation of symmetry should be employed. The rectangular prism is symmetric around all three axes meaning that only one octant needs be considered when calculating the demagnetization tensor field, $\mathbb{N}$. Obviously, the applied field, temperature and magnetization cannot *a priori* be assumed to be symmetric since realistic scenarios include both temporally and spatially varying magnetic fields and temperatures.

However, the nature of $\mathbb{N}$ is purely geometric and is thus only a function of $\mathbf{r}-\mathbf{r}'_{i,j,k}$, a', b', and c'. Since the grid is defined to be homogeneous, the calculation of $\mathbb{N}$ only has to be performed once (at the beginning of the iteration process). Furthermore, $\mathbb{N}$ needs only to be evaluated in one octant and from this result can be mirrored to the remaining part of the coordinate system. Finally, during the calculations needed for one iteration, the value of M is obtained from the previous iteration (or, in the case of the first iteration, from the initial guess), which means that the evaluations of the dot products between $\mathbb{N}$ and $\mathbf{M}$ needed in Eq. (7) are completely decoupled, which results in the possibility of maximized parallelization.

[1]P. M. Levy and D. P. Landau, J. Appl. Phys. **39**, 1128 (1968).
[2]J. A. Osborn, Phys. Rev. **67**, 351 (1945).
[3]A. Aharoni, J. Appl. Phys. **83**, 3432 (1998).
[4]R. I. Joseph and E. Schloemann, J. Appl. Phys. **36**, 1579 (1965).
[5]M. Beleggia and M. De Graef, J. Magn. Magn. Mater. **263**, L1 (2003).
[6]S. Tandon, M. Beleggia, Y. Zhu, and M. De Graef, J. Magn. Magn. Mater. **271**, 9 (2004).
[7]S. Tandon, M. Beleggia, Y. Zhu, and M. De Graef, J. Magn. Magn. Mater. **271**, 27 (2004).
[8]J. A. Brug and W. P. Wolf, J. Appl. Phys. **57**, 4685 (1985).
[9]O. Peksoy and A. Rowe, J. Magn. Magn. Mater. **288**, 424 (2005).
[10]M. Lu, Z. Yang, and F.-L. Wei, Int. J. Infrared Millim. Waves **19**, 1027 (1998).
[11]M. Schabes and A. Aharoni, IEEE Trans. Magn. **23**, 3882 (1987).
[12]A. H. Morrish, *The Physical Priciples of Magnetism* (Wiley, New York, 1965).
[13]A. Rowe and A. Tura, Int. J. Refrig. **29**, 1286 (2006).
[14]G. J. Liu, J. R. Sun, J. Z. Wang, T. Y. Zhao, and B. G. Shen, J. Phys.: Condens. Matter **19**, 466215 (2007).
[15]D. R. Lide, *CRC Handbook of Chemistry and Physics* (CRC, Boca Raton, FL, 2004).
[16]A. M. Tishin and Y. I. Spichkin, *The Magnetocaloric Effect and its Applications* (Institute of Physics, London, 2003).

Paper IX

Paper published in Journal of Magnetism and Magnetic Materials, 2010

Bjørk, R., Bahl, C. R. H., Smith, A. and Pryds, N.

Comparison of adjustable permanent magnetic field sources

Journal of Magnetism and Magnetic Materials, 322, 3664-3671, 2010

Journal of Magnetism and Magnetic Materials 322 (2010) 3664–3671

Contents lists available at ScienceDirect

Journal of Magnetism and Magnetic Materials

journal homepage: www.elsevier.com/locate/jmmm

Comparison of adjustable permanent magnetic field sources

R. Bjørk *, C.R.H. Bahl, A. Smith, N. Pryds

Fuel Cells and Solid State Chemistry Division, Risø National Laboratory for Sustainable Energy, Technical University of Denmark - DTU, Frederiksborgvej 399, DK-4000 Roskilde, Denmark

ARTICLE INFO

Article history:
Received 4 November 2009
Available online 23 July 2010

Keywords:
Magnetic field
Permanent magnet flux source
Halbach cylinder
Mangle

ABSTRACT

A permanent magnet assembly in which the flux density can be altered by a mechanical operation is often significantly smaller than comparable electromagnets and also requires no electrical power to operate. In this paper five permanent magnet designs in which the magnetic flux density can be altered are analyzed using numerical simulations, and compared based on the generated magnetic flux density in a sample volume and the amount of magnet material used. The designs are the concentric Halbach cylinder, the two half Halbach cylinders, the two linear Halbach arrays and the four and six rod mangle. The concentric Halbach cylinder design is found to be the best performing design, i.e. the design that provides the most magnetic flux density using the least amount of magnet material. A concentric Halbach cylinder has been constructed and the magnetic flux density, the homogeneity and the direction of the magnetic field are measured and compared with numerical simulation and a good agrement is found.

1. Introduction

A homogeneous magnetic field for which the flux density can be controlled is typically produced by an electromagnet. To generate a magnetic flux density of 1.0 T over a reasonably sized gap an electromagnet requires a large amount of power, typically more than a thousand watts, and additionally a chiller is needed to keep the electromagnet from overheating. This makes any application using such an electromagnet very power consuming.

Instead of using an electromagnet a permanent magnet configuration for which the flux density can be controlled by a mechanical operation can be used. A number of such variable permanent magnetic flux sources have previously been investigated separately [1,2], and presented in a brief overview [3] but no detailed investigations determining the relative efficiencies of the different designs have been published. Here five such designs are compared and the best performing design is found. The efficiency of some of the magnet designs discussed in this paper have also been analyzed elsewhere [4,5]. However, there only the efficiency of designs of infinite length is characterized. In this paper we consider designs of finite length, which is important as the flux density generated by a finite length magnet assembly is significantly reduced compared to designs of infinite length. Also we parameterize the optimal designs, allowing other researchers to build efficient magnet assemblies.

Examples of applications where an adjustable permanent magnet assembly can be used are nuclear magnetic resonance (NMR) apparatus [6], magnetic cooling devices [7] and particle accelerators [8]. The flux density source designed in this paper is dimensioned for a new differential scanning calorimeter (DSC) operating under magnetic field designed and built at Risø DTU [9], but the general results apply for any application in which a variable magnetic field source is needed.

2. Variable magnetic field sources

2.1. Design requirements

In the analysis of a variable magnetic field source some design constrains must be imposed, such as the minimum and maximum producible flux density. In this analysis the maximum flux density is chosen to be 1.5 T which is a useful flux density for a range of experiments. The minimum flux density is required to be <0.1 T both to allow measurements at low values of the magnetic flux density, as well as to allow placement of a sample with only small interaction with the magnetic field. Also a flux density of <0.1 T is more easily realizable in actual magnet assemblies than if exactly 0 T had been required. Ideally the flux density must be homogeneous across the sample at any value between the high and low values. The mechanical force needed to adjust the flux density is also considered.

The magnet assembly must be able to contain a sample that can be exposed to the magnetic field, and the sample must of

* Corresponding author. Tel.: +45 46775895.
E-mail address: rabj@risoe.dtu.dk (R. Bjørk).

0304-8853/$ - see front matter © 2010 Elsevier B.V. All rights reserved.
doi:10.1016/j.jmmm.2010.07.022

course be able to be moved in and out of the magnet assembly. The size of a sample can be chosen arbitrarily, and for this investigation a sample volume shaped as a cylinder with a radius of 10 mm and a length of 10 mm was chosen. To allow the sample to be moved we require that the clearance between the magnet and the sample must be at least 2.5 mm, in effect increasing the gap radius to 12.5 mm. The sample volume is sufficiently large to allow the magnet designs to be used in the DSC device discussed above.

2.2. Numerical analysis

Given the above design requirements five different permanent magnet designs have been selected for detailed investigation. In each of the designs it is possible to adjust the generated flux density by a mechanical operation. Numerical simulations of each design for a range of parameters were performed and the designs are evaluated based on the mean flux density in the sample volume. Each design was always centered on the sample cylinder.

All numerical work in this paper was done in three dimensions using the commercially available finite element multiphysics program, *Comsol Multiphysics* [10]. The equation solved in the simulations is the magnetic scalar potential equation,

$$-\nabla\cdot(\mu_0\mu_r\nabla V_{\mathrm{m}}-\mathbf{B}_{\mathrm{rem}})=0, \tag{1}$$

where V_{m} is the magnetic scalar potential, $\mathbf{B}_{\mathrm{rem}}$ is the remanent flux density, μ_0 is the permeability of free space and μ_r is the relative permeability, defined as $\partial B/\partial H$ to account for the remanence of the permanent magnets, and assumed to be isotropic.

Once the magnetic scalar potential has been found, the magnetic field, $\mathbf{H}$, can be found as

$$\mathbf{H}=-\nabla V_{\mathrm{m}}, \tag{2}$$

and subsequently the magnetic flux density, $\mathbf{B}$, can be determined.

The permanent magnets are modeled by the relation $\mathbf{B}=\mu_0\mu_r\mathbf{H}+\mathbf{B}_{\mathrm{rem}}$, which is justified because the intrinsic coercivity of a NdFeB magnet, which is used as a permanent magnet in present calculations, can be as high as 3 T [11]. The transverse susceptibility of the magnets is ignored, as the anisotropy field has a value of 8 T [12]. The remanence of the permanent magnets in all designs considered here is $B_{\mathrm{rem}}=1.2$ T and the relative permeability is $\mu_r=1.05$, in accordance with values for a standard NdFeB magnet [11].

An important issue to note is that the magnetostatic problem is scale invariant, i.e. if all dimensions are scaled by the same factor the magnetic field in a given point will be the same if this point is scaled as well. This means that quantities such as the average value and the homogeneity of the magnetic field in a scaled volume of space will be the same. Thus the conclusions of this paper apply equally to any sample volume that has the same relative dimensions as the sample volume used here, as long as the magnet designs are scaled appropriately.

In the following subsections the five designs are introduced and analyzed.

2.3. Concentric Halbach cylinders

The concentric Halbach cylinder consists of two Halbach cylinders, which are cylindrical permanent magnet assemblies that have a direction of magnetization that changes continuously as, in polar coordinates,

$$B_{\mathrm{rem},r}=B_{\mathrm{rem}}\cos(\phi),$$

$$B_{\mathrm{rem},\phi}=B_{\mathrm{rem}}\sin(\phi), \tag{3}$$

where B_{rem} is the magnitude of the remanent flux density [13,14].

For practical applications the Halbach cylinder is constructed from segments, each with a constant direction of magnetization. A Halbach cylinder with eight segments produces 90% of the flux density of a perfect Halbach cylinder while a configuration with 16 segments obtains 95% of the flux density [15].

If two Halbach cylinders are placed concentrically inside each other, the flux density in the inner cylinder bore can be adjusted by rotating one of the cylinders relative to the other. If the permanent magnets used to construct the Halbach cylinders have a permeability close to one, as is the case for NdFeB magnets, the total flux density of the concentric Halbach cylinder is approximately the vector sum of the flux densities produced by the individual cylinders. An illustration of the concentric Halbach cylinder design is shown in Fig. 1.

The concentric Halbach cylinder system is characterized by eight parameters, namely the internal radius, r_{in}, external radius, r_{ex}, and the length, L, of each of the two cylinders, and the number of segments of each cylinder. The segments of the two cylinders were always aligned in the high field position, as shown in Fig. 1.

The advantages of the concentric Halbach cylinder design is that adjusting the flux density by rotating either of the cylinders does not change the geometry of the device. Also, in the infinite length case with no segmentation, there is no torque when rotating one of the cylinders [16]. However, a small torque is present in real-world assemblies, due to segmentation and flux leakage through the cylinder bore [2]. The disadvantage of the concentric Halbach cylinders is that even though the cylinders are designed to have exactly the same flux density in the center of the cylinder bore, so that the flux density will be zero when they are offset by 180°, this will not completely cancel the magnetic field away from the center of the bore. This is because the cylinders have different internal radii which means that the flux loss through the ends of each cylinder will not be the same and the flux density will not cancel all the way out of the cylinder bore. This can be important when placing samples in the magnet, as they will respond to the gradient of the magnetic field as they are moved in and out of the cylinder bore.

The parameters varied for the modeling of this design are presented in Table 1. The internal radius of the outer Halbach cylinder was kept fixed at the external radius of the inner Halbach cylinder plus 2 mm to allow room for the inner cylinder to rotate. Both the inner and outer Halbach cylinder were modeled from eight segments to make the design economically affordable. Many of the above configurations do not produce a sufficiently low

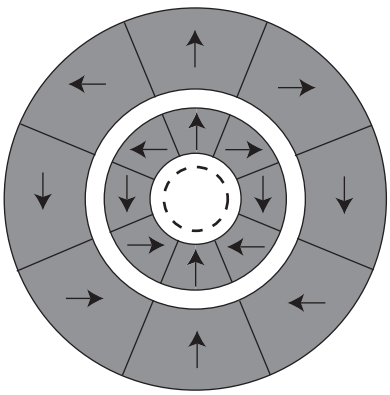

Fig. 1. A two dimensional illustration of the concentric Halbach cylinder. Each Halbach cylinder is segmented into eight parts. Shown as arrows is the direction of magnetization. The sample volume is shown as a dashed circle. In the configuration shown the total field in the sample volume is maximized.

Table 1
The parameters varied of each design.

	Concentric Halbach		Two half Halbach cylinders	Two linear Halbach array	Four rod mangle	Six rod mangle
	Inner magnet	Outer magnet				
Inner radius (mm)	12.5	21–37 (*) + 2	12.5	25–150[a] (5)	–	–
Outer radius (mm)	21–37 (*)	37–115 (*)	30–150 (10)	25–150[b] (5)	10–100 (2.5)	1–70 (1)
Length (mm)	35–95 (10)	35–95 (10)	30–300 (10)	25–150 (5)	10–250 (5)	10–600 (5)
Segments/rods	8	8	10	3	4	6

The number in parentheses denotes the step size. A asterisk denotes non-equidistant steps and no parentheses indicates a fixed value. For the two linear Halbach array [a]denotes the width and [b]denotes the height of a magnet block.

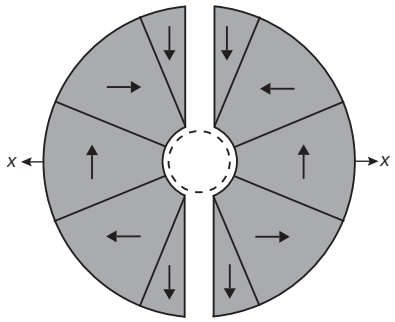

Fig. 2. A two dimensional illustration of the two half Halbach cylinders. In total 10 segments are used, of which several are identical. The direction of magnetization is shown as arrows. The sample volume is shown as a dashed circle. Notice the top and bottom gaps between the half-cylinders. This allows room for handling and securing the magnets. The half-cylinders are moved along the x-direction to control the flux density.

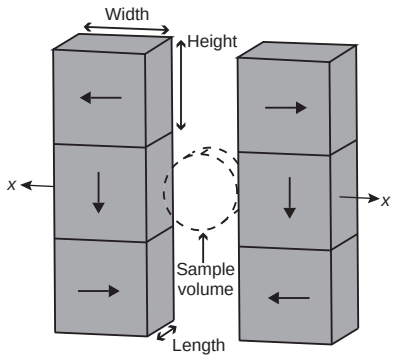

Fig. 3. A three dimensional illustration of two three block linear Halbach arrays. The high flux density region is created in between the two arrays, where the sample volume is placed. The arrays are moved along the x-direction to control the flux density.

magnetic flux density (<0.1 T) in the bore when the cylinders are oppositely aligned. These are not suitable designs and were not considered further.

The field in the exact center of a finite length Halbach cylinder can be calculated analytically by the following expression [17]

$$B(r=0,z=0)=B_{\mathrm{rem}}\left(\ln\left(\frac{r_{\mathrm{ex}}}{r_{\mathrm{in}}}\right)+\frac{z_0}{2\sqrt{z_0^2+r_{\mathrm{in}}^2}}-\frac{z_0}{2\sqrt{z_0^2+r_{\mathrm{ex}}^2}}-\ln\left(\frac{z_0+\sqrt{z_0^2+r_{\mathrm{ex}}^2}}{z_0+\sqrt{z_0^2+r_{\mathrm{in}}^2}}\right)\right), \quad (4)$$

where $z_0=L/2$. The calculated flux density must be corrected for segmentation of the Halbach cylinder. Using this expression the parameters that do not produce a concentric Halbach cylinder for which the field in the center is zero, could also have been found and disregarded. This expression is later compared with the results of the numerical simulations.

2.4. Two half Halbach cylinders

As previously mentioned it is not possible to adjust the flux density of a single particular Halbach cylinder. However, if the Halbach cylinder is split into two parts that can be moved away from each other the flux density between the half-cylinders can be controlled in this way. An illustration of this idea is shown in Fig. 2. This design is termed the two half Halbach cylinders. The design can be characterized by four parameters, namely the internal and external radii and the length of the identical half-cylinders as well as the number of segments. Notice that an additional gap has been included by removing some of the magnet from the top and bottom between the half-cylinders. This has been done to allow room for handling and securing the magnets.

The advantage of this design is that only a simple linear displacement is needed to control the flux density between the cylinders. However, the disadvantage is that there must be enough room to move the half-cylinders away from each other to lower the flux density, and when the half-cylinders are apart the flux density they each generate will influence nearby magnetic objects. Also, a substantial force will in some cases be needed to keep the two half Halbach cylinders close to each other to generate a high flux density.

The parameters varied for this design can again be seen in Table 1. The number of segments was fixed at ten, again to make the design economically affordable.

2.5. Two linear Halbach arrays

The linear Halbach array is a magnetic assembly that uses the same principle as the Halbach cylinder to generate a one-sided flux [13]. The linear Halbach array is characterized by the width, height and length of the identical blocks as well as the number of blocks used in the array. For the array considered here three blocks are used, as this is the minimum number of blocks needed to create a one-sided array. An adjustable flux density configuration can be made by placing two mirrored linear Halbach arrays opposite to each other, as with the two half Halbach cylinders. By moving the arrays closer or further apart the flux density between them can be controlled. An illustration of the two linear Halbach array design is shown in Fig. 3.

The sample volume can, because of its short length, be rotated, so that the arrays can be placed closer to each other. This

configuration has also been considered, although it might require an alternative method for mounting the sample than for the other designs considered here.

The advantage of the linear Halbach array is that it is easy to construct, as it can be made using simple rectangular magnet blocks. However, the design has the same disadvantages as the two half Halbach cylinders in that a large force will, in some cases, be needed to keep the arrays close together and a high flux density will still be generated when the arrays are moved apart, which could influence nearby magnetic objects.

For the sample position as shown in Fig. 3 the two linear Halbach arrays were separated by a distance of 25 mm, so that the sample volume fitted in between the arrays. For the alternative sample orientations the arrays were separated by a distance of 15 mm so that the rotated sample fitted between the arrays. For either of the sample positions the height, width and length of a rectangular permanent magnet block were independently varied as given in Table 1. Each array consists of three identical blocks.

One can envision designs that have a geometrical form "between" the two linear Halbach arrays and the two half Halbach cylinders. The performance of these will be comparable to the performance of either of the two linear Halbach arrays or the two half Halbach cylinders.

2.6. The mangle

The mangle is made up of identical transversely magnetized permanent magnet rods that can be rotated to alter the flux density at the center of the assembly [1]. The rods must be rotated alternately clockwise and counterclockwise to continuously alter the flux density in a homogeneous way. The design can be characterized by three parameters, namely the radius and the length of a rod as well as the number of rods used. An illustration of a mangle design with four cylinders in the orientation that generates a high flux density is shown in Fig. 4A. The conventional low flux density orientation for the four rod mangle, shown in Fig. 4B, does not produce a very low flux density, typically around 0.1–0.3 T across the sample volume (if magnet rods with a remanence of 1.2 T are used). An alternative orientation of the rods, shown in Fig. 4C, produces a much lower flux density, typically <0.05 T across the sample volume. Unfortunately there is no way to adjust the flux density from the configuration shown in Fig. 4A to that shown in Fig. 4C while maintaining homogeneity in the sample volume. Thus in the four rod mangle considered here we envision a design where the rods are rotated from the configuration shown in Fig. 4A to that in Fig. 4B and finally to that in Fig. 4C.

A six rod mangle design is also considered. The high flux density orientation of the rods is shown in Fig. 5A, while the low flux density configuration is shown in Fig. 5B. Notice that the rods have simply been turned 90° alternately. The low flux density

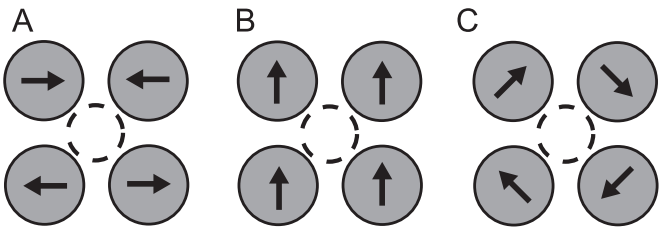

Fig. 4. A schematic drawing of the four rod mangle design. (A) shows the high flux density position of the four rod mangle design. The high flux density is created across the sample volume. (B) shows the low flux density configuration, as suggested by [1]. This position is reached by a 90° alternate rotation of the rods shown in (A). (C) shows an alternate position of the rods that generate a much lower flux density in the sample volume than the position shown in (B).

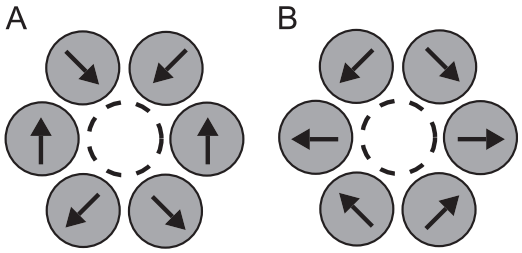

Fig. 5. A schematic drawing of the six rod mangle design. The high flux density position of the six rod mangle is shown in (A), while the low flux density position of the six rod mangle in shown in (B). In the latter figure the rods have been alternately rotated 90° from the position shown in (A).

orientation produce a flux density typically <0.1 T across the sample volume, so no alternate orientations need be considered.

The advantage of this design is economical as transversely magnetized rods are readily available. The design is also compact and produces a low stray flux density. The disadvantage is that the volume between the rods scales with the radius of the rods. Therefore the flux density can only be increased to a maximum value for a given sample volume, without increasing the size of the volume between the rods.

The parameters varied for both the four and six rod mangles are given in Table 1. The rods are always placed as closely as possible to each other or to the sample, depending on the mangle parameters.

3. Comparing the different designs

To find the best parameters for each design parameter variation simulations were conducted for each of the different designs with the parameters previously stated.

To allow the designs to be more easily compared, the best performing of each of the five different designs are selected. This is done by selecting the parameters that produce a high average flux density in the sample volume and at the same time has a low volume of magnet material. This approach has previously been used to optimize the Halbach cylinder design [15], but other optimization methods exist such as the figure of merit, M^*, which is almost identical to the optimization used here except that it also include the remanence of the magnets [5]. Also an optimization parameter for permanent magnet assemblies used in magnetic refrigeration devices exists [18]. In Fig. 6, both these optimally dimensioned designs, as well as the other parameter variations tried, are shown for the two half Halbach cylinder design. Some of the optimal designs have been indicated in the figure, and it is clearly seen that these produce a given flux density using the lowest amount of magnet material. The same analysis has been performed for the four other designs.

It is worth noting that the designs referred to here as "optimal" are not necessarily the global optimal designs. They are the optimal designs of the conducted parameter survey, and as such designs might exist outside the parameter space, or at resolutions smaller than the varied parameters that perform better than the designs referred to as optimal here. However, based on the detail of the parameter survey the potential for improvement will be small.

3.1. The best parameters for each design

The parametrization of the optimal designs of each individual design type have been found by analyzing the dimensions of the optimal designs for each flux density. For the concentric Halbach

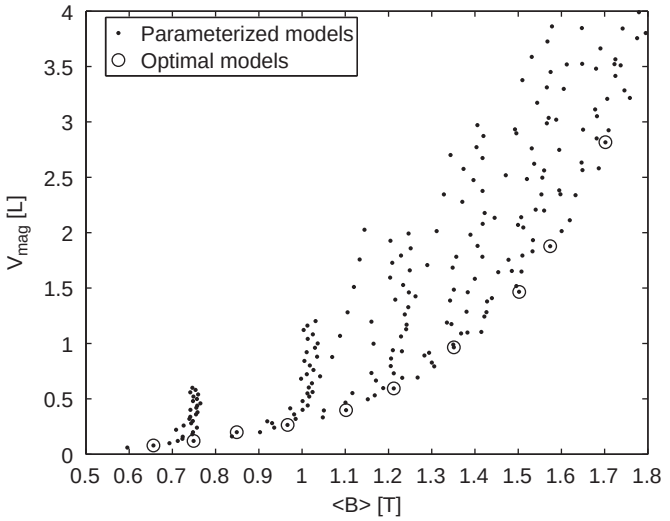

Fig. 6. The volume of the magnets as a function of the average flux density in the sample volume for the two half Halbach cylinders design. Some of the optimal designs are marked by circles.

cylinder the optimal designs fulfil

$$0.8 < \frac{r_{\text{inner, ex}}/r_{\text{inner,in}}}{r_{\text{outer,ex}}/r_{\text{outer,in}}} < 1 \quad \text{and} \quad 0.8 < \frac{L_{\text{inner}}}{L_{\text{outer}}} < 1, \tag{5}$$

where the first subscript denotes the inner or outer magnet and the second denotes the internal or external radius. However, this criteria is not enough, as some designs that fulfil these requirements produce a flux density in the low flux density configuration that is higher than 0.1 T. Thus the analytical expression for the flux density in the center of the system, Eq. (4), must be calculated to ensure that this will be < 0.1 T.

The optimal mangle designs are those where the radius, r, of the individual mangle rods is sufficiently small that the rods can be placed close to the sample without touching each other. For the four rod mangle, the relation $r \leq 32.5$ mm applies for the optimal designs. Also, the ratio of the radius to the length must be in the range of $0.2 < \text{radius/length} < 0.5$. Increasing the length of the rods increases the flux density in the sample volume.

For the six rod mangle only the designs that have $r \leq 10$ mm are optimal. Also, the ratio of the radius to the length must obey $0.05 < \text{radius/length} < 0.5$, where the lower bond is necessary to obtain a high flux density.

For the linear Halbach array with the sample volume as shown in Fig. 3 the optimal designs are parameterized by

$$\text{height} \simeq 0.22 \times \text{width} + 0.02 \text{ (mm)},$$

$$\text{length} \simeq 1.0 \times \text{width} + 0.05 \text{ (mm)}, \tag{6}$$

where the length, width and height are shown in Fig. 3.

For the linear Halbach array with the rotated sample volume the optimal designs are parameterized by

$$\text{height} \simeq 0.08 \times \text{width} + 0.02 \text{ (mm)},$$

$$\text{length} \simeq 1.3 \times \text{width} + 0.02 \text{ (mm)}, \tag{7}$$

where the dimensions are again shown in Fig. 3. Because the sample volume has been rotated a much smaller height and a longer length is now favored.

For the two half Halbach cylinders the optimal parameterized designs are characterized by the relation: radius $\simeq 0.95 \times$ length. This relation is in agreement with the optimal dimensions for a Halbach cylinder [15].

These parameterizations are obviously only valid for the sample volume with the relative dimensions as chosen here. If a different sample volume were chosen the relations would be different. However, if the sample volume is simply scaled by a factor then, owing to the linearity of the magnetostatic problem, the magnetic dimensions need simply be scaled by the same factor to produce the same flux density, and thus in this situation the parameterizations found above remain valid appropriately scaled.

The optimal designs for the different design types are shown in Fig. 7. The magnetic flux density produced by a given optimal design, i.e. a design whose dimensions follow the above parameterizations, can be found in Fig. 7 by calculating the volume of the magnet in the design.

It is seen that the concentric Halbach cylinder design is the optimal design as it produces a given magnetic flux density using the lowest amount of magnet material. An interesting observation is that the mangle designs are not able to produce a high flux density. This is because, as already stated, as the radius of the rods in the mangle increases the rods must be moved further away from each other, so as not to touch, and thus the volume in between them increases. The two half Halbach cylinders and the concentric Halbach cylinder do not perform identically due to the top and bottom gaps between the half-cylinders and due to the gap between the concentric cylinders.

It is also interesting to consider the homogeneity of the flux density in the sample volume. To characterizes the homogeneity, the best parameter set for each design that produces 1 ± 0.01 T in the high flux density position have been found. The six rod mangle is not able to produce this flux density and so it is not present in the figure. The flux density for these designs have then been varied either by rotation (mangle and concentric Halbach cylinder) or translation (two half Halbach cylinder and two linear Halbach array). Fig. 8 shows the standard deviation of the flux density, $\sqrt{\langle B^2 \rangle - \langle B \rangle^2}$, as a function of the average flux density, $\langle B \rangle$, for these optimal 1 T designs. All the design types produce a quite homogeneous flux density across the sample volume, but again the best design is the concentric Halbach cylinder design.

The high homogeneity of the concentric Halbach cylinder means that the difference between the flux density calculated

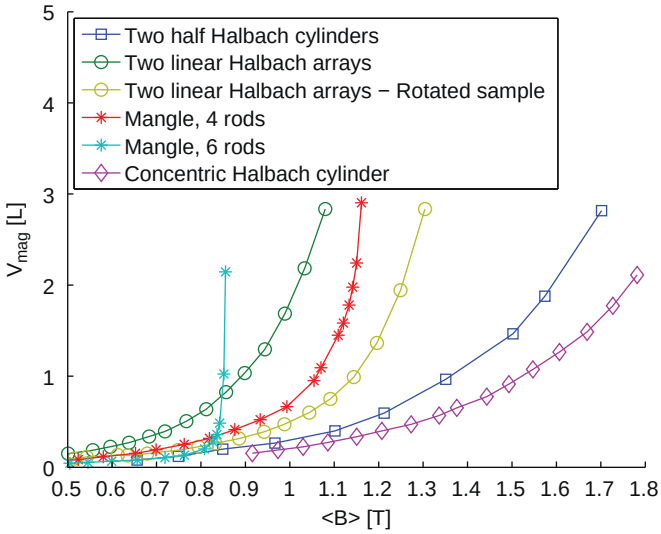

Fig. 7. The volume of the magnets as a function of the average flux density in the sample volume for the best individual designs for the six designs considered.

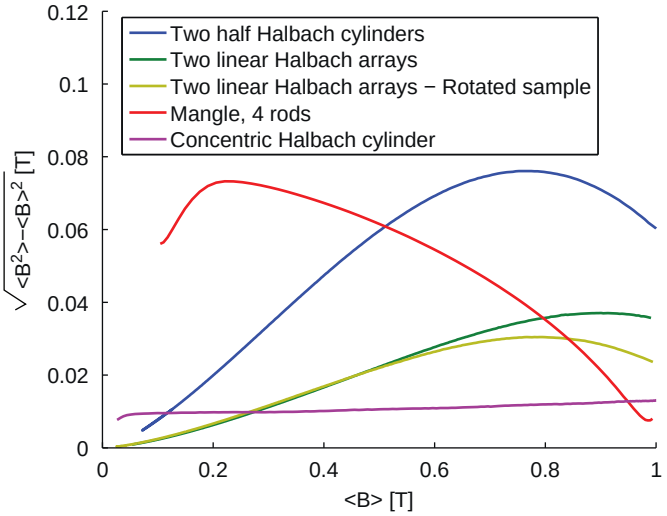

Fig. 8. The homogeneity, characterized by the standard deviation $\sqrt{\langle B^2\rangle-\langle B\rangle^2}$, for the optimal different types of designs that produce 1 T as a function of the average flux density. The mangle was turned from the position shown in Fig. 4A to that shown in Fig. 4B.

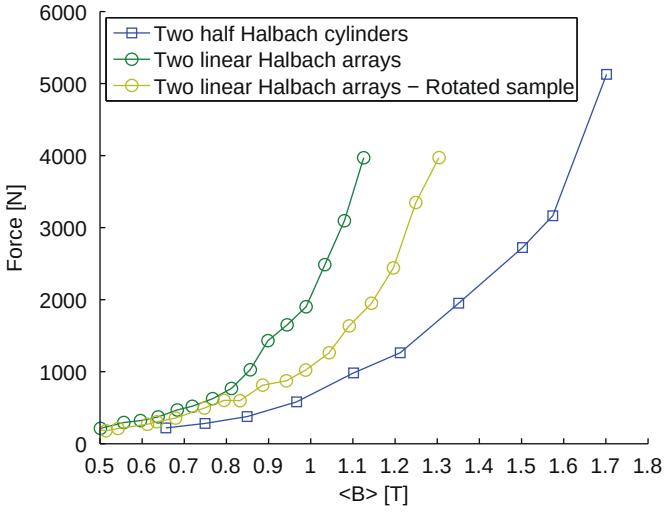

Fig. 9. The maximum force needed to keep the design at the maximum flux density.

using Eq. (4) and the numerically calculated mean flux density in the sample volume is <0.05 T in all considered cases.

In Fig. 9, the maximum force as a function of flux density for the two half Halbach cylinder and the linear Halbach array designs are shown. The force shown in the figure is the force on the optimal designs that is needed to keep the two halfs of each design as close together as the sample volume allows. As can be seen a substantial force is needed for the designs that generate a high flux density.

4. A constructed variable field source

An adjustable permanent magnet has been built based on the concentric Halbach cylinder design, as this is the best performing and most practical magnet design. A maximum flux density of 1.5 T was chosen as the desired value in the sample volume. The dimensions of the magnet are given in Table 2.

Table 2
The dimensions of the constructed concentric Halbach cylinder magnet.

	Inner magnet	Outer magnet
Internal radius (mm)	12.5	29.5
External radius (mm)	27.5	80
Length (mm)	55	65

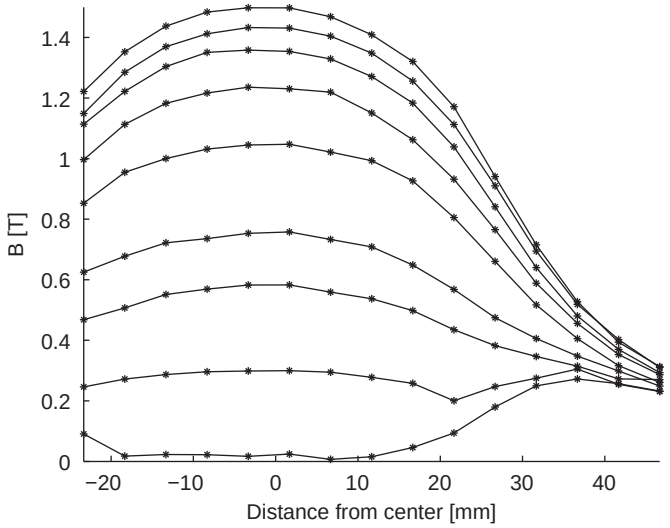

Fig. 10. The measured magnetic flux density as a function of distance from the center of the concentric Halbach cylinder. Between each measurement series the cylinders were rotated relative to each other by 22.5°. Due to of the design of the magnet it was only possible to measure down to −25 mm.

The magnet was constructed and using a Hall probe (AlphaLab Inc, Model: DCM) the flux density produced by the design was measured. Both components of the magnetic flux density in the plane perpendicular to the cylinder axis, as well as the component parallel to the axis, were measured at 5 mm intervals in the center of the cylinder for nine relative rotation positions of the two cylinders, each separated by 22.5°. The initial angle was chosen to be a close to a flux density of zero as possible. The norm of the vector sum of the three components of the magnetic flux density is shown in Fig. 10.

The uncertainty on the position of the Hall probe is estimated to be $\times 1$ mm. There is also an uncertainty in the 90° rotation of the Hall probe necessary to measure the two components of the flux density that are perpendicular to the cylinder axis. It is estimated that these uncertainties result in a total uncertainty of $\times 5\%$ for the magnetic flux density. The instrumental uncertainty of the Hall probe is $\times 0.2\%$, which is much less than the uncertainty due to the positioning of the Hall probe. No error bars are shown in Fig. 10 in order to maintain clarity in the plot.

The axial component of the magnetic flux density is included in the flux density shown in Fig. 10, but is quite small. At no point in the cylinder bore does the axial component exceed 0.15 T for any rotation angle, and in the center it is always <0.05 T for any rotation angle.

The measured values of the magnetic flux density have been interpolated to find the value at the center of the concentric cylinder. These values are shown in Fig. 11 as a function of the displacement angle, ϕ, between the two cylinders. A sine function of the form $B=\alpha\sin(0.5(\phi+\beta))$, where α and β are constants, has been fitted to the data as this is how the field should theoretically vary. This is so because the magnetic flux density produced by the inner and outer magnets is identical in the center and thus the

combined flux density can be found based on the law of cosine for an isosceles triangle. The fit is shown in Fig. 11 as well as the 95% confidence interval of the fit for a new measurement. The constants were determined to be $\alpha = 1.47 \pm 0.04\,\mathrm{T}$ and $\beta = 0 \pm 3^\circ$.

The magnet design has also been simulated numerically and the resulting flux densities are also shown in Fig. 11. A reasonable agreement between the measured flux density and the value predicted by simulation is seen. It is seen that the flux density can easily be adjusted by rotating the inner cylinder relative to the outer cylinder.

The homogeneity of the flux density has been investigated by measuring the flux density at four off-center positions. These are located 5.5 mm from the center along an angle corresponding to, respectively 0°, 90°, 180° and 270°. The results for three different displacement angles, $\phi = 0^\circ, 90^\circ, 180^\circ$, respectively, are shown in Fig. 12. The standard deviation, $\sqrt{\langle B^2\rangle - \langle B\rangle^2}$, can be calculated for the sample volume based on the data in Fig. 12. Using the four central data points to represent the sample volume one obtains $\sqrt{\langle B^2\rangle - \langle B\rangle^2} = 0.61 \times 10^{-2}$, 2.18×10^{-2} and 2.17×10^{-2} for $\phi = 0^\circ$, 90° and 180°, respectively. Thus the flux density distribution is quite homogeneous.

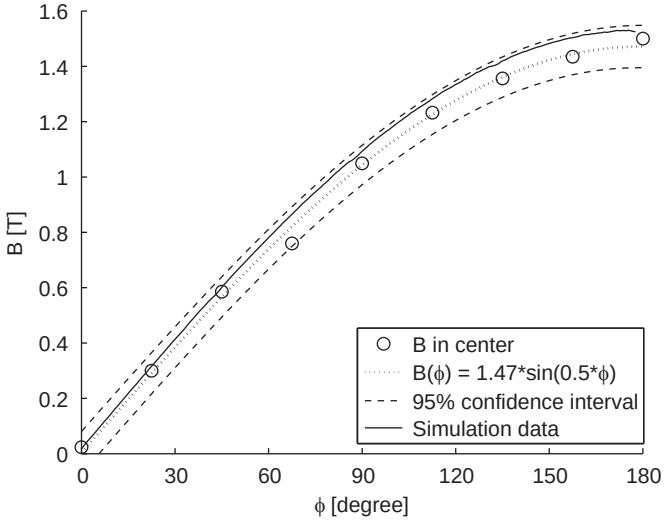

Fig. 11. The center value of the flux density as a function of rotation angle, ϕ. A sine function has been fitted to the data. Also shown are the results from numerical simulations.

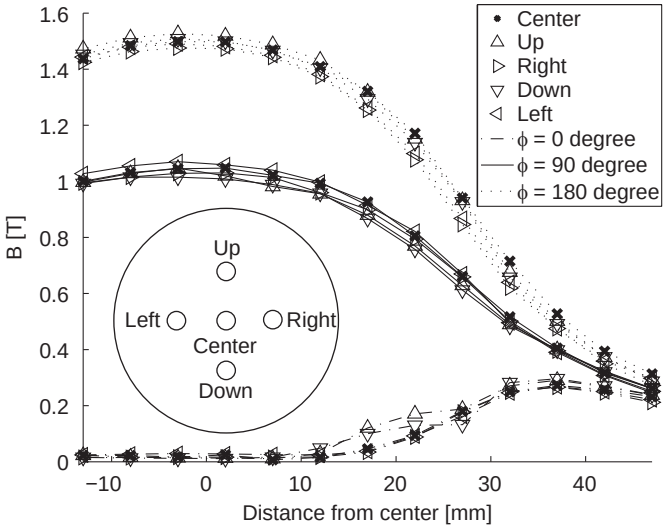

Fig. 12. The homogeneity of the measured magnetic flux density as a function of distance from the center of the concentric Halbach cylinder. The positions labeled *Up*, *Right*, *Down* and *Left* are located 5.5 mm from the center along the direction corresponding to, respectively, 0°, 90°, 180° and 270°.

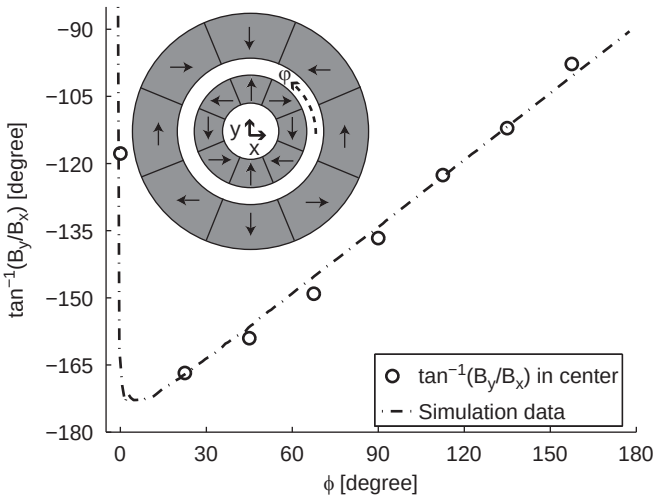

Fig. 13. The direction of the field as a function of rotation angle, ϕ in the coordinate system shown in the figure. The field changes direction by 180° when $\phi = 0$ is crossed, at which point $B = 0$.

The direction of the flux density changes as the cylinders are rotated with respect to each other. Fig. 13 shows the direction as a function of the rotation angle, ϕ, for the measured flux density as well as simulation data for the coordinate system as shown in the figure. A good agreement between these is seen.

The agreement between the measured magnetic flux density and the simulation results is limited by several factors. A perfect agreement is not expected as the transverse susceptibility for the magnets is ignored. However, the major source of error is estimated to be the positioning and rotation of the Hall probe in the conducted measurements, as described earlier.

For all the five designs it is important to consider the coercivity of the permanent magnets used. For, e.g. the concentric Halbach cylinder design when the cylinders are offset by 180° the flux density produced by the outer cylinder will be parallel and opposite to the remanence of parts of the inner cylinder, and if this flux density is higher than the coercivity of the magnets the direction of magnetization will be reversed, which will render the device useless [15,19]. For the simulated permanent magnets a remanence of 1.2 T was used. A typical industry NdFeB magnet with such a remanence has a high coercivity, $\mu_0 H_c = 3.2\,\mathrm{T}$, which is sufficiently strong to keep the direction of magnetization constant.

5. Conclusion

Five different variable permanent magnet designs, the concentric Halbach cylinder, the two half Halbach cylinders, the two linear Halbach arrays and the four and six rod mangles, were investigated and evaluated based on the generated magnetic flux density in a sample volume and the amount of magnetic material used. As the dipole field is scale invariant the conclusion holds for all sample volumes with the same relative dimensions as used here. The best performing design, i.e. the design that provides the highest magnetic flux density using the least amount of magnet material, was the concentric Halbach cylinder design. Based on this result a concentric Halbach cylinder was constructed and the magnetic flux density, the homogeneity and the direction of the

magnetic flux density were measured. These were compared with numerical simulation and a good agrement was found.

Acknowledgements

The authors would like to thank J. Geyti for his technical assistance. Also, the authors would like to acknowledge the support of the Programme Commission on Energy and Environment (EnMi) (Contract no. 2104-06-0032) which is part of the Danish Council for Strategic Research.

References

[1] O. Cugat, P. Hansson, J.M.D. Coey, IEEE Trans. Magn. 30 (1994) 4602.
[2] T.R. Ni Mhiochain, D. Weaire, S.M. McMurry, J.M.D. Coey, J. Appl. Phys. 86 (1999) 6412.
[3] J.M.D. Coey, J. Magn. Magn. Mater. 248 (2002) 441.
[4] M.G. Abele, Structures of Permanent Magnets, Wiley, 1993.
[5] J.M.D. Coey, T.R. Ni Mhiochain, in: High Magnetic Fields, Science and Technology, vol. 1, World Scientific, 2003.
[6] S. Appelt, H. Kühn, F. W Häsing, B. Blümich, Nat. Phys. 2 (2006) 105.
[7] A. Tura, A. Rowe. in: Proceedings of Second International Conference on Magnetic Refrigeration at Room Temperature, Portoroz, Solvenia, IIF/IIR:363, 2007.
[8] M. Sullivan, G. Bowden, S. Ecklund, D. Jensen, M. Nordby, A. Ringwall, Z. Wolf, IEEE 3 (1998) 3330.
[9] S. Jeppesen, S. Linderoth, N. Pryds, L.T. Kuhn, J.B. Jensen, Rev. Sci. Instrum. 79 (8) (2008) 083901.
[10] COMSOL AB, Tegnérgatan 23, SE-111 40 Stockholm, Sweden.
[11] Standard Specifications for Permanent Magnet Materials, Magnetic Materials Producers Association, 8 South Michigan Avenue, Suite 1000, Chicago, Illinois 60603, 2000.
[12] G. Zimmermann, J. Appl. Phys. 73 (1993) 8436.
[13] J.C. Mallinson, IEEE Trans. Magn. 9 (4) (1973) 678.
[14] K. Halbach, Nucl. Instrum. Methods 169 (1980).
[15] R. Bjørk, C.R.H. Bahl, A. Smith, N. Pryds, J. Appl. Phys. 104 (2008) 13910.
[16] R. Bjørk, C.R.H. Bahl, A. Smith, J. Magn. Magn. Mater. 322 (2010) 133.
[17] H. Zijlstra, Phillips J. Res. 40 (1985) 259.
[18] R. Bjørk, C.R.H. Bahl, A. Smith, N. Pryds, Int. J. Refrig. 33 (2010) 437.
[19] F. Bloch, O. Cugat, G. Meunier, J.C. Toussaint, IEEE Trans. Magn. 34 (1998) 5.

Paper X

Paper published in Journal of Magnetism and Magnetic Materials, 2010

Bjørk, R., Bahl, C. R. H. and Katter, M.

Magnetocaloric properties of $LaFe_{13-x-y}Co_xSi_y$ and commercial grade Gd

Journal of Magnetism and Magnetic Materials, 322, 3882-3888, 2010

Journal of Magnetism and Magnetic Materials 322 (2010) 3882–3888

Contents lists available at ScienceDirect

Journal of Magnetism and Magnetic Materials

journal homepage: www.elsevier.com/locate/jmmm

Magnetocaloric properties of $LaFe_{13-x-y}Co_xSi_y$ and commercial grade Gd

R. Bjørk [a,*], C.R.H. Bahl [a], M. Katter [b]

[a] Fuel Cells and Solid State Chemistry Division, Risø National Laboratory for Sustainable Energy, Technical University of Denmark - DTU, Frederiksborgvej 399, DK-4000 Roskilde, Denmark

[b] Vacuumschmelze GmbH & Co. KG, D-63450 Hanau, Germany

ARTICLE INFO

Article history:
Received 4 May 2010
Received in revised form
3 July 2010
Available online 10 August 2010

Keywords:
Magnetocaloric
Gadolinium
Magnetic refrigeration

ABSTRACT

The magnetocaloric properties of three samples of $LaFe_{13-x-y}Co_xSi_y$ have been measured and compared to measurements of commercial grade Gd. The samples have ($x=0.86$, $y=1.08$), ($x=0.94$, $y=1.01$) and ($x=0.97$, $y=1.07$) yielding Curie temperatures in the range 276–288 K. The magnetization, specific heat capacity and adiabatic temperature change have been measured over a broad temperature interval. Importantly, all measurements were corrected for demagnetization, allowing the data to be directly compared. In an internal field of 1 T the maximum specific entropy changes were 6.2, 5.1 and 5.0 J/kg K, the specific heat capacities were 910, 840 and 835 J/kg K and the adiabatic temperature changes were 2.3, 2.1 and 2.1 K for the three LaFeCoSi samples respectively. For Gd in an internal field of 1 T the maximum specific entropy change was 3.1 J/kg K, the specific heat capacity was 340 J/kg K and the adiabatic temperature change was 3.3 K. The adiabatic temperature change was also calculated from the measured values of the specific heat capacity and specific magnetization and compared to the directly measured values. In general an excellent agreement was seen.

1. Introduction

The magnetocaloric effect (MCE) is observed as a temperature change of a magnetic material when this is subjected to a changing external magnetic field. Such magnetocaloric materials (MCM) are interesting with respect to magnetic refrigeration, which is an emerging refrigeration technology based on the MCE that aims to provide environmentally friendly energy efficient cooling.

If an MCM with a positive magnetocaloric effect is subjected to a magnetic field and the conditions are kept adiabatic the temperature of the MCM will increase by the adiabatic temperature change, ΔT_{ad}. Had the conditions been kept isothermal the specific entropy would instead have been reduced by the isothermal entropy change, Δs. Both ΔT_{ad} and Δs are functions of temperature and magnetic field. These two properties, along with the specific heat capacity, c_p, which is also a function of temperature and magnetic field, are the three most important properties of an MCM with regard to application in magnetic refrigeration. Secondary properties such as the thermal conductivity, density and porosity can also be of importance, although these are in general not strong functions of temperature and magnetic field. A substantial number of magnetocaloric materials are known, each of whose properties has a different dependence on temperature and magnetic field [1]. The MCE is generally largest near the phase transition of the MCM, known as the Curie temperature, T_C.

For an MCM with a second order phase transition the measured magnetocaloric data are related as the adiabatic temperature change can be calculated as

$$\Delta T_{ad} = -\mu_0 \int_{H_i}^{H_f} \frac{T}{c_p} \left(\frac{\partial m}{\partial T}\right)_H dH, \quad (1)$$

once c_p and m are known.

For magnetic refrigeration an MCM must have a T_C that is around room temperature. As can be seen from Eq. (1) the change in magnetization must be substantial to provide a large ΔT_{ad}. Also, a high heat capacity provides a high thermal mass while a low heat capacity can cause a high adiabatic temperature change. The benchmark magnetocaloric material used in magnetic refrigeration is gadolinium (Gd), which has a T_C around 293 K and a ΔT_{ad} of ~ 3.5 K at T_C in a field of 1 T [2]. However, the Curie temperature of Gd cannot be tuned, and so the adiabatic temperature change will be low if the magnetic refrigerator is operated far from the Curie point.

In this paper we consider the properties of the magnetocaloric material, $LaFe_{13-x-y}Co_xSi_y$, referred to as LaFeCoSi, which displays a significant adiabatic temperature change and has a tuneable Curie temperature. The precursor of this material, $LaFe_{13-x}Si_x$, which has a $NaZn_{13}$-type lattice crystal structure, has a magnetocaloric effect due to an itinerant electron metamagnetic transition from a paramagnetic to a ferromagnetic state [3].

* Corresponding author.
E-mail address: rabj@risoe.dtu.dk (R. Bjørk).

0304-8853/$ - see front matter © 2010 Elsevier B.V. All rights reserved.
doi:10.1016/j.jmmm.2010.08.013

Previous measurements of the specific magnetization and the specific entropy change of different $LaFe_{13-x-y}Co_xSi_y$ compounds have been reported [4–10] as well as direct measurements of the adiabatic temperature change [11–13], and a single measurement of the specific heat capacity [14]. However, the published data are usually very widely spaced in external magnetic field and in general the published data have not been corrected for demagnetization effects, thus not allowing the different data to be compared. Also for LaFeCoSi no comparison between a measured adiabatic temperature change and a temperature change calculated using Eq. (1) have been reported. Importantly, if this relation can be verified experimentally only magnetization and heat capacity need to be measured to fully characterize the magnetocaloric properties of a magnetocaloric material.

Here we have measured each of the magnetocaloric properties, i.e. the magnetization, specific heat capacity and adiabatic temperature change, of three different sintered samples of $LaFe_{13-x-y}Co_xSi_y$. The chemical composition of these are $LaFe_{11.06}Co_{0.86}Si_{1.08}$, $LaFe_{11.05}Co_{0.94}Si_{1.01}$ and $LaFe_{10.96}Co_{0.97}Si_{1.07}$. These samples will be referred as Samples 1, 2 and 3 respectively.

The properties of the LaFeCoSi samples are compared with the properties of commercial grade gadolinium, here simply termed Gd. This gadolinium is much cheaper than pure gadolinium, but the purity is also lower. The commercial grade gadolinium contains 99.5% rare earth metal, of which 99.94% are gadolinium. This Gd grade has previously been used in an actual magnetic refrigeration device [15].

The properties of both pure and impure gadolinium have previously been analyzed, and the main conclusions of this analysis were that the impure gadolinium has a lower adiabatic temperature change and, depending on the amount and types of impurities of the sample, a small shift of a couple of degree of the Curie temperature is also seen [2].

2. Experimental setup

The magnetocaloric properties of both LaFeCoSi and commercial grade Gd have been measured using different lab equipment at Risø DTU.

Raw blocks of LaFeCoSi were prepared by powder metallurgy as described by Ref. [9]. The sintered blocks were cut into plates with dimensions $25\times20\times0.9\,mm^3$ utilizing the thermally induced decomposition and recombination (TDR) process [16]. From these plates, the samples for the various measurements were cut. The commercial grade Gd was obtained from China Rare Metal Material Co. in plates with dimensions $25\times40\times0.9\,mm^3$.

The magnetization was measured using a LakeShore 7407 Vibrating Sample Magnetometer (VSM). Isothermal magnetization measurements as a function of field were made at a ramp rate of 2.5 mT/s up to a maximum field of $\mu_0H_{ext}=1.6$ T and data were measured for every 5 mT. In a sample interval of ±10 K around the Curie temperature the measurements were taken at 1 K separation, while further from T_C the separation was larger. Data were measured from 250 to 310 K.

Once the magnetization has been determined the change in specific entropy can be calculated using

$$\Delta s_M=\mu_0\int_{H_i}^{H_f}\left(\frac{\partial m}{\partial T}\right)_H dH, \tag{2}$$

where H_i is the initial magnetic field and H_f is the final magnetic field.

Calorimetric data in applied fields up to $\mu_0H_{ext}=1.4$ T were obtained using a differential scanning calorimeter (DSC) with the magnetic field provided by a concentric Halbach cylinder, which is an adjustable permanent magnetic field source [17]. The specific heat capacity was measured at external field values of $\mu_0H_{ext}=0$, 0.25, 0.50, 0.75, 1.00 and 1.40 T in a temperature interval from 250 to 310 K with a ramp of 1 K/min and from 310 to 250 K with a ramp of -1 K/min. If no hysteresis is observed the calculated value of c_p from the two data sets are averaged. Data were taken every 12.5 ms. The DSC was calibrated using both copper and titanium reference samples.

Finally, the adiabatic temperature change was measured using an instrument designed at Risø DTU. A pneumatic piston moves a sample holder in and out of a magnetic field generated by the same permanent magnet as used for the DSC. A sliding track ensures that the direction of the sample holder with respect to the magnetic field is fixed. The entire setup is placed in a freezer, which is used to control the temperature. The ramp rate of the temperature was controlled by a 75 W light bulb and heat leakage to the surroundings. In general a complete sweep in temperature took around 9 h, during which time data were recorded. Due to this substantial time span, parasitic temperature gradients were kept as small as possible. The pneumatic piston was moved in and out of field every 5 s, with an actual movement time of no more than 100 ms. Because of the high sweep rate and the thermal isolation conditions can be assumed to be close to adiabatic. The temperature of the sample was recorded every 100 ms.

The sample is prepared by placing a type E thermocouple between two equally sized plates of the given sample which are then glued together. The sample is packed in isolating foam and placed in a sample holder together with a Hall probe (AlphaLab Inc, Model: DCM). Data were measured at external field values of $\mu_0H_{ext}=0.25$, 0.50, 0.75, 1.00 and 1.40 T in a temperature interval from 250 to 310 K. For each of the different materials all measurements were done on samples cut from the same large sample plate. The magnet is also cooled in the setup. This changes the magnetic field produced by the magnet slightly, but at 1 T the change is less than 3%.

2.1. Internal magnetic field

When subjecting a magnetic sample to an external magnetic field the internal field within the sample will depend on the geometry of the sample. It is extremely important to always report magnetocaloric properties as a function of internal field, as comparison with other or even identical materials is otherwise not meaningful [18]. If the sample has an ellipsoidal shape the internal field will be homogeneous and can be calculated if the magnetization of the sample is known [19]. If the sample has a non-ellipsoidal shape the internal field will not be homogeneous across the sample. However, an average internal magnetic field can be found. This average internal magnetic field, H_{int}, can be found by subtracting the demagnetization field $H_d=N_dM$, where N_d is the average demagnetization factor and M is the magnetization, from the applied external field, H_{ext},

$$H_{int}=H_{ext}-N_dM. \tag{3}$$

Assuming that the magnetic anisotropy is negligible the internal field, the external field and the magnetization are all very close to being parallel, so that only the magnitudes need to be considered.

If the sample has a rectangular (orthorhombic) shape the average demagnetization factor can be calculated according to Ref. [20]. This factor is a good approximation to the true demagnetization field [21].

Using the dimensions of the individual sample pieces and their respective demagnetization factors, given in Table 1, all measurements presented here have been corrected for demagnetization by the approximation in Ref. [20]. Thus, all measured properties are reported as a function of internal field. While this

correction is easy to perform it is not commonly done. In the papers previously published on LaFeCoSi corrections for demagnetization has not been performed making comparison with the present work difficult.

3. Results and discussion

The change in specific entropy was calculated by Eq. (2) using the measured magnetization data and employing a numerical integration scheme. These results are shown in Fig. 1.

The measured values of c_p, corrected for demagnetization and binned in 0.25 K intervals, are shown in Fig. 2. The 95% confidence interval resulting from the binning of the data is of the order of the width of the plotted lines.

The measured values of ΔT_{ad}, corrected for demagnetization and binned in 0.25 K intervals, are shown in Fig. 3. Again the 95% confidence interval resulting from the binning of the data is of the order of the width of the plotted lines. The adiabatic temperature has also been calculated using Eq. (1) using the measured magnetization and specific heat capacities. The results of these calculation are also shown in Fig. 3. In general a very good

Table 1
The dimensions and demagnetization factors for the different samples of LaFeCoSi and Gd.

	$LaFe_{13-x-y}Co_xSi_y$			Gd commercial grade	Unit
	$\begin{pmatrix} x=0.86 \\ y=1.08 \end{pmatrix}$ Sample 1	$\begin{pmatrix} x=0.94 \\ y=1.01 \end{pmatrix}$ Sample 2	$\begin{pmatrix} x=0.97 \\ y=1.07 \end{pmatrix}$ Sample 3		
Density	6980	7290	7160	7900	kg m^{-3}
VSM					
$a \times b \times c$	$0.82 \times 3.27 \times 1.81$	$0.85 \times 3.38 \times 1.96$	$0.87 \times 2.04 \times 3.38$	$0.90 \times 4.60 \times 2.26$	mm^3
N_d	0.27	0.27	0.16	0.26	–
DSC					
$a \times b \times c$	$1.94 \times 0.85 \times 3.66$	$2.47 \times 0.83 \times 2.50$	$2.21 \times 0.85 \times 3.17$	$2.04 \times 0.89 \times 2.78$	mm^3
N_d	0.14	0.20	0.17	0.19	–
ΔT_{ad}					
$a \times b \times c$	$7.36 \times 2.08 \times 5.33$	$5.60 \times 1.74 \times 7.70$	$9.90 \times 2.09 \times 10.23$	$5.42 \times 2.01 \times 9.48$	mm^3
N_d	0.24	0.15	0.15	0.14	–

The direction of the magnetic field is always along the *c*-axis.

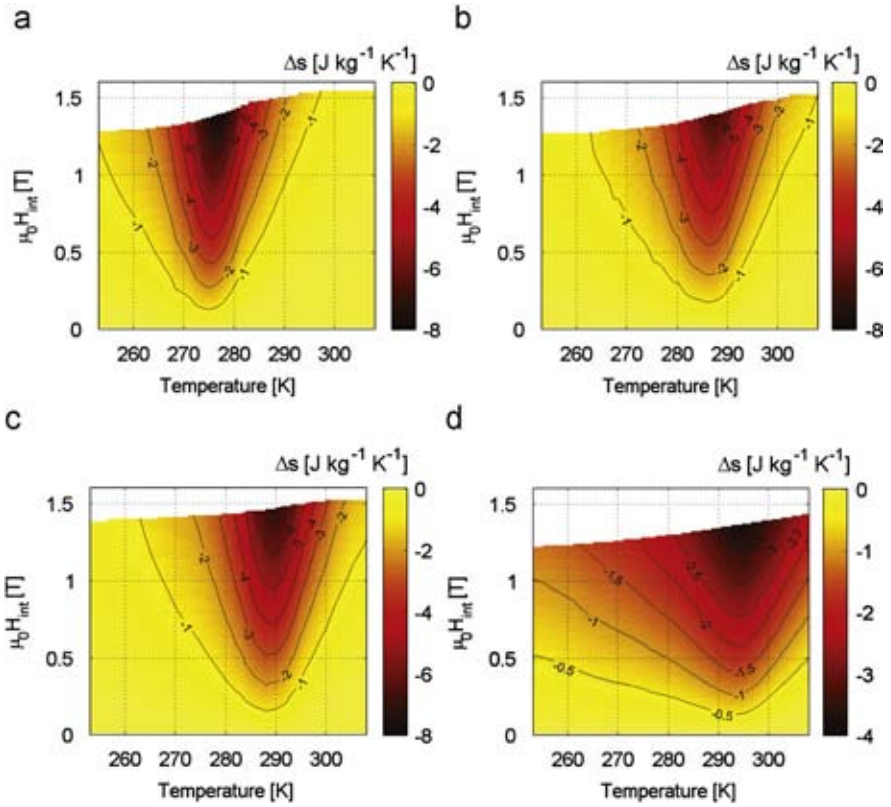

Fig. 1. (Color online) The change in specific entropy, Δs, as calculated from Eq. (2) as a function of temperature and internal field. (a) Specific entropy change of Sample 1. (b) Specific entropy change of Sample 2. (c) Specific entropy change of Sample 3. (d) Specific entropy change of Gd.

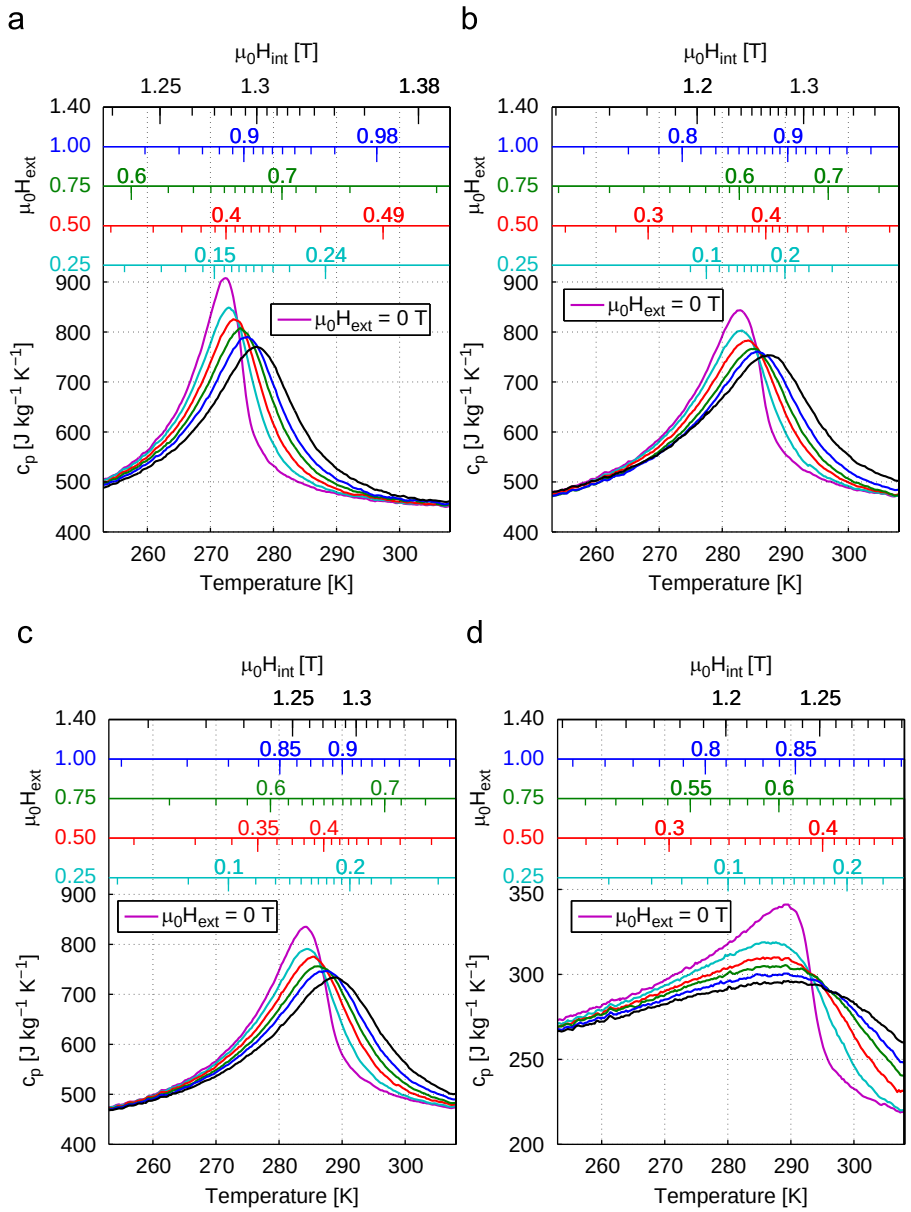

Fig. 2. The specific heat capacity, c_p, as a function of temperature for the internal field given in the top x-axis. Each of the top x-axis gives the internal field for the same colored curve. As the external field is increased the maximum value of the specific heat capacity decreases. (a) Specific heat capacity of Sample 1. (b) Specific heat capacity of Sample 2. (c) Specific heat capacity of Sample 3. (d) Specific heat capacity of Gd. (For interpretation of the references to color in this figure legend, the reader is referred to the web version of this article.)

agreement between the calculated and measured values of ΔT_{ad} is seen.

The adiabatic temperature change upon removal of the magnetic field has also been measured, i.e. $\Delta T_{ad,field\ off}$, although these are not shown in Fig. 3. A requisite for the reversibility of the MCE is that $\Delta T_{ad,field\ on}(T) = -\Delta T_{ad,field\ off}(T + \Delta T_{ad,field\ on}(T))$. This relation has been found to be true for all the measured data, and thus the MCE is reversible.

In both Figs. 2 and 3 the top x-axes show the internal magnetic field of the different samples, i.e. the external field corrected for demagnetization. For a given external field the internal field is a function of temperature, as the magnetization changes with temperature. Thus, here one can directly see how important it is to correct for demagnetization.

The position of the peak of both Δs, c_p and ΔT_{ad} changes between the three different samples of LaFeCoSi. Thus it is clearly seen that the peak position is tuneable.

It is known from literature that LaFeCoSi may contain an impurity phase of α–Fe. However, this will in general not greatly affect the magnetocaloric properties of LaFeCoSi. This is because the specific heat capacity of α–Fe is $c_p \sim 450\,\mathrm{J/kg\,K}$ which is close to the observed heat capacity of LaFeCoSi. The density for the α–Fe phase is $7.87\,\mathrm{kg\ m^{-3}}$ which is also close to that of the LaFeCoSi. For Sample 1 of LaFeCoSi X-ray diffraction has been performed and the results were reported in Ref. [14]. Here a 5% α–Fe content was identified and the structure of the LaFeCoSi was found to be of $NaZn_{13}$-type. As the remaining samples are manufactured in an identical manner to Sample 1 these are presumed to have the same low content of α–Fe as observed in similar series of LaFeCoSi materials [16].

In order to compare the LaFeCoSi and commercial grade Gd, each of the magnetocaloric properties has been interpolated for an internal field of 1 T. The results are shown in Figs. 4–6 as well as given in Table 2.

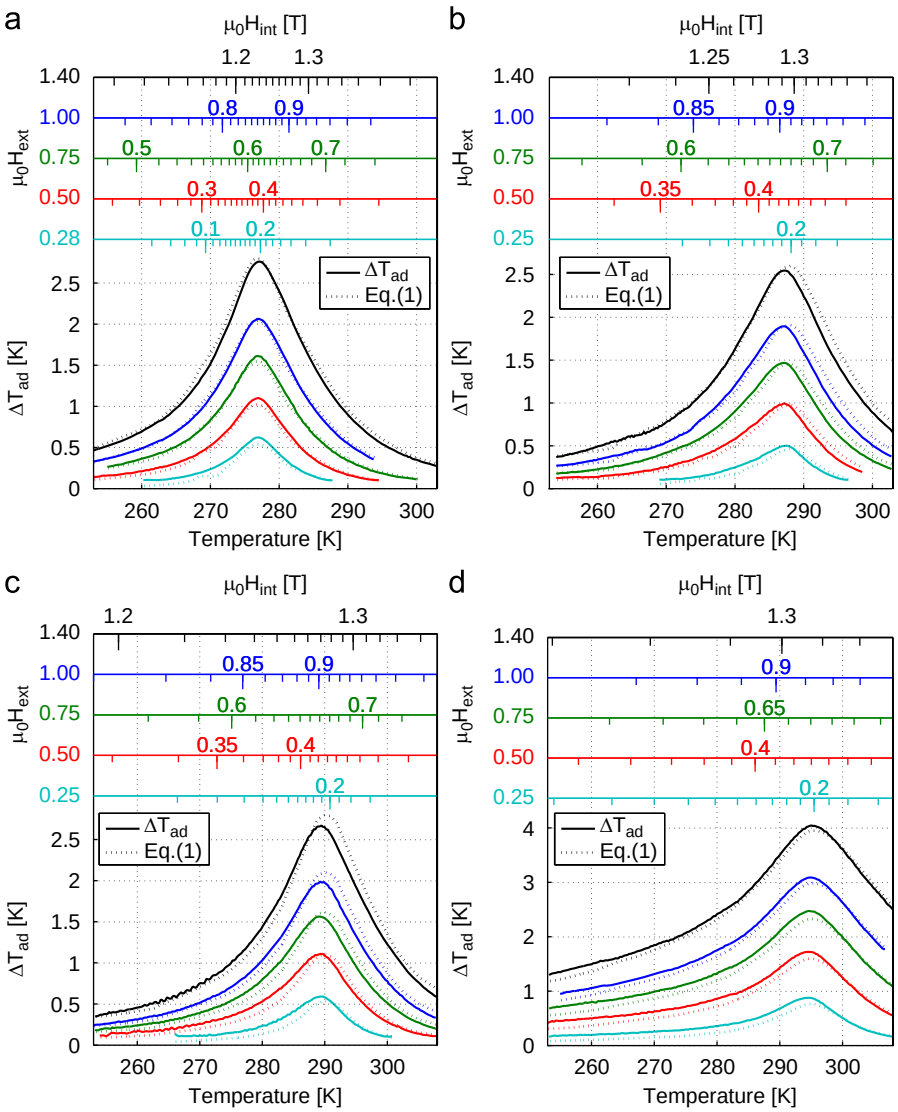

Fig. 3. The adiabatic temperature change, ΔT_{ad}, as a function of temperature for a change in magnetic field from zero to the internal field given in the top x-axis. Each of the top x-axis gives the internal field for the same colored curve. The figures also show the calculated ΔT_{ad} based on Eq. (1). The adiabatic temperature change increases with increasing external field. (a) Adiabatic temperature change of Sample 1. (b) Adiabatic temperature change of Sample 2. (c) Adiabatic temperature change of Sample 3. (d) Adiabatic temperature change of Gd. (For interpretation of the references to color in this figure legend, the reader is referred to the web version of this article.)

From the figures it is seen that although the specific entropy change of Gd is significantly lower than for the LaFeCoSi materials the adiabatic temperature change is larger over a broad interval. This is because the specific heat capacity of Gd is significantly lower than those of the LaFeCoSi materials. From these facts it is clear that the magnetocaloric properties and its application potential with regard to magnetic refrigeration cannot be judged from the specific entropy change alone. Also, it is seen that if only the adiabatic temperature change is considered the Curie temperature of a LaFeCoSi material must be below around 280 K for the material to outperform Gd.

One can consider the heat generated per cycle of the magnetocaloric effect. This is $Q = \Delta T_{ad} c_p$ and is shown in Fig. 8. From this figure one can see that the LaFeCoSi generates a larger heat over a large temperature interval than Gd. The cooling capacity of a regenerator is proportional to the generated heat, but the temperature span obtainable depends on the adiabatic temperature change and thus Gd will still be able to generate a larger no load temperature span than a single LaFeCoSi material.

In Fig. 7 the normalized interpolated value of $\Delta T_{ad}(T_{peak})$ and the interpolated normalized full width half maximum (FWHM) are shown as functions of internal magnetic field for Gd and LaFeCoSi, except for the FWHM curve for Gd, as the temperature span is not large enough to calculate this. Here one can see that $\Delta T_{ad}(T_{peak})$ scales similarly for Gd and LaFeCoSi. All three different LaFeCoSi materials display identical behavior, as could be expected. The adiabatic temperature change of a theoretical general second order magnetocaloric material scales with the magnetic field to the power of $\frac{2}{3}$ [22]. This relation is also shown in Fig. 7. It is seen that the scaling of both Gd and LaFeCoSi are very similar, both with a scaling close to the theoretical value.

The uncertainty of the measurements performed is not trivial to estimate. For e.g. the adiabatic temperature change the uncertainty of the thermocouple temperature measurement is of

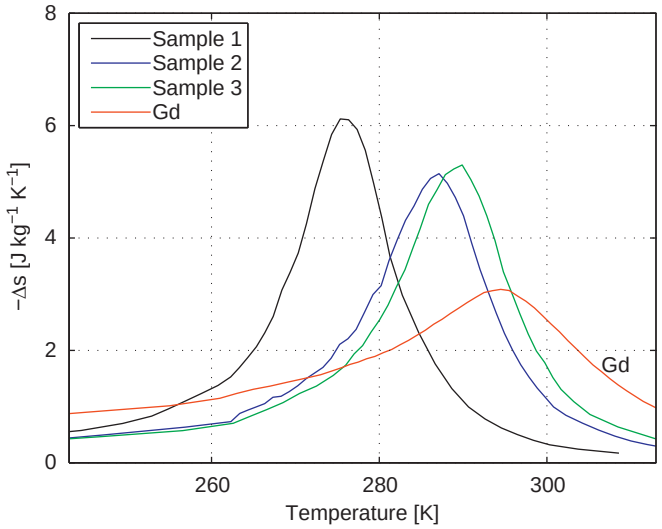

Fig. 4. The values of Δs interpolated at $\mu_0 H_{\text{int}} = 1$ T as a function of temperature for Gd and the three different samples of LaFeCoSi. The peak temperature increases with increasing sample number for the LaFeCoSi samples.

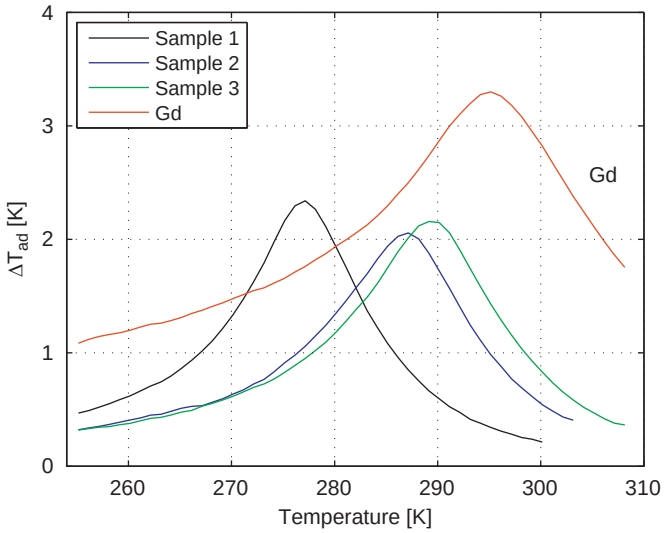

Fig. 6. The values of ΔT_{ad} interpolated at $\mu_0 H_{\text{int}} = 1$ T as a function of temperature for Gd and the three different samples of LaFeCoSi. The peak temperature increases with increasing sample number for the LaFeCoSi samples.

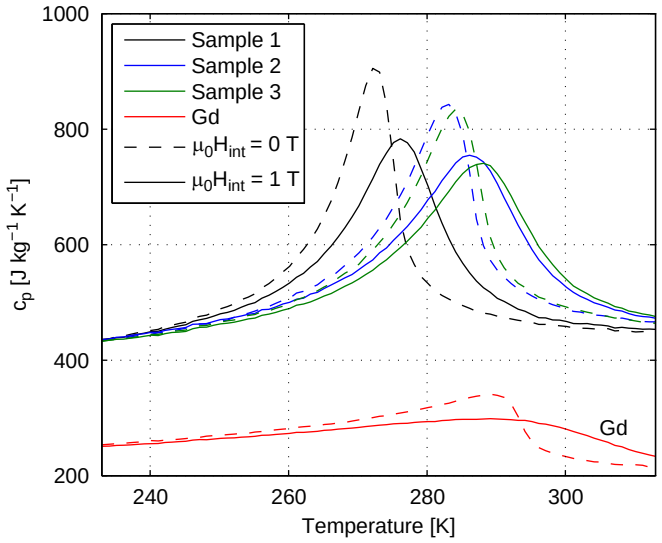

Fig. 5. The values of c_{p} interpolated at $\mu_0 H_{\text{int}} = 0$ and 1 T as a function of temperature for Gd and the three different samples of LaFeCoSi. The peak temperature increases with increasing sample number for the LaFeCoSi samples.

Table 2
The peak temperature and corresponding thermodynamic values for Δs, c_{p} and ΔT_{ad} of LaFeCoSi and Gd.

Variable	$LaFe_{13-x-y}Co_xSi_y$			Gd commercial grade	Unit
	$\begin{pmatrix} x=0.86 \\ y=1.08 \end{pmatrix}$ Sample 1	$\begin{pmatrix} x=0.94 \\ y=1.01 \end{pmatrix}$ Sample 2	$\begin{pmatrix} x=0.97 \\ y=1.07 \end{pmatrix}$ Sample 3		
Δs(1 T)					
Value	6.1	5.1	5.3	3.1	J/kg K
T_{peak}	275.8	287.1	289.8	294.8	K
ΔT_{95}	−1.5/+1.9	−1.8/+1.4	−2.2/+1.2	−3.4/+2.0	K
c_{p}(0 T)					
Value	910	840	835	340	J/kg K
T_{peak}	272.6	283.0	284.3	289.2	K
ΔT_{95}	−1.7/+1.3	−2.5/+2.0	−2.4/+2.0	−6.7/+3.0	K
c_{p}(1 T)					
Value	785	755	740	300	J/kg K
T_{peak}	276.1	286.1	288.2	289.2	K
ΔT_{95}	−2.7/+2.7	−3.5/+3.6	−4.3/+3.1	−19.0/+10.0	K
ΔT_{ad}(1 T)					
Value	2.3	2.1	2.2	3.3	K
T_{peak}	277.1	287.1	289.6	295.1	K
ΔT_{95}	−1.5/+1.4	−1.8/+1.6	−2.1/+1.6	−2.6/+2.6	K

The value of ΔT_{95} gives the band around T_{peak} in which the value of above 95% of the peak value. Note that the peak in c_{p} for Gd is very broad, making T_{peak} hard to determine accurately.

the order of 0.1 K, while the measurement uncertainty for the Hall probe (AlphaLab Inc, Model: DCM) is $\pm 2\%$. Systematic errors can, however, always be present. As previously mentioned the 95% confidence interval resulting from the binning of the data is of the order of the width of the plotted lines in Fig. 6. Thus the uncertainty of the individual measurement is small. As a measure of the uncertainty on the determination of the peak temperatures the band on which the parameters Δs, c_{p} and ΔT_{ad} are within 95% of their peak values, ΔT_{95}, has been computed and reported in Table 2. These values give the width of the peak and can be seen to change depending on the type of variable and material measured. Especially the 95% values of c_{p}(1 T) are seen to be quite large and thus here the uncertainty in the peak temperature is larger than for other types of variables and materials.

4. Conclusion

The magnetocaloric properties of Gd and three sample of LaFeCoSi with different chemical composition have been measured directly. The measurements were corrected for demagnetization, allowing the data to be directly compared. In an internal field of 1 T the specific entropy change was 6.2, 5.1 and 5.0 J/kg K, the specific heat capacity was 910, 840 and 835 J/kg K and the adiabatic temperature change was 2.3, 2.1 and 2.1 K for the three LaFeCoSi samples respectively. The peak temperature changes of the order of 1 K depending on the property measured, but are around 276,

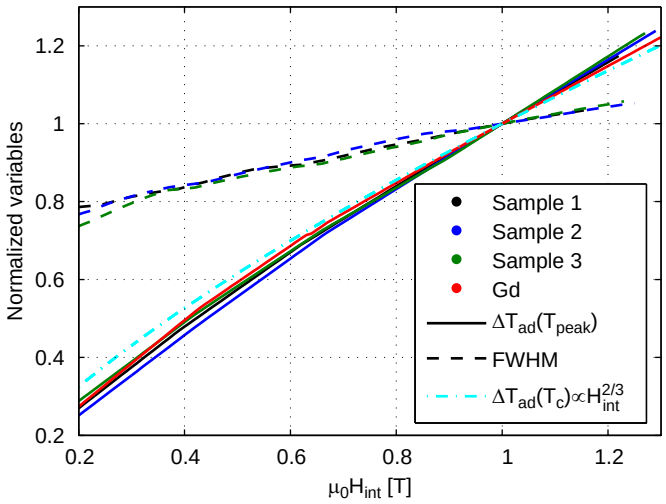

Fig. 7. The normalized peak value of ΔT_{ad} and normalized full width half maximum (FWHM) as a function of internal magnetic field for Gd and LaFeCoSi, except for the Gd FWHM curve which could not be calculated because of a too small temperature range. The scaling of the adiabatic temperature change at the Curie temperature for a theoretical general second order magnetocaloric material, which scales with the magnetic field to the power of $\frac{2}{3}$, is also shown. The scaling of the materials are seen to be almost identical.

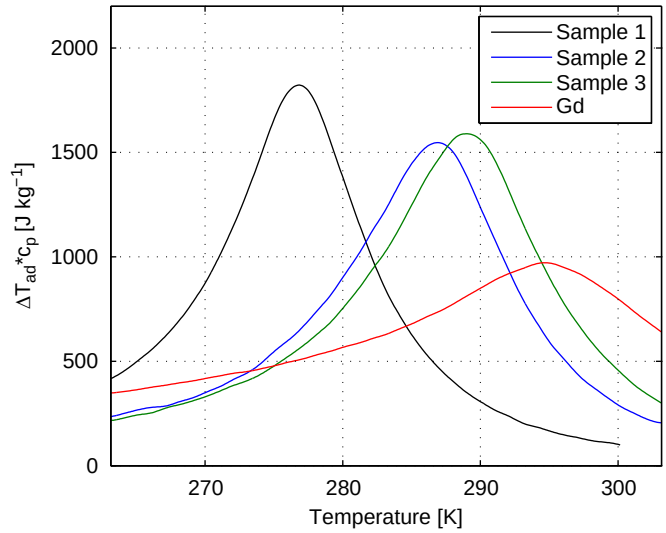

Fig. 8. The heat generated in one magnetocaloric cycle, $Q = \Delta T_{ad} c_p$, of Gd and LaFeCoSi at $\mu_0 H_{int} = 1$ T, based on the values shown in Figs. 5 and 6.

286 and 288 K for the three samples respectively. The corresponding values for all properties for Gd are 3.1, 340 J/kg K, 3.3 K and a peak temperature of 295 K. Thus, LaFeCoSi has a large enough magnetocaloric effect for practical application in magnetic refrigeration. Finally, an excellent agreement between the calculated adiabatic temperature change using Eq. (1) and the measured adiabatic temperature change was seen.

Acknowledgements

The authors would to thank J. Geyti for his technical help, and Dr. N. Pryds and Dr. A. Smith for fruitful discussions. The authors would like to acknowledge the support of the Programme Commission on Energy and Environment (EnMi) (Contract no. 2104-06-0032) which is part of the Danish Council for Strategic Research.

References

[1] K.A. Gschneidner Jr., V.K. Pecharsky, A.O. Tsokol, Rep. Prog. Phys. 68 (2005) 1479–1539.
[2] S. Dan'kov, A. Tishin, V. Pecharsky, K.A.J. Gschneidner, Phys. Rev. B 57 (6) (1998) 3478–3490.
[3] A. Fujita, Y. Akamatsu, K. Fukamichi, J. Appl. Phys. 85 (8) (1999) 4756–4758.
[4] F. Hu, X. Qian, J. Sun, G. Wang, X. Zhang, Z. Cheng, B. Shen, J. Appl. Phys. 92 (7) (2002) 3620–3623.
[5] F.-x. Hu, B.-g. Shen, J.-r. Sun, Appl. Phys. Lett. 80 (5) (2002) 826.
[6] X.B. Liu, Z. Altounian, J. Magn. Magn. Mater. 264 (2–3) (2003) 209–213.
[7] E. Passamani, C. Larica, J. Proveti, A. Takeuchi, A. Gomes, L. Ghivelder, J. Magn. Magn. Mater. 312 (1) (2007) 65–71.
[8] A. Saito, T. Kobayashi, H. Tsuji, J. Magn. Magn. Mater. 310 (2007) 2808–2810.
[9] M. Katter, V. Zellmann, G. Reppel, K. Uestuener, IEEE Trans. Magn. 44 (111) (2008) 3044–3047.
[10] A. Yan, K.-H. Muller, O. Gutfleisch, J. Alloy. Compd. 450 (1) (2008) 18.
[11] F. Hu, J. Gao, X. Qian, M. Ilyn, A. Tishin, J. Sun, B. Shen, J. Appl. Phys. 97 (10) (2005) 10M303.
[12] M. Ilyn, A. Tishin, F. Hu, J. Gao, J. Sun, B. Shen, J. Magn. Magn. Mater. 290–291 (2005) 712–714.
[13] M. Balli, O. Sari, J. Hu, P. Egolf, D. Fruchart, D. Gignoux, J. Huang, J. Appl. Phys. 106 (2) (2009) 023902.
[14] B.R. Hansen, M. Katter, Theil L. Kuhn, C.R.H. Bahl, A. Smith, C. Ancona-Torres, in: Proceedings of the 3rd International Conference on Magnetic Refrigeration at Room Temperature, Des Moines, Iowa, USA, 2009, pp. 67–73.
[15] C. Bahl, T. Petersen, N. Pryds, A. Smith, T. Petersen, Rev. Sci. Instrum. 79 (9) (2008) 093906.
[16] M. Katter, V. Zellmann, G.W. Reppel, K. Uestuener, in: Proceedings of the 3rd International Conference on Magnetic Refrigeration at Room Temperature, Des Moines, Iowa, USA, 2009, pp. 83–88.
[17] S. Jeppesen, S. Linderoth, N. Pryds, L.T. Kuhn, B.J. Jensen, Rev. Sci. Instrum. 79 (8) (2008) 083901.
[18] C.R.H. Bahl, K.K. Nielsen, J. Appl. Phys. 105 (1) (2009) 013916.
[19] J. Osborn, Phys. Rev. 67 (1945) 351–357.
[20] A. Aharoni, J. Appl. Phys. 83 (6) (1998) 3432–3434.
[21] A. Smith, K.K. Nielsen, D.V. Christensen, C.R.H. Bahl, R. Bjørk, J. Hattel, J. Appl. Phys. 107 (2010) 103910.
[22] H. Oesterreicher, F. Parker, J. Appl. Phys. 55 (1984) 4334–4338.

Paper XI

Paper published in International Journal of Refrigeration, 2010

Bjørk, R. and Engelbrecht, K.

The influence of the magnetic field on the performance of an active magnetic regenerator (AMR)

International Journal of Refrigeration, doi:10.1016/j.ijrefrig.2010.07.004, 2010

INTERNATIONAL JOURNAL OF REFRIGERATION XXX (2010) 1–12

available at www.sciencedirect.com

journal homepage: www.elsevier.com/locate/ijrefrig

The influence of the magnetic field on the performance of an active magnetic regenerator (AMR)

R. Bjørk, K. Engelbrecht*

Fuel Cells and Solid State Chemistry Division, Risø National Laboratory for Sustainable Energy, Technical University of Denmark – DTU, Frederiksborgvej 399, DK-4000 Roskilde, Denmark

ARTICLE INFO

Article history:
Received 9 February 2010
Received in revised form
1 July 2010
Accepted 11 July 2010
Available online xxx

Keywords:
Magnetic refrigerator
Magnetic field
Simulation
Modelling
Performance Variation

ABSTRACT

The influence of the time variation of the magnetic field, termed the magnetic field profile, on the performance of a magnetocaloric refrigeration device using the active magnetic regeneration (AMR) cycle is studied for a number of process parameters for both a parallel plate and packed bed regenerator using a numerical model. The cooling curve of the AMR is shown to be almost linear far from the Curie temperature of the magnetocaloric material. It is shown that a magnetic field profile that is 10% of the cycle time out of sync with the flow profile leads to a drop in both the maximum temperature span and the maximum cooling capacity of 20–40% for both parallel plate and packed bed regenerators. The maximum cooling capacity is shown to depend very weakly on the ramp rate of the magnetic field. Reducing the temporal width of the high field portion of the magnetic field profile by 10% leads to a drop in maximum temperature span and maximum cooling capacity of 5–20%. An increase of the magnetic field from 1 T to 1.5 T increases the maximum cooling capacity by 30–50% but the maximum temperature span by only 20–30%. Finally, it was seen that the influence of changing the magnetic field was more or less the same for the different regenerator geometries and operating parameters studied here. This means that the design of the magnet can be done independently of the regenerator geometry.

Influence du champ magnétique actif sur la performance d'un régénérateur magnétique actif

Mots clés : réfrigérateur magnétique ; champ magnétique ; simulation ; modélisation ; performance ; variation

* *Corresponding author*. Tel.: +45 46775800; fax: +45 46775858.
E-mail address: rabj@risoe.dtu.dk (R. Bjørk).

0140-7007/$ – see front matter
doi:10.1016/j.ijrefrig.2010.07.004

Please cite this article in press as: Bjørk, R., Engelbrecht, K., The influence of the magnetic field on the performance of an active magnetic regenerator (AMR), International Journal of Refrigeration (2010), doi:10.1016/j.ijrefrig.2010.07.004

Nomenclature

Variables

ΔT_{ad}	adiabatic temperature change (K)
T_c	Curie temperature (K)
$\dot{Q}$	cooling capacity (W)
T_{span}	temperature span (K)
T_{hot}	temperature of hot end of AMR (K)
T_{cold}	temperature of cold end of AMR (K)
$\dot{Q}_{max}$	maximum cooling capacity (W)
$T_{span,max}$	maximum or no load temperature span (K)
k	thermal conductivity ($W\,K^{-1}\,m^{-1}$)
h_{fluid}	height of fluid channel (m)
c_p	specific heat capacity ($J\,kg^{-1}\,K^{-1}$)
P	time period for hot/cold blow [s]
x_0	synchronization parameter (–)
H	magnetic field ($A\,m^{-1}$)
H_{max}	maximum magnetic field ($A\,m^{-1}$)
w_{top}	top width of magnetic field profile (–)
w_{total}	total width of magnetic field profile (–)
h_{plate}	height of plate of MCM (m)
$\dot{m}_{amp}$	mass flow rate ($kg\,s^{-1}$)
h	height of regenerator (m)
d_p	particle size (m)
R^2	goodness-of-fit statistic (–)
y_i	values of data set (–)
f_i	interpolated values (–)
$\bar{y}$	mean of the data set values (–)
L	linear function (–)
m	mass (kg)

Greek

τ_1	magnetization time step (s)
τ_2	cold to hot fluid flow time step (s)
τ_3	demagnetization time step (s)
τ_4	hot to cold fluid flow time step (s)
τ	cycle time (s)
Γ	"1D AMR correctness" parameter (-)
ρ	density ($kg\,m^{-3}$)
μ_0	permeability of free space ($m\,kg\,s^{-2}\,A^{-2}$)

1. Introduction

Magnetic refrigeration is an evolving cooling technology that has the potential for high energy efficiency using environmentally friendly refrigerants. Refrigeration is generated by utilizing the magnetocaloric effect (MCE), which is the temperature change that most magnetic materials exhibit when subjected to a changing magnetic field. This temperature change is called the adiabatic temperature change, ΔT_{ad}, and is a function of temperature and magnetic field. The temperature change is greatest near the Curie temperature, T_c, which varies with the magnetocaloric material (Pecharsky and Gschneidner, 2006). Because the MCE in the best magnetocaloric materials currently available exhibit a temperature change of no more than 4 K in a magnetic field of 1 T (Dan'kov et al., 1998), a magnetic refrigeration device must utilize a regenerative process to produce a large enough temperature span to be useful for refrigeration purposes. The most utilized process for this is called active magnetic regeneration (AMR) (Barclay, 1982).

A great number of magnetic refrigeration test devices have been built and examined in some detail, with focus on the produced temperature span and cooling power of the devices (Barclay, 1988; Yu et al., 2003; Gschneidner and Pecharsky, 2008). Detailed and extensive investigations of the AMR process using numerical modeling have previously been published (Hu and Xiao, 1995; Engelbrecht et al., 2005a,b; Allab et al., 2005; Siddikov et al., 2005; Shir et al., 2005; Petersen et al., 2008b; Nielsen et al., 2009, 2010), but so far little focus has been put into investigating how the properties and time variation of the magnetic field influence the theoretical performance of the AMR cycle. Here, a generic magnetic field that varies as a function of time during the AMR cycle is used to investigate the influence of the magnetic field on the performance of the AMR process. This time varying profile is called the magnetic field profile.

1.1. The AMR process

In the AMR process a heat transfer fluid and a magnetocaloric material (MCM), acting as a regenerator, are used to build up a temperature gradient that can be much larger than the adiabatic temperature change produced by the magnetocaloric material. The regenerator consists of a porous matrix of a solid magnetocaloric material through which a non-magnetic fluid can flow. This fluid transfers heat (positive or negative) to the solid material and through a movement of the fluid, by a piston or a pump, it is moved to heat exchangers in a cooled space or in contact with the environment. Most AMR devices either have a packed bed regenerator where the MCM is typically packed spheres (Okamura et al., 2005; Tura and Rowe, 2009) or a parallel plate regenerator (Zimm et al., 2007; Bahl et al., 2008). For a review of different magnetic refrigeration devices please see Gschneidner and Pecharsky (2008).

An AMR cycle proceeds in four steps. First the regenerator is magnetized. This raises the temperature of the solid due to the magnetocaloric effect. The temperature rise is a function of magnetic field but also of temperature, and thus of position in the regenerator. At the same time heat is transferred from the MCM to the heat transfer fluid in a time span, τ_1. The heat transfer fluid is then displaced towards the hot heat exchanger where the heat is released to the surroundings over a time span, τ_2. Next, the magnetic field in the regenerator is removed. This lowers the temperature of the MCM by the adiabatic temperature change so that the MCM is now colder than the entrained heat transfer fluid. Thus heat is transferred from the heat transfer fluid to the MCM, cooling the heat transfer fluid, through a time span, τ_3. Then the heat transfer fluid is displaced towards the cold heat exchanger, where heat can be absorbed from a heat load through a time span, τ_4. A total cycle lasts a time span τ, equal to $\tau_1+\tau_2+\tau_3+\tau_4$. The process then starts over again. Using this regenerative process a temperature span

Please cite this article in press as: Bjørk, R., Engelbrecht, K., The influence of the magnetic field on the performance of an active magnetic regenerator (AMR), International Journal of Refrigeration (2010), doi:10.1016/j.ijrefrig.2010.07.004

between the hot and cold end that is greater than the adiabatic temperature change can be achieved.

The performance of an AMR device depends on the process parameters specific to each AMR system. These are the shape and packing of the magnetocaloric material, the temperature of the surroundings and the properties of the MCM used, as well as the properties of the heat transfer fluid, flow system etc. The only parameter that is common to all AMR systems is the magnetic field. The magnet might be shaped differently in different AMR system, but the magnetic field generated by the magnet has the same effect on all AMR systems, namely that it drives the magnetocaloric effect that is the heart of the AMR. Thus the magnetic field sets a fundamental limit on the temperature span and cooling power that an AMR system can produce. Therefore it is interesting to investigate the influence of the magnetic field on the AMR performance.

The performance of an AMR is summed up in the cooling curve of the AMR. This curve shows the cooling capacity, $\dot{Q}$, as a function of temperature span, T_{span}, of the device, for a given set of process parameters. The temperature span is the difference between the temperature of the hot and the cold end, T_{hot} and T_{cold}, respectively. An example of a cooling curve is shown in Fig. 1. Examination of the figure shows that the cooling power produced by the AMR is highly dependent on temperature span. The most often-cited information that can be learned from a cooling curve are the maximum or no load temperature span, $T_{span,max}$, and the maximum refrigeration capacity, $\dot{Q}_{max}$. At $T_{span,max} \Leftrightarrow \dot{Q} = 0$ W, while at $\dot{Q}_{max} \Leftrightarrow T_{span} = 0$ K, where in the latter case all the cooling power generated by the device is used to move heat from the cold to the hot end. These two parameters are used to characterize the efficiency of an AMR throughout this paper. The shape of the cooling curve in between these two points is of course also of interest and is also investigated here.

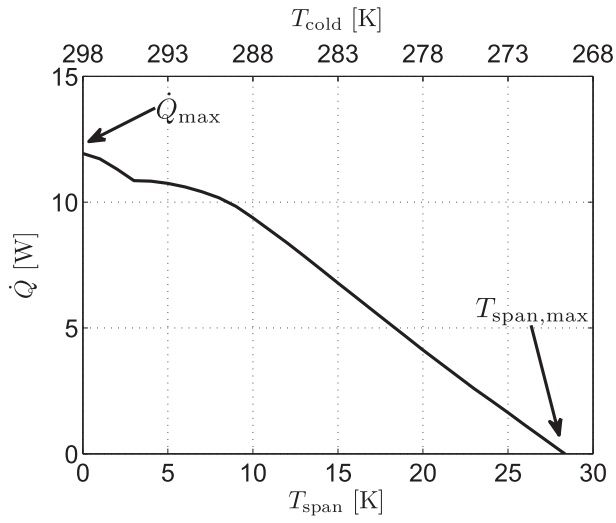

Fig. 1 – An example of a cooling curve showing $\dot{Q}$ as a function of T_{span}. The maximum temperature span, $T_{span,max}$, and the maximum refrigeration capacity, $\dot{Q}_{max}$, have been indicated. The temperature of the hot end of the regenerator was $T_{hot} = 298$ K and the Curie temperature of the MCM of $T_C = 293.6$ K.

The effect of the magnetic field on the performance of the AMR cycle is controlled by three parameters. The first of these parameters is the synchronization of the magnetic field with the AMR cycle, i.e. when in the AMR cycle the magnetocaloric material is subjected to the magnetic field. The second parameter is the ramp rate of the magnetic field, i.e. how quickly does the magnetic field change from its minimum to its maximum value and vice versa. And finally the last parameter is the maximum value of the magnetic field. A spatial variation of the magnetic field across the AMR is not considered here.

The influence of each of these parameters on the performance of the AMR is studied using a numerical model for a number of different set of AMR process parameters. Ideally the work presented here should be supported by experimental data, but conducting AMR experiments with changing magnetic fields are notoriously cumbersome, as most magnetic refrigerators use permanent magnets to generate the magnetic field, and for these the generated magnetic flux density can rarely be changed. Experiments would be possible if an electromagnet or an adjustable permanent magnet assembly was used, as in the AMR devices by Tura and Rowe (2007), Bahl et al. (2008).

2. The numerical model

A one-dimensional numerical model capable of modeling both packed bed and parallel plate regenerators is used to model the AMR process (Engelbrecht et al., 2006). This model is publicly available. For the packed bed regenerator the model has previously been compared with experimental data (Engelbrecht, 2008). For the parallel plate regenerator case the model has been compared with a more detailed two-dimensional model (Petersen et al., 2008a,b), where the latter has been compared with experimental data (Bahl et al., 2008). In the numerical model, the temperature span is an input parameter and the refrigeration capacity is calculated for the specified process parameters.

The one-dimensional model assumes that the fluid and solid temperature profiles are functions only of the flow direction. The cooling capacity of the AMR is determined by solving the coupled one-dimensional partial differential equations in space and time describing the temperature in the regenerator and in the fluid. Different regenerator parameters such as the position dependent Nusselt number, which determines the heat transfer between the regenerator and the fluid, and the friction factor are determined using established correlations. The model assumes that the edges of both the fluid and the solid are adiabatic except during the blow periods where the fluid enters the regenerator with the prescribed temperature of either the hot or the cold reservoir. The model starts from an initial temperature distribution and takes time steps until a cyclical steady state has been achieved. This state is reached when the dimensionless value of the absolute change in energy of the regenerator from cycle to cycle is less than a specified tolerance. The governing equations for the model are given in Engelbrecht et al. (2006) and Petersen et al. (2008a,b).

For the parallel plate regenerator model the comparison with the two-dimensional model lead to the definition of a "1D correctness" parameter, Γ, which is defined as

Please cite this article in press as: Bjørk, R., Engelbrecht, K., The influence of the magnetic field on the performance of an active magnetic regenerator (AMR), International Journal of Refrigeration (2010), doi:10.1016/j.ijrefrig.2010.07.004

$$\Gamma = \frac{\pi^2 k_{fluid}}{h_{fluid}^2 \rho_{fluid} c_{p,fluid}} \tau_1 \gg 1 \quad (1)$$

where the subscript "fluid" denotes a property of the heat transfer fluid, and where k is the thermal conductivity, ρ is the mass density, c_p is the specific heat capacity and h_{fluid} is the height of the fluid channel. A value much greater than one for Γ corresponds to an operating condition in which the one dimensional model produces comparable results to the two dimensional model.

2.1. The magnetic field profile

To separately study the effects of each of the properties of the magnetic field, a generic magnetic field profile is used. This profile is shown in Fig. 2 along with the fluid flow profile.

The generic magnetic field profile can be characterized by four parameters. The first parameter is the synchronization, denoted by x_0, which indicates the time in fractions of τ where the magnetic field profile begins to increase, relative to the AMR fluid flow cycle. The second parameter is the maximum value of the magnetic field, $\mu_0 H_{max}$, which is in general varied between 0.5 and 1.5 T, as this is the range obtainable with permanent magnets (Bjørk et al., 2010). The final two parameters are the top width, w_{top}, and the total width, w_{total}, of the temporal magnetic field profile, which are both defined in terms of τ. These also define the ramp rate.

3. AMR process parameters

The performance of the AMR as a function of magnetic field is studied for a number of process parameters. These must be chosen realistically if the results of the numerical model are to be relevant for magnetic refrigeration test devices. In all models and for all process parameters, a symmetric, or balanced, AMR flow cycle is used. The values of the fluid flow cycle parameters are always $\tau_1 = \tau_3 = 0.1$ and $\tau_2 = \tau_4 = 0.4$ in fractions of the total cycle time, τ. The length of the modeled regenerator is 50 mm. The heat transfer fluid is water with

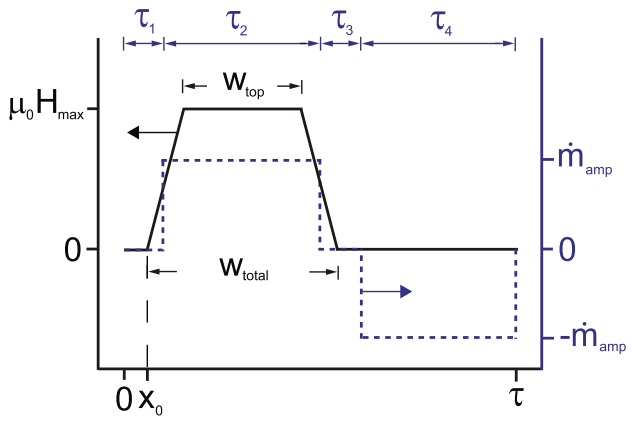

Fig. 2 – The generic magnetic field profile (full line) and the fluid flow cycle (dotted line) of the AMR cycle. The parameters of the magnetic field profile are indicated, as well as the AMR cycle time parameters τ_{1-4}.

Table 1 – Parallel plates regenerator parameters. As the parameters are varied individually, the table should not be read as rows but rather as what values the different parameters can assume. In total there are 54 sets of parameters, but 18 sets for $\tau = 0.5$ s are disregarded as the results would differ from a two dimensional AMR model.

h_{fluid} [m]	h_{plate} [m]	$\dot{m}_{amp}$ [kg s^{-1}]	τ [s]
0.00010	$1\times h_{fluid}$	$0.5 \times 7.27 \times 6/\tau \times h_{plate}$	0.5
0.00025	$2\times h_{fluid}$	$1 \times 7.27 \times 6/\tau \times h_{plate}$	6
0.00050	$3\times h_{fluid}$	$2 \times 7.27 \times 6/\tau \times h_{plate}$	

constant properties as given in Petersen et al. (2008a). The MCM is taken to be gadolinium, modeled using the mean field model (Morrish, 1965) with a Curie temperature of $T_c = 293.6$ K and properties as given in Petersen et al. (2008b). Although the mean field model does not exactly reproduce experimental data (Dan'kov et al., 1998; Liu et al., 2007), it is often used as the benchmark model for magnetocaloric AMR models (Petersen et al., 2008b; Nielsen et al., 2009) because it produces thermodynamically consistent data with smooth derivatives and different numerical models can be more easily compared if the same data set has been used as input. The temperature of the hot end of the AMR is kept fixed at $T_{hot} = 298$ K.

For the parallel plate regenerator three process parameters must be specified. These are the height of the fluid channel, h_{fluid}, the height of the plate, h_{plate}, and the mass flow rate, $\dot{m}_{amp}$. Here 54 different sets of parameters are considered. These are listed in Table 1, and have been chosen so that they span realistic values of the different parameters and yet produce similar results to the two-dimensional model mentioned previously. The mass flow rate has been chosen so that it is 7.27×10^{-3} kg s^{-1} for a 1 mm plate at $\tau = 6$ s (Petersen et al., 2008a). With the chosen values for the height of the plate and fluid channel the porosity is 50%, 66% and 75%, respectively.

For the cycle time of $\tau = 0.5$ s the result of the one dimensional model might deviate from a more detailed two dimensional model, as per the Γ parameter defined in Eq. (1). If $\Gamma < 3$ the set of process parameters are not considered further. For the $\tau = 0.5$ s parallel plate case these are the parameter sets where $h_{fluid} > 0.00010$ m. Thus a total of 18 sets of parameters are disregarded for the case of $\tau = 0.5$ s. For the case of $\tau = 6$ s, the lowest value of Γ occurs for $h_{fluid} = 0.00050$ m, where $\Gamma = 3.38$, thus all sets of parameters are within the defined requirement for Γ.

A spherical particle packed bed regenerator has also been considered. Here the process parameters are the height of the regenerator, h, the particle size, d_p, the mass flow rate, $\dot{m}_{amp}$, and the porosity. For a randomly packed sphere bed regenerator used in magnetic refrigeration the latter is generally near 0.36 (Okamura et al., 2005; Jacobs, 2009; Tura and Rowe, 2009) and therefore this parameter is fixed. The height of the regenerator, h, is chosen to be identical to three of the values from the parallel plate case, resulting in an equal regenerator volume and equal utilization for these cases. The utilization is given as $\Phi = \dot{m}_{fluid} c_{p,fluid} P / m_{solid} c_{p,solid}$ where P is the time period for either the hot or cold blow. All nine different heights from the parallel plate cases cannot be tried as this would

Please cite this article in press as: Bjørk, R., Engelbrecht, K., The influence of the magnetic field on the performance of an active magnetic regenerator (AMR), International Journal of Refrigeration (2010), doi:10.1016/j.ijrefrig.2010.07.004

Table 2 – Packed bed regenerator parameters. Similarly to the parallel plate parameter table, Table 1, the rows in this table are not to be understood as parameter sets, except for the $\dot{m}_{amp}$ column. Here, e.g., for the case of $h = 0.0002$ m the value of $\dot{m}_{amp} = 0.0001 \times [0.5\ 1\ 2] \times 7.27 \times 6/\tau$ kg s^{-1} and not any other values. Similarly for $h = 0.00075$ m the value is $\dot{m}_{amp} = 0.0005 \times [0.5\ 1\ 2] \times 7.27 \times 6/\tau$ kg s^{-1} and not any other values and so on. This ensures that $\dot{m}_{amp}$ is equal for the parallel plate and packed bed cases with the same regenerator volume. There are a total of 54 parameter sets.

h [m]	d_p [m]	$\dot{m}_{amp}$ [kg s^{-1}]	τ [s]
0.00020	0.00010	$0.0001 \times [0.5\ 1\ 2] \times 7.27 \times 6/\tau$	0.5
0.00075	0.00025	$0.0005 \times [0.5\ 1\ 2] \times 7.27 \times 6/\tau$	6
0.00150	0.00050	$0.0010 \times [0.5\ 1\ 2] \times 7.27 \times 6/\tau$	

result in too many parameter sets. As the height of the regenerator is increased the utilization will drop as the mass of magnetocaloric material is increased but the mass flow rate is kept constant. The particle size, d_p, is varied within reasonable values (Okamura et al., 2005; Engelbrecht et al., 2007; Tura and Rowe, 2009). The value of $\dot{m}_{amp}$ is calculated to give the same value as the parallel plate cases with the same regenerator geometry. Finally τ assumes the values of 0.5 and 6 s. The parameter sets are listed in Table 2.

4. The cooling curve

As previously mentioned the performance of an AMR, for a given set of process parameters, is summed up in the cooling curve which shows the cooling capacity, $\dot{Q}$, as a function of temperature span, T_{span}, of the device. The cooling curve is often assumed to be linear which would allow for interpolation to find $T_{span,max}$. This is useful because the model used here calculates $\dot{Q}$ for a chosen T_{span}. Here we have investigated the linearity by calculating the R^2 parameter of a linear least-squares fit to the cooling curve for a symmetric magnetic field profile, i.e. $w_{top} = 0.45$, $w_{total} = 0.55$ and $x_0 = 0$, for all parameters sets, and $T_{cold} = 260$ K to 298 K in steps of 1 K and at $\mu_0 H_{max} = 0.5$ T to 1.5 T in steps of 0.1 T for both the parallel plates and packed bed regenerator. The parameter R^2 is a goodness-of-fit statistic that measures of how well the fit approximates the data points, with an R^2 value of 1.0 indicating a perfect fit. The parameter is defined as

$$R^2 \equiv 1 - \frac{\sum_i (y_i - f_i)^2}{\sum_i (y_i - \bar{y})^2}, \tag{2}$$

where y_i are the values of the dataset, f_i are the interpolated values and $\bar{y}$ is the mean of the data.

The shape of a typical cooling curve displays a flattening around the Curie temperature. Here the temperature of the hot end, $T_{hot} = 298$ K, is larger than the Curie temperature of the MCM, $T_c = 293.6$ K, and thus this flattening will be present, as can also be seen in the cooling curve shown in Fig. 1.

The R^2 parameter is shown in Fig. 3 as a function of $T_{span,max}$ for two different linear functions. For this figure $T_{span,max}$ has been determined fairly accurately because the temperature has been varied in steps of 1 K. The functions are linear fits of the cooling curve from 298 K, i.e. at $\dot{Q}_{max}$, to $T_{span,max}$ and a linear fit from 285 K to $T_{span,max}$. The first fit is denoted $L(\dot{Q}(298), \dot{Q}(T_{span,max}))$ and the latter $L(\dot{Q}(285), \dot{Q}(T_{span,max}))$ in Fig. 3. As can clearly be seen from the figure the cooling curve is not linear from $\dot{Q}_{max}$ to $T_{span,max}$. However, if only the part after the flattening, i.e. $L(\dot{Q}(285), \dot{Q}(T_{span,max}))$, is fitted the R^2 parameter is in general higher than 0.998, and thus this part of the cooling curve is extremely close to being linear for both parallel plate and packed bed regenerators.

Having shown that the part of the cooling curve away from T_c can be fitted by a linear function, we wish to examine if the $T_{span,max}$ parameter can be estimated by only calculating the refrigeration capacity at a few selected temperature spans. In Fig. 4 four different linear functions have been used to calculate $T_{span,max}$, i.e. where $\dot{Q} = 0$. The first is a linear function between the two points $\dot{Q}(T_{cold} = 298)$ and $\dot{Q}(T_{cold} = 285)$, denoted $L(\dot{Q}(298), \dot{Q}(285))$. Using the same notation the three remaining functions are $L(\dot{Q}(285), \dot{Q}(260))$, $L(\dot{Q}(285), \dot{Q}(270))$

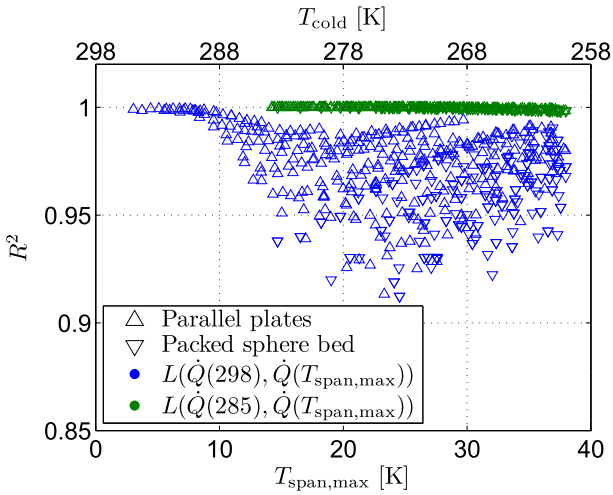

Fig. 3 – The goodness of fit parameter R^2 as a function of $T_{span,max}$ for parallel plates and packed bed for a linear fit to the full cooling curve and the cooling curve from 285 K to $T_{span,max}$.

Please cite this article in press as: Bjørk, R., Engelbrecht, K., The influence of the magnetic field on the performance of an active magnetic regenerator (AMR), International Journal of Refrigeration (2010), doi:10.1016/j.ijrefrig.2010.07.004

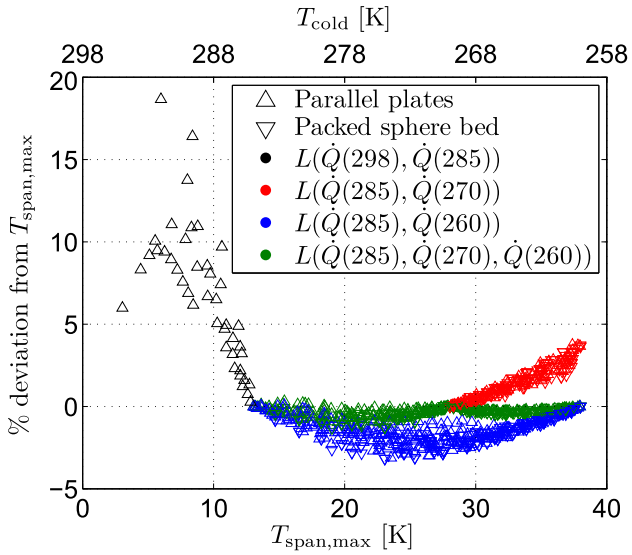

Fig. 4 – The deviation of the estimated $T_{span,max}$, based on different linear fits, from the true $T_{span,max}$. From T_{cold} = 285 K to 270 K the two linear functions $L(\dot{Q}(285), \dot{Q}(270))$ and $L(\dot{Q}(285), \dot{Q}(270), \dot{Q}(260))$ are identical, and thus only $L(\dot{Q}(285), \dot{Q}(270), \dot{Q}(260))$ is shown.

and $L(\dot{Q}(285), \dot{Q}(270), \dot{Q}(260))$, where the latter is a two-section linear function, which consists of a linear function from $\dot{Q}(285)$ to $\dot{Q}(270)$ and second from $\dot{Q}(270)$ to $\dot{Q}(260)$. Thus for the two-section linear function if $\dot{Q}(270)$ is negative $T_{span,max}$, is interpolated between $\dot{Q}(285)$ to $\dot{Q}(270)$ while the $\dot{Q}(270)$ is positive the linear function $\dot{Q}(270)$ to $\dot{Q}(260)$ is used. A negative value of $\dot{Q}$ simply means that the regenerator is not able to cool the heat load sufficiently. The $T_{span,max}$ parameter has been interpolated based on these linear functions and the deviation from the true $T_{span,max}$, found by linear interpolation of the data set where T_{cold} was varied in steps of 1 K, is shown in Fig. 4. If the value of $T_{span,max}$ is higher than 38 K i.e. so that $\dot{Q}(260)$ is positive, than the value is disregarded. This is the case for the remainder of this article.

From the figure it can be seen that all the linear functions provide an accurate estimate of $T_{span,max}$. However, the two-section linear function $L(\dot{Q}(285), \dot{Q}(270), \dot{Q}(260))$ provides the most precise estimate of $T_{span,max}$, i.e. one that is accurate to within 1.5% of the true value in the $T_{span,max}$ interval between 285 K and 260 K. In the interval between 298 K and 285 K the estimate of $T_{span,max}$ is not very accurate, but as there are few models that have this small a temperature span the linear interpolation will still be used. In the remainder of this work the refrigeration capacity will be calculated at T_{cold} = 298, 285, 270 and 260 K, and $T_{span,max}$ will be estimated based on these values using linear interpolation, unless otherwise stated.

5. Synchronization of the magnetic field

It is important to investigate the performance of the AMR cycle as a function of when in the AMR cycle the regenerator is subjected to the magnetic field. This is termed "synchronization" as it describes how synchronized the magnetic field profile is with the AMR fluid flow profile and it is characterized by the synchronization parameter, x_0, as shown previously in Fig. 2. In this article, a synchronized cycle occurs when the magnetic field profile begins to ramp up when τ_1 begins and begin to ramp down when τ_2 ends. A negative value of x_0 means that the magnetic field profile has been moved so that it begins earlier in the cycle compared to the synchronized case.

The effect of the synchronization on $\dot{Q}_{max}$ and $T_{span,max}$ has been investigated for all parameter sets for both the parallel plate and packed bed cases. A value of $\mu_0 H_{max}$ = 0.5, 1 and 1.5 T and a magnetic field profile with w_{top} = 0.45 and w_{total} = 0.55 were used in the synchronization study. The synchronization parameter, x_0, was varied from −0.1 to 0.1 in steps of 0.01, where 0 is the point at which the magnetic field profile is synchronized with respect to the AMR cycle for the values of w_{top} and w_{total} used here.

The results are shown in Figs. 5 and 6 which show $\dot{Q}_{max}$ and $T_{span,max}$ as a function of the synchronization parameter, x_0, for all process parameters and magnetic fields. As can be seen from the figures both $\dot{Q}_{max}$ and $T_{span,max}$ show a broad plateau around x_0 = 0. The behavior of $\dot{Q}_{max}$ and $T_{span,max}$ appears to be much the same across the different sets of AMR process parameters and different magnetic fields that were investigated. The parallel plates show a slightly larger drop in $T_{span,max}$ than the packed bed regenerator does. For all parameter sets a drop in performance between 20 and 40% is seen if the magnetic field is

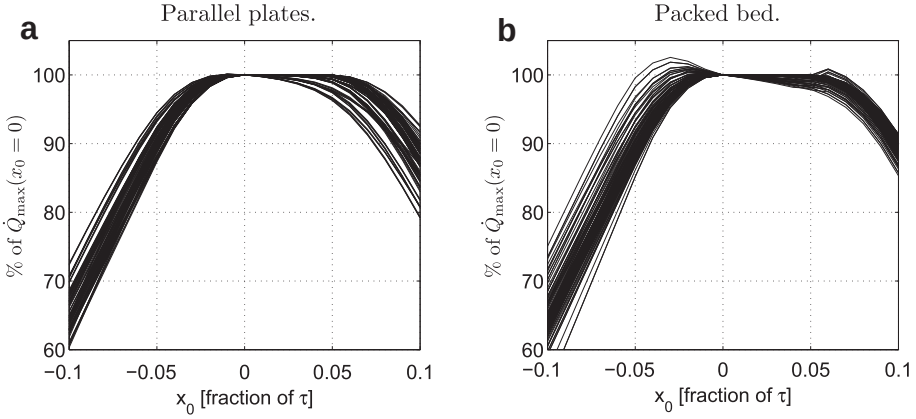

Fig. 5 – The maximum cooling capacity, $\dot{Q}_{max}$, as a function of the synchronization parameter, x_0, for all parameter sets.

Please cite this article in press as: Bjørk, R., Engelbrecht, K., The influence of the magnetic field on the performance of an active magnetic regenerator (AMR), International Journal of Refrigeration (2010), doi:10.1016/j.ijrefrig.2010.07.004

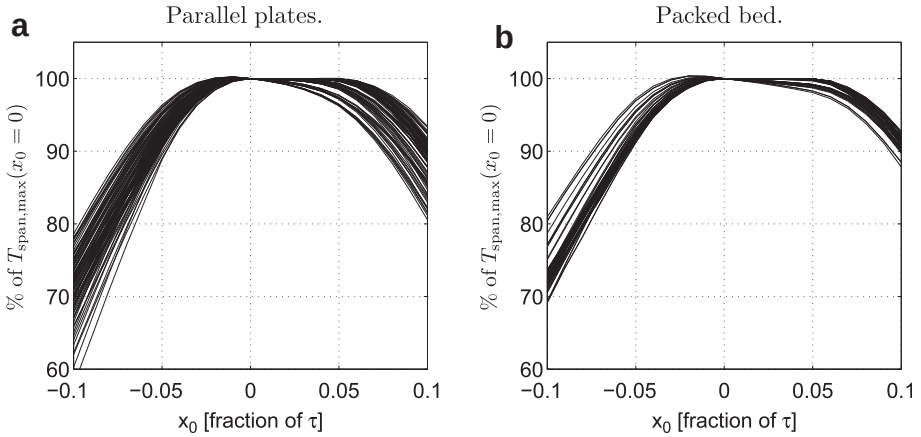

Fig. 6 – The no load temperature span, $T_{span,max}$, as a function of the synchronization parameter, x0, for all parameter sets.

ramped too early. A smaller performance drop is seen if the field is ramped too late. Shifting the magnetic field to earlier in the cycle can also provide a minimal increase in performance. Figs. 5 and 6 show that synchronization of the magnetic field and fluid flow is important; however, it has a small effect when the synchronization is within 5% of the cycle time.

6. Ramp rate of the magnetic field

It is also important to investigate the influence of the ramp rate, i.e. the speed of the increase from $\mu_0 H = 0$ T to $\mu_0 H_{max}$, on the performance of the AMR cycle. The ramp rate can be controlled by varying the w_{top} and w_{total} parameters as the ramp rate is given by Ramp Rate $= (w_{total} - w_{top})/2$ in fractions of τ.

In the simulations w_{top} is kept constant at 0.45 and $\mu_0 H_{max} = 1$ T. The total width, w_{total}, was varied from 0.46 to 0.65 in steps of 0.01, which means that the ramp rate was varied from 0.005 to 0.1 in fractions of τ. The synchronization parameter, x_0, was chosen such that the magnetic field profile always begins to ramp down at $t = \tau_1 + \tau_2$. In practice this means that the synchronization parameter was given as $x_0 = (0.55 - w_{total})/2$. It is ensured that the ramp of the magnetic field is always sufficiently numerically resolved in time.

The behavior of the AMR system, which was only examined at the maximum refrigeration capacity, is shown in Fig. 7 which shows $\dot{Q}_{max}$ as a function of w_{total} and the ramp rate for all process parameters. The maximum temperature span was not found due to the extensive computation time caused by the high numerical resolution required to resolve the field profiles with fast ramp rates. It is seen that the decrease in performance is only a few percent if a slow ramp rate is used. For a fast ramp rate no gain in performance is seen, but in a few cases a drop in performance is observed. This drop in performance can occur because the magnetic field profile with a slow ramp rate is wider, which can improve performance for some sets of process parameters. This will be considered in more detail shortly.

7. Maximum value of the magnetic field

Having determined the effect of synchronization and ramping of the magnetic field on the performance of the AMR, we now

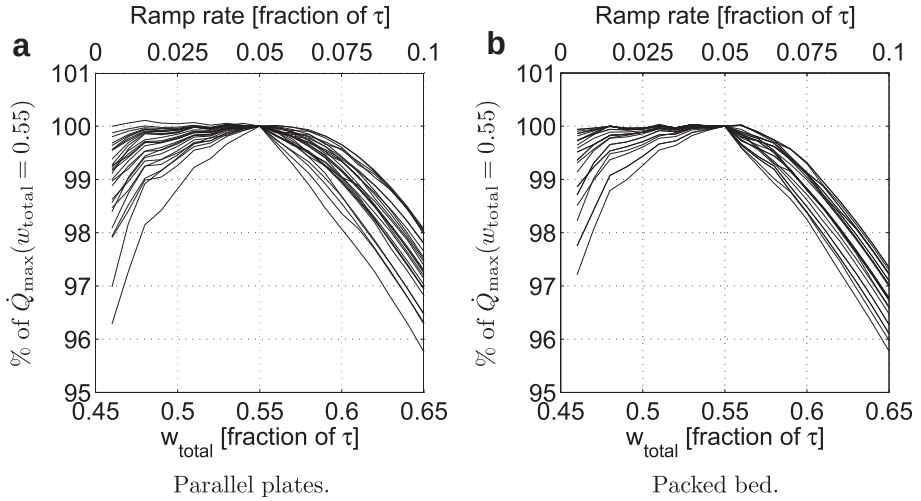

Fig. 7 – The maximum cooling capacity, $\dot{Q}_{max}$, as a function of w_{total} for the parallel plate and packed bed cases. The top x-axis shows the corresponding ramp rate. The lack of smoothness of the curves is due to the very small change of the refrigeration capacity with ramp rate, which is hard to resolve numerically.

Please cite this article in press as: Bjørk, R., Engelbrecht, K., The influence of the magnetic field on the performance of an active magnetic regenerator (AMR), International Journal of Refrigeration (2010), doi:10.1016/j.ijrefrig.2010.07.004

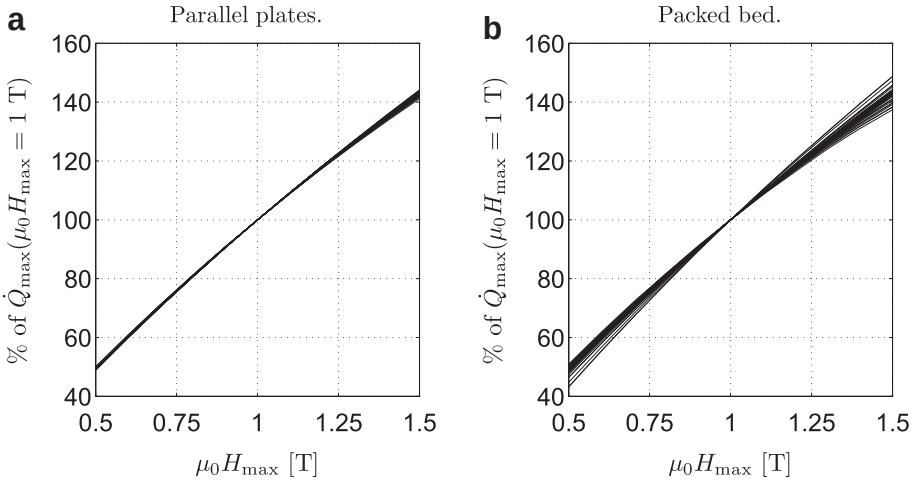

Fig. 8 – The maximum cooling capacity, $\dot{Q}_{max}$, as a function of $\mu_0 H_{max}$ for all parameter sets.

turn to the study of the effect of the maximum value of the magnetic field, $\mu_0 H_{max}$.

To study this, the magnetic field profile is chosen such that $w_{top} = 0.45$, $w_{total} = 0.55$ and $x_0 = 0$, i.e. a synchronized magnetic field profile. The value of $\mu_0 H_{max}$ was varied from 0.5 to 1.5 T in steps of 0.1 T. The temperature of the cold end of the regenerator was varied from 230 to 260 K in steps of 5 K and from 260 to 298 K in steps of 1 K in order to find $T_{span,max}$ and $\dot{Q}_{max}$. The larger temperature interval of the cold end temperature was considered in order to improve the estimate of $T_{span,max}$ produced by the high values of the magnetic field.

In Figs. 8 and 9 the maximum cooling capacity and temperature span are plotted as functions of $\mu_0 H_{max}$ for all process parameters. As can be seen from the figures $\dot{Q}_{max}$ scales almost identically for the different process parameters. In all cases $\dot{Q}_{max}$ has a stronger dependency on $\mu_0 H_{max}$ than $T_{span,max}$. Thus increasing the magnetic field increases $\dot{Q}_{max}$ more than $T_{span,max}$, e.g. increasing $\mu_0 H_{max}$ from 1 T to 1.5 T increases $\dot{Q}_{max}$ by ~40% but only $T_{span,max}$ by ~25%. The slope of increase for both $T_{span,max}$ and $\dot{Q}_{max}$ with respect to $\mu_0 H_{max}$ is below 1 for every parameter set modeled. This is due to the fact that, for mean field gadolinium, the adiabatic temperature change at the Curie temperature scales as a power law with an exponent of 2/3, i.e. $\Delta T_{ad}(T_c) = (\mu_0 H)^{2/3}$ (Oesterreicher and Parker, 1984). This is comparable with results from actual magnetocaloric materials (Bjørk et al., in press). This scaling, i.e. $\Delta T_{ad}(T_c) \propto (\mu_0 H)^{2/3}$, is also shown. As can be seen $T_{span,max}$ scales with an exponent that is slightly less than 2/3.

8. Width of the magnetic field

It is also of importance to examine the behavior of the AMR cycle with respect to the width of the magnetic field profile, i.e. the fraction of the AMR cycle in which the regenerator is subjected to the high magnetic field or correspondingly how long the regenerator is in the low field region. Here we consider a profile where the ramp time is kept constant at 5% of the total cycle time, i.e. $(w_{total} - w_{top})/2 = 0.05$. The w_{top}

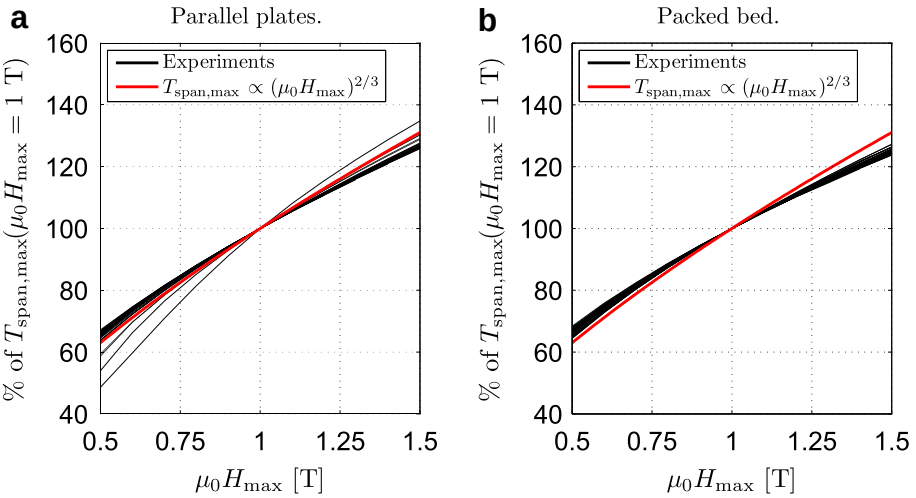

Fig. 9 – The no load temperature span, $T_{span,max}$, as a function of $\mu_0 H_{max}$ for all parameter sets. Also shown is $T_{span,max} \propto (\mu_0 H_{max})^{2/3}$.

Please cite this article in press as: Bjørk, R., Engelbrecht, K., The influence of the magnetic field on the performance of an active magnetic regenerator (AMR), International Journal of Refrigeration (2010), doi:10.1016/j.ijrefrig.2010.07.004

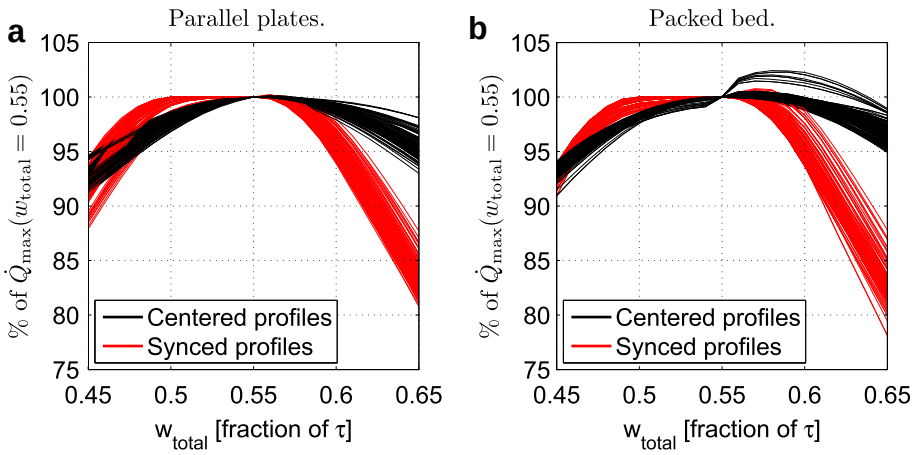

Fig. 10 – The maximum cooling capacity, $\dot{Q}_{max}$, as a function of w_{total} for the parallel plate and packed bed cases. Both centered profiles and synced profiles are shown.

parameter is varied from 0.35 to 0.55 in steps of 0.01, with the w_{total} parameter given by the ramp time, i.e. $w_{total} = w_{top} + 0.1$.

We consider two cases: one case where the magnetic field profile is centered on the flow profile, and one case where x_0 is changed so that the magnetic field profile begins to ramp down at the same time as the flow profile changes from $\dot{m}_{amp}$ to 0, i.e. at $t = \tau_1 + \tau_2$. The first type of profile will be referred to as the centered profile, whereas the latter will be referred to as the synced profile.

The fluid flow profile is kept fixed at the values introduced earlier, i.e. $\tau_1 = \tau_3 = 0.1$ and $\tau_2 = \tau_3 = 0.4$, respectively, in fractions of the total cycle time, τ. Thus as w_{top} is changed the width of the magnetic field profile will change from being "shorter" to "longer" than the fluid flow profile. This can be the case in e.g. a rotating AMR where the high field region can be smaller than the low field region or vice versa.

The modeling results are shown in Figs. 10 and 11, which show $\dot{Q}_{max}$ and $T_{span,max}$ as a function of w_{total}. As can be seen from the figures, a more or less identical behavior is seen for all parameter sets. The optimum w_{total} is approximately 0.55, and both $\dot{Q}_{max}$ and $T_{span,max}$ decrease as the value of w_{total} moves further from 0.55. In general a large width is worse than a short width for the values considered here. The drop in performance for both $\dot{Q}_{max}$ and $T_{span,max}$ for $w_{total} > 0.55$ is greater for the synced profiles than for the centered profiles.

The differences between the centered and synced profiles for all parameter sets are shown in Figs. 12 and 13. For both $\dot{Q}_{max}$ and $T_{span,\ max}$ it is seen that if the magnetic field profile has a small value of w_{total} it is better to sync the profile with the fluid flow profile, whereas for large values of w_{total} the centered profile has the best performance.

9. Discussion

In Table 3 the impact on performance is given for each of the magnetic field profile configurations tested.

For all the different magnetic field profiles tried it was seen that the influence of changing the magnetic field was more or less the same for the different regenerator geometries and operating parameters studied. This means that the design and optimization of the magnet can be done independently of the regenerator geometry. Thus, the optimum field strength and magnetized volume will be nearly the same for a packed sphere regenerator or parallel plate regenerator.

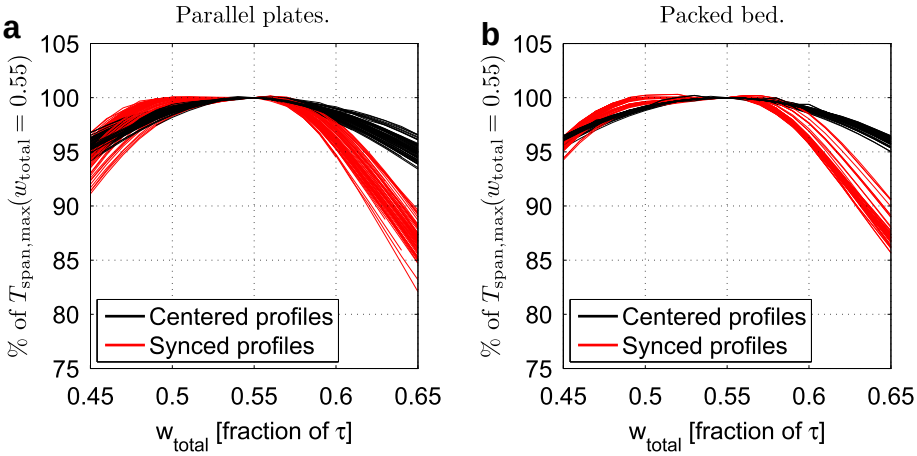

Fig. 11 – The no load temperature span, $T_{span,max}$, as a function of w_{total} for the parallel plate and packed bed cases. Both centered profiles and synced profiles are shown.

Please cite this article in press as: Bjørk, R., Engelbrecht, K., The influence of the magnetic field on the performance of an active magnetic regenerator (AMR), International Journal of Refrigeration (2010), doi:10.1016/j.ijrefrig.2010.07.004

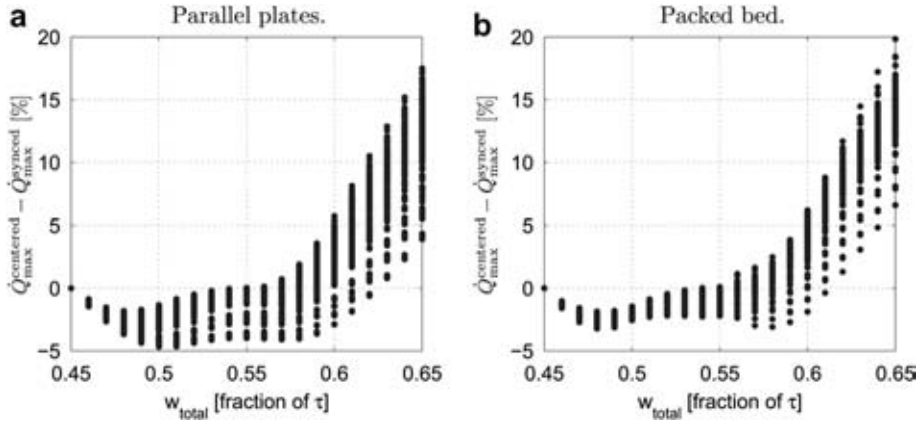

Fig. 12 – The difference in Q_{max} between the synced and centered profiles as a function of w_{total} for the parallel plate and packed bed cases.

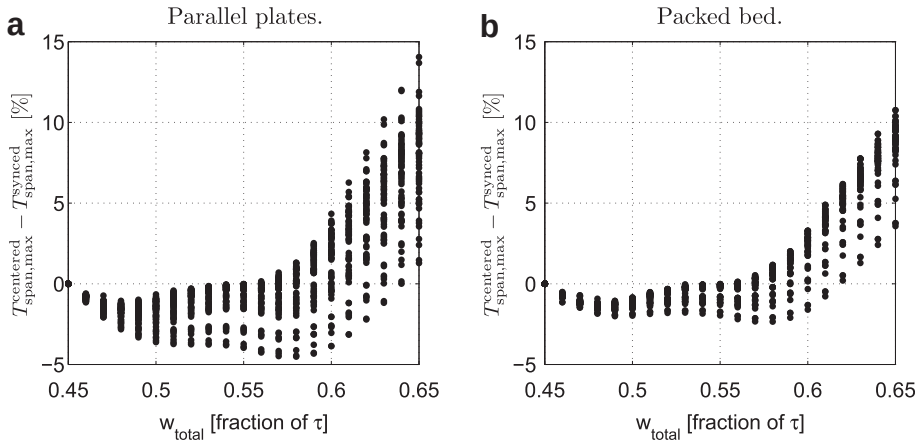

Fig. 13 – The difference in $T_{span,max}$ between the synced and centered profiles as a function of w_{total} for the parallel plate and packed bed cases.

Table 3 – The performance of the different tested profiles for a magnetic field profile characterized by the value in the "Change" column relative to the performance of a profile with the value given by "Reference value" column.

Case	Reference value	Change	Performance: parallel plate regenerator		Performance: packed bed regenerator	
			Q_{max}	$T_{span,max}$	Q_{max}	$T_{span,max}$
Synchronization	$x_0 = 0$	$x_0 = -0.1$	60–75%	60–80%	60–75%	70–80%
		$x_0 = 0.1$	80–95%	80–95%	85–90%	90–95%
Ramp rate	Rate = 0.05	Rate = 0.005	96–100%	–	97–100%	–
		Rate = 0.1	96–98%	–	96–98%	–
Maximum field	$\mu_0 H_{max} = 1$T	$\mu_0 H_{max} = 0.5$ T	50%	60–70%	40–50%	60–70%
		$\mu_0 H_{max} = 1.5$ T	140%	125%	130–150%	120–130%
Width (centered)	$w_{total} = 0.55$	$w_{total} = 0.45$	90-95%	95-100%	90-95%	95-100%
		$w_{total} = 0.65$	90-100%	90-100%	95-100%	95-100%
Width (synced)	$w_{total} = 0.55$	$w_{total} = 0.45$	85-95%	90-95%	90-95%	95-100%
		$w_{total} = 0.65$	80-90%	85-90%	80-90%	85-90%

Please cite this article in press as: Bjørk, R., Engelbrecht, K., The influence of the magnetic field on the performance of an active magnetic regenerator (AMR), International Journal of Refrigeration (2010), doi:10.1016/j.ijrefrig.2010.07.004

10. Conclusion

The influence of the magnetic field profile on the performance of an AMR was studied for different sets of process parameters. First, it was shown that when the hot and cold reservoir temperatures are adequately far from the Curie temperature of the magnetocaloric material, the cooling curve is almost linear. As the reservoir temperatures near the Curie temperature, the cooling curve flattens. Next, it was shown that a magnetic field profile that is 10% of the total cycle time out of sync with the flow profile will lead to a drop in both the maximum temperature span and the maximum cooling capacity of 20–40% for both parallel plate and packed bed regenerators. Also the maximum cooling capacity was shown to depend very weakly on the ramp rate of the magnetic field, whereas a drop in maximum temperature span and maximum cooling capacity of 5–20% was seen when the temporal width of the magnetic field curve was changed by 10%. It was shown that an increase of the magnetic field from 1 T to 1.5 T increased the maximum cooling capacity by 40% but the maximum temperature span by only 25%. The relative change in performance caused by changing the magnetic field was found to be the same for the different regenerator geometries and operating conditions tried, which means that the magnet can be designed and optimized independently of the regenerator geometry. Finally, a magnetic field width of 0.55 was found to be optimum.

Acknowledgements

The authors would like to thank Dr. C. R. H. Bahl for useful discussions. The authors would like to acknowledge the support of the Programme Commission on Energy and Environment (EnMi) (Contract No. 2104-06-0032) which is part of the Danish Council for Strategic Research.

REFERENCES

Allab, F., Kedous-Lebouc, A., Fournier, J., Yonnet, J., 2005. Numerical modeling for active magnetic regenerative refrigeration. IEEE Trans. Magnet. 41 (10), 3757–3759.

Bahl, C., Petersen, T., Pryds, N., Smith, A., Petersen, T., 2008. A versatile magnetic refrigeration test device. Rev. Scient. Instrum. 79 (9), 093906.

Barclay, J., 1982. The theory of an active magnetic regenerativ refrigerator. NASA STI/Recon Technical Report No. 83, pp. 34087.

Barclay, J.A., 1988. Magnetic refrigeration: a review of a developing technology. Adv. Cryogen. Eng. 33, 719–731.

Bjørk, R., Bahl, C., Katter, M. Magnetocaloric properties of $LaFe_{13-x-y}Co_xSi_y$ and commercial grade Gd. J. Magn. Magn. Mater., in press.

Bjørk, R., Bahl, C.R.H., Smith, A., Pryds, N., 2010. Review and comparison of magnet designs for magnetic refrigeration. Int. J. Refrigeration 33, 437–448.

Dan'kov, S., Tishin, A., Pecharsky, V., Gschneidner Jr., K.A., 1998. Magnetic phase transitions and the magnetothermal properties of gadolinium. Phys. Rev. B (Condensed Matter) 57 (6), 3478–3490.

Engelbrecht, K., 2008. A Numerical Model of an Active Magnetic Regenerator Refrigerator with Experimental Validation. Ph.D. thesis, University of Wisconsin, Madison.

Engelbrecht, K., Nellis, G., Klein, S., 2005a. A Numerical Model of an Active Magnetic Regenerator Refrigeration System. Technical Report ARTI-21CR/612–10075. University of Wisconsin, Madison.

Engelbrecht, K., Nellis, G., Klein, S., Boeder, A., 2005b. Modeling active magnetic regenerative refrigeration systems. In: Proceedings of the First International Conference on Magnetic Refrigeration at Room Temperature, Montreux, Switzerland, pp. 265–274.

Engelbrecht, K.L., Nellis, G.F., Klein, S.A., 2006. Predicting the performance of an active magnetic regenerator refrigerator used for space cooling and refrigeration. HVAC&R Res. 12 (4), 1077–1095.

Engelbrecht, K., Nellis, G.F., Sanford, A.K., Zimm, C.B., 2007. Recent developments in room temperature active magnetic regenerative refrigeration. HVAC&R Res. 13 (4), 525–542.

Gschneidner Jr., K.A., Pecharsky, V., 2008. Thirty years of near room temperature magnetic cooling: where we are today and future prospects. Int. J. Refrigeration 31 (6), 945–961.

Hu, J., Xiao, J., 1995. New method for analysis of active magnetic regenerator in magnetic refrigeration at room temperature. Cryogenics 35 (2), 101–104.

Jacobs, S., 2009. Modeling and optimal design of a multilayer active magnetic refrigeration system. In: Proceedings of the third International Conference on Magnetic Refrigeration at Room Temperature, Des Moines, Iowa, USA, pp 267–274.

Liu, G., Sun, J., Wang, J., Zhao, T., Shen, B., 2007. A comparison study of the entropy changes in materials with and without short-range magnetic order. J. Phys. Condens. Matter 19 (46), 466215.

Morrish, A.H., 1965. The Physical Priciples of Magnetism. John Wiley & Sons, Inc.

Nielsen, K., Bahl, C., Smith, A., Bjørk, R., Pryds, N., Hattel, J., 2009. Detailed numerical modeling of a linear parallel-plate active magnetic regenerator. Int. J. Refrigeration 32 (6), 1478–1486.

Nielsen, K., Bahl, C., Smith, A., Pryds, N., Hattel, J., 2010. A comprehensive parameter study of an active magnetic regenerator using a 2D numerical model. Int. J. Refrigeration 33 (4), 753–764.

Oesterreicher, H., Parker, F., 1984. Magnetic cooling near curie temperatures above 300k. J. Appl. Phys. 55, 4334–4338.

Okamura, T., Yamada, K., Hirano, N., Shigeo, N., 2005. Performance of a room-temperature rotary magnetic refrigerator. Proceedings of the First International Conference on Magnetic Refrigeration at Room Temperature, Montreux, Switzerland, pp. 319–324.

Pecharsky, V.K., Gschneidner Jr., K.A., 2006. Advanced magnetocaloric materials: What does the future hold? Int. J. Refrigeration 29 (8), 1239–1249.

Petersen, T.F., Engelbrecht, K., Bahl, C.R.H., Pryds, N., Smith, A., Petersen, T.F., Elmegaard, B., Engelbrecht, K., 2008a. Comparison between a 1d and a 2d numerical model of an active magnetic regenerative refrigerator. J. Phys. D Appl. Phys. 41 (10), 105002.

Petersen, T.F., Pryds, N., Smith, A., Hattel, J., Schmidt, H., Høgaard Knudsen, H.-J., 2008b. Two-dimensional mathematical model of a reciprocating room-temperature active magnetic regenerator. Int. J. Refrigeration 31 (3), 432–443.

Shir, F., Mavriplis, C., Bennett, L.H., Torre, E.D., 2005. Analysis of room temperature magnetic regenerative refrigeration. Int. J. Refrigeration 28 (4), 616–627.

Siddikov, B., Wade, B., Schultz, D., 2005. Numerical simulation of the active magnetic regenerator. Comput. Mathem. Appl. 49 (9–10), 1525–1538.

Please cite this article in press as: Bjørk, R., Engelbrecht, K., The influence of the magnetic field on the performance of an active magnetic regenerator (AMR), International Journal of Refrigeration (2010), doi:10.1016/j.ijrefrig.2010.07.004

Tura, A., Rowe, A., 2007. Design and testing of a permanent magnet magnetic refrigerator. In: Proceedings of the Second International Conference of Magnetic Refrigeration at Room Temperature, Portoroz, Slovenia, pp. 363–370.

Tura, A., Rowe, A., 2009. Progress in the characterization and optimization of a permanent magnet magnetic refrigerator. In: Proceedings of the Third International Conference on Magnetic Refrigeration at Room Temperature, Des Moines, Iowa, USA, pp. 387–392.

Yu, B., Gao, Q., Zhang, B., Meng, X., Chen, Z., 2003. Review on research of room temperature magnetic refrigeration. Int. J. Refrigeration 26 (6), 622–636.

Zimm, C., Auringer, J., Boeder, A., Chell, J., Russek, S., Sternberg, A., 2007. Design and initial performance of a magnetic refrigerator with a rotating permanent magnet. In: Proceedings of the Second International Conference of Magnetic Refrigeration at Room Temperature, Portoroz, Slovenia, pp. 341–347.

Please cite this article in press as: Bjørk, R., Engelbrecht, K., The influence of the magnetic field on the performance of an active magnetic regenerator (AMR), International Journal of Refrigeration (2010), doi:10.1016/j.ijrefrig.2010.07.004

Paper XII

Paper published in Journal of Magnetism and Magnetic Materials, 2010

Bjørk, R., Bahl, C. R. H., Smith, A., Christensen, D. V. and Pryds, N.

An optimized magnet for magnetic refrigeration

Journal of Magnetism and Magnetic Materials, 322, 3324-3328, 2010

Journal of Magnetism and Magnetic Materials 322 (2010) 3324–3328

Contents lists available at ScienceDirect

Journal of Magnetism and Magnetic Materials

journal homepage: www.elsevier.com/locate/jmmm

An optimized magnet for magnetic refrigeration

R. Bjørk *, C.R.H. Bahl, A. Smith, D.V. Christensen, N. Pryds

Fuel Cells and Solid State Chemistry Division, Risø National Laboratory for Sustainable Energy, Technical University of Denmark—DTU, Frederiksborgvej 399, DK-4000 Roskilde, Denmark

ARTICLE INFO

Article history:
Received 11 February 2010
Received in revised form
26 May 2010
Available online 9 June 2010

Keywords:
Halbach cylinder
Magnetic field
Permanent magnet flux source
Magnetic refrigeration

ABSTRACT

A magnet designed for use in a magnetic refrigeration device is presented. The magnet is designed by applying two general schemes for improving a magnet design to a concentric Halbach cylinder magnet design and dimensioning and segmenting this design in an optimum way followed by the construction of the actual magnet. The final design generates a peak value of 1.24 T, an average flux density of 0.9 T in a volume of 2 L using only 7.3 L of magnet, and has an average low flux density of 0.08 T also in a 2 L volume. The working point of all the permanent magnet blocks in the design is very close to the maximum energy density. The final design is characterized in terms of a performance parameter, and it is shown that it is one of the best performing magnet designs published for magnetic refrigeration.

1. Introduction

Magnetic refrigeration is a potentially energy efficient and environmentally friendly evolving cooling technology that uses the magnetocaloric effect (MCE) to generate cooling through a regenerative process called active magnetic regeneration (AMR).

At present, a great number of magnetic refrigeration test devices have been built and examined in some detail, with focus on the produced temperature span and cooling power of the devices [1–3]. A substantial number of magnet designs have also been published [4–11] (see Ref. [12] for a review), but for almost all magnet designs no argument is presented for the specific design and dimensioning of the magnet.

In this paper we present the full design approach of a magnet used for magnetic refrigeration. The magnet is designed by applying two general ways or schemes for improving a magnet design to a concentric Halbach cylinder design. The resulting design is dimensioned and segmented and is then characterized by comparing flux density measurements to a numerical simulation. Finally, the magnet design is compared to other magnet designs used in magnetic refrigeration.

2. Modeling the magnet design

The magnet is designed for a cylindrical rotating magnetic refrigeration device under construction at Risø DTU, in which plates of magnetocaloric material rotate in an air gap between an outer and inner cylindrical magnetic structure. The dimensions of the design, which have been chosen based on the desired temperature span and cooling capacity of the device, are such that the volume between the inner and the outer magnet is 4 L. The magnetic refrigeration device is designed such that the magnet must provide four high flux density regions and four low flux density regions in the air gap between the two magnets.

A similar magnetic refrigerator, i.e. with a stationary magnet and a rotating magnetocaloric material, was also considered in Ref. [11], where a magnet design that generates a magnetic field between 0.1 and 1 T in four low and four high field regions is presented. Rotary magnetic refrigerators where the magnet rotates and the magnetocaloric material is kept stationary are considered in, e.g., Refs. [13–15]. One of these designs uses rectangular magnets while the other two use highly irregularly shaped magnets. The generated magnetic field is between 1.0 and 1.9 T, although the latter value is based on a two dimensional numerical simulation which is known to overestimate the magnitude of the magnetic field except for very long assemblies.

Based on numerical modeling of the AMR process using the model of Ref. [16] the length of the Risø DTU device was chosen to be 250 mm [17]. Based on practical engineering requirements, as well as to allow ample room for the inner magnet, an external radius of the inner magnet of 70 mm and an internal radius of the outer magnet of 100 mm was chosen.

The regenerator itself can consist of either plates or a packed bed of magnetocaloric material. The dimensions, shape and stacking of the plates or the dimensions and shape of the packed bed can vary, and the performance of the refrigeration device will of course depend on these parameters. The magnetocaloric material is contained in a plastic structure with low heat conduction, so the heat transfer between the magnet and the magnetocaloric material is kept low. As the magnetocaloric

* Corresponding author.
E-mail address: rabj@risoe.dtu.dk (R. Bjørk).

0304-8853/$ - see front matter © 2010 Elsevier B.V. All rights reserved.
doi:10.1016/j.jmmm.2010.06.017

material is rotated in the magnetic field there will be an eddy current induced in the magnetocaloric material. The heating due to this eddy current is negligible because the magnetization is small and the rotation rate is only on the order of 1 Hz.

A magnet design that fulfils the requirement of generating four high and low flux density regions is the concentric Halbach cylinder design [18]. Here each cylinder is magnetized such that the remanent flux density at any point varies continuously as, in polar coordinates,

$$B_{\mathrm{rem},r} = B_{\mathrm{rem}}\cos(p\phi),$$
$$B_{\mathrm{rem},\phi} = B_{\mathrm{rem}}\sin(p\phi), \quad (1)$$

where B_{rem} is the magnitude of the remanent flux density and p is an integer [19,20]. Subscript r denotes the radial component of the remanence and subscript ϕ the tangential component. A magnet with four high and four low flux density regions, as described above, can be created by having a $p=2$ outer Halbach cylinder and a $p=-2$ inner Halbach cylinder. The concentric Halbach cylinder design is shown in Fig. 1.

This magnet design is the starting design for the optimized magnet design presented here. The design is improved by applying an algorithm to increase the difference in flux density between a high and low flux density region in an air gap in a magnetic structure, as described in Ref. [21]. The algorithm lowers the flux density in a given area by replacing magnet material enclosed by an equipotential line of the magnetic vector potential, A_z, with a soft magnetic material or vacuum.

Furthermore, the design is improved by replacing magnet material with a high permeability soft magnetic material where the component of the magnetic field along the remanence is not large and negative, i.e. where, $\mu_0\mathbf{H}\cdot\hat{\mathbf{B}}_{\mathrm{rem}} > -\gamma$, with an appropriately chosen positive γ, as here a high permeability soft magnetic material will produce a similar value of $|\mathbf{B}|$ as the magnet produces [21–23].

These two improvements are applied to the design using a numerical two dimensional model implemented in the commercially available finite element multiphysics program *Comsol Multiphysics* [24] and using magnets with a remanence of 1.44 T and a relative permeability of 1.05, which are the properties of standard neodymium-iron-boron (NdFeB) magnets [25]. A two dimensional model is used as the magnet design is symmetric along the length of the design and the ratio of the gap to the length of the assembly is much smaller than 1, making end effects relatively unimportant.

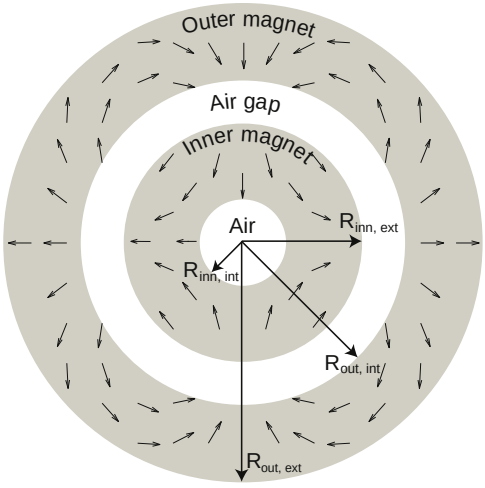

Fig. 1. The concentric Halbach cylinder design. The direction of magnetization is shown as arrows. The different radii have been indicated.

For the algorithm the equipotential line of A_z is chosen to be the line that goes through the point ($r=100$ mm, $\phi=22.5^\circ$), i.e. the point on the internal radius of the outer magnet, half way between the center of the high and low flux density regions, as this equipotential line encircles the low flux density region. Iron is used as the soft magnetic material as it has a very high permeability as well as being easily workable and reasonable priced. A value of $\gamma=0.125$ T is used for replacing magnet material with iron where the component of the magnetic field along the remanence is not large and negative.

2.1. Dimensioning of the design

The remaining dimensions of the magnet design, i.e. the external radius of the outer magnet, $R_{\mathrm{out,ext}}$, and the internal radius of the inner magnet, $R_{\mathrm{inn,int}}$, are chosen based on a parameter variation of the concentric Halbach design where the two improvements discussed above have been applied. The external radius of the outer magnet was varied from 110 to 155 mm in steps of 5 mm and the internal radius of the inner magnet was varied from 10 to 50 mm in seven equidistant steps. The optimization parameter is taken as the difference in flux density between the high and low flux density regions to the power of 0.7 as a function of the cross-sectional area of the magnet; this is shown in Fig. 2. Here $\langle B^{0.7}_{\mathrm{high}}\rangle$ denotes the average of the flux density to the power of 0.7 in the high field region and similarly $\langle B^{0.7}_{\mathrm{low}}\rangle$ for the low flux density region. For this design the high and low flux density regions are defined to be of the same size and span an angle of 45° each making them adjacent.

The reason the power of 0.7 is chosen is that the adiabatic temperature change of a second order magnetocaloric material scales with the magnetic field to the power of 0.7 at the Curie temperature [12,26]. Thus it is this value that is important to the performance of a magnet used in magnetic refrigeration.

To limit the cost of the magnet, a cross-section of $A_{\mathrm{mag}}=0.025$ m^2 was chosen. Based on this value and Fig. 2 the optimal design was chosen. This design has an external radius of the outer magnet of 135 mm and an internal radius of the inner magnet of 10 mm.

The original concentric Halbach cylinder design and the design after the application of the different improvements are shown in Fig. 3 for the dimensions found above.

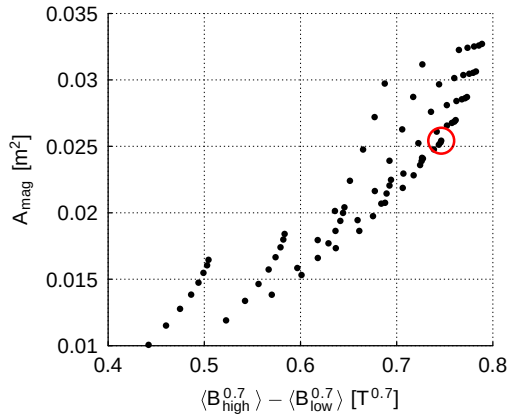

Fig. 2. The difference in flux between the high and low flux density regions to the power of 0.7 as a function of the cross-sectional area of the magnet, A_{mag}, for a range of different external radii of the outer magnet, $R_{\mathrm{out,ext}}$, and internal radii of the inner magnet, $R_{\mathrm{inn,int}}$. The area is used as the model is two-dimensional. The chosen set of dimensions have been encircled.

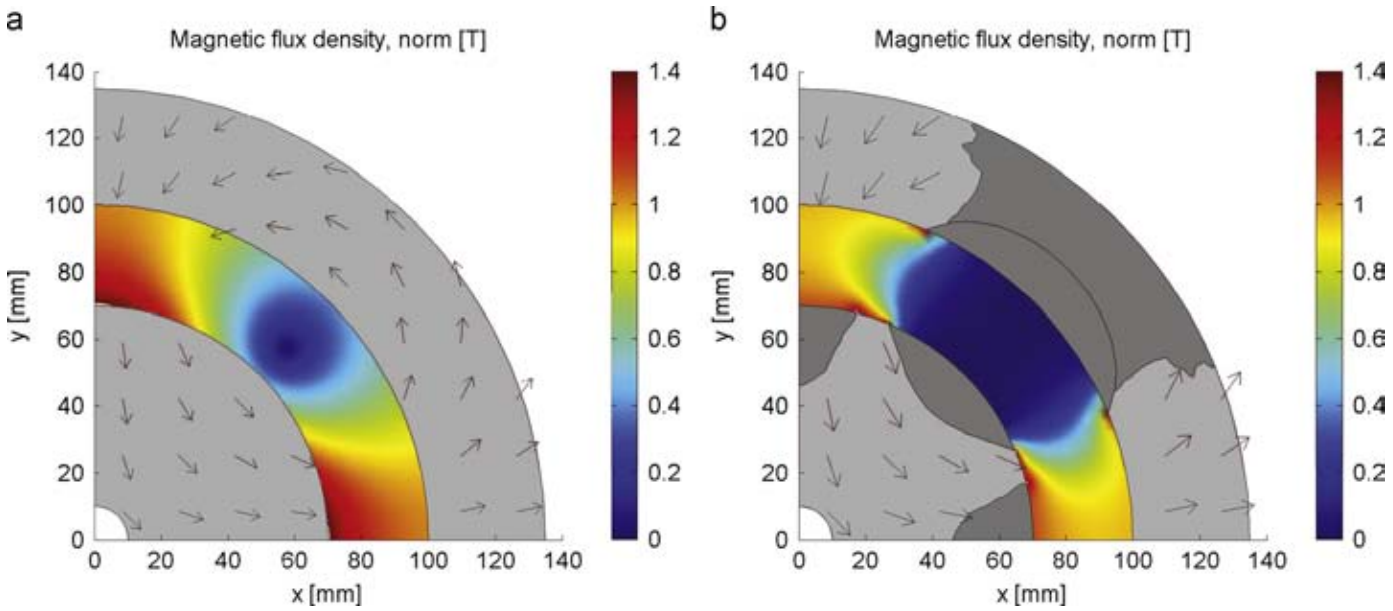

Fig. 3. (a) shows a quadrant of the a concentric Halbach cylinder with $p_{\text{outer}}=2$ and $p_{\text{inner}}=-2$. The remaining quadrants can be obtained by mirroring along the coordinate axes. The magnetization is shown as black arrows on the magnets, which are light grey. Iron is dark grey. The flux density in the air gap between the cylinders is shown as a color map. (b) shows the same design after the two improvement schemes have been applied. The line in the iron region in the outer magnet separates the iron regions generated by the two improvement schemes, and it is only shown for reference. (For interpretation of the references to colour in this figure legend, the reader is referred to the web version of this article.)

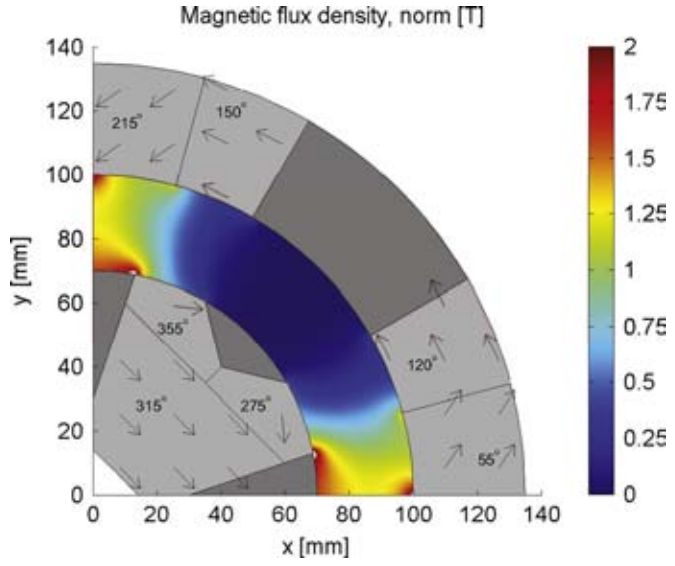

Fig. 4. The segmentation of the final design. The direction of magnetization has been found by maximizing $\langle B_{\text{high}}^{0.7}\rangle - \langle B_{\text{low}}^{0.7}\rangle$. The direction of magnetization is indicated on each segment. The small white areas in the air gap have a flux density higher than the maximum value on the color bar. (For interpretation of the references to colour in this figure legend, the reader is referred to the web version of this article.)

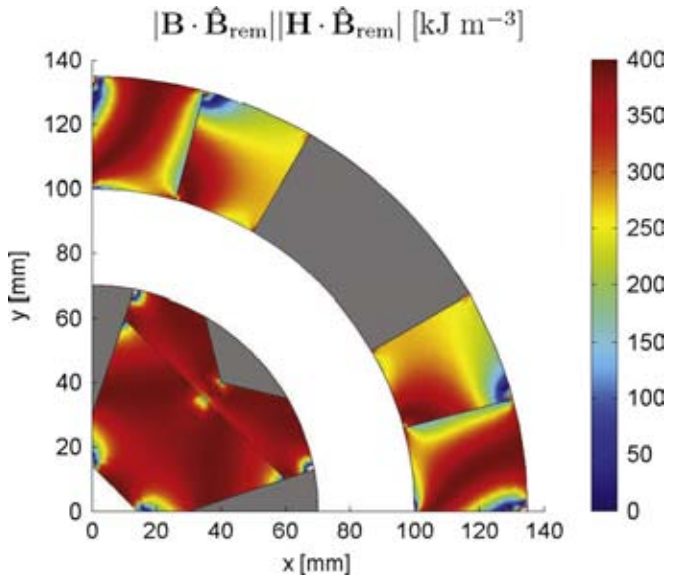

Fig. 5. (Color online) The working point, $|\mathbf{B}\cdot\hat{\mathbf{B}}_{\text{rem}}||\mathbf{H}\cdot\hat{\mathbf{B}}_{\text{rem}}|$, of the magnets. The maximum working point for a 1.44 T remanence magnet, as is used here, is 400 kJ m^{-3}.

3. The physical magnet

3.1. Segmentation of the final design

To allow construction of the magnet, the design shown in Fig. 3(b) must be segmented. The number of segments is an important parameter as the more segments used the more expensive the manufacturing process becomes. Generally it is the total number of segments that determines the cost together with the overall magnet volume, due to the handling of the individual segments. However, segments with different geometric shapes introduce an additional cost as these must be separately manufactured. If different segments have the same geometrical shape but different directions of magnetization these introduce little additional cost as the same molds and fixation tools can be used [27].

The segmentation of the optimized design is done manually. The size of the iron regions is decreased a bit in order to generate a higher flux density in the high flux density region. In order to find the optimal direction of magnetization of the individual segments an optimization procedure has been applied. The optimization routine used is a modified version of the *Matlab* function `FMINSEARCH` [28], called `FMINSEARCHBND`, which finds the minimum of an unconstrained multivariable function with

boundaries using a derivative-free method [29]. A Comsol model with a predefined geometry is used as input, with the direction of magnetization as variables. The optimization criteria is that the difference between $\langle B^{0.7}_{\text{high}} \rangle$ and $\langle B^{0.7}_{\text{low}} \rangle$ be maximized. The segmentation of the magnet design and the resulting directions of magnetization are shown in Fig. 4.

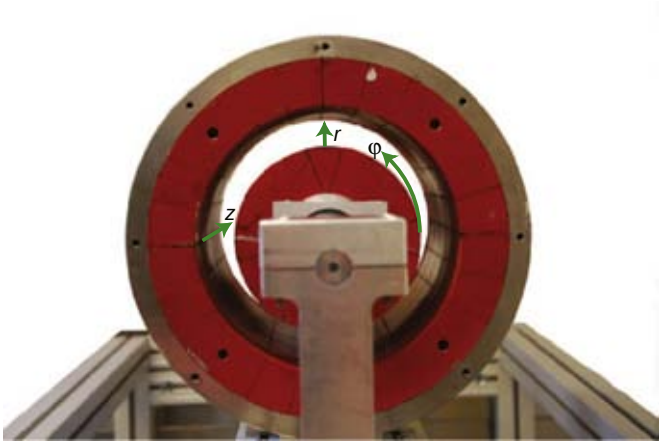

Fig. 6. A photo of the actual constructed magnet (in red) including a stand and an outer stainless steel casing. The coordinate system used for the measurements of the flux density is also shown. (For interpretation of the references to colour in this figure legend, the reader is referred to the web version of this article.)

The effectiveness of the magnet design can be judged from the working point of the magnets, i.e. the size of the magnetic field times the size of the flux density, both measured in the direction of the remanence: $|\mathbf{B}\cdot\hat{\mathbf{B}}_{\text{rem}}||\mathbf{H}\cdot\hat{\mathbf{B}}_{\text{rem}}|$. In Fig. 5 the working point is shown as calculated from a model of the magnet design. For magnets with a remanence of 1.44 T, as is used here, the maximum energy density, i.e. the optimal working point $(|\mathbf{B}\cdot\hat{\mathbf{B}}_{\text{rem}}||\mathbf{H}\cdot\hat{\mathbf{B}}_{\text{rem}}|)_{\text{max}}$, is 400 kJ m^{-3} [30]. As can be seen from the figure most parts of the magnets are close to the maximum energy density thus illustrating the efficiency of the design.

3.2. The final design realized

The magnet design shown in Fig. 4 has been constructed and a photo of the magnet is shown in Fig. 6. The magnet has a length of 250 mm.

All spatial components of the flux density in the air gap have been measured using a Hall probe (AlphaLab Inc, Model: DCM) as a function of angle, radius and length of the device. A three dimensional simulation of the design has also been performed. The measured flux density was found to be periodic with a period of 90°, as expected. The measured flux density for the first 90° and the results of the simulation are shown in Fig. 7. An excellent agreement between the simulated and measured flux density is seen.

In the four high field regions the peak flux density is around 1.24 T while it is very close to 0 T in the four low field regions. The

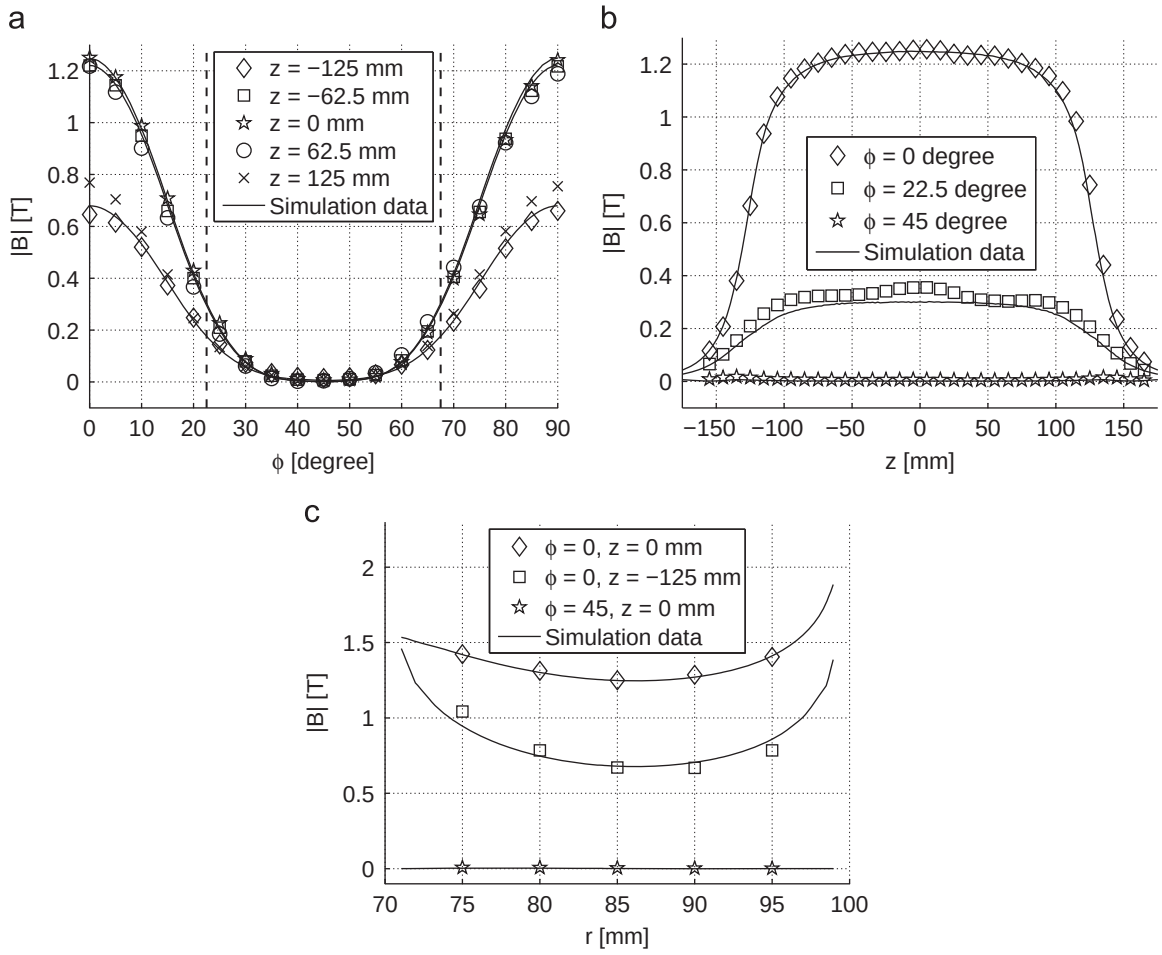

Fig. 7. Measurements of the flux density as a function of angle ϕ, length z, and radius r, in the middle of the air gap of the magnet compared with numerical simulations. The dashed vertical lines on Fig. (a) separate the high and low flux density regions. (a) $|B|$ as function of ϕ in the middle of the air gap, $r=85$ mm. (b) $|B|$ as function of z in the middle of the air gap, $r=85$ mm. (c) $|B|$ as function of r.

gradient between the high and low field regions is quite sharp, but it is clear that the field is not homogeneous in the high field region. However, as the magnetocaloric effect scales with the magnetic field to the power of 0.7 it is preferable to have a zero flux density in the low field region rather than to have part of the flux density gradient in the low field region. Therefore the gradient is concentrated in the high field region. The field is also seen to drop off only at the very ends of the device, i.e. $|z| > 100$ mm. Finally the field is seen to be slightly larger radially near the inner and outer magnet compared to the center of the air gap, but the difference is small and is not expected to have an impact on the performance of the AMR.

3.3. Performance of the magnet

The performance of the magnet with regards to magnetic refrigeration can be evaluated using the Λ_{cool} parameter [31], which is defined as

$$\Lambda_{\text{cool}} \equiv (\langle B_{\text{high}}^{0.7} \rangle - \langle B_{\text{low}}^{0.7} \rangle) \frac{V_{\text{field}}}{V_{\text{mag}}} P_{\text{field}}, \quad (2)$$

where V_{mag} is the volume of the magnet(s), V_{field} is the volume where a high flux density is generated and P_{field} is the fraction of an AMR cycle that magnetocaloric material is placed in the high flux density volume. Note that V_{mag} is the volume of permanent magnet material used, excluding any soft magnetic material as the price of this material is in general significantly lower than permanent magnet material. Also, the magnet design presented above has not been optimized with respect to the total weight of the design. More soft magnetic material than needed is present, as the saturation magnetization of the soft magnetic material is not reached. This was done for ease of construction.

Other published magnet designs for magnetic refrigeration devices have a Λ_{cool} parameter between 0.03 and 0.21 [12]. The magnet designed here has $V_{\text{mag}} = 7.3$ L, $V_{\text{field}} = 2.0$ L, $\langle B_{\text{high}}^{0.7} \rangle = 0.91$ T and $\langle B_{\text{low}}^{0.7} \rangle = 0.15$ T. Assuming $P_{\text{field}} = 1$, as is the aim of the device, the design achieves $\Lambda_{\text{cool}} = 0.21$, thus equaling the best performing magnet published to date. The rotary magnetic refrigeration devices mentioned earlier, Refs. [11,13–15] have $\Lambda_{\text{cool}} = 0.13$, 0.11, 0.21 and 0.03, respectively.

For this particular design the choice of the high and low flux density regions is rather arbitrary and so they could have been chosen to span less than 45°. This would lead to a higher value for $\langle B_{\text{high}}^{0.7} \rangle$ and a lower value of $\langle B_{\text{low}}^{0.7} \rangle$, but also to a lower value of V_{field}. It has been verified that Λ_{cool} attains the highest value for this design when the high and low flux density regions combined span the entire air gap circumference, i.e. as done here.

4. Conclusion

The complete process of designing a magnet for use in a magnetic refrigeration device has been described. Two different ways for improving the performance of a magnet design were applied to a concentric Halbach magnet design which was dimensioned and subsequently segmented once the optimal dimensions had been found. The direction of magnetization was also optimized for each of the individual segments. The final design generates a peak value of 1.24 T, an average flux density of 0.9 T in a volume of 2 L using 7.3 L of magnet, and has an average low flux density of 0.08 T. The difference in flux to the power of 0.7 is $0.76\,\text{T}^{0.7}$. The working point of the magnets is close to the maximum energy density possible. Finally the flux density of the design has been measured and compared with a three dimensional numerical simulation of the design, and an excellent agreement was seen. A magnetic refrigeration device utilizing the magnet is under construction at Risø DTU.

Acknowledgements

The authors would like to acknowledge the support of the Programme Commission on Energy and Environment (EnMi) (Contract no. 2104-06-0032) which is part of the Danish Council for Strategic Research. The authors also wish to thank F. B. Bendixen and P. Kjeldsteen for useful discussions.

References

[1] J.A. Barclay, Adv. Cryog. Eng. 33 (1988) 719.
[2] B. Yu, Q. Gao, B. Zhang, X. Meng, Z. Chen, Int. J. Refrig. 26 (6) (2003) 622.
[3] K.A. Gschneidner Jr., V.K. Pecharsky, Int. J. Refrig. 31 (6) (2008) 945.
[4] A. Coelho, S. Gama, A. Magnus, G. Carvalho, in: Proceedings of 3rd International Conference on Magnetic Refrigeration at Room Temperature, Des Moines, Iowa, USA, 2009, p. 381.
[5] C. Dupuis, A.J. Vialle, U. Legait, A. Kedous-Lebouc, D. Ronchetto, in: Proceedings of 3rd International Conference on Magnetic Refrigeration at Room Temperature, Des Moines, Iowa, USA, 2009, p. 437.
[6] K. Engelbrecht, J.B. Jensen, C.R.H. Bahl, N. Pryds, in: Proceedings of 3rd International Conference on Magnetic Refrigeration at Room Temperature, Des Moines, Iowa, USA, 2009, p. 431.
[7] Y. Kim, S. Jeong, in: Proceedings of 3rd International Conference on Magnetic Refrigeration at Room Temperature, Des Moines, Iowa, USA, 2009, p. 393.
[8] O. Sari, M. Balli, G. Trottet, P. Bonhote, P. Egolf, C. Muller, J. Heitzler, S. Bour, in: Proceedings of 3rd International Conference on Magnetic Refrigeration at Room Temperature, Des Moines, Iowa, USA, 2009, p. 371.
[9] L. Tagliafico, F. Scarpa, G. Tagliafico, F. Valsuani, F. Canepa, S. Cirafici, M. Napoletano, C. Belfortini, in: Proceedings of 3rd International Conference on Magnetic Refrigeration at Room Temperature, Des Moines, Iowa, USA, 2009, p. 425.
[10] Z. Zheng, H. Yu, X. Zhong, D. Zeng, Z. Liu, Int. J. Refrig. 32 (2009) 78.
[11] J. Tušek, S. Zupan, A. Sarlah, I. Prebil, A. Poredos, Int. J. Refrig. 33 (2) (2010) 294.
[12] R. Bjørk, C.R.H. Bahl, A. Smith, N. Pryds, Int. J. Refrig. 33 (2010) 437.
[13] C. Vasile, C. Muller, Int. J. Refrig. 29 (8) (2006) 1318.
[14] T. Okamura, R. Rachi, N. Hirano, S. Nagaya, in: Proceedings of 2nd International Conference on Magnetic Refrigeration at Room Temperature, Portoroz, Slovenia, 2007, p. 377.
[15] C. Zimm, J. Auringer, A. Boeder, J Chell, S. Russek, A. Sternberg, in: Proceedings of 2nd International Conference on Magnetic Refrigeration at Room Temperature, Portoroz, Slovenia, 2007, p. 341.
[16] K.K. Nielsen, C.R.H. Bahl, A. Smith, R. Bjørk, N. Pryds, J. Hattel, Int. J. Refrig. 32 (6) (2009) 1478.
[17] K.K. Nielsen, K. Engelbrecht, C.R.H. Bahl, A. Smith, J. Geyti, 2009, Private communication. Unpublished.
[18] R. Bjørk, C.R.H. Bahl, A. Smith, J. Magn. Magn. Mater. 322 (2010) 133.
[19] J.C. Mallinson, IEEE Trans. Magn. 9 (4) (1973) 678.
[20] K. Halbach, Nucl. Instrum. Methods 169 (1980).
[21] R. Bjørk, C.R.H. Bahl, A. Smith, N. Pryds, IEEE Trans. Magn., 2010, submitted for publication.
[22] F. Bloch, O. Cugat, G. Meunier, J.C. Toussaint, IEEE Trans. Magn. 34 (5) (1998) 2465.
[23] J.M.D. Coey, T.R. Ni Mhiochain, in: F. Herlach, N. Miura (Eds.), High Magnetic Fields (Permanent Magnets), vol. 25, World Scientific, 2003.
[24] COMSOL AB, Tegnérgatan 23, SE-111 40 Stockholm, Sweden.
[25] Standard Specifications for Permanent Magnet Materials, Magn. Mater. Prod. Assoc., Chicago, USA, 2000, ⟨www.intl-magnetics.org⟩.
[26] V.K. Pecharsky, K.A. Gschneidner Jr., Int. J. Refrig. 29 (8) (2006) 1239.
[27] F.B. Bendixen, 2009. Private communication.
[28] Matlab, version 7.7.0.471 (R2008b) (2008).
[29] J. D'Errico, ⟨http://www.mathworks.com/matlabcentral/fileexchange/8277⟩, Release: 4 (7/23/06) (2006).
[30] Vacuumschmelze GMBH & Co, KG. Pd 002—Vacodym/Vacomax (2007).
[31] R. Bjørk, C.R.H. Bahl, A. Smith, N. Pryds, J. Appl. Phys. 104 (1) (2008) 13910.

Paper XIII

Paper presented at the 4th International Conference on Magnetic Refrigeration at Room Temperature, 2010

Bahl, C. R. H., Engelbrecht, K., Bjørk, R., Eriksen, D., Smith, A. and Pryds, N.

Design concepts for a continuously rotating active magnetic regenerator

Proceedings of the 4rd International Conference on Magnetic Refrigeration at Room Temperature, Baotou, China, 2010

DESIGN CONCEPTS FOR A CONTINUOUSLY ROTATING ACTIVE MAGNETIC REGENERATOR

C.R.H. BAHL, K. ENGELBRECHT, R. BJØRK, D. ERIKSEN, A. SMITH AND N. PRYDS

Fuel Cells and Solid State Chemistry Divison, Risø National Laboratory for Sustainable Energy, Technical University of Denmark, Frederiksborgvej 399, 4000 Roskilde, Denmark
Email: chrb@risoe.dtu.dk

ABSTRACT

Design considerations for a prototype magnetic refrigeration device with a continuously rotating AMR are presented. Building the AMR from stacks of elongated plates of the perovskite oxide material $La_{0.67}Ca_{0.33-x}Sr_xMn_{1.05}O_3$, gives both a low pressure drop and allows grading of the Curie temperature along the plates. This may be accomplished by a novel technique where a compositionally graded material may be tape cast in one piece. The magnet assembly is based on a novel design strategy, to create alternating high- and low magnetic field regions within a magnet assembly. Focus is on maximising the magnetic field in the high field regions but also, importantly, minimising the flux in the low field regions. The design is iteratively optimised through 3D finite element magnetostatic modelling.

1. INTRODUCTION

Over the last ten years a number of prototype magnetic refrigeration devices relying on the active magnetic regeneration (AMR) principle have been built and tested, see, e.g. Gschneidner *et al.*(2008), Zimm *et al.* (2007), Tura and Rowe (2007), Okamura *et al.* (2006) and Tusek *et al.* (2009). These have included a broad range of different design ideas including reciprocating pistons and rotating discs of magnetocaloric material. Although magnetic refrigeration promises high energy efficiency without the use of a gaseous refrigerant the components of any device, especially the magnet field source and the magnetocaloric regenerator, will potentially be costly. Thus it is of the utmost importance to carefully consider the design of any device minimising any waste of space or materials. Conventionally designs have been focussed towards lowering the pressure loss in the regenerator, using as little magnet material as possible, fast operation etc. In addition to these ideas, we suggest the following design constraints:

- *Continuous rotation of the magnetocaloric parts:*
  Arranging the magnetocaloric material in a continuously rotating structure gives a smooth movement facilitating high frequency operation.
- *Use of cheap magnetocaloric parts that are easily processed:*
  Raw materials and especially processing can be very expensive.
- *Continuous use of the magnetised volume and magnetocaloric material:*
  As the magnetic flux is expensive to generate the magnetised regions should continuously be filled with magnetocaloric material that is continuously in use.
- *Continuous flow of heat transfer fluid through a part of the regenerator:*
  The fluid is not interrupted. This reduces pumping losses.

Each of these points should be addressed when designing a magnetic refrigeration device. In the following we will outline how the above points influenced the design of the prototype device under construction at Risø DTU.

2. DESIGN OF THE PROTOTYPE

The basic design of the prototype device is a rotating cylinder of magnetocaloric material. Two concentric multi-pole magnet assemblies are mounted around and within the cylinder. Thus when rotating the cylinder each part of it will successively experience high and low magnetic field regions, see Figure 1

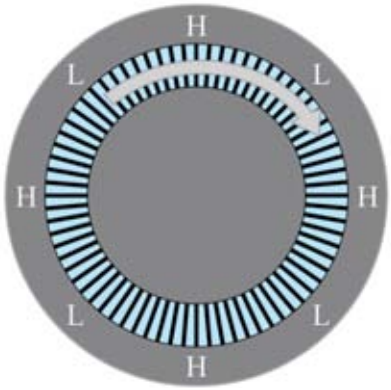

Figure 1: Sketch showing the alternating high and low field regions, as well as the rotating regenerator.

To allow for the passage of a heat transfer fluid the cylinder of magnetocaloric material should be porous. A geometry consisting of radially mounted plates was chosen as this minimises the pressure loss across the regenerator, while allowing assembly of the regenerator with a chosen plate spacing and distance. Also, this geometry of radially arranged thin plates reduces the magnetostatic demagnetisation field which can otherwise significantly reduce the MCE (Bahl and Nielsen, 2009). Other structures such as monolithic honeycombed structure are also considered for future application (Pryds *et al.*, 2010).

The angular extent of the high and low field regions of the magnet must be the same in order to have a continuous use of the magnetocaloric material and a balanced cycle. A four pole magnet assembly was chosen, the details of which will be discussed below. Thus there are eight equally spaced regions of the magnet cylinders, four high magnetic field and four low magnetic field regions. This results in a smooth rotation of the magnetocaloric cylinder as an equal amount of material is always entering the high magnet field region and there is no jolting of the cylinder. Also, the magnetic forces needed to pull the plates out of the high field region are balanced by those resulting from plates being attracted into the high field regions. Thus the only work needed to rotate the cylinder is the magnetic work resulting from differences in magnetisation due to temperature differences between the plates and mechanical drag due to external parts such as seals.

During rotation, heat transfer fluid flows between the plates in alternating directions. There are fluid inlets and outlets arranged so that the flow is in phase with the magnetisation and demagnetisation of the plates in the different regions of the magnet.

3. REGENERATOR MATERIALS

When making the choice of which magnetocaloric material to use in the refrigeration device it is important to consider magnetocaloric performance, cost and whether there are any adverse properties to be aware of. When considering cost it is important to include both the raw material price and the cost of processing the material into the desired geometry. In price estimates of the benchmark magnetocaloric material Gd, often only the raw material price is quoted. However, processing into, e.g. thin sheets, can easily increase the price ten-fold. Although the magnetocaloric performance of Gd

is very high, it does have some adverse properties. These include corrosion issues if care is not taken when handling the material and when choosing heat transfer fluids. Also, the softness of Gd makes it difficult to work with thin plates (< 0.5 mm) as these will easily flex and bend.

A viable alternative to Gd is the perovskite oxide material $La_{0.67}Ca_{0.33-x}Sr_xMn_{1.05}O_3$ (LCSM). Even very thin plates (~0.2 mm) are stiff and will not bend. Also, being an oxide material, corrosion and toxicity are not issues. Importantly, the material is very cheap and easy to manufacture and process in large quantities. The adiabatic temperature change in an applied field of 1 T is about 1 K, which is significantly below the ~3 K of Gd, but due to the higher heat capacity of LCSM the entropy change per volume is only 30 % below that of Gd. The Curie temperature of LCSM can be accurately tuned by altering the chemical composition. This allows for a functional grading of a regenerator with a profile of Curie temperatures closely matching the working temperature profile within the regenerator, enhancing the performance.

Recently, a novel technique of tape casting up to ten different compositions of LCSM into one plate has been developed at Risø DTU. Powders of the ten materials are suspended into slurries, ensuring a matching of the viscosities. Bands of these slurries are applied side-by-side onto a moving tape, with equal height being ensured by a doctor blade. The tapes are subsequently dried, sintered and cut into the desired shapes. An example of such a 0.3 mm thick tape consisting of ten bands of LCSM is shown in Figure 2.

Figure 2: Graded Plate of LCSM 250 mm x 20 mm x 0.3 mm. The plate is cut from a larger sheet, tape cast in one piece, consisting of 10 discrete regions of LCSM.

Due to the stiffness of the LCSM material if can easily be stacked into rigid structures. Such stacks can then be used to build up structures of magnetocaloric material.

4. MAGNET ASSEMBLY

The desired properties of the magnet assembly are that it has a cylindrical bore of alternating high and low field regions. These should, as discussed above, be of equal angular extent and adjacently placed. A maximum utilisation of the magnet material and thus a minimum stray field is a requirement. This lends itself towards a cylindrical bore that is significantly longer than it is thick. The starting point of the design is two concentric multi-pole Halbach cylinders (Coey, 2002), as these contain all the available magnetic flux within the bore, see Figure 3.

Both theory (Oesterreicher and Parker, 1984) and experiment (Dong *et al.*, 2008) have shown that the magnetic entropy change and also the adiabatic temperature change are approximately proportional to $H^{2/3}$, where H is the magnetic field. This is valid for materials exhibiting second order phase transition at temperatures close to the Curie temperature. Thus the temperature change when rotating the magnetocaloric material from a low field region to a high field region is

$$\Delta T_{\mathrm{ad}} \sim H_{\mathrm{high}}^{2/3} - H_{\mathrm{low}}^{2/3} \qquad (1)$$

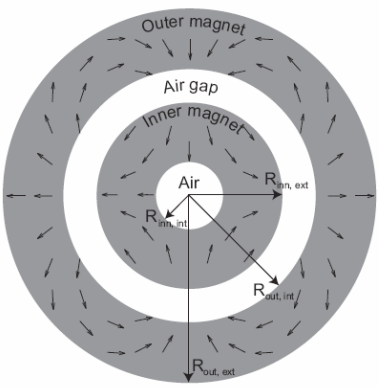

Figure 3: Two concentric quadropole Halbach type cylinders. The inner magnet directs the field outward, while the outer one directs the field inward.

where the subscripts high and low indicate the high and low field regions, respectively. Therefore, it is even more important to minimise the magnetic field in the low field region than to maximise it in the high field region. Having the two regions situated adjacently means that any stray field from the high field region must be kept out of the low field region.

A procedure has been developed at Risø DTU, to improve the performance of magnet assemblies (Bjørk *et al.*, 2010a; Bjørk *et al*. 2010b). Using a 2D numerical modelling approach, parts of the magnet assembly which are contributing to the field in the low field regions are removed. Details of this iterative procedure are discussed elsewhere (Bjørk *et al.*, 2010a; Bjørk *et al*. 2010b). The resulting field experienced by a plate rotating around with the regenerator is shown in Figure 4, where a comparison between the field before and after the improvement is shown. Although the field in the high field region has decreased after the improvement, it is apparent that the field in the low field region has been almost removed giving a higher ΔT_{ad} according to Eq. (1). Also, the improvement procedure gives a significant reduction in the amount of magnet material required to produce the desired adiabatic temperature change.

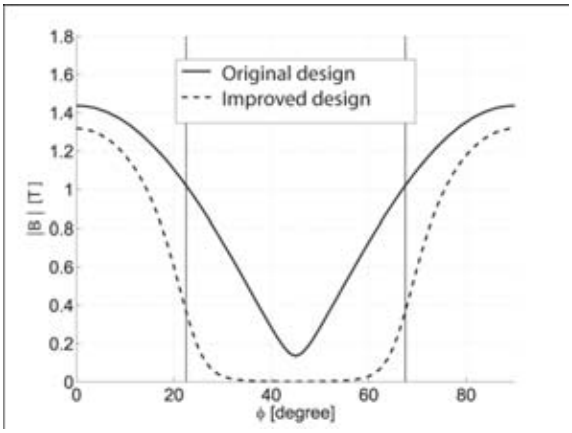

Figure 4: The magnetic flux $B = \mu_0 H$ in the centre of the gap between the magnets as a function of the rotation angle. Adapted from Bjørk *et al.* (2010b).

5. ACTUAL DESIGN

A prototype magnetic refrigeration device is at presently being constructed at Risø DTU based on the design considerations outlined above.

Using the improvement approach detailed above a magnet assembly has been designed and built. This has four high field regions, each with a maximum flux of 1.24 T, and four low field regions which have minimum fluxes below 0.01 T. Using the magnet performance metric presented in Bjørk *et al.* (2010c) the design has a Λ_{cool} of 0.21, equalling the best design published so far. The magnet assembly has been built to accommodate a cylindrical regenerator consisting of 200 mm long LCSM plates, see Figure 5.

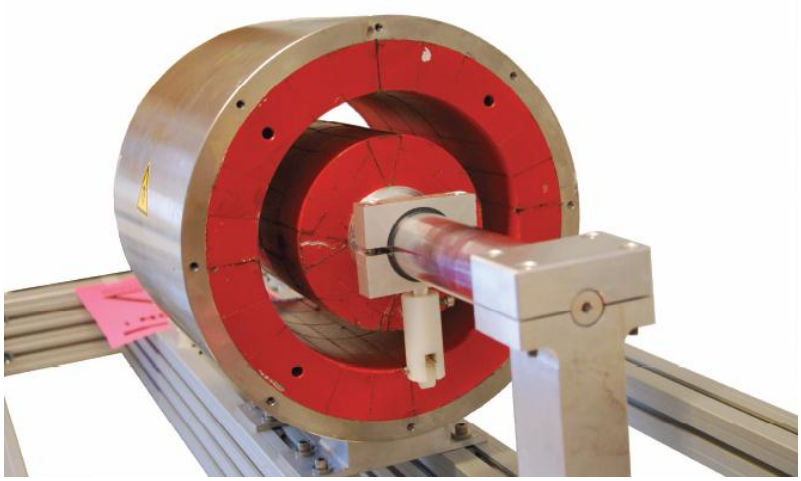

Figure 5: Picture of the actual magnet assembly used for the prototype at Risø DTU.

It was decided to use 24 individual compartments with stacks of parallel LCSM plates in the place of the radially arranged plates. Although this does mean that not all the magnetic field is utilised at all times, it gives an increased versatility as well as an increased structural strength of the prototype. Figure 6 shows such a compartment with a stack of 0.4 mm thick Al plates glued in for testing.

Figure 6: One of the 24 compartments from the regenerator. The one shown contains a stack of Al plates.

Dividing the regenerator into compartments will reduce the balancing of the system and make the rotation less smooth. However, numerical simulations have shown that as the number of compartments is high compared to the number of magnet poles such that unbalance will be insignificant.

This 24 compartment regenerator and the four pole magnet will form the basis of the prototype. During rotation, a complex flow distribution system will divide the flow from the pump into each of the compartments in phase with the regions of the magnet. A sketch of the full system is given in Figure 7.

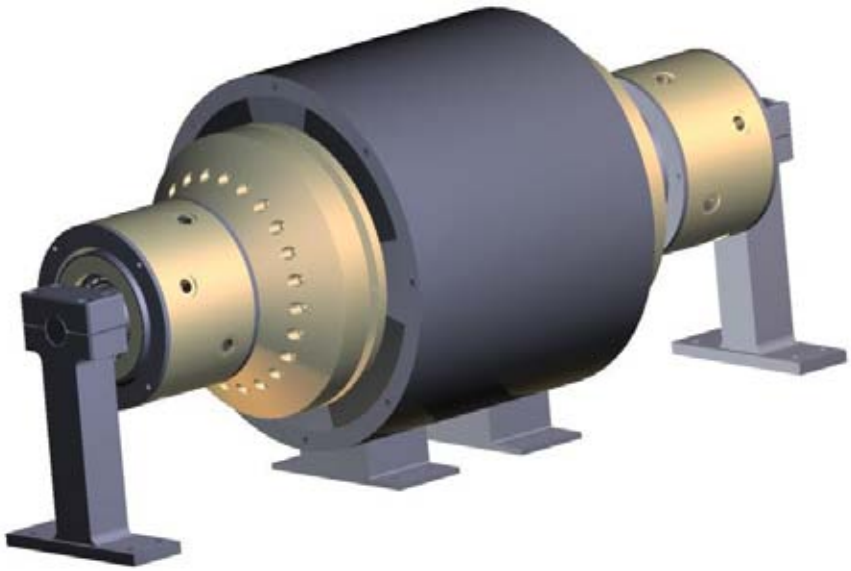

Figure 7. Picture showing a CAD model of the final system, including magnet, regenerator (not visible) and flow distributors. Not shown are the motor, pump and piping system.

6. CONCLUSION

Based on a number of design constraints a prototype AMR refrigeration device has been designed and partly constructed at Risø DTU. The system has a continuously rotating regenerator built from the cheap and easily processed magnetocaloric material $La_{0.67}Ca_{0.33-x}Sr_xMn_{1.05}O_3$ (LCSM). A novel magnet design allows for the maximum utilisation of the magnet field, with the high and low field regions adjacently placed. For practical reasons the regenerator has been divided into 24 individual compartments, reducing the utilisation of the magnet field. However, in future a continuous regenerator may be conceived. The flow system has been designed for a continuous non-interrupted flow of heat transfer fluid. Although the regenerator is divided into compartments a continuous flow is still possible due to the high number of these.

REFERENCES

Bahl CRH, Nielsen KK. 2009, The effect of demagnetization on the magnetocaloric properties of gadolinium, *J. Appl. Phys.* 105: 013916.

Bjørk R, Bahl CRH, Smith A, Christensen D, Pryds N. 2010a, An optimized magnet for magnetic refrigeration, *J. Magn. Magn. Mater.* In Press.

Bjørk R, Bahl CRH, Smith A, Pryds N. 2010b, Optimization of permanent magnet assemblies, *Submitted*.

Bjørk R, Bahl CRH, Smith A, Pryds N. 2010c, Review and comparison of magnet designs for magnetic refrigeration, *Int. J. Refrig.* 33: 437-448.

Coey JMD. 2001, Permanent magnet applications, *J. Magn. Magn. Mater.* 248: 441-456.

Dong QY, Zhang HW, Sun JR, Shen BG, Franco V. 2008, A phenomenological fitting curve for the magnetocaloric effect of materials with a second-order phase transition, *J. Appl. Phys.* 103: 116101.

Gschneidner Jr. KA ,Pecharsky VK. 2008, Thirty years of near room temperature magnetic cooling: Where we are today and future prospects, *Int. J. of Refrig.* 31: 945-961.

Oesterreicher H, Parker F. 1984, Magnetic cooling near curie temperatures above 300 K, *J. Appl. Phys.* 55: 4334-4338.

Okamura T, Yamada K, Hirano N, Nagaya S. 2006, Performance of a room-temperature rotary magnetic refrigerator, *Int. J. of Refrig.* 29: 1327-1331.

Pryds N, Clemens F, Biering I, Nielsen PH, Menon M, Brodersen K, Bjørk R, Bahl CRH, Engelbrecht K, Nielsen KK, Smith A. 2010, Monolithic perovskite for magnetic regenerator, *In preparation*.

Tura A, Rowe A. 2007, Design and testing of a permanent magnet magnetic refrigerator, *Proc. of the 2nd Internat. Conf. of Magnetic Refrigeration at Room Temperature, Portoroz, Slovenia*, IIF/IIR: 363-370.

Tusek J, Zupan S, Sarlah A, Prebil I, Poredos A. 2009, Development of a rotary magnetic Refrigerator, *Proc. of the 3rd Internat. Conf. on Magnetic Refrigeration at Room Temperature, Des Moines, USA*, IIR/IIF: 409-414.

Zimm C, Auringer J, Boeder A, Chell J, Russek S, Sternberg A. 2007, Design and initial performance of a magnetic refrigerator with a rotating permanent magnet, *Proc. of the 2nd Internat. Conf. of Magnetic Refrigeration at Room Temperature, Portoroz, Slovenia*, IIF/IIR: 341-347.

Paper XIV

Paper accepted for publication in Journal of Applied Physics, 2010

Christensen, D. V., Bjørk. R., Nielsen, K. K., Bahl, C. R. H., Smith. A. and Clausen, S.

Spatially resolved measurement of the magnetocaloric effect and the local magnetic field using thermography

Journal of Applied Physics, 108, 063913, 2010

Spatially resolved measurements of the magnetocaloric effect and the local magnetic field using thermography

D. V. Christensen,[1,2,a)] R. Bjørk,[1] K. K. Nielsen,[1,3] C. R. H. Bahl,[1] A. Smith,[1] and S. Clausen[4]
[1]*Fuel Cells and Solid State Chemistry Division, Risø National Laboratory for Sustainable Energy, Technical University of Denmark, Frederiksborgvej 399, DK-4000 Roskilde, Denmark*
[2]*The Niels Bohr Institute, University of Copenhagen, Blegdamsvej 17, DK-2100 Copenhagen, Denmark*
[3]*Department of Mechanical Engineering, Technical University of Denmark, Building 425, Niels Koppels Alle, DK-2800 Kongens Lyngby, Denmark*
[4]*Plasma Physics and Technology Division, Risø National Laboratory for Sustainable Energy, Technical University of Denmark, Frederiksborgvej 399, DK-4000 Roskilde, Denmark*

(Received 29 March 2010; accepted 9 August 2010; published online 22 September 2010)

The magnetocaloric effect causes a magnetic material to change temperature upon application of a magnetic field. Here, spatially resolved measurements of the adiabatic temperature change are performed on a plate of gadolinium using thermography. The adiabatic temperature change is used to extract the corresponding change in the local magnetic field strength. The measured temperature change and local magnetic field strength are compared to results obtained with a numerical model, which takes demagnetization into account and employs experimental data. © *2010 American Institute of Physics*. [doi:10.1063/1.3487943]

I. INTRODUCTION

The applied magnetic field, $\mathbf{H}_{\text{appl}}$, differs from the local magnetic field, $\mathbf{H}$, in a magnetic material. The difference arises as the magnetization, $\mathbf{M}$, itself produces a magnetic field, known as the demagnetizing field, $\mathbf{H}_{\text{dem}}$, which tends to decrease the local magnetic field inside the body. In general the demagnetizing field varies spatially and is highly dependent on the geometry and the magnetization of the body. Since the demagnetizing field depends on the magnetization, which in turn generally depends on the local magnetic field, the demagnetizing field can typically only be evaluated analytically in the few cases where both the magnetization and the demagnetizing field are homogeneous. This is fulfilled only in ellipsoidal bodies[1] and a few other cases such as infinite cylinders or infinite sheets.

When the local magnetic field in a finite, nonellipsoidal body is needed, a commonly used approach is to assume a homogeneous magnetization throughout the body. The position dependence of the local magnetic field can then be expressed as

$$\mathbf{H}(\mathbf{r}) = \mathbf{H}_{\text{appl}}(\mathbf{r}) + \mathbf{H}_{\text{dem}}(\mathbf{r}) = \mathbf{H}_{\text{appl}}(\mathbf{r}) - \mathbb{N}(\mathbf{r}) \cdot \mathbf{M}, \qquad (1)$$

where the demagnetization tensor field, $\mathbb{N}(\mathbf{r})$, has been evaluated for a range of geometries, see e.g. Refs. 2 and 3, and a general expression has been given using a Fourier space approach.[4] However, as the local magnetic field varies spatially the assumption of a homogeneous magnetization is often invalid. When this is the case the demagnetizing field can be solved numerically as in, e.g., Refs. 5 and 6.

Another approach is to determine the local magnetic field experimentally. Due to the strong shape dependence of the demagnetizing field this must be done without altering the shape of the sample. One way of achieving this is to determine the local field indirectly by measuring an observable that depends on the local magnetic field. As shown in Refs. 5 and 7 one such observable is the magnetocaloric effect, which manifests itself as an adiabatic temperature change, ΔT_{ad}, if the local magnetic field in a magnetocaloric material changes in time.

Here, measurements of the adiabatic temperature change in a plate of gadolinium are performed using thermography as described in Sec. II. The measurements are compared to a numerical model introduced in Sec. III, which corrects for the demagnetization and employs measurements of the magnetization and adiabatic temperature change in samples of gadolinium. Finally, the results of the measured and calculated adiabatic temperature change and corresponding local magnetic field changes are discussed in Sec. IV.

II. EXPERIMENTAL

The experiment was carried out using a $40 \times 25 \times 0.9$ mm^3 plate of gadolinium with a purity of 99.9% obtained from China Rare Metal Material Co. The relevant dimensions and defined coordinate system are given in the illustration of the experimental setup in Fig. 1. Two layers of black paint were applied to the plate, and the plate was mounted in a plastic cylinder with a hole of the same size as the plate allowing transmission of thermal radiation. To ensure approximately adiabatic conditions the plate was mounted such that only the faces with $x=0$ and $x=25$ mm were in contact with the thermally insulating cylinder. Using a stepper motor the cylinder was moved into the center of a Halbach magnet with a magnetic field profile as seen in Fig. 2. When thermal equilibrium was reached at 295 K, the cylinder was moved out of the magnet in 0.7 s resulting in a negative adiabatic temperature change. During the movement the intensity of the thermal radiation was recorded in

a)Electronic mail: dennischristensen@stud.ku.dk.

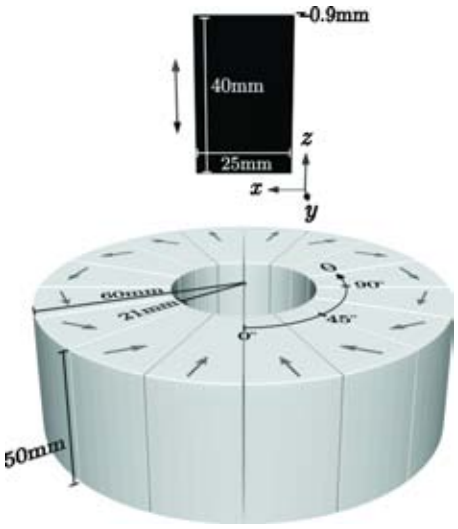

FIG. 1. (Color online) The thermographic measurements were performed by moving a plate of gadolinium out of a Halbach magnet, while recording the thermal radiation. The dimensions of the plate and Halbach magnet are given in the figure along with the defined coordinate system of the plate and the angle θ between the applied field and the y-direction (chosen normal to the plate). For the configuration shown here $\theta=0°$. The Halbach magnet consists of 16 segments of permanent magnets each with a magnetization direction given by the arrows.

real-time using an infrared camera of the type Cedip FLIR Titanium SC7000. The camera was calibrated by measuring the intensity of the thermal radiation from a black body at two temperatures and interpolating linearly.

The experimental setup allows for variation in the angle θ in the xy-plane between the direction of the applied field and the y-direction, where the y-direction is chosen to be normal to the plate as illustrated in Fig. 1. Three orientations were investigated: $\theta=0°$ (i.e., $\mathbf{H}_{\text{appl}}$ parallel to the y-direction), $\theta=45°$ and $\theta=90°$ (i.e., $\mathbf{H}_{\text{appl}}$ parallel to the x-direction).

To confirm that the temperature change in the plate is adiabatic, the plate was moved out of the applied field and the difference between the temperature of the surroundings and the average temperature of the plate was monitored over time. For both $\theta=0°$ and $\theta=90°$ the temperature difference, $|\Delta T|$, was well-described by a exponentially decaying function, $|\Delta T| \propto \exp(-t/\tau)$, with a characteristic time constant, τ, of approximately a minute. Since the characteristic time for the temperature relaxation is almost two orders of magnitude larger than the time it takes to moves the plate out of the magnet, the plate can be considered in adiabatic conditions.

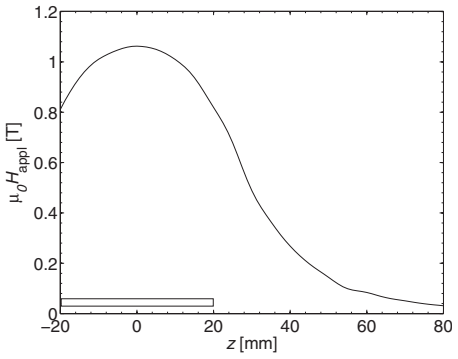

FIG. 2. The experimentally measured magnetic field strength, $\mu_0 H_{\text{appl}}$, of the Halbach magnet as a function of the distance, z, from the center of the magnet (from Ref. 8). The field strength is approximately constant in the xy-plane. The horizontal bar shows the spatial extent of the plate when placed inside the magnet.

Using the measured adiabatic temperature change as a function of the local magnetic field, taken from Ref. 9, the thermographically obtained adiabatic temperature change is converted into the corresponding change in the local magnetic field strength. The measurements in Ref. 9 are obtained using a type E thermocouple and the results have been corrected for demagnetization and thus represent the adiabatic temperature change without shape effects. Hence, the spatially varying adiabatic temperature change is directly measured in real-time using thermography, whereas the local magnetic field strength is determined indirectly.

III. MODEL

To predict the adiabatic temperature change a numerical model was developed, which operates in two steps.

First, the model solves for the spatially varying local magnetic field inside the plate when situated in the center of the Halbach magnet. The local field is calculated using the iterative, magnetostatic demagnetization approach described in Ref. 6 and the experimentally measured magnetization from Ref. 9. Assuming a negligible stray field at a distance of 100 mm from the center of the magnet, the magnetic field change is given directly by the calculated local magnetic field.

Second, the local magnetic field change is converted into the corresponding adiabatic temperature change using the aforementioned measurements of the adiabatic temperature change reported in Ref. 9. It is important to clarify that the measurements in Ref. 9 represent the adiabatic temperature change as a function of the local field, whereas the temperature change obtained using the model described here includes shape effects, which enter via the demagnetizing field.

When developing the model a few simplifying assumptions have been made: As the y-dimension of the plate is only 0.9 mm, heat transfer will, to some degree, smooth out the temperature variations in the y-direction; therefore the model averages the adiabatic temperature change in this direction. During the time it takes to move the plate out of the field (0.7 s), heat transfer is neglected in the x-direction and z-direction and between the plate and the surroundings. Furthermore, the applied magnetic field has been assumed homogeneous in the xy-plane.

IV. RESULTS AND DISCUSSION

The simulated and measured adiabatic temperature change and the corresponding changes in the local magnetic field strength are shown in Fig. 3. Since the stray field of the Halbach magnet is negligible, the change in the local magnetic field strength is also a direct measure of the local field. When the plate is moved out of the Halbach magnet, the center of the plate ($z=20$ mm) is subjected to a 30% higher applied magnetic field change compared to the field at the edges ($z=0$ mm and $z=40$ mm), see Fig. 2. This causes the

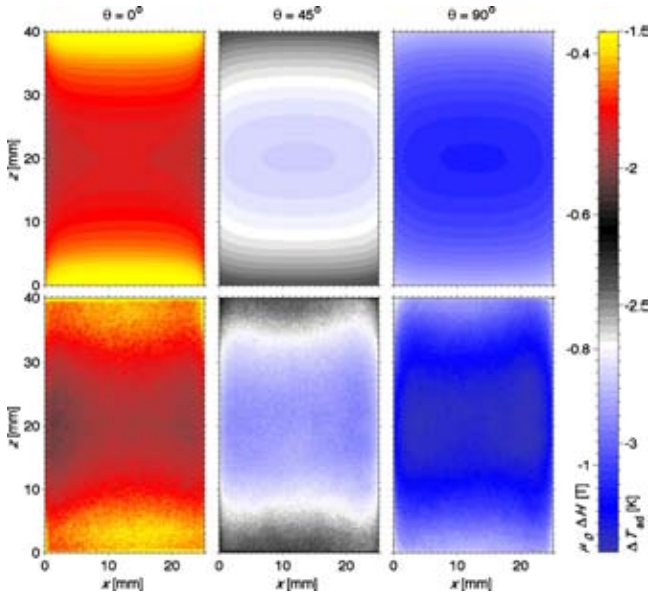

FIG. 3. (Color online) Simulated (first row) and measured (second row) adiabatic temperature change, ΔT_{ad}, and corresponding local magnetic field change, $\mu_0 \Delta H$, resulting from removing a plate of gadolinium from the applied magnetic field of a Halbach magnet. The angle θ between the applied magnetic field and the y-axis is 0°, 45°, and 90° in the first, second and third column, respectively. Note that the color scale is the same for all figures.

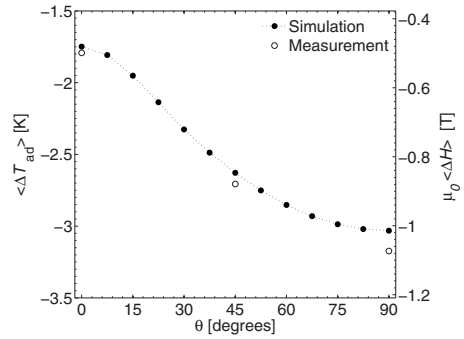

FIG. 4. Average adiabatic temperature change, $\langle \Delta T_{ad} \rangle$, and corresponding local magnetic field change, $\mu_0 \langle \Delta H \rangle$, as a function of the angle θ between the applied field and the y-axis.

plate to experience a varying local magnetic field change and consequently a gradient in the adiabatic temperature change along the z-direction as observed in Fig. 3. In the model the applied magnetic field is assumed homogeneous in the xy-plane, and hence the uneven temperature distribution observed along the x-direction in the first row of Fig. 3 is solely due to the demagnetizing field. For $\theta = 45°$ and $\theta = 90°$ the applied field is, however, slightly larger at $x = 0$ mm and $x = 25$ mm compared to $x = 12.5$ mm resulting in the largest temperature change near the edges and not at the center as predicted by the model. The difference between the model and the observed data is small and can be attributed to the inhomogeneous applied field. Hence the model is able to reproduce the spatial dependence of the changes in the temperature and local magnetic field strength, thereby validating the demagnetization approach described in Ref. 6.

The average change in the temperature and local magnetic field strength for various applied field orientations is given in Fig. 4. Here, the change in the average local magnetic field strength is increased by 50% when applying the magnetic field along the x-direction compared to the y-direction. The dependence of the sample orientation is a result of the demagnetizing field, since the average local magnetic field strength without taking demagnetization into account is independent of the angle θ assuming a homogeneous applied field in the xy-plane. Reducing the demagnetizing field increases the absolute value of the adiabatic temperature change from 1.8 to 3.2 K clearly showing the importance of taking the demagnetizing field into account as noted in Refs. 5 and 7.

The significant decrease in the absolute temperature change upon removal of a magnetic field oriented perpendicular to the plate has important consequences for magnetic cooling. Here, the temperature increase and decrease in a magnetocaloric material caused by application or removal of an applied magnetic field replaces the compression and expansion of a gas used in conventional cooling; for a review of magnetic cooling see Ref. 11. Therefore, increasing the magnitude of the adiabatic temperature change improves the efficiency of the cooling, hence making it important to choose geometries of the magnetocaloric materials and an orientation of the applied field, which minimize the demagnetizing field.

Furthermore, Fig. 3 suggests that a detailed description of the adiabatic temperature change requires a spatial resolution due to the observed inhomogeneities. Here, these inhomogeneities are caused by an inhomogeneous applied magnetic field and the demagnetizing field. In addition, numerical simulations[6] predict that the local magnetic field, and consequently the adiabatic temperature change, is highly inhomogeneous when the material is subject to an inhomogeneous temperature distribution or when the Curie temperature varies with position inside the material. Both conditions are often met in magnetic refrigeration as the temperature span between the surrounding and the inside of the refrigerator causes the magnetocaloric material to experience a temperature gradient. Since the adiabatic temperature change is maximized at temperatures around the Curie temperature, one often utilizes graded materials where the Curie temperature changes with position in order to match the temperature gradient. The effect of material grading and the temperature gradient can also be investigated experimentally using the thermographic technique presented here if a heat source and sink is placed in either end of a graded material.

Though the thermographic method described here provides a simple way of mapping the spatial dependence of the local magnetic field and adiabatic temperature change in real-time, it is subject to some limitations. First, the thermographic measurements only probe the surface temperature. Second, only the magnitude of the local magnetic field can be determined making it possible to extract the demagnetizing field from Eq. (1) only when the dominant component of the local magnetic field is along the applied field or when the direction can be deduced from symmetry considerations. For example, consider an applied magnetic field oriented along the x-axis, y-axis or z-axis. For these orientations the local magnetic field must be invariant under 180° rotation around

the axis of the applied field, and consequently the mean of the local magnetic field can only have a nonzero component parallel with the applied field. Third, the material of interest must exhibit a measurable adiabatic temperature change. Several such materials have been reviewed in Ref. 10.

V. CONCLUSION

The spatially varying adiabatic temperature change in a plate of gadolinium was measured directly using thermography, and the adiabatic temperature change was converted into the corresponding change in the local magnetic field strength. The measured change in the temperature and local magnetic field strength was compared to the results from a numerical model, which utilizes a magnetostatic demagnetization approach and experimentally measured data. The model is able to predict both the spatial dependence and the magnitude of the measured temperature and local magnetic field change hence validating the demagnetization approach. The adiabatic temperature change and local magnetic field strength are found to be highly dependent on the orientation of the applied field due to the demagnetizing field.

ACKNOWLEDGMENTS

The authors thank the support of the Programme Commission on Energy and Environment (EnMi) (Contract No. 2104-06-0032), which is part of the Danish Council for Strategic Research.

[1] J. A. Osborn, Phys. Rev. **67**, 351 (1945).
[2] R. I. Joseph and E. Schloemann, J. Appl. Phys. **36**, 1579 (1965).
[3] K. Tang, H. W. Zhang, Q. Y. Wen, and Z. Y. Zhong, Physica B **363**, 96 (2005).
[4] M. Beleggia and M. De Graef, J. Magn. Magn. Mater. **263**, L1 (2003).
[5] O. Peksoy and A. Rowe, J. Magn. Magn. Mater. **288**, 424 (2005).
[6] A. Smith, K. K. Nielsen, D. V. Christensen, C. R. H. Bahl, R. Bjørk, N. Pryds, and J. Hattel, J. Appl. Phys. **107**, 103910 (2010).
[7] C. R. H. Bahl and K. K. Nielsen, J. Appl. Phys. **105**, 013916 (2009).
[8] K. K. Nielsen, R. Bjørk, J. B. Jensen, C. R. H. Bahl, N. Pryds, A. Smith, A. Nordentoft, and J. Hattel, Eighth IIR Gustav Lorentzen Conference on Natural Working Fluids, Copenhagen, September 7–10, 2008.
[9] R. Bjørk, C. R. H. Bahl, and M. Katter, J. Magn. Magn. Mater. **322**, 3882 (2010).
[10] K. A. Gschneidner, Jr., V. K. Pecharsky, and A. O. Tsokol, Rep. Prog. Phys. **68**, 1479 (2005).
[11] K. A. Gschneidner, Jr. and V. K. Pecharsky, Int. J. Refrig. **31**, 945 (2008).

Paper XV

Paper submitted to IEEE Transactions on Magnetics, 2010

Bjørk, R., Bahl, C. R. H., Smith, A., Pryds, N.

Improving magnet designs with high and low field regions

Submitted to IEEE Transactions on Magnetics, 2010

Improving magnet designs with high and low field regions

R. Bjørk, C. R. H. Bahl, A. Smith and N. Pryds
Fuel Cells and Solid State Chemistry Division, Risø National Laboratory for Sustainable Energy
Technical University of Denmark - DTU, Building 228, P.O. Box 49, DK-4000 Roskilde, Denmark
e-mail: rabj@risoe.dtu.dk

***Abstract*—A general scheme for increasing the difference in flux density between a high and a low field region by removing unnecessary magnet material is presented. This is important in, e.g., magnetic refrigeration where magnet arrays has to deliver high field regions in close proximity to low field regions. Also, a general way to replace magnet material with a high permeability soft magnetic material where appropriate is discussed. These schemes are applied to a concentric Halbach cylinder design resulting in a reduction of the amount of magnet material used by 42% while increasing the difference in flux density between a high and a low field region by 45%.**

I. Introduction

Magnetic refrigeration is a potentially highly energy efficient and environmentally friendly cooling technology, based on the magnetocaloric effect. In this technology a magnetocaloric material is moved in and out of a magnetic field, in order to generate cooling. The magnetic field is usually generated by permanent magnets (1; 2). In such magnet designs used in magnetic refrigeration it is very important to obtain a large difference in flux density between the high and the low flux density regions, between which the magnetocaloric material is moved in order to generate the magnetocaloric effect. This is because the magnetocaloric effect scales with the magnetic field to the power of 0.7 near the Curie temperature for most magnetocaloric materials of interest, and in particular for the benchmark magnetocaloric material Gd (3; 4). Because of this scaling it is very important that the magnetic field in a low field region is very close to zero. This is especially a problem in rotary magnetic refrigerators (2; 5; 6; 7) where the high and low magnetic field regions are constrained to be close together. Here it is crucial to ensure that flux does not leak from the high field region into the low field region.

The permanent magnet structure can be designed from the ground up to accommodate this criterion, e.g., by designing the structure through Monte Carlo optimization (8), or by optimizing the direction of magnetization of the individual magnets in the design (9; 10). However, the resulting design may be unsuitable for construction. Here we present a scheme that applied to a given magnet design will lower the flux density in the low flux density region, thus increasing the difference in flux density, and lower the amount of magnet material used at the same time. No general way to improve the flux density difference for a magnet design for magnetic refrigeration has previously been presented.

II. Physics of the scheme

The properties of field lines of the magnetic flux density can be exploited to minimize the magnetic flux in a given area. A field line is a curve whose tangent at every point is parallel to the vector field at that point. These lines can be constructed for any vector field. The magnitude of the magnetic flux density, $\mathbf{B}$, is proportional to the density of field lines. For a two

dimensional problem, as will be considered here, with a static magnetic field, lines of constant magnetic vector potential, A_z, are identical to field lines of $\mathbf{B}$ if the Lorenz gauge, i.e. $\nabla \cdot \mathbf{A} = 0$, is chosen (11). We begin by calculating a field line of the magnetic flux density, $\mathbf{B}$, i.e. an equipotential line of constant A_z, that encloses the area in which the flux density is to be minimized. All field lines enclosed by the calculated field line are confined to the enclosed area as field lines do not cross. These enclosed field lines are creating the flux density inside the calculated area. This procedure will only work for a two dimensional case, as in three dimensions a field line will not enclose a volume. Here a surface of field lines that enclose the volume must be used instead.

If we remove all magnet material enclosed within the chosen field line, it might be thought that no field lines should be present inside the area and the flux density should be zero. However, this is not precisely the case as by removing some magnet material the magnetostatic problem is no longer the same, and a new solution, with new field lines of $\mathbf{B}$, must be calculated. Thus a new field line that confines the area in which we wish to minimize the flux density can be found and the procedure can be iteratively repeated.

It must be made clear that the magnet material inside the calculated field line, i.e. the material that is removed, does contribute a non-zero flux density to areas outside the enclosing field line. This can be seen by considering each little piece of a magnet as a dipole, which will generate a flux density at any point in space. Thus by removing the enclosed magnet material the flux density will also be lowered in the high flux density region. However, this is more than compensated by the lowering of $||\mathbf{B}||$ in the low flux density region, due to the fact that the high flux density region is farther away from the removed material. This makes it possible to increase the *difference* between the high and low flux density regions.

Field lines that do not pass through the high flux density region do not contribute to the flux density there. The scheme can also be used to remove the magnet material enclosed by these field lines.

The scheme must be run until a stopping criterion has been reached. This can be, e.g., that the flux density in the low flux density region has dropped below a certain value or that the volume of magnetic material has been reduced by a certain fraction. This is to ensure that the flux density in the high flux density region is not significantly reduced. In some cases successive applications of the scheme might result in removal of all magnet material. If, for example, one tried to remove the flux density on one side of an ordinary bar magnet by applying the scheme, one would simply remove slices of the bar magnet, until the magnet would be removed completely. This does result in zero flux density, but does not leave any region with flux at all.

As an additional improvement, the removed magnet material can be replaced by a high permeability soft magnetic material, to shield the low flux density area from field lines from the new magnet configuration. This will lower the flux density in the low flux density region further. If the magnet material is replaced by air the scheme is henceforth referred to as improvement scheme (Air), while if magnet material is replaced by soft magnetic material the reference term is improvement scheme (Iron). The difference between these two cases is illustrated in the next section.

Due to the high permeability of the soft magnetic material one would not necessarily have to replace all the enclosed magnet material with a soft magnetic material. Removing the magnet material and using only a small layer of soft magnetic material along the edge of the remaining magnet to shield the low flux density region will in general result in the same magnetic field as replacing all the magnet material with soft magnetic material. This will be an attractive option if the weight of the final assembly is an issue. However, the only difference between these two solutions is the amount of soft

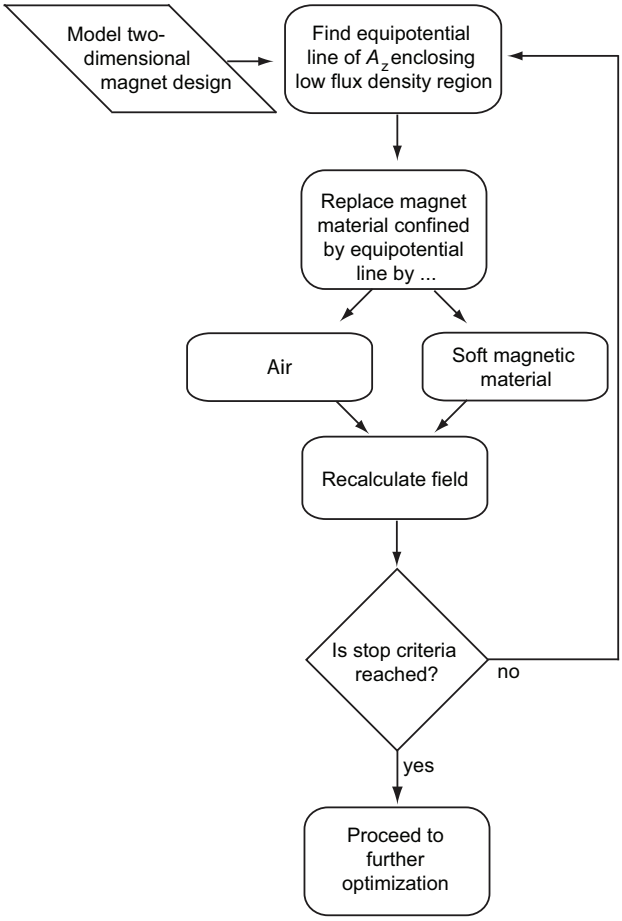

Fig. 1. The flow diagram for the improvement scheme.

magnetic material used, and this option will not be considered further here.

In practice the scheme is implemented numerically and applied to a numerical simulation of a magnet design. The scheme is presented as a flow diagram in Fig. 1.

III. Applying the scheme

The improvement scheme is best illustrated through an example. Here we consider the concentric Halbach cylinder design, which is a cylindrical magnet with an air gap in between an outer and inner cylindrical magnet structure (12). Each cylinder is magnetized such that the remanent flux density at any point varies continuously as, in polar coordinates,

$$\begin{aligned} B_{\mathrm{rem},r} &= B_{\mathrm{rem}} \cos(p\phi) \\ B_{\mathrm{rem},\phi} &= B_{\mathrm{rem}} \sin(p\phi), \end{aligned} \tag{1}$$

where B_{rem} is the magnitude of the remanent flux density and p is an integer (13; 14). The subscript r denotes the radial component of the remanence and the subscript ϕ the tangential component. A positive value of p produces a field that is directed into the cylinder bore, and a negative value produces a field that is directed outwards from the cylinder.

As an example we consider a magnet with four high and four low flux density regions which can be created by having a $p = 2$ outer Halbach cylinder and a $p = -2$ inner Halbach cylinder and with dimensions $R_{\mathrm{inn,int}} = 10$ mm, $R_{\mathrm{inn,ext}} = 120$ mm, $R_{\mathrm{out,int}} = 150$ mm and $R_{\mathrm{out,ext}} = 220$ mm, which are indicated in Fig. 2. The scheme could be equally well applied to any magnetic circuit with adjacent high and low flux density regions where the aim is to increase the difference between these regions.

In the example setup magnets with a remanence of $B_{\mathrm{rem}} = 1.4$ T and a relative permeability of $\mu_{\mathrm{r}} = 1.05$ which are the properties of standard neodymium-iron-boron (NdFeB) magnets (15) are used. We define the high and low flux density regions to be of the same size and to span an angle of 45 degree each.

The improvement scheme will be applied to this design using a numerical two dimensional model implemented in the commercially available finite element multiphysics program *Comsol Multiphysics* (16).

As an equipotential line of A_{z} that encircles the low flux density region is chosen the equipotential line of A_{z} that goes through the point $r = 135$ mm, $\phi = 22.5°$, i.e. the point in the middle of the air gap, half way between the centers of the high and low flux density regions. This equipotential line is shown in Fig. 2(b).

The improvement scheme in which the magnet material is replaced by air is shown in Fig. 3, while the same scheme where the magnet material is replaced by iron is shown in Fig. 4. Iron was chosen as the soft magnetic material because it has a very high permeability as well as being easily workable

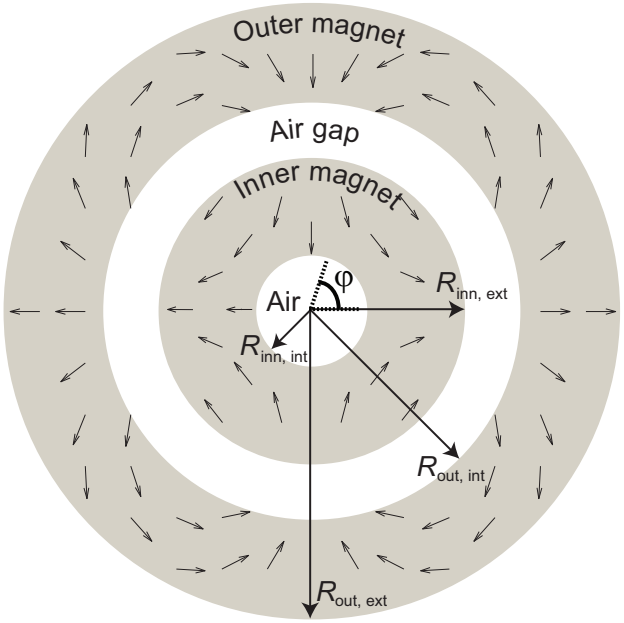

(a) The full concentric Halbach cylinder.

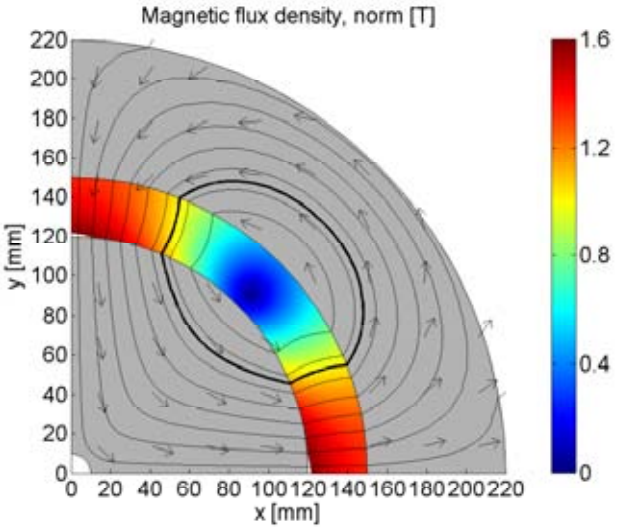

(b) A quadrant of the concentric Halbach cylinder design.

Fig. 2. (Color online) The full concentric Halbach cylinder (a) and a quadrant of the design (b). The magnetization is shown as black arrows on the magnets, which are grey. The flux density in the air gap between the cylinders is shown as a color map. In (b) the equipotential line of A_z which encloses the low flux density region is shown as a thick black line, whereas other contours of A_z are shown as thin black lines. It is magnet material inside the thick black line that is removed.

and reasonably priced.

It is seen that applying the improvement scheme does reduce the flux density in the low flux density region, but the flux density in the high flux density region also decreases as more and more magnet material is removed.

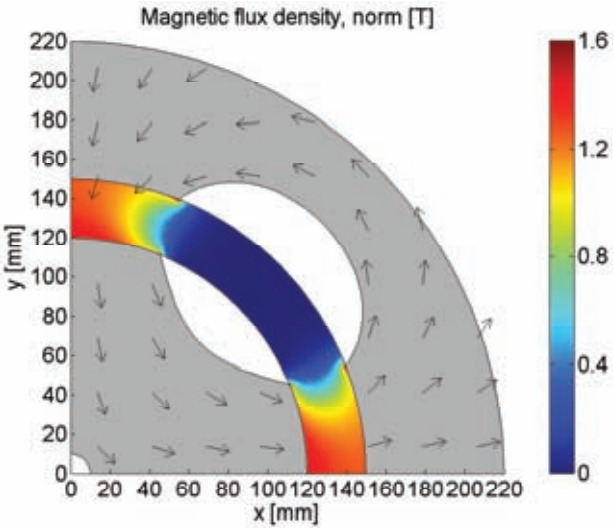

(a) Iteration 1.

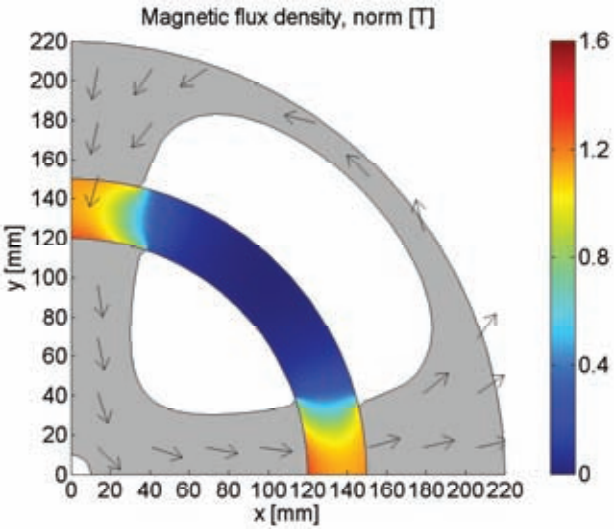

(b) Iteration 6.

Fig. 3. (Color online) The improvement scheme (Air) applied to a quadrant of the magnet design. The first iteration step and the sixth step are shown. The first iteration step corresponds to Fig. 2(b) where the magnet material enclosed by the thick black line has been removed.

The effects of applying the two versions of the improvement scheme are shown in Fig. 5, which shows the magnetic flux density in the middle of the air gap as a function of the angle, ϕ.

It is seen from the figure that some flux is lost in the high flux density region, but the flux density in the low flux density region is also almost completely removed. Substituting with a soft magnetic material lowers the flux density in the low field region more than by substituting with air.

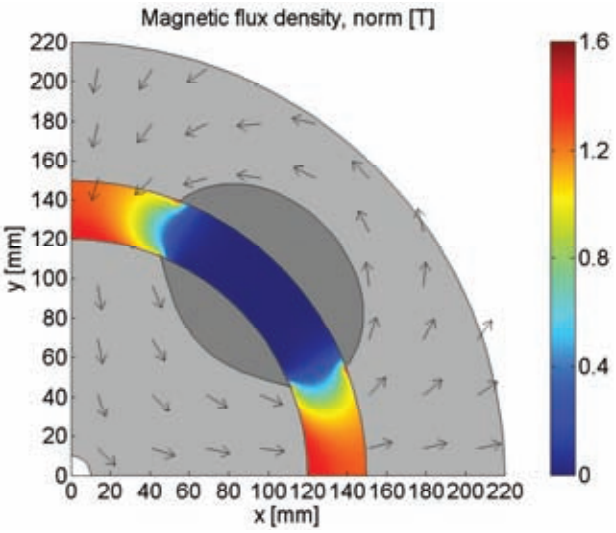

(a) Iteration 1.

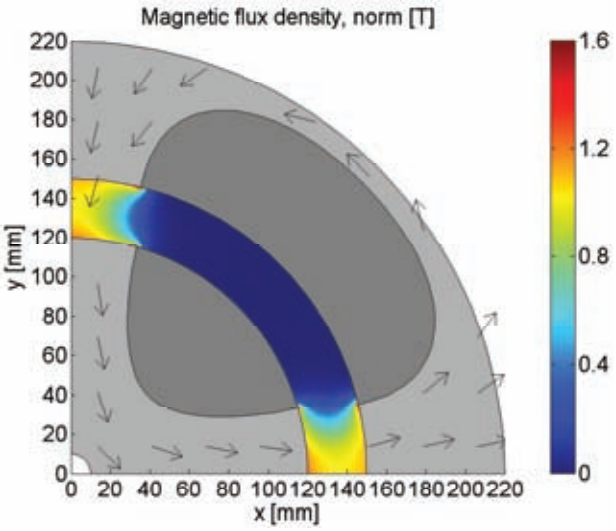

(b) Iteration 3.

Fig. 4. (Color online) The improvement scheme (Iron) applied to a quadrant of the magnet design. The first iteration step and the third step are shown. The first iteration is identical to the first iteration in Fig. 3, expect that iron has been substituted instead of air. Areas of iron are indicated by dark grey.

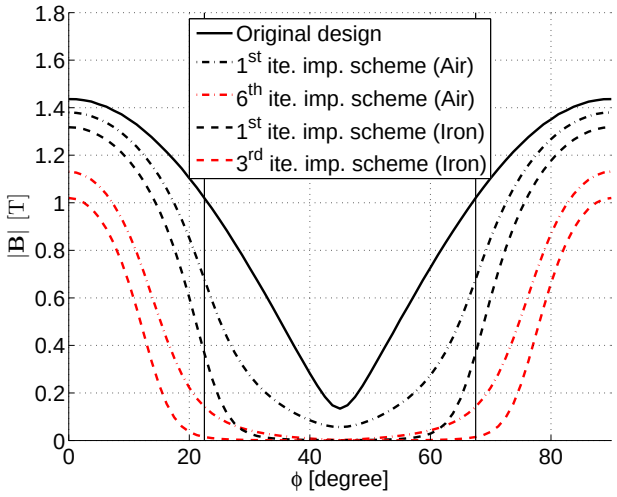

Fig. 5. (Color online) The flux density as a function of angle in the middle of the air gap for the models shown in Figs. 3 and 4. The vertical lines separate the high and low flux density regions.

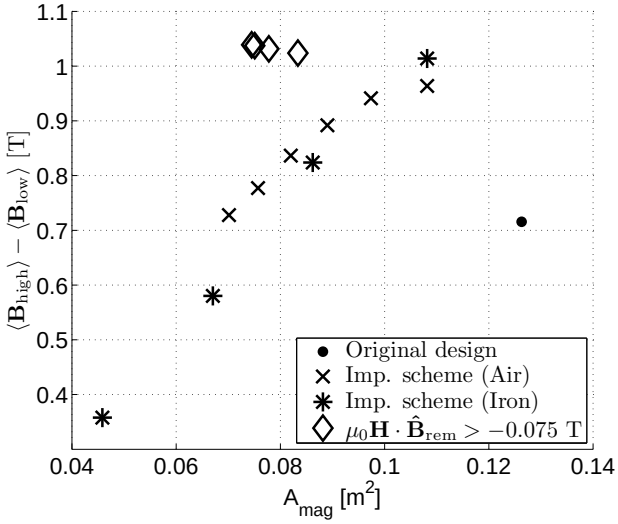

Fig. 6. The difference in flux density as a function of the cross-sectional area of the magnet for the improvement scheme. Decreasing values of A_{mag} indicates further iteration steps. Also shown is the difference in flux gained by replacing magnet material with a high permeability soft magnetic material where the applied magnetic field is parallel or almost parallel to the magnetization. This has been done on the model with a single application of the improvement scheme (Iron), i.e. the model with the highest flux difference.

The effect of applying the scheme is shown in Fig. 6 where the difference in flux density as a function of the cross-sectional area of the magnet is plotted. Both improvement schemes (Air) and (Iron) are shown. As can clearly be seen applying the optimization schemes at first reduces the cross-sectional area of the magnet, A_{mag}, while at the same time improving the difference in flux density between the high and the low flux density regions. The largest difference in flux density is obtained after only one iteration for both the improvement scheme (Air) and improvement scheme (Iron). In the latter case, which is also the best case, the amount of magnet material used is reduced by 15% and the difference in flux density is increased by 41%.

IV. Further design considerations

The magnetic design produced by applying the improvement scheme might not be easily manufacturable, as is the case for the example considered above. Also, for this example the direction of magnetization varies continuously which also unsuitable for manufacturing purposes. To overcome these problems the design must be segmented into regular pieces of permanent magnets, each with a constant direction of magnetization, and pieces of high permeability soft magnetic material. This segmentation can be accomplished in numerous ways, and is in itself a process that must be optimized. It must also be considered whether the added manufacturing cost of the magnet design is worth the increased difference in flux density and the lowered material cost. However, before segmenting a design an additional way of lowering the amount of permanent magnet material used in a given magnet design should also be considered.

As also stated in Ref. (17) and (18) it is advantageous to replace magnet material with a high permeability soft magnetic material if the applied magnetic field is parallel to the remanence. In an ideal hard magnet the anisotropy field is infinite which mean that components of the magnetic field, $\mathbf{H}$, and $\mathbf{B}$ that are perpendicular to the direction of the remanence, $\hat{\mathbf{B}}_{\rm rem}$, have no effect on the magnet. Here $\hat{\mathbf{B}}_{\rm rem} = \mathbf{B}_{\rm rem}/||\mathbf{B}_{\rm rem}||$, i.e. the unit vector in the direction of $\mathbf{B}_{\rm rem}$. Here we also propose to replace magnet material that has a small negative component of $||\mathbf{H} \cdot \hat{\mathbf{B}}_{\rm rem}||$, as this has a poor working point far from the maximum energy density. This will of course affect the flux density generated in the air gap, so care must be taken not to remove to much magnetic material. We thus propose to replace magnet material where

$$\mu_0 \mathbf{H} \cdot \hat{\mathbf{B}}_{\rm rem} > -\gamma \ , \tag{2}$$

where γ is a positive number. The value for γ can be changed depending on the demagnetization curve for the magnet material being used, however in general γ must be chosen small, i.e. on the order of at most 0.1 T.

Having replaced magnet material by soft magnetic material according to Eq. (2) and resolved the magnetic system, the magnet design must be investigated if there are now new regions where Eq. (2) holds and magnet material can be replaced. The result of performing this replacement with a value of $\gamma = 0.075$ T to the model produced by a single application of the improvement scheme (Iron) is shown in Fig. 7. For this model the magnet material is replaced three successive times until the change in magnet volume from one iteration to the next is less than 5%, at which point replacing the small remaining areas does not change the flux density significantly. The result of the replacement is also shown in Fig. 6. By replacing magnet material with high permeability soft magnetic material the amount of magnet material is reduced by an additional 27% compared to the original design while the difference in flux density was increased slightly by 4%, again compared to the original design.

When replacing magnet material by soft magnetic material it is important to ensure that the shapes of the replaced segments are not such that the demagnetization of the segments are high as this can reduce the internal field in the soft magnetic material. However, as a high permeability material is used, even a very small field will cause the material to saturate, and thus this problem can be ignored except for cases with extremely high demagnetization.

As can be seen from Figs. 6 and 7 replacing magnet material with soft magnetic material can also reduce the manufacturability of the magnet design, and thus the same consideration as with the improvement scheme applies. Here we will not consider segmentating the concentric Halbach cylinder design, as the design is only meant to serve as an example and also because no clear optimum segmentation procedure can be suggested. In Ref. (19) we apply the present improvement schemes to a magnet design which is then segmentated and constructed. The resulting magnet show high performance for magnetic refrigeration.

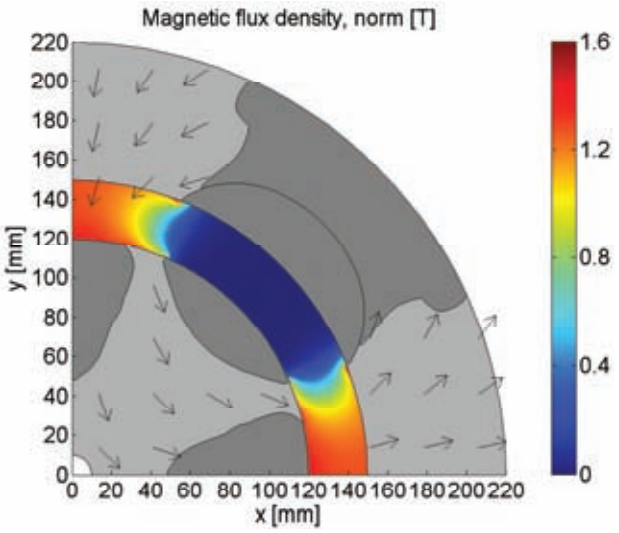

Fig. 7. (Color online) Replacing magnet material with a high permeability soft magnetic material where the applied magnetic field is parallel or almost parallel to the remanence on the model shown in Fig. 4 (a) three successive times results in the magnet design shown. The line in the iron region in the outer magnet separates the iron regions generated by the improvement scheme and the parallel replacement method and it is only shown for reference.

V. Conclusion

An algorithm for improving the difference in flux density between a high and a low flux density region in an air gap in a magnetic structure has been presented and as an example applied to a concentric Halbach magnet design. For the design considered, applying the scheme reduces the amount of magnet material used by 15% and increases the difference in flux density by 41%. For the design considered here it was also shown that by replacing magnet material with a high permeability soft magnetic material where the applied magnetic field is parallel or almost parallel to the remanence the amount of magnet material used can be reduced by an additional 27% compared to the original design while the difference in flux density was increased slightly by 4%, again compared to the original design.

Acknowledgements

The authors would like to acknowledge the support of the Programme Commission on Energy and Environment (EnMi) (Contract No. 2104-06-0032) which is part of the Danish Council for Strategic Research.

References

[1] K. A. Gschneidner Jr and V. K. Pecharsky, Int. J. Refrig. 31 (6), 945 (2008).

[2] R. Bjørk, C. R. H. Bahl, A. Smith, and N. Pryds, Int. J. Refrig. 33, 437 (2010).

[3] V. K. Pecharsky and K. A. Gschneidner Jr, Int. J. Refrig. 29 (8), 1239 (2006)

[4] R. Bjørk, C. R. H. Bahl and M. Katter, Submitted to J. Magn. Magn. Mater. (2010).

[5] T. Okamura, R. Rachi, N. Hirano, and S. Nagaya, Proc. 2nd Int. Conf. on Magn. Refrig. at Room Temp. 377 (2007).

[6] C. Zimm, J. Auringer, A. Boeder, J. Chell, S. Russek, and A. Sternberg, Proc. 2nd Int. Conf. on Magn. Refrig. at Room Temp., 341 (2007).

[7] J. Tušek, S. Zupan, A. Sarlah, I. Prebil, and A. Poredos, Proc. 3rd Int. Conf. on Magn. Refrig. at Room Temp., 409 (2009).

[8] W. Ouyang, D. Zarko, T. A. Lipo, Conference Record of the 2006 IEEE Industr. Appl. Conf. Forty-First IAS Annual Meeting 4, 1905 (2006).

[9] A. E. Marble, IEEE. Trans. Mag. 44 (5), 576 (2008).

[10] J. Choi and J. Yoo, IEEE. Trans. Mag. 44 (10) (2008).

[11] Z. Haznadar, and Z. Stih. Electromagnetic Fields, Waves and numerical methods. IOS Press (2000).

[12] R. Bjørk, A. Smith, and C. R. H. Bahl, J. Magn. Magn. Mater. 322, 133 (2010).

[13] J. C. Mallinson, IEEE Trans. Magn. 9 (4), 678 (1973).

[14] K. Halbach, Nucl. Instrum. Methods 169 (1980).

[15] Standard specifications for permanent magnet materials, Int. Mag. Assoc., Chicago, USA, (2000).

[16] COMSOL AB, Tegnrgatan 23, SE-111 40 Stockholm, Sweden.

[17] F. Bloch, O. Cugat, G. Meunier, and J. C. Toussaint, IEEE Trans. Magn. 34 (5), 2465 (1998).

[18] J. M. D. Coey and T. R. Ni Mhiochain, Permanent magnets. In: High Magnetic Fields, Edt: F. Herlach and N. Miura, World Scientific Publishing, 25 (2003).

[19] R. Bjørk, C. R. H. Bahl, A. Smith, D. V. Christensen and N. Pryds. Accepted for publication in J. Magn. Magn. Mater., (2010).

Paper XVI

Paper submitted to Journal of the American Ceramic Society, 2010

Pryds, N., Clemens, F., Menon, M., Nielsen, P. H., Brodersen, K., Bjørk, R., Bahl, C. R. H., Engelbrecht, K., Nielsen, K. K. and Smith, A.

Monolithic perovskite for magnetic regenerator

Journal of the American Ceramic Society, 2010

A Monolithic Perovskite structure for use as a Magnetic Regenerator

***Nini Pryds*[*], *Frank Clemenc*[**], *Mohan Menon*[*], *Pernille H. Nielsen*[*], *Karen Brodersen*[*], *Rasmus Bjørk*[*], *Christian R. H. Bahl*[*], *Kurt Engelbrecht*[*], *Kaspar K. Nielsen*[#*], *Anders Smith*[*]**

[*]Fuel Cells and Solid state Chemistry Division, Risø DTU, Technical University of Denmark, DK-4000, Roskilde, Denmark, [**]EMPA Dübendorf, Laboratory for High Performance Ceramics, Überlandstrasse 129, 8600 Dübendorf, Switzerland, [#]Technical University of Denmark, Department of Mechanical Engineering, Produktionstorvet, building 425, 2800 Kgs. Lyngby, Denmark

ABSTRACT: A $La_{0.67}Ca_{0.26}Sr_{0.07}Mn_{1.05}O_3$ (LCSM) perovskite was prepared for the first time as a ceramic monolithic regenerator used in a regenerative magnetic refrigeration device. The parameters influencing the extrusion process and the performance of the regenerator, such as the nature of the monolith paste and the influence of the sintering on the adiabatic temperature change, were investigated. Comparisons between the extruded monolithic structure before and after the sintering showed that an increase of the adiabatic temperature change was seen after the sintering. Furthermore, calculations show that the performance of the monolithic structure is potentially superior to a parallel plate regenerator, indicating the potential cost and structural benefit of using such structure, i.e. a mechanically stable ceramic thin wall structure which can be produced in one processing step.

*Author to whom correspondence should be addressed. E-mail: nipr@risoe.dtu.dk

Introduction

Magnetic refrigeration is a promising technology for energy efficient and environmentally friendly space cooling and refrigeration. The technology uses magnetic materials as the active components and non-volatile fluids, e.g. water, for heat transfer[1]. The temperature of magnetic materials changes when they are subjected to a change in magnetic field. This so-called magnetocaloric effect is due to interaction of the spin and lattice degrees of freedom of the magnetic material. The magnetic field aligns the spins, lowering their entropy; which, under adiabatic conditions, leads to higher lattice entropy resulting in an increase of the temperature of the material. The adiabatic magnetisation/demagnetisation cycle is reversible for LCSM, and the theoretical efficiency of the entire cooling cycle may be as much as 60% greater than for conventional compressor based refrigerators [2].

A wide range of different types of materials, from metals to ceramics, exhibit the magnetocaloric effect [3]. Generally, the magnetocaloric effect manifests itself as a reversible increase in temperature when the magnetic material is placed in a magnetic field, and the maximum magnetocaloric effect occurs near the Curie temperature. The process of choosing a magnetocaloric material for a specific magnetic refrigeration application is complex. A large magnetocaloric effect, corrosion resistance, the ability to adjust the Curie temperature, ease of fabrication, and cost are important in nearly every practical application. Magnetic ceramics materials are very stable at room temperature, can be compositionally tuned to adjust the Curie temperature, and do not corrode in water. This makes them an attractive option for use as regenerators for magnetic refrigeration systems. Families of functional materials with a large magnetocaloric effect (MCE) have been found in several perovskite-type manganese oxides such as Ca- and Sr-doped lanthanum manganites, $La_{0.67}Ca_{0.33-x}Sr_xMnO_{3\pm\delta}$ ($0 \leq x \leq 0.33$)[4]. These samples show a substantial magnetocaloric effect (e.g. ΔT~0.5-1.4K depending on the exact composition) in a temperature range around their respective Curie temperature which makes the

compounds suitable for air-conditioning and refrigeration applications. By varying the composition parameter $\boldsymbol{x}$ the Curie temperature can be adjusted between 267 K ($\boldsymbol{x}$ = 0) and 369 K ($\boldsymbol{x}$ = 0.33)[4],

The performance of the magnetic refrigeration system is strongly affected by the heat transfer and magnetocaloric characteristics of the regenerator and its geometry[5,6]. Perovskite-type oxides can be processed into different geometries such as parallel plates and monolithic perforated cylinders which may have much lower pressure losses than typical magnetic regenerator geometries such as packed particles. For a regenerator consisting of magnetocaloric plates, reducing the regenerator plate thickness as well as the gap distances between the plates can improve the regenerator performance[5,7]. However, a reduction of wall thickness causes a reduction of the mechanical strength and makes the fabrication of such a regenerator very difficult, especially when it must be assembled with hundreds of plates separated by small distances of 0.1-0.5 mm. In order to overcome this problem, a single monolithic structure is suggested. Achieving the goal of producing a one-piece magnetic regenerator can be a breakthrough in the manufacturability and commercialization of a magnetic cooling device. Monolithic structures can be viewed as two-dimensional assemblies of long, parallel channels through which the heat transfer fluid may flow. Fine monolithic structures have the following benefits: (1) the surface area is increased and thereby the heat transfer to and from the fluid medium, (2) the channels are straight and parallel so that the flow is not obstructed and the pressure drop across the monolith is low and (3) a complete complex monolithic structure is made as a single part. Monolithic structures are often produced through the process of extrusion. These complex structures have been used so far almost exclusively for catalytic systems in power plant and automotive emission control systems[8].

In the present work, the fabrication of a monolithic regenerator for magnetic refrigeration, made of a perovskite type ceramic material using a thermoplastic extrusion process, was investigated. The fabrication of such a magnetic refrigeration regenerator made of complex

ceramic powders has not previously been reported and it is the main topic of this work. To optimize the extrusion process the different process parameters are investigated, including the effect of mixing ratios (vol% binder/vol% powder) on the homogeneity of the feedstock and the pressure drop during extrusion. The fabricated monolithic regenerator is tested and evaluated in a magnetic cooling device from which preliminary results are presented.

Experimental procedure

Powders with the composition of $La_{0.67}Ca_{0.26}Sr_{0.07}Mn_{1.05}O_3$ (LCSM) were prepared by the solid-state reaction (SSR) method with the starting materials Calcium oxide (CaO, 99.9%), Lanthanum oxide (La_2O_3, 99.99%), Manganese oxide (MnO_2, 99.9%) and Strontium carbonate ($SrCO_3$, 99.9%). The powder was then calcined at an elevated temperature of 1473 K (heating and cooling rate of 100 K/h) for 16 h followed by additional heat treatment at 1573 K (heating and cooling rate of 100 K/h) for additionally 6 h. After calcination and ball milling, the powder was coated with stearic acid (97% pure stearic acid, Fluka Chemie AG). The coating method procedure has been described previously[9]. Before the coating process the specific surface area and the density of the powder were measured using BET (SA3100, Beckman-Coulter Inc) and a helium pycnometer (Micromeritics, AccuPyc 1330), respectively. To achieve sufficient plasticity for the honeycomb production, a thermoplastic binder system based on low density polyethylene (PEBD 1700MN 18C – Lacqtene Elf Atochem S.A.) was used. The two main advantages in using thermoplastic binder systems and not the conventional water based feedstocks are (1) possible formation of carbonates is avoided and (2) phase separation due to the high extrusion pressure can be eliminated easily. In a first series, blends with three different contents of stearic acid coated LCSM powder were mixed (HAAKE PolyLab Rheomix 600, Thermo Fisher Scientific) and the viscosity was evaluated using a capillary rheometer (RH7-2 Flowmaster, Rosand Precision Limited, Malvern) with a 1 mm capillary die configuration. Based on the results from these investigations, a 52 vol.% LCSM compound was prepared with a high shear mixer (HAAKE

PolyLab Rheomix 3000, Thermo Fisher Scientific). To achieve a homogenous ceramic-polymer blend, the composition was mixed with roller blade rotors and a frequency of 10 rpm until the torque reached equilibrium. The extrusion was performed in a pilot-scale piston extruder with a cylinder diameter of 45 mm and heating option up to 523 K at EMPA, Switzerland. The die head honeycombed structures (36 mm in diameter, 0.5 mm wall thickness and 1 mm channel width) were first extruded with a SiC (Silicon Carbide) paste in order to polish the die head channels. In order to keep the flows of the feedstock continuous without blocking the extruder head during the process, the whole setup was preheated to a temperature between 423 K and 473 K for about 30-40 min. before and during the extrusion process. The speed of the piston varies between 5 and 50 mm/min. Following the extrusion, sintering took place under the following conditions: (1) heating the sample to 473 K at a rate of 60 K/h, (2) heating to 593 K at 10 K/h and holding the sample for 2 h, (3) heating to 973 K at 5 K/h and finally (4) heating to 1523 K at 30 K/h for 0.5 h and cooling down to room temperature at 50 K/h. The powders and the sintered samples were checked by X-ray diffraction using a STOE diffractometer with Cu-K_α radiation and differential scanning calorimetry (DSC) using a Netzsch DSC 200F3 Maia for phase purity and their magnetic transition temperatures. The Curie temperatures were defined as the position of the maximum peak heights of the phase transition peaks.

Results

Preparation of the powder and the feedstocks

Before preparation of the feedstock, the powder was ball milled to an average grain size of approximately 2 µm as confirmed by laser scattering particle analysis and XRD patterns were then taken from the LCSM sample after the calcination. The observed peaks in XRD patterns after the calcinations confirmed that the sample remained single phase without any secondary phase. All the observed peaks were assigned to the formation of a crystalline perovskite phase (based on JCPDS data). The heat capacity and the transition temperature of the LCSM were

measured from the DSC at zero magnetic field, see Fig. 1. From the DSC measurement the transition temperature was found to be 290 K, as was expected for this composition[9]. One of the main parameters in the preparation of the feedstock is to maximize the powder volume fraction in the compound in order to ensure extrudability and to ensure that there is no contamination after kneading and extrusion. Maximizing the amount of powder has another important outcome as the cooling capacity of a magnetic refrigeration device is directly related to the amount of magnetocaloric material. To achieve this, LCSM powder and polyethylene were mixed in different volume ratios to get a stable and reproducible mixing process and to reach a homogeneous distribution of the ceramic particles in the thermoplastic matrix. The density and surface area of the uncoated powder were 5.68 g/cm^3 and 4.21 m^2/g, respectively. Figure 2 shows the pressure versus the extrusion speed for powder content between 52 and 58 vol.%, measured in front of a capillary die with a diameter of 1 mm and a length of 16 mm. These results confirmed high viscosity of the mixture where 58 vol% ceramic powder was used, compared to the other mixtures with lower powder content. Fig. 2b presents apparent viscosity curves depending on shear rate and ceramic powder portion.

A general challenge in extrusion is the dimensional control, i.e. maintaining uniform shrinkage during drying and sintering. The shrinkage of these mixtures measured for different volume fraction of the ceramic feedstock show that, for the investigated ratios, the variation in the shrinkage of the volume contraction is approx. 40-45% regardless of the fraction of powder/binder. The highest volume fraction that was therefore used 58 vol% of LCSM and 42 vol% binder, giving a ratio of 1.38.

Extrusion and sintering of the monolithic structure

A die head with the dimensions that give an extruded part which fits the magnetic refrigeration test device has been designed, taking into account the experimentally determined shrinkage. Based on obtained results and the pressure limitation of the die head, a mixture of 650 g LCSM

powder, 19 g stearic acid and 74 g polyethylene binder was used to extrude the honeycomb structure in this study, which is equal to the 52 vol.% powder content (ratio of 1.38). The wall thickness (for each channel) and channel width of the extruded honeycomb were designed to be 0.5 and 1.0 mm, respectively.

Prior to the final extrusion experiment, tests were performed at different temperatures and piston velocities. Good monolithic structures could be extruded at 423 K with a piston speed of 5 mm/min. A piston force of 4 kN, corresponding to a pressure of 2.5 MPa, was necessary to extrude the 52 vol.% LCSM compound through the orifice of the honeycomb die. Increasing the piston speed from 5 to 50 mm/min, the corresponding pressure increased up to 22 MPa which is significantly over the maximum allowed pressure of the honeycomb die (10 MPa). Decreasing the temperature to 403 K, the pressure reached a maximum of 13 MPa when using a piston speed of 5 mm/min.

A monolithic squared microchannel structure with a wall thickness of approx. 0.5 mm was fabricated and is shown in Figure 3. A slight distribution in wall-thickness can be seen and some channels also seem to be slightly skewed. Spatial variations in the mold might be the reason for this. After cooling the monolith was cut to a length of 4 cm corresponding to the length of the regenerator. Due to the fact that the fraction volume of the binder was relatively high, the monolith could not maintain its shape upon sintering. Furthermore, the binder burnout has not been optimized with respect to heating rates and holding temperatures which resulted in the sagging of the monolith. Thus, for the present implementation of the monolith in the magnetic refrigeration test device we have chosen to use the unsintered monolith as a regenerator. Hence, the total weight of the monolith contains both the LCSM and the binder, thus lowering the magnetocaloric effect.

Measurement of the magnetocaloric effect and the performance of the monolith

The adiabatic temperature change, ΔT_{ad}, is the temperature increase or decrease of a magnetocaloric material upon application or removal of a magnetic field under adiabatic conditions. Samples taken from the monolith before and after sintering have been measured in a ΔT_{ad} measurement device at Risø DTU[10]. The results are shown in Fig. 4. Measurements were done with an applied magnetic field change of 1 T, as this is in the range of practical magnetic fields for a commercial magnetic refrigerator. Demagnetization effects due to the shape of the sample have been taken into account and the internal fields of the samples during the measurements is indicated in the upper scale of Fig.4.

As expected, there is a significant difference between ΔT_{ad} in the two measurements. The lower value for the sample prior to sintering is partly due to the dilution of the thermal mass of the magnetocaloric material with the thermal mass of the binder material. Also, the LCSM powder prior to sintering may be of a more nano-crystalline nature. In similar materials, this has previously been observed to lead to a reduction of the magnetocaloric effect along with a broadening of the phase transition[11,12].

Differential scanning calorimetry was performed using a device built at Risø DTU in which samples can also be subjected to an applied magnetic field[17]. The samples in zero applied magnetic field shows a peak at the Curie temperature of the sintered sample with a value close to the expected[4]. In a magnetic field of 1 T the peak in heat capacity is broadened, as expected. However, in the unsintered sample at zero magnetic field there is no distinct clear peak (see Fig. 5). This may be due to a broadening of the transition, due to nano-crystallinity or a non-uniform composition. The increased level of the measured heat capacity is due to the high heat capacity of the binder (about 2000 J/ kg K) compared to LCSM (Fig. 5). Table 1 summarizes the results of these investigations.

A reciprocating active magnetic regenerator test machine has been used to test the monolith. The magnetic field is provided by a Halbach cylinder type permanent magnet with an average

flux density in the bore of 1.03 T. The magnet, which is described by Bjørk et al.[13], has a bore of 42 mm and a height of 50 mm. Magnetisation and demagnetisation of the regenerator is achieved by moving the regenerator vertically relatively to the stationary magnet by means of a stepper motor. The test device is described in more detail by Bahl et al.[1]. In order to determine the best operating parameters, preliminary tests of the monolithic regenerator (81.7 g) were carried out for a range of experiments where the fluid flow rates, piston stroke lengths and cycle times were varied. In these preliminary results, a maximum temperature span of 0.9 K for the non-sintered regenerator was found for a piston stroke of 9 mm, fluid velocity of 1 mm/s and a cycle time of 21 s. For comparison with the performance of other magnetic refrigeration devices the value of the utilization was calculated using the following equation

$$\varphi = \frac{\dot{m} c_{p,f} P}{m_s c_{p,s}} \quad (1)$$

where the mass flow rate of the heat transfer fluid is denoted $\dot{m}$, the flow period of either blow is P and the mass of the regenerator is m_s. Subscripts f and s denote fluid and solid, respectively. The utilization is a dimensionless number, which describes the amount of moved thermal fluid mass to the amount of thermal mass in the regenerator. For the optimal operating conditions presented here the value of the utilization is 0.18.

Passive regenerator experiments

Regardless whether the regenerator is operated as an Active Magnetic Regenerator (AMR) or as a passive regenerator the regenerator geometry has a large impact on the device performance.

A highly effective passive regenerator will in general also perform well when operated actively.

In the following experiments the extruded monolithic structured regenerator was therefore tested as a passive regenerator. In devices using passive magnetic or nonmagnetic materials, a thermal wave-front propagates back and forth within the regenerator. In this mode the applied magnetic field remains zero throughout all experiments. One end of the regenerator exchanges heat with

the ambient through a secondary heat exchanger thus maintaining the ambient temperature at that end at all times. At the other end of the regenerator an electric heater is situated. In this way a temperature difference between the two ends may be obtained and maintained by the regenerative process. The effectiveness of such a passive regenerator is given by[14]

$$\mathbf{Eff} = \mathbf{1} - \frac{\int_0^{\tau} [(T]_{hot} - T_{f,exit}) dt}{T_{hot} - T_{cold}} \quad (2)$$

where T_{hot} is the temperature at the end of the regenerator with the heater, T_{cold} is the temperature at the end of the regenerator thermally connected to the ambient and $T_{f,exit}$ is the temperature of the fluid exiting the regenerator. Finally, the total cycle time is denoted τ. Equation 2 can interpreted as one minus the heater power necessary to maintain a reservoir temperature divided by the maximum energy required to heat the fluid from the cold reservoir temperature to the hot temperature. For the experiments considered here, the heater power in the hot reservoir is held constant and the cold reservoir temperature is fixed. Therefore, the temperature span achieved in each experiment is a direct measurement of the regenerator effectiveness. Thus, the passive regenerator performance is reported as the temperature span in this work.

Numerical model

In order to evaluate the experimental results obtained from operating the monolithic structure passively, a well-established numerical model was used to predict the regenerator performance in terms of expected temperature spans. The model is one-dimensional and it solves the governing regenerator equations for the coupled heat transfer between a solid and a fluid in counter-flow

operation. The model is presented in detail in ref. 15 and it is available for public usage. The governing equations solved are

$$A\epsilon\rho_f c_f \frac{\partial T_f}{\partial t} = -\dot{m}c_f \frac{\partial T_f}{\partial x} - \frac{Nuk_f}{D_h} aA(T_f - T_s) \quad (3)$$

$$A(1-\epsilon)\rho_s c_s \frac{\partial T_s}{\partial t} = \frac{Nuk_f}{D_h} aA(T_f - T_s) \quad (4)$$

where A, ϵ, ρ_f, c_f, $\dot{m}$, T_f, Nu, k_f, D_h, a, T_s are the cross sectional area, porosity of the structure, mass density of the heat transfer fluid, specific heat of the heat transfer fluid, mass flow rate, temperature of the fluid, the Nusselt number describing the heat transfer between the solid and fluid, thermal conductivity of the fluid, hydraulic diameter of the regenerator, specific surface area of the regenerator and temperature of the solid, respectively. The equations are solved in time and space along the direction of the flow.

Several parameters are needed for the model. The specific surface area is found as the wetted perimeter of one channel divided by the unit cross section of a channel, which is this case corresponds to $a = {4 \times 1 \text{ mm}}/{(1.5 \text{ mm})^2} = 1778 \text{ m}^{-1}$. The porosity is given by the void cross section fraction of the unit cross section of a channel, i.e. $\epsilon = {(1 \text{ mm})^2}/{(1.5 \text{ mm})^2} = 0.44$. Finally, the hydraulic diameter is given by four times the flow cross sectional area divided by the wetted perimeter of one channel, i.e. $D_h = {4(1 \text{ mm})^2}/{4 \times 1 \text{ mm}} = 1 \text{ mm}.$

For square channels, as considered here, the Nusselt number has been found to be 2.98[16].

Experimental and modeling results

The thermal utilization, as defined in Eq. (1), and the mass flow rate were varied for different values of the heater power. In this way the temperature span of the regenerator, when operating passively, could be obtained throughout a relevant parameter space. The results presented in Fig. 6 were obtained with a heater power of 0.4 W and those in Fig. 7 at a heater power of 1.7 W. In

both figures the temperature span, i.e. the difference between the hot and cold side temperatures, is given as a function of the thermal utilization and at different mass flow rates.

The model predictions are seen to be in qualitatively good agreement with the experimental results. The trend as a function of the utilization is clear. At higher utilizations the temperature span decreases and thus the effectiveness of the regenerator is degraded. It is also evident from the results that at larger mass flow rates the regenerator is less efficient than at the smaller mass flow rate. This is explained from the fact that as the mass flow rate increases the fluid velocity will increase also. The time for local heat transfer between the solid and the fluid is thus decreased and is therefore less efficient resulting in an overall less efficient regenerator. The model is based on a single perfect channel of the monolith. Although, as mentioned before, some of the channels seem to be slightly skewed the model was able to capture correctly the behavior of the regenerator. These results indicate indirectly that the overall geometry of the monolithic regenerator after extrusion is as expected on average without major distortion of the shape which could affect the performance.

Discussion

Much of the effort to improve the performance of magnetic refrigeration is centered on the search for new magnetic materials with a large magnetocaloric effect and new designs of permanent magnet systems producing strong magnetic fields. However, the geometry of the regenerator has an equally large impact on the device performance. Even so, the question of the processability of candidate magnetocaloric materials into a relevant geometry has hitherto not been experimentally investigated in much detail. In this study, we have succeeded in fabricating for the first time a monolithic ceramic regenerator made of LCSM.

The key to the fabrication of high quality monolithic structure lies in the quality of the extrusion dies and in achieving a lower viscosity with a higher solid loading of the LCSM material. As discussed above, polymeric additives are necessary to provide sufficient plasticity for the material

to be extruded. The demand to provide sufficient plasticity for the material introduces other difficulties, such as diluting the magnetocaloric effect and the lack of rigidity of the structure during sintering if the ratio powder/binder is low. The amount and type of plasticizers added is determined by empirical evaluation rather than by scientific approach. Indeed, this remains one of the most poorly understood areas of ceramic processing. Sintering is an essential step in producing a dense and structurally stable ceramic microstructure. In the present investigation, a tendency of the structure to collapse was observed during sintering for the extruded material with the high powder volume fraction content. The tendency to collapse is associated with the presence of excess polymer between the oxide particles, which accounts for the viscoplastic creep which makes the structure too soft to retain its shape. Water based paste might be a promising route in the future to avoid this problem.

Taking into consideration the fact that the monolith was not sintered, i.e. the ΔT_{ad} is only 0.26 K, the results indicate that during the testing of the monolith, the measured temperature span was found to be almost four times larger than the adiabatic temperature change suggesting the possibility for good future performance of such a structure providing that the binder is removed. For a better monolith performance, the external parameter such as the channel dimension, i.e. the wall thickness, needs to be optimized for high kinetic performance balanced against low pressure drop regardless of whether the monolith in a non-sintered or sintered state.

Parallel plate regenerators with small plate spacings (1 mm or less) received a huge interest owing to their theoretically high thermal performance (i.e., high heat transfer coefficient due to a large specific surface area) with low pressure drops. However, a novel manufacturing technique offers the possibility to obtain a monolithic ceramic structure which overcomes some of the limitations of producing parallel plate regenerator by increasing the surface area while maintaining a high amount of material and structural rigidity of the structure. Figure 8 shows a comparison between a parallel plate and monolithic regenerator. The plate regenerator performance was predicted for a regenerator with 1 mm plate spacing and a plate thickness of

1.27 mm, resulting in porosity equal to the monolithic regenerator. As seen from this figure the characteristics provided by the monolithic design seem to be similar to parallel plate. However, the monolithic structure provide a larger surface area for heat transfer of the MCM and more importantly the intrinsic brittle character of the ceramic materials is overcome by making the regenerator monolithic leading to a stable structure which can be produced by one processing step. Although the passive regenerator performance could not be compared directly to an active regenerator the present results indicate that the monolithic regenerator perform well as a passive regenerator. These results indicated that if we are able to sinter the monolith, and by that obviously removing the binder, we can achieve a high performance of the active regenerator.

Further work on understanding the parameters influencing the extrudability of magnetic regenerators as well as the parameters influencing the sintering of the monolith is needed.

Conclusion

$La_{0.67}Ca_{0.26}Sr_{0.07}Mn_{1.05}O_3$ (LCSM) perovskite was prepared for the first time as a ceramic monolith for use as a magnetic regenerator. The parameters influencing the extrusion process and the performance of the regenerator, such as the nature of the monolith paste and the influence of sintering on the adiabatic temperature change, were investigated. A tendency of the structure to collapse was observed during sintering due to the high ratio of binder to powder.

The present results indicate that the monolithic regenerator perform well as a passive regenerator suggesting that if we are able to sinter the monolith while maintain its shape we can achieve a high performance of the active regenerator. Further comparison between a parallel plate regenerator and monolith structure show similar performance indicating the potential financial and structural benefits of using such a structure, i.e. a stable ceramic thin wall structure which can be produced by a one-step processing technique.

Acknowledgements

The authors thank Mr. Jørgen Geyti for his technical help as well as Dr. Carlos Eugenio Ancona-Torres for helping with the DSC measurements. This project is supported by the Programme Commission on Energy and Environment (EnMi) (Contract no. 2104-06-0032) which is part of the Danish Council for Strategic Research.

References

[1]C. R. H. Bahl, T. F. Petersen, N. Pryds, A. Smith, A versatile magnetic refrigeration test device, Review of Scientific Instruments, **79** [9] 093906 (2008).

[2]C. R. H. Bahl, A. Smith, N. Pryds, S. Linderoth, Magnetic Refrigeration – an Energy Efficient Technology for the Future, Presented at: Risø International Energy Conference 2009. Risø (DK), 14 – 16 Sep., 2009, In: Energy solutions for CO2 emission peak and subsequent decline: Proceedings, p. 107-115-Roskilde : Risø National Laboratory for Sustainable Energy, 2009

[3]K. Gschneidner, V. Pecharsky, A. Tsokol,. Recent developments in magnetocaloric materials. Rep. Prog. Phys., **68** 1479–1539 (2005)

[4]Dinesen A R, Linderoth S and Mørup S, Direct and indirect measurement of the magnetocaloric effect in $La_{0.67}Ca_{0.33-x}Sr_xMnO_{3+/-\delta}$ (x is an element of [0; 0.33]). J. Phys.: Condens. Matter, **17** 6257-6269 (2005)

[5]L. Peng, G. Maoqiong and W.Jianfeng, Geometric optimization of an active magnetic regenerative refrigerator via second-law analysis, J. Appl. Phys., **104** 103536 (2008)

[6]K.K. Nielsen, C.R.H. Bahl, A. Smith, N. Pryds, J. Hattel, A comprehensive parameter study of an Active Magnetic Regenerator using a 2D numerical model, Int. J. Refrig. **33** 753-764 (2010)

[7]P. Li, M. Gong, G. Yao and J. Wu, "A practical model for analysis of active magnetic regenerative refrigerators for room temperature applications", International Journal of Refrigeration, **29** 1259-1266 (2006),

[8]P. Avila, M. Montes and E. E. Miró, Monolithic reactors for environmental applications A review on preparation technologies, Chemical Engineering Journal, **109** 11–36 (2005)

[9]P. Bardhan, Ceramic honeycomb filters and catalysts, Current Opinion in Solid State and Materials Science, **2** [5] 577-583 (1997)

[9]Heiber, J., Clemens, F., Graule, T. and Hülsenberg, D., Thermoplastic extrusion to highly-loaded thin green fibres containing $Pb(Zr,Ti)O_3$. Adv. Eng. Mater., **7** 404–408 (2005)

[10]R. Bjørk, C. R. H. Bahl and M. Katter, Magnetocaloric properties of $LaFe_{13-x-y}Co_xSi_y$ and commercial grade Gd, Journal of Magnetism and Magnetic Materials, **322**, 3882-3888 (2010).

[11]M. Pękała and V. Drozd, Magnetocaloric effect in nano- and polycrystalline $La_{0.8}Sr_{0.2}MnO_3$ manganites, Journal of Non-Crystalline Solids, **354** 5308–5314 (2008)

[12]M. Pękała, V. Drozd, J.F. Fagnard, P. Vanderbemden and M. Ausloos, Magnetocaloric effect in nano- and polycrystalline manganite $La_{0.7}Ca_{0.3}MnO_3$. Appl. Phys. A, **90** 237–241 (2008)

[13] R. Bjørk, C. R. H. Bahl, A. Smith, N. Pryds, Review and comparison of magnet designs for magnetic refrigeration**,** In: International Journal of Refrigeration, 33 [3] 437-448 (2010)

[14] G. D. Dragutinovic, and B. S. Baclic, 1998, ***Operation of Counterflow Regenerators***,

Computational Mechanics Inc., Billerica, MA.

[15] K. Engelbrecht, 2008, PhD thesis, University of Wisconsin, Madison.

[16] Kays, W. M. and M. E. Crawford, 1980, ***Convective Heat and Mass Transfer***, McGraw-Hill, New York.

[17] S. Jeppesen, S. Linderoth, N. Pryds, L. T. Kuhn, and J. B. Jensen, Indirect measurement of the magnetocaloric effect using a novel differential scanning calorimeter with magnetic field, Review of Scientific Instruments, **79**, 083901 (2008)

Figure Caption

Figure 1. DSC scan of the powder at zero field after calcination at 1573K.

Figure 2. Rheological results of the three different ceramic blends (52, 54, 58 vol.-% LCSM). The experiment was done with a 1 mm die at 413 K. (a) pressure vs. piston speed and (b) shear rate vs. apparent shear viscosity (the lines are linear fits to the data points).

Figure 3. 52 vol.-% LCSM extruded honeycomb structure. The compound was extruded at 423 K with a piston speed of 5 mm/min.

Figure 4. The adiabatic temperature change (a) before and (b) after sintering. The top x-axis indicates the internal magnetic field of the sample.

Figure 5. The heat capacity measured for sintered and non sintered samples at zero and 1 T field.

Figure 6. Temperature span as a function of utilization as defined in Eq. (1) at a constant heat load of 0.4 W.

Figure 7. Temperature span as a function of utilization as defined in Eq. (1) at a constant heat load of 1.7 W.

Figure 8. Comparison between a parallel and monolithic regenerator. The temperature span for these two structures is plotted as a function of utilization

Tables

Table 1. Summary of the magnetocaloric measurements.

	Measurements of the adiabatic temperature			Measurements of the heat capacity		
Materials/properties	ΔT_{ad} (K)	T_c (K)	$\mu_0 H_{int}$ (T)	Peak C_p (J/kgK)	T_c (K)	$\mu_0 H_{int}$ (T)
LCSM – non-sintered	0.26	298	0.96	750.	292	0.94
LSCM – sintered	0.78	300	0.96	600	292	0.94

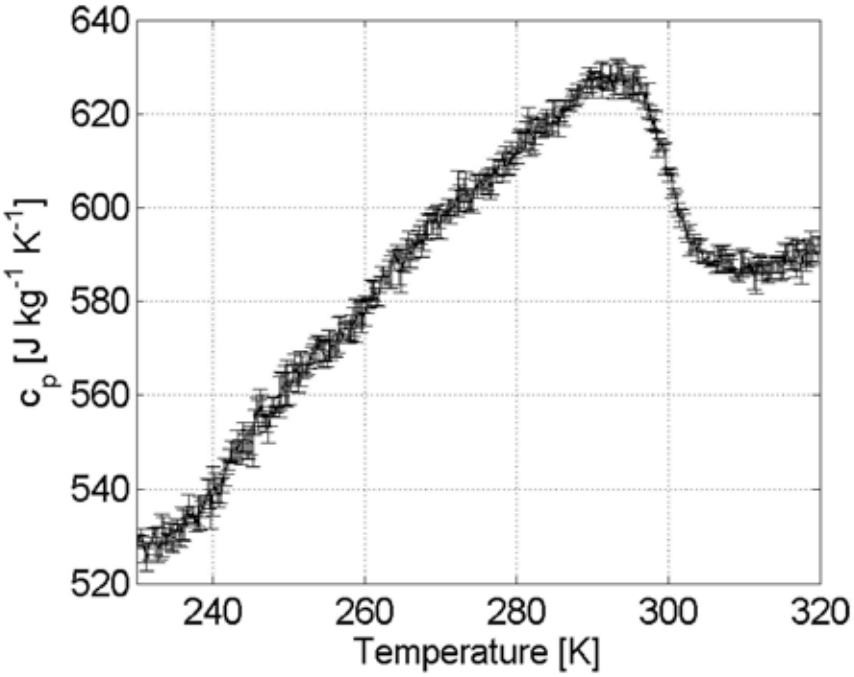

Figure 1. DSC scan of the powder at zero field after calcination at 1573K.

DSC scan of the powder at zero field after calcination at 1573K.
165x154mm (600 x 600 DPI)

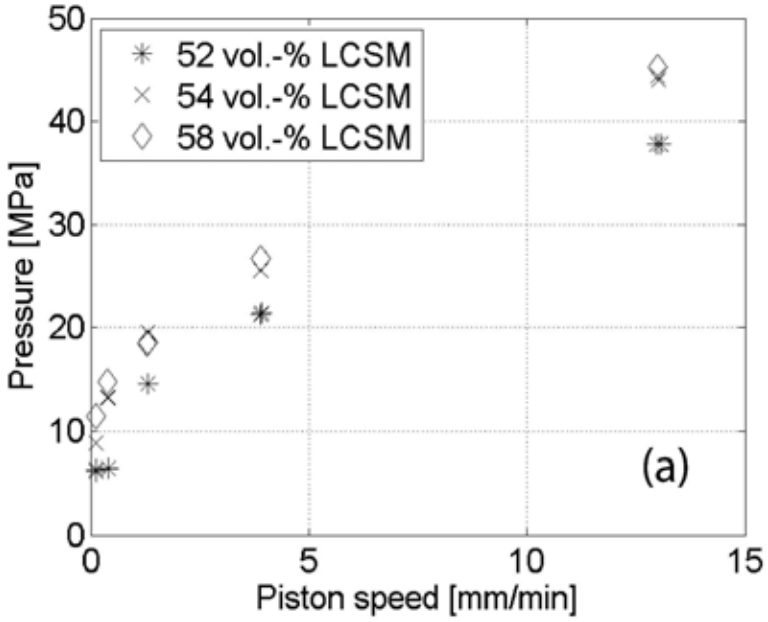

Figure 2a. Pressure vs. piston speed .

(a) pressure vs. piston speed
178x169mm (600 x 600 DPI)

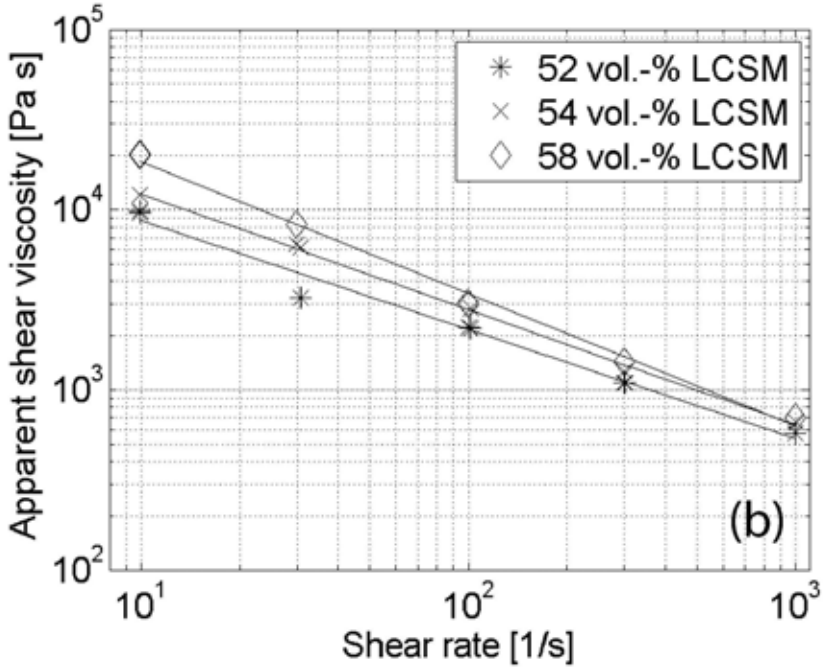

Figure 2b (b) shear rate vs. apparent shear viscosity (the lines are fits to the data points)

(b) shear rate vs. apparent shear viscosity (the lines are linear fits to the data points).
165x179mm (600 x 600 DPI)

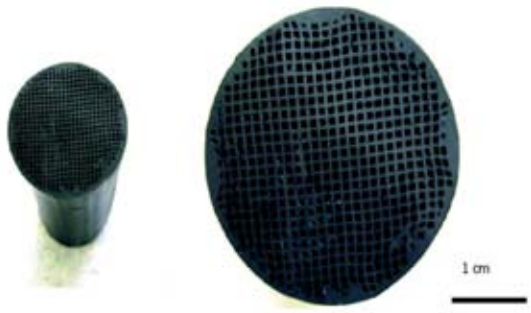

Figure 3. 52 vol.-% LCSM extruded honeycomb structure. The compound was extruded at 423 K with a piston speed of 5 mm/min.

52 vol.-% LCSM extruded honeycomb structure. The compound was extruded at 423 K with a piston speed of 5 mm/min.
283x233mm (600 x 600 DPI)

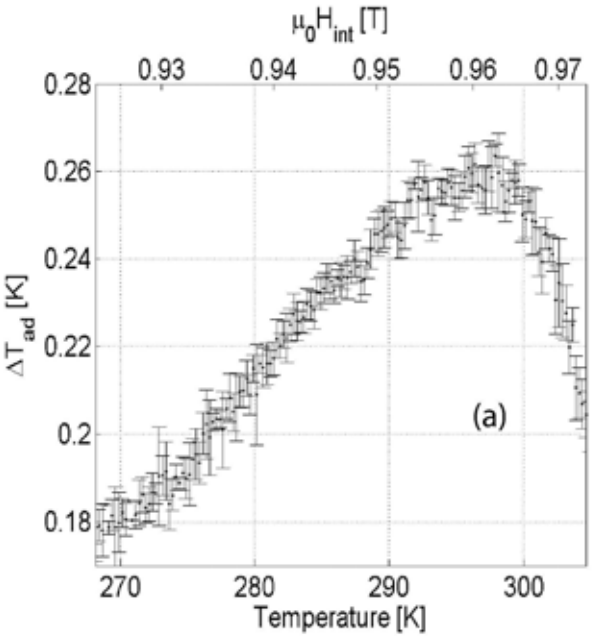

Figure 4. The adiabatic temperature change (a) before and (b) after sintering. The top x-axis indicates the internal magnetic field of the sample.

The adiabatic temperature change (a) before and (b) after sintering. The top x-axis indicates the internal magnetic field of the sample.
250x215mm (600 x 600 DPI)

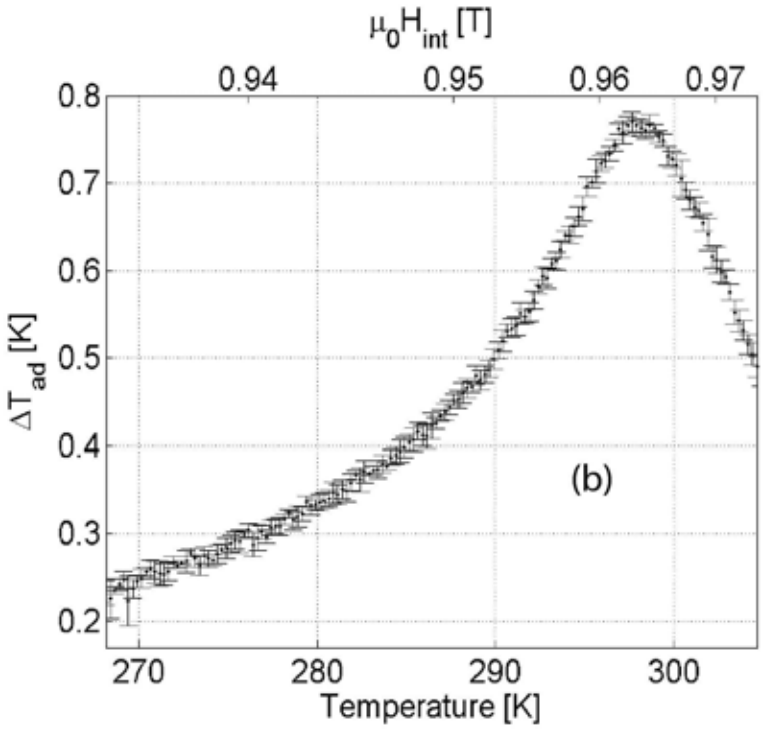

Figure 4. The adiabatic temperature change (a) before and (b) after sintering. The top x-axis indicates the internal magnetic field of the sample.

The adiabatic temperature change (a) before and (b) after sintering. The top x-axis indicates the internal magnetic field of the sample.
223x214mm (600 x 600 DPI)

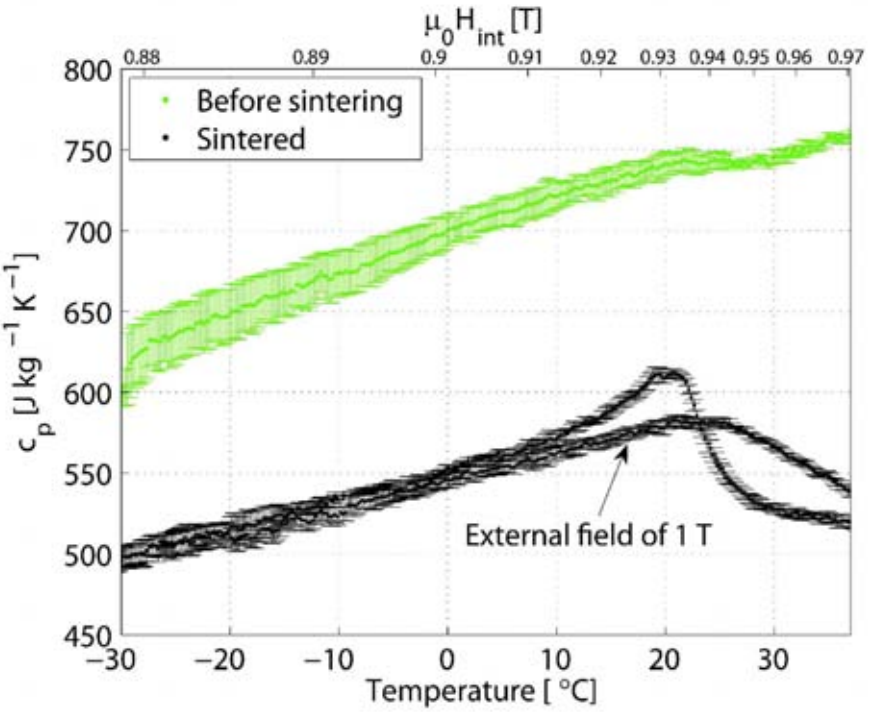

Figure 5. The heat capacity measured for sintered and non sintered samples at zero and 1 T field.

The heat capacity measured for sintered and non sintered samples at zero and 1 T field.
208x208mm (600 x 600 DPI)

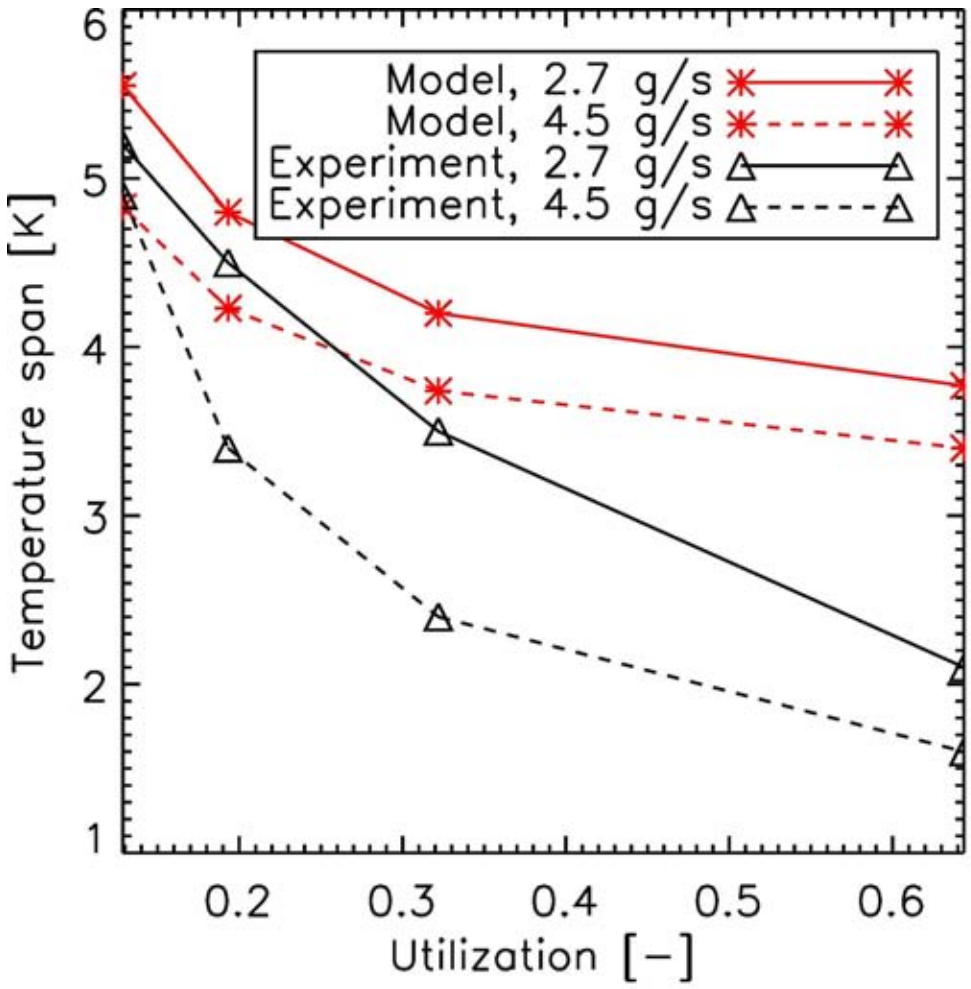

Figure 6 Temperature span as a function of utilization as defined in eq. (1) at a constant heat load of 0.4 W.

Temperature span as a function of utilization as defined in Eq. (1) at a constant heat load of 0.4 W.
169x198mm (600 x 600 DPI)

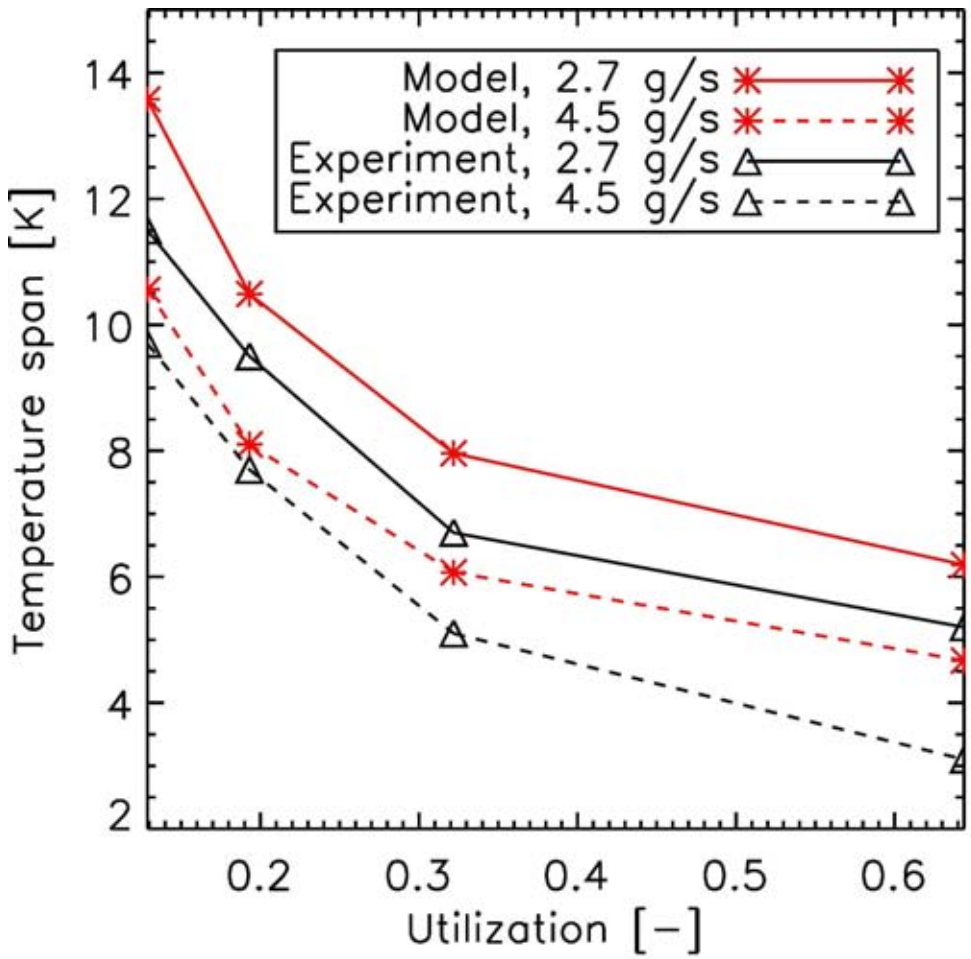

Figure 7 Temperature span as a function of utilization as defined in eq. (1) at a constant heat load of 1.7 W.

Temperature span as a function of utilization as defined in Eq. (1) at a constant heat load of 1.7 W.
174x209mm (600 x 600 DPI)

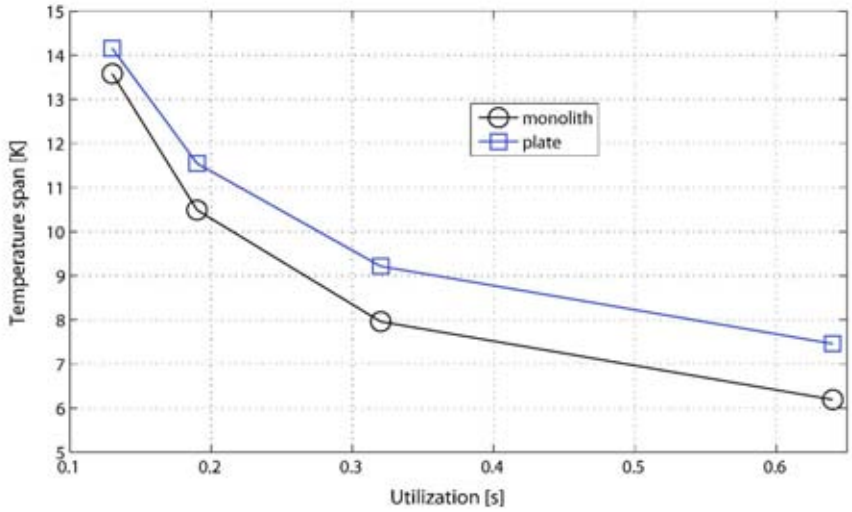

Figure 8 Comparison between a parallel and monolithic regenerator. The temperature span for these two structures is plotted as a function of utilization.

Comparison between a parallel and monolithic regenerator. The temperature span for these two structures is plotted as a function of utilization
239x181mm (600 x 600 DPI)

Bibliography

Aharoni, A., 1998. Demagnetizing factors for rectangular ferromagnetic prisms. Journal of Applied Physics 83 (6), 3432–3434.

Allab, F., Kedous-Lebouc, A., Fournier, J. M., Yonnet, J. P., 2005. Numerical modeling for active magnetic regenerative refrigeration. IEEE Transactions on Magnetics 41 (10), 3757–3759.

Appelt, S., Kühn, H., Häsing, F. W., Blümich, B., 2006. Chemical analysis by ultrahigh-resolution nuclear magnetic resonance in the earths magnetic field. Nature Physics 2, 105–109.

Ashcroft, N. W., Mermin, D., 1976. Solid State Physics. Saunders College.

Atallah, K., Howe, D., Mellor, P. H., 1997. Design and analysis of multi-pole halbach (self-shielding) cylinder brushless permanent magnet machines. Eighth International Conference on Electrical Machines and Drives (Conf. Publ. No.444), 376–380.

Bahl, C. R. H., Nielsen, K. K., 2009. The effect of demagnetization on the magnetocaloric properties of gadolinium. Journal of Applied Physics 105 (1), 013916.

Bahl, C. R. H., Petersen, T. F., Pryds, N., Smith, A., Petersen, T. F., 2008. A versatile magnetic refrigeration test device. Review of Scientific Instruments 79 (9), 093906.

Bahl, C. R. H., Smith, A., Pryds, N., Kuhn, L. T., Linderoth, S., 2009. A refrigeration device and a method of refrigerating. EU Patent WO2009024412.

Bakker Magnetics, 2008. NdFeB specs, www.bakkermagnetics.com.

Barclay, J. A., 1982. The theory of an active magnetic regenerativ refrigerator. NASA STI/Recon Technical Report N 83, 34087.

Bendixen, F. B., 2009. Private communication.

Bleaney, B., Bleaney, B., 1957. Electricity and Magnetism. Oxford Press.

Blumenfeld, P. E., Prenger, F. C., Sternberg, A., Zimm, C., 2002. Magnetic refrigerators - high temperature superconducting magnetic refrigeration. Advances in Cryogenic Engineering 47 (A), 1019.

Bohigas, X., Molins, E., Roig, A., Tejada, J., Zhang, X. X., 2000. Room-temperature magnetic refrigerator using permanent magnets. IEEE Transactions on Magnetics 36, 538–544.

Brown, G. V., 1976. Magnetic heat pumping near room temperature. Journal of Applied Physics 47 (8), 3673–3680.

Buchelnikov, V. D., Taskaev, S. V., Bychkov, I. V., Chernets, I. A., Denisovskiy, A. N., 2007. The prototype of effective device for magnetic refrigeration. Proceedings of the 2nd International Conference of Magnetic Refrigeration at Room Temperature, Portoroz, Slovenia, 371–376.

Burriel, Tocadoa, L., Palacios, E., Tohei, T., Wada, H., 2005. Square-shape magnetocaloric effect in Mn_3GaC. Journal of Magnetism and Magnetic Materials 290, 715718.

Chell, J., 2009. Private communication.

Chell, J., Zimm, C. B., 2006. Permanent magnet assembly. US Patent 7148777.

Chen, Y. G., Tang, Y. B., Wang, B. M., Xue, Q. X., Tu, M. J., 2007. A permanent magnet rotary magnetic refrigerator. Proceedings of the 2nd International Conference of Magnetic Refrigeration at Room Temperature, Portoroz, Slovenia, 309–313.

Coelho, A., Gama, S., Magnus, A., Carvalho, G., 2009. Prototype of a gd-based rotating magnetic refrigerator for work around room temperature. Proceedings of the 3rd International Conference on Magnetic Refrigeration at Room Temperature, Des Moines, Iowa, USA, 381–386.

Coey, J. M. D., Ni Mhiochain, T. R., 2003. High Magnetic Fields (Permanent magnets). World Scientific, Ch. 2, pp. 25–47.

Comsol Multiphysics, 2005. Comsol Multiphysics Model Library, third ed. COMSOL AB, Chalmers Teknikpark 412 88 G.

Comsol Multiphysics, A., 2008. Tegnergatan 23, SE-111 40 Stockholm, Sweden.

Dan'kov, S. Y., Tishin, A. M., Pecharsky, V. K., Gschneidner Jr, K. A., 1998. Magnetic phase transitions and the magnetothermal properties of gadolinium. Physical Review B (Condensed Matter) 57 (6), 3478–3490.

de Oliveira, N. A., 2008. Magnetocaloric effect under applied pressure and the barocaloric effect in the compounds RCo_2 (R = Er, Ho and Dy). Journal of Physics: Condensed Matter 20 (17), 175209.

D'Errico, J., 2006. Http://www.mathworks.com/matlabcentral/fileexchange/8277, Release: 4 (7/23/06).

Dupuis, C., Vialle, A. J., Legait, U., Kedous-Lebouc, A., Ronchetto, D., 2009. New investigations in magnetic refrigeration device, amr cycle and refrigerant bed performance evaluation. Proceedings of the 3rd International Conference on Magnetic Refrigeration at Room Temperature, Des Moines, Iowa, USA, 437–442.

Engelbrecht, K., 2008. A numerical model of an active magnetic regenerator refrigerator with experimental validation. Ph.D. thesis, University of Wisconsin Madison.

Engelbrecht, K., Jensen, J. B., Bahl, C. R. H., Pryds, N., 2009. Experiments on a modular magnetic refrigeration device. Proceedings of the 3rd International Conference on Magnetic Refrigeration at Room Temperature, Des Moines, Iowa, USA, 431–436.

Engelbrecht, K., Nellis, G., Klein, S., 2005a. A numerical model of an active magnetic regenerator refrigeration system. Tech. Rep. Tech. Rep. ARTI-21CR/61210075, University of Wisconsin-Madison.

Engelbrecht, K., Nellis, G., Klein, S., 2006. Predicting the performance of an active magnetic regenerator refrigerator used for space cooling and refrigeration. HVAC and R Research 12 (4), 1077–1095.

Engelbrecht, K., Nellis, G., Klein, S., Boeder, A., 2005b. Modeling active magnetic regenerative refrigeration systems. Proceedings of the 1st International Conference on Magnetic Refrigeration at Room Temperature, Montreux, Switzerland, 265–274.

Engelbrecht, K., Nellis, G., Klein, S., Zimm, C., 2007. Recent developments in room temperature active magnetic regenerative refrigeration. HVAC and R Research 13 (4), 525–542.

Gschneidner Jr, K. A., Pecharsky, V. K., 2008. Thirty years of near room temperature magnetic cooling: Where we are today and future prospects. International Journal of Refrigeration 31 (6), 945–961.

Gschneidner Jr, K. A., Pecharsky, V. K., Tsokol, A. O., 2005. Recent developments in magnetocaloric materials. Rep. Prog. Phys 68, 1479–1539.

Halbach, K., 1980. Design of permanent multipole magnets with oriented rare earth cobalt material. Nuclear instruments and methods 169.

Haznadar, Z., Stih, Z., 2000. Electromagnetic Fields, Waves and numerical methods. IOS Press.

Hu, J. C., Xiao, J. H., 1995. New method for analysis of active magnetic regenerator in magnetic refrigeration at room temperature. Cryogenics 35 (2), 101–104.

Jacobs, S., 2009. Modeling and optimal design of a multilayer active magnetic refrigeration system. Proceedings of the 3rd International Conference on Magnetic Refrigeration at Room Temperature, Des Moines, Iowa, USA, 267–274.

Jensen, J. H., Abele, M. G., 1996. Maximally efficient permanent magnet structures. Journal of Applied Physics 79 (2), 1157–1163.

Jeppesen, S., Linderoth, S., Pryds, N., Kuhn, L. T., Jensen, J. B., 2008. Indirect measurement of the magnetocaloric effect using a novel differential scanning calorimeter with magnetic field. Review of Scientific Instruments 79 (8), 083901.

Kim, Y., Jeong, S., 2009. Investigation on the room temperatre active magnetic regenerative refrigerator with permanet magnet array. Proceedings of the 3rd International Conference on Magnetic Refrigeration at Room Temperature, Des Moines, Iowa, USA, 393–400.

Lee, S. J., Kenkel, J. M., Pecharsky, V. K., Jiles, D. C., 2002. Permanent magnet array for the magnetic refrigerator. Journal of Applied Physics 91 (10), 8894–8896.

Lide, D. (Ed.), 2004. CRC Handbook of Chemistry and Physics. CRC Press.

Lim, J. K., Frigola, P., Travish, G., Rosenzweig, J. B., Anderson, S. G., Brown, W. J., Jacob, J. S., Robbins, C. L., Tremaine, A. M., 2005. Adjustable, short focal length permanent-magnet quadrupole based electron beam final focus system. Physical review special topics-accelerators and beams 8 (7), 072401.

Lu, D. W., Xu, X. N., Wu, H. B., Jin, X., 2005. A permanent magnet magneto-refrigerator study on using Gd/Gd-Si-Ge/ Gd-Si-Ge-Ga alloys. Proceedings of the 1st International Conference on Magnetic Refrigeration at Room Temperature, Montreux, Switzerland, 1–6.

Mallinson, J. C., 1973. One-sided fluxes - a magnetic curiosity? IEEE Transactions on magnetics 9 (4), 678 – 682.

Matlab, 2008. Version 7.7.0.471 (R2008b).

MMPA Standard, 2000. Standard specifications for permanent magnet materials, the International Magnetics Association, 8 South Michigan Avenue, Suite 1000, Chicago, Illinois 60603, www.intl-magnetics.org.

Morrish, A. H., 1965. The Physical Priciples of Magnetism. John Wiley & Sons, Inc.

Ni Mhiochain, T. R., Weaire, D., McMurry, S. M., D., C. J. M., 1999. Analysis of torque in nested magnetic cylinders. Journal of Applied Physics 86, 6412–6425.

Nielsen, K., Bahl, C., Smith, A., Pryds, N., Hattel, J., 2010. A comprehensive parameter study of an active magnetic regenerator using a 2d numerical model. International Journal of Refrigeration 33 (4), 753–764.

Nielsen, K. K., 2009. Private communication.

Nielsen, K. K., Bahl, C. R. H., Smith, A., Bjørk, R., Pryds, N., Hattel, J., 2009. Detailed numerical modeling of a linear parallel-plate active magnetic regenerator. International Journal of Refrigeration 32 (6), 1478–1486.

Nikly, G., Muller, C., 2007. Technical and economical criteria to design and realize a magnetocaloric heat pump. Proceedings of the 2nd International Conference of Magnetic Refrigeration at Room Temperature, Portoroz, Slovenia, 59–70.

Oesterreicher, H., Parker, F. T., 1984. Magnetic cooling near curie temperatures above 300k. Journal of Applied Physics 55, 4334–4338.

Okamura, T., 2009. Private communication.

Okamura, T., Rachi, R., Hirano, N., Nagaya, S., 2007. Improvement of 100w class room temperature magnetic refrigerator. Proceedings of the 2nd International Conference of Magnetic Refrigeration at Room Temperature, Portoroz, Slovenia, 377–382.

Okamura, T., Yamada, K., Hirano, N., S., N., 2005. Performance of a room-temperature rotary magnetic refrigerator. Proceedings of the 1st International Conference on Magnetic Refrigeration at Room Temperature, Montreux, Switzerland, 319–324.

Osborn, J. A., 1945. Demagnetizing factors of the general ellipsoid. Physical Review 67, 351–357.

Pecharsky, V. K., Gschneidner Jr, K. A., 2006. Advanced magnetocaloric materials: What does the future hold? International Journal of Refrigeration 29 (8), 1239–1249.

Peng, Q., McMurry, S. M., Coey, J. M. D., 2003. Cylindrical permanent-magnet structures using images in an iron shield. IEEE Transactions on Magnetics 39 (42), 1983–1989.

Petersen, T. F., Engelbrecht, K., Bahl, C. R. H., Pryds, N., Smith, A., Elmegaard, B., 2008a. Comparison between a 1d and a 2d numerical model of an active magnetic regenerative refrigerator. Journal of Physics D: Applied Physics 41 (10), 105002.

Petersen, T. F., Pryds, N., Smith, A., Hattel, J., Schmidt, H., Høgaard-Knudsen, H. J., 2008b. Two-dimensional mathematical model of a reciprocating room-temperature active magnetic regenerator. International Journal of Refrigeration 31 (3), 432–443.

Potenziani, E., Clarke, J. P., Leupold, H. A., 1987. The production of laminar fields with permanent magnets. Journal of Applied Physics 61, 3466–3467.

Richard, M. A., Rowe, A. M., Chahine, R., 2004. Magnetic refrigeration: Single and multimaterial active magnetic regenerator experiments. Journal of Applied Physics 95 (4), 2146–2150.

Rowe, A., 2009a. Performance metrics for active magnetic refrigerators. Proceedings of the 3rd International Conference on Magnetic Refrigeration at Room Temperature, Des Moines, Iowa, USA, 195–206.

Rowe, A., 2009b. Private communication.

Rowe, A., Dikeos, J., Tura, A., 2005. Experimental studies of near room-temperature magnetic refrigeration. Proceedings of the 1st International Conference on Magnetic Refrigeration at Room Temperature, Montreux, Switzerland, 325–333.

Rowe, A., Tura, A., 2006. Experimental investigation of a three-material layered active magnetic regenerator. International Journal of Refrigeration 29 (8), 1286–1293.

Russek, S. L., Zimm, C., 2006. Potential for cost effective magnetocaloric air conditioning systems. International Journal of Refrigeration 29 (8), 1366–1373.

Sari, O., Balli, M., Trottet, G., Bonhote, P., Egolf, P., Muller, C., Heitzler, J., Bour, S., 2009. Initial results of a test-bed magnetic refrigeration machine with practical running conditions. Proceedings of the 3rd International Conference on Magnetic Refrigeration at Room Temperature, Des Moines, Iowa, USA, 371–380.

Schenk, O., Gärtner, K., 2002. Two-level scheduling in pardiso: Improved scalability on shared memory multiprocessing systems. Parallel Computing 28.

Schenk, O., Gärtner, K., Fichtner, W., Stricker, A., 2001. Pardiso: A high-performance serial and parallel sparse linear solver in semiconductor device simulation. Journal of Future Generation Computers Systems 18, 69–78.

Shir, F., Bennett, L. H., Della Torre, E., Mavriplis, C., Shull, R. D., 2005a. Transient response in magnetocaloric regeneration. IEEE Transactions on Magnetics 41 (6), 2129–2133.

Shir, F., Mavriplis, C., Bennett, L. H., Torre, E. D., 2005b. Analysis of room temperature magnetic regenerative refrigeration. International Journal of Refrigeration 28 (4), 616–627.

Siddikov, B. M., Wade, B. A., Schultz, D. H., 2005. Numerical simulation of the active magnetic regenerator. Computers & Mathematics with Applications 49 (9-10), 1525–1538.

Tagliafico, L. A., Scarpa, F., Tagliafico, G., Valsuani, F., Canepa, F., Cirafici, S., Napoletano, M., Belfortini, C., 2009. Design and assembly of a linear reciprocating magnetic refrigerator. Proceedings of the 3rd International Conference on Magnetic Refrigeration at Room Temperature, Des Moines, Iowa, USA, 425–430.

Tishin, A. M., Spichkin, Y. I., 2003. The magnetocaloric Effect and its Applications. Institute of Physics Publishing, Temple Back, Bristol, UK.

Tura, A., Rowe, A., 2007. Design and testing of a permanent magnet magnetic refrigerator. Proceedings of the 2nd International Conference of Magnetic Refrigeration at Room Temperature, Portoroz, Slovenia, 363–370.

Tura, A., Rowe, A., 2009. Progress in the characterization and optimization of a permanent magnet magnetic refrigerator. Proceedings of the 3rd International Conference on Magnetic Refrigeration at Room Temperature, Des Moines, Iowa, USA, 387–392.

Tušek, J., Zupan, S., Sarlah, A., Prebil, I., A., P., 2009. Development of a rotary magnetic refrigerator. Proceedings of the 3rd International Conference on Magnetic Refrigeration at Room Temperature, Des Moines, Iowa, USA, 409–414.

Vacuumschmelze GMBH & Co, KG, 2007. PD 002 - Vacodym/Vacomax - Edition 2007, www.vacuumschmelze.de.

Vasile, C., Muller, C., 2006. Innovative design of a magnetocaloric system. International Journal of Refrigeration 29 (8), 1318–1326.

Vuarnoz, D., Kitanovski, A., Diebold, M., Gendre, F., Egolf, P. W., 2007. A magnetic heat pump with porous magneto caloric material. Physica Status Solidi (C) Current Topics in Solid State Physics 4 (12), 4552–4555.

Warburg, E., 1881. Magnetische untersuchungen. Ann.Phys.(Leipzig) 13, 141–164.

Xia, Z. P., Zhu, Z. Q., Howe, D., 2004. Analytical magnetic field analysis of halbach magnetized permanent-magnet machines. IEEE Transactions on Magnetics 40 (41), 1864–1872.

Xu, X. N., Lu, D. W., Yuan, G. Q., Han, Y. S., Jin, X., 2004. Studies of strong magnetic field produced by permanent magnet array for magnetic refrigeration. Journal of Applied Physics 95 (11), 6302–6307.

Zheng, Z. G., 2009. Private communication.

Zheng, Z. G., Yu, H. Y., Zhong, X. C., Liu, Z. W., Zeng, D. C., You, S. H., 2007. A practical model for performance analysis of a reciprocating room temperature magnetic regenerator. Proceedings of the 2nd International Conference of Magnetic Refrigeration at Room Temperature, Portoroz, Slovenia, 223–228.

Zheng, Z. G., Yu, H. Y., Zhong, X. C., Zeng, D. C., Liu, Z. W., 2009. Design and performance study of the active magnetic refrigerator for room-temperature application. International journal of refrigeration 32, 7886.

Zhu, Z., Howe, D., Bolte, E., Ackermann, B., 1993. Instantaneous magnetic field distribution in brushless permanent magnet dc motors. i. open-circuit field. IEEE Transactions on Magnetics 29 (12), 124–135.

Zimm, C., Auringer, J., Boeder, A., Chell, J., Russek, S., Sternberg, A., 2007. Design and initial performance of a magnetic refrigerator with a rotating permanent magnet. Proceedings of the 2nd International Conference of Magnetic Refrigeration at Room Temperature, Portoroz, Slovenia, 341–347.

Zimm, C., Boeder, A., Chell, J., Sternberg, A., Fujita, A., Fujieda, S., Fukamichi, K., 2006. Design and performance of a permanent-magnet rotary refrigerator. International Journal of Refrigeration 29 (8), 1302–1306.

Zimm, C., Jastrab, A., Pecharsky, V. K., Gschneidner Jr, K. A., Osborne, M., Anderson, I., 1998. Cryocoolers: Regenerative - description and performance of a near-room temperature magnetic refrigerator. Advances in Cryogenic Engineering 43 (B), 1759.

Zimmermann, G., 1993. Determination of magnetic anisotropy by transverse susceptibility measurement-an application to NdFeB. Journal of Applied Physics 73 (12), 8436–8440.

Risø DTU is the National Laboratory for Sustainable Energy. Our research focuses on development of energy technologies and systems with minimal effect on climate, and contributes to innovation, education and policy. Risø has large experimental facilities and interdisciplinary research environments, and includes the national centre for nuclear technologies.

Risø DTU
National Laboratory for Sustainable Energy
Technical University of Denmark

Frederiksborgvej 399
PO Box 49
DK-4000 Roskilde
Denmark
Phone +45 4677 4677
Fax +45 4677 5688

www.risoe.dtu.dk